TESIS DE LA UNIVERSIDAD DE ZARAGOZA

2019 138

Javier Sánchez Laínez

MOF-based Polymeric Membranes for CO2 Capture

Departamento

Ingeniería Química y Tecnologías del Medio Ambiente

Director/es

Zornoza Encabo, Beatriz
Coronas Ceresuela, Joaquín

ISSN 2254-7606

Prensas de la Universidad Universidad Zaragoza

ISSN 2254-7606

Universidad Zaragoza
1542

Tesis Doctoral

MOF-BASED POLYMERIC MEMBRANES FOR CO2 CAPTURE

Autor

Javier Sánchez Laínez

Director/es

Zornoza Encabo, Beatriz
Coronas Ceresuela, Joaquín

UNIVERSIDAD DE ZARAGOZA

Ingeniería Química y Tecnologías del Medio Ambiente

2019

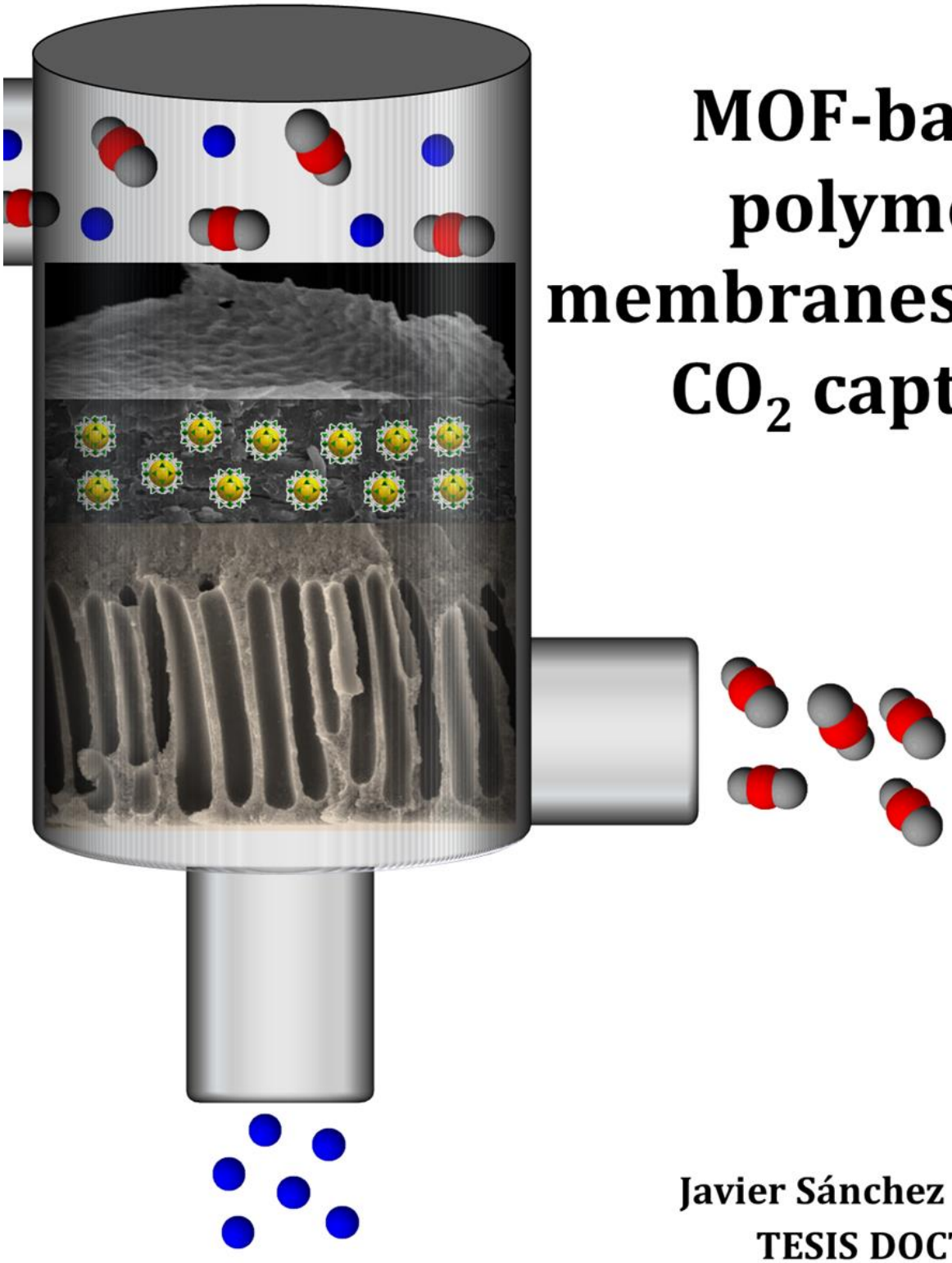

MOF-based polymeric membranes for CO_2 capture

Javier Sánchez Laínez

TESIS DOCTORAL

2019

ÁREA DE INGENIERÍA QUÍMICA,
DEPARTAMENTO DE INGENIERÍA QUÍMICA
Y TECNOLOGÍAS DEL MEDIO AMBIENTE

MOF-based Polymeric Membranes for CO_2 Capture

Memoria para optar al
grado de Doctor por la
Universidad de Zaragoza
presentada por

D. Javier Sánchez Laínez

Julio 2019

D. Joaquín Coronas Ceresuela, Catedrático de Universidad en el Departamento de Ingeniería Química y Tecnologías del Medio Ambiente de la Universidad de Zaragoza, y Dña. Beatriz Zornoza Encabo, Investigadora Posdoctoral, del Departamento de Energía y Medioambiente en el Instituto de Carboquímica de Aragón (ICB-CSIC),

CERTIFICAN

Que la presente memoria titulada:

MOF-based Polymeric Membranes for CO_2 Capture

Ha sido realizada bajo su dirección por **D. Javier Sánchez Laínez** en el Departamento de Ingeniería Química y Tecnologías del Medio Ambiente de la Universidad de Zaragoza, y autorizan su presentación como compendio de publicaciones para optar al grado de Doctor por la Universidad de Zaragoza.

Y para que así conste, firman el presente certificado en Zaragoza, a 20 de marzo de 2019.

Fdo.: Dr. Joaquín Coronas Ceresuela

Fdo.: Dr. Beatriz Zornoza Encabo

A Marina,
porque mi mayor descubrimiento eres tú.

A los que siguen presentes aun faltando,
y de su falta hacen su presencia especial.

"Erfolg hat drei Buchstaben: TUN!"
Johann Wolfgang von Goethe

Agradecimientos

A mis directores de tesis, Beatriz Zornoza y Joaquín Coronas, por su ayuda, consejo y enseñanzas.

A Carlos Téllez, por todas sus ideas y apoyo en las distintas reuniones.

A Adrián, Inés, Alberto y Enrique, porque no solo me han ayudado con mi investigación sino que también he aprendido mucho de ellos, y lo más importante, me han enseñado a enseñar.

A todos mis compañeros del CREG, tanto los que ya se han ido como con los que sigo compartiendo despacho, porque sin su ayuda esta tesis habría sido muy dura y por el maravilloso clima de trabajo que me brindan.

A los técnicos del LMA, por toda su ayuda y paciencia con las diferentes técnicas de caracterización.

A mis padres, por su apoyo durante el primer periodo de mi trayectoria profesional.

A mi mujer, por tener que sufrir mi pasión por mi trabajo.

A todos vosotros, ¡gracias de todo corazón!

La tesis doctoral, que se presenta con esta memoria titulada "**MOF-based Polymeric Membranes for CO_2 Capture**", se estructura como un compendio a partir de las siguientes publicaciones científicas, lo que se hace constar en cumplimiento del Reglamento sobre Tesis Doctorales de la Universidad de Zaragoza (artículo 20, apartado a), aprobado según el acuerdo de 20 de diciembre de 2013 del Consejo de Gobierno de la Universidad:

1. J. Sánchez-Laínez, B. Zornoza, Á. Mayoral, Á. Berenguer-Murcia, D. Cazorla-Amorós, C. Téllez, J. Coronas. **Beyond the H_2/CO_2 upper bound: one-step crystallization and separation of nano-sized ZIF-11 by centrifugation and its application in mixed matrix membranes**. Journal of Materials Chemistry A, 3 (2015) 6549-6556.
2. J. Sánchez-Laínez, B. Zornoza, S. Friebe, J. Caro, S. Cao, A. Sabetghadam, B. Seoane, J. Gascon, F. Kapteijn, C. L. Guillouzer, G. Clet, M. Daturi, C. Tellez, J. Coronas. **Influence of ZIF-8 particle size in the performance of polybenzimidazole mixed matrix membranes for pre-combustion CO_2 capture and its validation through interlaboratory test**. Journal of Membrane Science, 515 (2016) 45-53.
3. J. Sánchez-Laínez, B. Zornoza, C. Téllez, and J. Coronas. **On the chemical filler–polymer interaction of nano-and micro-sized ZIF-11 in PBI mixed matrix membranes and their application for H_2/CO_2 separation**. Journal of Materials Chemistry A, 4 (2016), 14334-14341.
4. J. Sánchez-Laínez, A. Veiga, B. Zornoza, S.R. Balestra, S. Hamad, A.R. Ruiz-Salvador, S. Calero, C. Téllez, J. Coronas. **Tuning the separation properties of zeolitic imidazolate framework core–shell structures via post-synthetic modification**. Journal of Materials Chemistry A, 5 (2017), 25601-25608.
5. J. Sánchez-Laínez, B. Zornoza, A. F. Orsi, M. M. Łozińska, D. M. Dawson, S. E. Ashbrook, S. M. Francis, P. A. Wright, V. Benoit, P. L. Llewellyn, C. Téllez, J. Coronas. **Synthesis of ZIF-93/11 hybrid nanoparticles *via* post-synthetic modification of ZIF-93 and their use for H_2/CO_2 separation**. Chemistry–A European Journal, 24, (2018), 11211–11219.
6. J. Sánchez-Laínez, B. Zornoza, C. Téllez, J. Coronas. **Asymmetric polybenzimidazole membranes with thin selective skin layer containing ZIF-8 for H_2/CO_2 separation at pre-combustion capture conditions**. Journal of Membrane Science, 563 (2018), 427-434.
7. J. Sánchez-Laínez, B. Zornoza, M. Carta, R. Malpass-Evans, N. B. McKeown, C. Téllez, J. Coronas. **Hydrogen separation at high temperature with dense and asymmetric membranes based on PIM-EA(H2)-TB/PBI blends**. Industrial and Engineering Chemistry Research, 57 (2018) 16909–16916.
8. J. Sánchez-Laínez, L. Paseta, M. Navarro, B. Zornoza, C. Téllez, and J. Coronas. **Ultrapermeable Thin Film ZIF-8/Polyamide Membrane for**

H_2/CO_2Separation at High Temperature without Using Sweep Gas. Advanced Materials Interfaces, 2018, 1800647.

9. J. Sánchez-Laínez, S. Friebe, B. Zornoza, A. Mundstock, I. Strauß, C. Téllez, J. Coronas. **Polymer-Stabilized Percolation Membranes based on nano-sized zeolitic imidazolate frameworks for H_2/CO_2 Separation.** ChemNanoMat, 4 (2018), 698-703.
10. J. Sánchez-Laínez, I. Gracia-Guillén, B. Zornoza, C. Téllez, J. Coronas. **Thin supported MOF based mixed matrix membranes of Pebax® 1657 for biogas upgrade**. New Journal of Chemistry, 43 (2019), 312-319.

Además, el doctorando ha participado activamente en lo relativo a las correspondientes medidas de separación de gases en las siguientes publicaciones, de las que es coautor:

1. A. Perea-Cachero, J. Sánchez-Laínez, Á. Berenguer-Murcia, D. Cazorla-Amorós, C. Téllez, J. Coronas. **A new zeolitic hydroxymethylimidazolate material and its use in mixed matrix membranes based on 6FDA-DAM for gas separation.** Journal of Membrane Science, 544 (2017), 88-97.
2. J. Benito, J. Sánchez-Laínez, B. Zornoza, S. Martín, M. Carta, R. Malpass-Evans, C. Téllez, N. B McKeown, J. Coronas, I. Gascón. **Ultrathin Composite Polymeric Membranes for CO_2/N_2 Separation with Minimum Thickness and High CO_2 Permeance.** ChemSusChem, 10 (2017), 4014-4017.
3. A. Perea-Cachero, J. Sánchez-Laínez, B. Zornoza, E. Romero, C. Téllez, J. Coronas. **Nanosheets of MIL-53 (Al) applied in membranes with improved CO_2/N_2 and CO_2/CH_4 selectivities.** Dalton Transactions, 48 (2019), 3392-3403.
4. J. Benito, J. Vidal, J. Sánchez-Laínez, B. Zornoza, C. Téllez, S. Martín, K. J Msayib, B. Comesaña-Gándara, N. B McKeown, J. Coronas, I. Gascón. **The fabrication of ultrathin films and their gas separation performance from polymers of intrinsic microporosity with two-dimensional (2D) and three-dimensional (3D) chain conformations.** Journal of Colloid and Interface Science, 536 (2019), 474-482.

Finalmente, esta tesis doctoral también opta a la mención de doctorado internacional, por lo que el resumen, las conclusiones y parte de la memoria vienen escritos en inglés para cumplir con la normativa descrita en el artículo 18 del Capítulo II del Título IV del Acuerdo de 20/12/2013 del Consejo de Gobierno de la Universidad de Zaragoza relativo al Reglamento sobre Tesis Doctorales.

Marco de la tesis doctoral

La presente tesis doctoral se ha realizado en el Grupo CREG (Grupo de Investigación en Catálisis, Separaciones Moleculares e Ingeniería de Reactores), que forma parte del Departamento de Ingeniería Química y Tecnologías del Medio Ambiente (IQTMA) de la Universidad de Zaragoza. El grupo se encuentra adscrito al Instituto Universitario de Nanociencia de Aragón (INA) (incluido desde mediados de 2018 en el Instituto de Ciencia de Materiales de Aragón (ICMA, CSIC)) y está reconocido por el Gobierno de Aragón como grupo de investigación de excelencia (T43-17R) desde 2004.

Académicamente, esta tesis se enmarca dentro del programa de doctorado de "Ingeniería Química y del Medio Ambiente" del mencionado departamento, y ha sido financiada mediante el programa de ayudas para contratos predoctorales para la Formación de Profesorado Universitario del Ministerio de Educación (FPU 2014) y por los siguientes proyectos, a los que se agradece su financiación:

- "Grupo de Investigación en Catálisis, Separaciones Moleculares e Ingeniería de Reactores (CREG)" (286261/1, 2 y 3, grupo consolidado T43-17R de excelencia del Gobierno de Aragón, 01/01/2014 - 31/12/2018).

- "Innovaciones en MOFs para aplicaciones energética y medioambientalmente eficientes: nanofiltración y catálisis en biorefinerías" (MAT2013-40556-R, Ministerio de Economía y Competitividad, Gobierno de España, periodo 2014-2016).

- "Energy Efficient MOF-based Mixed Matrix Membranes for CO_2 Capture (M^4CO_2)" *(European Union Seventh Framework Programme (FP7/2007-2013) under grant agreement n° 608490*, periodo 2014-2017).

- "Avances en membranas de fibra hueca basadas en MOFs y grafeno enfocadas a procesos eficientes" (MAT2016-77290-R, Ministerio de Economía y Competitividad, Gobierno de España, desde 2017).

Índice de contenido

General introduction: summary, objectives and thesis structure

The present thesis book is structured in 15 chapters that can be divided into two main blocks: memory and results. The memory is formed by chapters 1, 2 and 3. Chapter 1 contains a general introduction where the CO_2 separation processes are described and the role of the membrane technology is explained. The concept of membrane is fully developed, from their different types, the fabrication processes and the gas transport mechanisms. The different polymers used in this work are explained and also the metal-organic frameworks (MOFs) that will be used as fillers, everything reinforced with an updated bibliography about gas separation results. Chapter 2 refers to the methodology, including the synthesis of MOFs, the preparation of membranes and the characterization and measurements performed. Finally, chapter 3 contains the list of references. The second block refers to the results and discussion. It comprises chapters 4 to 14 and corresponds to the journal publications previously listed, whose thematic unity will be explained throughout this summary. The last section (chapter 15) details the main conclusions of the whole work. A glossary with technical terms is also included at the end of the book to facilitate the reading.

Carbon dioxide (CO_2) is one of the most important pollutants at industrial level. Due to the augment in the emissions of this greenhouse gas into the atmosphere and to its contribution to the global warming, decreasing the atmospheric CO_2 concentration has currently become one the most challenging environmental issues. Besides, CO_2 appears as an important contaminant in fuels such as natural gas or biogas, being necessary its removal to obtain a clean fuel that can meet the legal specifications. Although chemical absorption, physical absorption or cryogenic distillation are available technologies for CO_2 separation, the energetic costs of these processes are really high. Gas separation by membrane technology can mean an alternative owing to its low energy consumption, its small carbon footprint and its easy operation and scale-up.

Hence, the main objective of this thesis is the development of improved membranes for CO_2 separation. The research has primarily focused on the H_2/CO_2 separation for pre-combustion CO_2 capture, but also membranes suitable for processes of post-

combustion capture (i.e. CO_2/N_2 separation) as well as for natural gas and biogas upgrading (CO_2/CH_4 mixtures) have been studied. These membranes have been prepared from existing polymers with good gas separation properties for the corresponding mixture. The polyimide Matrimid®, polybenzimidazole (PBI) and the polyamide (PA) formed by the reaction of trimesoyl chloride (TMC) with m-phenylenediamine (MPD) have been the polymers chosen for pre-combustion CO_2 capture, while the post-combustion separation and biogas purification has been tackled with the polymers of intrinsic microporosity (PIMs) PIM-1 and PIM-EA(H_2)-TB, the polyimide 6FDA-DAM and the block copolymer Pebax® 1657.

Although the gas separation performance of bare polymeric membranes is limited to the intrinsic separation capacity of the polymer itself, new composites can be prepared to obtain enhanced membranes with superior properties. On the whole, the main approach followed in this research to improve the gas separation properties of the pristine polymeric membranes has been building multicomponent systems, consisting in the mixture of the above mentioned polymers with other phases. The most common way of building these composites has been through the preparation of mixed matrix membranes (MMMs). MMMs consist of the dispersion of inorganic/metal-organic fillers within a polymeric matrix so that the permeability and selectivity of the membranes can be improved through the synergistic combination of the two components. Metal-organic frameworks (MOFs) have been used as disperse phase in this work. They are highly porous crystalline materials formed by the coordination of metal ions or clusters with organic linkers. Due to the presence of these organic linkers in their structure, MOFs have a better affinity for the polymeric chains than inorganic fillers, making the MOF-polymer interface interactions easier to control in order to avoid non-selective voids.

In chapter 4 the use of membranes of Matrimid® for H_2/CO_2 separation is explained, where ZIF-11 is used as filler to develop MMMs. Nevertheless, PBI has been the most used polymer in this thesis for pre-combustion CO_2 capture. The preparation of PBI MMMs with ZIF-8 as filler is explained in chapter 5, where the influence of the particle size, as well as its incorporation as wet and dry filler, are discussed. Besides, the reproducibility of the membranes has been confirmed by a European interlaboratory Round Robin test involving three different institutions. ZIF-11 has also

been used as filler to improve the gas separation properties of PBI, which can be seen in chapter 6.

Although existing MOFs have been used for the preparation of MMMs, a big effort to develop new structures with better compatibility with the polymers has been also made in this thesis. In chapter 4 the synthesis of nano-sized ZIF-11 with an average size of 36±6 nm is explained. This material has been obtained following a new synthesis route based on a centrifugation process, which allowed the formation of much smaller particles than those of the conventional microcrystalline ZIF-11 (i.e. 1.9±0.9 μm) but maintaining the same chemical composition and thermal stability properties and analogous H_2 and CO_2 adsorption properties. The use of this material as filler with Matrimid® as polymer is explained in chapter 4. Its use as filler in MMMs is also explained in chapter 6, where the evolution of nano- and micro-sized ZIF-11 when embedded into a PBI polymeric matrix is studied.

The effort for obtaining new MOFs has also focused on the synthesis of hybrid materials. Chapter 7 explains the formation of ZIF-7/8 hybrid core-shell frameworks *via* the post-synthetic modification of ZIF-8 with benzimidazole. This reaction has led to the full conversion of ZIF-8 into ZIF-7 and it has been monitored quantifying the liberated 2-methylimidazole by gas chromatography coupled with mass spectroscopy. This has allowed adjusting the reaction kinetics to the shrinking core model, providing the diffusion coefficient of benzimidazole inside the pores and the reaction kinetic constant. ZIF-93/11 hybrid nanoparticles have also been developed in chapter 8. The hybrid ZIF was also obtained *via* post-synthetic modification, in this case of ZIF-93, in a benzimidazole solution. Conversely to the case of ZIF-7/8 hybrid, the reaction was not complete. The use of different solvents (MeOH and DMAc) and reaction times led to differences in the quantity of benzimidazole incorporated to the framework, from 7.4 to 23%. Both hybrids, ZIF-7/8 and ZIF-93/11, have been used as fillers with PBI MMMs and the gas separation performance of these membranes for the separation of H_2/CO_2 mixtures is compared to those prepared with the pure MOFs (i.e. ZIF-7, ZIF-8, ZIF-11 and ZIF-93) in the corresponding chapters.

The gas separation performance of the polymers has not only been enhanced by the addition of filler nanoparticles. A big effort has been made to reduce the thickness

of the membranes in favor to higher gas fluxes. Following this idea, PBI membranes have been obtained in an asymmetric configuration on P84® supports in chapter 9, representing a new way of preparing flat PBI membranes. These membranes have been prepared with the phase inversion method, resulting in membranes with a 1 μm selective skin layer that show an unprecedented gas separation capacity for pre-combustion CO_2 capture, much superior to dense membranes, under harsh operating conditions (250 °C and 6 bar feed). PBI membranes have also been optimized by blending this polymer with PIM-EA(H_2)-TB in chapter 10. The mixture of both polymers forms a homogeneous blend that improves the gas permeances of the corresponding asymmetric PBI membranes.

The thinnest membranes obtained in this thesis have been the thin-film nanocomposites developed in chapter 11. They consist of 50-100 nm thick polyamide flat membranes supported on P84®, obtained by the interfacial polymerization of MPD and TMC and containing ZIF-8 nanoparticles. The membranes show outstanding separation values with such high gas fluxes that the can be measured without sweep gas. They also show a high thermal stability, with a stable performance at 180 ^{0}C for at least seven days.

The validity of ZIF-7, ZIF-8 and the developed ZIF-7/8 core-shells for H_2/CO_2 separation has also been checked in chapter 12 by the preparation of Polymer-Stabilized Percolation Membranes (PSPM). This work, achieved during a research stay of three months in the University of Hannover (*Leibniz Universität Hannover,* Germany), consists in the compression of pellets of these ZIF nanoparticles (up to 74 wt% loading) and their stabilization with gas-impermeable epoxy resin, providing a gas transport-selective percolation network where only the ZIF is responsible for the gas separation.

Finally, membranes for post-combustion CO_2 capture and biogas upgrading are developed in chapters 13 and 14. Chapter 13 shows the preparation of MMMs for CO_2/N_2 and CO_2/CH_4 separation from PIM-1/6FDA-DAM heterogeneous blends with ZIF-8 as filler. The filler nanoparticles show better compatibility with 6FDA-DAM than with PIM-1, as they preferentially locate near the interphase between the polymers, helping to the filler dispersion. Chapter 14 explains the preparation of thin

MMMs with 2-3 μm thickness of Pebax® 1657 on P84® and polytrimethylsilylpropyne (PTMSP). Nanoparticles of the MOFs: ZIF-8, MIL-101(Cr), UiO-66 and ZIF-7/8 core-shells have been selected as fillers since all of them are MOFs with high CO_2 adsorption capacity but different pore size distribution. These membranes have been applied for the separation CO_2/CH_4 mixtures where a synergistic compatibility between Pebax® 1657 and P84® is noticed.

In addition to all the empirical work, several mathematical models have also been developed in this thesis to understand the gas flux though the prepared membranes. In chapter 6, the Maxwell-Wagner-Sillar model has been used to calculate the H_2 and CO_2 permeabilities of nZIF-11 and ZIF-11. In chapter 9 a resistance in series model is provided to understand the flux through the structure of the asymmetric PBI membranes. Chapter 10 shows an empirical model where the influence of the amount of PIM and the feed pressure in the gas separation performance of PIM-EA(H_2)-TB/PBI blends is correlated. Finally, to calculate the permeability though the MMMs with PIM-1/6FDA-DAM blends, a coupled Maxwell model has been proposed in chapter 13. This model has also calculated the gas separation properties of ZIF-8. **Table 1** shows a summary of the thesis structure.

Table 1. Structure and organization of the thesis.

Chapter	Section	Reference	Description
Chapter 1	Introduction	-	CO_2 separation proceses, membrane technology, MOFs and polymeric materials.
Chapter 2	Methodology	-	Synthesis of MOFs, membrane preparation, gas separation analysis and characterization techniques.
Chapter 3	Bibliography	-	-
Chapter 4	Results	*J. Mater. Chem. A, 3 (2015) 6549-6556*	Synthesis of nZIF-11 and its use as filler in Matrimid® MMMs applied for H_2/CO_2 separation.
Chapter 5	Results	*J. Membr. Sci., 515 (2016) 45-53*	MMMs of PBI with ZIF-8 of different sizes. H_2/CO_2 separation results validated by a Round Robin test.
Chapter 6	Results	*J. Mater. Chem. A, 4 (2016), 14334-14341*	nZIF-11 and ZIF-11 as fillers in PBI MMMs for H_2/CO_2 separation.
Chapter 7	Results	*J. Mater. Chem. A, 5 (2017), 25601-25608*	Synthesis of ZIF-7/8 core-shells and its use as fillers in PBI MMMs applied for H_2/CO_2 separation.
Chapter 8	Results	*Chem.–A Eur. J., 24 (2018), 11211–11219*	Synthesis of ZIF-93/11 hybrid and its use as fillers for PBI MMMs applied for H_2/CO_2 separation.
Chapter 9	Results	*J. Membr. Sci., 563 (2018), 427-434*	Preparation of integrally skinned asymmetric membranes of PBI containing ZIF-8 and its application for H_2/CO_2 separation.
Chapter 10	Results	*Ind. Eng. Chem. Res., 57 (2018) 16909–16916*	Blends of PBI with PIM-EA(H_2)-TB as dense and asymmetric membrane applied for H_2/CO_2 separation.
Chapter 11	Results	*Adv. Mater. Interfaces, (2018), 1800647*	Thin-film nanocomposites of polyamide with ZIF-8 for H_2/CO_2 separation.
Chapter 12	Results	*ChemNanoMat, 4 (2018), 698-703*	Polymer-Stabilized Percolation Membranes prepared with ZIF-7(III), ZIF-8 and ZIF-7/8 for H_2/CO_2 separation.
Chapter 13	Results	-	Heterogenous blends of PIM-1 and 6FDA-DAM containing ZIF-8 for the separation of CO_2/N_2 and CO_2/CH_4 mixtures.
Chapter 14	Results	*New J. Chem, 43 (2019), 312-319*	Thin MMMs of Pebax® 1657 containing ZIF-8, MIL-101(Cr), UiO-66 and ZIF-7/8 for CO_2/CH_4 separation.
Chapter 15	Conclusions	-	-

CAPÍTULO 1

INTRODUCCIÓN

1.1. Procesos de Separación de CO_2

El dióxido de carbono (CO_2) es un gas incoloro, inodoro y que no resulta tóxico. Sin embargo, a nivel industrial es considerado uno de los principales gases contaminantes por dos motivos diferentes, uno energético y otro medioambiental. Por un lado, hace que disminuya el poder calorífico de mezclas de combustibles gaseosos en las que está presente, resultando imprescindible su separación para obtener una mayor eficiencia energética. Por otro lado, al tratarse de un gas de efecto invernadero contribuye al calentamiento global y con ello al cambio climático, siendo necesaria su captura en aquellos procesos en los que el CO_2 es emitido a la atmósfera. A continuación, se estudiará este gas como contaminante, describiendo los procesos industriales en los que aparece y las condiciones en la que debe darse su separación.

1.1.1. El CO_2 como contaminante atmosférico en la generación de energía

A pesar de que el CO_2 es uno de los gases minoritarios de la atmósfera, diferentes investigaciones han demostrado que contribuye de manera clara al efecto invernadero. Aunque no es el gas con el mayor efecto, puesto que el metano o el vapor de agua muestran capacidades de absorción de radiación superiores, sus emisiones a la atmósfera son mucho mayores que las de estos otros. De hecho, el aumento creciente de su concentración en la atmósfera desde la Primera Revolución Industrial es una de las preocupaciones medioambientales actuales más importantes.

La amenaza del cambio climático ha provocado un movimiento político a nivel mundial. La Unión Europea, a través del SET-Plan y del CCS Technology Roadmap 2050, ya acordó en 2011 apoyar el desarrollo de tecnologías de captura y almacenamiento que fueran competitivas a partir de 2020.[1] Un objetivo ambicioso con el que se pretende reducir entre un 80-95% las emisiones de CO_2 comparadas con las de 1990. Además, el protocolo de Kioto fue actualizado en 2015 por la reunión del clima de París (COP 21), donde se fijó el objetivo de mantener el aumento de la temperatura media del planeta por debajo de 2 °C con respecto a los niveles preindustriales. Este acuerdo fue ratificado durante la cumbre del clima COP 24 de diciembre de 2018 en Katowice (Polonia). Las tecnologías de captura y almacenamiento de CO_2 (CAC) juegan un papel esencial en el sector de la generación de electricidad y en otras industrias donde se generan grandes cantidades de CO_2,

como las relativas al cemento y al acero, para hacer de este objetivo una realidad. Estas tecnologías constan de tres etapas: separación, transporte y almacenamiento geológico del CO_2; y se clasifican en tres grupos en función de la etapa del proceso de la combustión en el que actúe la separación (**Figura 1.1**):[2]

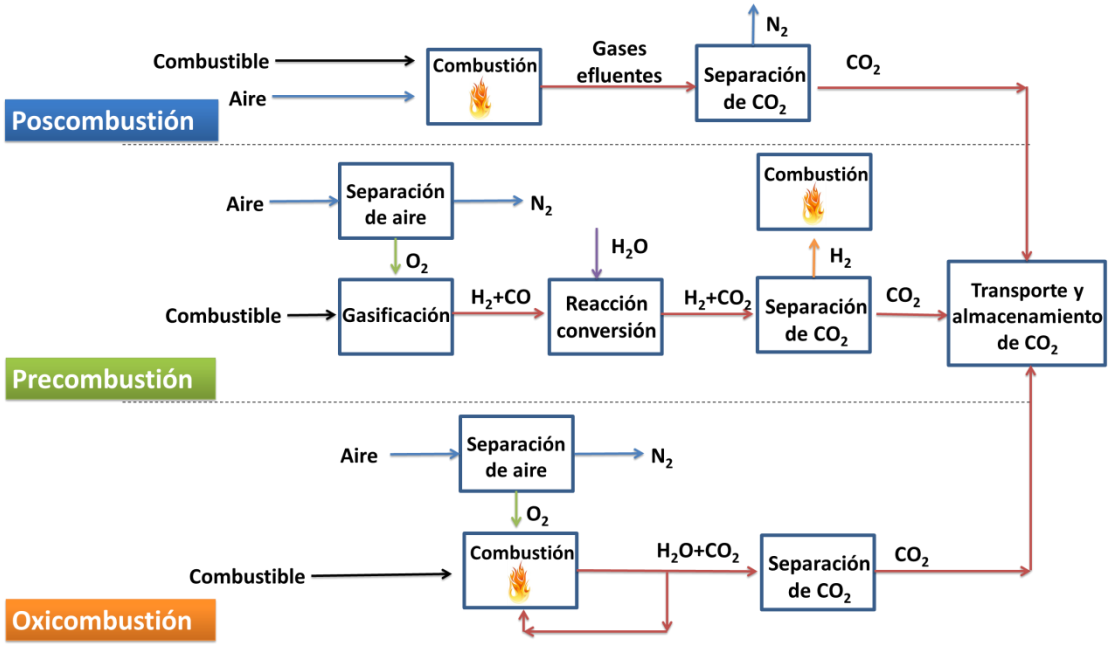

Figura 1.1. Representación esquemática de las tecnologías de captura de CO_2.

- Poscombustión: se basa en incorporar una etapa de captura posterior a la combustión y básicamente consiste en la separación de una mezcla CO_2/N_2. Los gases de escape que contienen el CO_2 pasan por una torre de absorción, donde dicho gas reacciona de manera selectiva con un absorbente haciendo que se absorba químicamente y separándose del resto. Existen varios tipos de disolventes de CO_2 que pueden actuar como absorbentes: carbonato potásico, hidróxido de sodio, amoniaco, entre otros. Pero los más difundidos son los geles de aminas (una mezcla de aminas primarias y secundarias con agua). La ventaja de esta tecnología es que es fácil de incorporar a centrales energéticas ya existentes, ya que es la que exige menos modificaciones en la planta. Sin embrago, el CO_2 queda muy diluido en los gases de salida (3-20 %) y sale a baja presión (1 bar), lo que dificulta su captura.[3] Además hay impurezas de SO_x y NO_x que hay que tener en cuenta.

- Precombustión: Este tipo de captura implica la separación de mezclas H_2/CO_2 a elevada presión y temperatura (15-20 bar y 190-210 °C, respectivamente) y donde el H_2 tiene una alta concentración (~45 vol %).[4] El combustible se somete a un proceso de gasificación en el que se convierte en gas de síntesis, es decir, una mezcla de monóxido de carbono e hidrógeno. El monóxido de carbono se oxida posteriormente con vapor de agua mediante una reacción de intercambio a dióxido de carbono y se separa del hidrógeno, el cual se usa como combustible en el proceso de combustión. El resultado es un gas de salida libre de CO_2, ya que la combustión de hidrógeno solo produce vapor de agua. A este proceso global se lo denomina *ciclo combinado con gasificación integrada (IGCC)*. Aunque la captura en precombustión es más eficiente que poscombustión, las condiciones de operación extremas hacen que el proceso sea más complicado. Además, existe una penalización energética debido a los equipos necesarios para la gasificación del combustible.[5]

- Oxicombustión: Esta tecnología se caracteriza porque se alimenta oxígeno puro al reactor, en lugar de aire, junto con el combustible. Realmente el proceso no implica la separación de CO_2 en ningún momento, ya que la mezcla a separar es O_2/N_2. Debido al alto poder oxidante del oxígeno, se recircula parte del CO_2 de los gases de escape al reactor para diluir el oxígeno entrante. El problema de esta tecnología es el coste añadido que conlleva fraccionar el aire para obtener el oxígeno puro necesario.[6]

1.1.2. El CO_2 como contaminante en biogás y gas natural

Tanto el biogás como el gas natural son mezclas con un alto interés energético por su alto contenido en CH_4, un combustible muy útil en la generación de electricidad y de calor. El gas natural constituye una importante fuente de energía fósil. Consiste en una mezcla de hidrocarburos gaseosos ligeros que se extrae de yacimientos independientes, de yacimientos petrolíferos o de minas de carbón. Su composición varía en función del yacimiento, pero consta por lo general de un 70-80% de CH_4, junto con otros gases como CO_2, etano, propano, butano, He, N_2, impurezas y trazas de hidrocarburos más pesados. Al igual que con otros combustibles fósiles, el gas natural se debe purificar antes de su uso, una tarea cada vez más difícil por el agotamiento de

los pozos. La **Tabla 1.1** muestra la composición más común en los pozos, y la que es necesaria alcanzar para su comercialización.

Tabla 1.1. Composición del gas natural.[7]

Componenete	Composición en pozo	Composición comercial
CH_4	70-80 %	90 %
CO_2	5-20 %	2 %
C_2H_6	3-4 %	3-4 %
De C_3 a C_5	~3 %	~3 %
C_6 y superior	0,5-1 %	0,5-1 %
N_2	~1-4 %	<4 %
H_2S	<100 ppm	<4 ppm
H_2O	saturada	<100 ppm

El biogás, por otro lado, es una fuente de energía alternativa. Se trata de un gas combustible que se genera en medios naturales o en dispositivos específicos por las reacciones de biodegradación de la materia orgánica, mediante la acción de microorganismos en condiciones anaeróbeas. La composición del biogás depende principalmente de dos factores: los materiales empleados en la digestión y la tecnología utilizada para el proceso.[8] El biogás suele contener concentraciones similares de CO_2 y CH_4, además de trazas de otros gases, como muestra la **Tabla 1.2.** Su poder calorífico oscila entre los 15 y 30 MJ/Nm^3. [9]

Tabla 1.2. Composición típica del biogás según su procedencia.[10]

Componenete	Desechos agrícolas	Lodos cloacales	Desechos de vertedero
CH_4	50-80 %	50-80 %	50-70 %
CO_2	20-50 %	20-50 %	30-50 %
H_2O	Saturado	Saturado	Saturado
H_2	0-2 %	0-5 %	0-2 %
H_2S	100-700 ppm	0-1 %	0-8 %

El CO_2 es la principal impureza tanto del gas natural como del biogás, ya que es la que está en mayor proporción. Por lo tanto, la purificación de estas mezclas de gases se puede estudiar como la separación de mezclas CO_2/CH_4. La presencia de CO_2 en el gas

natural o en el biogás reduce su poder calorífico y hace que las corrientes de gas sean ácidas y corrosivas. Eliminar este gas es necesario para evitar la corrosión de tuberías y obtener una pureza que cumpla con lo exigido por la legislación, es decir, una concentración de CO_2 inferior al 2%.[11]

1.1.3. La tecnología de membranas en la separación de mezclas de CO_2

Con la tecnología actual, el modo de captura de CO_2 más efectivo para las mezclas CO_2/N_2 y CO_2/CH_4 es la absorción química en disoluciones acuosas de aminas, como monoetanolamina o diaetanolamina.[12] La corriente gaseosa entra en un absorbedor donde puede llegar a retenerse un 85-90 % del CO_2. Tras ello el líquido absorbente es regenerado en un segundo reactor, donde se aplica calor en forma de vapor de agua para desorber el CO_2. Sin embargo, esta tecnología es problemática por la alta cantidad de energía necesaria en el proceso de regeneración, además de las grandes pérdidas de agua y la degradación de las aminas que se producen.[13] Para el caso de mezclas H_2/CO_2, dos disolventes comerciales ampliamente utilizados de nuevo en procesos de absorción química son el Selexol® (basado en glicol) y el Rectisol® (que utiliza metanol refrigerado).[14]

Otras tecnologías disponibles para la separación de mezclas de CO_2 son la destilación criogénica o la adsorción física a presión. Pero estas tecnologías también tienen sus propias limitaciones que derivan de problemas relativos a la corrosión, un gran consumo energético, un alto coste y una baja capacidad.[15] La tecnología de membranas supone una alternativa prometedora por su bajo consumo energético, pequeña huella de carbono y fácil operación y escalado.[16]

La primera aplicación industrial a gran escala de la tecnología de membranas para la separación de gases la llevó a cabo en los años 80 la empresa *Permea* (ahora filial de *AirProducts*) con el desarrollo de sistemas de fibra hueca para la recuperación de H_2.[17] Se trataba de membranas de fibra hueca de polisulfona destinadas a la separación de este gas en la producción de amoniaco. Por otro lado, los primeros sistemas de membranas para la eliminación de CO_2 del gas natural estaban basados en acetato de celulosa y fueron introducidos a mitad de los años 80 por *Cynara* (ahora parte de *Natco*), *Grace Membrane Systems Separex* (ahora parte de *UOP*) y *GMS* (ahora parte de *Kvaerner*).[18] En la pasada década el acetato de celulosa empezó a ser

desplazado por otros polímeros más modernos como poliimidas (*Air Liquide*) y perfluoropolímeros (*ABB/MTR*).[19] Hoy en día, diferentes compañías como *UOP, Air Products and Chemicals, Dow, DuPont y Grace* producen unidades de membrana para la separación de gases a escala industrial. Proteus®, de *Membrane Technology & Research Inc.*, es una membrana comercial que ofrece una selectividad H_2/CO_2 de aproximadamente 11 con una permeación de H_2 de 500 GPU operando a 150 °C.[20]

Aunque las plantas de generación de energía basadas en procesos de precombustión (separación de mezclas H_2/CO_2) son más elaboradas y costosas que las plantas de combustión tradicionales, la separación de CO_2 con membranas es más fácil y barata debido a las altas presiones de operación y la alta concentración de gas en este diseño. Además, el uso de membranas produce la corriente de CO_2 a alta presión, lista para el transporte, mientras que no son necesarias presiones tan altas de la corriente de H_2 en la combustión.[12] Diferentes investigaciones han concluido que una selectividad H_2/CO_2 superior a 10 puede reducir significativamente los costes de la captura.[16, 21]

La separación CO_2/N_2 en procesos de poscombustión se hace más complicada porque las condiciones del gas de salida son justamente las contrarias. La corriente se genera a baja presión y en grandes cantidades, con una concentración de CO_2 muy diluida. Esta baja presión parcial de CO_2 hace que la fuerza impulsora se convierta en el parámetro limitante del proceso, con lo que es necesario aumentarla con otros medios como: presurizar el gas de alimentación, hacer vacío en el lado del permeado o utilizar un gas de barrido en el lado del permeado.

Otro aspecto a tener en cuenta es la temperatura de proceso. Mientras que la separación H_2/CO_2 se ve favorecida con el aumento de la temperatura, no es así para mezcla CO_2/N_2 debido a que el flujo de CO_2 a través de la membrana suele estar condicionado por la adsorción de este gas, que disminuye a temperaturas altas. Por otro lado, la separación de H_2 de CO_2 es complicada debido a la proximidad entre los diámetros cinéticos de ambas moléculas (0,29 y 0,33 nm, respectivamente).

Respecto a la mezcla CO_2/CH_4, algunos yacimientos de gas natural están tan agotados que poseen altas concentraciones de CO_2, lo que los convierte en económicamente inaccesibles. La tecnología de membranas podría hacer económica la

recuperación de metano de estos depósitos, ya que con esta tecnología la separación es más sencilla cuanto mayor es la concentración de CO_2. Además, las membranas tienen la capacidad de soportar las altas presiones con las que sale la mezcla del pozo. Por otra parte, es preciso tener en cuenta que las membranas deben tolerar la presencia de contaminantes (humedad, H_2S, etc.), debido a la variedad de los componentes encontrados en la alimentación de gas natural.

1.2. Tecnología de membranas

En este apartado de la tesis doctoral se va a explicar el concepto de membrana así como los diferentes tipos y métodos de fabricación y los procedimientos de mejora existentes. Además se expondrán los mecanismos de transporte que definen el flujo de gases a través de una membrana.

1.2.1. Definición de membrana

Una membrana consiste en una barrera semipermeable que permite el paso de determinados compuestos de un lado a otro mediante la acción de una fuerza impulsora: gradiente de presión, de concentración, de temperatura o de potencial eléctrico, mientras que otros son rechazados.[22] De esta manera el flujo que es capaz de pasar a través de la membrana recibe el nombre de *permeado*, mientras que el que es rechazado se denomina *retenido o rechazo* (ver **Figura 1.2**).

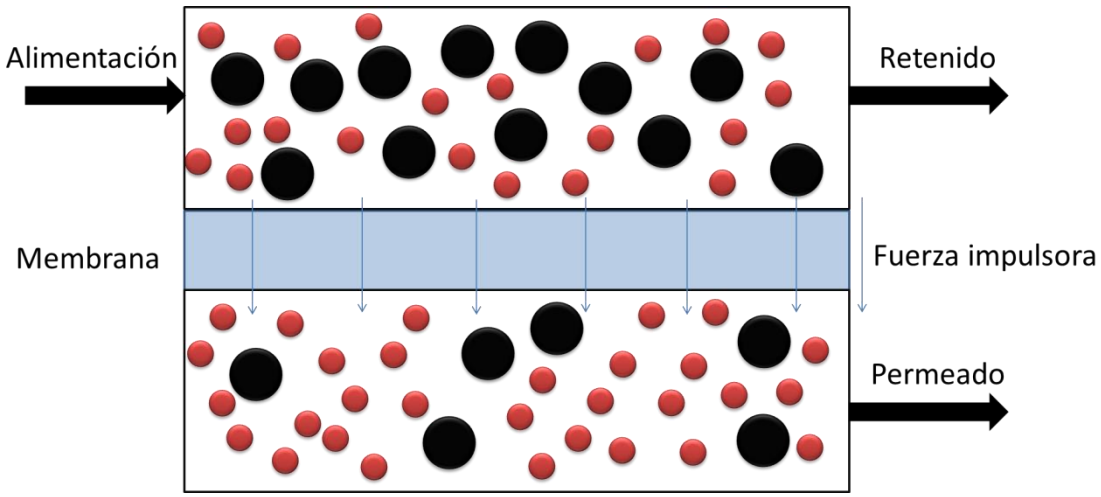

Figura 1.2. Esquema de funcionamiento de una membrana.

La tecnología de membranas tiene diferentes aplicaciones. Los procesos más usuales basados en esta tecnología pueden clasificarse en base al tipo de fuerza impulsora aplicada, tal y como muestra la **Tabla 1.3**:

Tabla 1.3. Aplicación de las membranas atendiendo a la fuerza impulsora del proceso.[23]

Presión (ΔP)	Concentración (ΔC)	Temperatura (ΔT)	Potencial eléctrico (ΔE)
Microfiltración Ultrafiltración Nanofiltración Ósmosis inversa	Separación de gases Pervaporación Diálisis Contactores de membrana	Ósmosis térmica Destilación con membranas	Electrodiálisis

Todos estos procesos se llevan a cabo en fase líquida, excepto los de pervaporación y separación de gases que se realizan en fase vapor y gas, respectivamente. El proceso de separación de gases, en concreto de mezclas de CO_2, es el estudiado en esta tesis doctoral.

1.2.2. Tipos de membranas

Las membranas pueden clasificarse siguiendo diferentes criterios: naturaleza, estructura o configuración, tal y como se observa en la **Figura 1.3**.[24]

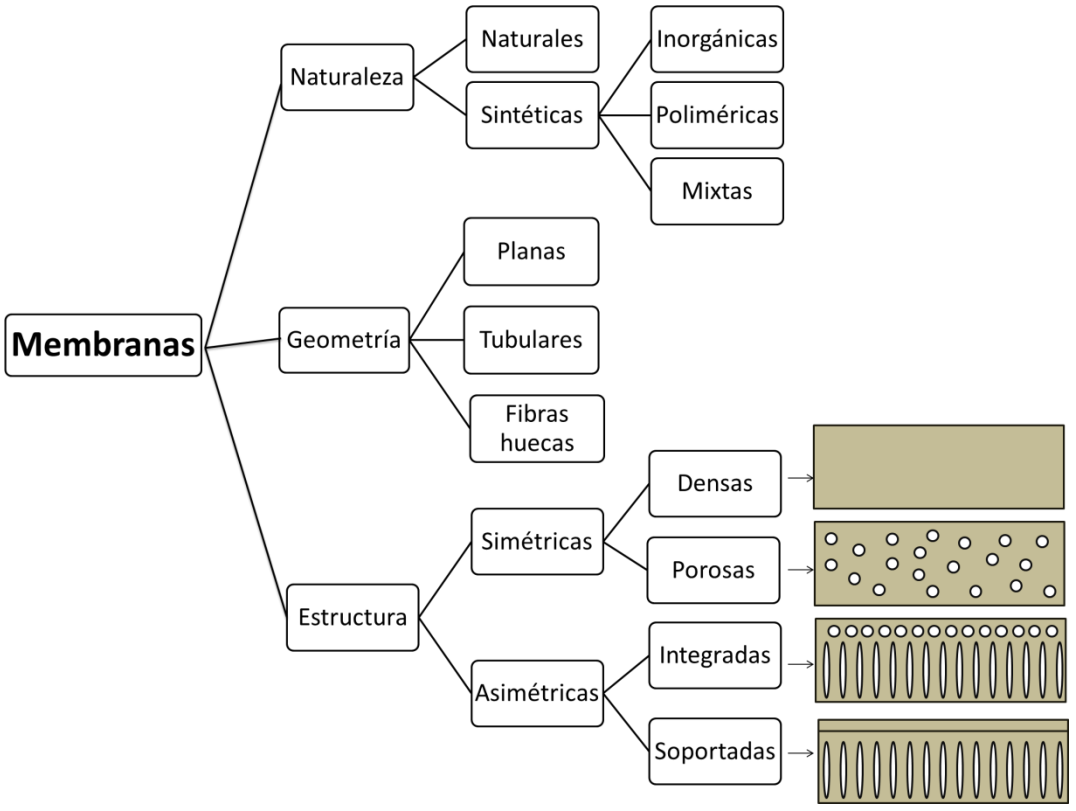

Figura 1.3 Esquema de clasificación de las membranas.

Según su *naturaleza*, las membranas pueden ser **naturales** o **sintéticas**. Las membranas sintéticas pueden ser a su vez **poliméricas**, **inorgánicas** o **mixtas**. En este último caso consisten en una combinación de las dos primeras.

Según su *geometría*, las membranas pueden ser **planas**, **tubulares** o de **fibra hueca**. Las membranas tubulares poseen una relación de área superficial de permeación por volumen de módulo superior a las planas, y las de fibra hueca muy superior a las otras dos. Es por ello que es el modelo de configuración más atractivo comercialmente.[25]

Según su *estructura*, las membranas pueden ser **simétricas** o **asimétricas**. Las membranas simétricas pueden ser a su vez **densas** o **porosas** y se caracterizan por ser homogéneas, es decir, todo el espesor de la membrana es selectivo para la separación de compuestos. Las membranas asimétricas en cambio son heterogéneas. Constan de una capa superior más densa, que es la que es selectiva a la separación, y de una capa inferior altamente porosa, que le aporta resistencia mecánica evitando que la membrana se rompa. Cuando estas membranas se forman en un solo paso mediante un proceso de inversión de fases, se habla de **"membranas integradas"**; cuando se forma en dos etapas, de **"membranas soportadas".** En este último caso, se comienza preparando el soporte altamente poroso y en un segundo paso se deposita una membrana densa sobre él mediante técnicas como dip-coating, spin-coating...etc, que es la que constituye la capa selectiva al flujo.

1.2.3. Métodos de preparación de membranas poliméricas planas

Todos los métodos de formación de membranas orgánicas planas comprenden tres pasos bien diferenciados.

- Primero, disolver del polímero en un disolvente afín.
- Segundo, extender la disolución polimérica para formar una lámina plana.
- Por último, eliminar el disolvente para obtener una lámina sólida, que es la membrana.

Los diferentes métodos existentes para la fabricación de membranas poliméricas planas se explican a continuación.

- *Casting* o volcado

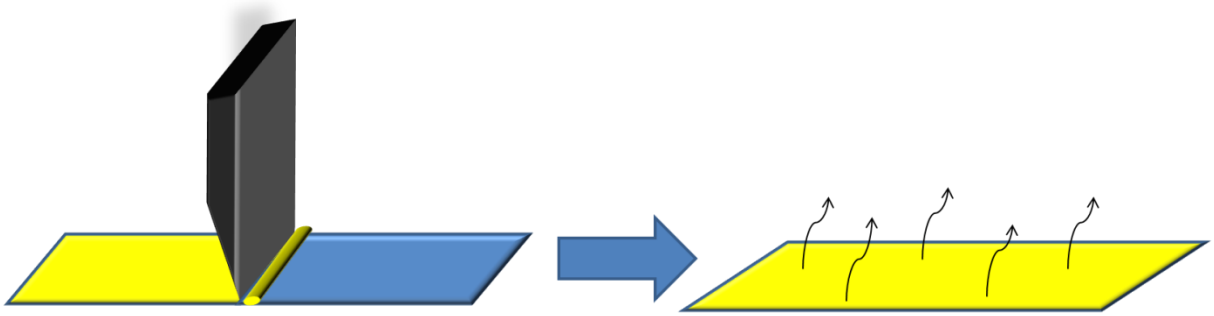

Figura 1.4. Esquema de fabricación de membranas por *casting*.

Las membranas simétricas, densas o porosas se forman generalmente por *casting* (volcado) y evaporación (ver **Figura 1.4**). El proceso comienza con la disolución del polímero en un disolvente adecuado para obtener la denominada "disolución de *casting*". Una vez obtenida una disolución homogénea, esta se vuelca sobre una superficie completamente plana y nivelada se extiende para formar una lámina, dejando tras ello evaporar el disolvente. Una vez seca, el resultado es una lámina polimérica cuya estructura será densa o porosa en función del polímero utilizado y de las condiciones aplicadas. Este proceso también se puede utilizar para obtener membranas soportadas. En este caso la disolución polimérica se extiende generalmente sobre un soporte poroso no selectivo.

- Inversión de fases

Las membranas asimétricas se suelen fabricar mediante un mecanismo de inversión de fases, un proceso que fue desarrollado en los años 60 por Loeb y Sourirajan.[26] Esta técnica comienza como en el caso anterior por la disolución del polímero y el volcado para formar una lámina, pero en lugar de dejar evaporar el disolvente, la membrana se sumerge en un baño de coagulación constituido por un no-disolvente, normalmente agua. Esto produce la precipitación rápida del polímero formándose la capa superior densa. Esta capa densa actúa como una barrera disminuyendo el acceso del agua en las capas más interiores, lo que lleva a la formación de la subestructura porosa.

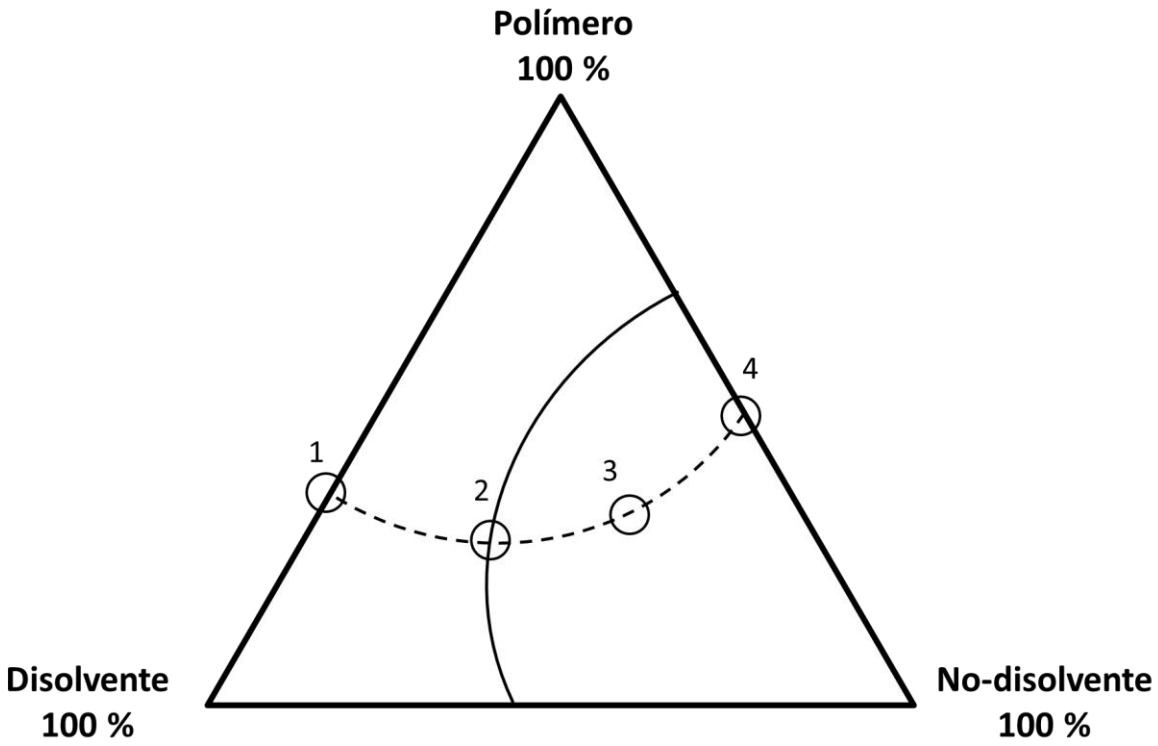

Figura 1.5. Diagrama ternario explicativo del proceso de inversión de fases.

Este proceso es fácil de explicar utilizando un diagrama ternario como el de la **Figura 1.5**. El diagrama consiste en un triángulo equilátero donde cada vértice corresponde a una concentración del 100% en uno de los tres compuestos; los lados (1 y 4), a mezclas bicomponentes y los puntos interiores (2 y 3) son mezclas de los tres componentes. El interior del diagrama tiene dos zonas separadas por la curva binodal. La zona izquierda corresponde a concentraciones donde los tres componentes son completamente miscibles y solo hay una fase en el sistema. Y la zona derecha, a concentraciones donde hay una fase sólida (rica en polímero) en equilibrio con una fase líquida (pobre en polímero).

Al comienzo del proceso se tiene una disolución de *casting*, que corresponde al punto 1. Cuando se forma la película y se pone en contacto con el no-disolvente, el sistema se desplaza de acuerdo con la trayectoria que describe la línea discontinua. Cuando la película se introduce en el baño de coagulación se produce un intercambio líquido-líquido entre el disolvente y el no-disolvente, ya que el disolvente tiene más afinidad por él que por el polímero. De esta manera, cuando llega al punto 2, el polímero en la superficie de la lámina comienza a precipitar rápidamente, pero las dos

fases formadas no tienen tiempo de aglomerarse y generan una fina microestructura. Cuando se alcanza el punto 3, la capa superior de la lámina se vuelve una barrera sólida, disminuyendo el flujo saliente de disolvente y el entrante de no-disolvente a las capas inferiores. Esto hace que disminuya la velocidad de precipitación, y por consiguiente que aumente el tamaño medio de poro en estas capas. Finalmente, cuando se alcanza la concentración del punto 4, todo el disolvente ha salido de la lámina y el resultado es una membrana sólida.[23]

- Recubrimiento por inmersión: *dip-coating*

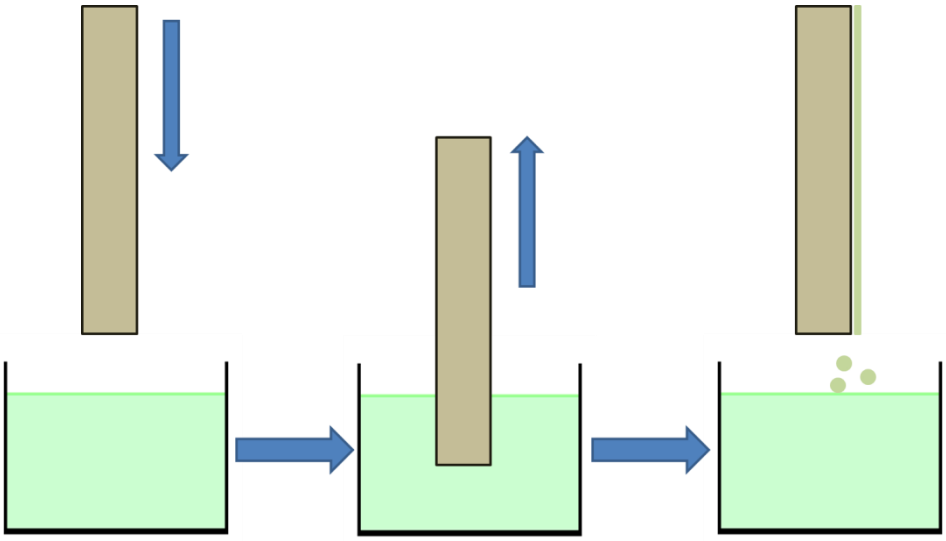

Figura 1.6. Esquema de preparación de membranas por *dip-coating*.

El método de *dip-coating* o recubrimiento por inmersión es uno de los más sencillos y más comúnmente utilizados en la fabricación de membranas multicapa. El método consiste en sumergir un soporte en una disolución polimérica para después sacarlo. De esta manera, el soporte queda impregnado en la disolución, y cuando se seca, queda adherida una membrana sobre el soporte, como muestra la **Figura 1.6**.[27] Los parámetros que controlan el espesor de la membrana depositada son la concentración del polímero en la disolución, el tiempo de inmersión, la velocidad de inmersión y el proceso de secado (temperatura, humedad relativa, atmósfera, etc.) El modelo de Landau y Levich[28] permite estimar el grosor de la capa depositada mediante la expresión que muestra la **Ecuación 1.1**:

$$l = 0.944\, Ca^{1/6} \left(\frac{\eta U}{\rho g}\right)^{\frac{1}{2}}$$ **Ecuación 1.1**

donde Ca es un número de capilaridad definido como $Ca = \frac{\eta U}{\sigma}$, η es la viscosidad del líquido, U es la velocidad con la que se retira la membrana, σ la tensión superficial del líquido, ρ la densidad del líquido y g la aceleración de la gravedad.

- Recubrimiento mediante giro: *spin-coating*

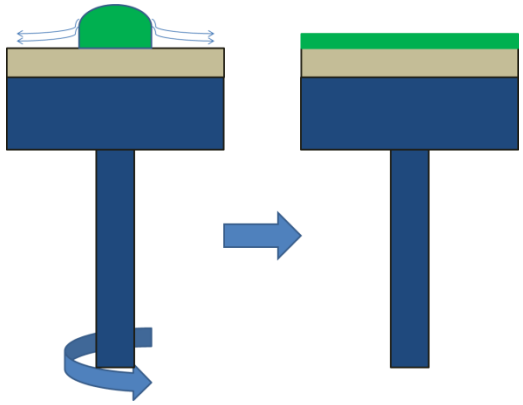

Figura 1.7. Esquema de fabricación de membranas por *spin coating*.

Este método, esquematizado en la **Figura 1.7**, se utiliza para preparar membranas soportadas. Consiste en fijar el soporte sobre un sustrato horizontal y depositar sobre él una cantidad determinada de disolución de polímero. Entonces se hace girar el soporte a una determinada velocidad para que la disolución se extienda sobre el soporte como efecto de la fuerza centrífuga, de manera que se genera una lámina sobre él que una vez seca se transforma en una membrana.[29]

- Polimerización interfacial

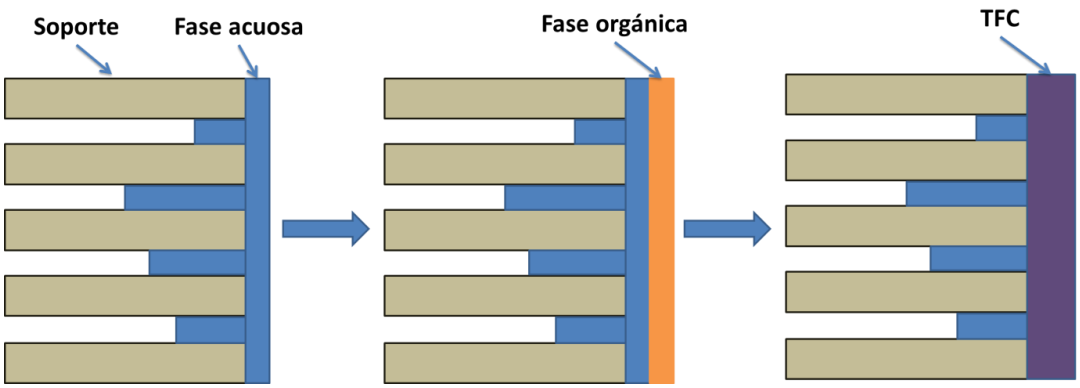

Figura 1.8. Esquema de fabricación de membranas por polimerización interfacial.

El método de preparación de membranas por polimerización interfacial[30] fue creado por John Cadotte, y *North Star Research* continuó desarrollando esta tecnología.[31] La polimerización interfacial implica la polimerización por condensación de dos monómeros multifuncionales que inicialmente están disueltos en fases diferentes: agua y un disolvente orgánico. El proceso viene detallado en la **Figura 1.8** y comienza empapando el soporte con la disolución acuosa del primer monómero, para después añadir la disolución orgánica del segundo. Al entrar en contacto las disoluciones se produce una rápida reacción de polimerización en la interfase que provoca que el polímero precipite formando una lámina densa muy delgada.[32] Los materiales más comunes usados en polimerización interfacial son aminas multifuncionales aromáticas o alifáticas para la fase acuosa, y cloruro de trimesoilo (TMC), cloruro de isoftaloilo (IPC) y cloruro de tetraftaloilo (TPC) para la orgánica.

1.2.4. Procedimientos de mejora en membranas poliméricas

Las membranas poliméricas presentan por lo general una limitación en su eficiencia para la separación de gases. Las membranas que son muy permeables suelen ser poco selectivas, y del mismo modo, las membranas que son muy selectivas tienden a tener escasa permeabilidad. Esto hace que los resultados de membranas poliméricas se encuentren lejos de la región comercialmente atractiva (altos flujos y selectividades). Este compromiso entre permeabilidad y selectividad fue definido por Lloyd M. Robeson, que ya en 1991 definió el llamado "límite superior de Robeson"[33] utilizando más de 300 referencias bibliográficas de membranas poliméricas. En 2008 este límite fue actualizado incorporando además nuevas mezclas de interés industrial, como CO_2/N_2.[34] El límite superior es una expresión del tipo $P_i = k \cdot \alpha_{ij}^n$, donde P_i es la permeabilidad del gas más permeable, α es el factor de separación (P_i/P_{ij}) y n es el exponente de la ecuación potencial. Estos parámetros no tienen valores arbitrarios. Se observó que al representar $-1/n$ frente a d_{ij} (donde d_{ij} es la diferencia entre los diámetros moleculares de los dos gases a separar $(d_j - d_i)$) se daba una relación linear. Los límites de Robeson los utilizan normalmente los investigadores para comparar sus resultados experimentales y verificar el rendimiento de las membranas.

A modo de ejemplo, la **Figura 1.9** muestra el límite superior de Robeson de 1991 y 2008 para la separación H_2/CO_2 (líneas negras), donde los puntos en rojo son los

resultados experimentales bibliográficos de membranas poliméricas puras hasta esa fecha.

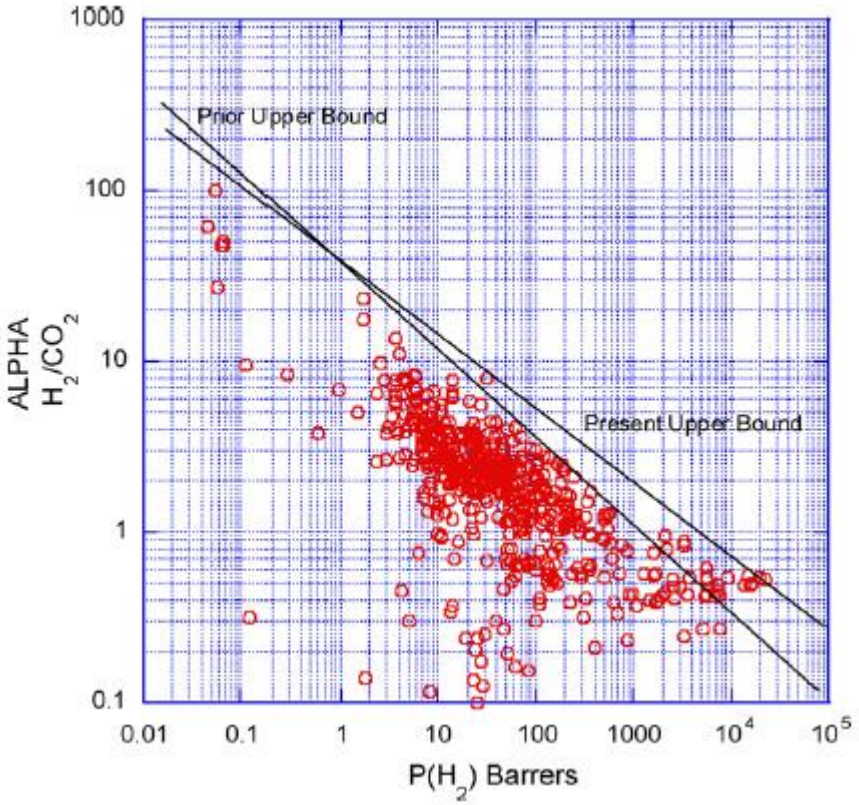

Figura 1.9. Límite superior de Robeson de 1991 (*Prior Upper Bound*) y 2008 (*Present Upper Bound*) para la mezcla H_2/CO_2 (*reprinted from "The upper bound revisted, L. M. Robeson, J. Membr. Sci.* ***2008****, 320, 390-400", copyright 2008, with permission from Elsevier*).[34]

El desafío de las membranas poliméricas está en traspasar el límite superior de Robeson y alcanzar la zona comercialmente atractiva. Las membranas poliméricas pueden mejorar su rendimiento en separación de gases de diferentes maneras, entre las que destacan: el control de su microestructura, los postratamientos, (tratamientos que se aplican a posteriori una vez que se ha preparado la membrana), la mezcla de polímeros o la incorporación de materiales inorgánicos o metalorgánicos para formar membranas híbridas o también llamadas mixtas.

- *Annealing* térmico

El *annealing* es una técnica por la que una membrana se somete a altas temperaturas, pero por debajo de la de transición vítrea, durante un determinado periodo de tiempo. De esta manera se consigue que las cadenas poliméricas tengan energía suficiente para reordenarse en un nuevo estado de equilibrio en el que

aumenta el empaquetamiento y disminuye el volumen libre de la membrana. Por consiguiente, este postratamiento suele conllevar un aumento de la selectividad de la membrana, pero también un descenso de su permeabilidad. Esta técnica se ha utilizado con poliimidas como Matrimid®,[35-37] 6FDA[38, 39] o P84®[40] para evitar la plastificación.

La plastificación es un fenómeno que se debe a la disolución de gases condensables como: CO_2, H_2O, H_2S en una membrana polimérica, impidiendo el correcto empaquetamiento de las cadenas poliméricas y facilitando la movilidad entre segmentos de estas.[41] Se genera por tanto un hinchamiento del polímero que suele provocar una disminución en la selectividad de la membrana deteriorando su rendimiento. En polímeros termoplásticos se suele ver este fenómeno en función de la presión de alimentación. A presiones bajas de CO_2, por ejemplo, la permeabilidad de la membrana disminuye con el aumento de presión debido a la saturación gradual de micro huecos en la membrana. Conforme la presión sigue aumentando se observa un punto de inflexión en la permeabilidad, que empieza a aumentar de forma irreversible en el caso de que se retorne a los valores previos de presión. La presión a la que se da este mínimo se denomina presión de plastificación.[41] Puede verse un esquema del proceso en la **Figura 1.10**. Además de la presión, la plastificación guarda también relación con el espesor de la membrana, ya que se ha demostrado que este fenómeno se acelera en membranas ultrafinas de menos de 1 μm de espesor en comparación con membranas densas más espesas.[42]

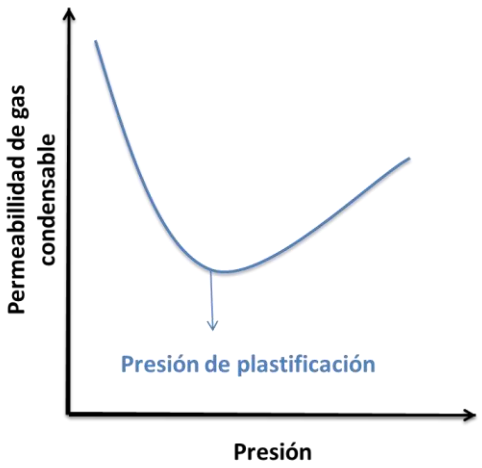

Figura 1.10. Presión de plastificación en membranas poliméricas.

- Entrecruzamiento (*crosslinking*)

El entrecruzamiento es una técnica que tiene el fin de aumentar la interacción entre las cadenas poliméricas de una membrana mediante medios físicos o químicos, mejorando así su eficiencia de separación de gases. Mediante el *crosslinking* se puede: (1) reducir el grado de cristalinidad del polímero al interrumpir regularmente las cadenas poliméricas,[43] (2) aumentar la resistencia mecánica del polímero, (3) ayudar a prevenir fenómenos de plastificación[44,45] y (4) mejorar la selectividad de las membranas al disminuir el espaciado entre cadenas poliméricas.

El entrecruzamiento físico puede producirse mediante un tratamiento térmico a alta temperatura[44],[46] o con radiación ultravioleta.[47, 48] Sin embargo, el más utilizado es un entrecruzamiento químico, en el que se utiliza un reactivo que posee algún grupo funcional que puede interaccionar con las cadenas poliméricas facilitando su enlace. El entrecruzamiento químico se ha utilizado ampliamente con diferentes poliamidas[49] o polietileno[50, 51] para reducir la plastificación y mejorar la capacidad de separación de las membranas. Chung y cols.[52] llevaron a cabo un entrecruzamiento de membranas 6FDA-dureno con trimetilendiamina (TMEDA) y la selectividad H_2/CO_2 aumentó de 1 a 101 después del tratamiento. Hosseini y cols.[53] también utilizaron entrecruzamiento químico con membranas de polibenzimidazol (PBI) para mejorar el rendimiento de la separación de gases. La **Figura 1.11** muestra el mecanismo de entrecruzamiento de este polímero con p-xyleno. El resultado de esta investigación fueron membranas con una permeabilidad de H_2 de 3,6 Barrer y una selectividad H_2/CO_2 de 26,1. Esto significó un aumento de la selectividad de casi el triple, pero un descenso de la permeabilidad del 34%. El PBI también se ha dopado con ácidos como H_3PO_4 o H_2SO_4, logrando alcanzar selectividades H_2/CO_2 de 140 a 150ºC, aunque de nuevo de la mano de una reducción drástica de la permeabilidad.[54] Esta tendencia es típica en las membranas tratadas mediante entrecruzamiento químico, ya que la proximidad entre cadenas poliméricas termina penalizando la permeabilidad de los gases.

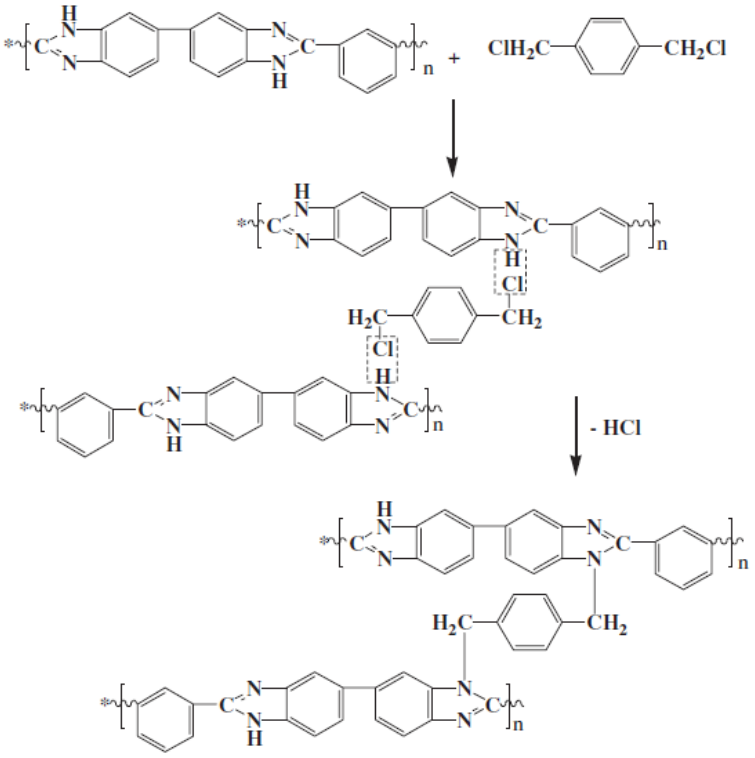

Figura 1.11. Esquema del mecanismo de entrecruzamiento de polibenzimidazol con p-xyleno.[55] *Reprinted from Chemical Engineering Science, 61(17), Kai Yu Wang, Youchang Xiao, Tai-Shung Chung, Chemically modified polybenzimidazole nanofiltration membrane for the separation of electrolytes and cephalexin, 5807-5817, copyright (2006) with permission from Elsevier.*

- Reparación con PDMS

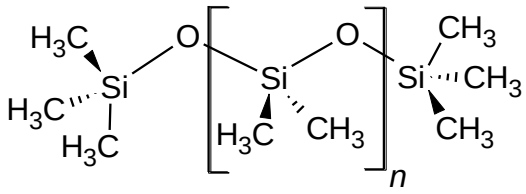

Figura 1.12. Estructura química del PDMS.

El polidimetilsiloxano (PDMS), cuya estructura química puede verse en la **Figura 1.12**, es un elastómero ampliamente utilizado para la reparación de membranas. Realmente fue uno de los primeros polímeros empleados para la fabricación de membranas[56-58] pero actualmente tiene mayor importancia esta otra aplicación. De hecho, gracias a las reparaciones con PDMS las membranas de separación de gases han podido tener aplicación industrial.[59] El método seguido para reparar membranas es normalmente por *dip-coating*. Las membranas se sumergen en una disolución de PDMS durante un determinado tiempo y luego se retiran, de manera que una capa de elastómero queda adherida en la superficie de la misma. La disolución de PDMS es

capaz de colarse por todos los entresijos de la membrana, cubriendo así todos los defectos responsables del flujo viscoso que penalizan la selectividad (ver esquema en la **Figura 1.13**).

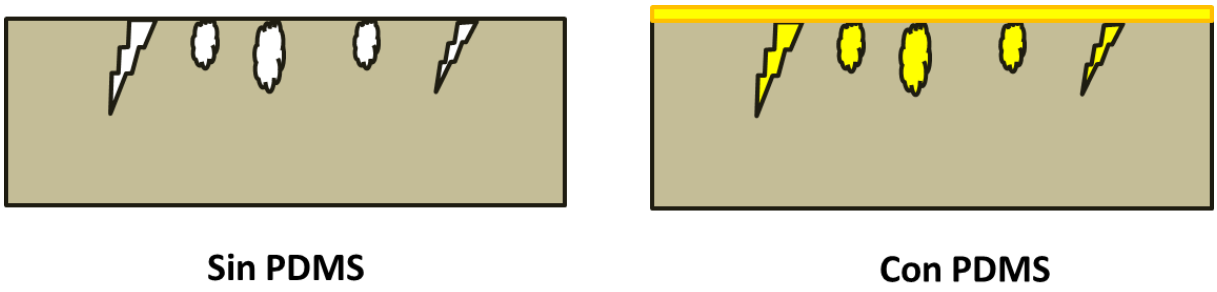

Figura 1.13. Esquema explicativo de la reparación de membranas con PDMS.

Esta técnica de reparación es especialmente útil con membranas asimétricas, que son las que más defectos críticos presentan debido a la finura de su capa selectiva. El aumento en la selectividad suele venir de la mano de un descenso en la permeabilidad de la membrana debido a la adición de una nueva resistencia en serie al flujo.

- Mezcla (*blending*) de polímeros

El *blending* consiste en la mezcla de dos polímeros sin que se produzcan enlaces covalentes entre las cadenas de cada uno.[60] Existen dos tipos. Cuando la mezcla de los dos polímeros es completa a nivel molecular, se habla de *blending* homogéneo. Cuando por el contrario no es así, el *blending* es heterogéneo. En este caso se pueden observar dominios de un polímero repartidos en la matriz polimérica del otro. El *blending* homogéneo es el que resulta interesante para la separación de gases, porque en el segundo caso las inhomogeneidades suelen disminuir la resistencia mecánica de las membranas.

Se considera que los polímeros están íntimamente mezclados, y que por lo tanto el *blending* es homogéneo, cuando presentan una única temperatura de transición vítrea (Tg). El valor de la Tg del polímero mezclado depende de la proporción inicial de cada polímero y puede estimarse con la ecuación de Fox (**Ecuación 1.2**):

$$\frac{1}{T_g} = \frac{W_1}{T_{g1}} + \frac{W_2}{T_{g2}} \qquad \textbf{Ecuación 1.2}$$

donde T_{g1} y T_{g2} son las temperaturas de transición vítreas en K de los polímeros individuales y W_1 y W_2 son las fracciones másicas de los polímeros en la mezcla.

La Tg es la temperatura a la que se da una pseudotransición termodinámica en polímeros termoplásticos. Al superar la Tg, los enlaces secundarios entre los segmentos poliméricos son mucho más débiles que el movimiento térmico de los mismos, lo que hace que el polímero se vuelva gomoso. Es un punto intermedio de temperatura entre el estado fundido y el estado rígido del material. Al disminuir de nuevo la temperatura por debajo de la Tg, las propiedades del material no vuelven a ser las originales debido a cambios en el volumen libre.[61]

El *blending* pretende conseguir una sinergia entre las propiedades ventajosas de cada polímero que ayude a superar las limitaciones individuales de cada uno por separado. Un ejemplo de blending es la mezcla de pequeñas cantidades de polibenzimidazol (PBI) con poliimidas, como Matrimid®, P84® o Torlon®.[62, 63] El PBI es un polímero con buena estabilidad térmica pero genera membranas frágiles, mientras que a las poliimidas les sucede lo contrario. La buena miscibilidad entre estos polímeros se debe a la afinidad entre los grupos N-H del primero y C=O del segundo, que permite construir enlaces de hidrógeno entre ellos.[64] De esta manera la fragilidad de las membranas se ve reforzada por los segmentos de poliimida y la resistencia térmica de las membranas es superior gracias a la contribución del PBI. Estas investigaciones mostraron como la incorporación de PBI provocó un aumento en la selectividad, pero un descenso de la permeabilidad de las membranas. El aumento en la selectividad se atribuye principalmente a un aumento en la selectividad por difusión, ya que el PBI tiene un mayor efecto de tamizado molecular, mientras que el descenso en la selectividad se debe a la reducción de volumen libre por los fuertes enlaces de hidrógeno dados entre ambos polímeros.

Las poliimidas también se han mezclado con polímeros de microporosidad intrínseca (PIMs)[65] para mejorar la permeabilidad de las membranas. Así destaca el blending de PIM-1 con Matrimid®.[66] La incorporación de cantidades pequeñas de PIM-1 (5, 10 % en peso) logró mejorar la permeabilidad hasta en un 75 % de las membranas con una reducción mínima de la selectividad CO_2/CH_4. El PIM-1 también se ha mezclado con polietilienglicol (PEG),[67] siendo en este caso el último el

componente minoritario con proporciones no superiores al 3,5 % en peso. Las membranas mostraron excelentes resultados en la separación de mezclas CO_2/N_2 y CO_2/CH_4, superiores a los del PIM-1 puro, con permeabilidades de CO_2 cercanas a los 2000 Barrer y selectividades CO_2/N_2 y CO_2/CH_4 de 16 y 39, respectivamente. En este caso el aumento de selectividad se debió a la mejora en la solubidad del CO_2 favorecida por el PEG.

- Membranas mixtas

Las membranas mixtas o híbridas, del inglés *mixed matrix membranes* o MMMs, consisten en la incorporación de compuestos inorgánicos o metalorgánicos como material de relleno en el seno de matrices poliméricas, como muestra el esquema de la **Figura 1.14**. De esta manera se consigue potenciar las propiedades ventajosas de cada fase, detalladas en la **Tabla 1.4**, mejorando las capacidades permeoselectivas de la membrana.

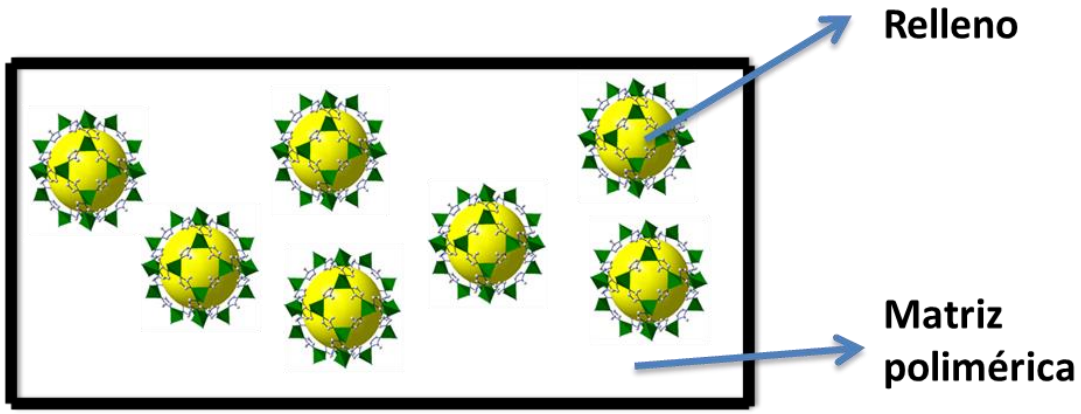

Figura 1.14. Esquema de una membrana mixta.

Tabla 1.4. Propiedades de las membranas poliméricas e inorgánicas/metalorgánicas.

	Membranas poliméricas	Membranas inorgánicas/ metalorgánicas
Ventajas	Procesabilidad Precio asequible Resistencia mecánica	Alta permeabilidad y selectividad Alta estabilidad térmica y química Buena resistencia a la erosión
Desventajas	Capacidad de separación limitada Baja estabilidad térmica y química Poco estables ante contaminantes	Precio elevado Poca resistencia mecánica Baja reproducibilidad Difícil escalado

El efecto de incorporar materiales metalorgánicos en matrices poliméricas depende de su estructura química, química superficial y del tipo de partículas. Los materiales utilizados como relleno se pueden clasificar en porosos y no porosos.[68] Los materiales no porosos mejoran las propiedades de separación porque aumentan la tortuosidad y reducen la difusión de moléculas grandes. Además también pueden alojarse entre las cadenas poliméricas, lo que hace que aumente el volumen libre.[69] Por lo general, los materiales de relleno porosos actúan como tamices moleculares en la matriz mixta, discriminando las moléculas de gas de acuerdo con su tamaño.[70] Estas partículas tienen tamaños de poro precisos con altas permeabilidades y selectividades superiores al límite superior de Robeson.[34] Por ello, cuando estos materiales de relleno se añaden a la matriz polimérica el flujo de gas aumenta, ya que los materiales de relleno son más permeables que los polímeros, pero además también lo hace la selectividad por el mecanismo de tamizado molecular ya citado. Es por ello importante que el tamaño de poro del material de relleno esté comprendido entre los de los diámetros cinéticos de las moléculas de los gases a separar.

El uso de membranas mixtas para separación de gases se puede decir que comenzó en 1972, cuando Paul y Kemp encontraron una mejora en el rendimiento de la separación de CO_2 y CH_4 al añadir zeolita 5A a PDMS debido al fenómeno de adsorción preferencial del CO_2 causado por la zeolita.[71] Así las zeolitas fueron los primeros materiales en utilizarse como relleno de membranas híbridas, primero en polímeros elastómeros, como PDMS[72] o acetato de celulosa,[73] y posteriormente en termoplásticos, como diferentes polisulfonas. [74,75] Aparte de las zeolitas, los materiales que tradicionalmente más se han utilizado en membranas mixtas son los óxidos metálicos, los carbones activos y los nanotubos de carbono. Sin embargo, en los últimos años ha ido creciendo cada vez más el uso de compuestos metalorgánicos porosos (MOFs) como material de relleno debido a sus propiedades interesantes para la separación de gases. La descripción de estos materiales, así como su uso en membranas mixtas, se detallará en el apartado 1.3.

1.2.5. Mecanismos de transporte de gas

Los mecanismos de transporte de gas se clasifican en cuatro tipos: flujo de Poiseuille o viscoso, difusión Knudsen, tamizado molecular y disolución-difusión. Los

tres primeros explican el transporte de gases en membranas porosas, mientras que el último lo explica en membranas densas. De este modo los primeros pueden explicar también el transporte a través de compuestos metalorgánicos, mientras que el último solo sirve para membranas poliméricas. Un esquema explicativo de estos mecanismos de transporte puede verse en la **Figura 1.15**.

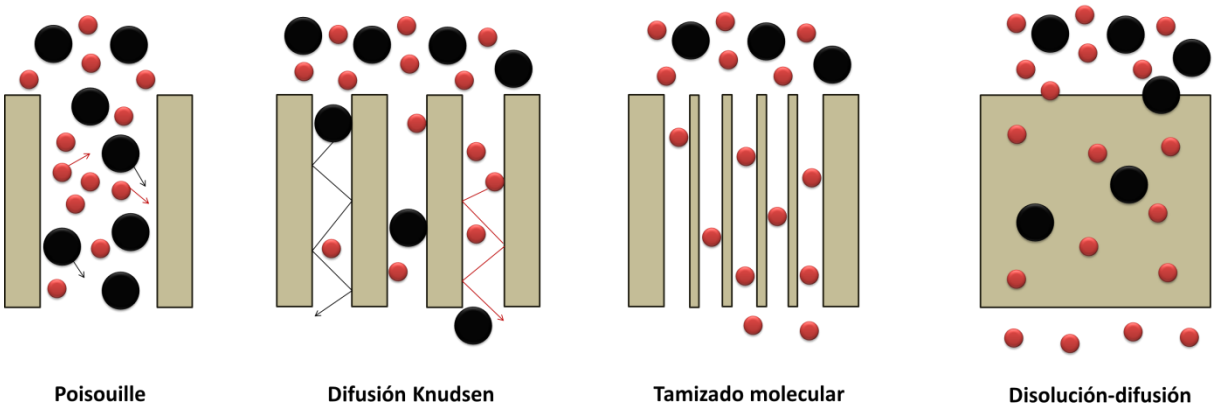

Figura 1.15. Diferentes mecanismos de transporte posibles a través de una membrana.

- Flujo tipo Poiseuille

El flujo de Poiseuille o viscoso se da cuando el diámetro del poro de las membranas (d) es mayor que camino libre medio (λ) de los gases penetrantes. Este tipo de transporte se produce en membranas con poros grandes y no conlleva la separación de gases, por lo que es un flujo indeseado y suele estar ligado a defectos. El camino libre medio se refiere a la distancia media que recorre una molécula de gas entre colisiones y se representa con la **Ecuación 1.3**

$$\lambda = \frac{3\eta}{2P}\left(\frac{\pi RT}{2M}\right)^{0,5} \qquad \textbf{Ecuación 1.3}$$

donde η es la viscosidad del gas, P es la presión, T es la temperatura, R es la constante universal de los gases y M la masa molecular del gas.

- Difusión Knudsen

La difusión Knudsen se da en membranas con tamaños de poro comprendidos entre aproximadamente 5 y 10 nm. Cada uno de los gases fluye a través de la membrana de manera casi independiente cuando se produce la difusión Knudsen.

Cuando se alimenta una mezcla equimolar, la selectividad Knudsen es inversamente proporcional a la raíz cuadrada del cociente de las masas moleculares de cada gas, como expresa la **Ecuación 1.4**

$$\alpha_{a/b} = \sqrt{\frac{M_b}{M_a}} \qquad \textbf{Ecuación 1.4}$$

donde M_a y M_b, son las masas moleculares de cada uno de los gases.

- Tamizado molecular

El mecanismo de tamizado molecular se basa en la exclusión por tamaños de cada uno de los gases que forman la mezcla de alimentación. Se da en membranas con poros inferiores a 0,7 nm de diámetro. Según este mecanismo de transporte, los gases de menor diámetro cinético y con mayores difusividades son capaces de permear a través de la membrana, mientras que las moléculas más grandes son retenidas. Es el mecanismo de transporte típico de las zeolitas y de los compuestos metalorgánicos porosos.

- Modelo de disolución-difusión

Este mecanismo explica el transporte de gases a través de membranas densas poliméricas, el cual consta de tres etapas:[76] (1) los gases se absorben en el polímero en el lado de la alimentación, (2) los gases difunden a través de la membrana debido a un gradiente de concentración, y por último, (3) los gases se desorben en el lado del permeado.

La ley de Fick de la difusión (**Ecuación 1.5**) puede explicar este mecanismo de separación. El flujo de gas se define de acuerdo con esta ley en función de una diferencia de concentraciones:

$$J_i = -D\frac{dc}{dx} \qquad \textbf{Ecuación 1.5}$$

donde J es el flujo de gas (mol cm^{-2} s^{-1}), D es el coeficiente de difusión efectivo (cm^2 s^{-1}), x es la posición (cm) y c la concentración (mol cm^{-3}).

Integrando esta ecuación se obtiene la **Ecuación 1.6**:

$$J_i = -D\frac{(C_2 - C_1)}{l} \qquad \textbf{Ecuación 1.6}$$

donde *l* corresponde al espesor de la membrana y C_2 y C_1, la concentración del gas a cada lado de la misma. De acuerdo con la ley de Henry, la concentración gaseosa puede expresarse como el producto de un coeficiente de solubilidad (S) y la presión (P), tal y como muestra la **Ecuación 1.7**:

$$C = S \cdot P \qquad \textbf{Ecuación 1.7}$$

De manera que la **Ecuación 1.7** puede expresarse como:

$$J_i = -D \cdot S\frac{(P_2 - P_1)}{l} \qquad \textbf{Ecuación 1.8}$$

Hay dos parámetros claves que determinan el rendimiento intrínseco de una membrana en separación de gases: la **permeabilidad y la selectividad**. La primera está relacionada con el caudal que fluye a través de la membrana, y la segunda con su capacidad de separación. La permeabilidad (P_i) se define para cada uno de los gases (i) según la **Ecuación 1.9**:

$$P_i = \frac{l \cdot J_i}{\Delta P \cdot A} \qquad \textbf{Ecuación 1.9}$$

donde *l* es el espesor de la membrana, *Ji* el caudal de gas, ΔP la diferencia de presión a ambos lados de la membrana, y *A* el área de permeación. La unidad más utilizada para la permeabilidad es el Barrer, en honor al catedrático Richard Mailing Barrer, que ejerció una gran influencia en el campo de las zeolitas,[77] siendo 1 Barrer = 10^{-10} cm^3(STP) cm cm^{-2} s^{-1} $cmHg^{-1}$. Para algunas membranas es imposible determinar el grosor exacto de la capa selectiva responsable de la separación. En estos casos se define el flujo a través de la membrana como permeación, que no tiene en cuenta este espesor (**Ecuación 1.10**).

$$Q_i = \frac{J_i}{\Delta P \cdot A} \qquad \textbf{Ecuación 1.10}$$

La unidad más utilizada para definir la permeación es el GPU (del inglés *Gas Permeation Unit*), siendo 1 GPU = 10^{-6} cm^3(STP) cm^{-2} s^{-1} $cmHg^{-1}$. De esta manera, permeación y permeabilidad se relacionan según la **Ecuación 1.11** de la siguiente manera (siendo iguales para el espesor de 1 μm):

$$P_i(Barrer) = Q_i(GPU) \cdot l(\mu m) \qquad \textbf{Ecuación 1.11}$$

Existen otras unidades que se suelen utilizar para definir la permeación, como las del sistema internacional (mol m^{-2} s^{-1} Pa^{-1}). Su equivalencia en GPU se muestra en la **Tabla 1.5**.

Tabla 1.5. Tabla de equivalencias para la conversión entre unidades de permeación.[78]

GPU	10^{-7} cm^3(STP) cm^{-2} s^{-1} kPa^{-1}	10^{-10} mol m^{-2} s^{-1} Pa^{-1}	10^{-3} m^3(STP) m^{-2} h^{-1} bar^{-1}
10^{-6} cm^3(STP) cm^{-2} s^{-1} $cmHg^{-1}$	7,50	3,35	2,70

La selectividad ideal (α^*_{ij}) se define como el cociente de las permeabilidades de dos gases puros (**Ecuación 1.12**).

$$\alpha^*_{ij} = \frac{P_i}{P_j} \qquad \textbf{Ecuación 1.12}$$

donde P_i y P_j son las permeabilidades de los gases i y j a través de la membrana.

Cuando se calcula el cociente de las permeabilidades de dos gases medidos en mezcla se habla de selectividad real. En general, el valor de selectividad real es menor que el ideal debido a la existencia de interacciones y competencias entre los gases de la alimentación. Incluso puede darse la polarización de la concentración para membranas muy permeables. En algunos casos se prefiere utilizar el también el factor de separación en lugar de la selectividad. Este se define como el cociente entre la composición del flujo de alimentación al flujo de permeado, que se expresa como muestra la **Ecuación 1.13**:

$$\alpha_{ij} = \frac{y_i/x_i}{y_j/x_j} \qquad \textbf{Ecuación 1.13}$$

donde y_i e y_j son las fracciones molares de las especies gaseosas i y j en el lado del permeado, mientras que x_i y x_j, las fracciones molares en el lado de la alimentación. Cuando la diferencia de presión parcial de cada gas entre la alimentación y el permeado es muy grande, el factor de separación se aproxima a la selectividad (ver **Ecuación 1.14**).[79]

$$\alpha_{ij} = \frac{y_i/x_i}{y_j/x_j} = \frac{1}{x_i/x_j}\frac{P_i}{P_j}\frac{p_{f,i} - p_{p,i}}{p_{f,j} - p_{p,j}} \approx \frac{P_i}{P_j} = \alpha_{ij}^{*} \qquad \textbf{Ecuación 1.14}$$

De acuerdo con el modelo de disolución-difusión,[76] como puede derivarse de la **Ecuación 1.15**, la permeabilidad de un gas i puede definirse como el producto de un coeficiente de difusión efectivo, D_i, y un coeficiente de adsorción efectivo, S_i:

$$P_i = D_i \cdot S_i \qquad \textbf{Ecuación 1.15}$$

S_i indica cuanto gas puede retener la membrana en equilibrio con una fugacidad de gas dada, y D_i está relacionado con la movilidad de las moléculas penetrantes en la membrana. Para un par de gases *i*, *j* la selectividad, $\alpha_{i/j}$, se define de acuerdo con la **Ecuación 1.16**:

$$\alpha_{ij} = \left(\frac{D_i}{D_j}\right) \cdot \left(\frac{S_i}{S_j}\right) = \alpha_{ij}^{D} \cdot \alpha_{ij}^{S} \qquad \textbf{Ecuación 1.16}$$

α_{ij}^{D} se denomina selectividad por difusividad, D_i/D_j, y está relacionada con la rapidez con la que difunden los gases por la membrana debido a las diferencias en sus diámetros cinéticos. Por otro lado, α_{ij}^{S} es la selectividad por solubilidad S_i/S_j, y se debe a la adsorción preferencial de unos gases sobre otros. La solubilidad es un parámetro termodinámico que depende de tanto la capacidad de condensación del gas como de su afinidad con el polímero. Por el contrario, la difusividad es un parámetro cinético y depende del tamaño y forma de las moléculas gaseosas y de la movilidad y el grado de empaquetamiento de las cadenas poliméricas.[80]

El transporte de gases a través de una membrana mixta (MMM) consiste en una combinación del mecanismo de disolución–difusión en la fase continua polimérica y del transporte permeoselectivo en la fase discreta. En este último hay dos contribuciones a tener en cuenta: (i) las interacciones adsorbato-superficie, relativas a

la interacción física y química entre los gases y las partículas de relleno, y (ii) la exclusión por tamaños, relativas a las diferencias entre el tamaño de poro de las partículas de relleno y el tamaño y forma de las moléculas de gas.[81]

1.2.6. Adsorción de gas en polímeros

La adsorción de las moléculas de gas en polímeros se explica por el modelo de **adsorción dual**,[82,83] que consiste en una combinación de los modelos de Henry y Langmuir, de manera que las moléculas gaseosas pueden adsorberse de uno o dos modos. En los sitios de adsorción de Henry, las moléculas de gas experimentan mecanismos de disolución ordinarios en la matriz polimérica. En los de Langmuir, el polímero muestra procesos de relleno de cavidades. De acuerdo con las leyes de Henry y Langmuir (**Ecuación 1.17** y **Ecuación 1.18**), las concentraciones de gases, C_D y C_H son, respectivamente:

$$C_D = k_D p \qquad \textbf{Ecuación 1.17}$$

$$C_H = \frac{C'_H b p}{1 + bp} \qquad \textbf{Ecuación 1.18}$$

Combinado ambas ecuaciones se obtiene la concentración, C, global según el modelo de adsorción dual (**Ecuación 1.19**):

$$C = C_D + C_H = k_D p + \frac{C'_H b p}{1 + bp} \qquad \textbf{Ecuación 1.19}$$

donde, k_D es el coeficiente de la ley de Henry, y C'_H y b son la constante de saturación de hueco y el parámetro de afinidad de Langmuir, respectivamente. El parámetro k_D representa la cantidad de gas penetrante disuelto en la matriz polimérica en condiciones de equilibrio. El parámetro de solubilidad se obtiene dividiendo entre la presión como muestra la **Ecuación 1.20**:

$$S = \frac{C}{P} = S_D + S_H = k_D + \frac{C'_H b}{1 + b} \qquad \textbf{Ecuación 1.20}$$

donde S es la solubilidad del gas penetrante, y S_D y S_H, las solubilidades basadas en las leyes de Henry y Langmuir, respectivamente.

La solubilidad de un polímero está relacionada con su fracción de volumen libre.[84] La adsorción tipo Langmuir se da en polímeros por debajo de su temperatura de transición vítrea debido a la existencia de estados de no equilibrio con exceso de volumen libre. Por ello la solubilidad en polímeros termoplásticos es más alta que en elastómeros. Por otro lado, las constantes del coeficiente de la ley de Henry y las constantes de afinidad de Langmuir aumentan con la condensabilidad del gas que permea.[85]

1.2.7. Factores que afectan a las propiedades del transporte de gases en una membrana

- Tamaño de las moléculas gaseosas

El tamaño de las moléculas de gas afecta a los coeficientes de difusión, ya que las moléculas más pequeñas son las que más rápido difunden. El coeficiente de difusión es proporcional a la velocidad media y al camino libre medio de las moléculas gaseosas. De este modo los gases que mejor difunden son los que corresponden a moléculas con diámetros cinéticos compatibles con el tamaño de los huecos entre cadenas poliméricas. Los polímeros termoplásticos suelen tener las mayores selectividades debido a una gran selectividad por difusión. La **Tabla 1.6** muestra los diámetros cinéticos y las temperaturas críticas de gases comunes en procesos con membranas:[86]

Tabla 1.6. Listado con los diámetros cinéticos y las temperaturas críticas de diferentes gases.

	H_2	CO_2	O_2	N_2	CH_4
Diámetro cinético (nm)	0,289	0,330	0,346	0,364	0,380
Temperatura crítica, T_c (K)	33	304	155	126	191

Otro factor que influye en la difusión, además del tamaño de las moléculas, es su forma. Por ejemplo, las moléculas lineales tienen coeficientes de difusión más altos que otras con la misma masa molecular pero de forma esférica, y por tanto más voluminosas, como ocurre con el CO_2.[87] La relación entre el coeficiente de difusión, D, y el volumen crítico del gas penetrante (o volumen de van der Waals, V_c), se da según la **Ecuación 1.21**:[88]

$$D = \frac{\tau}{V_c^{\eta}}$$ **Ecuación 1.21**

donde τ y η son parámetros específicos de cada gas.

- Condensabilidad de los gases

La condensabilidad de los gases afecta a la solubilidad de los mismos en el polímero. La solubilidad aumenta cuanta más alta es la condensabilidad de los gases, que viene dada por su temperatura crítica. La separación de mezclas CO_2/N_2 y CO_2/CH_4 es relativamente sencilla porque en ambos casos el CO_2 difunde más rápido y muestra una solubilidad mayor que los otros dos gases. Por lo que tanto la selectividad por difusión como por solubilidad se ven favorecidas. Sin embrago, la separación de gases se vuelve complicada cuando hay un efecto competitivo entre la difusión y la solubilidad. Es el caso de la mezcla H_2/CO_2, típica de los procesos de captura en precombustión. El H_2 difunde más rápido por su menor diámetro cinético, pero el CO_2 es un gas más condensable, y su solubilidad en el polímero es mayor. Trabajar a temperaturas elevadas favorece la selectividad por difusión pero penaliza la selectividad por disolución, y viceversa. Esto hace que para algunos polímeros, como el polibenzimidazol, se encuentre una temperatura de operación intermedia con un valor de selectividad óptimo.[89]

- Presión de operación

La presión de alimentación influye en la adsorción de los gases en la matriz polimérica de la membrana. El efecto de la presión sobre la difusión es diferente para gases condensables que para los no condensables. Para los gases no condensables el incremento de presión no tiene apenas efecto en la permeabilidad. Sin embargo, para los gases condensables, un aumento en la presión de alimentación conlleva un aumento de la permeabilidad. De hecho, cuando la presión aumenta hasta un valor determinado puede producirse el fenómeno de plastificación (fenómeno descrito en la página 43).

- Temperatura de operación

La temperatura es un factor que afecta tanto a la difusión como a la solubilidad de los gases. La difusión es un fenómeno cinético relacionado con la velocidad con la que las moléculas de gas atraviesan la membrana. La relación del coeficiente de difusión con la temperatura viene dada por la ecuación de Arrhenius (**Ecuación 1.22**):

$$D = D_0 \, exp\left(-\frac{E_D}{RT}\right) \qquad \textbf{Ecuación 1.22}$$

donde D_O es un factor pre-exponencial, E_D la energía de activación de la difusión, R la constante universal de los gases y T la temperatura. Por otro lado la solubilidad es un parámetro termodinámico y su variación con la temperatura sigue la ley de van't Hoff (**Ecuación 1.23**).

$$S = S_0 \, exp\left(-\frac{\Delta H_S}{RT}\right) \qquad \textbf{Ecuación 1.23}$$

donde S_O es una constante y ΔH_S la entalpía de adsorción. Dado que la permeabilidad es el producto de la difusión y la solubilidad, las dos ecuaciones pueden englobarse como muestra la **Ecuación 1.24**:

$$P = P_0 \, exp\left(-\frac{E_P}{RT}\right) \qquad \textbf{Ecuación 1.24}$$

donde $P_O = D_O \cdot S_O$ es una constante y $E_P = E_D + \Delta H_S$ es la energía de activación de la permeación. Normalmente un aumento de la temperatura conlleva un aumento del coeficiente de difusión y una disminución de la solubilidad. Pero como el valor absoluto de E_P suele ser mayor que el de ΔH_S, la permeación de las membranas aumenta con la temperatura para la mayoría de los polímeros.[90]

- Volumen libre

La fracción de volumen libre (FFV) del polímero influye en la difusión de los gases. Cuanto mayor es este volumen libre, mayor es el coeficiente de difusión, y por tanto, mayor la permeabilidad del polímero, tal y como muestra la **Ecuación 1.25**:[91]

$$D = A\,exp\left(-\frac{B}{FVV}\right)$$ **Ecuación 1.25**

donde A y B son constantes específicas de cada polímero.

- Movilidad de las cadenas poliméricas

La movilidad de las cadenas poliméricas afecta al coeficiente de difusión de los gases penetrantes. Esta movilidad es importante ya que debe haber espacio suficiente entre los segmentos de polímero para permitir el paso de las moléculas de gas. Por ejemplo, la presencia de grupos aromáticos rígidos reduce la movilidad de las cadenas haciendo disminuir la permeabilidad de las membranas.[92]

1.2.8. Modelos de permeación para membranas mixtas con materiales de relleno porosos: modelos ideales

Los modelos de permeación para membranas mixtas con materiales de relleno porosos se utilizan para predecir la permeabilidad de los gases en membranas de este tipo. Para ello los modelos utilizan tres parámetros: la permeabilidad de la fase continua (polímero), P_c, la permeabilidad de la fase dispersa (material de relleno), P_d, y la fracción volumétrica de cada fase, Φ.

La permeabilidad efectiva de un gas en una membrana mixta, P_{eff}, viene dada por modelos de dos resistencias. El valor mínimo de P_{eff} se da cuando el mecanismo de transporte a través de la membrana equivale a un modelo de resistencias en serie (**Ecuación 1.26**):

$$P_{eff} = \frac{P_c P_d}{\Phi_c P_d + \Phi_d P_c}$$ **Ecuación 1.26**

Por el contrario, cuando se asume que las dos fases trabajan en paralelo a la dirección del flujo de gas se obtiene el valor máximo de la **Ecuación 1.27**:

$$P_{eff} = \Phi_c P_c + \Phi_d P_d$$ **Ecuación 1.27**

El modelo de media geométrica asume la distribución aleatoria de las fases y la permeabilidad efectiva se calcula como la media geométrica de la permeabilidad de ambas según la **Ecuación 1.28**:[93]

$$P_{eff} = P_c^{\Phi_c} P_d^{\Phi_d} \qquad \textbf{Ecuación 1.28}$$

Maxwell utilizó la teoría de potenciales eléctricos a través de un medio heterogéneo para obtener un modelo que describe el flujo de gas a través de una membrana mixta compuesta por una distribución homogénea de partículas esféricas que no contactan entre sí (**Ecuación 1.29**).[94]

$$P_{eff} = P_c \cdot \frac{P_d + 2P_c - 2\Phi_d(P_c - P_d)}{P_d + 2P_c + \Phi_d(P_c - P_d)} \qquad \textbf{Ecuación 1.29}$$

Este modelo de Maxwell solo es aplicable a membranas mixtas cuyo relleno son partículas esféricas y para cargas bajas (hasta el 20 % vol.). El modelo de Maxwell-Wagner-Sillar,[94] mostrado en la **Ecuación 1.30**, permite calcular la permeación de una membrana mixta donde el material de relleno son elipsoides:

$$P_{eff} = P_c \cdot \frac{n \cdot P_d + (1-n)P_c + (1-n)(P_d - P_c) \cdot \Phi_d}{n \cdot P_d + (1-n)P_c - n(P_d - P_c) \cdot \Phi_d} \qquad \textbf{Ecuación 1.30}$$

donde *n* corresponde al factor de forma del material de relleno. Es un modelo que supone una ampliación del anterior, ya que acepta partículas de diferentes geometrías. Para n=1/3, las partículas son esféricas y la expresión se reduce a la ecuación de Maxwell (**Ecuación 1.29**).

Otros modelos alternativos que permiten estimar el flujo en membranas mixtas son los de Böttcher e Higuchi[95], Chiew y Glandt [96] o la ecuación de Bruggeman,[97] (**Ecuación 1.31**) precisa hasta cargas del 60 % vol.

$$\left(\frac{P_{eff}}{P_c}\right)^{-1/3} \left[\frac{P_{eff}/P_c - P_d/P_c}{1 - P_d/P_c}\right] = (1 - \Phi_d) \qquad \textbf{Ecuación 1.31}$$

1.2.9. Modelos de permeación para membranas mixtas con materiales de relleno porosos: Desviación de las predicciones teóricas

Para que una membrana mixta tenga un rendimiento de separación adecuado es necesaria una buena interacción entre el material de relleno y la matriz polimérica, sin que existan huecos no selectivos entre ambas fases y sin que los poros del material de relleno estén bloqueados al flujo de gas. Además, las partículas del material de relleno deben estar homogéneamente distribuidas a lo largo de la sección de la membrana para que su efecto sea máximo. Sin embargo, existen varios casos de imperfecciones que pueden darse en estos materiales compuestos, y que provocan que el transporte de gases a través de las membranas se aleje de las predicciones de los modelos ideales anteriores. A continuación se explican los casos que causan estas discrepancias:[98]

- Caso 1: mala interacción entre el material de relleno y la matriz polimérica

Si la interacción material de relleno-polímero es pobre, las cadenas poliméricas no se adhieren completamente a la superficie de los materiales de relleno, dando lugar a la formación de canales preferentes entre ambas fases. En este caso, la permeabilidad del gas en la fase dispersa y alrededor de las partículas en mucho mayor que en la fase continua ($P_d >> P_c$) y la **Ecuación 1.29** se transforma en esta otra:

$$P_{eff} = P_c \left[\frac{1 + 2\Phi_d}{1 - \Phi_d}\right] \qquad \textbf{Ecuación 1.32}$$

La formación de huecos no selectivos en la interfase permite un flujo cortocircuitado de gas alrededor de las partículas de material de relleno. A cargas bajas esto conlleva un aumento de la permeabilidad mientras la selectividad se mantiene constante. Sin embargo, a cargas elevadas se produce un descenso en la selectividad de la membrana, y con ello empeora el rendimiento de la separación.[99]

- Caso 2: bloqueo de los poros del material de relleno

El bloqueo, bien sea parcial o total, de la porosidad de las partículas del material de relleno por parte de la fase polimérica provoca que la permeabilidad de la fase

dispersa sea mucho menor que la de la fase continua (Pd<<Pc), con lo que la ecuación de Maxwell (**Ecuación 1.29**) cambia a la siguiente expresión:

$$P_{eff} = P_c \left[\frac{P_c - \Phi_d P_c}{P_c + 0{,}5\Phi_d P_c}\right] \qquad \textbf{Ecuación 1.33}$$

Esto significa que las partículas de material de relleno son obstáculos impermeables al flujo y su adición a la fase polimérica no supone ningún cambio en las propiedades de transporte de la membrana. Aunque puede ocurrir que la adición de estas partículas de relleno afecte al empaquetamiento de las cadenas poliméricas, lo que influenciaría indirectamente a la permeabilidad.[100]

- Caso 3: misma permeabilidad de las fases continua y dispersa

Si la permeabilidad de la fase continua es exactamente igual que la de la fase dispersa (P_c=P_d), la **Ecuación 1.29** se simplifica a la siguiente expresión:

$$P_{eff} = P_c \qquad \textbf{Ecuación 1.34}$$

Esto significa que la presencia del material de relleno no tiene influencia en las propiedades de transporte de una membrana para un gas concreto. En este caso, la membrana mixta mostrará una permeabilidad idéntica que la de una membrana de polímero puro, aunque la selectividad podría ser diferente ya que los diferentes gases pueden ser afectados de manera diferente por la presencia de las partículas de relleno.

- Caso 4: rigidificación del polímero

Se produce cuando las cadenas poliméricas en contacto con las partículas de material de relleno pierden su movilidad respecto a las del resto del polímero. Esto afecta negativamente a la permeabilidad de los gases, que disminuye, pero dado que afecta a los dos gases que permean, en algunos casos puede producir un aumento de la selectividad.[101]

1.3. Materiales metalorgánicos

Este apartado describe la naturaleza y propiedades de los materiales metalorgánicos para explicar su utilidad en la separación de gases. Se profundizará en concreto en los *zeolitic imidazolate frameworks (ZIFs)*, que se integran en la subfamilia de estos materiales que más se van a utilizar en esta tesis doctoral.

1.3.1. Concepto de material metalorgánico (MOF)

Los compuestos metalorgánicos porosos, del inglés *metalorganic frameworks (MOFs)*, también denominados polímeros de coordinación, son una familia de materiales porosos cristalinos cuyos primeros trabajos se publicaron a finales de los 90.[102-105] Están formados por iones o clústeres metálicos coordinados con ligandos orgánicos multidireccionales que actúan como enlazadores en estructuras de red 1-D, 2-D ó 3-D.

Los MOF son materiales con gran superficie específica, como demuestran los grandes valores de área BET que poseen, por ejemplo, MOF-177 (4500 m^2/g),[106] MOF-210 (6240 m^2/g)[107] o MIL-101 (4230 m^2/g).[108] Pero sin duda la mayor ventaja de los MOF respecto de otros materiales porosos es la posibilidad de ajustar el tamaño y la forma de sus poros, desde el rango de los microporos a los mesoporos, lo que genera materiales adecuados para aplicaciones concretas. Esto se consigue cambiando el tipo de ligando orgánico o su coordinación con los centros metálicos. Por ejemplo, la elección adecuada del ligando orgánico posibilita determinar el tamaño, la forma y funcionalidad química de las cavidades de la superficie interna.[109] Todas estas propiedades hacen que los MOF sean compuestos interesantes con aplicaciones potenciales en energía limpia: adsorción y separación de gases de gases[110-112] y su uso en membranas; además de otras relacionadas con la catálisis[113,114] o la liberación de fármacos.[115]

El proceso de síntesis de cualquier MOF consta de tres etapas diferenciadas:

- Disolución de la fuente de metal (generalmente una sal) y del ligando orgánico en un disolvente afín.
- Reacción: ambas disoluciones se mezclan y se da lugar la reacción de cristalización. Dependiendo de los medios de reacción, la síntesis puede ser

hidrotermal, solvotermal, en microondas, electroquímica, mecánica, por ultrasonidos... etc.

- Activación: consiste en la eliminación de los restos de ligando que no han reaccionado, así como las moléculas huésped de disolvente que se encuentran atrapadas en el interior de los poros de los MOF. La activación se suele dar por intercambio líquido-líquido con disolventes de menor punto de ebullición y/o térmicamente. La correcta activación de los MOF es lo que determina su superficie específica y la accesibilidad a sus poros.

La naturaleza parcialmente orgánica de estos compuestos permite una buena interacción con las cadenas poliméricas, también de naturaleza orgánica, al formar membranas mixtas.

1.3.2. Zeolitic imidazolate framewoks (ZIFs)

Dentro de los MOF destaca una subfamilia denominada *zeolitic imidazolate framewoks* (ZIFs), que se podría traducir como "compuestos de tipo zeolítico basados en imidazolatos". Estos MOF fueron descubiertos en paralelo e independientemente por los grupos de Yaghi[116] y Chen,[117] y reciben su nombre porque forman estructuras cristalinas con topologías similares a las de las zeolitas (SOD, RHO, LTA...). Están formados por iones de Zn(II) o Co(II) coordinados tetraédricamente con los átomos de nitrógeno de moléculas de imidazol (ligando orgánico),[118] donde el enlace metal-imidazolato-metal forma un ángulo aproximado de 145°, análogo al que se da en el enlace O-Si-O de las zeolitas,[119] como puede verse en la **Figura 1.16.**

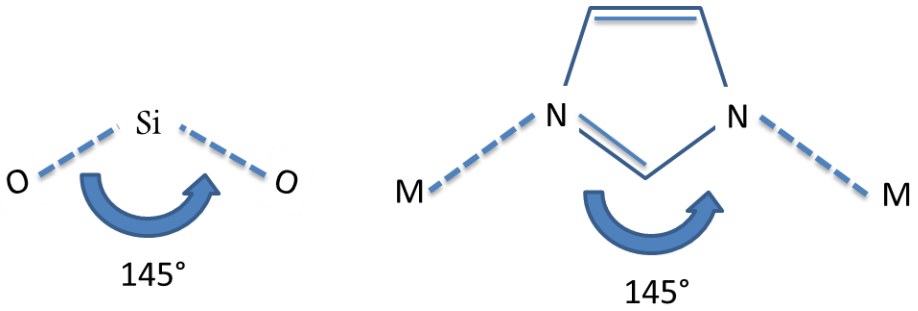

Figura 1.16. Esquema general de la estructura química de un ZIF.

El tipo de ligando orgánico utilizado así como su funcionalización influye en la topología de los cristales y en el tamaño de los poros.[120] La microporosidad de estos

materiales sumado a la escasa adsorción de CO_2 que presentan,[121] hace que sean los materiales ideales para mejorar el rendimiento de las membranas por tamizado molecular en los procesos de separación de CO_2. A continuación, se detallarán los diferentes ZIF utilizados en esta tesis doctoral para la preparación de membranas mixtas:

- ZIF-7

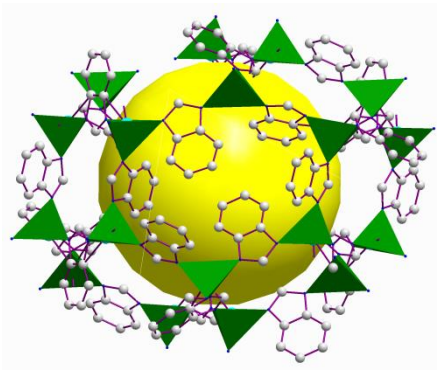

Figura 1.17. Esquema del ZIF-7. Esta estructura ha sido representada con el programa Diamond 3.2 utilizando el correspondiente fichero CIF.[122]

Se trata de un MOF compuesto por átomos de Zn(II) coordinados con ligandos benzimidazolato (bIm), tal y como muestra la **Figura 1.17**. Su fórmula molecular es $Zn(bIm)_2$ y su masa molar puede estimarse como 301,56 g/mol. Cristaliza formando una estructura tipo **sod** y posee poros de 0,43 nm conectados por ventanas de poro de 0,30 nm.[123] Esta distribución porosa tan pequeña hace que este material sea interesante para la separación de H_2 respecto de otros gases de tamaño mayor. La síntesis original se llevó a cabo en DMF[116] para obtener cristales con tamaños de micras. Más adelante se consiguió su síntesis en EtOH[123] con ese mismo tamaño, e incluso reducirla a tamaño nanométrico, de nuevo en DMF.[124]

Se ha reportado que el ZIF-7 presenta tres fases diferentes: ZIF-7(I), ZIF-7(II) y ZIF-7(III). El ZIF-7(I) corresponde al MOF original, cuya descripción es la dada anteriormente. El ZIF-7(II) es un ZIF-7 con una distribución de poro más estrecha y se considera que es un ZIF-7(I) distorsionado. Este material se obtiene mediante una transición de fase en la que el ZIF-7(I) pierde las moléculas de DMF alojadas en el interior de su estructura a altas temperaturas. Este cambio puede revertirse sumergiendo el ZIF-7 en DMF, con lo que vuelve a la estructura del ZIF-7(I).[122]

También se ha observado que esta transición puede darse con la adsorción de CO_2. Aguado y cols.[125] descubrieron que la transición de fases de ZIF-7(I) a ZIF-7(II) explica el fenómeno de "respiración" que se observa durante la adsorción de este gas, es decir, la estructura es capaz de hincharse dilatando los poros para permitir la entrada de moléculas de gas con un tamaño mayor que el de la ventana de poro. Es un comportamiento que se da en otros MOF, como el MIL-53,[126] y que refleja la flexibilidad de estas estructuras.

Finalmente, el ZIF-7(III) es la fase más densa del ZIF-7. Se obtiene al poner en contacto el ZIF-7(I) o el ZIF-7(II) con un disolvente polar (agua, metanol...) a alta temperatura, siendo esta transición de fase irreversible. Se trata de un material laminar cuya apertura de poro se estima en 0,21 nm, considerablemente menor que la del ZIF-7(I). Este material se ha conseguido exfoliar mostrando resultados muy interesantes en la separación del mezclas H_2/CO_2.[127] Las transiciones de fase del ZIF-7 se esquematizan en la **Figura 1.18**.

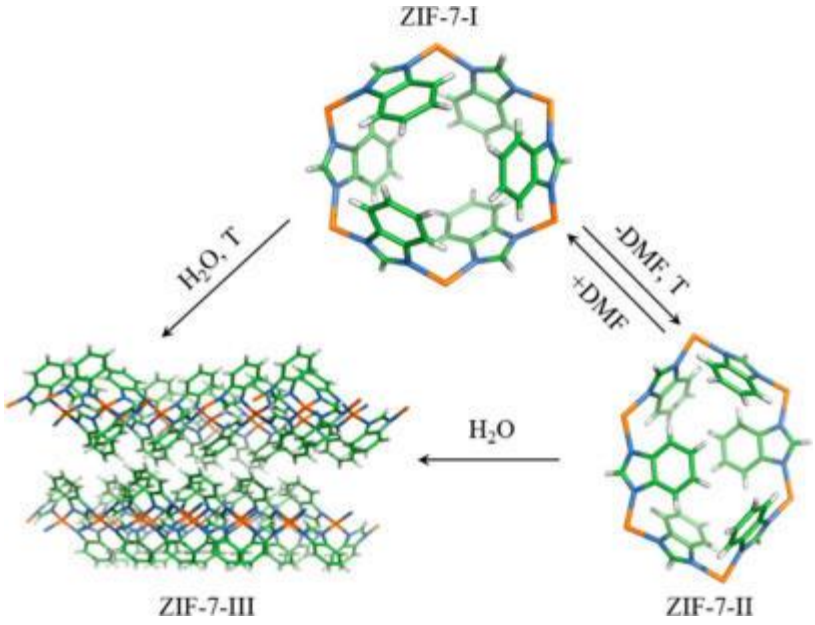

Figura 1.18. Esquema de las transiciones de fase del ZIF-7[122]. *Reprinted with permission from Chem. Mater.* ***2014*** *26 (5), 1767-1769.* ***DOI:*** *10.1021/cm500407f. Copyright 2014. American Chemical Society.*

- ZIF-8

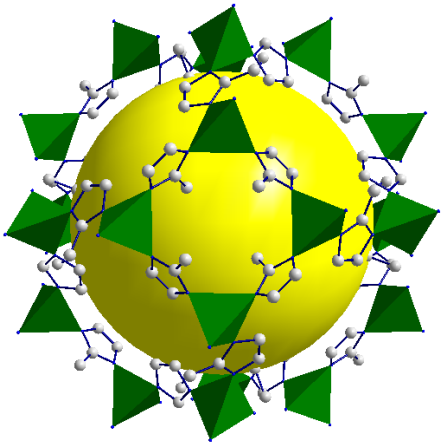

Figura 1.19. Esquema del ZIF-8. Esta estructura ha sido representada con el programa Diamond 3.2 utilizando el correspondiente fichero CIF (CCDC code VELVOY).[116]

El ZIF-8 es probablemente el ZIF más desarrollado en la bibliografía en lo que a caracterización, simulación y aplicaciones se refiere. De hecho, es uno de los pocos MOF que estan disponibles comercialmente. Lo comercializa BASF con el nombre de Basolite® Z1200.

Este compuesto está formado por átomos de Zn(II) coordinados con ligandos 2-metilimidazolato (mIm), como se muestra en la **Figura 1.19**. Su fórmula molecular es $Zn(mIm)_2$ y su masa molar es de 229,50 g/mol. Cristaliza formando una estructura **sod** y posee poros de 1,16 nm conectados por ventanas de poro de 0,34 nm. Es un MOF con una extraordinaria resistencia química, ya que se ha demostrado que es capaz de permanecer inalterado tras sumergirse en metanol, benzeno o agua hirviendo durante 7 días o hidróxido de sodio concentrado durante 24 h.[116]

Desde que el ZIF-8 se obtuvo por primera vez mediante síntesis solvotermal,[116, 117] han aparecido nuevas rutas de síntesis para este material, entre las que destacan las síntesis: por microondas,[128] por ultrasonidos,[129] electroquímica,[130] mecánica,[131] conversión sol-gel[132] y microfluídica.[133] El uso de diferentes disolventes y métodos ha dado lugar a un amplio rango de tamaños de partícula, desde la escala nanométrica a la micrométrica.

Una de las propiedades más destacadas del ZIF-8 es el llamado "*gate-opening*". Este fenómeno implica que durante la adsorción de gases ciertos enlaces en el poro son capaces de romperse al alcanzar una determinada presión, dejando entrar a moléculas

de gas cuyo diámetro cinético es mayor que la ventana de poro. Esto explica como el ZIF-8 es capaz de mostrar adsorción de N_2, un gas con un diámetro cinético de 0,36 nm frente a los 0,34 nm de ventana de poro del ZIF.

- ZIF-11

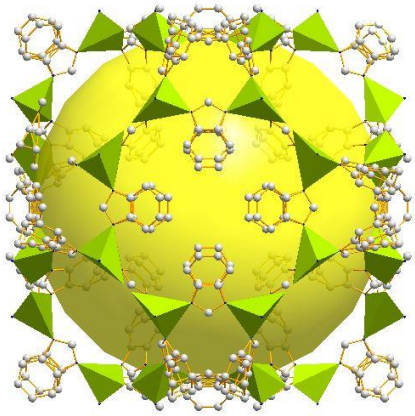

Figura 1.20. Esquema del ZIF-11. Esta estructura ha sido representada con el programa Diamond 3.2 utilizando el correspondiente fichero CIF (CCDC code VEJZOA).[116]

El ZIF-11 es un material que posee la misma composición química que el ZIF-7, es decir, está también compuesto por átomos de Zn(II) coordinados con ligandos benzimidazolato. Sin embargo, en este caso el material cristaliza formando una estructura tipo **rho**, como puede verse en la **Figura 1.20**, lo que hace que aunque las ventanas de poro sean igual que las del ZIF-7 (0,30 nm) sus cavidades sean más grandes (1,46 nm).[123] La proximidad de las aperturas de poro al diámetro cinético del hidrógeno (0,29 nm) hace que este material sea ideal para el tamizado molecular de este gas respecto de otros con diámetros cinéticos superiores. De hecho, simulaciones moleculares han estimado que el ZIF-11 presenta una permeabilidad de 5830 Barrer de H_2 y una selectividad H_2/CO_2 de 262,[134] convirtiéndolo en un buen candidato para la captura de CO_2 en procesos de precombustión.

A día de hoy solo pueden encontrarse síntesis de ZIF-11 para partículas de tamaño micrométrico. Entre ellas aparecen rutas solvotermales,[116, 135] hidrotermales[123] y por ultrasonidos.[136] Al igual que ocurre con el ZIF-7, este ZIF es capaz de transformarse en una fase densa cuando se pone en contacto con medios polares, bien durante su síntesis[137] o tras ella.[116]

- ZIF-93

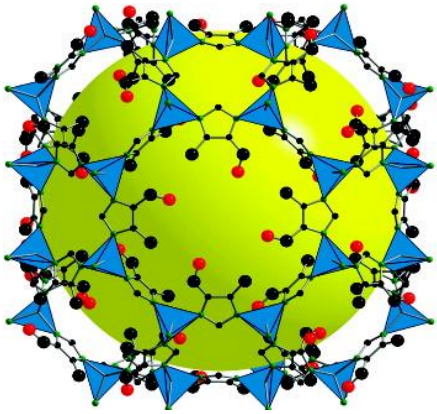

Figura 1.21. Esquema del ZIF-93.[138] *Reprinted with permission from J. Am. Chem. Soc.* ***2010****, 132, 11006-11008.* ***DOI:*** *10.1021/ja104035j. Copyright 2010. American Chemical Society.*

El ZIF-93 es un material con estructura **rho** constituido por iones de Zn(II) coordinados con ligandos 4-metil-5-imidazolatocarboxialdehído (almeIm), que le confieren un tamaño de poro de 0,36 nm.[139] Su fórmula molecular es $Zn(almeIm)_2$ y su masa molar es de 283,72 g/mol. La síntesis original se obtuvo en DMF para dar lugar a cristales micrométricos,[138] pero también pueden encontrarse en la literatura recetas para sintetizar cristales con tamaño de nanómetos en MeOH.[140]

La **Tabla 1.7** muestra un resumen con las propiedades de los diferentes ZIF explicados.

Tabla 1.7. Resumen de las propiedades físicas de los diferentes ZIFs.

ZIF	Metal	Ligando	Estructura	Densidad (g/mL)	Ventana de poro (nm)
ZIF-7	Zn (II)	bIm	**sod**	1,24	0,30
ZIF-7(III)	Zn (II)	bIm	**mon**	1,58	0,21
ZIF-8	Zn (II)	mIm	**sod**	1,30	0,34
ZIF-11	Zn (II)	bIm	**rho**	1,10	0,30
ZIF-93	Zn (II)	almeIm	**rho**	-	0,36

1.3.3. ZIF híbridos

Desde su aparición en los años 90, se ha reportado un gran número de síntesis de nuevos ZIF. Esto hace que en la actualidad sea complicado encontrar nuevas estructuras, y por ello, muchas investigaciones se centran en la síntesis de compuestos híbridos, creando estructuras que permitan combinar las propiedades ventajosas de cada MOF por separado. En lo que a la separación de gases se refiere, resulta

interesante combinar diferentes ligandos orgánicos dentro de la misma estructura para modificar el tamaño de poro de los MOF, ajustándolo al rango adecuado en función de la mezcla gaseosa a separar.

Esta mezcla de ligandos puede encontrarse en la literatura en la síntesis directa por vía solvotermal de ZIF híbridos. Thompson y cols.[141] publicaron la síntesis de los híbridos ZIF-7/90 y ZIF-7/8. En su trabajo, los ZIF híbridos se obtuvieron haciendo reaccionar en una mezcla de MeOH y DMF las cantidades adecuadas de la fuente de metal y ambos ligandos: benzimidazolato y carboxialdehido-2-imidazolato para el ZIF-7/90 y bezilimidazolato y 2-metilimidazolato para el ZIF-7/8. El híbrido ZIF-7/8 también se ha sintetizado en su variante que utiliza Co(II) como fuente de metal (ZIF-9/67[142]) y mediante síntesis por microondas, con la que se redujo el tiempo de síntesis a solo 90 s.[143] Como resultado se obtuvieron ZIF híbridos con diferente proporción de ligandos en su estructura en función de las cantidades añadidas al medio de reacción. También las series del ZIF-68 al ZIF-70,[144] del ZIF-78 al ZIF-82[145] y del ZIF-300 al ZIF-302[146], constituyen ZIF hibridos con una mezcla de ligandos en su estructura. Los últimos forman una estructura tipo **cha** y los dos primeros una tipo **gme**. Todos ellos combinan 2-metilimidazolato o NO_2-metilimidazolato con derivados de benzimidazolato.

Sin embargo, problemas derivados de la solubilidad limitada de los ligandos orgánicos, la baja estabilidad térmica y/o química o la mala compatibilidad entre grupos funcionales pueden hacer que la síntesis directa de un material híbrido sea imposible. De este modo, la modificación postsintética aparece como una alternativa útil, una técnica que consiste en modificar la estructura del MOF una vez sintetizado. Mediante este tipo de síntesis se pueden obtener materiales de alta complejidad y gran funcionalidad, siempre que el MOF no se destruya durante la reacción química.

La modificación postsintética de un MOF puede clasificarse en dos tipos: covalente o dativa, en función de los enlaces que se forman o rompen en el proceso, aunque también pueden darse las dos a la vez.[147] La **modificación postsintética covalente** se define como el uso de un reactivo para modificar un componente del MOF tras la síntesis del mismo, formando un nuevo enlace covalente. Por lo general, el objetivo es modificar el ligando orgánico del MOF original para funcionalizarlo. Por otro lado, la

modificación postsintética dativa consiste en utilizar un reactivo que forma un enlace dativo con algún componente del MOF. Normalmente se utiliza un metal o ligando que se añade a la estructura del MOF original. Un esquema de ambos tipos puede verse en la **Figura 1.22**.

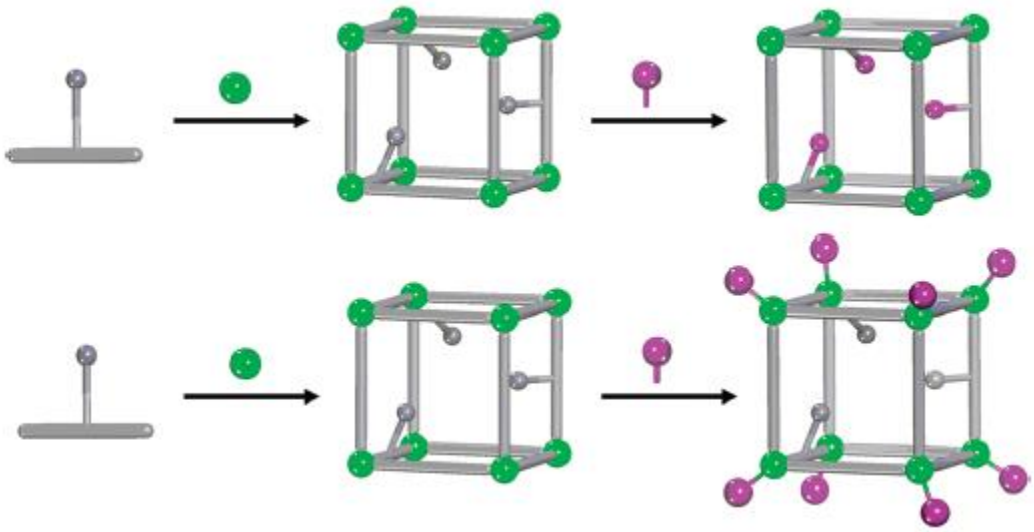

Figura 1.22. Esquema de modificación postsintética covalente (arriba) y dativa (abajo).[147] *Reprinted with permission from Chem. Rev., **2012**, 112 (2), pp 970–1000. **DOI:** 10.1021/cr200179u. Copyright 2012. American Chemical Society.*

Cuando la modificación postsintética se produce de fuera a dentro de la partícula puede formarse un tipo de estructura híbrida especial con estructura núcleo-cáscara o *core-shell*, como se esquematiza en la **Figura 1.23**. En ella, el MOF original se encuentra en el interior de la partícula híbrida (núcleo), mientras que las moléculas añadidas durante la modificación postsintética se asientan en el exterior, formando la corteza.

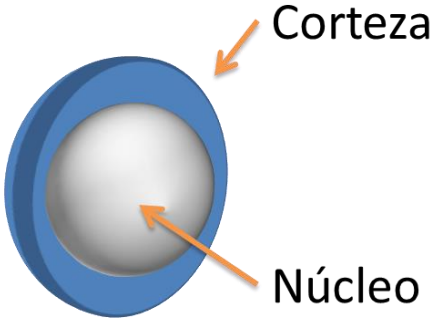

Figura 1.23. Esquema de la estructura de una *core-shell*.

La modificación postsinética se ha aplicado con éxito a un gran número de MOF, como: IRMOF-3[148-153], MIL-53(Al),[154] MIL-53(Al)-NH_2,[155-157] MIL-101(Fe)-NH_2,[158] MIL-101(Cr),[159] UiO-66-NH_2,[160, 161] UiO-66-Br,[162] HKUST-1.[105] Dentro de la familia de los ZIF, el ZIF-90 y el SIM-1 (también conocido por ZIF-94) se han modificado también mediante esta técnica. El ZIF-90 se ha transformado en ZIF-91, y posteriormente en ZIF-92 mediante una reacción en MeOH a 60 °C, utilizando disoluciones de $NaBH_4$ y etanolamina, respectivamente.[163] El SIM-1 se ha tratado con dodecilamina en MeOH anhidro a temperatura ambiente para generar SIM-2(C_{12})[164] y también con alquilaminas para obtener el ZIF-93.[165] Además de estos dos materiales, Liu y cols.[166] modificaron el ZIF-8 mediante una reacción de intercambio de ligandos utilizando diferentes compuestos orgánicos derivados del imidazol, obteniendo estructuras de tipo *core-shell* que mejoraban la estabilidad hidrotermal del ZIF-8, ya que se prevenía la densificación del mismo.

1.3.4. Membranas de MOF puro

Es posible fabricar membranas formadas únicamente por MOF haciendo cristalizar estos materiales en forma de capas continuas sobre soportes cerámicos o poliméricos, tanto planos como tubulares. Existen diferentes técnicas que permiten formar capas continuas de MOF como: la deposición capa a capa, la siembra reactiva, el uso de esprai, la síntesis por microondas o la contradifusión.[167-170] Respecto a los ZIF, en la bibliografía pueden encontrarse membranas soportadas de: ZIF-7, ZIF-8, ZIF-22, ZIF-69 y ZIF-90 aplicadas para la separación de mezclas de CO_2. Los resultados más representativos aparecen recogidos en la **Tabla 1.8**. Como puede verse, las selectividadades obtenidas de CO_2 respecto de otros gases son bastante limitadas, pero cabe destacar entre ellos algún resultado positivo. Por ejemplo, Li y cols.[124] prepararon membranas continuas de ZIF-7 sobre soportes de alúmina que mostraron buenos resultados de separación de mezclas H_2/CO_2. A 220 °C la membrana alcanzó una permeación de H_2 de $4{,}5x10^{-8}$ mol m^{-2} s^{-1} Pa^{-1} y una selectividad H_2/CO_2 de 13,6. También destacan las membranas de ZIF-90 fabricadas por Huang y cols.[163] El uso de 3-aminopropiltrietoxisilano (APTES) como enlace covalente entre el ZIF y el soporte de alúmina permitió mejorar la selectividad de las membranas, especialmente para la mezcla H_2/CO_2, cuya selectividad se triplicó, alcanzando valores de 21. Es interesante

cómo la fácil cristalización de algunos de estos ZIF ha permitido preparar membranas continuas sobre soportes poliméricos de fibra hueca.[171–173]

Tabla 1.8. Resultados de separación de gases con membranas de MOF puro.

Año de publicación y ref.	MOF	Soporte	T (°C)	P alimentación	Permeación (x10^{-7} mol m^{-2} $s^{-1}Pa^{-1}$)		Selectividad		
					H_2	CO_2	H_2/CO_2	CO_2/N_2	CO_2/CH_4
2010[124]	ZIF-7	Disco de Al_2O_3	220	1 bar	0,45	0,03	13,6	1,3	1,0
2016[174]	ZIF-8	Fibra de silicon nitride	25	2,5 bar	4,0	0,34	11,7*	–	–
2016[175]	ZIF-8	Fibra Al_2O_3–ZnO	25	1 bar	18,0	3,2	5,7	1,8	2,1
2013[176]	ZIF-8	HCT tubular	25	1 bar	7,3	1,4	5,4	1,7	2,0
2012[177]	ZIF-8	cerámica YSY tubular	22	1 bar	15,4	4,0	3,9	2,9	3,3
2011[178]	ZIF-8	Disco de α-Al_2O_3	22	1 bar	3,6	1,3	2,8	1,2	1,6
2009[179]	ZIF-8	Disco de TiO_2	25	1 bar	0,50	–	4,5	–	–
2009[180]	ZIF-8	α- Al_2O_3 tubular	25	1 bar	–	240	–	–	7,0*
2017[181]	ZIF-9 (III)	Ni poroso	-10	1,3 bar	0,34	–	22,2	–	–
2010[182]	ZIF-22	Disco de TiO_2	50	1 bar	1,9	0,30	7,2	1,2	1,0
2010[183]	ZIF-69	Disco de Al_2O_3	25	1 bar	–	0,36	–	–	3,3
2012[163]	ZIF-90**	Disco de Al_2O_3	225	1 bar	3,0	0,14	21,6	–	3,7
2010[184]	ZIF-90	Disco de Al_2O_3	200	1 bar	7,2	0,99	7,3	1,7	2,2
2014[185]	ZIF-7	Fibra hueca de PSF	35	1 bar	0,02	–	2,4*	13,6*	13,5*
2014[185]	ZIF-8	Fibra hueca de PSF	35	1 bar	0,05	–	2,6*	7,1*	6,1*
2012[186]	ZIF-8	Polietersulfona	100	1,5 bar	4,0	–	10,8	–	–
2017[187]	ZIF-8/ZIF-9	P84®	150	1 bar	0,84	–	9,6	–	–
2012[188]	ZIF-90	Torlon	35	1 bar	1,9	–	1,8	3,5	1,5

*Mezcla equimolar

** Posfuncionalizado con 3-aminopropiltrietoxisilano (APTES)

Respecto a este tipo de membranas de MOF puro destaca una investigación muy novedosa desarrollada recientemente en el grupo de Caro sobre las denominadas *Polymer-Stabilized Percolation Membranes (PSPMs)*.[189] Estas membranas están fomadas por partículas de materiales microporosos agregados por compresión y cohesionados entre sí gracias al poder aglutinante de una resina epoxi impermeable al flujo de gas. Esta investigación supone una técnica de preparación para este tipo de membranas muy diferente a las mencionadas anteriormente. En su trabajo desarrollaron membranas con MIL-140A, las cuales medidas a 1 bar y 25 °C para una mezcla de gases H_2/CO_2 (50/50 v/v) arrojaron valores de permeación de H_2 de $2x10^{-8}$ mol m^{-2} s^{-1} Pa^{-1} y selectividades H_2/CO_2 de 8,0. También prepararon membranas con ZIF-8. En este caso se obtuvieron valores de $9x10^{-10}$ mol m^{-2} s^{-1} Pa^{-1} de H_2 y una selectividad H_2/CO_2 de 8,2.

1.4. Materiales poliméricos

Los polímeros son los materiales actualmente más desarrollados para la fabricación de membranas comerciales. Estos materiales se pueden clasificar en dos grandes grupos en función de su temperatura de transición vítrea (Tg) en comparación con la temperatura de operación: **termoplásticos y elastómeros**. Los **elastómeros** son polímeros cuya Tg es inferior a la temperatura de operación. Son polímeros de tipo gomoso que cuentan generalmente con un gran volumen libre (la fracción de volumen no ocupada por nubes de electrones de las moléculas de polímero), lo que hace que sus permeabilidades sean generalmente altas. El mecanismo de separación de estas membranas se debe principalmente a diferencias en la solubilidad de los gases. De este modo los gases más condensables, como el CO_2, son los que más permean. En la captura de CO_2, estos gases resultan apropiados para la separación de mezclas CO_2/N_2 y CO_2/CH_4. No así para la mezcla H_2/CO_2, para la que se suelen obtener selectividades inferiores a la unidad. Los **termoplásticos**, por otro lado, son polímeros cuya Tg es superior a la temperatura de operación. Al contrario que los elastómeros, muestran estructuras más compactas con un volumen libre mucho menor. Este mayor empaquetamiento hace que la separación de gases se dé principalmente por diferencias en la difusión entre estos. Las moléculas de menor diámetro cinético son las que más permean y esta diferencia se ve más favorecida con el aumento de la temperatura. Estos polímeros son ideales para la separación de mezclas de H_2 con otros gases, como por ejemplo las mezclas de precombustión en la captura de CO_2.

Tabla 1.9. Clasificación de los distintos tipos de polímero.

Elastómeros	Termoplásticos
Polidimetilsiloxano (PDMS)	Acetato de celulosa
Poli(1-trimetilsilil, 1-propino) (PTMSP)	Policarbonatos
Copolímeros basados es óxido de	Polifenoles
etileno o propileno/amida (Pebax®)	Poliimidas (PI)
	Poliamidas (PA)
	Polisulfona (PSF)
	Polibenzimidazoles (PBI)
	Polímeros de microporosidad intrínseca (PIM)

Los polímeros más interesantes para separación de gases, tanto a nivel comercial como de investigación, pueden verse en la **Tabla 1.9**.

El objetivo de este apartado es explicar las propiedades más características de los polímeros que se han utilizado en el desarrollo de esta tesis doctoral y realizar una búsqueda bibliográfica sobre los resultados de separación de gases con las membranas fabricadas con ellos en diferentes configuraciones. Dichos resultados se recopilan de manera conjunta en el apartado 1.4.6 "Valores de separación de gases". La búsqueda referente a membranas mixtas (MMMs) se ha limitado a las que contienen ZIF como material de relleno, ya que esta subfamilia de MOF es la que va a ser considerada en el experimental de esta tesis doctoral, además de ser la más estudiada para la fabricación de estas membranas.

1.4.1. Membranas de polibenzimidazol (PBI)

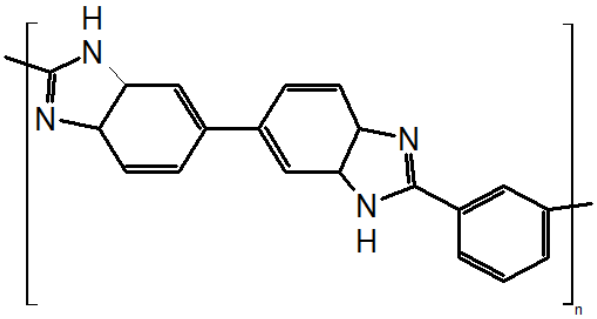

Figura 1.24. Estructura química del PBI.

En 1961 Vogel y Marvel[190] sintetizaron los primeros polibenzimidazoles aromáticos (PBI). Sus primeras aplicaciones fueron para ropa ignífuga y no se utilizaron para fabricar membranas hasta la decada de los 90. Los PBI son una clase de polímeros heterocíclicos que suelen sintetizarse mediante una reacción de condensación entre *bis-o-diaminas aromáticas* y *dicarboxilatos*, y en los que la molécula de benzimidazol es la unidad monomérica que se repite en la cadena.[191] De ellos, el único que existe comercialmente a día de hoy es el poli(2,2′-(*m*-fenileno)-5,5′-bibenzimidazol), detallado en la **Figura 1.24**, al que referirá el texto a partir de ahora como PBI. La primera casa en comercializarlo fue *Hoechst Celanese* en 1983, aunque es *PBI Performance Products* el mayor productor a día de hoy.

Se trata de un polímero con una alta estabilidad térmica (Tg de 427 °C[62]), buena resistencia química y un alto módulo de compresión. En lo que se refiere a la separación de gases, posee una alta selectividad de H_2 respecto de otros gases de diámetro cinético mayor (CO_2, N_2, CH_4, etc.) debido a la proximidad entre sus cadenas

poliméricas. Sin embargo, las principales desventajas de las membranas de PBI son su baja permeabilidad y su fragilidad, lo que hace difícil procesarlas.[192] Otro de los problemas de este material es su escasa solubilidad, que solo es posible en los disolventes DMAc, DMF o DMSO y a alta temperatura. Es por ello que muchos investigadores han funcionalizado el polímero para que sea soluble en disolventes más comunes, aunque ello provoca una pérdida en la capacidad de separación del material.[193-195]

En lo que respecta a la captura de CO_2, los resultados encontrados en la bibliografía corresponden a la captura en precombustión (separación H_2/CO_2), ya que, como se ha mencionado anteriormente, este polímero permite la separación de moléculas de H_2 respecto de otras más voluminosas. En la literatura pueden encontrarse membranas de PBI de diferentes configuraciones: membranas planas densas, tanto de polímero puro como membranas mixtas, y membranas de fibra hueca. La **Tabla 1.11** muestra los datos más actuales de membranas densas de PBI puro. Puede verse que existe una gran dispersión de datos en lo que respecta a la permeabilidad y a la selectividad de las membranas, debido a las diferentes formas de preparación en cada publicación. Pero en general se aprecia cómo el polímero es altamente selectivo para la mezcla H_2/CO_2, aunque se trata de membranas poco permeables que no logran alcanzar la centena de Barrer, ni siquiera operando a alta temperatura.

Respecto a las membranas mixtas de PBI con ZIF como material de relleno, no existe un gran número de publicaciones al respecto. Los resultados disponibles en la bibliografía pueden verse en la **Tabla 1.12** donde lo más curioso es que las membranas que contienen ZIF-8 son las que presentan mejores resultados de separación. Este resultado es inesperado ya que la ventana de poro de este MOF (0,34 nm) es mayor que los diámetros cinéticos de H_2 y CO_2 (0,29 y 0,33 nm, respectivamente), por lo que teóricamente no debería tamizar esta mezcla. Los valores de selectividad no mejoran en gran medida los que muestra el polímero puro, pero la incorporación del material de relleno sí tiene un efecto notable en el aumento de la permeabilidad de ambos gases.

En lo referente a membranas asimétricas, solo pueden encontrarse en la literatura valores de separación de gases para membranas de fibra hueca. Estos valores aparecen

resumidos en la **Tabla 1.13**. Destaca el uso de recubrimientos de PDMS para la reparación de las fibras. No existen muchas publicaciones al respecto pero puede verse como, en general, el rendimiento de la separación de gases es mejor que el de las membranas densas de la **Tabla 1.11**. Aún más limitada es la existencia de datos relativos a membranas asimétricas que contengan ZIF. Destaca el trabajo del grupo de Chung en el que se incorpora ZIF-8 en fibras huecas de PBI alcanzando valores de 64,5 GPU de H_2 a 180 °C con una selectividad H_2/CO_2 de 12,3.[196]

1.4.2. Membranas basadas en poliimidas (PI)

Las poliimidas (PI) son polímeros rígidos, con alto punto de fusión y temperatura de transición vítrea y térmicamente estables que se obtienen por policondensación de dianhidros y diaminas.[197] Las propiedades de separación de las PI cambian en función de los monómeros utilizados. Por ejemplo, introducir grupos fluorados hace que disminuya la densidad de empaquetamiento de las cadenas poliméricas aumentando el volumen libre. Esto favorece la solubilidad del CO_2 mejorando el rendimiento de la separación en mezclas como CO_2/CH_4. Son polímeros que poseen una alta selectividad en la separación de diversas mezclas de gases. Sin embargo, la principal desventaja de las poliamidas es que muestran tendencia a la plastificación y al envejecimiento,[198] por lo que su estabilidad con el tiempo es limitada. El envejecimiento es un fenómeno que se debe a que los polímeros termoplásticos son materiales que se encuentran en un estado inherente de no equilibrio. Por ello sufren gradualmente reordenamientos moleculares a un estado de equilibrio que afecta sus las propiedades físicas, entre ellas su permeabilidad y selectividad.[199] Las poliimidas que se han utilizado en el desarrollo de esta tesis doctoral han sido Matrimid® 5218, P84® y 6FDA-DAM.

- Matrimid® 5218

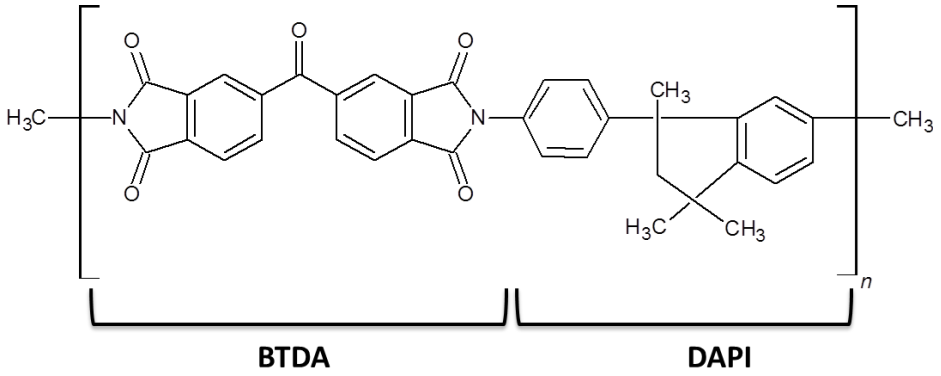

Figura 1.25. Estructura química de la Matrimid 5218®.

La Matrimid® 5218, comercializada entre otras casas por *Huntsman*, es una poliimida que consiste en unidades monoméricas de *dianhídrido tetracarboxílico-3,3´,4,4´-benzofenona (BTDA)* y *diaminofenil (DAPI)*.[35]. Su estructura puede verse en la **Figura 1.25**. Es un polímero soluble en una gran cantidad de disolventes, entre ellos: cloroformo, THF, DMF, DMAc, y con una Tg de 316 °C. Resulta adecuado para preparar membranas para la separación de todas las mezclas de CO_2: H_2/CO_2, CO_2/N_2 y CO_2/CH_4. En bibliografía pueden encontrarse valores de membranas densas (**Tabla 1.14**) así como de membranas planas asimétricas (**Tabla 1.15**), ambas tanto de polímero puro como de MMMs.

- P84®

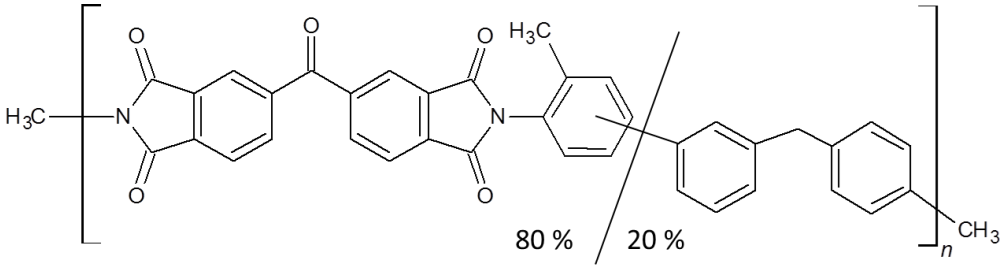

Figura 1.26. Esquema de la estructura química del P84®.

El P84® es una copoliimida comercial (fabricada por *Evonik*) constituida por un 80 % de *dianhídrido tetracarboxílico-3,3´,4,4´-benzofenona (BTDA)* y un 20 % de *metilendiamina (MDI)*, como puede verse en la **Figura 1.26**. El dianhidro utilizado en la polimerización es distinto al de la Matrimid®, lo que le da al P84® propiedades de separación diferentes y muestra una mayor resistencia a la plastificación.[200] Además, su solubilidad es más limitada, ya que solo puede disolverse en DMF, DMAc o DMSO,

lo que le aporta a su vez una gran resistencia química ante disolventes como tolueno, hidrocarburos, alcoholes y cetonas.[201] Posee también una estabilidad térmica elevada, con una Tg de 315°C.[200] La bibliografía para este polímero es limitada, ya que es un material que suele utilizarse para la fabricación se soportes. Aun así, la **Tabla 1.16** muestra valores de separación de gases de membranas densas de polímero puro.

- 6FDA-DAM

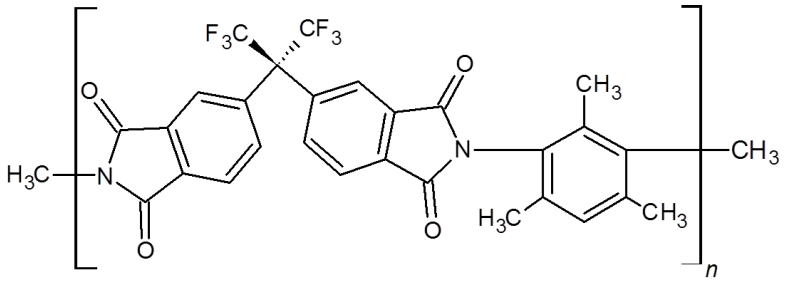

Figura 1.27. Estructura química de la poliamida 6FDA-DAM.

A diferencia de las poliimida Matrimid® y P84®, el 6FDA-DAM no se ha comercializado todavía a gran escala y solo existen síntesis de laboratorio o ventas en pequeños lotes (por ejemplo, por la compañía *Akrom Polymer Systems*). Esto hace que la masa molecular del polímero sea diferente para cada síntesis publicada. Se trata de una copoliimida compuesta por el dianhidro 6FDA (*2,2-bis(3,4-carboxifenil)hexafluoropropano*) y la diamina DAM (*2,4,6-trimetil-1,3-fenilendiamina*). Este último posee una alta fracción de volumen libre con cadenas más flexibles que se traduce en grandes permeabilidades de cientos de Barrer.[202] Al igual que la Matrimid®, es soluble en un gran número de disolventes y posee una Tg de 377 °C.[203] Este polímero da buenos resultados para la separación de mezclas CO_2/CH_4 y CO_2/N_2. Sin embargo, muestra selectividad menor a la unidad (selectividad inversa) para la mezcla H_2/CO_2. Esto hace que solo alcance valores ligeramente superiores a la unidad con el aumento de temperatura, lo que no lo convierte en un polímero apropiado para esta mezcla. En la literatura pueden encontrarse resultados de separación de gases para membranas densas de polímero puro y MMMs (**Tabla 1.17** y **Tabla 1.18**, respectivamente).

1.4.3. Membranas de polímeros de microporosidad intrínseca (PIM)

Los polímeros de microporosidad intrínseca (PIM) deben su nombre a que poseen una gran superficie específica (700-900 m^2/g)[204] y volumen libre. Esto se debe a que las cadenas poliméricas son de tipo escalonado y rígido, por lo que forman un entramado retorcido que favorece un empaquetamiento poco compacto.[205] Los PIM muestran un tamaño de poro inferior a 2 nm, es decir, en el rango de los microporos. Esto hace que las membranas de estos materiales muestren permeabilidades altísimas, del orden de miles de Barrer, acompañadas de selectividades modestas. Esto se debe a que las cadenas poliméricas aún tienen algo de flexibilidad, lo que hace fluctuar el tamaño de los poros.[206] Son polímeros termoplásticos con una alta estabilidad térmica, cuya Tg es superior a la temperatura de degradación del polímero (350 °C), por lo que no se puede determinar su valor exacto.[207]

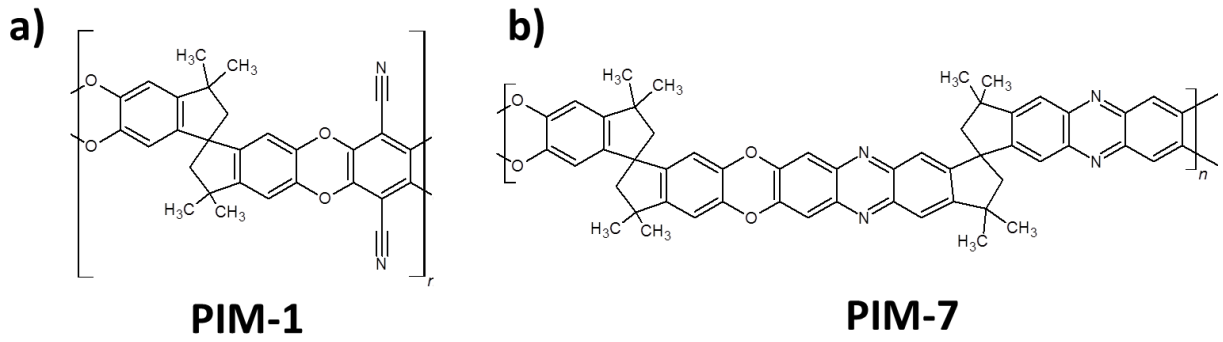

Figura 1.28. Estructura química del PIM-1 (a) y el PIM-7 (b).

Los PIM fueron sintetizados por primera vez en 2004 por Bud y cols.,[65] y una de las características más interesantes de estos polímeros es que su envejecimiento es reversible tras sumergir las membranas en etanol o metanol, que permiten recuperar los valores originales de permeación.[208] El polímero que más se han publicado para separación de gases es el PIM-1, cuya estructura puede verse en la **Figura 1.28**. Este polímero se obtiene mediante la polimerización por condensación de *5,5,6,6-tetrahidroxi-3,3,3,3- tetrametil-1,10-espirobisindano* con *tetrafluoro ftalonitrilo*.[209] La **Tabla 1.19** muestra los resultados encontrados en la bibliografía hasta la fecha. Destaca que el orden de permeabilidad de los gases es CO_2 >H_2 >CH_4 >N_2, lo que lo hace diferente a la mayoría de los polímeros termoplásticos, donde lo común es que el H_2 permee más que el CO_2 y el N_2 más que el CH_4. El mecanismo de separación de estos polímeros se debe a diferencias en la solubilidad de los gases. Esto hace que sean

los gases más condensables los que más permean y sean apropiados para mezclas CO_2/N_2 y CO_2/CH_4, pero no así para las mezclas H_2/CO_2, ya que el polímero presenta selectividad inversa. Las MMMs fabricadas con este polímero y ZIF son muy escasas. Solo se han publicado resultados con ZIF-8, ZIF-67 y ZIF-71, como muestra la **Tabla 1.20**, y tampoco se observa una mejora de las membranas con respecto a los valores del polímero puro.

Otro polímero para el que se ha publicado su uso en separación de gases es el PIM-7 (ver **Figura 1.28**). Se obtiene de la reacción del monómero *5,5,6,6-tetrahidroxi-3,3,3,3-trimetil-1,10-espirobisidano* con *7,7-,8,8-tetracloro-benacil-3,3,3-,3-tetrametil-1,1-espirobisidano*.[204] Este polímero tiene un rendimiento semejante al del PIM-1, pero con menores permeabilidades. Resultados bibliográficos a 25 °C muestran flujos de H_2 de 860 Barrer y de CO_2 de 1100 Barrer. Además, posee unas selectividades H_2/CO_2, CO_2/N_2 y CO_2/CH_4 de 0,78; 26,2 y 17,7; respectivamente.[204]

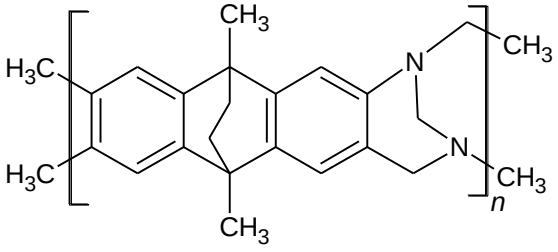

Figura 1.29. Estructura química del PIM-EA-TB.

Recientemente, Carta y cols. han publicado una modificación del PIM-1 en el que se añaden grupos de etanoantraceno (EA) y base de Tröger (TB) (*2,8-dimetil-6H,12H-5,11-metanodibenzo[b,f][1,5]diazocina*) dando lugar al PIM-EA-TB.[210] Su estructura puede verse en la **Figura 1.29**. La principal diferencia respecto a los otros PIM es que posee una estructura más rígida, lo que le permite tener una selectividad H_2/CO_2 superior a la unidad incluso a temperatura ambiente. Su permeabilidad a 25 °C es de 7760 Barrer de H_2 y de 7140 Barrer de CO_2 y tiene unas selectividades H_2/CO_2, CO_2/N_2 y CO_2/CH_4 de 1,1; 13,6 y 10,2; respectivamente.[204]

1.4.4. Membranas de Pebax®

Los copolímeros compuestos por bloques de poliéter flexible (PE) y de poliamida rígida (PA) son más conocidos bajo el nombre comercial de Pebax®, fabricados por la empresa francesa *Arkema*. Se trata de copolímeros semicristalinos que combinan las

propiedades de polímeros termoplásticos y elastómeros. La proporción poliamida/poliéter, que se indica con un código concreto, puede ser diferente y afecta a las propiedades del material, tal y como refleja la **Tabla 1.10**. Estos copolímeros cuentan también con dos temperaturas de fusión, cada una correspondiente a los segmentos de PE y PA.

Tabla 1.10. Propiedades físicas de algunos polímeros Pebax® [211]

Código	Contenido de PA (% peso)	Tm (PE) (°C)	Tm (PA) (°C)	Cristalinidad en el bloque de PA (% vol.)
2533	20	10	126	3
3533	30	18	155	6
4033	46	21	30	14
1657	40	49	204	-

En el copolímero, el bloque rígido de poliamida proporciona la resistencia mecánica del material compuesto, mientras que el transporte de gases se da principalmente a través del bloque blando de poliéter.[212] Son materiales que muestran elevadas selectividades CO_2/N_2 (30-80) y CO_2/CH_4 (15-20), aunque su permeabilidad es limitada. Como ocurre con los PIM, estos polímeros no son adecuados para la separación de H_2. Uno de los copolímeros más utilizados para separación de gases es el Pebax® 1657.[212] Como muestra la **Tabla 1.21**, se ha utilizado para la fabricación de membranas densas, tanto autosoportadas como soportadas, en las que se deposita una capa fina de Pebax® sobre un soporte plano muy permeable. Respecto a MMMs de Pebax® con ZIF, hasta la fecha solo se han publicado resultados con ZIF-7 y ZIF-8 (**Tabla 1.22**), y solo con el primero se mejoraban los resultados del polímero puro.

1.4.5. Membranas finas soportadas (*thin-film composites, TFC*) de poliamidas (PA)

El difícil procesado de las poliamidas hace que no existan muchos trabajos de investigación en la literatura respecto a la fabricación de membranas densas o asimétricas como con los polímeros anteriores. Sin embargo, la preparación de membranas finas soportadas o en inglés *thin-film composites (TFC)* sí ha merecido cierto número de estudios. La combinación de altos flujos de agua y grandes retenciones de sales ha hecho que las membranas finas de poliamida fabricadas por

polimerización interfacial tengan una implementación exitosa en procesos industriales a gran escala, especialmente en ósmosis inversa y nanofiltración.[213] Su alto rendimiento se debe a la formación de una capa selectiva extremadamente fina conseguida por este proceso de polimerización. Aunque menos abundantes, algunas aplicaciones respecto a la separación de mezclas de CO_2 pueden encontrarse también en la literatura. Zhao y cols.[214] desarrollaron membranas con *tetraamina de trimetileno (TETA)* y *cloruro de trimesoilo (TMC)* sobre soportes de polisulfona para la separación de mezclas CO_2/CH_4, alcanzando valores de 13,3 GPU de CO_2 y una selectividad CO_2/CH_4 de 94,1 a una presión de alimentación 1,1 atm. Yu y cols.[215] llevaron a cabo la polimerización interfacial de *3,3-diamino-N-metildipropilamina (DNMDAm)* y *TMC* en soportes de polisulfona para fabricar membranas que mostraban una permeación de CO_2 de 173 GPU y selectividades CO_2/N_2 y CO_2/CH_4 de 70 y 37, respectivamente. La separación de mezclas CO_2/N_2 también fue investigada por Wang et. al.,[30] cuyas membranas basadas en *TMC* y *3,5-diaminobenzoato sódico* sobre polisulfona recubierta con PDMS mostraron una permeación de CO_2 de 5831 GPU y una selectividad CO_2/N_2 de 86 a 0.11 MPa.

Respecto a la separación de mezclas de precombustión (H_2/CO_2) destaca el trabajo del grupo de Pinnau. Este ha desarrollado recientemente membranas finas por polimerización interfacial capaces de alcanzar una permeación de H_2 de 500 GPU y una selectividad H_2/CO_2 de 50.[216] Sin embargo, estas membranas no pueden sobrepasar temperaturas de operación de 140 °C debido al uso de soportes de polisulfona. La captura en precombustión, en cambio, necesita de membranas fabricadas con materiales con una alta resistencia mecánica y térmica capaces de aguantar las condiciones de operación intensivas del proceso. En el campo de la precombustión también destaca el trabajo de Shan y cols.,[217] que han fabricado membranas mediante la polimerización interfacial de bezimidazol sobre soportes de alúmnina, dando como resultado a 150 °C un flujo de H_2 de 24,2 GPU con una selectividad H_2/CO_2 de 40.

1.4.6. Valores de separación de gases

- Membranas de PBI

Tabla 1.11. Valores de separación de gases de membranas de PBI denso.

Año de publicación y ref.	Tipo de análisis	Temperatura (^{0}C)	Presión de alimentación	Permeabilidad H_2 (Barrer)	Selectividad H_2/CO_2 (-)
2018[54]	Individual	150	8-15 atm	27,0	16,0
				1,5*	140
2017[53]	Individual	35	11 atm	2,0	12,0
	Mezcla**	100		10,0	11,0
		150		25,0	11,0
		200		40,0	12,0
2017[218]	Individual	30	1,5 bar	2,2	4,1
		30***		1,3	16,5
2017[219]	Individual	30	1,5 bar	5,2	12,5
2017[220]	Individual	150	5 bar	45,5	1,4
		200		77,4	4,1
2016[221]	Individual	30	206,8 kPa	5,4	6,5
		200		33,1	7,1
2016[222]	Individual	35	5 bar	3,6	9,5
2014[194]	Individual	30	1,3-3,4 bar	2,8	10,8
		200		50,0	24,0
		250		76,8	23,0
2013[223]	Individual	35	3,5 atm	4,1	8,9
	Mezcla**		2 atm	2,9	7,1
2011[89]	Individual	35	3,5 atm	3,7	8,7
	Mezcla**	35	7 atm	2,9	7,1
		60		13,7	6,8
		80		22,3	8,8
		120		37,7	9,3
		150		53,1	8,7
		180		70,2	8,4
2006[195]	Individual	35	20 atm	0,60	3,8
2003[224]	Individual	25	3,4 bar	0,10	9,1
		340		18,0	4,5
	Mezcla**	25		0,10	1,0
		250		13,3	20,0
		320		11,0	3,0

*Dopado con H_3PO_4

** Proporción H_2/CO_2 50/50 (v/v)

*** Tras ser tratado a 300 °C

Tabla 1.12. Valores de separación de gases de MMMs de PBI.

Año de publicación y ref.	ZIF	Carga (% peso)	Tipo de análisis	T (^{0}C)	Presión de alimentación	Permeabilidad H_2 (Barrer)	Selectividad H_2/CO_2 (-)
2011[89]	ZIF-7	10	Individual	35	3,5 atm	7,7	12,9
		25				15,4	11,9
		50				26,2	14,9
		25	Mezcla*		7,0 atm	6,3	6,8
		50				13,3	7,2
		25	Mezcla*	180	7,0 atm	60	6,5
		50				450	8,2
2013[223]	ZIF-8	30	Individual	35	3,5 atm	82,5	12,0
		60				1613	4,1
		30	Mezcla*		2,0 atm	39,0	6,8
		60				670	2,2
		30	Mezcla*	230	2,0 atm	470	26,3
		60				2015	12,3
2012[196]	ZIF-8	15	Individual	35	3,5 atm	28,5	13,0
		20				36,4	12,1
		30				106	12,3
		35				239	7,0
		60				1750	4,1
2014[225]	ZIF-11	16	Individual	25	-	67,8	5,0
		29				133	5,6
		39				465	3,7
2013[226]	ZIF-90	10	Individual	35	3,5 atm	12,7	14,6
		25				18,3	20,6
		45				24,5	25,0
		35	Mezcla*	35		18,0	5,0
		45		180		227	13,3

* Proporción H_2/CO_2 50/50 (v/v)

Tabla 1.13. Valores de separación de gases de membranas asimétricas de PBI.

Año de publicación y ref.	Tipo de análisis	Recubrimiento de PDMS	T (^{0}C)	Presión de alimentación	Permeación H_2 (GPU)	Selectividad H_2/CO_2 (-)
2014[227]	Individual	No	250	-	500	19,0
2012[228]	Individual	No	138	1,3-3,4 bar	2,0	58,0
		No	187		3,0	50,0
		No	238		5,5	42,0
		No	250		4,7	43,0
	Mezcla*	No	250		7,0	47,6
2012[229]	Individual	No	20	1-6 bar	65,1	3,1
	Individual	Sí			26,7	4,7
2011[230]	Individual	No	100	5-8 bar	0,33	7,9
		No	200		0,62	12,8
		No	300		0,99	21,7
		No	400		2,3	27,3
2010[231]	Individual	No	35	10 atm	38,7	6,9
	Individual	Sí			29,3	11,1
* Proporción H_2/CO_2 50/50 (v/v)						

- Membranas de poliimida

Tabla 1.14. Valores de separación de gases para membranas de Matrimid® pura y MMMs.

Año de publicación y ref.	ZIF	Carga (% peso)	Tipo de análisis	T (^{0}C)	Presión de alimentación	Permeabilidad H_2 (Barrer)	Selectividad H_2/CO_2 (-)	Permeabilidad CO_2 (Barrer)	Selectividad CO_2/N_2 (-)	Selectividad CO_2/CH_4 (-)
2014[232]	ZIF-8	0	Individual	35	3,5 bar	-	-	9,0	-	34,5
		15				-	-	26,0	-	35,0
2014[233]	ZIF-8	0	Individual	35	5 bar	-	-	8,7	-	26,2
		10				-	-	12,8	-	36,2
		20				-	-	17,4	-	42,0
		30				-	-	21,3	-	45,9
2012[234]	ZIF-8	0	Individual	35	4,5 bar	-	-	10,7	-	34,0
		10				-	-	12,0	-	35,0
		25				-	-	23,2	-	39,0
2012[235]	ZIF-8	0	Individual	22	4 bar	32,7	4,1	8,1	22,4	35,1
		5				38,1	3,8	10,1	21,4	38,7
		10				52,6	3,8	13,7	21,7	30,4
		20				63,5	3,8	16,6	18,9	36,2
		30				112	3,9	28,7	17,1	24,8
2010[236]	ZIF-8	0	Individual	25	2,7 bar	28,9	3,0	9,5	30,7	39,8
		20				31,2	3,5	9,0	30,1	51,1
		30				47,2	3,3	14,2	24,1	38,2
		40				71,2	3,0	24,6	23,4	27,8
		50				18,1	3,8	4,7	26,2	125
		60				35,8	4,4	8,1	18,4	80,8

Continuación de **Tabla 1.14**

Año de publicación y ref.	ZIF	Carga (% peso)	Tipo de análisis	T (^{0}C)	Presión de alimentación	Permeabilidad H_2 (Barrer)	Selectividad H_2/CO_2 (-)	Permeabilidad CO_2 (Barrer)	Selectividad CO_2/N_2 (-)	Selectividad CO_2/CH_4 (-)
2010[236]	ZIF-8	0	Mezcla*	25	2,7 bar	-	2,6	-	-	42,1
		50				-	3,5	-	-	89,1
		60				-	7,0	-	-	80,1
2018[237]	ZIF-11	0	Individual	35	4 bar	17,3	4,1	-	-	16,2
		10				28,1	4,2	-	-	23,3
		20				54,9	4,7	-	-	27,3
		30				103	3,3	-	-	43,0
		40				28,4	2,8	-	-	66,7
2010[179]	ZIF-90	0	Mezcla*	25	2 bar	-	-	-	-	34,0
		15				-	-	-	-	35,0
* Proporción CO_2/CH_4 de 10/90 (v/v)										

Tabla 1.15. Membranas asimétricas de Matrimid®.

Año de publicación y ref.	ZIF	Carga (% peso)	Tipo de análisis	T (^{0}C)	Presión de alimentación	Permeación H_2 (GPU)	Selectividad H_2/CO_2 (-)	Permeación CO_2 (GPU)	Selectividad CO_2/N_2 (-)	Permeación CO_2 (GPU)	Selectividad CO_2/CH_4 (-)
2011[238]	ZIF-8	0	Mezcla*	35	10 bar	-	-	10,5	18,1	9,9	17,9
		10				-	-	15,0	18,1	17,2	18,3
		20				-	-	18,1	18,1	20,9	18,3
		30				-	-	18,8	19,1	21,6	19,6
* Proporción CO_2/N_2 y CO_2/CH_4 de 35/65 (v/v)											

Tabla 1.16. Valores de separación de gases para membranas densas de P84®.

Año de publicación y ref.	Tipo de análisis	T (^{0}C)	Presión de alimentación	Permeabilidad H_2 (Barrer)	Selectividad H_2/CO_2 (-)	Permeabilidad CO_2 (Barrer)	Selectividad CO_2/N_2 (-)	Permeabilidad CO_2 (Barrer)	Selectividad CO_2/CH_4 (-)
2003[200]	Individual	25	4 bar	-	-	8,70	37,8	-	-
	Mezcla*		10-30 bar	-	-	0,60	38,2	-	-
2007[239]	Individual	30	40 bar	-	-	-	-	14,4	33,4
2012[240]	Individual	25	1 bar	-	-	0,89	20,2	-	-
* Proporción CO_2/N_2 de 20/80 (v/v)									

Tabla 1.17. Valores de separación de gases de membranas de 6FDA-DAM puro.

Año de publicación y ref,	Tipo de análisis	T (^{0}C)	Presión de alimentación	Permeabilidad CO_2 (Barrer)	Selectividad CO_2/N_2 (-)	Permeabilidad CO_2 (Barrer)	Selectividad CO_2/CH_4 (-)
2016[241]	Mezcla*	25	3 bar	-	-	380	31,0
2014[242]	Individual	35	7 bar	-	-	817	17,6
2013[243]	Individual	35	7 bar	20,3	15,3	20,3	18,0
2000[244]	Individual	35	1 MPa	467	14,5	467	15,9
* Proporción CO_2/CH_4 de 50/50 (v/v)							

Tabla 1.18. Valores de separación de gases de MMMs de 6FDA-DAM.

Año de publicación y ref.	ZIF	Carga (% peso)	Tipo de análisis	T (^{0}C)	Presión de alimentación	Permeabilidad CO_2 (Barrer)	Selectividad CO_2/N_2 (-)	Permeabilidad CO_2 (Barrer)	Selectividad CO_2/CH_4 (-)
2017[245]	ZIF-94	0	Mezcla*	25	3 bar	450	12,9	-	-
		10				780	24,7	-	-
		20				960	23,6	-	-
		30				1000	17,8	-	-
		40				2000	22,9	-	-
2017[246]	ZIF-11	0	Individual	30	4 bar	-	-	20,6	32,7
		10				-	-	110	31,3
		20				-	-	258	31,0
		30				-	-	73,1	30,4
2010[179]	ZIF-90	0	Mezcla**	25	2 bar	-	-	390	24,0
		15				-	-	720	37,0

* Proporción CO_2/N_2 de 15/85 (v/v)

** Proporción CO_2/CH_4 de 50/50 (v/v)

- Membranas de PIM-1

Tabla 1.19. Valores de separación de gases de membranas de PIM-1 puro.

Año de publicación y ref.	Tipo de análisis	T (ºC)	P alimentación	Permeabilidad H_2 (Barrer)	Permeabilidad CO_2 (Barrer)	Selectividad H_2/CO_2 (-)	Selectividad CO_2/N_2 (-)	Selectividad CO_2/CH_4 (-)
2016[247]	Individual	25	1 bar	-	8280	-	14,4	-
2015[248]	Individual	25	1 atm	-	3620	-	21,0	-
2013[209]	Individual	25	1 atm	2936	5303	0,55	21,0	16,6
2012[46]	Individual	35	3,5 atm	2696	3375	0,80	20,7	7,1
2011[249]	Individual	25	1 bar	1450	4790	0,30	20,0	10,9
2008[250]	Individual	25	1 atm	2330	3500	0,67	15,0	9,7
2008[208]	Individual	24	1 atm	1630	4390	0,37	24,0	14,2
2005[204]	Individual	30	300 mbar	1300	2300	0,57	25,0	18,4

Tabla 1.20. Valores de separación de gases de MMMs de PIM-1.

Año de publicación y ref.	ZIF	Carga (% peso)	Tipo de análisis	T (ºC)	P alimentación	Permeabilidad H_2 (Barrer)	Permeabilidad CO_2 (Barrer)	Selectividad H_2/CO_2 (-)	Selectividad CO_2/N_2 (-)	Selectividad CO_2/CH_4 (-)
2018[251]	ZIF-67	0	Individual	30	2 bar	2219	4521	0,5	20,2	12,5
		5				2504	4685	0,5	21,1	13,4
		10				2813	4895	0,6	22,7	14,6
		20				3542	5206	0,7	24,2	16,8
		30				4532	6128	0,7	15,5	12,0
2015[252]	ZIF-71	0	Individual	35	3,5 atm	-	3295	-	20,1	10,2
		10				-	4271	-	19,4	11,3
		20				-	5942	-	20,0	11,9
		30				-	8377	-	18,3	11,2

Continuación de **Tabla 1.20**

Año de publicación y ref.	ZIF	Carga (% peso)	Tipo de análisis	T (^{0}C)	P alimentación	Permeabilidad H_2 (Barrer)	Permeabilidad CO_2 (Barrer)	Selectividad H_2/CO_2 (-)	Selectividad CO_2/N_2 (-)	Selectividad CO_2/CH_4 (-)
2013[253]	ZIF-8	0	Individual	25	1 bar	1630	4390	0,40	24,4	14,2
		11				2560	4815	0,53	19,3	15,0
		28				2980	4270	0,70	21,9	18,6
		36				5745	6820	0,84	17,9	13,4
		43				6680	6300	1,06	18,0	14,7

- Membranas de Pebax®

Tabla 1.21. Valores de separación de gases para membranas soportadas de Pebax® 1657.

Año de publicación y ref.	Soporte	Tipo de análisis	T (^{0}C)	P alimentación	Permeación de CO_2 (GPU)	Selectividad CO_2/N_2 (-)	Selectividad CO_2/CH_4 (-)
2015[254]	PSF	CO_2/N_2 (15/85 (v/v))	25 °C	1 bar	670	62,0	-
2015[255]	PVDF/PSF	CO_2/N_2 (23/77(v/v))	25 °C	7 bar	550	45,0	-
2015[256]	PAN	Individual	25 °C	1-4 bar	13,5	-	18,0
2015[257]	-	Individual	35 °C	4-10 bar	2,5	78,0	-
2014[258]	PES	CO_2/N_2 (10/90 (v/v))	25 °C	3 bar	1275	46,0	-
2008[259]	PAN	CO_2/N_2 (25/75 (v/v))	20 °C	8 bar	93,0	70,0	-
2007[260]	-	Individual	30 °C	20 bar	3,7	-	21,2
2004[261]	PSF	CO_2/N_2 (15/85 (v/v))	25 °C	1 bar	61,0	32,0	

Tabla 1.22. Valores de separación de gases de MMMs de Pebax® 1657.

Año de publicación y ref.	ZIF	Carga (% peso)	Tipo de análisis	T (ºC)	P alimentación	Permeación CO_2 (GPU)	Selectividad CO_2/N_2 (-)	Selectividad CO_2/CH_4 (-)
2018[262]	ZIF-8	0	Individual	20	10 bar	1,6	48,0	-
		5				2,0	59,6	-
		10				2,4	54,6	-
		15				2,7	44,8	-
		20				3,1	40,5	-
2017[263]	ZIF-8	0	Individual	25	4 bar	1,8	39,9	18,0
		11				2,3	31,7	16,5
		21				4,3	44,5	17,9
		33				2,4	30,1	12,2
2017[264]	ZIF-7	0	Mezcla*	25	2-15 bar	220	41,9	13,6
		10				247	45,3	14,7
		20				260	43,0	15,8
		30				300	47,5	17,0
2013[265]	ZIF-7	0	Individual	20	-	287	34,0	14,0
		8				291	68,0	23,0
		22				137	97,0	30,0
		34				39,0	105	44,0

* Proporción CO_2/N_2 y CO_2/CH_4 20/80 (v/v)

CHAPTER 2

METODOLOGY

2.1. Synthesis of common MOFs

Different metal-organic frameworks (MOFs) have been prepared in this thesis with the aim of being used as fillers that can improve the gas separation performance of polymeric membranes. All the materials synthesized followed similar procedures consisting in four steps: (i) dissolution of the metal source and the linker, (ii) crystallization reaction, (iii) washing and (iv) thermal activation. This procedure can be seen in the scheme of **Figure 2.1**.

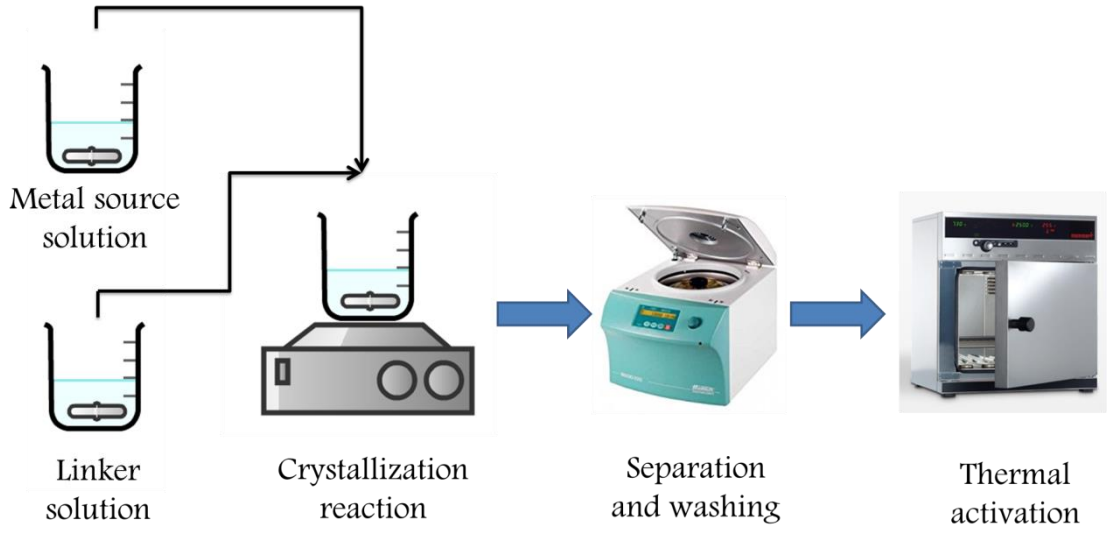

Figure 2.1. General scheme of the synthesis of MOFs.

ZIF-7, ZIF-8 and ZIF-11 were prepared following non-solvothermal routes at room temperature. ZIF-7 was synthesized in DMF according to a recipe developed by Caro's group.[124] ZIF-8 was prepared as nanoparticles with two different sizes (50 and 150 nm). The 50 nm ZIF-8 was synthesized following the method reported by Cravillon et. al.[266] and the synthesis of 150 nm ZIF-8 was performed following a recipe based on a report involving a MeOH/H_2O mixture as solvent. [267] Finally, ZIF-11 was synthesized in a mixture of MeOH, toluene and NH_4OH.[123]

UiO-66 was prepared solvothermally in DMF at 120 °C[268] and the synthesis of MIL-101(Cr) was performed microwave-assisted in distilled water.[269] **Table 2.1** contains a summary of the different reaction conditions and the chapter of the thesis were full experimental details can be found.

Table 2.1.Synthesis conditions for common MOFs.

MOF	Metal source	Ligand	Type of synthesis	Reaction medium and temperature	Washing	Thermal activation	Particle size	Chapter
ZIF-7	$Zn(NO_3)_2 \cdot 6H_2O$	Benzimidazole	Non-solvothermal	DMF, RT	MeOH	100 °C, 18 h	50 nm	7
ZIF-8	$Zn(NO_3)_2 \cdot 6H_2O$	2-methylimidazole	Non-solvothermal	MeOH/H_2O, RT	MeOH	100 °C, 18 h	50-150 nm	5,7,9,10,11, 12, 13, 14
ZIF-11	$Zn(CH_3COO)_2 \cdot 2H_2O$	Benzimidazole	Non-solvothermal	MeOH, toluene, NH_4OH, RT	MeOH	100 °C, 18 h	2.5 μm	4,6,8
UiO-66	$ZrCl_4$	Benzene-1,4-dicarboxylic acid	Solvothermal	DMF/$H_2$0 120 °C	DMF/MeOH	300 °C, 3 h	33 nm	14
MIL-101 (Cr)	$CrCl_3 \cdot 6H_2O$	Terephthalic acid	Microwave-assisted	$H_2$0, 180 °C	DMF/MeOH	100 °C, 18 h	25 nm	14

2.2. Modification of existing ZIFs

Part of the work in this thesis has comprised the development of zeolitic imidazolate frameworks (ZIFs) with adapted features for the CO_2 separation. This way, some existing ZIFs in the literature were modified to obtain new nanoparticles more suitable for their use in membranes for gas separation. The novelty of this research is related to the synthesis of ZIF-11 nanoparticles, ZIF-7/8 core-shells and hybrid ZIF-93/11 frameworks.

2.2.1. Nano-sized ZIF-11 (nZIF-11)

ZIF-11 nanoparticles were prepared in a centrifuge, meaning a novel route for the synthesis of MOFs and also the first time that this ZIF was achieved in nanometric size. Firstly, bIm (0.24 g) was dissolved in 6.4 g of MeOH, together with 9.2 g of toluene and 2.4 g of NH_4OH. In parallel, $Zn(CH_3COO)_2{\cdot}2H_2O$ (0.22 g) was dissolved in 3.2 g of MeOH. Both solutions were cooled separately to 18 °C and then mixed in a centrifuge flask of 50 mL at 10000 rpm and during 5 min at that temperature. The solid collected was washed with MeOH three times for the complete removal of toluene and dried at 100 °C overnight. The whole process is described in **Figure 2.2**.

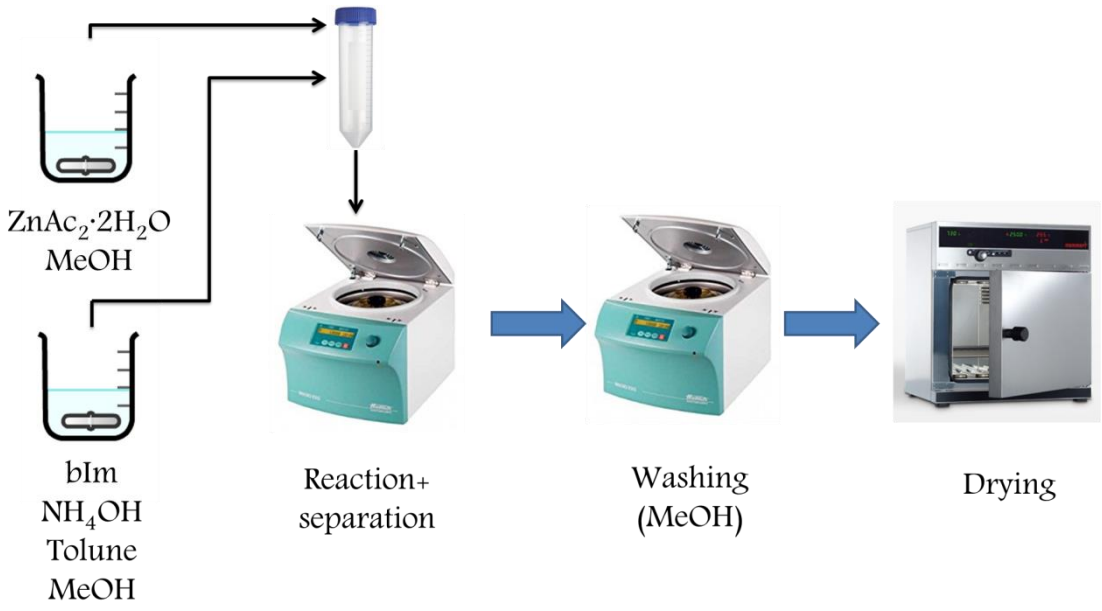

Figure 2.2. Scheme of the synthesis route of nZIF-11.

2.2.2. ZIF-7/8 core-shells

The ZIF-7/8 core-shells were prepared *via* post-synthetic modification of ZIF-8 (see **Figure 2.3**). An initial amount of bIm was added to DMF at 65 ^{0}C to obtain a concentration of 13 g/L. Once solved, ZIF-8 was added to the solution (3.3 g/L); which was stirred. The solid was collected by centrifugation at the corresponding reaction time (depending on the desired mIm/bIm proportion in the hybrid nanoparticle) and washed 3 times with MeOH and dried at 110 ^{0}C overnight. The mIm/bIm proportion in the ZIF-7/8 hybrid was calculated assuming that all the liberated mIm had been replaced by bIm during the reaction. Different initial bIm concentrations and temperatures were also tested to study their influence on the reaction time. For example, the ZIF-7/8 hybrid with 10 %mol of bIm was obtained in 3 days at 65 ^{0}C and with an initial bIm concentration in the reaction medium of 6.5 g/L, or at 30 ^{0}C with a bIm concentration of 13 g/L.

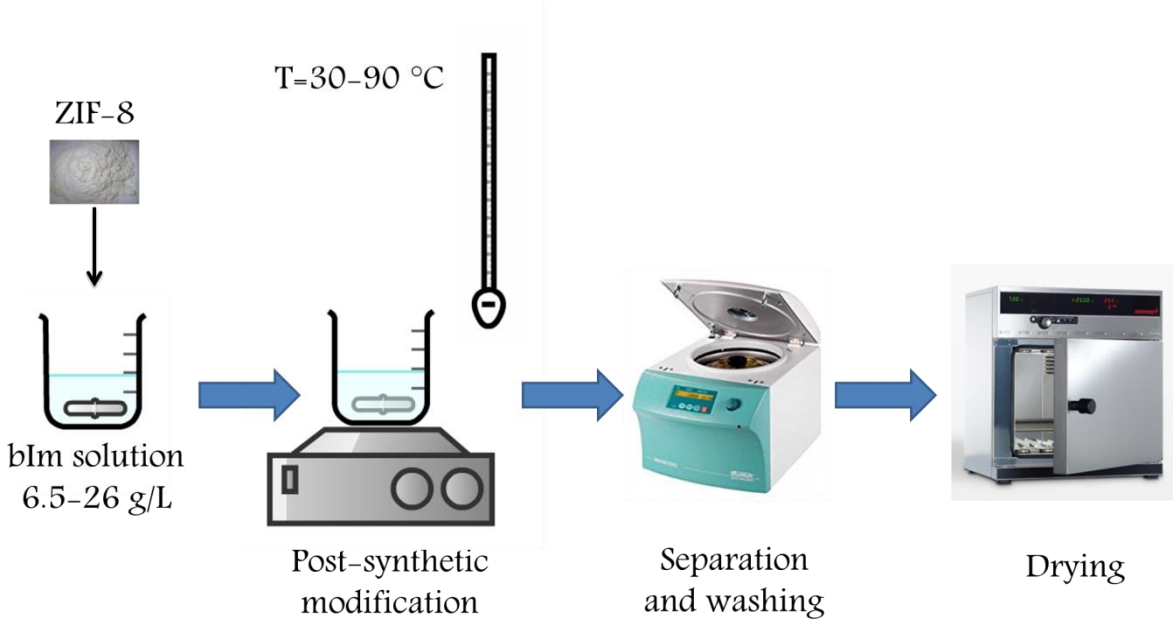

Figure 2.3. Scheme of the synthesis route of ZIF-7/8 core-shells.

2.2.3. ZIF-93/11

The ZIF-93/11 hybrid material was also prepared *via* post-synthetic modification, in this case starting with ZIF-93 (see **Figure 2.4**). Two different solvents were used: DMAc and MeOH. For the synthesis in the first solvent, bIm (1.25 g) was dissolved in

DMAc (30 mL) and ZIF-93 (0.2 g) was added to the solution. The suspension was stirred (30 °C, 3 days). The solid was collected by centrifugation, washed with MeOH under reflux (18 h), cooled, collected by centrifugation again and then dried (110 °C, overnight). For synthesis in MeOH, bIm (1.25 g) was dissolved in a mixture of MeOH (6.4 g), toluene (9.2 g) and NH_4OH (2.4 g). Then, ZIF-93 (0.2 g) was added to the solution. The suspension was stirred (30 °C, 3 h) and the solid was collected by centrifugation and washed 3 times with MeOH. The solid was then dried (110 °C, overnight).

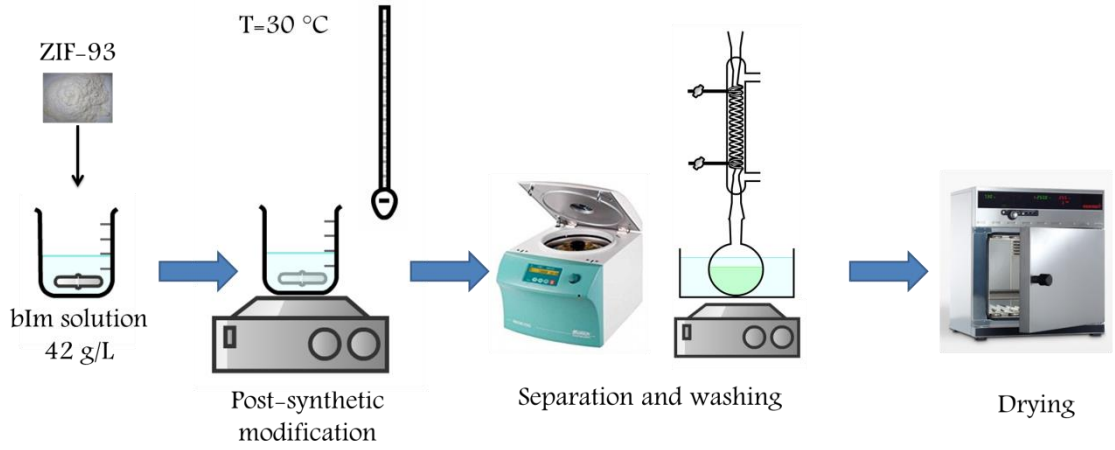

Figure 2.4. Scheme of the synthesis route of ZIF-93/11 hybrid nanoparticles.

2.3. Membrane preparation

2.3.1. Preparation of dense mixed matrix membranes (MMMs)

Dense MMMs were prepared in this thesis with Matrimid® and PBI as polymeric phases and using the different MOFs previously described as fillers. The general procedure (the solution casting method) can be seen in **Figure 2.5** and consists of six steps: (i) Filler dispersion, (ii) polymer dissolution, (iii) casting and film formation, (iv) solvent evaporation, (v) washing and (vi) thermal activation. Pure polymeric membranes were prepared analogously but just skipping the first step, since they contain no filler.

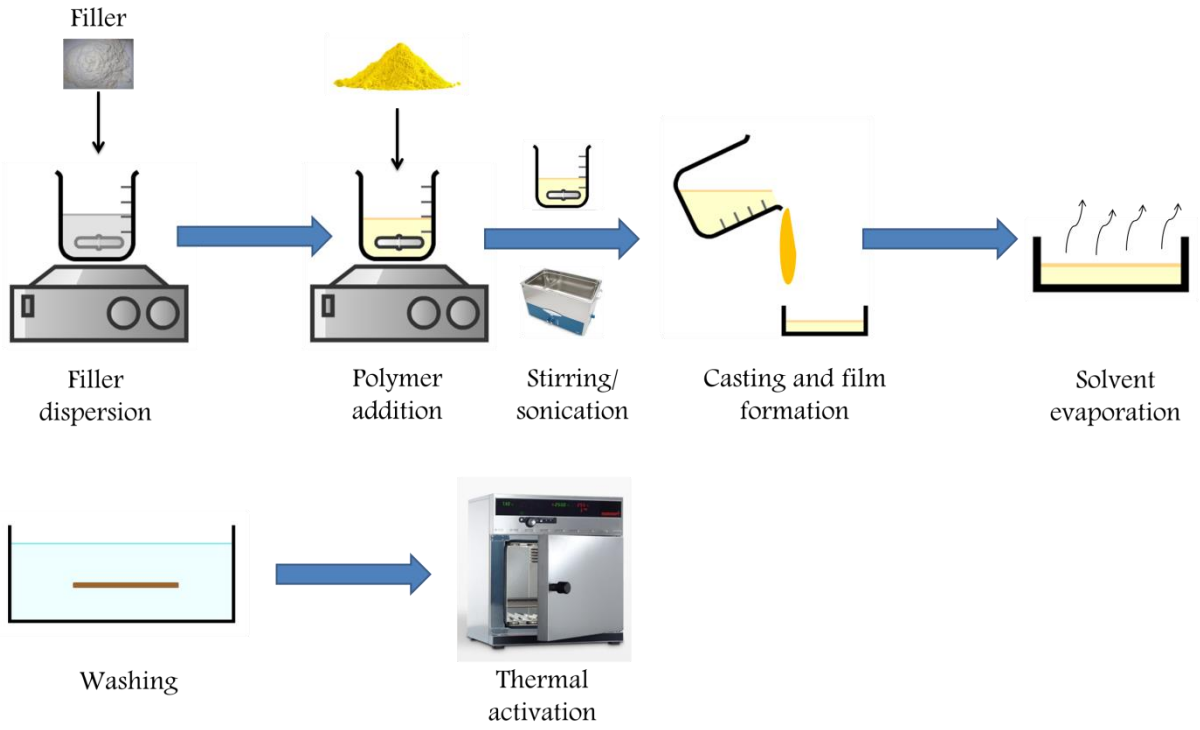

Figure 2.5. Scheme of the general procedure for the preparation of MMMs following the solution casting method.

The peculiarities for each polymer were the following:

- Matrimid® MMMs

a) Fillers used: ZIF-11 and nZIF-11.

b) Polymer form: powder.

c) Solvent used: chloroform.

d) Casting conditions: room temperature.

e) Washing: none.

f) Thermal activation. 180 °C and 10 mbar for 24 h.

- PBI MMMs

a) Fillers used: ZIF-7, ZIF-8, ZIF-7/8 core-shells, nZIF-11, ZIF-11, ZIF-93 and ZIF-93/11 hybrid.

b) Polymer form: commercial solution at 26 wt% (Celazole® S26).

c) Solvent used: N,N-Dimethylacetamide.

d) Casting conditions: 90 °C.

e) Washing: MeOH/H_2O.

f) Thermal activation. 130 ^{0}C and 10 mbar for 24 h.

Table 2.2 shows a summary of the different dense MMMs prepared, including the ZIF loading and the operating conditions in gas separation tests.

Table 2.2. Summary of the dense MMMs prepared in this thesis.

Filler	Polymer	Loading (wt%)	Feed pressure (bar)	Temperature (°C)
ZIF-7	PBI	20	3	180
ZIF-8	PBI	10-40	3-6	150-180
ZIF-7/8 core-shell	PBI	10-32	3	180-250
nZIF-11	Matrimid®	10-25	3	35-200
	PBI	10-32	3	70-200
ZIF-11	Matrimid®	10	3	35
	PBI	10-55	3	70-200
ZIF-93	PBI	20	3	180
ZIF-93/11	PBI	20	3	180

2.3.2. Preparation of integrally skinned asymmetric flat membranes

These membranes represent an evolution of the dense membranes previously explained since their much thinner selective layer allows higher permeation fluxes and better selectivity, as it will be seen in the following results section. Besides, the asymmetric configuration of these membranes is similar to that found in hollow fibers, which is the type of membranes commercially available. This way the preparation of flat membranes in asymmetric configuration approaches the level of the research necessary for real industrial products.

Two polymers have been used to prepare flat asymmetric membranes: PBI and P84®. PBI membranes were developed to obtain high selective membranes for pre-combustion CO_2 capture (i.e. H_2/CO_2 separation). They were also loaded with ZIF-8 to form asymmetric MMMs. The polyimide P84®, though, was used to prepare asymmetric porous supports that could provide mechanical stability to the PBI

membranes. Thanks to the quality of this support it was also used for the development of supported Pebax® and polyamide membranes, as it will be shown later.

The asymmetric membranes were prepared following the phase inversion method. A dope solution of P84® or PBI in DMAc (23 and 20 wt%, respectively) was prepared. The dope concentrations were chosen near the critical values for each polymer so that a thin skin layer with fewer defects could be formed.[270] The polymer solution was cast using an *Elcometer 4340 Automatic Film Applicator* and immediately immersed into the coagulation bath at 25 ^{0}C. After precipitation, the membranes were kept in a DI water bath and then rinsed with alcohol in order to remove the remaining DMAc. The films were dried at 100 ^{0}C for one day prior to use. PBI membranes containing ZIF-8 were prepared analogously. In this case, ZIF-8 nanoparticles were dispersed in DMAc and commercial PBI solution (26 wt%) was added in three steps until a 20 wt% dope solution was obtained. A scheme explaining the process can be seen in **Figure 2.6**. Once dried, the membranes had to be healed with PDMS following a dip-coating procedure. The detailed experimental procedures can be found in chapter 9.

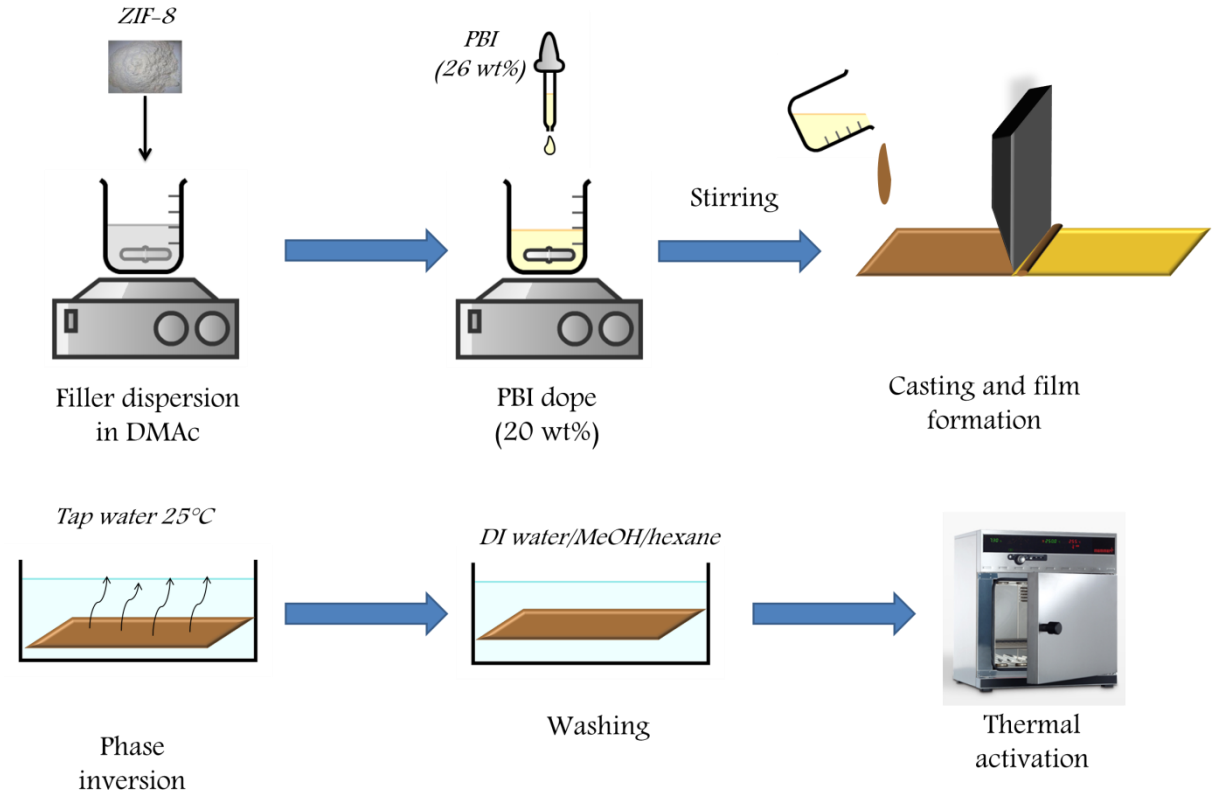

Figure 2.6. Scheme of the preparation of flat asymmetric membranes *via* phase inversion.

2.3.3. Preparation of supported membranes

Supported membranes were prepared in this thesis on the above described P84® supports. Two different polymers were used as selective layer: polyamide and Pebax® 1657, which allowed dealing with different gas separations. MOFs were also embedded in both polymers, providing supported MMMs.

Polyamide membranes were prepared by interfacial polymerization (IP) and they incorporated ZIF-8 nanoparticles. The P84® support was placed in a glass filtration holder and soaked firstly with a solution of m-phenylenediamine (MPD) in distilled water. Then, a solution of trimesoyl chloride (TMC) in hexane with dispersed ZIF-8 nanoparticles was added and the PA thin film was synthesized. The remaining hexane and rest of the unreacted monomers were washed out with DI water at 80 ^{0}C and finally, the membrane was dried at 100 ^{0}C. A scheme of the procedure can be seen in **Figure 2.7** while the full experimental details are shown in chapter 11.

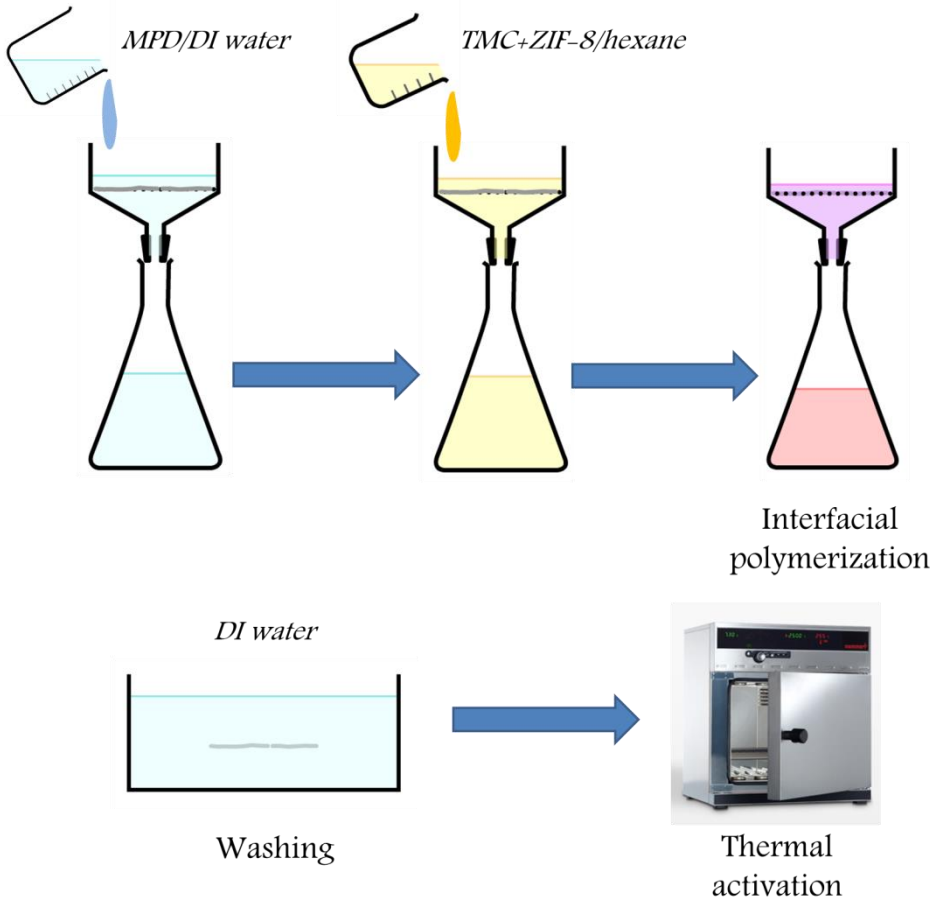

Figure 2.7. Scheme of the preparation of supported polyamide membranes *via* interfacial polymerization.

Thin films of Pebax® 1657 were prepared following a solution-casting procedure. The polymer solution was prepared in an EtOH/H_2O mixture and cast on the asymmetric porous P84® using the same film applicator as before. Afterwards, the membrane was kept at room temperature for 1 day for complete solvent evaporation. In the case of the Pebax® MMMs, the corresponding amount of MOF (ZIF-8, UiO-66, MIL-101(Cr) or ZIF-7/8 core-shells) was dispersed in the EtOH/H_2O mixture solvent previous to the addition of the polymer. Then the suspension was cast on the polymeric supports and allowed to dry, as explained above (see **Figure 2.8**). These membranes were applied for biogas upgrading (i.e. CO_2/CH_4 separation) and dense polytrimethylsilylpropyne (PTMSP) was also used as support. The experimental details can be seen completely in chapter 14.

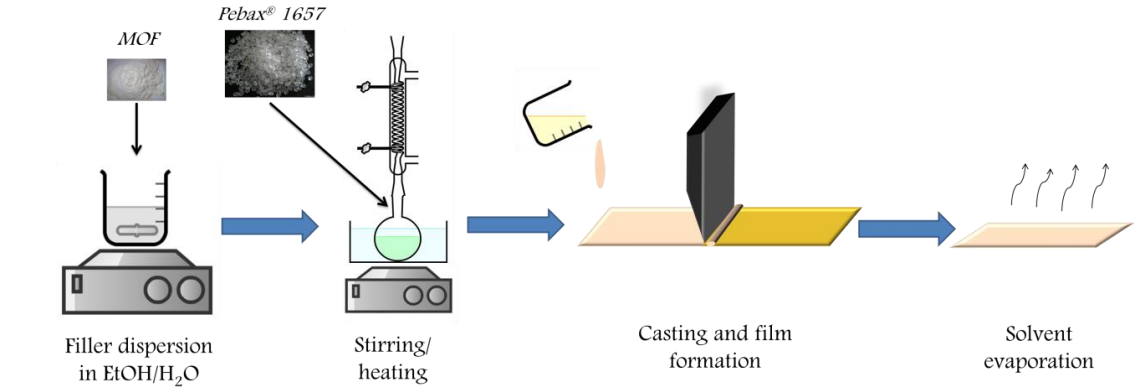

Figure 2.8. Scheme of the preparation of supported Pebax® 1657 membranes.

2.3.4. Preparation of polymer-stabilized percolation membranes (PSPMs)

These membranes consist of a percolation network of a nanoporous component (zeolite or MOF) obtained by pressing a powder, followed by the infiltration of the intercrystalline space by a gas-impermeable polymer to force gas transport exclusively through the percolation network of the embedded nanoporous material. This way they mean a middle point between MMMs, owing to the use of a polymeric matrix, and pure MOF membranes, because the used polymer is not permeable to the gas and only the MOF plays the gas separation role. These membranes were prepared during a research stay in the University of Hannover (*Leibniz Universität Hannover*, LUH) using ZIF-7(III), ZIF-8 and ZIF-7/8 core-shells as fillers (all of them synthesized at the University of Zaragoza). The work is fully developed in chapter 12 and a scheme of the general procedure can be seen in **Figure 2.9**.

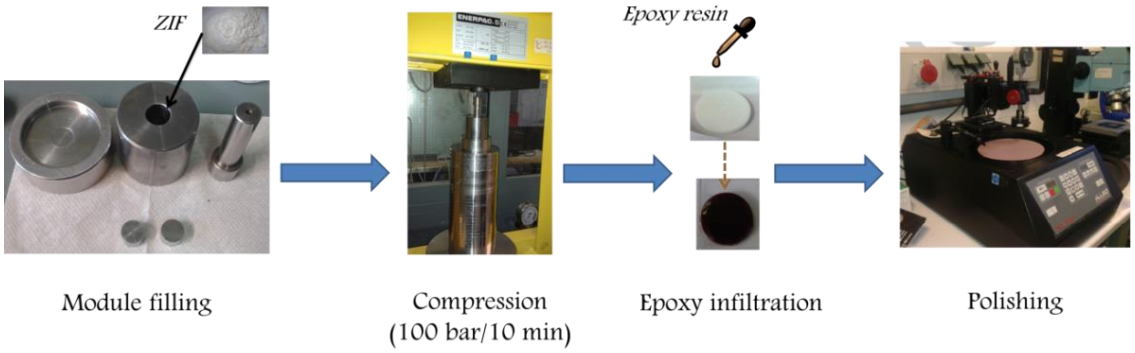

Figure 2.9. Scheme of the preparation of PSPMs.

2.3.5. Preparation of polymer blends

Polymers of intrinsic microporosity (PIMs) have been used to fabricate blended composites for gas separation. Membranes based on combinations of PBI with PIM-EA(H_2)-TB and 6FDA-DAM with PIM-1 have been prepared. The former led to homogenous blends in form of dense and asymmetric membranes useful for CO_2 capture in pre-combustion conditions (H_2/CO_2 separation). The latter were prepared in the form of dense membranes heterogeneously blended that were applied for post-combustion CO_2 capture and biogas upgrading (CO_2/N_2 and CO_2/CH_4 separation, respectively). The synthesis routes were similar to those previously explained in sections 2.3.1 and 2.3.2 and they are fully developed in chapters 10 and 13.

2.3.6. Comparison among different membrane configurations

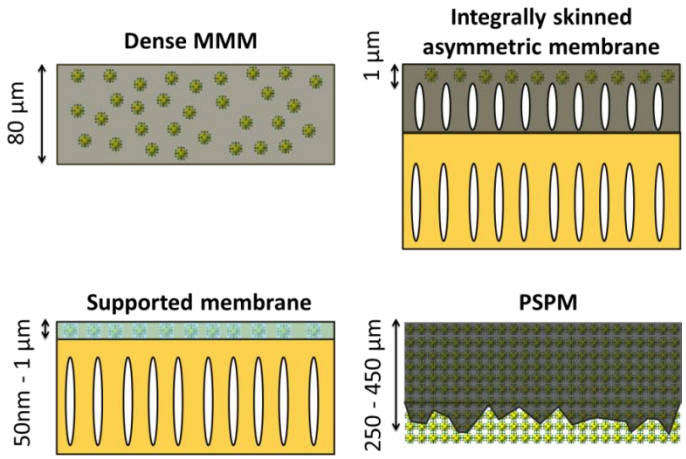

Figure 2.10. Scheme of the different membrane configurations used in this work. The thickness of the gas selective layer is also shown.

In **Figure 2.10** a scheme of the different membrane configurations previously explained can be seen. The gas selective layer of each composite is also indicated. **Table 2.3** contains the information of the polymers and fillers used for their preparation, as well as the chapters where they can be found.

Table 2.3. Summary of the polymers and fillers used in this thesis to prepare membranes with different configurations.

Type of membrane	Polymer	Filler	Chapter
Dense MMM	Matrimid® PBI 6FDA-DAM PIM-1 PIM-EA(H_2)-TB PIM-EA(H_2)-TB/blends PIM-1/6FDA-DAM blends	ZIF-7 ZIF-8 ZIF-7/8 nZIF-11 ZIF-11 ZIF-93 ZIF-93/11	4, 5, 6, 7, 8, 10, 13
Integrally skinned asymmetric membrane	PBI P84®	ZIF-8	9, 10
Supported membrane	Pebax® Polyamide	ZIF-8 UiO-66 MIL-101(Cr) ZIF-7/8	11, 14
PSPM	Epoxy resin	ZIF-7(III) ZIF-8 ZIF-7/8	12

2.4. Gas separation analysis

Mixed-gas analysis was performed with all the membranes prepared in this thesis in a gas separation setup whose scheme can be seen in **Figure 2.11**. The membranes (circular areas of 3.14 or 15.2 cm^2) were introduced into a module consisting of two stainless steel pieces and a 316LSS macroporous disk support (from Mott Co.) with a 20 μm nominal pore size, gripped inside with silicone or viton o-rings.

The permeation module was placed in a UNE 200 Memmert oven to control the temperature of the experiments (35-250 °C). For pre-combustion CO_2 capture and biogas upgrading, the gas separation measurements were carried out by feeding an equimolar mixture (25/25 cm^3(STP) min^{-1}) at 3-6 bar to the feed side by means of two flow-mass controllers (Alicat Scientific). For post-combustion capture the CO_2 concentration in the feed flow was 10 %vol. The permeate side of the membrane was

swept with a stream of Ar or He at 1 bar. Concentrations of H_2, N_2, CH_4 and CO_2 in the outgoing streams were analyzed by an Agilent 3000A online gas microchromatograph equipped with a thermal conductivity detector. Permeability was calculated in Barrer (10^{-10} cm^3(STP) cm cm^{-2} s^{-1} $cmHg^{-1}$) once the steady-state of the exit stream was reached (for at least 3 h), and the separation selectivity was calculated as the ratio of permeabilities. When the thickness of the membranes was impossible to determine, permeance instead of permeability was calculated in GPU (10^{-6} cm^3(STP) cm^{-2} s^{-1} $cmHg^{-1}$). The different operating conditions are summarized in **Table 2.4**.

Table 2.4. Operating conditions for the different gas separation tests.

Separation process	Gas mixture	Temperature (°C)	Feed pressure (bar)
Pre-combustion CO_2 capture	H_2/CO_2 (50/50 (v/v))	35-250	1-6
Post-combustion CO_2 capture	CO_2/N_2 (10/90 (v/v))	35	3
Biogas upgrading	CO_2/CH_4 (50/50 (v/v))	35	3-5

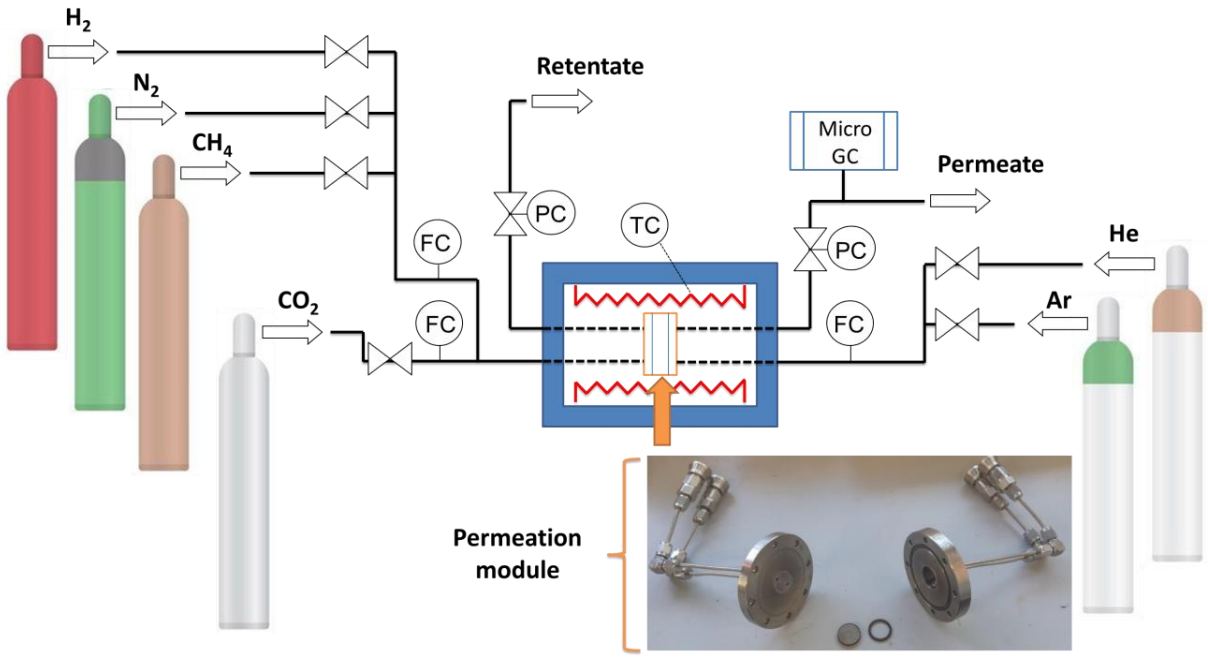

Figure 2.11. Scheme of the gas separation setup.

2.5. Characterization techniques

2.5.1. X-ray diffraction (XRD)

XRD diffraction is an analytical technique that allows the phase identification of a crystalline material and can provide information of its unit cell characteristics. In an X-ray diffractometer, monochromatic X-rays are directed onto the sample. The sample and the detector rotate within a certain range of angles (θ), while the intensity of the reflected X-rays is recorded and the detector converts the signal into a count rate. When the angle of the incident X-rays impinging on the sample satisfies the Bragg´s law ($2d \cdot sin(\theta) = n \cdot \lambda$), a constructive interference occurs and an intensity peak appears. In this equation, d refers to the distance between crystallographic planes, n is a positive integer number and λ is the wavelenght of the XRD radiation. The d-spacing can explain the packing density since of a material since it is related to distance among the central atoms of close planes.

Powder XRD spectra of MOFs and MMMs were acquired using a D-Max Rigaku X-ray diffractometer with a copper anode and a graphite monochromator to select CuKα radiation (λ = 1.540 Å), taking data from 2θ=2.5° to 40° at a scan rate of 0.03 ° s^{1}.

2.5.2. Thermal analysis

- Thermogravimetric analysis (TGA)

Thermogravimetric analysis (TGA) measures the amount of weight change of a material as a function of increasing temperature and time, in an inert (N_2, Ar, He…) or oxidizing (air) atmosphere. This technique determines the temperature and the weight change of decomposition reactions, making a quantitative composition analysis possible. It can also be used to determine the presence of water and other residual solvents in the sample, allowing verifying the right activation of MOFs and membranes.

TGA analyses were carried out using a Mettler Toledo TGA/STDA 851e. The samples (4 mg), placed in 70 μL alumina pans, were heated in an air or nitrogen flow from 25 to 900 °C at a heating rate of 5, 10 and 20 °C min^{-1}.

- Differential scanning calorimetry (DSC)

Differential scanning calorimetry (DSC) measures the amount of energy absorbed or released by a sample while it is heated or cooled, providing quantitative data on endothermic and exothermic processes. DSC can be used to measure the melting temperature, the heat of fusion or the glass transition temperature of a sample. All of them phase transition processes that imply energy changes.

DSC analysis was performed on a Mettler Toledo DSC822e. Samples (10 mg) placed in 70 μL aluminum pans were heated in 40 mL of nitrogen flow from 25 to 500 ^{0}C at a heating rate of 10 ^{0}C min^{-1}.

2.5.3. Electron microscopy

Electron microscopy is used to generate high-resolution images of objects whose size is too small to be seen with a light microscope.

- Scanning electron microscopy (SEM)

The scanning electron microscope (SEM) impinges a high-energy electron beam on the surface of solid samples. This way, the signals deriving from the electron-sample interactions reveal information about the external morphology of the sample. The SEM is also capable of performing elemental analyses of selected point locations on the sample, quantifying its chemical compositions (EDS, energy-dispersive X-ray spectroscopy)

The accelerated electrons contain kinetic energy that is dissipated when they crash onto the solid sample. This collision produces secondary electrons, backscattered electrons, diffracted backscattered electrons and photons (characteristic X-rays used for the EDS analysis). Secondary electrons and backscattered electrons are commonly used for the sample imaging. The secondary electrons are useful to show the morphology and topography of the samples, while the backscattered electrons are more valuable for contrasts in the composition of multiphase samples.

SEM images of MOFs and membranes were obtained using a FEI Inspect F50 model scanning electron microscope, operated at 20 kV. Cross-sections of membranes were

prepared by freeze-fracturing after immersion in liquid N_2 and subsequently coated with Pt.

- Transmission electron microscopy (TEM)

The transmission electron microscope (TEM) also uses a high-energy electron beam (100-400 kV). In this case the beam passes through the sample and the interactions between the electrons and the atoms forms the image. The sample must be thin enough (<100 nm) to transmit sufficient electrons to form an image with minimum energy loss. Elemental analysis is also possible with this microscopy and the characterization of crystalline samples by electron diffraction.

TEM images of the MOFs were obtained using a FEI Tecnai F30 microscope, operated at 300 kV. This TEM, fitted with a SuperTwin® lens allowing a point resolution of 1.9 Å, is equipped for spectroscopy experiments performed in EDS (X-Ray Microanalysis). The samples were prepared by dispersion of the powder in ethanol before placing a few drops of the suspension onto the copper carbon coated microgrid.

2.5.4. Spectroscopy

- Fourier transform infrared spectroscopy (FTIR)

In this kind of spectroscopy, infrared radiation passes through a sample. Some of the radiation is absorbed by this sample and the rest of it is transmitted. The resulting spectrum represents the molecular absorption and transmission, creating a one-of-a-kind molecular fingerprint of the sample. The term "Fourier-transform" stands for the use of Fourier transformation to convert the raw data into the actual spectrum. Infrared spectroscopy can be useful for the qualitative analysis of a material. Besides, the size of the peaks in the spectrum is related to the amount of material present.

Fourier transform infrared spectroscopy (FTIR) was performed on a Bruker Vertex 70 FTIR spectrometer equipped with a deuterated triglycine sulfate (DTGS) detector and a Golden Gate diamond ATR accessory. Powder samples and membranes were measured in a diffuse reflectance module. Both spectra were recorded by averaging 40 scans in the 4000-600 cm^{-1} wavenumber range at a resolution of 4 cm^{-1}.

- Raman spectroscopy

The Raman spectroscopy is based on the inelastic scattering of monochromatic light from a laser source and provides information about vibrational, rotational and other low frequency transitions in molecules. The photons of the laser light are absorbed by the sample and then reemitted. This way the frequency of the reemitted photons changes in comparison with the original monochromatic frequency, which is called the Raman effect. The Raman effect is based on the interaction between the electrons of the sample and the monochromatic light, which can create an induced dipole moment within the molecule based on its polarizability.

In this thesis, membranes were characterized by Raman spectroscopy using a WiTec Alpha300 Confocal Raman Microscope, with a 785 nm laser excitation beam.

- Nuclear magnetic resonance spectroscopy (NMR)

Nuclear magnetic resonance spectroscopy (NMR) is an analytical technique that can be used with solutions and solid-state samples and it is based on the magnetic properties of certain atomic nuclei. This type of spectroscopy determines the physical and chemical properties of atoms in molecules, providing detailed information about their structure and chemical environment.

NMR spectroscopy is only applicable to samples containing nuclei with spin. Isotopes of particular interest are ^{1}H, ^{13}C, ^{19}F and ^{31}P, all of them with a spin of ½. In the presence of an external magnetic field, two spin states exist: one aligns with the magnetic field and the other opposes it. All the nuclei in the sample do not give resonant signals at the same frequency values, because the electrons surrounding the nuclei move in response to the applied magnetic field, generating local magnetic fields that oppose the much stronger field applied. This electron movement has a shielding effect for the protons, making it necessary to increase the magnetic field to achieve resonance. Such increments are very small, normally ppm, and they are dependent on the chemical environment of the proton.

^{13}C NMR Spectra were recorded in a Bruker Avance III WB400 spectrometer with 4 mm zirconia rotors spun at the magic angle in N_2 at 10 kHz. ^{1}H-^{13}C CP spectra were measured using a ^{1}H $\pi/2$ pulse length of 3.0 μs, with a contact time (ramp) of 3 ms, a

spinal 64 proton decoupling sequence of 5.3 μs pulse length, and a recycle delay of 5 s. 3000 scans were acquired for each spectrum.

- X-ray photoelectron spectroscopy (XPS)

X-ray photoelectron spectroscopy (XPS) is an analytical technique capable of providing elemental and chemical state information from the outer 10 nm of the surface of a solid sample. This technique is based on the photoelectric effect. When the sample is irradiated with X-rays of known energy, photoelectrons can be emitted and their kinetic energy is analyzed with an electrostatic or electromagnetic analyzer. This way, the binding energy of the electronic orbit from which they have been emitted can be calculated using the Einstein's photoelectric equation. The binding energies are sensitive to the chemical environment of the atom and therefore chemical information about the sample can be obtained. Usually, the binding energy will increase as chemical state number increases.

XPS measurements were performed with an Ultra DLD (Kratos Tech.) with Al K_α emission (1486.6 eV) operated at 15 kV and 10 mA for the X-ray source. The samples were previously cleaned with an Ar^+ ion beam, working at 15 kV and 20 mA. All binding energies were corrected for charging of the samples by calibration of the C 1s peak at 284.9 eV. For the measurement with membranes, their cross-section was prepared by freeze-fracturing in liquid nitrogen, as for SEM analysis.

2.5.5. Gas adsorption analysis

Gas sorption analysis provides useful information about the textural properties of porous solids such as their surface area and pore size distribution. Before performing a gas sorption analysis, the solid must be degassed to remove contaminants (other adsorbed gases and humidity) that would interfere in the analysis. The sample degassing is carried out heating it under vacuum or a flow of dry inert gas. After that, the test is performed under isotherm conditions. Small amounts of gas are injected into the evacuated sample chamber as the gas pressure increases. The gas molecules interact with the surface of every pore in the solid, being adsorbed layer by layer until the saturation pressure is reached. The quantity of gas adsorbed in equilibrium at each pressure constitutes the adsorption isotherm. Adsorption isotherms can be classified in six different types according to IUPAC and when fitted to a certain adsorption model,

such as *Brunauer-Emmet-Teller (BET)* or *Barret-Joyner-Halenda (BJH),* the surface area and pore size distribution can be calculated.

Gas sorption tests have been performed with several gases in this thesis, depending on the pore size of the sample. Nitrogen adsorption/desorption isotherms were obtained using a Micromeritics Tristar 3000 surface area and porosity analyzer, after previously degassing the samples generally at 200 ^{0}C for 8 h under vacuum. Carbon dioxide adsorption isotherms were measured using a volumetric adsorption analyzer (Micromeritics ASAP 2020) at 0 ^{0}C up to 120 kPa after degassing at 200 ^{0}C for 8 h.

CHAPTER 3

BIBLIOGRAPHY

[1] F. H. Soriano, F. Mulatero, *Energy Policy* **2011**, *39*, 3582-3590.

[2] PTE CO_2, *https://www.pteco2.es/es/tecnologias/captura* **(10/01/2019)**.

[3] S. D. Kenarsari, D. Yang, G. Jiang, S. Zhang, J. Wang, A. G. Russell, Q. Wei, M. Fan, *RSC Adv.* **2013**, *3*, 22739-22773.

[4] Z. Dai, L. Ansaloni, L. Deng, *Ind. Eng. Chem. Res.* **2016**, *55*, 5983-5992.

[5] E. S. Rubin, H. Mantripragada, A. Marks, P. Versteeg, J. Kitchin, *Prog. Energy Comb. Sci.* **2012**, *38*, 630-671.

[6] Y. Tan, E. Croiset, M. A. Douglas, K. V. Thambimuthu, *Fuel* **2006**, *85*, 507-512.

[7] A. Tabe-Mohammadi, *Sep. Sci. Technol.* **1999**, *34*, 2095-2111.

[8] N. Abatzoglou, S. Boivin, *Biofuels, Bioprod. Biorefin.* **2009**, *3*, 42-71.

[9] M. Harasimowicz, P. Orluk, G. Zakrzewska-Trznadel, A. Chmielewski, *J. Hazard. Mater.* **2007**, *144*, 698-702.

[10] S. Rasi, A. Veijanen, J. Rintala, *Energy*, **2007**, *32*, 1375-1380.

[11] W. Burgers, P. Northrop, H. Kheshgi, J. Valencia, *Energy Procedia* **2011**, *4*, 2178-2184.

[12] B. Seoane, J. Coronas, I. Gascon, M. E. Benavides, O. Karvan, J. Caro, F. Kapteijn, J. Gascon, *Chem. Soc. Rev.* **2015**, *44*, 2421-2454.

[13]Global CCS Institute, *http://cdn.globalccsinstitute.com/sites/default/files/publications/116211/global-status-ccs-2013.pdf* **(10/11/2017)**.

[14] J. Franz, P. Maas, V. Scherer, *Appl. Energy* **2014**, *130*, 532-542.

[15] D. Aaron, C. Tsouris, *Sep. Sci. Technol.* **2005**, *40*, 321-348.

[16] T. C. Merkel, M. Zhou, R. W. Baker, *J. Membr. Sci.* **2012**, *389*, 441-450.

[17] L. Clements, P. Bhat, *Meeting Amer. Inst. Chem. Eng* **1986**.

[18] R. W. Baker, *Ind. Eng. Chem. Res.* **2002**, *41*, 1393-1411.

[19] R. W. Baker, K. Lokhandwala, *Ind. Eng. Chem. Res.* **2008**, *47*, 2109-2121.

[20] J. Ciferno, S. Plasynski, *Report DOE/NETL* **2010**.

[21] M. C. Woods, P. Capicotto, J. Haslbeck, N. Kuehn, M. Matuszewski, L. Pinkerton, M. Rutkowski, R. Schoff, V. Vaysman, *National Energy Technology Laboratory* **2007**.

[22] Y. Osada, T. Nakagawa, *Membrane science and technology*, CRC Press **1992**.

[23] R. W. Baker, *John Wiley & Sons, Ltd.* **2004**, 96-103.

[24] J. D. Perry, K. Nagai, W. J. Koros, *MRS Bull* **2006**, *31*, 745-749.

[25] P. Cote, Z. Alam, J. Penny, *Desalination* **2012**, *288*, 145-151.

[26] S. Loeb, S. Sourirajan, *Adv. Chem. Ser.* **1963**, *38*, 117.

[27] A. Car, C. Stropnik, W. Yave, K. Peinemann, *J. Membr. Sci.*, **2008**, 307, 88-95.

[28] L. Landau, B. Levich, *Dyn. Curved Fronts* **1988**, 141-153.

[29] P. A. Gurr, J. M. Scofield, J. Kim, Q. Fu, S. E. Kentish, G. G. Qiao, *J. Polym. Sci. Part A: Polym. Chem.* **2014**, *52*, 3372-3382.

[30] M. Wang, Z. Wang, S. Li, C. Zhang, J. Wang, S. Wang, *Energy Environ. Sci.* **2013**, *6*, 539-551.

[31] R. W. Baker, *Encyclopedia of Polymer Science and Technology* **2003**.

[32] J. Mulder, *Basic principles of membrane technology*, Springer Science & Business Media **2012**.

[33] L. M. Robeson, *J. Membr. Sci.*, **1991**, 62, 165-185.

[34] L. M. Robeson, *J. Membr. Sci.* **2008**, *320*, 390-400.

[35] A. Bos, I. Pünt, M. Wessling, H. Strathmann, *Sep. Purif. Technol.* **1998**, *14*, 27-39.

[36] A. Bos, I. Pünt, M. Wessling, H. Strathmann, *J. Polym. Sci., Part B: Polym. Phys.* **1998**, *36*, 1547-1556.

[37] J. Krol, M. Boerrigter, G. Koops, *J. Membr. Sci.* **2001**, *184*, 275-286.

[38] H. Kawakami, M. Mikawa, S. Nagaoka, *J. Membr. Sci.* **1996**, *118*, 223-230.

[39] X. Duthie, S. Kentish, S. Pas, A. Hill, C. Powell, K. Nagai, G. Stevens, G. Qiao, *J. Polym. Sci., Part B: Polym. Phys.* **2008**, *46*, 1879–1890.
[40] F. Cacho-Bailo, G. Caro, M. Etxeberría-Benavides, O. Karvan, C. Téllez, J. Coronas, *RSC Adv.* **2016**, *6*, 5881–5889.
[41] J. Chiou, J. W. Barlow, D. R. Paul, *J Appl. Polym. Sci.* **1985**, *30*, 2633–2642.
[42] C. Zhou, T. Chung, R. Wang, Y. Liu, S. H. Goh, *J. Membr. Sci.* **2003**, *225*, 125–134.
[43] S. L. Liu, L. Shao, M. L. Chua, C. H. Lau, H. Wang, S. Quan, *Prog. Polym. Sci.* **2013**, *38*, 1089–1120.
[44] A. M. Kratochvil, W. J. Koros, *Macromolecules* **2008**, *41*, 7920–7927.
[45] H. Eguchi, D. J. Kim, W. J. Koros, *Polymer* **2015**, *58*, 121–129.
[46] F. Y. Li, Y. Xiao, T. Chung, S. Kawi, *Macromolecules* **2012**, *45*, 1427–1437.
[47] J. S. Kang, J. Won, H. C. Park, U. Y. Kim, Y. S. Kang, Y. M. Lee, *J. Membr. Sci.* **2000**, *169*, 229–235.
[48] L. Rosu, I. Sava, D. Rosu, *Appl. Surf. Sci.* **2011**, *257*, 6996–7002.
[49] K. Vanherck, G. Koeckelberghs, I. F. Vankelecom, *Prog. Polym. Sci.* **2013**, *38*, 874–896.
[50] L. Shao, S. Quan, X. Cheng, X. Chang, H. Sun, R. Wang, *Int. J. Hydrogen Energy* **2013**, *38*, 5122–5132.
[51] S. Quan, S. Li, Z. Wang, X. Yan, Z. Guo, L. Shao, *J. Mater. Chem. A* **2015**, *3*, 13758–13766.
[52] T. Chung, L. Shao, P. S. Tin, *Macromol. Rapid Commun.* **2006**, *27*, 998–1003.
[53] L. Zhu, M. T. Swihart, H. Lin, *J. Mater. Chem. A* **2017**, *5*, 19914–19923.
[54] L. Zhu, M. T. Swihart, H. Lin, *Energy Environ. Sci.* **2018**, *11*, 94–100.
[55] K. Y. Wang, Y. Xiao, T. Chung, *Chem. Eng. Sci.* **2006**, *61*, 5807–5817.
[56] A. Car, C. Stropnik, K. Peinemann, *Desalination*, **2006**, *200*, 424–426.
[57] M. Fang, C. Wu, Z. Yang, T. Wang, Y. Xia, J. Li, *J. Membr. Sci.* **2015**, *474*, 103–113.
[58] T. Merkel, R. Gupta, B. Turk, B. Freeman, *J. Membr. Sci.* **2001**, *191*, 85–94.
[59] B. Freeman, I. Pinnau, *Trends Polym. Sci.* **1997**, *5*, 167–173.
[60] S. Sridhar, B. Smitha, T. Aminabhavi, *Separation Purif. Rev.* **2007**, *36*, 113–174.
[61] D. Turnbull, M. H. Cohen, *J. Chem. Phys.* **1961**, *34*, 120–125.
[62] S. S. Hosseini, T. S. Chung, *J. Membr. Sci.* **2009**, *328*, 174–185.
[63] S. S. Hosseini, M. M. Teoh, T. S. Chung, *Polymer* **2008**, *49*, 1594–1603.
[64] P. Musto, F. Karasz, W. MacKnight, *Macromolecules* **1991**, *24*, 4762–4769.
[65] P. M. Budd, B. S. Ghanem, S. Makhseed, N. B. McKeown, K. J. Msayib, C. E. Tattershall, *Chem. Commun.* **2004**, 230–231.
[66] W. Yong, F. Li, Y. Xiao, P. Li, K. Pramoda, Y. Tong, T. Chung, *J. Membr. Sci.* **2012**, *407*, 47–57.
[67] X. Mei Wu, Q. Gen Zhang, P. Ju Lin, Y. Qu, A. Mei Zhu, Q. Lin Liu, *J. Membr. Sci.*, **2015**, *493*, 147–155.
[68] T. Chung, L. Y. Jiang, Y. Li, S. Kulprathipanja, *Prog. Polym. Sci.* **2007**, *32*, 483–507.
[69] S. Bertelle, T. Gupta, D. Roizard, C. Vallières, E. Favre, *Desalination* **2006**, *199*, 401–402.
[70] C. V. Funk, D. R. Lloyd, *J. Membr. Sci.* **2008**, *313*, 224–231.
[71] D. PAUL, D. KEMP, **1972**, *164*, 22–26.
[72] J. Duval, B. Folkers, M. Mulder, G. Desgrandchamps, C. Smolders, *J. Membr. Sci.* **1993**, *80*, 189–198.
[73] S. Kulprathipanja, R. Neuzil, N. Li, *US Patent* **1988**, *4*, 219.
[74] T. M. Gür, *J. Membr. Sci.* **1994**, *93*, 283–289.
[75] M. G. Süer, N. Baç, L. Yilmaz, *J. Membr. Sci.* **1994**, *91*, 77–86.
[76] J. Wijmans, R. Baker, *J. Membr. Sci.* **1995**, *107*, 1–21.
[77] S. Stern, J. Polym. Sci., Part A-2: Polym. Phys. **1968**, *6*, 1933–1934.
[78] Z. Dai, L. Ansaloni, L. Deng, *Green Energy Environ.* **2016**, *1*, 102–128.

[79] D. F. Sanders, Z. P. Smith, R. Guo, L. M. Robeson, J. E. McGrath, D. R. Paul, B. D. Freeman, *Polymer*, **2013**, *54*, 4729-4761.
[80] W. Koros, G. Fleming, *J. Membr. Sci.* **1993**, *83*, 1-80.
[81] J. Li, R. J. Kuppler, H. Zhou, *Chem. Soc. Rev.* **2009**, *38*, 1477-1504.
[82] R. Barrer, J. Barrie, J. Slater, *J. Polym. Sci., Part A: Polym. Chem.* **1958**, *27*, 177-197.
[83] D. Paul, W. Koros, J. Polym. Sci., Part B: Polym. Phys. **1976**, *14*, 675-685.
[84] S. Jordan, W. Koros, *Macromolecules* **1995**, *28*, 2228-2235.
[85] Z. P. Smith, D. F. Sanders, C. P. Ribeiro, R. Guo, B. D. Freeman, D. R. Paul, J. E. McGrath, S. Swinnea, *J. Membr. Sci.* **2012**, *415-416*, 558-567.
[86] S. Matteucci, Y. Yampolskii, B. D. Freeman, I. Pinnau, *Mater. Sci. Membr. Gas Vapor Sep.* **2006**, *1*, 1-2.
[87] A. Berens, H. Hopfenberg, *J. Membr. Sci.* **1982**, *10*, 283-303.
[88] J. P. O'connell, J. Prausnitz, B. Poling, *McGraw-Hill Companies-Inc.New Delhi.doi* **2001**, *10*, 0070116822.
[89] T. Yang, Y. Xiao, T. Chung, *Energy Environ. Sci.* **2011**, *4*, 4171-4180.
[90] J. M. Henis, Commercial and practical aspects of gas separation membranes, CRC Press: Boca Raton, FL **1994**.
[91] S. V. Wroblewski, *Annalen der Physik* **1879**, *244*, 29-52.
[92] T. Kim, W. Koros, G. Husk, K. O'brien, *J. Membr. Sci.* **1988**, *37*, 45-62.
[93] E. E. Gonzo, M. L. Parentis, J. C. Gottifredi, *J. Membr. Sci.* **2006**, *277*, 46-54.
[94] R. Bouma, A. Checchetti, G. Chidichimo, E. Drioli, *J. Membr. Sci.* **1997**, *128*, 141-149.
[95] J. Petropoulos, J. Polym. Sci., Part B: Polym. Phys. **1985**, *23*, 1309-1324.
[96] Y. Chiew, E. Glandt, *J. Colloid Interface Sci.* **1983**, *94*, 90-104.
[97] G. Banhegyi, *Colloid Polym. Sci.* **1986**, *264*, 1030-1050.
[98] M. R. Khdhayyer, E. Esposito, A. Fuoco, M. Monteleone, L. Giorno, J. C. Jansen, M. P. Attfield, P. M. Budd, *Sep. Purif. Technol.* **2017**, *173*, 304-313.
[99] T. T. Moore, W. J. Koros, *J. Mol. Struct.* **2005**, *739*, 87-98.
[100] K. Althumayri, W. J. Harrison, Y. Shin, J. M. Gardiner, C. Casiraghi, P. M. Budd, P. Bernardo, G. Clarizia, J. C. Jansen, *Philos. Trans. A. Math. Phys. Eng. Sci.* **2016**, *374*, 20150031-20150031.
[101] M. Moaddeb, W. J. Koros, *J. Membr. Sci.* **1997**, *125*, 143-163.
[102] F. Serpaggi, G. Férey, *Microporous Mesoporous Mater.* **1999**, *32*, 311-318.
[103] H. Li, M. Eddaoudi, M. O'Keeffe, O. M. Yaghi, *Nature* **1999**, *402*, 276-279.
[104] S. Kitagawa, M. Kondo, *Bull. Chem. Soc. Jpn.* **1998**, *71*, 1739-1753.
[105] S. S. Chui, S. M. Lo, J. P. Charmant, A. G. Orpen, I. D. Williams, *Science* **1999**, *283*, 1148-1150.
[106] H. Furukawa, M. A. Miller, O. M. Yaghi, *J. Mater. Chemi.* **2007**, *17*, 3197-3204.
[107] H. Furukawa, N. Ko, Y. B. Go, N. Aratani, S. B. Choi, E. Choi, A. O. Yazaydin, R. Q. Snurr, M. O'Keeffe, J. Kim, O. M. Yaghi, *Science* **2010**, *329*, 424-428.
[108] P. L. Llewellyn, S. Bourrelly, C. Serre, A. Vimont, M. Daturi, L. Hamon, G. De Weireld, J. Chang, D. Hong, Y. Kyu Hwang, *Langmuir* **2008**, *24*, 7245-7250.
[109] M. Eddaoudi, J. Kim, N. Rosi, D. Vodak, J. Wachter, M. O'Keeffe, O. M. Yaghi, *Science* **2002**, *295*, 469-472.
[110] G. Ferey, C. Serre, *Chem. Soc. Rev.* **2009**, *38*, 1380-1399.
[111] B. Zornoza, C. Tellez, J. Coronas, J. Gascon, F. Kapteijn, *Microporous Mesoporous Mater.* **2013**, *166*, 67-78.
[112] H. B. T. Jeazet, C. Staudt, C. Janiak, *Dalton Trans.* **2012**, *41*, 14003-14027.
[113] H. Jiang, T. Akita, T. Ishida, M. Haruta, Q. Xu, *J. Am. Chem. Soc.* **2011**, *133*, 1304-1306.

[114] J. Gascon, U. Aktay, M. D. Hernandez-Alonso, G. P. M. van Klink, F. Kapteijn, *J. Catal.* **2009**, *261*, 75-87.

[115] P. Horcajada, C. Serre, M. Vallet-Regí, M. Sebban, F. Taulelle, G. Férey, *Angew. Chem.* **2006**, *118*, 6120-6124.

[116] K. S. Park, Z. N. Ni, A. P. Cô te, J. Y. Choi, R. Huang, F. J. Uribe-Romo, H. K. Chae, M. O'Keeffe, O. M. Yaghi, *PNAS* **2006**, *103*, 10186-10191.

[117] X. Huang, Y. Lin, J. Zhang, X. Chen, *Angew. Chem.* **2006**, *118*, 1587-1589.

[118] Y. Lee, J. Kim, W. Ahn, *Korean J. Chem. Eng.* **2013**, *30*, 1667-1680.

[119] H. Hayashi, A. P. Cote, H. Furukawa, M. O'Keeffe, O. M. Yaghi, *Nat. Mater.* **2007**, *6*, 501-506.

[120] K. Díaz, L. Garrido, M. López-González, L. F. Del Castillo, E. Riande, *Macromolecules* **2009**, *43*, 316-325.

[121] A. Perea-Cachero, J. Sánchez-Laínez, Á. Berenguer-Murcia, D. Cazorla-Amorós, C. Téllez, J. Coronas, *J. Membr. Sci.*, **2017**, *544*, 88-97.

[122] P. Zhao, G. I. Lampronti, G. O. Lloyd, M. T. Wharmby, S. Facq, A. K. Cheetham, S. A. Redfern, *Chem. Mater.* **2014**, *26*, 1767-1769.

[123] M. He, J. Yao, Q. Liu, Z. Zhongb, H. Wang, *Dalton Trans.* **2013**, *42*, 16608–16613.

[124] Y.-S. Li, F.-Y. Liang, H. Bux, A. Feldhoff, W.-S. Yang, J. Caro, *Andgew. Chem. Int. Ed.* **2010**, 548–551.

[125] S. Aguado, G. Bergeret, M. P. Titus, V. Moizan, C. Nieto-Draghi, N. Bats, D. Farrusseng, *New J. Chem.* **2011**, *35*, 546-550.

[126] S. Couck, T. Rémy, G. V. Baron, J. Gascon, F. Kapteijn, J. F. Denayer, *Phys. Chem. Chem. Phys.* **2010**, *12*, 9413-9418.

[127] T. Rodenas, I. Luz, G. Prieto, B. Seoane, H. Miro, A. Corma, F. Kapteijn, i Xamena, Francesc X Llabrés, J. Gascon, *Nat. Mater.* **2015**, *14*, 48-55.

[128] J. Park, S. Park, S. Jhung, *J. Korean Chem. Soc.* **2009**, *53*, 553-559.

[129] H. Cho, J. Kim, S. Kim, W. Ahn, *Microporous Mesoporous Mater.* **2013**, *169*, 180-184.

[130] A. Martinez Joaristi, J. Juan-Alcañiz, P. Serra-Crespo, F. Kapteijn, J. Gascon, *Cryst. Growth Des.* **2012**, *12*, 3489-3498.

[131] P. J. Beldon, L. Fábián, R. S. Stein, A. Thirumurugan, A. K. Cheetham, T. Friščić, *Angew. Chem. Int. Ed.* **2010**, *49*, 9640-9643.

[132] Q. Shi, Z. Chen, Z. Song, J. Li, J. Dong, *Angew. Chem.* **2011**, *123*, 698-701.

[133] Y. Lee, M. Jang, H. Cho, H. Kwon, S. Kim, W. Ahn, *Chem. Eng. J.* **2015**, *271*, 276-280.

[134] A. W. Thornton, D. Dubbeldam, M. S. Liu, B. P. Ladewig, A. J. Hilla, M. R. Hill, *Energy Environ. Sci.* **2012**, *5*, 7637–7646.

[135] W. Morris, N. He, K. G. Ray, P. Klonowski, F. Hiroyasu, I. N. Daniels, Y. A. Houndonougbo, M. Asta, O. M. Yaghi, B. B. Laird, *J. Phys. Chem.* **2012**, *116*, 24084–24090.

[136] B. Seoane, J. M. Zamaro, C. Tellez, J. Coronas, *CrystEngComm* **2012**, *14*, 3103-3107.

[137] B. Reif, F. Fabisch, M. Hovestadt, M. Hartmann, W. Schwieger, *Microporous Mesoporous Mater.* **2017**, *243*, 65-68.

[138] W. Morris, B. Leung, H. Furukawa, O. K. Yaghi, N. He, H. Hayashi, Y. Houndonougbo, M. Asta, B. B. Laird, O. M. Yaghi, *J. Am. Chem. Soc.* **2010**, *132*, 11006-11008.

[139] K. G. Ray, D. L. Olmsted, J. M. Burton, Y. Houndonougbo, B. B. Laird, M. Asta, *Chem. Mater.* **2014**, *26*, 3976-3985.

[140] X. Liu, Y. Li, Y. Ban, Y. Peng, H. Jin, W. Yang, K. Li, *Mater. Lett.* **2014**, *136*, 341-344.

[141] J. A. Thompson, C. R. Blad, N. A. Brunelli, M. E. Lydon, R. P. Lively, C. W. Jones, S. Nair, *Chem. Mater.* **2012**, *24*, 1930-1936.

[142] C. Zhang, Y. Xiao, D. Liu, Q. Yang, C. Zhong, *Chem. Commun.* **2013**, *49*, 600–602.
[143] F. Hillman, J. Brito, H. Jeong, *ACS Appl. Mater. Interfaces* **2018**, *10*, 5586–5593.
[144] R. Banerjee, A. Phan, B. Wang, C. Knobler, H. Furukawa, M. O'Keeffe, O. M. Yaghi, *Science* **2008**, *319*, 939–943.
[145] R. Banerjee, H. Furukawa, D. Britt, C. Knobler, M. O'Keeffe, O. M. Yaghi, *J. Am. Chem. Soc.* **2009**, *131*, 3875–3877.
[146] N. T. Nguyen, H. Furukawa, F. Gándara, H. T. Nguyen, K. E. Cordova, O. M. Yaghi, *Angew. Chem. Int. Ed.* **2014**, *53*, 10645–10648.
[147] S. M. Cohen, *Chem. Rev.* **2011**, *112*, 970–1000.
[148] Z. Wang, S. M. Cohen, *J. Am. Chem. Soc.* **2007**, *129*, 12368–12369.
[149] K. K. Tanabe, Z. Wang, S. M. Cohen, *J. Am. Chem. Soc.* **2008**, *130*, 8508–8517.
[150] M. J. Ingleson, J. P. Barrio, J. Guilbaud, Y. Z. Khimyak, M. J. Rosseinsky, *Chem. Commun.* **2008**, 2680–2682.
[151] S. J. Garibay, Z. Wang, K. K. Tanabe, S. M. Cohen, *Inorg. Chem.* **2009**, *48*, 7341–7349.
[152] Z. Wang, S. M. Cohen, *Angew. Chem.* **2008**, *120*, 4777–4780.
[153] D. Britt, C. Lee, F. J. Uribe-Romo, H. Furukawa, O. M. Yaghi, *Inorg. Chem.* **2010**, *49*, 6387–6389.
[154] M. Meilikhov, K. Yusenko, R. A. Fischer, *J. Am. Chem. Soc.* **2009**, *131*, 9644–9645.
[155] T. Ahnfeldt, D. Gunzelmann, T. Loiseau, D. Hirsemann, J. Senker, G. Férey, N. Stock, *Inorg. Chem.* **2009**, *48*, 3057–3064.
[156] C. Volkringer, S. M. Cohen, *Angew. Chem. Int. Ed.* **2010**, *49*, 4644–4648.
[157] S. J. Garibay, Z. Wang, S. M. Cohen, *Inorg. Chem.* **2010**, *49*, 8086–8091.
[158] K. M. Taylor-Pashow, J. D. Rocca, Z. Xie, S. Tran, W. Lin, *J. Am. Chem. Soc.* **2009**, *131*, 14261–14263.
[159] S. Bernt, V. Guillerm, C. Serre, N. Stock, *Chem. Communi.* **2011**, *47*, 2838–2840.
[160] V. Guillerm, F. Ragon, M. Dan-Hardi, T. Devic, M. Vishnuvarthan, B. Campo, A. Vimont, G. Clet, Q. Yang, G. Maurin, *Angew. Chem. Int. Ed.* **2012**, *51*, 9267–9271.
[161] M. Kandiah, S. Usseglio, S. Svelle, U. Olsbye, K. P. Lillerud, M. Tilset, *J. Mater. Chem.* **2010**, *20*, 9848–9851.
[162] S. J. Garibay, S. M. Cohen, *Chem. Commun.* **2010**, *46*, 7700–7702.
[163] A. Huang, J. Caro, *Angew. Chem. Int. Ed.* **2011**, *50*, 4979–4982.
[164] J. Canivet, S. Aguado, C. Daniel, D. Farrusseng, *ChemCatChem* **2011**, *3*, 675–678.
[165] F. Cacho-Bailo, M. Etxeberría-Benavides, O. Karvan, C. Téllez, J. Coronas, *CrystEngComm* **2017**, *19*, 1545–1554.
[166] X. Liu, Y. Li, Y. Ban, Y. Peng, H. Jin, H. Bux, L. Xu, J. Caro, W. Yang, *Chem. Commun.* **2013**, *49*, 9140–9142.
[167] S. Qiu, M. Xue, G. Zhu, *Chem. Soc. Rev.* **2014**, *43*, 6116–6140.
[168] E. D. Bloch, W. L. Queen, R. Krishna, J. M. Zadrozny, C. M. Brown, J. R. Long, *Science* **2012**, *335*, 1606–1610.
[169] Y. Zhang, X. Feng, S. Yuan, J. Zhou, B. Wang, *Inorg. Chem. Front.* **2016**, *3*, 896–909.
[170] E. Adatoz, A. K. Avci, S. Keskin, *Sep. Purif. Technol.* **2015**, *152*, 207–237.
[171] A. J. Brown, N. A. Brunelli, K. Eum, F. Rashidi, J. R. Johnson, W. J. Koros, C. W. Jones, S. Nair, *Science* **2014**, *345*, 72–75.
[172] F. Cacho-Bailo, G. Caro, M. Etxeberría-Benavides, O. Karvan, C. Téllez, J. Coronas, *Chem. Commun.* **2015**, *51*, 11283–11285.
[173] F. Cacho-Bailo, S. Catalan-Aguirre, M. Etxeberria-Benavides, O. Karvan, V. Sebastian, C. Tellez, J. Coronas, *J. Membr. Sci.* **2015**, *476*, 277–285.

[174] J. Wang, N. Li, Z. Li, J. Wang, X. Xu, C. Chen, *Ceram. Int.* **2016**, *42*, 8949-8954.
[175] X. Wang, M. Sun, B. Meng, X. Tan, J. Liu, S. Wang, S. Liu, *Chem. Commun.* **2016**, *52*, 13448-13451.
[176] K. Tao, L. Cao, Y. Lin, C. Kong, L. Chen, *J. Mater. Chem. A* **2013**, *1*, 13046-13049.
[177] Y. Pan, B. Wang, Z. Lai, *J. Membr. Sci.* **2012**, *421-422*, 292-298.
[178] Y. Pan, Z. Lai, *Chem. Commun.* **2011**, *47*, 10275-10277.
[179] T. Bae, J. S. Lee, W. Qiu, W. J. Koros, C. W. Jones, S. Nair, *Angew. Chem. Int. Ed.* **2010**, *49*, 9863-9866.
[180] S. R. Venna, M. A. Carreon, *J. Am. Chem. Soc.* **2009**, *132*, 76-78.
[181] F. Cacho-Bailo, M. Etxeberria-Benavides, O. David, C. Téllez, J. Coronas, *ACS Appl. Mater. Interfaces* **2017**, *9*, 20787-20796.
[182] A. Huang, H. Bux, F. Steinbach, J. Caro, *Angew. Chem.* **2010**, *122*, 5078-5081.
[183] Y. Liu, E. Hu, E. A. Khan, Z. Lai, *J. Membr. Sci.* **2010**, *353*, 36-40.
[184] A. Huang, W. Dou, J. Caro, *J. Am. Chem. Soc.* **2010**, *132*, 15562-15564.
[185] F. Cacho-Bailo, S. Catalán, M. Etxeberría-Benavides, O. Karvan, V. Sebastián, C. Téllez, J. Coronas, *J. Membr. Sci.* **2015**, *476*, 277-285.
[186] L. Ge, W. Zhou, A. Du, Z. Zhu, *J. Phys. Chem. C* **2012**, *116*, 13264-13270.
[187] F. Cacho-Bailo, I. Matito-Martos, J. Perez-Carbajo, M. Etxeberría-Benavides, O. Karvan, V. Sebastián, S. Calero, C. Téllez, J. Coronas, *Chem. Sci.* **2017**, *8*, 325-333.
[188] A. J. Brown, J. Johnson, M. E. Lydon, W. J. Koros, C. W. Jones, S. Nair, *Angew. Chem. Int. Ed.* **2012**, *51*, 10615-10618.
[189] S. Friebe, A. Mundstock, D. Schneider, J. Caro, *Chem. Eur. J.* **2017**, *23*, 6522-6526.
[190] H. Vogel, C. Marvel, J. Polym. Sci., Part A: Polym. Chem. **1961**, *50*, 511-539.
[191] O. Olabisi, K. Adewale, *Handbook of thermoplastics*, CRC press **2016**.
[192] T. Chung, J Macromol. Sci., Part C: Polym. Rev. **1997**, *37*, 277-301.
[193] H. Borjigin, K. A. Stevens, R. Liu, J. D. Moon, A. T. Shaver, S. Swinnea, B. D. Freeman, J. Riffle, J. E. McGrath, *Polymer* **2015**, *71*, 135-142.
[194] X. Li, R. P. Singh, K. W. Dudeck, K. A. Berchtold, B. C. Benicewicz, *J. Membr. Sci.* **2014**, *461*, 59-68.
[195] S. C. Kumbharkar, P. B. Karadkar, U. K. Kharul, *J. Membr. Sci.* **2006**, *286*, 161-169.
[196] T. Yang, G. M. Shi, T. Chung, *Adv. Energy Mater.* **2012**, *2*, 1358-1367.
[197] S. Matteucci, *Freeman, BD, Eds* **2005**.
[198] F. Dautzenberg, M. Mukherjee, *Chem. Eng. Sci.* **2001**, *56*, 251-267.
[199] L. Cui, W. Qiu, D. R. Paul, W. J. Koros, *Polymer*, **2011**, *52*, 3374-3380.
[200] J. Barsema, G. Kapantaidakis vd, N. Van der Vegt, G. Koops, M. Wessling, *J. Membr. Sci.* **2003**, *216*, 195-205.
[201] L. S. White, *J. Membr. Sci.* **2002**, *205*, 191-202.
[202] J. Liu, T. Bae, W. Qiu, S. Husain, S. Nair, C. W. Jones, R. R. Chance, W. J. Koros, *J. Membr. Sci.* **2009**, *343*, 157-163.
[203] K. Tanaka, M. Okano, H. Toshino, H. Kita, K. Okamoto, *J. Polym. Sci., Part B: Polym. Phys.* **1992**, *30*, 907-914.
[204] P. M. Budd, K. J. Msayib, C. E. Tattershall, B. S. Ghanem, K. J. Reynolds, N. B. McKeown, D. Fritsch, *J. Membr. Sci.* **2005**, *251*, 263-269.
[205] N. B. McKeown, P. M. Budd, *Chem. Soc. Rev.* **2006**, *35*, 675-683.
[206] P. M. Budd, N. B. McKeown, *Polym. Chem.* **2010**, *1*, 63-68.

[207] N. Du, H. B. Park, G. P. Robertson, M. M. Dal-Cin, T. Visser, L. Scoles, M. D. Guiver, *Nat. Mater.* **2011**, *10*, 372-375.

[208] P. M. Budd, N. B. McKeown, B. S. Ghanem, K. J. Msayib, D. Fritsch, L. Starannikova, N. Belov, O. Sanfirova, Y. Yampolskii, V. Shantarovich, *J. Membr. Sci.* **2008**, *325*, 851-860.

[209] P. Li, T. Chung, D. Paul, *J. Membr. Sci.* **2013**, *432*, 50-57.

[210] M. Carta, R. Malpass-Evans, M. Croad, Y. Rogan, J. C. Jansen, P. Bernardo, F. Bazzarelli, N. B. McKeown, *Science* **2013**, *339*, 303-307.

[211] J. H. Kim, S. Y. Ha, Y. M. Lee, *J. Membr. Sci.* **2001**, *190*, 179-193.

[212] V. Bondar, B. Freeman, I. Pinnau, *J. Polym. Sci., Part B: Polym. Phys.* **2000**, *38*, 2051-2062.

[213] M. J. Raaijmakers, N. E. Benes, *Prog. Polym. Sci.* **2016**, *63*, 86-142.

[214] J. Zhao, Z. Wang, J. Wang, S. Wang, *J. Membr. Sci.* **2006**, *283*, 346-356.

[215] X. Yu, Z. Wang, Z. Wei, S. Yuan, J. Zhao, J. Wang, S. Wang, *J. Membr. Sci.* **2010**, *362*, 265-278.

[216] Z. Ali, F. Pacheco, E. Litwiller, Y. Wang, Y. Han, I. Pinnau, *J. Materi. Chem. A* **2018**, *6*, 30-35.

[217] M. Shan, X. Liu, X. Wang, I. Yarulina, B. Seoane, F. Kapteijn, J. Gascon, *Sci. Adv.* **2018**, *4*, eaau1698.

[218] V. Giel, Z. Morávková, J. Peter, M. Trchová, *J. Membr. Sci.* **2017**, *537*, 315-322.

[219] V. Giel, M. Perchacz, J. Kredatusová, Z. Pientka, *Nanoscale Res. Lett.* **2017**, *12*, 3.

[220] H. S. M. Suhaimi, C. P. Leo, A. L. Ahmad, *Chem. Eng. Technol.* **2017**, *40*, 631-638.

[221] J. R. Klaehn, C. J. Orme, E. S. Peterson, *J. Membr. Sci.* **2016**, *515*, 1-6.

[222] Z. Hu, Z. Kang, Y. Qian, Y. Peng, X. Wang, C. Chi, D. Zhao, *Ind. Eng. Chem. Res.* **2016**, *55*, 7933-7940.

[223] T. Yang, T. Chung, *Int. J. Hydrogen Energy* **2013**, *38*, 229-239.

[224] D. R. Pesiri, B. Jorgensen, R. C. Dye, *J. Membr. Sci.* **2003**, *218*, 11-18.

[225] L. Li, Y. Jianfeng, X. Wang, Y. Chen, H. Wang, *J. Appl. Polym. Sci.* **2014**, *131*, 41056.

[226] T. Yang, T. Chung, *J. Mater. Chem. A* **2013**, *1*, 6081-6090.

[227] R. P. Singh, G. J. Dahe, K. W. Dudeck, C. F. Welch, K. A. Berchtold, *Energy Procedia* **2014**, *63*, 153-159.

[228] K. A. Berchtold, R. P. Singh, J. S. Young, K. W. Dudeck, *J. Membr. Sci.* **2012**, *415*, 265-270.

[229] S. Kumbharkar, K. Li, *J. Membr. Sci.* **2012**, *415*, 793-800.

[230] S. Kumbharkar, Y. Liu, K. Li, *J. Membr. Sci.* **2011**, *375*, 231-240.

[231] S. S. Hosseini, N. Peng, T. S. Chung, *J. Membr. Sci.* **2010**, *349*, 156-166.

[232] J. A. Thompson, J. T. Vaughn, N. A. Brunelli, W. J. Koros, C. W. Jones, S. Nair, *Microporous Mesoporous Mater.* **2014**, *192*, 43-51.

[233] S. Shahid, K. Nijmeijer, *J. Membr. Sci.* **2014**, 470, 166-177.

[234] J. A. Thompson, K. W. Chapman, W. J. Koros, C. W. Jones, S. Nair, *Microporous Mesoporous Mater.* **2012**, *158*, 292-299.

[235] Q. Song, S. Nataraj, M. V. Roussenova, J. C. Tan, D. J. Hughes, W. Li, P. Bourgoin, M. A. Alam, A. K. Cheetham, S. A. Al-Muhtaseb, *Energy Environ. Sci.* **2012**, *5*, 8359-8369.

[236] M. J. C. Ordonez, K. J. Balkus Jr., J. P. Ferraris, I. H. Musselman, *J. Membr. Sci.* **2010**, *361*, 28-37.

[237] A. B. Yumru, M. Safak Boroglu, I. Boz, *Greenhouse Gases Sci. Technol.* **2018**, *8*, 529–541.

[238] S. Basu, A. Cano-Odena, I. F. Vankelecom, *Sep. Purif. Technol.* **2011**, *81*, 31-40.

[239] S. Sridhar, R. Veerapur, M. Patil, K. Gudasi, T. Aminabhavi, *J. Appl. Polym. Sci.* **2007**, *106*, 1585-1594.

[240] Y. Shen, A. C. Lua, *Chem. Eng. J.* **2012**, *188*, 199-209.

[241] A. Sabetghadam, B. Seoane, D. Keskin, N. Duim, T. Rodenas, S. Shahid, S. Sorribas, C. L. Guillouzer, G. Clet, C. Tellez, M. Daturi, J. Coronas, F. Kapteijn, J. Gascon, *Adv. Funct. Mater.* **2016**, *26*, 3154-3163.

[242] L. Xu, C. Zhang, M. Rungta, W. Qiu, J. Liu, W. J. Koros, *J. Membr. Sci.* **2014**, *459*, 223-232.
[243] W. Qiu, L. Xu, C. Chen, D. R. Paul, W. J. Koros, *Polymer* **2013**, *54*, 6226-6235.
[244] C. K. Yeom, J. M. Lee, Y. T. Hong, K. Y. Choi, S. C. Kim, *J. Membr. Sci.* **2000**, *166*, 71-83.
[245] M. Etxeberria-Benavides, O. David, T. Johnson, M. M. Łozińska, A. Orsi, P. A. Wright, S. Mastel, R. Hillenbrand, F. Kapteijn, J. Gascon, *J. Membr. Sci.* **2018**, *550*, 198-207.
[246] M. Safak Boroglu, A. B. Yumru, *Sep. Purif. Technol.* **2017**, *173*, 269-279.
[247] T. Mitra, R. S. Bhavsar, D. J. Adams, P. M. Budd, A. I. Cooper, *Chem. Commun.* **2016**, *52*, 5581-5584.
[248] S. J. Smith, B. P. Ladewig, A. J. Hill, C. H. Lau, M. R. Hill, *Sci. Rep.* **2015**, *5*, 7823.
[249] C. R. Mason, L. Maynard-Atem, N. M. Al-Harbi, P. M. Budd, P. Bernardo, F. Bazzarelli, G. Clarizia, J. C. Jansen, *Macromolecules* **2011**, *44*, 6471-6479.
[250] C. L. Staiger, S. J. Pas, A. J. Hill, C. J. Cornelius, *Chem. Mater.* **2008**, *20*, 2606-2608.
[251] X. Wu, W. Liu, H. Wu, X. Zong, L. Yang, Y. Wu, Y. Ren, C. Shi, S. Wang, Z. Jiang, *J. Membr. Sci.* **2018**, *548*, 309-318.
[252] L. Hao, K. Liao, T. Chung, *J. Mater. Chem. A* **2015**, *3*, 17273-17281.
[253] A. F. Bushell, M. P. Attfield, C. R. Mason, P. M. Budd, Y. Yampolskii, L. Starannikova, A. Rebrov, F. Bazzarelli, P. Bernardo, J. Carolus Jansen, M. Lanč, K. Friess, V. Shantarovich, V. Gustov, V. Isaeva, *J. Membr. Sci.* **2013**, *427*, 48-62.
[254] P. Li, Z. Wang, W. Li, Y. Liu, J. Wang, S. Wang, *ACS Appl. Mater. Interfaces* **2015**, *7*, 15481-15493.
[255] Y. Wang, T. Hu, H. Li, G. Dong, W. Wong, V. Chen, *Energy Procedia* **2014**, *63*, 202-209.
[256] E. Esposito, G. Clarizia, P. Bernardo, J. C. Jansen, Z. Sedláková, P. Izák, S. Curcio, B. d. Cindio, F. Tasselli, *Chem. Eng. Process. Process Intensif.* **2015**, *94*, 53-61.
[257] Y. Wang, H. Li, G. Dong, C. Scholes, V. Chen, *Ind. Eng. Chem. Res.* **2015**, *54*, 7273-7283.
[258] Y. Li, S. Wang, H. Wu, R. Guo, Y. Liu, Z. Jiang, Z. Tian, P. Zhang, X. Cao, B. Wang, *ACS Appl. Mater. Interfaces* **2014**, *6*, 6654-6663.
[259] A. Car, C. Stropnik, W. Yave, K. Peinemann, *Sep. Purif. Technol.* **2008**, *62*, 110-117.
[260] S. Sridhar, R. Suryamurali, B. Smitha, T. Aminabhavi, *Colloids Surf. Physicochem. Eng. Aspects* **2007**, *297*, 267-274.
[261] L. Liu, A. Chakma, X. Feng, *Chem. Eng. J.* **2004**, *105*, 43-51.
[262] W. Zheng, R. Ding, K. Yang, Y. Dai, X. Yan, G. He, *Sep. Purif. Technol.* ***2018***, *DOI: 10.1016/j.seppur.2018.04.010*.
[263] L. Xu, L. Xiang, C. Wang, J. Yu, L. Zhang, Y. Pan, *Chin. J. Chem. Eng.* **2017**, *25*, 882-891.
[264] P. D. Sutrisna, J. Hou, M. Y. Zulkifli, H. Li, Y. Zhang, W. Liang, D. D'Alessandro, V. Chen, *J. Mater. Chem. A* **2018**, *6*, 918-931.
[265] T. Li, Y. Pan, K. Peinemann, Z. Lai, *J. Membr. Sci.* **2013**, *425*, 235-242.
[266] J. Cravillon, S. Muenzer, S. Lohmeier, A. Feldhoff, K. Huber, M. Wiebcke, *Chem. Mater.* **2009**, *21*, 1410-1412.
[267] N. Liédana, A. Galve, C. Rubio, C. Téllez, J. Coronas, *ACS Appl. Mater. Interfaces* **2012**, *4*, 5016-5021.
[268] L. Hou, L. Wang, N. Zhang, Z. Xie, D. Dong, *Polym. Chem.* **2016**, *7*, 5828-5834.
[269] N. A. Khan, I. J. Kang, H. Y. Seok, S. H. Jhung, *Chem. Eng. J.* **2011**, *166*, 1152-1157.
[270] T. S. Chung, S. K. Teoh, X. Hu, *J. Membr. Sci.* **1997**, *133*, 161-175.

CHAPTERS 4–14

RESULTS

Chapter 4: Beyond the H_2/CO_2 upper bound: one-step crystallization and separation of nano-sized ZIF-11 by centrifugation and its application in mixed matrix membranes

J. Sánchez-Laínez, B. Zornoza, Á. Mayoral, Á. Berenguer-Murcia, D. Cazorla-Amorós, C. Téllez, J. Coronas. Journal of Materials Chemistry A, 3 (2015) 6549-6556. DOI: 10.1039/C4TA06820C. Reproduced by permission of The Royal Society of Chemistry.

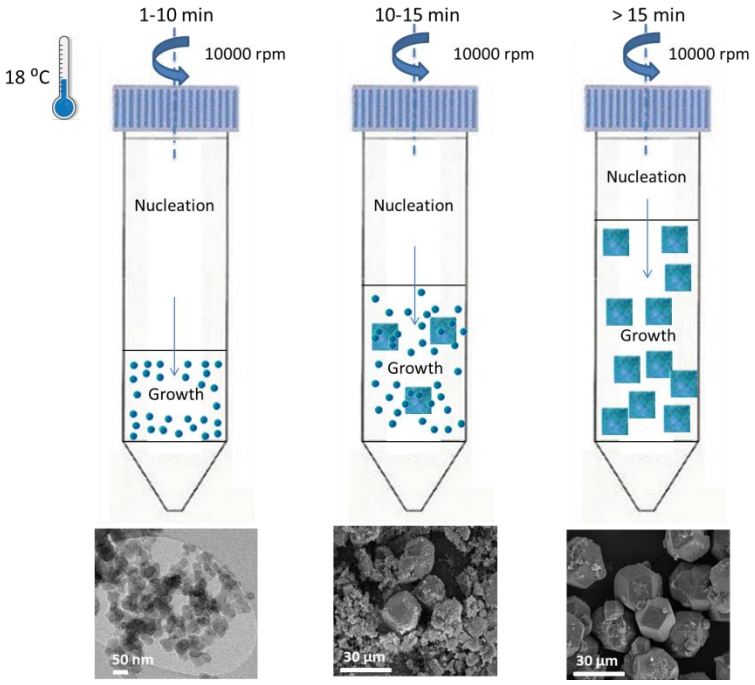

Category:

- Synthesis of new MOFs
- Type of membrane: self-supported MMMs
- Gas separation: pre-combustion CO_2 capture

Journal of Materials Chemistry A

PAPER

View Article Online
View Journal | View Issue

Cite this: J. Mater. Chem. A, 2015, 3, 6549

Beyond the H_2/CO_2 upper bound: one-step crystallization and separation of nano-sized ZIF-11 by centrifugation and its application in mixed matrix membranes†

Javier Sánchez-Laínez,[a] Beatriz Zornoza,[a] Álvaro Mayoral,[b] Ángel Berenguer-Murcia,[c] Diego Cazorla-Amorós,[c] Carlos Téllez[a] and Joaquín Coronas*[a]

Received 11th December 2014
Accepted 15th February 2015

DOI: 10.1039/c4ta06820c

www.rsc.org/MaterialsA

The synthesis of nano-sized ZIF-11 with an average size of 36 ± 6 nm is reported. This material has been named nano-zeolitic imidazolate framework-11 (nZIF-11). It has the same chemical composition and thermal stability and analogous H_2 and CO_2 adsorption properties to the conventional microcrystalline ZIF-11 (*i.e.* 1.9 ± 0.9 μm). nZIF-11 has been obtained following the centrifugation route, typically used for solid separation, as a fast new technique (pioneering for MOFs) for obtaining nanomaterials where the temperature, time and rotation speed can easily be controlled. Compared to the traditional synthesis consisting of stirring + separation, the reaction time was lowered from several hours to a few minutes when using this centrifugation synthesis technique. Employing the same reaction time (2, 5 or 10 min), micro-sized ZIF-11 was obtained using the traditional synthesis while nano-scale ZIF-11 was achieved only by using centrifugation synthesis. The small particle size obtained for nZIF-11 allowed the use of the wet MOF sample as a colloidal suspension stable in chloroform. This helped to prepare mixed matrix membranes (MMMs) by direct addition of the membrane polymer (polyimide Matrimid®) to the colloidal suspension, avoiding particle agglomeration resulting from drying. The MMMs were tested for H_2/CO_2 separation, improving the pure polymer membrane performance, with permeation values of 95.9 Barrer of H_2 and a H_2/CO_2 separation selectivity of 4.4 at 35 °C. When measured at 200 °C, these values increased to 535 Barrer and 9.1.

Introduction

Zeolitic imidazolate frameworks (ZIFs) are a subfamily of metal–organic frameworks (MOFs) in which a metal cation of Zn^{2+} or Co^{2+} is linked to the nitrogen atoms of deprotonated imidazole molecules forming tetrahedral frameworks in zeolite-like topologies.[1] ZIFs constitute highly porous frameworks with extraordinarily high thermal and chemical stabilities. They have a great number of potential applications such as gas sorption,[2] gas separation,[3,4] drug delivery[5] and catalysis.[6,7] Due to its small pore size, ZIF-11 is one of the most promising ZIFs for gas separation. It forms a RHO type zeolitic structure where Zn^{2+} is the metal ion and benzimidazole (bIm) the organic linker.[8] The well-defined porous structure with large cavities of 14.6 Å connected through pore apertures of 3 Å, similar to the kinetic diameter of H_2 (2.9 Å), makes it ideal for hydrogen separation by the sieving process.[9] It has been estimated by molecular simulation that at room temperature ZIF-11 can achieve a H_2/CO_2 selectivity of 262 with a H_2 permeability of 5830 Barrer. It is thus a perfect candidate for pre-combustion capture.[10] However, its applications are still underdeveloped, mainly due to its micrometric size, *i.e.* due to the lack of a synthesis method to produce nano-sized ZIF-11.

MOF nanoparticles are of great interest in the engineering world due to their unique physical, chemical and optical properties and their high surface to volume ratio.[11] Many researchers have focused their efforts on reducing the crystal size to the nanoscale besides reducing the synthesis time through several methods beyond solvothermal synthesis,[12] including ultrasound bath,[13] microwave-assisted crystallization,[14] microemulsion,[15] microfluidics,[16] *etc.* However, precise control over the size and shape of MOFs still remains a challenge.[17] Some ZIFs have already been synthesized as nanoparticles, such as ZIF-7 (ref. 18) or ZIF-8,[19] but this has not been achieved for ZIF-11 since the material was first obtained by

[a]Chemical and Environmental Engineering Department, Instituto de Nanociencia de Aragón (INA), Universidad de Zaragoza, 50018 Zaragoza, Spain. E-mail: coronas@unizar.es; Fax: +34 976 761879; Tel: +34 976 762471

[b]Laboratorio de Microscopías Avanzadas (LMA), Nanoscience Institute of Aragón (INA), Universidad de Zaragoza, 50018 Zaragoza, Spain

[c]Alicante Materials Institute and Inorganic Chemistry Department, University of Alicante, 03080 Alicante, Spain

† Electronic supplementary information (ESI) available. See DOI: 10.1039/c4ta06820c

Yaghi's group.[9] A friendlier alternative to the common amide-based solvents such as *N*,*N*-dimethylformamide (DMF) and *N*,*N*-diethylformamide (DEF), which are difficult to remove from pores,[20] is the use of methanol.[21] In this procedure, reported by He *et al.*,[21] toluene was also used as a structure director in the synthesis of ZIF-11, but still within the 1–4 μm size range.

During the synthesis of zeolites, which have a similar topology to that of ZIFs, amorphous precursors can be obtained. These precursors show no crystallinity but present pore dimensions and topologies very close to those of zeolites, having similar properties.[22] Analogous structures can also be obtained in the synthesis of MOFs, as already reported for HKUST-1 or MIL-89.[23,24]

In this work nano-sized ZIF-11 (nZIF-11) has been synthesized under centrifugal acceleration, with physical and chemical properties similar to the microcrystalline ZIF-11. nZIF-11 has been integrated in the commercial polyimide Matrimid® continuous phase, forming mixed matrix membranes (MMMs), which are capable of enhancing the performance of the pure polymer in the H_2/CO_2 separation process, focusing on H_2 purification and the so-called precombustion CO_2 capture. The filler was used as a colloidal suspension, similar to the Chung *et al.* procedure with nano-sized ZIF-7 and DMF.[25]

Experimental

Chemicals

Zinc acetate dihydrate ($Zn(CH_3COO)_2 \cdot 2H_2O$), benzimidazole (bIm, $C_7H_6N_2$, 98%), ammonium hydroxide (NH_3, 28–30% aqueous solution), chloroform (anhydrous) and toluene (≥99.5%) were purchased from Sigma Aldrich. Methanol (HPLC grade) was purchased from Scharlau. Matrimid® 5218 was kindly supplied by Huntsman Advanced Materials.

Nano-sized ZIF-11 synthesis

0.24 g of bIm (2 mmol) was dissolved in 6.4 g of methanol (400 mmol), together with 9.2 g of toluene (100 mmol) and 2.4 g of ammonium hydroxide (40 mmol). 0.22 g of zinc acetate dihydrate (1 mmol) was dissolved in 3.2 g of methanol (200 mmol). Both solutions were cooled separately to 18 °C and then mixed in a 50 mL centrifuge flask at 10 000 rpm at the same temperature. The centrifugation time varied between 1 and 30 min. Note that 1 min is the time needed to achieve the rotation speed mentioned above. The solid collected was washed with methanol three times for the complete removal of toluene and dried at 100 °C overnight for characterization purposes. The molar composition of the mixture was Zn : bIm : NH_3 : CH_3-OH : toluene = 1 : 2 : 40 : 300 : 100.[21]

Micro-sized ZIF-11 synthesis

The same reactant amounts and steps as in the previous procedure were applied. However, instead of centrifuging, the mixture was stirred from a few minutes to 3 h at room temperature before collecting the solid by centrifugation at 10 000 rpm and washing it.

MMM fabrication

When using the material as a filler for MMMs, instead of being dried, the methanol-collected ZIF-11 nanoparticles were further washed with chloroform to avoid agglomeration. After the third centrifugation, the particles were re-suspended in chloroform prior to use. The suspension concentration was calculated for each membrane loading: 10, 15 and 25 wt%, and the corresponding amount of polyimide Matrimid® powder was added. The addition of polymer to the nZIF-11 dispersion was done in two stages while stirring and the resulting solution was further stirred overnight. The casting solution was stirred three times and sonicated alternatively for 90 min and cast into a Petri dish at room temperature. The Petri dishes were left covered overnight for slow evaporation of the solvent. After that, the membranes were peeled off from the Petri dishes and treated in a vacuum oven at 180 °C and 10 mbar for 24 h for complete removal of the remaining solvent.

Membrane thicknesses were measured using a Digimatic Micrometer (measurement range from 0 to 30 mm with an accuracy of ±1 μm). Several points (9) equally distributed on the membrane were measured per membrane and the arithmetic average was used for the membrane thickness. In this work, the MMMs obtained have a thickness of 87 ± 12 μm. For permeation testing of the membranes, circular areas of 15.2 cm^2 were cut from the films.

Characterization of samples

Powder X-ray diffraction (XRD) spectra of nano-MOFs and MMMs were acquired using a D-Max Rigaku X-ray diffractometer with a copper anode and a graphite monochromator to select CuKα radiation ($\lambda = 1.540$ Å), taking data from $2\theta = 2.5°$ to 40° at a scan rate of 0.03° s^{-1}. Thermogravimetric analyses (TGA) were carried out using a Mettler Toledo TGA/STDA 851e. Samples (10 mg) placed in 70 μL alumina pans were heated in an air flow from 25 to 900 °C at a heating rate of 10 °C min^{-1}. Scanning electron microscopy (SEM) images of MOFs and membranes were obtained using an Inspect F50 model scanning electron microscope (FEI), operated at 20 kV. Cross-sections of membranes were prepared by freeze-fracturing after immersion in liquid N_2 and subsequently coated with Pt. Transmission electron microscopy (TEM) images of the MOF were obtained using a FEI Tecnai F30 microscope, operated at 300 kV. The samples were prepared by dispersion of the powder in ethanol before placing a few drops of the suspension onto the copper carbon coated microgrid. Fourier transform infrared spectroscopy (FTIR) was performed on a Bruker Vertex 70 FTIR spectrometer equipped with a DTGS detector and a Golden Gate diamond ATR accessory. Powder samples were prepared by the KBr wafer technique and the measurements were done in a diffuse reflectance module. Both spectra were recorded by averaging 40 scans in the 4000–600 cm^{-1} wavenumber range at a resolution of 4 cm^{-1}. The particle size was obtained using ImageJ 1.49b software. At least 300 particles were counted for the nano-sized samples and 30 for the micro-sized, as the particle density observed in SEM images is much lower. NMR spectra were recorded in a Bruker Avance III WB400

spectrometer with 4 mm zirconia rotors spun at the magic angle in N_2 at 10 kHz. ^1H–^{13}C CP spectra were measured using a ^1H $\pi/2$ pulse length of 3.0 μs, with a contact time (ramp) of 3 ms, a spinal 64 proton decoupling sequence of 5.3 μs pulse length, and a recycle delay of 5 s. 3000 scans were acquired for each spectra.

High and low pressure adsorption analysis

High pressure hydrogen and carbon dioxide adsorption measurements were carried out in an automatic volumetric apparatus (Quantachrome iSorb HP1) to perform hydrogen isotherm experiments up to 4 MPa and carbon dioxide isotherm experiments up to 3.4 MPa. The manifold of the apparatus was kept at 35 °C. In the case of hydrogen, the sample cell was refrigerated at the adsorption temperature (−196 °C) by means of a thermostatted liquid nitrogen deposit which pumped the necessary amount of cryogenic liquid into a Dewar deposit to ensure a constant liquid nitrogen level and a stable sample temperature throughout the experiment. For the CO_2 experiments, a circulator bath set to 0 °C was employed. The manifold volume was calibrated with a standard volume, performing helium isotherm measurements prior to each experiment. In order to ensure that the apparatus was leak-free, hydrogen leak tests were executed at 9 and 15 MPa for 28 h, the resulting leak rate being below 10^{-6} torr (torr^{-1} s^{-1}). The bulk gas amounts were calculated by the modified Benedict–Webb–Rubin equation of state,[26] and the cell volume was calculated taking into account the correction described in the literature.[27] Prior to the adsorption, the sample was degassed at 150 °C for 4 h under vacuum. After that, the sample was loaded in the sample holder, and then evacuated at 150 °C for 4 h under vacuum. Sample masses ranged between 0.5 and 1.0 g to ensure accurate measurements.

Carbon dioxide adsorption isotherms of ZIF-11 and nZIF-11 (synthesis of 5 min and 1 min) were also measured using a volumetric adsorption analyzer (Micromeritics ASAP 2020) at 0 °C up to 120 kPa after degassing at 200 °C for 8 h. In all cases, hydrogen, carbon dioxide and helium gases used in the experiments were 99.9995% pure.

Gas separation analysis

Mixture permeability analyses were performed for polyimide based MMMs with nZIF-11 loadings of 10, 15 and 25 wt%, and ZIF-11 with 10 wt% loading for comparison. The membranes were introduced into a module consisting of two stainless steel pieces and a 316LSS macroporous disk support (from Mott Co.) with a 20 μm nominal pore size, gripped inside with silicone o-rings. The permeation module was placed in a UNE 200 Memmert oven to control the temperature of the experiments. Gas separation measurements were carried out by feeding an equimolar mixture of H_2/CO_2 (25/25 cm^3(STP) min^{-1}) at 330 kPa to the feed side by means of two flow-mass controllers (Alicat Scientific, MC-100CCM-D), while the permeate side of the membrane was swept with a 1 cm^3(STP) min^{-1} mass-flow controller stream of Ar at 124 kPa (Alicat Scientific, MC-5CCM-D). Concentrations of H_2 and CO_2 in the outgoing streams were analyzed using an Agilent 3000A online gas microchromatograph equipped with a thermal conductivity detector. Permeability was calculated in Barrer (10^{-10} cm^3(STP) cm (cm^{-2} s^{-1} cmHg^{-1})) once the steady-state of the exit stream (for at least 3 h) was reached, and the separation selectivity was calculated as the ratio of permeabilities.

Colloidal suspension stability

A study was performed in order to prove the stability of the colloidal suspension and the need for keeping it wet to avoid agglomeration. Amounts (0.19 g) of wet and dry nZIF-11 were separately dispersed in chloroform (27.3 g). Both suspensions were left still for 20 days so as to observe changes in their homogeneity.

Results and discussion

nZIF-11 characterization

The synthesis method (traditional stirring + separation *vs.* direct centrifugation) and the reaction time appear to be the critical variables in the formation of nZIF-11 or ZIF-11.

During synthesis by centrifugation two different zones may appear inside the centrifuge tube, a nucleation zone in the upper part (from which the centrifugal force removes nucleated particles) and a growth zone at the bottom consisting of the settled nuclei (see Fig. 1). For synthesis times lower than 10 min, ZIF-11 nanoparticles that settled down from the nucleation to the growth zone were not able to grow because the process ended too early and thus remained nano-sized. For times between 10 and 15 min some of the crystals that settled down (the older crystals) had time to grow while others did not, thus a heterogeneous distribution of nano- and micro-sized crystals appeared. Eventually, for times higher than 15 min, the nucleation and growth zones were not separated, resulting in a micro-sized distribution.

XRD spectra of ZIF-11 powder, synthesized at different times and by different methods (conventional stirring and centrifugation), are represented together with the simulated spectra of ZIF-11 in Fig. 2a. For 1 and 2 min an amorphous band for angles between 10 and 22° appears, showing that the material was not yet completely crystalline. All the spectra show the characteristic

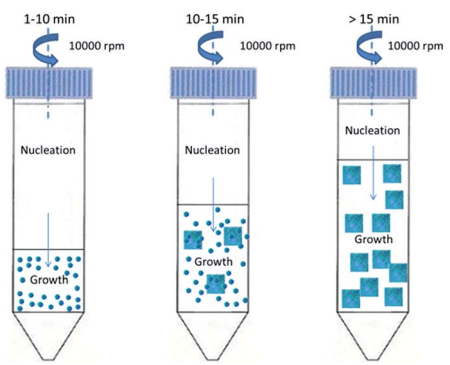

Fig. 1 Crystal size distribution scheme for the centrifugation crystallization process at 18 °C.

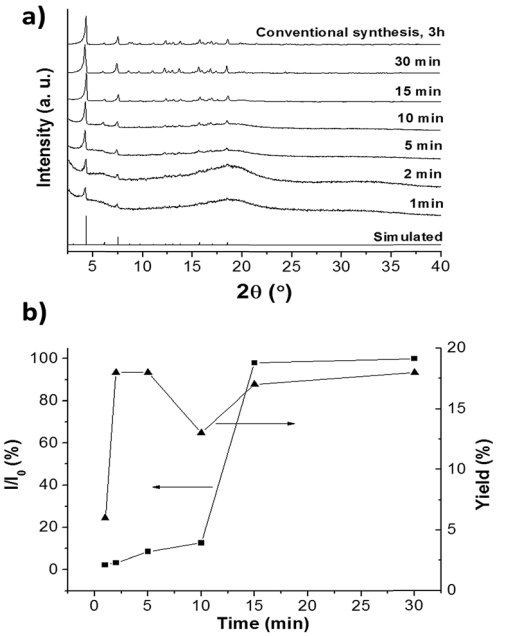

Fig. 2 (a) XRD patterns of ZIF-11 samples synthesized at different reaction times and (b) evolution of crystallinity (calculated from the main peak at 4.3°) and synthesis yield with time.

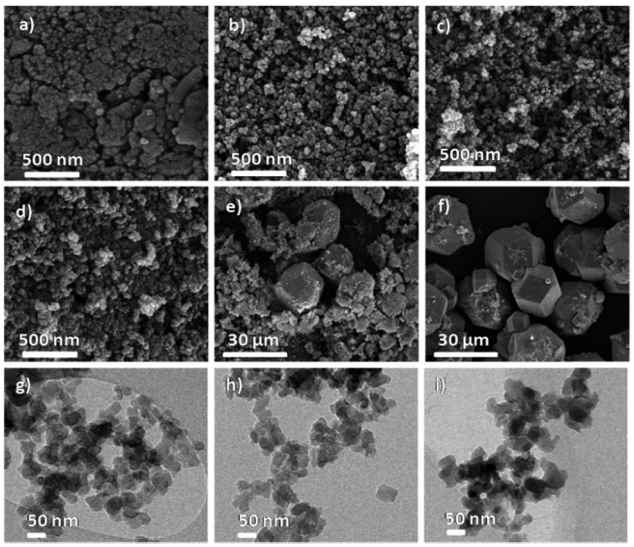

Fig. 3 SEM images of ZIF-11 samples synthesized by centrifugal acceleration at different reaction times: (a) 1 min, (b) 2 min, (c) 5 min, (d) 10 min, (e) 15 min, and (f) 30 min; TEM images at: (g) 2 min, (h) 5 min and (i) 10 min. The TEM image at 1 min can be seen in the ESI (Fig. S1†).

peaks of ZIF-11 at angles lower than 10°, their width not matching the crystal nanosize when calculated with the Scherrer equation. The presence of few micrometric crystals of ZIF-11, evidenced in TEM images but not through SEM inspection (probably due to coating with nano-sized particles), must be responsible for these crystalline features. In fact, the evolution of crystallinity with time is also shown in Fig. 2b, where the absolute intensity of the highest peak of ZIF-11 ($2\theta = 4.3°$) is represented. The plot shows very low values for times under 5 min, low values from 5 to 10 min, and a big increase at 15 min.

The results are consistent with the products obtained. Low intensities correspond to times when nZIF-11 is predominant. At 15 min the first micrometric-sized crystals of ZIF-11 are obtained, and therefore the crystallinity of the mixture greatly increased. In any event, the relative crystallinity of about 8% reached after 5 min (2% after 1 min) would indicate a small amount of micro-sized particles, most of the material corresponding to nZIF-11. Fig. 2b also shows the nZIF-11 synthesis yield, calculated as the MOF obtained (mol) per metal cation used (mol) as the reagent. The value is near 20% for all cases except for the 1 min sample, which is two-thirds lower.

SEM images (Fig. 3a–f) reveal a non-defined particle shape for 1 min reaction time. For 2 min the first nanoparticles appear, their shape similar to those of the samples obtained at 5 and 10 min. At 15 min micro-sized crystals are evident and the nanoparticles finally disappear at 30 min. TEM images reveal a more accurate shape of the nanoparticles for times below 15 min (see Fig. 3g–i). These nano-sized particles did not exhibit electron diffraction. We hypothesize that the critical energy dose reached by the nanoparticles would have been responsible for destroying the possible electron-diffraction pattern.[28] In agreement with the XRD patterns (shown in Fig. 2a), the TEM images also show the presence of a small proportion of micro-sized crystals. These were covered by the nanometric particles that could not be observed in SEM images and have SAED (selected area electron diffraction) features similar to micro-sized crystals. Fig. S2† shows SAED patterns along [110] and [100] directions of ZIF-11 micro-sized particles which can be indexed to the $Im\bar{3}m$ space group corresponding to the RHO type structure.

The corresponding normalized cumulative number of particles is represented in Fig. S3a† as a function of the particle size. From this plot, an average size for each sample was obtained at $N/N_T = 0.5$. The diameter increases from 36 ± 6 nm for the 5 min sample to 17 ± 2 μm corresponding to 30 min synthesis time. In addition, the differential distribution was calculated (Fig. S3b†), providing the predominant particle diameter (mode). The average and predominant sizes are shown in Table S1.† The values are similar to the corresponding averages except for the 15 min sample, at which time both micro- and nano-sized crystals are depicted.

This one-step centrifugation process contrasts with the traditional synthesis, where crystals grow when stirred and are then collected by centrifugation. In this case, micro-sized crystals are obtained even for very low stirring times (see Fig. S4†).

The thermal stability of nZIF-11 in open air was measured by TGA (Fig. 4). It can be seen how each synthesized sample has almost the same thermal stability, with an onset temperature over 400 °C, much higher than that of the organic ligand bIm (200 °C). This means that the nano-sized ZIF-11 is as stable as the micrometric ZIF-11, as both sizes are included among the different samples measured. This suggests the same nature of the chemical bond between the ligand and metal in both the nano- and micro-sized materials. The residue weight remaining

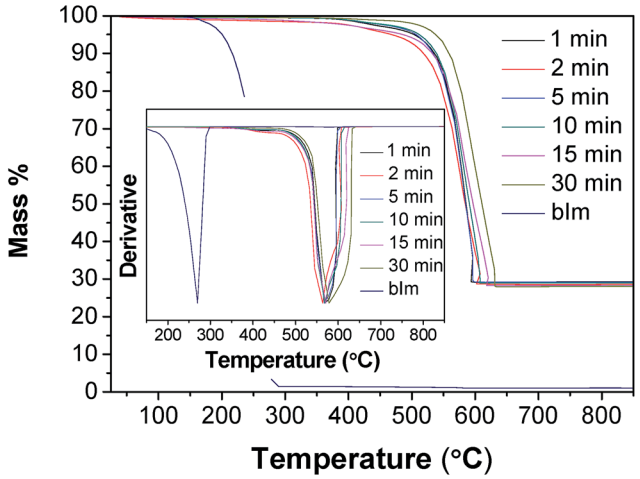

Fig. 4 TGA and derivative curves (inset) in air of the ZIF-11 samples synthesized at different reaction times. TGA of ligand bIm is shown for comparison.

at the end of the analysis (≈25 wt% for all nano- and micro-sized samples) is due to the oxidation of Zn metal to ZnO. Moreover, TGA also proves the need for three washes with methanol for the complete removal of toluene (used during the synthesis as a co-solvent and structuring agent) from the pores of ZIF-11 (Fig. S5†).

The FTIR spectra are explained in detail in the ESI.† The same bands for nZIF-11 and micro-sized ZIF-11 were found (Fig. S6†) proving that both types of crystal have the same bond structure, consistent with the thermal stability shown by the TGA results.

Fig. 5 shows the measured ^{13}C NMR spectra of micro- and nano-sized ZIF-11 (1 and 5 min), compared to the simulated spectrum of bIm. The characteristic bIm peaks at 122.9 (C5, C6) and 115.4 ppm (C4, C7) are slightly shifted to 122.5 and 115.9 ppm, respectively. However, the largest differences occur for the signals corresponding to C8, C9 (137.9 ppm) and C2 (141.5 ppm), close to nitrogen atoms coordinated to the metallic

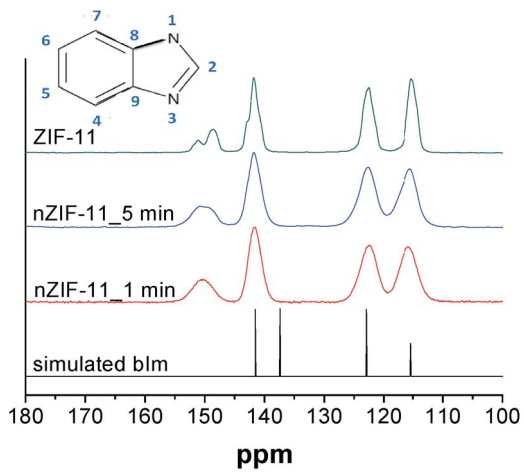

Fig. 5 ^{13}C NMR spectra of nZIF-11, ZIF-11 and the organic ligand.

clusters, displaced in ZIF-11 type materials to 141.8 and about 150 ppm (split into 148.6 and 151.1 for ZIF-11), respectively. These chemical shifts of ^{13}C signals are indicative of the presence of anionic [bIm$^-$], consistent with the deprotonation of bIm during ZIF-11 formation.[32] Besides the splitting of the signal at about 150 ppm seen in the micro-sized ZIF-11 spectrum, slight differences of about 1 ppm between the micro- and nano-sized ZIF-11 peaks can be observed. In any event, the 5 min sample tends to be more similar to the micro-sized ZIF-11 than the 1 min sample. Like the previous characterizations, ^{13}C NMR suggests strong similarities in the chemical bond between both nano- and micro-sized samples, as well as subtle differences in the ZIF-11 ligand (bIm) coordination which may be due to both the lack of crystallinity and the higher external area (explained below) that nZIF-11 particles exhibit as compared to ZIF-11.

Gas adsorption measurements

Gas adsorption was measured for nZIF-11 to study its porosity. The compound was unable to adsorb N_2 at low relative pressures due to its narrow microporosity, proving that, as in the case of microcrystalline ZIF-11, the pore aperture is smaller than the N_2 molecule kinetic diameter (3.64 Å). Nevertheless, the nano-sized ZIF did show H_2 and CO_2 adsorption which indicates the presence of narrow microporosity as observed with ZIF-11.[9]

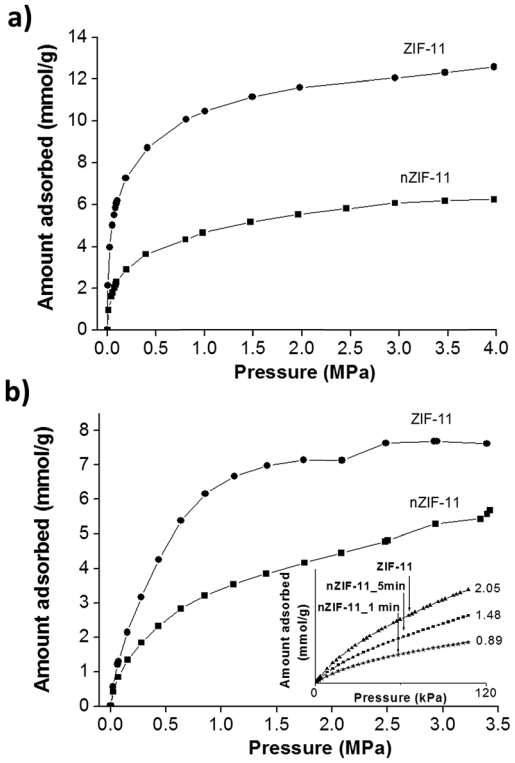

Fig. 6 (a) H_2 excess adsorption isotherms at 77 K of micro- and nano-sized ZIF-11 from 0 to 40 bar and (b) absolute CO_2 adsorption isotherms for both samples at 273 K; inset: CO_2 adsorption isotherm at 273 K from 0 to 120 kPa.

Fig. 6a shows a H_2 uptake of 6 mmol g^{-1} at 77 K and 4 MPa for nZIF-11, which is half of the amount adsorbed by the micro-sized MOF as found in the literature.[9] In Fig. 6b a CO_2 uptake of 5.9 mmol g^{-1} at 273 K and 3.4 MPa can be seen for nano-sized ZIF-11, which is approximately 30% less than the amount adsorbed by the micro-sized ZIF-11 sample under the same conditions. The inset in Fig. 6b shows the low pressure CO_2 adsorption isotherms for both samples, together with the 1 min sample, where nZIF-11 depicts an intermediate sorption capacity. The micropore volume was calculated by applying the Dubinin–Radushkevich equation to the low pressure region of the CO_2 absolute adsorption isotherms (up to 0.3 MPa).[29] The values obtained were 0.16 and 0.11 $cm^3\ g^{-1}$ for micro- and nano-sized ZIF-11, respectively.

Under the experimental conditions studied, H_2 adsorption occurred in the microporous material[30] which explains the similar shape of both adsorption isotherms in Fig. 6a. Then, the lower adsorption of H_2 in nZIF-11 compared to the micro-sized ZIF-11 indicates the lower amount of micropores in the former. However, CO_2 adsorption at 0 °C and up to 3.4 MPa (Fig. 6b) is sensitive to the whole range of porosity since the isotherm reaches a maximum relative fugacity close to 1.[29] The wider knee of the high pressure CO_2 isotherm for nZIF-11 suggests that this material has a wider pore size distribution and some amount of large pores, and a larger external surface. This may be a consequence of the difference in crystallinity of both materials, which may give rise to a broader pore size distribution in the case of nZIF-11, contrary to its micro-sized counterpart which has a narrower knee in the CO_2 adsorption isotherm. Furthermore, as other authors have noted,[29] upon reaching pressures above around 2.5 MPa, CO_2 may condense in the mesoporosity (or intercrystalline space) of the samples. In this sense, the slope of the isotherm from this pressure and the upward curvature found in the last three adsorption data points found for the nano-sized sample are indicative of these wider pores, which once again may derive from the lower crystallinity of the sample.

It should be noted that CO_2 has been extensively reported in the literature as a suitable adsorbate for the characterization of narrow porosity (*i.e.* for pores of sizes around 3 Å, which correspond to the narrower cavities found for ZIF-11)[9] of adsorbents of markedly different chemical nature, not only carbon materials and carbon molecular sieves,[29] but also microporous crystalline inorganic oxides such as zeolites[31] and mesoporous materials such as MCM-41.[32] Thus, the results reported in this study serve to heighten the relevance of the crystallinity of ZIF-11 in the development of its porous texture.

Membrane characterization and performance

As a proof of application, ZIF-11 nanoparticles (specifically nZIF-11_5 min) in both dried and wet conditions were integrated in the Matrimid® continuous phase in the form of MMMs. More stable, colloidal dispersions were obtained when nZIF-11 was processed in wet conditions without drying. In fact, Fig. S7† shows its stability in chloroform for more than 20 days. The use of wet particles avoided agglomeration that occurs when using the dried nanoparticles. Thus, MMMs comprising nominal loadings of 10, 15 and 25 wt% in a dry basis of wet nZIF-11 (actual loadings tested by TGA being 9.1, 13.5 and 22.6 wt%, respectively) were prepared. The discrepancy between nominal and actual loadings comes from the use of the MOF in wet conditions without prior drying, only taking as reference the average yield calculated for the nZIF-11 synthesis.

The cross-sections of the membranes containing nominal loadings of 10, 15 and 25 wt% of nZIF-11 and 10 wt% micro-sized ZIF-11 (where large hexagonal ZIF-11 particles are evident) are shown in Fig. 7. SEM images reveal the homogeneous dispersion and excellent adhesion of the filler particles within the polymeric phase.

Fig. 8a shows the H_2/CO_2 gas separation performance for a 50/50 mixture at 35 °C and 2 bar of driving force. At least 2–3 MMMs of each loading were fabricated and measured, except for the 25 wt% loading, to provide error estimations. The integration of nZIF-11 in membranes enhanced the permeability for both gases, achieving a higher selectivity in comparison with the pure polymer. However, while permeability continuously increased as a function of the membrane loading, selectivity decreased for the 15 wt% MMMs and then remained constant. This suggests the presence of non-selective voids owing to some deterioration in the interaction between the MOF and the polymer at these high loadings.[33] This oscillating

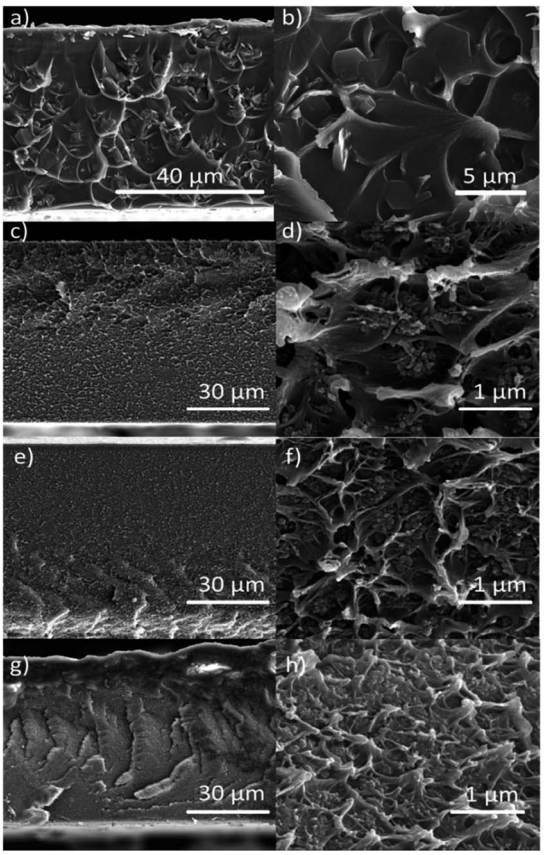

Fig. 7 SEM images of Matrimid® MMMs 10 wt% loading with micro-sized ZIF-11 as the filler (a and b) and 10 wt% (c and d), 15 wt% (e and f) and 25 wt% (g and h) loading with nZIF-11_5 min as the filler.

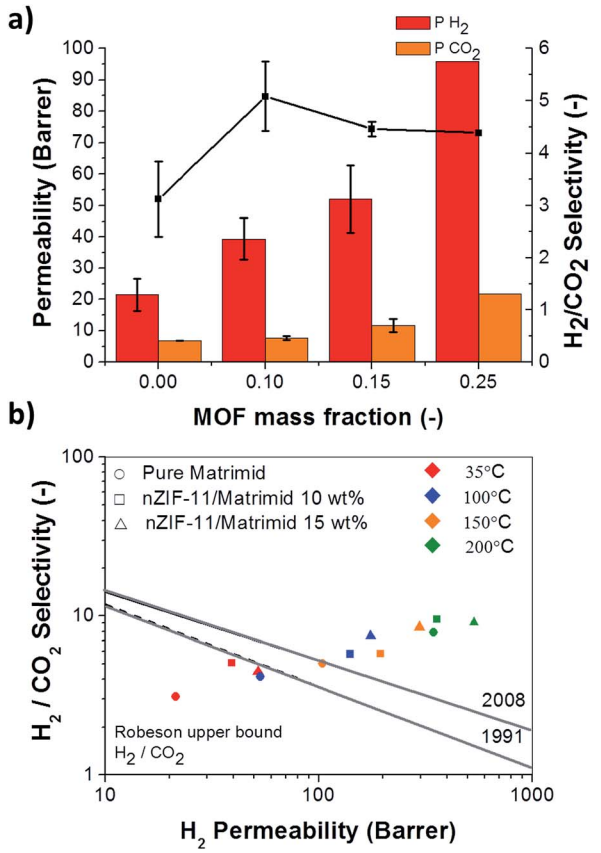

Fig. 8 Gas separation performance of Matrimid® MMMs containing nZIF-11_5 min at 35 °C (a) and as a function of the temperature (b).

behavior has also been reported in the literature for Matrimid® MMMs comprising ZIF-8.[34] These results are also in good agreement with the single published paper reporting micro-sized ZIF-11 in the form of MMMs.[35] In this case ZIF-11 was embedded in PBI polymer giving rise to an improvement in permeability when increasing the loading ($PH_2 = 17.2$ Barrer for the pure polymer membrane to 67.8 Barrer for 16.1 wt% loading and 133 Barrer for 29.7 wt%) but the selectivity barely improved over the pure polymer ($\alpha H_2/CO_2 = 5.0$ for PBI, 5.6 for 16.1 wt% loading and 3.7 for 29.7 wt%).

In addition, 10 wt% nZIF-11 MMMs produced higher H_2 permeability and H_2/CO_2 selectivity (44.5 Barrer and 5.6, respectively) than the corresponding MMMs with micro-sized ZIF-11 (38.3 Barrer and 4.8, respectively). In any event, the highest loading membrane (25 wt%) produced 95.9 Barrer of H_2 with a H_2/CO_2 selectivity of 4.4.

Thus, in order to improve the membrane performance, experiments at high temperature (35–200 °C range) were carried out with 10 and 15 wt% MMMs (Fig. 8b). Matrimid® has a high thermal stability with a glass transition temperature of about 320 °C.[36] Raising the temperature has a beneficial effect on the separation performance, surpassing the Robeson upper bound[37] over 100 °C. Although only the Robeson upper bound at 35 °C is represented, it only shifts upwards slightly with increasing temperature[38] and the measured values would continue being over it. In any event, permselectivity results of nZIF-11 MMMs at each temperature are always higher than those of the bare polymer membrane. As expected, the permeability increased due to a higher diffusion of the penetrants, while CO_2 adsorption on the MOF and its solution in the polymer decreased. All membranes showed permeation at least 300 Barrer higher at 200 °C than at 35 °C. Selectivity also increased with temperature, duplicating its value from the lowest to the highest temperature for each membrane. The best result obtained with 15 wt% loading of nZIF-11 corresponds to 535 Barrer of H_2 with a H_2/CO_2 selectivity of 9.1. A comparison with other MMMs containing ZIFs found in the literature regarding this mixture is included in the ESI (Table S2†).

Even though high selectivity values are expected due to the small pore apertures of ZIF-11 (3.0 Å) and the molecular size of both molecules of H_2 (2.9 Å) and CO_2 (3.3 Å), the flexibility of the ZIFs plays an important role leading to lower values than predicted as suggested by Bux *et al.*[39]

Apparent activation energy was calculated for H_2, the fastest permeating compound in the binary mixture, resulting in values of 14.7 kJ mol^{-1} for the pure polymer and 15.7 and 16.8 kJ mol^{-1} for the 10 wt% and 15 wt% loaded MMMs, respectively. This increase in the activation energy as a function of the filler loading suggests the positive influence of the ZIF microporosity on the transport properties of the membrane. Activated transport in the case of H_2/CO_2 has recently been found when testing MMMs comprising polysulfone and the filler MSS-Z8 (silica-ZIF-8 core shell spheres with ordered meso-microporosity) with 32 wt% loading at high temperature (120 °C), giving rise to higher H_2 permeabilities with similar selectivities.[40]

Conclusions

Nano-sized MOF ZIF-11 (nZIF-11) has been synthesized through a new technique based on centrifugal acceleration for obtaining nanoparticles. This technique makes possible the synthesis and separation of the MOF material in only one step. From the characterization carried out, the nanoparticles (36 ± 6 nm) showed the same thermal stability as, and similar bond structure in terms of both FTIR and NMR and analogous H_2 and CO_2 adsorption capacities to the micrometric particles.

Due to their smaller size, nZIF-11 particles were easily integrated with high loading (10–25 wt%) in a polymeric continuous phase to produce mixed matrix membranes. It was necessary to keep the filler in a wet state to avoid agglomeration. Mixed matrix membranes containing nZIF-11 displayed a high performance for H_2/CO_2 separation, which improved at high temperatures due to the simultaneous increase in both permeability (because of H_2 activated diffusion) and H_2/CO_2 selectivity (because of the decrease in CO_2 adsorption and solution).

Acknowledgements

Financial support from the Spanish MINECO (MAT2013-40566-R, CTQ2012-31762, and RyC-2009-03913), the Aragón Government and the ESF is gratefully acknowledged. In addition, research leading to these results has received funding from the

European Union Seventh Framework Programme (FP7/2007–2013) under grant agreement no. 608490, project M4CO2. Finally, the use of the Servicio General de Apoyo a la Investigación-SAI (Universidad de Zaragoza) is acknowledged.

Notes and references

1 Y. Lee, J. Kim and W. Ahn, *Korean J. Chem. Eng.*, 2013, **30**, 1667–1680.
2 G. Ferey and C. Serre, *Chem. Soc. Rev.*, 2009, **38**, 1380–1399.
3 B. Zornoza, C. Tellez, J. Coronas, J. Gascon and F. Kapteijn, *Microporous Mesoporous Mater.*, 2013, **166**, 67–78.
4 H. B. T. Jeazet, C. Staudt and C. Janiak, *Dalton Trans.*, 2012, **41**, 14003–14027.
5 P. Horcajada, C. Serre, M. Vallet-Regí, M. Sebban, F. Taulelle and G. Férey, *Angew. Chem., Int. Ed.*, 2006, **118**, 6120–6124.
6 H. Jiang, T. Akita, T. Ishida, M. Haruta and Q. Xu, *J. Am. Chem. Soc.*, 2011, **133**, 1304–1306.
7 J. Gascon, U. Aktay, M. D. Hernandez-Alonso, G. P. M. van Klink and F. Kapteijn, *J. Catal.*, 2009, **261**, 75–87.
8 J. C. Tan, T. D. Bennett and A. K. Cheetham, *Proc. Natl. Acad. Sci. U. S. A.*, 2010, **107**, 9938–9943.
9 K. S. Park, Z. N. Ni, A. P. Côté, J. Y. Choi, R. Huang, F. J. Uribe-Romo, H. K. Chae, M. O'Keeffe and O. M. Yaghi, *Proc. Natl. Acad. Sci. U. S. A.*, 2006, **103**, 10186–10191.
10 A. W. Thornton, D. Dubbeldam, M. S. Liu, B. P. Ladewig, A. J. Hilla and M. R. Hill, *Energy Environ. Sci.*, 2012, **5**, 7637–7646.
11 S. K. Nune, P. K. Thallapally, A. Dohnalkova, C. Wang, J. Liu and G. J. Exarhos, *Chem. Commun.*, 2010, **46**, 4878–4880.
12 J. Cravillon, S. Muenzer, S. Lohmeier, A. Feldhoff, K. Huber and M. Wiebcke, *Chem. Mater.*, 2009, **21**, 1410–1412.
13 L. Qiu, Z. Li, Y. Wu, W. Wang, T. Xu and X. Jiang, *Chem. Commun.*, 2008, 3642–3644.
14 B. Zornoza, A. Martinez-Joaristi, P. Serra-Crespo, C. Tellez, J. Coronas, J. Gascon and F. Kapteijn, *Chem. Commun.*, 2011, **47**, 9522–9524.
15 D. Tanaka, A. Henke, K. Albrecht, M. Moeller, K. Nakagawa, S. Kitagawa and J. Groll, *Nat. Chem.*, 2010, **2**, 410–416.
16 L. Paseta, B. Seoane, D. Julve, V. Sebastian, C. Tellez and J. Coronas, *ACS Appl. Mater. Interfaces*, 2013, **5**, 9405–9410.
17 M.-H. Pham, G.-T. Vuong, A.-T. Vu and T.-O. Do, *Langmuir*, 2011, **27**, 15261–15267.
18 Y.-S. Li, F.-Y. Liang, H. Bux, A. Feldhoff, W.-S. Yang and J. Caro, *Angew. Chem., Int. Ed.*, 2010, 548–551.
19 Y. Pan, Y. Liu, G. Zeng, L. Zhao and Z. Lai, *Chem. Commun.*, 2011, **47**, 2071–2073.
20 W. Morris, N. He, K. G. Ray, P. Klonowski, F. Hiroyasu, I. N. Daniels, Y. A. Houndonougbo, M. Asta, O. M. Yaghi and B. B. Laird, *J. Phys. Chem.*, 2012, **116**, 24084–24090.
21 M. He, J. Yao, Q. Liu, Z. Zhongb and H. Wang, *Dalton Trans.*, 2013, **42**, 16608–16613.
22 A. Corma and M. J. Diaz-Cabanas, *Microporous Mesoporous Mater.*, 2006, **89**, 39–46.
23 J. Gascon, S. Aguado and F. Kapteijn, *Microporous Mesoporous Mater.*, 2008, **113**, 132–138.
24 S. Surble, F. Millange, C. Serre, G. Ferey and R. I. Walton, *Chem. Commun.*, 2006, 1518–1520.
25 T. Yang, Y. Xiao and T. Chung, *Energy Environ. Sci.*, 2011, **4**, 4171–4180.
26 C. Zhang, X. S. Lu and A. Z. Gu, *Int. J. Hydrogen Energy*, 2004, **29**, 1271–1276.
27 T. Kiyobayashi, H. T. Takeshita, H. Tanaka, N. Takeichi, A. Zuttel, L. Schlapbach and N. Kuriyama, *J. Alloys Compd.*, 2002, **330**, 666–669.
28 R. F. Egerton, P. Li and M. Malac, *Micron*, 2004, **35**, 399–409.
29 D. Cazorla-Amoros, J. Alcaniz-Monge, M. A. de la Casa-Lillo and A. Linares-Solano, *Langmuir*, 1998, **14**, 4589–4596.
30 M. Jorda-Beneyto, F. Suarez-Garcia, D. Lozano-Castello, D. Cazorla-Amoros and A. Linares-Solano, *Carbon*, 2007, **45**, 293–303.
31 J. Garcia-Martinez, D. Cazorla-Amoros and A. Linares-Solano, *Stud. Surf. Sci. Catal.*, 2000, **128**, 485–494.
32 Á. Berenguer-Murcia, D. Cazorla-Amorós and Á. Linares-Solano, *Adsorpt. Sci. Technol.*, 2011, **29**, 443–455.
33 R. Mahajan, R. Burns, M. Schaeffer and W. J. Koros, *J. Appl. Polym. Sci.*, 2002, **86**, 881–890.
34 M. J. C. Ordonez, K. J. Balkus Jr, J. P. Ferraris and I. H. Musselman, *J. Membr. Sci.*, 2010, **361**, 28–37.
35 L. Li, Y. Jianfeng, X. Wang, Y. Chen and H. Wang, *J. Appl. Polym. Sci.*, 2014, **131**, 41056.
36 B. Zornoza, C. Téllez and J. Coronas, *J. Membr. Sci.*, 2011, **368**, 100–109.
37 L. M. Robeson, *J. Membr. Sci.*, 2008, **320**, 390–400.
38 B. W. Rowe, L. M. Robeson, B. D. Freeman and D. R. Paul, *J. Membr. Sci.*, 2010, **360**, 58–69.
39 H. Bux, F. Liang, Y. Li, J. Cravillon, M. Wiebcke and J. Caro, *J. Am. Chem. Soc.*, 2009, **131**, 16000–16001.
40 S. Sorribas, B. Zornoza, C. Téllez and J. Coronas, *J. Membr. Sci.*, 2014, **452**, 184–192.

Journal of Materials Chemistry A RSCPublishing

ARTICLE

Supporting Information

MOF characterization

TEM

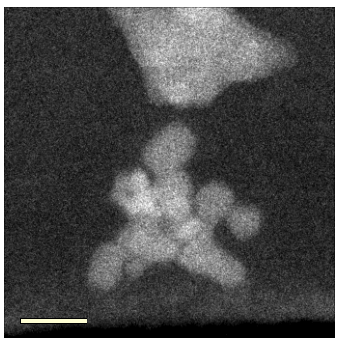

Figure S1. nZIF-11 TEM image at 1min

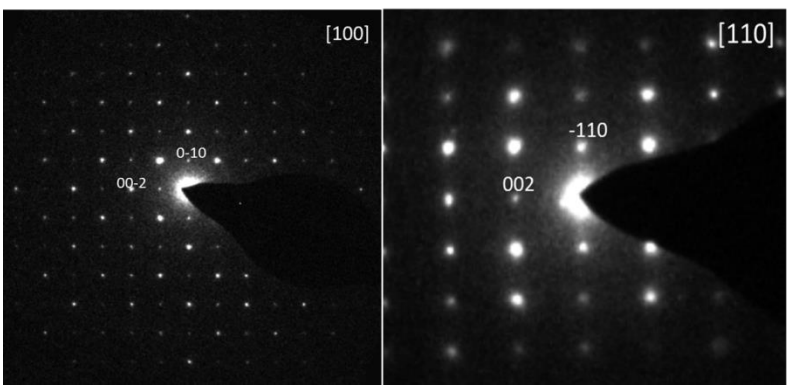

Figure S2. SAED patterns along [110] and [100] directions of ZIF-11 micro-sized particles

Crystal size distribution

Table S1. Average and predominant size of the different samples synthesized by centrifugal acceleration.

Sample	2 min	5 min	10 min	15 min	30 min
Average size (µm)	0.039±0.006	0.035±0.006	0.036±0.006	1.90±1.55	16.61±2.33
Predominant size (µm)	0.042	0.024	0.031	0.300	14.051

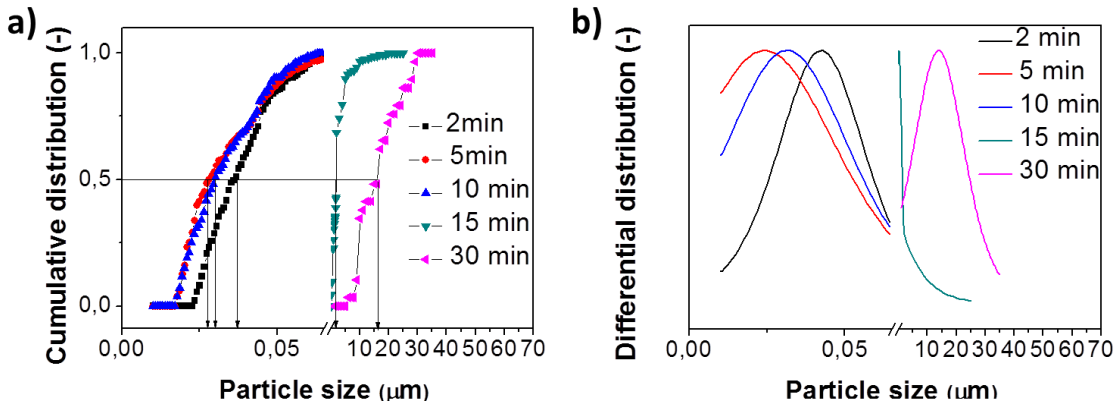

Figure S3. (a) Cumulative distribution and (b) differential distribution of the different samples synthesized by centrifugation.

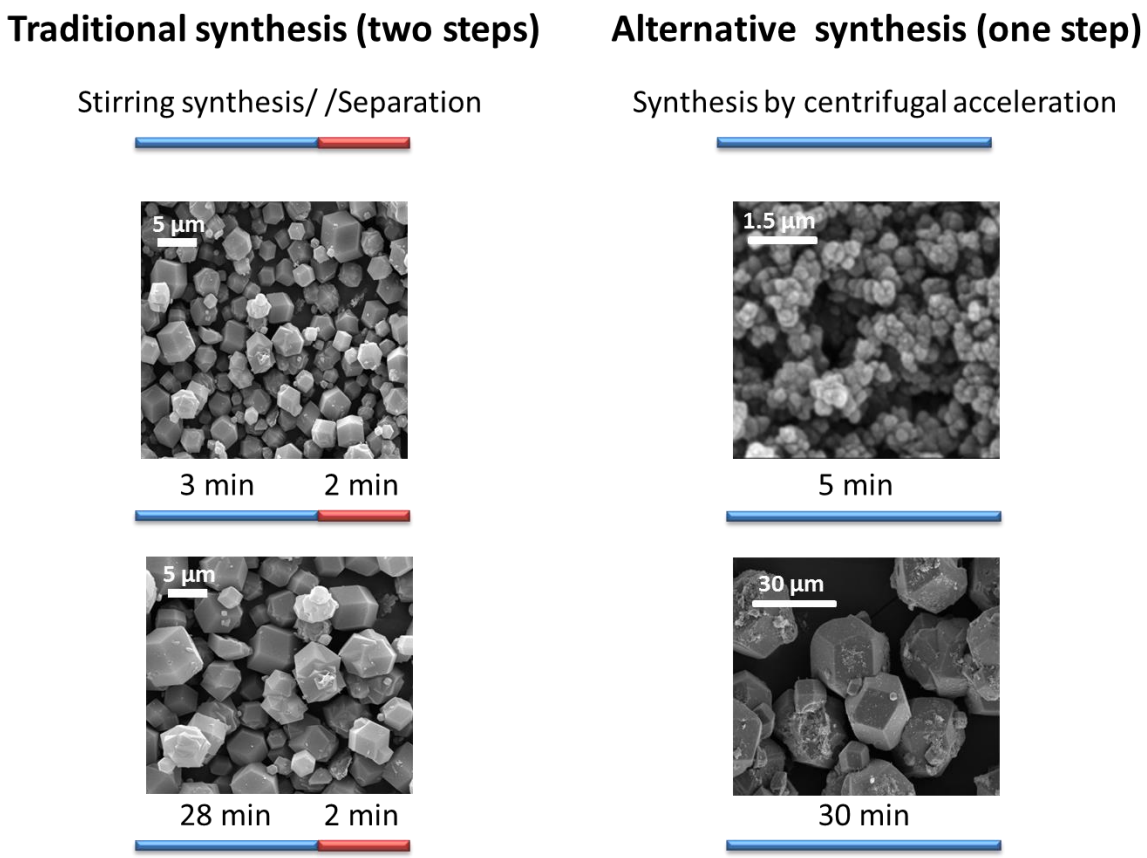

Figure S4. Crystal growth comparison between traditional and centrifugal syntheses.

Thermogravimetric analysis

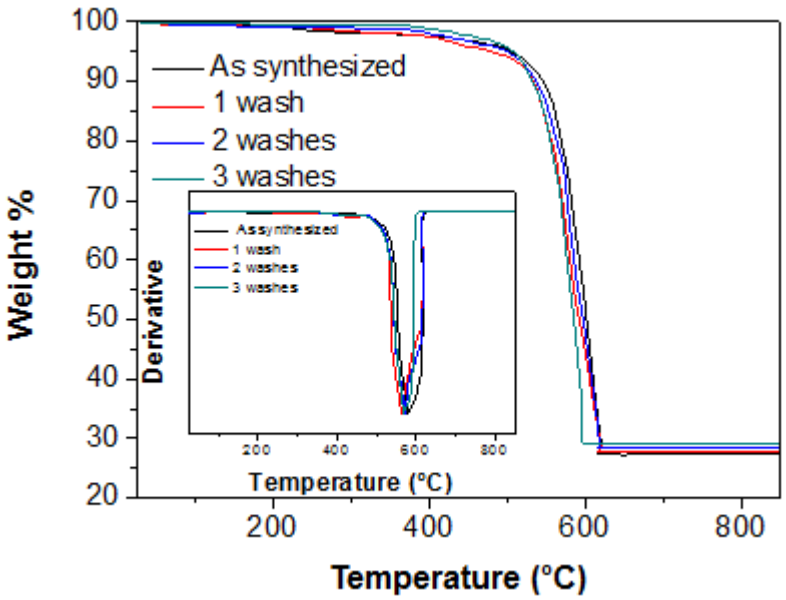

Figure S5. TGA and derivative (insert) of nZIF-11 as synthesized and for different washes.

Small weight loss at around 400 ^{0}C in Fig. S3 corresponds to residual toluene remaining in the particle pores. As the number of washes increases, this weight loss becomes smaller until it finally disappears for 3 washes.

FTIR analysis

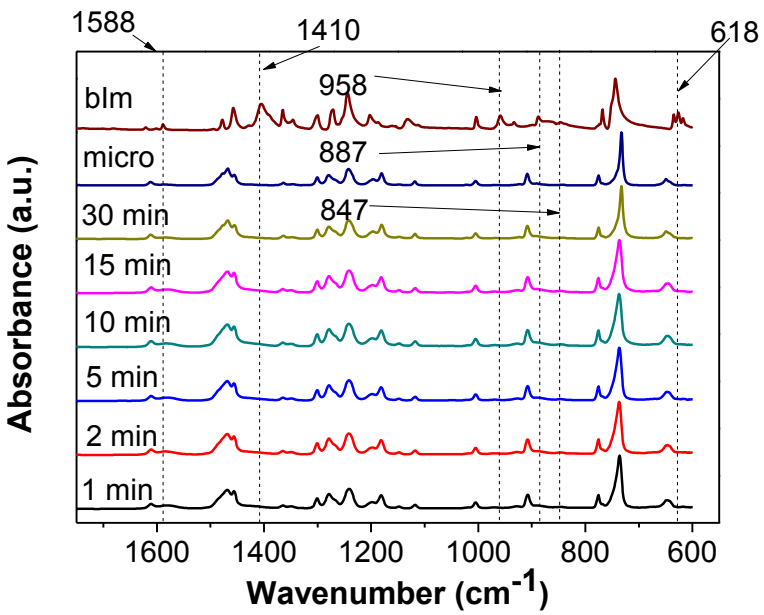

Figure S6. FTIR spectra of the samples synthesized at different times, micro-sized ZIF-11 and organic linker.

Fig. S4 shows the FTIR spectra of all the samples synthesized by centrifugal acceleration within times from 1 to 30 min, together with those of the micro-sized crystals and the organic linker. They are represented only from 2000 to 500 cm^{-1} so that the more representative peaks become better defined. The band found in the region 1620-1450 cm^{-1} is derived essentially from aromatic C-C and C-N stretching modes.[1] It can also be appreciated the C-N stretch mode at 1584 cm^{-1}.[2] The band in the region of 600-1500 cm^{-1} is attributed to the entire ring stretching or bending, while the C-C stretches in the aromatic ring is associated with the peak at 1611 cm^{-1}.[3] Differences between the organic liker and the MOF can be observed. Peaks at 1410, 958, 887 and 847 cm^{-1}, present in bIm spectrum and related to benzene CH-wag, ring stretch, imidazole ring bend and imidazole CH-wag respectively, disappear in ZIF-11 spectra, even when synthesizing the MOF for only 1 min in the centrifuge. The peaks at 1588 and 618 cm^{-1}, caused by N-H in plane bend and In-plane ring bend, respectively, move to higher wavelengths.[4]

Colloidal suspension stability

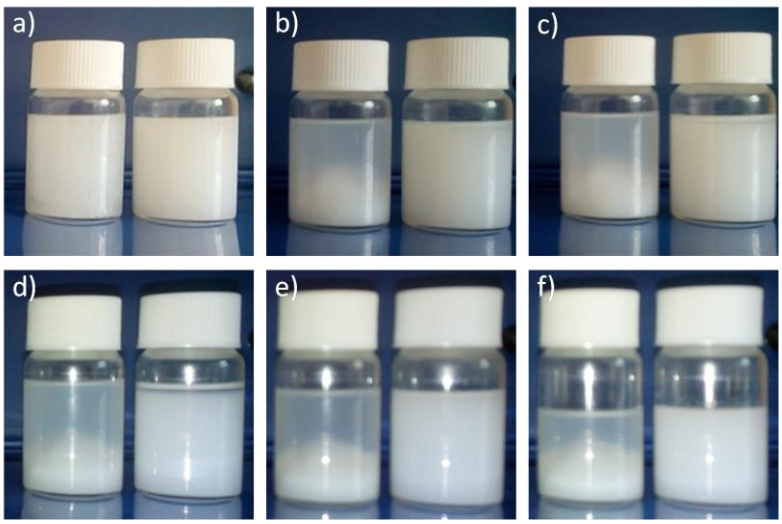

Figure S7. Pictures of nZIF-11 suspensions in chloroform taken at different times: a) 0 hours , b) 1 hour, c) 2 hours, d) 1 day, e) 8 days and f) 20 days. In each one picture the left one correspond to the previously dried MOF sample where the right one is the colloidal MOF suspension.

The colloidal suspension stability study shows how the material dispersed after drying starts to precipitate in only one hour, while the wet one keeps stable for 20 days. Agglomeration explains this behaviour. When dried, the material tends to aggregate and cannot be fully dispersed though sonication, which make it precipitate fast. On the other hand, when the material is kept in wet state it continues fully dispersed and can remain stable for days.

Membrane performance

Table S2. H_2/CO_2 gas separation performance for different MMMs collected from literature.

ZIF	Polymer	Loading [%wt]	Temperature [ºC]	H_2Permeability [Barrer]	H_2/CO_2 selectivity	Reference
ZIF-8	Matrimid®	40	35	71.22	2.90	5
ZIF-7	PBI	-	220	293	13.6	6
ZIF-7	PBI	50	120	202	9.2	7
ZIF-8	PBI	60	35	669.9	2.8	8
ZIF-8	PBI	60	35	1749.9	4.1	9
ZIF-11	PBI	39.5	35	464.7	3.6	10
ZIF-90	PBI	45	180	228	13.21	11
ZIF-8	PIM-1	43	35	14430	0.74	12
MSS-Z8[a]	PSF	32	35 120	56.1 224.1	2.2 3.7	13
nZIF-11[b]	Matrimid®	25 15	35 200	95.9 535	4.4 9.1	-

a Silica-(ZIF-8) core shell spheres.

bThis work.

References

1 Morgan, K. *J.Chem.Soc.*, **1961**, 2343-2347.
2 Hu, Y.; Kazemian, H.; Rohani, S.; Huang, Y.; Song, Y. *Chem. Commun.* **2011**, *47*, 12694-12696.
3 Hu, H.; Liu, S.; Chen, C.; Wang, J.; Zou, Y.; Lin, L.; Yao, S. *Analyst*, **2014**.
4 Morsy, M.; Al-Khaldi, M.; Suwaiyan, A. *J. Phys. Chem. A* **2002**, *106*, 9196-9203.
5 M. J. C. Ordonez, K. J. Balkus Jr., J. P. Ferraris and I. H. Musselman, J. Membr. Sci., 2010, 361, 28-37.
6 Y. Li, F. Liang, H. Bux, W. Yang and J. Caro, J. Membr. Sci., 2010, 354, 48-54.
7 T. Yang, Y. Xiao and T. Chung, Energy Environ. Sci., 2011, 4, 4171-4180.
8 T. Yang and T. Chung, Int. J. Hydrogen Energy, 2013, 38, 229-239.
9 T. Yang, G. M. Shi and T. Chung, Adv. Energy Mater., 2012, 2, 1358-1367.
10 L. Li, Y. Jianfeng, X. Wang, Y. Chen and H. Wang, J. Appl. Polym. Sci., 2014, 131, 41056.
11 T. Yang and T. Chung, J. Mater. Chem. A, 2013, 1, 6081-6090.
12 A. F. Bushell, M. P. Attfield, C. R. Mason, P. M. Budd, Y. Yampolskii, L. Starannikova, A. Rebrov, F. Bazzarelli, P. Bernardo, J. Carolus Jansen, M. Lanč, K. Friess, V. Shantarovich, V. Gustov and V. Isaeva, J. Membr. Sci., 2013, 427, 48-62.
13 S. Sorribas, B. Zornoza, C. Téllez and J. Coronas, J. Membr. Sci., 2014, 452, 184-192.

Chapter 5: Influence of ZIF-8 particle size in the performance of polybenzimidazole mixed matrix membranes for pre-combustion CO_2 capture and its validation through interlaboratory test

J. Sánchez-Laínez, B. Zornoza, S. Friebe, J. Caro, S. Cao, A. Sabetghadam, B. Seoane, J. Gascon, F. Kapteijn, C. L. Guillouzer, G. Clet, M. Daturi, C. Tellez, J. Coronas. Journal of Membrane Science, 515 (2016) 45-53. DOI: 10.1016/j.memsci.2016.05.039. Permission conveyed through Copyright Clearance Center, Inc.

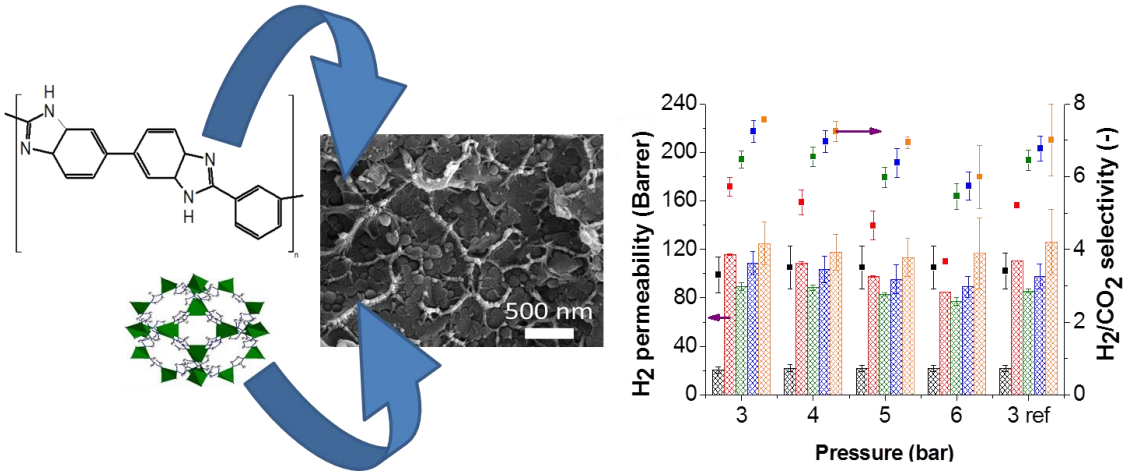

Category:

- Type of membrane: self-supported MMMs
- Gas separation: pre-combustion CO_2 capture

Journal of Membrane Science 515 (2016) 45–53

Contents lists available at ScienceDirect

Journal of Membrane Science

journal homepage: www.elsevier.com/locate/memsci

Influence of ZIF-8 particle size in the performance of polybenzimidazole mixed matrix membranes for pre-combustion CO_2 capture and its validation through interlaboratory test

Javier Sánchez-Laínez [a], Beatriz Zornoza [a], Sebastian Friebe [b], Jürgen Caro [b], Shuai Cao [c], Anahid Sabetghadam [d], Beatriz Seoane [d], Jorge Gascon [d], Freek Kapteijn [d], Clément Le Guillouzer [e], Guillaume Clet [e], Marco Daturi [e], Carlos Téllez [a], Joaquín Coronas [a,*]

[a] Chemical and Environmental Engineering Department and Instituto de Nanociencia de Aragón (INA), Universidad de Zaragoza, 50018 Zaragoza, Spain
[b] Institut für Physikalische Chemie und Elektrochemie, Leibniz Universität, 30167 Hannover, Germany
[c] Johnson Matthey Technology Center, Sonning Common, Reading RG4 9NH, United Kingdom
[d] Catalysis Engineering-Chemical Engineering Department, Delft University of Technology, 2628 BL Delft, The Netherlands
[e] Laboratoire Catalyse et Spectrochimie, ENSICAEN, Université de Caen Normandie, CNRS, 14050 Caen, France

ARTICLE INFO

Article history:
Received 2 October 2015
Received in revised form
18 February 2016
Accepted 23 May 2016
Available online 25 May 2016

Keywords:
ZIF-8
Polybenzimidazole (PBI)
Mixed matrix membrane
Pre-combustion CO_2 capture
Interlaboratory test

ABSTRACT

The preparation and performance of mixed matrix membranes (MMMs) based on polybenzimidazole (PBI) and ZIF-8 nanoparticles of different average sizes (50, 70 and 150 nm) as filler are reported. MMMs containing 10 and 20 wt% of ZIF-8 were tested for H_2/CO_2 separation (pre-combustion CO_2 capture) at 150 °C and feed pressures from 3 to 6 bar. The addition of ZIF-8 resulted in a clear improvement in membrane performance. Embedding 20 wt% of ZIF-8 resulted in a H_2 permeability increase of six times and the H_2/CO_2 selectivity increased nearly by 55% compared to the bare PBI polymer membrane. Both permeability and selectivity improved as the filler size increased, due to the lower degree of agglomeration of the largest particles, that may be less active owing to their smaller external surface area. MMMs synthesized using dry 150 nm ZIF-8 filler showed a better performance than those containing wet filler. Apart from agglomeration concerns favoring wet filler handling as evidenced by infrared characterization, the MMM preparation with wet filler is simpler than with dry filler. Finally, the reproducibility of the membranes was confirmed by a European interlaboratory Round Robin test involving three different institutions.

1. Introduction

Global climate change is one of the most threatening environmental problems currently. The mitigation policies involve the development of new technologies for CO_2 capture, the most abundant greenhouse gas, to reduce its concentration in the atmosphere [1]. Among the so-called carbon capture and storage technologies (CCS), pre-combustion capture consists in removing carbon dioxide from fuel prior to combustion. For this purpose, the fuel is first gasified and converted to a syngas mixture where CO is further oxidized to CO_2 *via* water-gas-shift reaction. At the end a H_2/CO_2 mixture is obtained, which has to be separated [2]. There are different technologies that can be employed for this separation, such as cryogenic distillation, chemical absorption or physical sorption. However, these technologies have their own limitations, either high corrosion, large energy consumption, high cost and low capacity [3]. Membrane technologies are promising alternatives for gas separation because of their low energy consumption, small carbon footprint, and easy operation and scale up [4]. Moreover, the high pressure at which the pre-combustion mixture is obtained provides the necessary driving force for the separation.

Gas permeation in polymeric membranes is controlled by the solution-diffusion mechanism. In a pre-combustion mixture, the diffusion and solubility selectivities show opposite trends. The first parameter favors the transport of the smallest molecule (H_2, with a kinetic diameter of 0.29 nm *vs.* CO_2, 0.33 nm) while the latter, the sorption of the most condensable gas (CO_2 with a critical temperature of 304 K *vs.* H_2, 33 K), favors the selective permeation of CO_2 [5]. This explains why the separation of H_2 from CO_2 is more complicated when compared to that of other gas pairs and usually high temperatures are necessary in order to minimize CO_2 adsorption.

* Corresponding author.
E-mail address: coronas@unizar.es (J. Coronas).

http://dx.doi.org/10.1016/j.memsci.2016.05.039
0376-7388/

From all the available polymers, the use of polybenzimidazole (PBI) membranes for the separation of H_2/CO_2 mixtures seems to be promising. PBI has high thermal stability, good chemical resistance, impressive compression strength and high intrinsic H_2/CO_2 selectivity. However, its major drawbacks are low permeability and relatively high brittleness [6].

According to the different results found in literature, PBI membranes have been prepared in different forms to be tested for this gas separation: as hollow fibers [7,8] and as supported [9] and self-supported flat membranes. In the last case, different procedures have been applied to enhance the polymer performance, such as PBI functionalization [10,11], thermal rearrangement [12], combination with ionic liquids[13,14] and polymer blending [15–17]. In any event, the properties of the polymer can be also modified by the incorporation of nanostructured fillers dispersed in a continuous polymeric phase, forming mixed matrix membranes (MMMs) [15,18–20], which are possible candidates for commercialization [21]. They combine the advantageous properties of both phases: easy processing of the organic polymer, and great separation performance and high thermal and chemical stability of the nanostructured fillers. By selecting fillers with a narrow distribution of microporosity, the performance of PBI membranes can be improved by the sieving properties of the former. However, this separation remains challenging due to the above mentioned similar kinetic diameters of H_2 and CO_2. Indeed, as shown by the Robeson's upper bound [22] for this separation, H_2/CO_2 selectivities higher than 10 are hardly achieved [23].

Zeolitic imidazolate frameworks (ZIFs) are a subfamily of metal-organic frameworks (MOFs) in which a divalent metal cation (i.e. Zn^{2+} or Co^{2+}) is linked to the nitrogen atoms of deprotonated imidazole molecules, forming tetrahedral frameworks with zeolite-like topologies [24]. ZIFs constitute crystalline, highly porous materials with extraordinarily high thermal and chemical stabilities. Among them, ZIF-8 is probably the most widely studied ZIF in the literature. It consists of a metal cation of Zn^{2+} coordinated with molecules of the organic linker 2-methylimidazole (2-mIm) forming a SOD zeolitic topology with large cavities of 1.16 nm connected through smaller windows of 0.34 nm. Thus, the permeance of H_2 (kinetic diameter of 0.29 nm) is expected to be favored over that of CO_2 (0.33 nm), despite the well-known flexibility of ZIF-8. The extraordinary chemical resistance of ZIF-8 has been proven previously, remaining unaltered after immersion in boiling methanol, benzene and water for seven days and in concentrated sodium hydroxide at 100 °C for 24 h [25]. For that reason, this MOF is expected to be stable in the aggressive solvents used to dissolve PBI, such as N,N-dimethylacetamide (DMAc) or N-methyl-2-pyrrolidone (NMP), even though Ostwald ripening during MMMs preparation has been reported [26].

MMMs based on PBI have already been prepared with different types of ZIFs, *e.g.* ZIF-7 [19], ZIF-11 [20], ZIF-90 [27] and ZIF-8. The latter has been the most widely used embedded in PBI membranes, not only for gas separation [8,11,28,29], but also for pervaporation processes [30,31]. Since ZIF-8 was first obtained solvothermally [25,32], new synthesis methods for this MOF have been developed with different solvents giving rise to a whole range of particle sizes, such as: microwave-assisted [33], sonochemical [34] electrochemical [35] and mechanochemical [36] syntheses, dry-gel conversion [37], microfluidics [38] and centrifugal acceleration [23]. The size and shape of the particles used as fillers in the fabrication of MMMs are crucial to obtain both a good dispersion and a good integration within the polymeric phase avoiding voids and further defects derived from a poor interaction [39,40].

In this work, different ZIF-8 nanoparticles in dry state with average sizes of 50, 70 and 150 nm have been integrated in commercial PBI polymer at two different loadings: 10 and 20 wt%. The obtained MMMs were tested at 150 °C and pressures from 3 to 6 bar to study their performance in the separation of H_2 from a H_2/CO_2 binary mixture in comparison with the pure polymeric membranes. The results show a relationship between particle size and separation performance, probably due to agglomeration issues. Furthermore, 150 nm ZIF-8 has also been used as a colloidal liquid suspension to be integrated in wet state in the polymeric phase for comparison with the membranes prepared from dried powder. The membranes prepared with the wet-state filler have also been measured at three different European universities, in an interlaboratory Round Robin test, providing results of multiple independent scientists following the same procedure in different laboratories. This kind of collaboration has already been performed in several chemical fields, such as pyrolysis of aerosols [41] and liquids [42], encapsulation [43], osmosis membranes [44] and adsorption [45]. To the best of our knowledge, neither the influence of the filler particle size in the membranes performance nor the results reproducibility through an interlaboratory Round Robin test have ever been tested for these ZIF-8/PBI MMMs.

2. Experimental section

2.1. MOFs synthesis

ZIF-8 was synthesized in several laboratories from different countries with different sizes: University of Zaragoza -UNIZAR- (150 nm), Leibniz University Hannover -LUH- (70 nm) and Johnson Mattey Co. -JM- (50 nm). In all cases the synthesis was done following similar recipes based on reports involving MeOH [46] and MeOH-water mixture [47] as solvents.

In the synthesis method of 150 nm ZIF-8 at UNIZAR, 0.47 g of zinc nitrate hexahydrate ($Zn(NO_3)_2 \cdot 6H_2O$, > 98%, Sigma Aldrich) was dissolved in 10 mL of MeOH (Scharlau) and 10 mL of distilled water. Besides, 1.0 g of 2-methylimidazole (mIm, $C_4H_6N_2$, > 99%, Sigma Aldrich), was dissolved in 10 mL of MeOH, and the two solutions were mixed and stirred for 2 h. The final product was collected by centrifugation (10000 rpm, 10 min), washed once with MeOH, and dried at 110 °C overnight.

The synthesis for 70 nm ZIF-8 was developed at LUH. 734.4 mg of $Zn(NO_3)_2 \cdot 6H_2O$ (> 98%, Sigma Aldrich) was first dissolved in 50 mL MeOH (Carl Roth). A second solution consisting of 810.6 mg mIm (> 99%, Sigma Aldrich) in 50 mL MeOH was prepared in parallel. The latter was then poured into the first solution under stirring. After the completed addition the resulting solution was kept for 1 h without stirring, followed by centrifugation and several washing steps with MeOH. The final product was then dried at 70 °C in overnight.

Finally, the ZIF-8 (50 nm) nanoparticles were synthesized at JM. Typically, a solution of $Zn(NO_3)_2 \cdot 6H_2O$ (2.933 g, 9.87 mmol) in 200 mL of MeOH was rapidly poured into a solution of mIm (6.489 g, 79.04 mmol) in 200 mL of MeOH under stirring with a magnetic bar. The mixture slowly turned turbid and after 30 min the nanocrystals were separated from the milky dispersion by centrifugation and washed with fresh MeOH for three times. The nanocrystals were then dried at room temperature in air for 16 h.

2.2. MMM preparation

All the membranes were prepared at UNIZAR. The standard membrane preparation was carried out with dry ZIF-8 particles. For each membrane loading (10 and 20 wt%) the necessary amount of ZIF-8 of different sizes (50, 70 and 150 nm) was weighted and dispersed in a certain quantity of DMAc (> 99.5%, Sigma Aldrich), calculated for each membrane loading in order to obtain a solvent concentration of 90 wt% in the final casting solution. After that, the

corresponding amount of PBI solution was added. The commercial PBI (comprising 26 wt% PBI with 1.5 wt% LiCl as stabilizer in N,N-dimethylacetamide), purchased from PBI Performance Products, was diluted to 15 wt% (also in DMAc) to avoid problems related to viscosity. The resulting solution was further stirred overnight. The casting solution was stirred three times and sonicated alternatively for 15 min each, and cast into a Petri dish located in an oven at 90 °C. The Petri dishes were left uncovered overnight to allow the evaporation of the solvent. After that, the membranes were peeled off from the Petri dishes and washed in MeOH for 8 h. Finally, the membranes were treated in a vacuum oven at 130 °C (temperature reached after a heating rate of 0.7 °C/min) and 10 mbar for 24 h for completing the removal of the remaining solvent.

When using the large 150 nm ZIF-8 particles in wet state as filler for MMMs, the methanol-collected nanoparticles (150 nm; wet synthesis) were washed/exchanged with DMAc. After the second centrifugation, the particles were re-suspended in DMAc prior to use. The suspension concentration was calculated for each membrane loading: 10 and 20 wt%, and the corresponding amount of PBI (15 wt% solution) was added. This procedure is similar to that used previously to prepare MMMs comprising ZIF-11 and Matrimid® [23].

Membrane thicknesses were assessed by a Digimatic Micrometer (measurement range from 0 to 30 mm with an accuracy of ± 1 μm). Several points (9) equally distributed across the membrane were measured per membrane and the arithmetic average was used to calculate the membrane thickness. In this work, MMMs with a thickness of 106 ± 11 μm were obtained.

2.3. Characterization of samples

Powder X-ray diffraction (XRD) patterns of MOFs and MMMs (Fig. S1, supporting information) were acquired using a D-Max Rigaku X-ray diffractometer with a copper anode and a graphite monochromator to select CuKα radiation (λ=1.540 Å), taking data from 2θ=2.5° to 40° at a scan rate of 0.03°/s. Thermogravimetric analyses (TGA) were carried out using Mettler Toledo TGA/STDA 851e. Samples (10 mg) placed in 70 μL alumina pans were heated in an air flow of 40 mL/min from 25 to 900 °C at a heating rate of 10 °C/min. Scanning electron microscopy (SEM) images of MOFs and membranes were obtained using an Inspect F50 model scanning electron microscope (FEI), operated at 20 kV. Cross-sections of membranes were prepared by freeze-fracturing after immersion in liquid N_2 and subsequently coated with Pt. Particle size was obtained using ImageJ 1.49b software, where at least 60 particles were counted for each sample. The membranes were also analyzed at several locations by the use of an IR microscope (Thermo Nicolet iN10MX) in the transmission mapping mode.

2.4. Gas separation performance

Gas separation tests were performed in the setups of three different institutions at 150 °C and at different feed pressures from 3 to 6 bar. The exit stream was analyzed by gas chromatography. Permeability was calculated in Barrer (10^{-10} cm^3(STP) cm/(cm^2 s cm Hg)) once the steady-state was reached (after about 3 h). One stabilization curve measured at TUDelft is shown as an example in the supporting information (Fig. S2). The separation selectivity was calculated as the ratio of the permeabilities of H_2 and CO_2. The different setups are described as follows.

2.4.1. UNIZAR setup

All types of PBI based MMMs, with 10 and 20 wt% of ZIF-8 and different sizes of filler particles were tested for H_2/CO_2 mixed gas separation. The membranes, 15.2 cm^2 in area, were assembled into a module consisting of two stainless steel pieces and a 316LSS macroporous disk support (from Mott Co.) with a 20 μm nominal pore size, gripped inside with silicone O-rings. The permeation module was placed in a UNE 200 Memmert oven to control the temperature of the module. Gas separation measurements were carried out by feeding an equimolar H_2/CO_2 mixture (90/90 cm^3(STP)/min) at the different operating pressures to the feed side by means of two mass flow controllers (Alicat Scientific, MC-100CCM-D), while the permeate side of the membrane was swept with a 2 cm^3(STP)/min mass flow controlled stream of Ar at 1 bar (Alicat Scientific, MC-5CCM-D). Concentrations of H_2 and CO_2 in the permeate were analyzed online by an Agilent 3000 A micro-gas chromatograph equipped with a thermal conductivity detector (TCD).

2.4.2. TUDelft setup

Only bare PBI membranes and MMMs with 10 wt% of ZIF-8 (150 nm; wet-state) were tested for gas separation in this setup. Round membrane areas of 4.90 cm^2 were cut from the casted films, placed on a macroporous support 316 L with 20 μm nominal pore size and mounted in a flange between Viton® O-rings. This flange fit in a permeation module that was located inside an oven using the permeation setup described elsewhere [48]. The H_2/CO_2 separation measurements were carried out in a home-made set-up employing an equimolar flow mixture of H_2/CO_2 (65/65 cm^3(STP)/min) as feed. He (3.3 cm^3 (STP)/min) was used as sweep gas for the permeate stream (atmospheric), while the trans-membrane pressure was adjusted in the range of the operating pressures using a back-pressure controller at the retentate side. An online gas chromatograph (Interscience Compact GC) equipped with a packed Carboxen 1010 PLOT (30 m × 0.32 mm) column and TCD and FID detectors was used to analyze the permeate stream.

2.4.3. LUH setup

Also bare PBI membranes and MMMs with 10 wt% of ZIF-8 (150 nm; wet-state) were tested in this setup. Neat PBI membranes and 10 wt% ZIF-8/PBI-MMMs were cut out with the help of a hollow punch, resulting in a membrane area of 2.54 cm^2. These membranes were placed into the same module as TUDelft. In addition, a porous α-Al_2O_3 support (2.5 μm pores in top layer, Fraunhofer IKTS, Germany) was used to prevent cracking during the measurement. The permeation module was sealed with O-rings (FKM 70 Vi 370) and wrapped with a heating tape and aluminum foil to control the temperature during the measurements. Gas separation measurements were carried out by feeding an equimolar mixture of H_2/CO_2 (25/25 cm^3(STP) /min) at different pressures by means of two mass flow controllers. The permeate side of the membrane was swept with a 1 cm^3 (STP)/min of Ar at 1 bar. Concentrations of H_2 and CO_2 in the permeate were analyzed by an Agilent Technologies 7890B online gas chromatograph equipped with a TCD.

3. Results and discussion

3.1. MOFs characterization

Three different types of ZIF-8 were synthesized and characterized before using them as fillers in PBI based MMMs. Representative SEM images of the different samples are shown in Fig. 1, where the different particle size (from 50 to 150 nm) and morphology are envisaged. While the smallest particles are almost spherical, the largest ZIF has well defined edges, according to the typical rhombic dodecahedron shape of ZIF-8. This morphological evolution has been previously reported and, as in most crystalline materials, is induced by changes of saturation levels during crystal

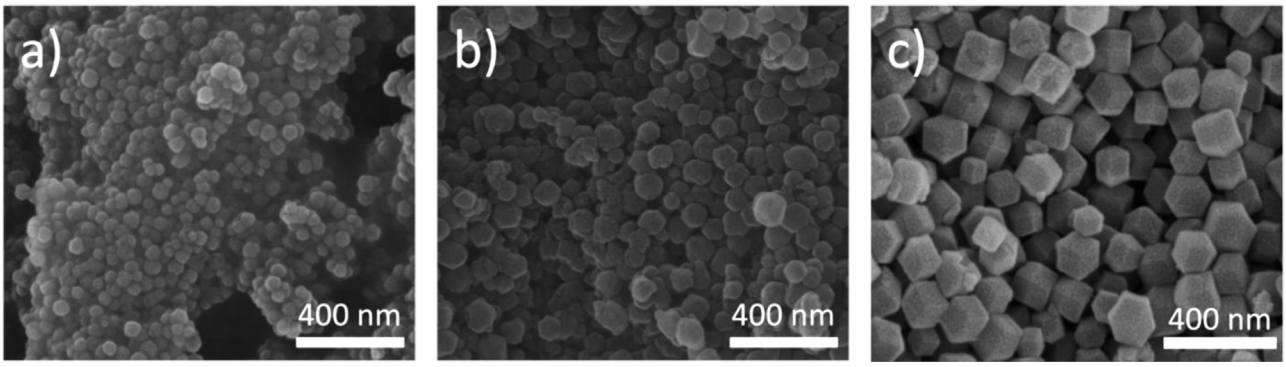

Fig. 1. SEM images of ZIF-8 nanoparticles with different sizes: (a) 50 nm, (b) 70 nm and (c) 150 nm used as filler.

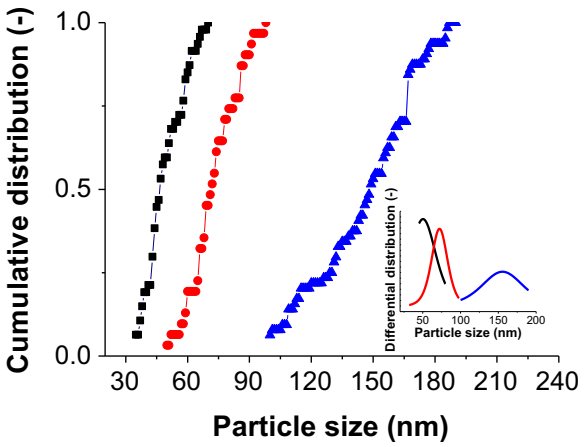

Fig. 2. Cumulative and differential (inset) particle size distribution of the ZIF-8 nanoparticle samples used as filler: 50 nm (black, square), 70 nm (red, circle) and 150 nm (blue, triangle). (For interpretation of the references to color in this figure legend, the reader is referred to the web version of this article.)

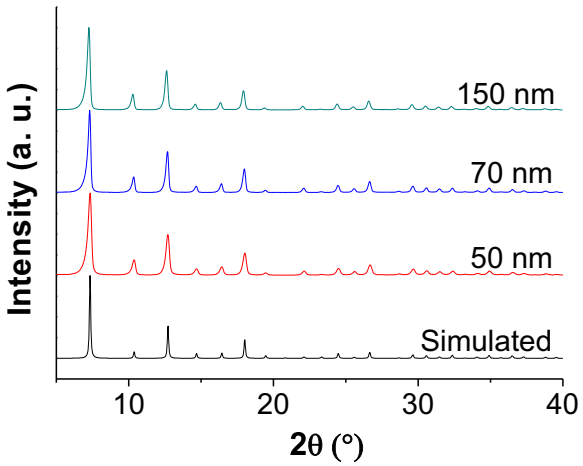

Fig. 3. XRD spectra of the different ZIF-8 nanoparticles synthesized.

growth [49,50].

Fig. 2 shows the normalized cumulative number of particles as a function of the particle size. From this plot, average particle sizes for each sample (47 ± 7, 72 ± 13 and 150 ± 60 nm) were obtained at $N/N_T = 0.5$, N and N_T being the number and total number of particles, respectively. In addition, the differential distributions were calculated (inset), providing predominant particle sizes (modes), whose values (51, 72 and 156 nm) are similar to the corresponding averages.

Finally, the XRD patterns of the ZIF-8 with sizes between 50 and 150 nm are represented in Fig. 3. All the samples show a pattern with identical shape and reflections at the same positions, proving that they constitute the same kind of MOF. Moreover, the height and width of the different peaks is equivalent for all samples, with slightly differences in the FWHM between 0.24 and 0.31°, disregarding their size, which also indicates high crystallinity.

3.2. Membrane characterization

The membranes were characterized by the use of an IR microscope to evaluate the impact of the preparation method on their homogeneity. Fig. 4 shows typical spectra recorded over the 10 wt% MOF loading membranes obtained with different dry-state MOF particle sizes and the 150 nm particles in wet state, as well as over the 20 wt% MOF loading membranes with 150 nm ZIF-8 synthesized in dry and wet state. PBI shows very intense bands in the 1300–1700 cm^{-1} range and below 900 cm^{-1} which hinder any comparison with ZIF-8 vibrations. In the 1250–950 cm^{-1} range, PBI shows bands at 957, 989, 1019, 1102, 1118, 1174 and 1231 cm^{-1}. From data recorded on benzimidazole [51] or PBI [52,53], these are mainly attributed to benzene-ring vibrations and in-plane C-H deformation bands. In this range ZIF-8 also shows bands at 954 and 994 cm^{-1} and two intense bands at 1146 and 1179 cm^{-1}, the latter being attributed to C–N ring vibrations [54,55].

For 10 wt% MOF loading, it can be observed that only in the case of the 150 nm dry particles, the bands attributed to ZIF-8 clearly appeared, at 1179, 1147, 997 and 954 cm^{-1}. This implies that some parts of the membranes contain sufficient amount of MOF to be detected and could be due to some agglomeration of the MOF particles. This was observed directly by eyes on this membrane. In addition, compared to the bands of the polymer, the intensities of ZIF-8 bands were different at the various spots analyzed, confirming the surface heterogeneity of this membrane. By contrast, for this MOF loading, the other membranes, which visually looked more homogeneous, did not exhibit the peaks of pure ZIF-8 at these positions. This indicates that “islands” of pure MOF could not be detected by the IR microscope on these samples. Noteworthy, the membrane preparation using the larger particles (150 nm) and a wet filler yielded similar results as MMMs made with smaller particles. For these membranes, additional bands to those of the polymer and different from those of pure ZIF-8 were observed at ca. 1136, 1024 and 1005 cm^{-1}. They are clearly evidenced on the difference spectra (Fig. 4b) and were also present on the 150 nm dry filler membrane sample as weak shoulders. The doublet at 1024 and 1005 cm^{-1} also changed with the particle size. In particular, the band at 1024 cm^{-1} decreased between 50 nm, 70 nm and 150 nm (wet) and was nearly absent on the 150 nm (dry). These bands are in the range of the C-H ring deformation bands of methyl imidazole [55–57]. Their shifts with

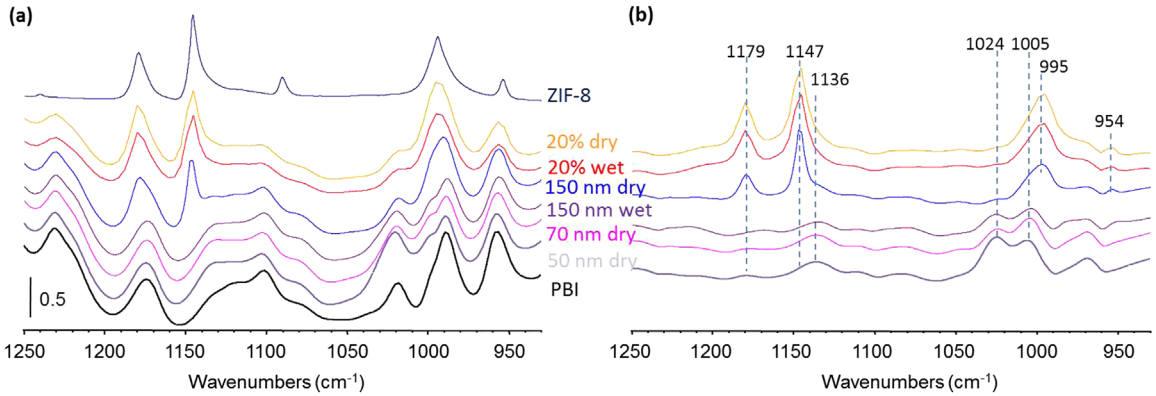

Fig. 4. IR characterization of PBI MMMs containing 10 wt% ZIF-8 of different sizes: 50 nm, 70 nm and 150 nm; as well as 20 wt% 150 nm ZIF-8. 150 nm ZIF-8 both in dry and wet state. Spectra are compared with those of pure PBI and ZIF-8 (a); Spectra of the MMMs after subtraction of the PBI (b).

respect to the expected positions could be attributed to chemical interactions between MOF and polymer or to a distortion of the MOF ligand structure of ZIF-8 upon interaction with the polymer. Their intensities inversely proportional to the particle sizes and to the MOF dispersion could thus indicate a more complete mixing of both phases.

At 20 wt% MOF loading, membranes prepared in dry or wet state did not show any difference. Both showed the prominent features due to ZIF-8, as the 10 wt% MOF in dry state membrane. At this loading, both membranes looked visually homogeneous. Nevertheless, the broad peaks of ZIF-8 indicate that for such MOF loading larger domains of ZIF-8 are likely to occur within the membrane.

3.3. Interlaboratory round-robin test: permeation performance

In order to check the reproducibility of the membrane permeation testing, pure PBI membranes and those prepared with the wet-state filler (150 nm) at 10 wt% loading were measured at three different European universities (UNIZAR from Zaragoza-Spain, LUH from Hannover-Germany and TUDelft from Delft-The Netherlands) in an interlaboratory Round Robin test.

Table 1 shows the H_2 permeability and the H_2/CO_2 selectivity for the membranes measured at each university, together with the average values calculated from the last tests, once steady-state was reached. Discrepancies were the highest for the permeability values for the pure PBI membranes, but less in the other cases. The MMM containing 10 wt% (actual loading measured by TGA of 9.6 ± 1.1 wt%) of ZIF-8 contributed to the checking of each experimental setup and measuring methodology with lower errors. All these differences could be related to: (i) different GC analytical errors of each setup; (ii) the use of the different permeation modules at each institution, leading to differences in effective permeation area; and (iii) the use of different sweep gases (He *vs.* Ar). In addition, the backpermeation of sweep gas (in particular of He) may result in an artificially higher permeability and should be carefully verified. Finally, to prove whether the different testing conditions could be under these discrepancies, one MMM was tested at UNIZAR under different feed and sweep conditions. The results are contained in Table S1, where it can be seen how the performance differences are similar to those in the Round Robin testing.

On the whole, a relatively good coherence among the different measurements can be appreciated, which assures the reproducibility of the membranes prepared and reported test results. In any event, these results confirm the suitability of the MMM approach to improve the performance of the pure polymer in the H_2/CO_2 separation by adding ZIF-8 filler. Moreover, the membranes could be tested in different setups, what is not usually reported.

MMMs based on PBI, containing ZIF-8 of different sizes (50, 70 and 150 nm) in dry state, were used in this experiment in order to study the influence of the filler size on the membranes performance. Besides, the results for MMMs with 150 nm ZIF-8 were compared with those from the previous experiment (150 nm; wet-state). All these tests were performed at UNIZAR.

Table 1
Gas separation results for H_2/CO_2 separation (50/50 vol%) of pure PBI membranes and 10 wt% ZIF-8/PBI MMMs tested at 150 °C at UNIZAR, LUH and TUDelft. Up to 4 different membranes were tested by each partner. The pressure of the equimolar feed mixture H_2/CO_2 was varied between 3 and 6 bar, the permeate side was at 1 bar of the sweep gas (Ar or He).

	UNIZAR	LUH	TUDelft	Average	UNIZAR	LUH	TUDelft	Average
	Pure PBI membranes							
P (bar)	**pH_2 (Barrer)**				**α (H_2/CO_2)**			
3	25.2 ± 2.4	32.5 ± 0.6	–	29 ± 5	3.3 ± 0.5	3.8 ± 0.2	–	3.7 ± 0.2
4	27.2 ± 3.0	31.1 ± 0.4	34.5 ± 1.7	31 ± 4	3.5 ± 0.6	4.0 ± 0.3	4.3 ± 0.0	3.9 ± 0.4
5	26.8 ± 2.7	30.7 ± 1.1	33.7 ± 4.7	30 ± 3	3.5 ± 0.6	4.1 ± 0.3	3.9 ± 0.4	3.8 ± 0.3
6	26.7 ± 2.7	–	33.2 ± 2.9	30 ± 5	3.5 ± 0.6	–	4.1 ± 0.2	3.8 ± 0.4
3 ref	26.7 ± 2.7	33.7 ± 0.4	–	30 ± 5	3.4 ± 0.5	3.9 ± 0.3	–	3.7 ± 0.4
	10 wt% ZIF-8/PBI MMMs							
P (bar)	**pH_2 (Barrer)**				**α (H_2/CO_2)**			
3	35.2 ± 1.2	46.4 ± 1.3	–	41 ± 8	4.6 ± 0.4	4.7 ± 0.3	–	4.7 ± 0.1
4	36.9 ± 1.6	44.7 ± 1.7	40.2 ± 6.6	41 ± 4	4.7 ± 0.4	5.0 ± 0.3	4.1 ± 0.3	4.6 ± 0.5
5	36.4 ± 1.9	42.7 ± 1.2	39.6 ± 3.8	40 ± 3	4.5 ± 0.4	5.0 ± 0.2	4.2 ± 0.5	4.6 ± 0.4
6	37.7 ± 1.3	–	38.6 ± 3.1	38 ± 1	4.3 ± 0.6	–	4.2 ± 0.3	4.3 ± 0.1
3 ref	38.5 ± 1.2	45.8 ± 0.4	–	42 ± 5	4.7 ± 0.2	4.9 ± 0.1	–	4.8 ± 0.1

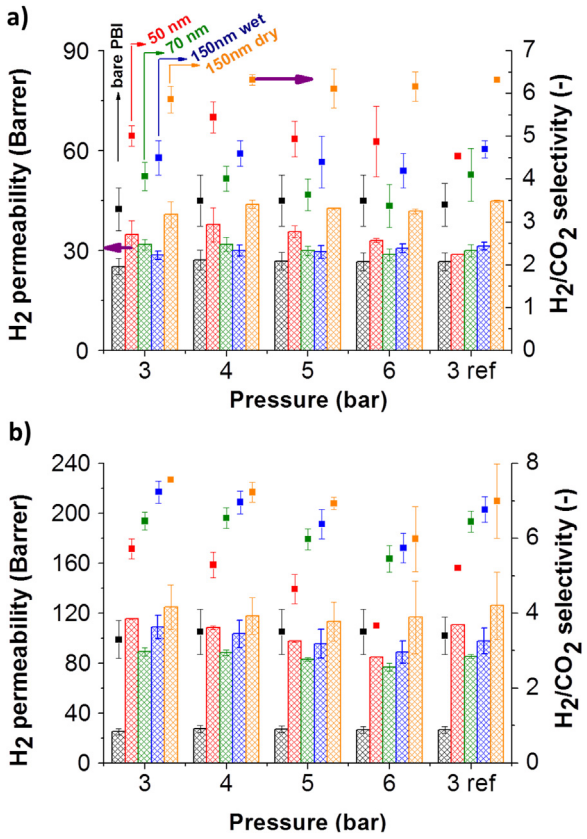

Fig. 5. Mixed gas separation performance of pure PBI (black) and PBI MMMs containing ZIF-8 of different sizes: 50 nm (red), 70 nm (green) and 150 nm in wet (blue) and dry state (orange) at loadings of 10 (a) and 20 wt% (b) and at different feed pressures from 3 to 6 bar at 150 °C, permeate side at 1 bar of the sweep gas Ar. The bars indicate the H_2 permeability, the squares give the (H_2/CO_2) selectivity. The "3 ref" data show the stability of the MMM after working at different feed pressures by repeating the 3 bar initial measurement. This testing was performed at UNIZAR. (For interpretation of the references to color in this figure legend, the reader is referred to the web version of this article.)

3.4. Permeation performance of MMMs containing ZIF-8 filler of different sizes

Fig. 5 shows the H_2/CO_2 gas separation performance for a 50/50 mixture at 150 °C and 3, 4, 5 and 6 bar of feed pressure. At least 2–3 MMM samples of each loading were fabricated and measured to provide the corresponding error estimations. The integration of each type of ZIF-8 improved the membrane performance clearly. When embedding 10 wt% of ZIF-8, H_2 permeability was doubled while giving rise to a nearly 40% increase in selectivity compared to the bare polymer membrane (Fig. 5a). This evidences the important role that the presence of microporous ZIF-8 plays in the gas transport through the membranes. No significant changes in the permeabilities of hydrogen were observed with increasing pressure from 3 to 6 bar, while the H_2/CO_2 selectivities decreased by 9%, probably due to the enhancement of CO_2 adsorption with pressure. However, when reducing the pressure from 6 bar to the reference pressure (3 bar) a slight increase in both permeability and selectivity was found compared to the original values at 3 bar but only for the membranes containing 150 nm ZIF-8.

Comparing the results of membranes prepared with wet and dry filler, it can be concluded that the membranes containing dry ZIF-8 (10 wt%) showed a better performance in terms of permeability and selectivity, increasing these values by a 20% when compared with membranes prepared with wet ZIF-8. The MOF treatment before preparing the casting solution may be responsible for this behavior because, in the case of dry ZIF-8, the material was dried at 110 °C while for the wet-state MOF, a solvent exchange with DMAc was carried out. Besides, the dry sample, with no remains of solvent molecules in its porosity, may interact better with polymer chains (it is worth mentioning that bulky caffeine can penetrate ZIF-8) [47], leading to an improvement in the interaction between filler and polymeric matrix. In fact, it has been demonstrated that partially activated and non-activated fillers give rise to worse performance membranes [58]. In any event, the use of the wet material as filler must not be discarded. It would be environmentally friendlier, since the energy consumption for the drying stage could be avoided and it simplifies the possible industrial processing of the MMMs.

In order to achieve a deeper insight into the filler size influence on the membrane performance, PBI MMMs were fabricated at higher loadings (20 wt%) and tested under the same conditions (Fig. 5b). In this case, the H_2 permeability of each MMM was at least six times higher when compared to the pure polymer with the H_2/CO_2 selectivity increasing with the filler size (approximately by 55% for the 150 nm size). For this loading a clear decreasing tendency with rising pressure from 3 to 6 bar is observed for permeability and selectivity. Also in this case, the membranes containing dry ZIF-8 performed better than those with the filler added in wet state, although the difference was not as high as for 10 wt% MMMs. This result is in coherence with the IR characterization, which showed a difference in the particle dispersion for 10 wt% loaded MMMs, while this was not appreciated for 20 wt% loadings. Apart from the simplicity, the use of wet MOF for MMMs is more suitable due to less agglomeration and easier dispersion.

In both cases, at loadings of 10 wt% the separation selectivity shows an irregular trend with particle size, while at 20 wt%, the separation selectivity improved as the filler size increased. In terms of permeability, this irregular trend can be related to the simultaneous occurrence of counteracting effects. On the one hand, large particles show less agglomeration, which has a positive effect on the particle dispersion. On the other, they have a lower external surface area, weakening the interaction with the polymeric phase [59], and less exchange area between continuous and filler phase. The agglomeration of hydrophobic ZIF-8 particles due to the formation of bridges between external surface groups would be lower than in case of hydrophilic silicates and zeolites, which exhibit a strong tendency to establish T–O–T condensation bonds, T being Si or Al [60]. In any event, this positive effect with particle size is clearer with selectivity than with permeability, where the data show no statistical difference, especially at 20% loading. Moreover, increasing the amount of ZIF up to 20 wt% has a positive effect on the membranes performance, since both permeability and selectivity increase. The behavior of increasing permeability with the filler loading is in agreement with the literature, where generally an optimum of selectivity at a certain amount of loading is found [58], and is consequence of the ZIF microporosity which favors H_2 transport over that of CO_2.

Finally, Fig. 6 shows a Robeson graph with permeability and selectivity values obtained for the MMMs containing dry ZIF-8 of 150 nm with 10 and 20 wt% loadings and bare PBI membranes tested at 3 bar and 150 °C, i.e. H_2 permeabilities of 40.8 and 124.9 Barrer and H_2/CO_2 selectivities of 5.8 and 7.6, respectively. These values are represented together with others found in the literature for PBI based MMMs and different types of ZIFs as fillers [19,20,27–29], whose particle size and embedding state can be seen in Table 2. It can be seen that the results from this work are in good agreement with the literature, especially with ZIF-7/PBI MMMs (25 wt% ZIF-7 loading tested also at 150 °C) [19]. However, when the results are compared with other MMMs containing ZIF-8 [28,29], there seem to be greater discrepancy due to both the differences in filler loading (up to 60 wt%) and testing temperatures (25, 35 and 230 °C).

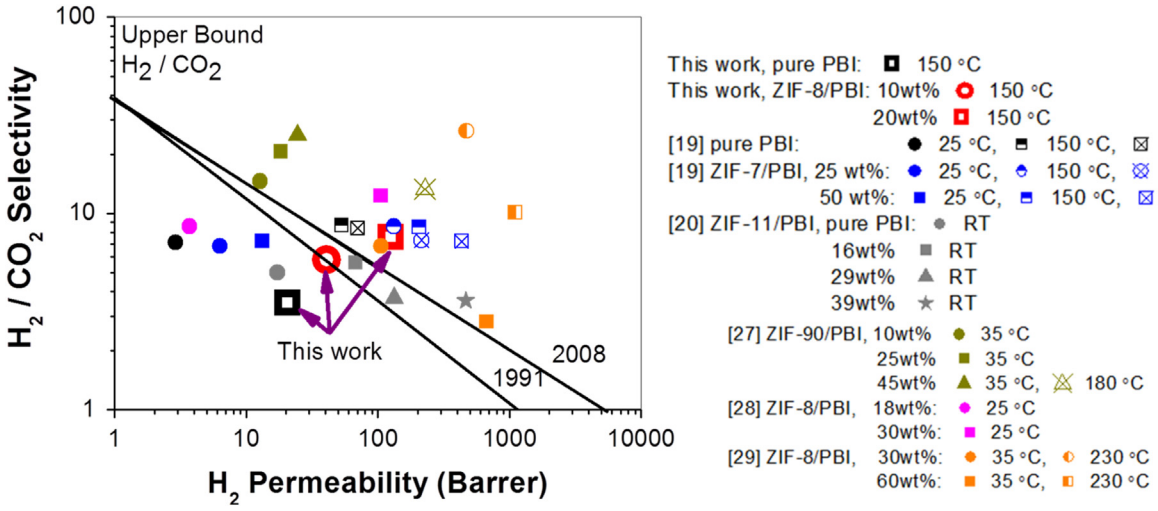

Fig. 6. ZIF/PBI mixed matrix membranes: comparison between selective permeation performance in this work and results from literature. (For interpretation of the references to color in this figure legend, the reader is referred to the web version of this article.)

Table 2
Particle size and embedding state of different ZIFs found in literature that have been used as filler in PBI based MMMs for H_2/CO_2 gas separation and the main achievements obtained.

ZIF	Particle size	State	Main achievements	Reference
ZIF-7	ca. 30 nm	wet	ZIF-7 nano-particles were embedded in wet state into PBI without much ZIF agglomeration, enhancing the membrane performance.	Yang et al. [19]
ZIF-8	ca. 45 nm	wet	The first time that ZIF-8 and PBI were combined for energy-related applications. Best reported data for H_2-selective polymeric materials to date.	Yang et al. [28]
ZIF-8	ca. 45 nm	wet	The incorporation of ZIF-8 nanoparticles enhanced the membrane performance. Impurities present in the feed gas (CO and water vapor) had insignificant impact on the H_2/ CO_2 separation performance.	Yang et al. [29]
ZIF-90	80–200 nm	wet	ZIF-90 nanocrystals were synthesized *via* a specially designed route. Mixed gas permeation results showed that the ZIF-90-PBI membranes suffer a significant performance drop, still possessing a good gas separation performance, though.	Yang et al. [27]
ZIF-11	ca. 2 μm	dry	ZIF-11 showed a good compatibility with PBI as they have the same benzimidazole structure. ZIF-11/PBI composite membrane exhibited potential for hydrogen separation.	Li et al. [20]
ZIF-8	50, 70, 150 nm	dry/wet	Membrane performance improves the higher the particle size of the filler is and when it is embedded in dry state. Good agreement in results obtained through interlaboratoty testing.	This work

4. Conclusions

MMMs based on PBI and ZIF-8 filler of different sizes have been prepared at loadings of 10 and 20 wt%. Spectroscopic characterizations confirmed the MOF particle dispersion in the polymer and their mutual interactions; specific vibrations were found possibly witnessing for the organic ligand interacting with the polymeric chain. These membranes have been tested in the H_2/CO_2 separation at 150 °C and feeding pressures from 3 to 6 bar, conditions relevant for the pre-combustion capture of CO_2. The integration of each type of ZIF-8 clearly enhanced the membranes performance, evidencing the important role that the microporous structure of the ZIF plays in the gas transport through the membranes. This improvement is more evident as the particle size of the filler increases from 50 to 150 nm, probably due to agglomeration issues. When embedding 10 wt% of ZIF-8, H_2 permeability was doubled giving rise to a considerable increase in selectivity of nearly 40% compared to the bare polymer membrane. This improvement was even more relevant at 20 wt% loading, with a H_2 permeability at least six times higher and an increase in selectivity of about twofold. On the whole, both permeability and selectivity values decreased as the feeding pressure rose, and the data show no statistical difference in permeability as a function of particle size, especially at 20% loading, while the selectivities barely do.

Besides, the membranes prepared with dry ZIF-8 showed a better performance in terms of hydrogen permeability and H_2/CO_2 selectivity than the MMMs containing wet ZIF-8. However, together with the IR evidences of more homogeneous dispersion in the MMM, the handling of the wet filler should not be discarded when having in mind the possible scale up due to other considerations such as simplicity of the procedure. When the MOF loading was sufficiently high (20 wt%), the permselectivity results improved due to the lower aggregation of the largest particles, less active relating to their external surface area. Finally, the reproducibility of the membrane permeation analyzing methodology has been demonstrated by a European interlaboratory Round Robin test involving three different institutions.

Acknowledgments

Financial support from the Spanish MINECO (MAT2013-40556-R), the Aragón Government (T05) and the ESF is gratefully acknowledged. The research leading to these results has received funding from the European Union Seventh Framework Programme (FP7/2007–2013) under Grant Agreement no. 608490, project M4CO2. All the microscopy work was done in the Laboratorio de Microscopías Avanzadas at the Instituto de Nanociencia de Aragón (LMA-INA). The use of the Servicio General de Apoyo a la Investigación-SAI (Universidad de Zaragoza) is acknowledged. J.G. and B.S. gratefully acknowledge financial support from the European Research Council under the European Union's Seventh

Framework Programme (FP/2007–2013)/ERC Grant Agreement no. 335746, CrystEng-MOF-MMM.

Appendix A. Supplementary material

Supplementary data associated with this article can be found in the online version at http://dx.doi.org/10.1016/j.memsci.2016.05.039.

References

[1] T. Stocker, D. Qin, G. Plattner, M. Tignor, S.K. Allen, J. Boschung, et al., Climate change 2013: The Physical Science Basis 2013, Cambridge University Press, Cambridge, UK, and New York, 2014.

[2] E.S. Rubin, H. Mantripragada, A. Marks, P. Versteeg, J. Kitchin, The outlook for improved carbon capture technology, Prog. Energy Combust. Sci. 38 (2012) 630.

[3] D. Aaron, C. Tsouris, Separation of CO_2 from flue gas: a review, Sep. Sci. Technol. 40 (2005) 321.

[4] T.C. Merkel, M. Zhou, R.W. Baker, Carbon dioxide capture with membranes at an IGCC power plant, J. Membr. Sci. 389 (2012) 441.

[5] J. Wijmans, R. Baker, The solution-diffusion model: a review, J. Membr. Sci. 107 (1995) 1.

[6] T. Chung, A critical review of polybenzimidazoles: historical development and future R&D, J. Macromol. Sci. Part C Polym. Rev. 37 (1997) 277.

[7] S. Kumbharkar, Y. Liu, K. Li, High performance polybenzimidazole based asymmetric hollow fibre membranes for H_2/CO_2 separation, J. Membr. Sci. 375 (2011) 231.

[8] B.P. Biswal, A. Bhaskar, R. Banerjee, U.K. Kharul, Selective interfacial synthesis of metal–organic frameworks on a polybenzimidazole hollow fiber membrane for gas separation, Nanoscale 7 (2015) 7291.

[9] K.A. Berchtold, R.P. Singh, J.S. Young, K.W. Dudeck, Polybenzimidazole composite membranes for high temperature synthesis gas separations, J. Membr. Sci. 415 (2012) 265.

[10] S.C. Kumbharkar, P.B. Karadkar, U.K. Kharul, Enhancement of gas permeation properties of polybenzimidazoles by systematic structure architecture, J. Membr. Sci. 286 (2006) 161.

[11] A. Bhaskar, R. Banerjee, U. Kharul, ZIF-8@ PBI-BuI composite membranes: elegant effects of PBI structural variations on gas permeation performance, J. Mater. Chem. A 2 (2014) 12962.

[12] S.H. Han, J.E. Lee, K. Lee, H.B. Park, Y.M. Lee, Highly gas permeable and microporous polybenzimidazole membrane by thermal rearrangement, J. Membr. Sci. 357 (2010) 143.

[13] L. Liang, Q. Gan, P. Nancarrow, Composite ionic liquid and polymer membranes for gas separation at elevated temperatures, J. Membr. Sci. 450 (2014) 407.

[14] A.S. Rewar, R.S. Bhavsar, K. Sreekumar, U.K. Kharul, Polybenzimidazole based polymeric ionic liquids (PILs): effects of controlled degree of N-quaternization on physical and gas permeation properties, J. Membr. Sci. 481 (2015) 19.

[15] S.S. Hosseini, T.S. Chung, Carbon membranes from blends of PBI and polyimides for N_2/CH_4 and CO_2/CH_4 separation and hydrogen purification, J. Membr. Sci. 328 (2009) 174.

[16] X. Li, R.P. Singh, K.W. Dudeck, K.A. Berchtold, B.C. Benicewicz, Influence of polybenzimidazole main chain structure on H_2/CO_2 separation at elevated temperatures, J. Membr. Sci. 461 (2014) 59.

[17] N.P. Panapitiya, S.N. Wijenayake, D. Nguyen, Y. Huang, I.H. Musselman, K. J. Balkus, et al., Gas separation membranes derived from high performance immiscible polymer blends compatibilized with small molecules, ACS Appl. Mater. Interfaces (2015).

[18] S. Choi, J. Coronas, E. Jordan, W. Oh, S. Nair, F. Onorato, et al., Layered silicates by swelling of AMH-3 and nanocomposite membranes, Angew. Chem. Int. Ed. 47 (2008) 552.

[19] T. Yang, Y. Xiao, T. Chung, Poly-/metal-benzimidazole nano-composite membranes for hydrogen purification, Energy Environ. Sci. 4 (2011) 4171.

[20] L. Li, Y. Jianfeng, X. Wang, Y. Chen, H. Wang, ZIF-11/Polybenzimidazole composite membrane with improved hydrogen separation performance, J. Appl. Polym. Sci. 131 (2014) 41056.

[21] B. Seoane, J. Coronas, I. Gascon, M.E. Benavides, O. Karvan, J. Caro, et al., Metal–organic framework based mixed matrix membranes: a solution for highly efficient CO_2 capture? Chem. Soc. Rev. 44 (2015) 2421.

[22] L.M. Robeson, The upper bound revisited, J. Membr. Sci. 320 (2008) 390.

[23] J. Sánchez-Laínez, B. Zornoza, Á. Mayoral, Á. Berenguer-Murcia, D. Cazorla-Amorós, C. Téllez, et al., Beyond the H_2/CO_2 upper bound: one-step crystallization and separation of nano-sized ZIF-11 by centrifugation and its application in mixed matrix membranes, J. Mater. Chem. A (2015).

[24] Y. Lee, J. Kim, W. Ahn, Synthesis of metal-organic frameworks: a mini review, Korean J. Chem. Eng. 30 (2013) 1667.

[25] K.S. Park, Z.N. Ni, A.P. Côté, J.Y. Choi, R. Huang, F.J. Uribe-Romo, et al., Exceptional chemical and thermal stability of zeolitic imidazolate frameworks, Proc. Natl. Acad. Sci. USA 103 (2006) 10186–10191.

[26] J.A. Thompson, K.W. Chapman, W.J. Koros, C.W. Jones, S. Nair, Sonication-induced Ostwald ripening of ZIF-8 nanoparticles and formation of ZIF-8/polymer composite membranes, Microporous Mesoporous Mater. 158 (2012) 292.

[27] T. Yang, T. Chung, Room-temperature synthesis of ZIF-90 nanocrystals and the derived nano-composite membranes for hydrogen separation, J. Mater. Chem. A 1 (2013) 6081.

[28] T. Yang, G.M. Shi, T. Chung, Symmetric and asymmetric zeolitic imidazolate frameworks (ZIFs)/polybenzimidazole (PBI) nanocomposite membranes for hydrogen purification at high temperatures, Adv. Energy Mater. 2 (2012) 1358.

[29] T. Yang, T. Chung, High performance ZIF-8/PBI nano-composite membranes for high temperature hydrogen separation consisting of carbon monoxide and water vapor, Int. J. Hydrogen Energy 38 (2013) 229.

[30] G.M. Shi, H. Chen, Y. Jean, T.S. Chung, Sorption, swelling, and free volume of polybenzimidazole (PBI) and PBI/zeolitic imidazolate framework (ZIF-8) nanocomposite membranes for pervaporation, Polymer 54 (2013) 774.

[31] G.M. Shi, T. Yang, T.S. Chung, Polybenzimidazole (PBI)/zeolitic imidazolate frameworks (ZIF-8) mixed matrix membranes for pervaporation dehydration of alcohols, J. Membr. Sci. 415 (2012) 577.

[32] X. Huang, Y. Lin, J. Zhang, X. Chen, Ligand-directed strategy for zeolite-type metal–organic frameworks: zinc (ii) imidazolates with unusual zeolitic topologies, Angew. Chem. Int. Ed. 118 (2006) 1587.

[33] J. Park, S. Park, S. Jhung, Microwave-syntheses of zeolitic imidazolate framework material, ZIF-8, J. Korean Chem. Soc. 53 (2009) 553.

[34] H. Cho, J. Kim, S. Kim, W. Ahn, High yield 1-L scale synthesis of ZIF-8 via a sonochemical route, Microporous Mesoporous Mater. 169 (2013) 180.

[35] A. Martinez Joaristi, J. Juan-Alcañiz, P. Serra-Crespo, F. Kapteijn, J. Gascon, Electrochemical synthesis of some archetypical Zn_2, Cu_2, and Al_3 metal organic frameworks, Cryst. Growth Des. 12 (2012) 3489.

[36] P.J. Beldon, L. Fábián, R.S. Stein, A. Thirumurugan, A.K. Cheetham, T. Friščić, Rapid room-temperature synthesis of zeolitic imidazolate frameworks by using mechanochemistry, Angew. Chem. Int. Ed. 49 (2010) 9640.

[37] Q. Shi, Z. Chen, Z. Song, J. Li, J. Dong, Synthesis of ZIF-8 and ZIF-67 by steam-assisted conversion and an investigation of their tribological behaviors, Angew. Chem. Int. Ed. 123 (2011) 698.

[38] Y. Lee, M. Jang, H. Cho, H. Kwon, S. Kim, W. Ahn, ZIF-8: a comparison of synthesis methods, Chem. Eng. J. 271 (2015) 276.

[39] T. Rodenas, I. Luz, G. Prieto, B. Seoane, H. Miro, A. Corma, et al., Metal–organic framework nanosheets in polymer composite materials for gas separation, Nat. Mater. 14 (2015) 48.

[40] T. Rodenas, M. van Dalen, E. García-Pérez, P. Serra-Crespo, B. Zornoza, F. Kapteijn, et al., Visualizing MOF mixed matrix membranes at the nanoscale: towards structure-performance relationships in CO_2/CH_4 separation over NH2–MIL-53 (Al)@ PI, Adv. Funct. Mater. 24 (2014) 249.

[41] H. Schmid, L. Laskus, H.J. Abraham, U. Baltensperger, V. Lavanchy, M. Bizjak, et al., Results of the "carbon conference" international aerosol carbon round robin test stage I, Atmos. Environ. 35 (2001) 2111.

[42] E. Jakab, O. Faix, F. Till, T. Székely, Thermogravimetry/mass spectrometry study of six lignins within the scope of an international round robin test, J. Anal. Appl. Pyrolysis 35 (1995) 167.

[43] S. Rosinski, G. Grigorescu, D. Lewinska, L. Ritzén, H. Viernstein, E. Teunou, et al., Characterization of microcapsules: recommended methods based on round-robin testing, J. Microencapsul. 19 (2002) 641.

[44] T.Y. Cath, M. Elimelech, J.R. McCutcheon, R.L. McGinnis, A. Achilli, D. Anastasio, et al., Standard methodology for evaluating membrane performance in osmotically driven membrane processes, Desalination 312 (2013) 31.

[45] S. Kaskel, P. Llewellyn, F. Rodriguez-Reinoso, N.A. Seaton, Characterization Measurements of Common Reference Nanoporous Materials by Gas Adsorption(Round Robin Tests): Nigel Seaton, Francisco R Reinoso, Philip Llewellyn, Stefan Kaskel (Eds.), Characterisation of Porous Solids VIII : Proceedings of the 8th International Symposium on the Characterisation of Porous Solids, RSC, Cambridge, 2009.

[46] J. Cravillon, S. Muenzer, S. Lohmeier, A. Feldhoff, K. Huber, M. Wiebcke, Rapid room-temperature synthesis and characterization of nanocrystals of a prototypical zeolitic imidazolate framework, Chem. Mater. 21 (2009) 1410.

[47] N. Liédana, A. Galve, C. Rubio, C. Téllez, J. Coronas, CAF@ ZIF-8: one-step encapsulation of caffeine in MOF, ACS Appl. Mater. Interfaces 4 (2012) 5016.

[48] B. Zornoza, A. Martinez-Joaristi, P. Serra-Crespo, C. Tellez, J. Coronas, J. Gascon, et al., Functionalized flexible MOFs as fillers in mixed matrix membranes for highly selective separation of CO_2 from CH_4 at elevated pressures, Chem. Commun. 47 (2011) 9522.

[49] J. Cravillon, C.A. Schröder, H. Bux, A. Rothkirch, J. Caro, M. Wiebcke, Formate modulated solvothermal synthesis of ZIF-8 investigated using time-resolved in situ X-ray diffraction and scanning electron microscopy, CrystEngComm 14 (2012) 492.

[50] B. Seoane, S. Castellanos, A. Dikhtiarenko, F. Kapteijn, J. Gascon, Multi-scale crystal engineering of metal organic frameworks, Coord. Chem. Rev. (2015).

[51] M. Cordes, J. Walter, Infrared and Raman studies of heterocyclic compounds—II Infrared spectra and normal vibrations of benzimidazole and bis-(benzimidazolato)-metal complexes, Spectrochim. Acta Part A Mol. Spectrosc. 24 (1968) 1421.

[52] P. Musto, F. Karasz, W. MacKnight, Fourier transform infra-red spectroscopy on the thermo-oxidative degradation of polybenzimidazole and of a polybenzimidazole/polyetherimide blend, Polymer 34 (1993) 2934.

[53] P. Christensen, S. Jones, An in situ FTIR study of undoped PolyBenzoImadazole as a function of relative humidity, Polym. Degrad. Stab. 105 (2014) 211.

[54] Q. Song, S. Nataraj, M.V. Roussenova, J.C. Tan, D.J. Hughes, W. Li, et al., Zeolitic

imidazolate framework (ZIF-8) based polymer nanocomposite membranes for gas separation, Energy Environ. Sci. 5 (2012) 8359.
[55] G. Kumari, K. Jayaramulu, T.K. Maji, C. Narayana, Temperature induced structural transformations and gas adsorption in the zeolitic imidazolate framework ZIF-8: a Raman study, J. Phys. Chem. A 117 (2013) 11006.
[56] T. Lane, I. Nakagawa, J. Walter, A. Kandathil, Infrared investigation of certain imidazole derivatives and their metal chelates, Inorg. Chem. 1 (1962) 267.
[57] M. Cordes, Infrared and Raman spectra of heterocyclic compounds—I the infrared studies and normal vibrations of imidazole, Spectrochim. Acta Part A Mol. Spectrosc. 24 (1968) 237.
[58] B. Zornoza, S. Irusta, C. Téllez, J. Coronas, Mesoporous silica sphere- polysulfone mixed matrix membranes for gas separation, Langmuir 25 (2009) 5903.
[59] S. Ersolmaz, C. Oral, M. Tatlıer, A. Senatalar, B. Schoeman, J. Sterte, Effect of zeolite particle size on the performance of polymer–zeolite mixed matrix membrane, J. Membr. Sci. 175 (2000) 285.
[60] D. Julve, J. Ramos, J. Perez, M. Menéndez, Analysis of Mercury porosimetry Curves of precipitated Silica, as an example of compressible porous solids, J. Non Cryst. Solids 357 (2011) 1319.

Supplementary Data

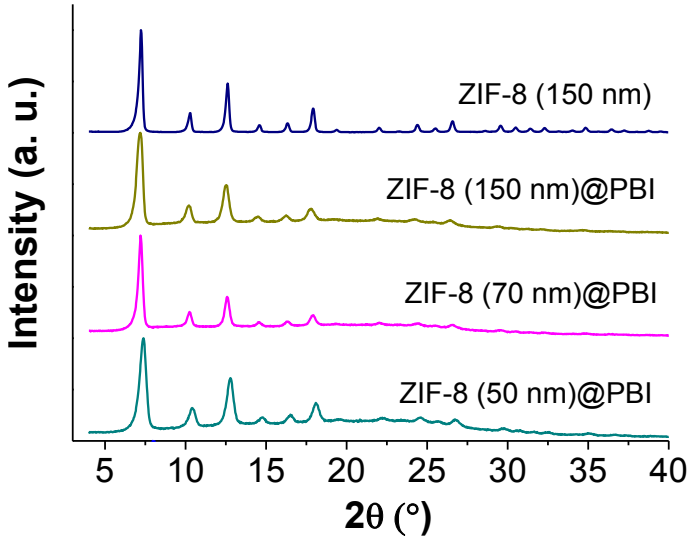

Figure S1. XRD patterns of MMMs with 20 wt% loading containing ZIF-8 of different sizes as filler.

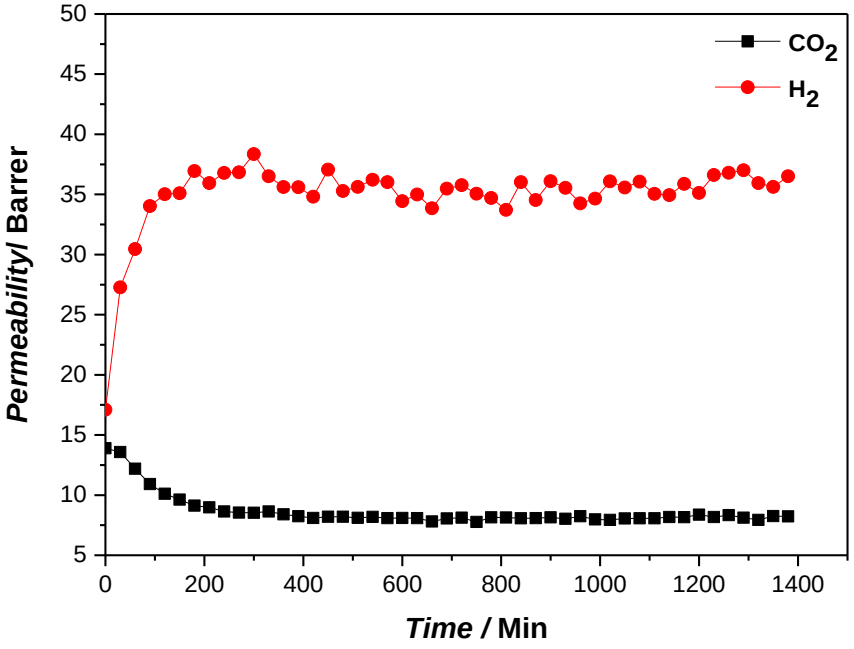

Figure S2. Stabilization curve for pure PBI membrane.

Table S1. Gas separation performance of one ZIF-8/PBI 10 wt% (wet) MMM tested under different feed and sweep flows, and sweep flow gas (Ar vs. He).

Sweep gas	Feed flow H_2/CO_2 (mL/min)	Sweep flow (mL/min)	PH_2 (Barrer)	PCO_2 (Barrer)	α (H_2/CO_2)
Ar	90/90	1	35.6	9.4	3.8
		2	35.1	9.2	3.8
		3	34.3	9.2	3.7
		4	34.1	9.2	3.7
	25/25	2	38.5	9.1	4.3
	65/65		35.8	9.3	3.9
	90/90		35.1	9.2	3.8
He	90/90	2	44.7	10.2	4.4

Chapter 6: On the chemical filler–polymer interaction of nano-and micro-sized ZIF-11 in PBI mixed matrix membranes and their application for H_2/CO_2 separation

J. Sánchez-Laínez, B. Zornoza, C. Téllez, and J. Coronas. Journal of Materials Chemistry A, 4 (2016), 14334-14341 DOI: 10.1039/C6TA06438H. Reproduced by permission of The Royal Society of Chemistry.

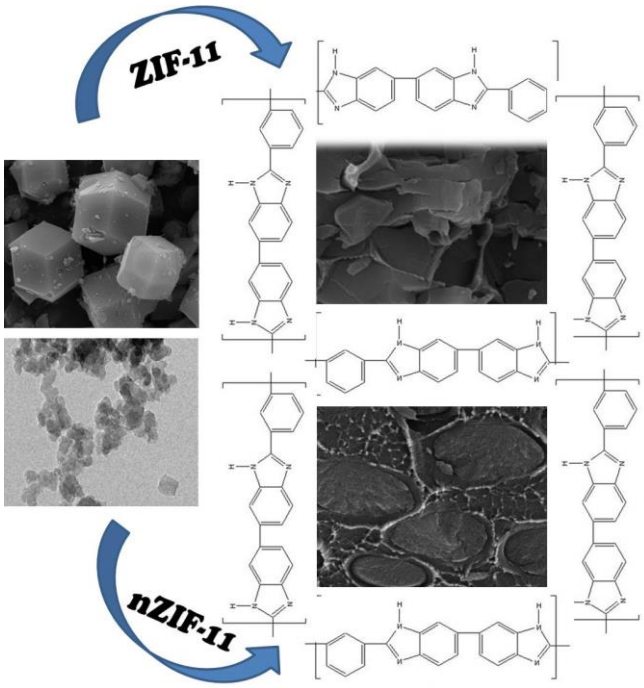

Category:

- Type of membrane: self-supported MMMs
- Gas separation: pre-combustion CO_2 capture

Journal of Materials Chemistry A

PAPER

View Article Online
View Journal | View Issue

Cite this: J. Mater. Chem. A, 2016, 4, 14334

On the chemical filler–polymer interaction of nano- and micro-sized ZIF-11 in PBI mixed matrix membranes and their application for H_2/CO_2 separation†

Javier Sánchez-Laínez, Beatriz Zornoza,* Carlos Téllez and Joaquín Coronas

Received 28th July 2016
Accepted 30th August 2016

DOI: 10.1039/c6ta06438h

www.rsc.org/MaterialsA

The evolution of nano- and micro-sized ZIF-11 (nZIF-11 and ZIF-11, respectively) when embedded into a PBI polymeric matrix is studied. The prepared membranes, with loadings up to 55 wt%, have been characterized through several techniques (XRD, SEM, FTIR, TGA, ^{13}C NMR and XPS) and the changes in the morphology of the fillers upon combination with PBI, as well as in the chemical environment of their main atoms (interactions between the linker of the filler and the benzyl rings of the polymeric bIm units) are discussed. All the membranes have been tested at temperatures ranging between 70 and 200 °C to study their H_2/CO_2 separation performance. The integration of both types of MOF in the polymeric phase improves not only the hydrogen permeability but also the selectivity in comparison with the pure polymer in all cases. H_2 permeability increases due to a better diffusion of the penetrants, while CO_2 adsorption on the MOF and solution in the polymer decreases. The best result obtained corresponds to the membrane with 55 wt% loading of ZIF-11, with 495 Barrer of H_2 permeability and a H_2/CO_2 selectivity of 7.0.

Introduction

Gas separation by membrane technology is more efficient than other separation operations such as distillation and absorption processes in terms of both energy cost and separation selectivity. Due to the limitations in the separation performance of polymeric membranes,[1] several solutions have been proposed. Various polymers have been modified with inorganic fillers such as zeolites or mesoporous silicas to produce mixed matrix membranes (MMMs).[2,3] However, it is the embedding of metal organic framework (MOF) crystals within a polymeric phase and the corresponding gas separation application which has been most extensively studied in recent years.[4–6] Due to the organic linkers present in their structure, MOFs have a better affinity for the polymeric chains than inorganic fillers. The MOF–polymer interface interactions are easier to control in order to avoid non-selective voids between the phases. Furthermore, the selection of the appropriate linkers or the use of post-synthetic functionalization together with the flexibility of MOFs in chemical design and in pore size and shape may facilitate interactions with the polymer and adjust their cavities to a particular application.[7]

Zeolitic imidazolate frameworks (ZIFs) are a subfamily of MOFs in which a metal cation of Zn^{2+} or Co^{2+} is linked to the nitrogen atoms of deprotonated imidazole molecules forming tetrahedral frameworks in zeolite-like topologies.[8] ZIFs constitute highly porous frameworks with extraordinary thermal and chemical stabilities. A striking feature of these materials is that the structure adopted by a given ZIF is determined by link–link interactions rather than by the structure directing agents used in zeolite synthesis.[9] ZIF-11 is especially promising for gas separation owing to its small pore dimensions and to the fact that it can be obtained following several synthesis routes such as solvothermal[10] and non-solvothermal[11] synthesis, sonocrystallization[12] and centrifugal acceleration.[13] It forms a *rho* type zeolitic structure where Zn^{2+} is the metal ion and benzimidazole (bIm) the organic linker.[14] Its well-defined porous structure with large cavities of 1.46 nm connected through pore apertures of 0.3 nm, similar to the kinetic diameter of H_2 (0.29 nm), makes it ideal for hydrogen separation over larger molecules by the sieving process.[10] A H_2/CO_2 selectivity of 262 with a H_2 permeability of 5830 Barrer of ZIF-11 at room temperature has been estimated by molecular simulation, and it is considered a perfect candidate for pre-combustion capture[15] among the different MOFs studied in the literature for CO_2 capture and separation.[16]

Nevertheless, despite all its advantageous properties for gas separation, the micrometric size of ZIF-11 hinders its integration within a polymeric phase when the objective is the formation of thin MMMs. For this reason a nano-sized ZIF-11

Chemical and Environmental Engineering Department, Instituto de Nanociencia de Aragón (INA), Universidad de Zaragoza, 50018 Zaragoza, Spain. E-mail: bzornoza@unizar.es

† Electronic supplementary information (ESI) available: TGA and derivative of the different membranes prepared, EDX mapping, stability study in DMAc and intrinsic properties of the fillers. See DOI: 10.1039/c6ta06438h

(nZIF-11) with an average size of 36 ± 6 nm was successfully synthesized in a previous study.[13] The same chemical composition and thermal stability properties and analogous H_2 and CO_2 adsorption properties as those of the conventional microcrystalline ZIF-11 (*i.e.* 1.9 ± 0.9 μm) were observed.

The use of polybenzimidazole (PBI) membranes for the separation of H_2/CO_2 mixtures has been widely reported.[17–22] PBI is a polymer with high thermal stability, good chemical resistance, impressive compression strength and high intrinsic H_2/CO_2 selectivity. However, its major drawbacks are low permeability and brittleness.[23] Several types of MOFs, such as ZIF-7[18], ZIF-8[24–26]and ZIF-90[27], have been embedded in the PBI continuous phase. MMMs comprising micro-sized ZIF-11 in PBI have hitherto been reported only once, but containing loadings up to 40 wt% and tested at room temperature only.[19] The present work additionally examines membranes containing nano-sized ZIF-11, the use of higher loadings for micro-sized ZIF-11 (up to 55 wt%) and testing at higher temperatures (up to 200 °C). This is of paramount importance for obtaining the best of this high performance polymer. However, ZIF-11 has already shown some lack of chemical stability when exposed to certain experimental conditions.[10] For this reason, it is necessary to explore the evolution of this ZIF in the polymeric matrix in order to ensure that its full properties, suitable for hydrogen separation, are maintained.

In this work nano-sized ZIF-11 (nZIF-11) and micro-sized ZIF-11 have been integrated in a commercial PBI continuous phase in the form of MMMs. The evolution in the morphology of both fillers has been observed by SEM, while changes in chemical bonds at the filler–polymer interphase have been studied by FTIR, NMR and XPS characterization. Furthermore, the crystallinity of the filler inside the polymeric matrix has been checked by XRD analysis. These MMMs, tested at temperatures from 70 to 200 °C, were evaluated for their performance in the separation of H_2/CO_2 mixtures.

Experimental

Chemicals

Zinc acetate dihydrate ($Zn(CH_3COO)_2 \cdot 2H_2O$), benzimidazole (bIm, $C_7H_6N_2$, 98%), ammonium hydroxide (NH_3, 28–30% aqueous solution), toluene (≥99.5%), and *N*,*N*-dimethylacetamide (DMAc, ≥99.5%) were purchased from Sigma Aldrich. Methanol (HPLC grade) was purchased from Scharlau. Commercial PBI solution comprising 26 wt% PBI with 1.5 wt% LiCl as stabilizer in DMAc solvent was purchased from PBI Performance Products.

MOFs synthesis

The synthesis method of nZIF-11 follows the same procedure used in our previous work.[13] 0.24 g of bIm (2 mmol) was dissolved in 6.4 g of methanol (400 mmol), together with 9.2 g of toluene (100 mmol) and 2.4 g of ammonium hydroxide (40 mmol). 0.22 g of zinc acetate dihydrate (1 mmol) was dissolved in 3.2 g of methanol (200 mmol). Both solutions were cooled separately to 18 °C and then mixed in a centrifuge flask of 50 mL. The synthesis reaction took place during centrifugation at 10 000 rpm for 5 min at that temperature. This procedure prevents the production of large ZIF-11 particles. The solid collected was washed with methanol and centrifuged at 10 000 rpm three times for the complete removal of toluene and dried at 100 °C overnight. The molar composition of the mixture was Zn : bIm : NH_3 : CH_3OH : toluene = 1 : 2 : 40 : 300 : 100.[11] For the micro-sized ZIF-11 synthesis, the same reactant amounts and steps as in the previous procedure were applied. However, instead of centrifuging, the mixture was stirred for 15 min at room temperature before collecting the solid by centrifugation at 10 000 rpm and washing it.

MMM preparation

The required amount of ZIF-11 and nZIF-11 was weighed for each membrane loading, from 10 to 55 wt%, and the corresponding amount of PBI solution was added (previously diluted in DMAc to 15 wt% concentration to avoid problems deriving from viscosity). The resulting solution was further stirred overnight. The casting solution was three times stirred and sonicated alternately for 90 min total time and cast into a Petri dish leveled inside an oven at 90 °C. The Petri dishes were left uncovered overnight to allow the evaporation of the solvent. After that, the membranes were peeled off from the Petri dishes and washed for 8 h in MeOH. Finally, the membranes were treated in a vacuum oven at 130 °C and 10 mbar for 24 h for complete removal of the remaining solvent.

When using nZIF-11 as filler for MMM fabrication, the material was kept in a wet state to minimize agglomeration, *i.e.* the methanol-collected ZIF-11 nanoparticles were further washed with DMAc. After the second centrifugation, the particles were re-suspended in DMAc prior to use. The suspension concentration was calculated for each membrane loading, 10, 16 and 32 wt%, and the corresponding amount of PBI 15 wt% solution was added. The same procedure was previously used to fabricate MMMs with nZIF-11 and Matrimid®.[13] The membrane thicknesses were tested by a Digimatic Micrometer (measurement range from 0 to 30 mm with an accuracy of ±1 μm). Several equally distributed points (9) on each membrane were measured and the arithmetic mean was taken as the membrane thickness. The MMMs obtained in this work had a thickness of 119 ± 12 μm. For permeation testing of the membranes, circular areas of 15.2 cm^2 were cut from the films.

Characterization of samples

Powder X-ray diffraction (XRD) spectra of the MOFs and MMMs were acquired using a D-Max Rigaku X-ray diffractometer with a copper anode and a graphite monochromator to select CuKα radiation (λ = 1.540 Å), taking data from $2\theta = 2.5°$ to 40° at a scan rate of $0.03° \ s^{-1}$. Thermogravimetric analyses (TGA) were carried out using a Mettler Toledo TGA/STDA 851e. Samples (10 mg) placed in 70 μL alumina pans were heated in air flow from 25 to 900 °C at a heating rate of 10 °C min^{-1}. Scanning electron microscopy (SEM) images of the MOFs and membranes were obtained using an Inspect F50 model scanning electron microscope (FEI), operated at 20 kV. Cross-sections of

membranes were prepared by freeze-fracturing after immersion in liquid nitrogen and subsequent coating with Pt. Fourier transform infrared spectroscopy (FTIR) was performed on a Bruker Vertex 70 FTIR spectrometer equipped with a DTGS detector and a Golden Gate diamond ATR accessory. Powder samples were prepared by the KBr wafer technique and the measurements were done in a diffuse reflectance module. Both spectra were recorded by averaging 40 scans in the 4000–600 cm^{-1} wavenumber range at a resolution of 4 cm^{-1}. NMR spectra were recorded in a Bruker Avance III WB400 spectrometer with 4 mm zirconia rotors spun at the magic angle in N_2 at 10 kHz. ^1H–^{13}C CP spectra were measured using a ^1H $\pi/2$ pulse length of 3.0 μs, with a contact time (ramp) of 3 ms, a spinal 64 proton decoupling sequence of 5.3 μs pulse length, and a recycle delay of 5 s. 3000 scans were acquired for each spectrum. The chemical shifts were reported relative to TMS. XPS measurements were performed with an Ultra DLD (Kratos Tech.) with Al K_α emission (1486.6 eV) operated at 15 kV and 10 mA for the X-ray source. The samples were previously cleaned with an Ar^+ ion beam, working at 15 kV and 20 mA. The spectra of C 1s and N 1s were recorded and analyzed with Casa XPS software by curve fitting into two or three peaks. All binding energies were corrected for charging of the samples by calibration of the C 1s peak at 284.9 eV. The cross-section of the membranes was also prepared by freeze-fracturing in liquid nitrogen.

Gas separation analysis

Mixed gas analyses were performed for neat PBI membranes and PBI based MMMs with ZIF-11 and nZIF-11. The membranes were placed in a module consisting of two stainless steel pieces and a 316LSS macroporous disk support (from Mott Co.) with a 20 μm nominal pore size, and gripped inside with Viton O-rings. The permeation module was placed in a UNE 200 Memmert oven to control the temperature of the experiments. Gas separation measurements were carried out by feeding a H_2/CO_2 equimolar mixture (90/90 cm^3 (STP) min^{-1}) at 330 kPa to the feed side by means of two mass-flow controllers (Alicat Scientific, MC-100CCM-D), while the permeate side of the membrane was swept with a 2 cm^3 (STP) per min mass-flow controller stream of Ar at 124 kPa (Alicat Scientific, MC-5CCM-D). Concentrations of H_2 and CO_2 in the outgoing streams were analyzed by an Agilent 3000A online gas microchromatograph equipped with a thermal conductivity detector. Permeability was calculated in Barrer (10^{-10} cm^3 (STP) cm (cm^2 s cmHg)$^{-1}$) once the steady-state of the exit stream was reached (for at least 3 h), and the separation selectivity was calculated as the ratio of permeabilities.

Results and discussion

Membrane characterization

Micro- and nano-sized ZIF-11 particles were successfully embedded in the PBI polymeric phase. Fig. 1 shows the cross-sections of the membranes comprising nominal loadings of 10, 16 and 32 wt% of nZIF-11 (actual loadings tested by TGA being 11.0, 15.0 and 30.9 wt%, respectively, as inferred from Fig. S1†),

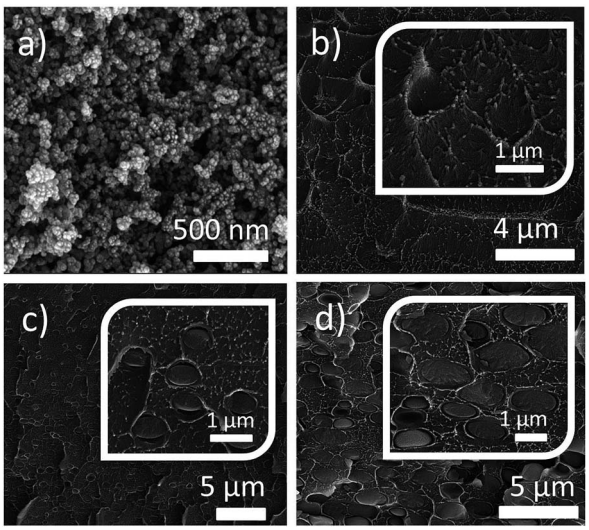

Fig. 1 SEM images of (a) nZIF-11, and PBI MMMs prepared with nZIF-11 as filler at several loadings: (b) 10 wt%, (c) 16 wt%, and (d) 32 wt%.

while those containing 10, 16, 32, 45 and 55 wt% micro-sized ZIF-11 can be seen in Fig. 2 (12.2, 17.0, 31.5, 42.3 and 55.6 wt%, respectively, as inferred from Fig. S2†). Note that MMMs with higher loadings than 32 wt% were also prepared with nZIF-11 but were broken during handling due to their excessive brittleness. As expected, SEM images revealed a homogeneous dispersion and excellent adhesion of the filler particles within the polymeric phase. However, changes in the morphology of both types of fillers are evident. It can be observed how micro-sized ZIF-11 (Fig. 2a) lost its rhombic dodecahedron form of *ca.*

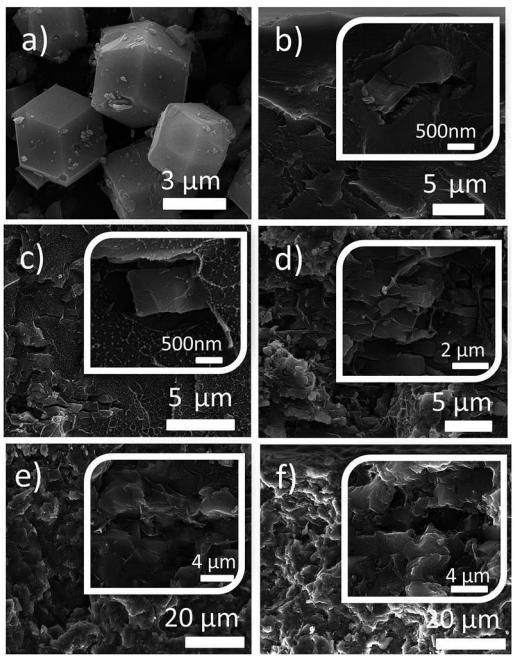

Fig. 2 SEM images of (a) ZIF-11, and PBI MMMs prepared with ZIF-11 as filler at several loadings: (b) 10 wt%, (c) 16 wt%, (d) 32 wt%, (e) 45 wt% and (f) 55 wt%.

2.5 μm in size, becoming particles of around 3–4 μm length and 600–800 nm width, thus changing their aspect ratio from 1 to 5. In the case of nZIF-11 (Fig. 1a), the morphology changes are more acute. When embedded in the PBI polymeric phase, this material transformed and grew into lentil-shaped particles whose final size was dependent on the membrane loading from unappreciable particles revealed by EDX analysis (Fig. S3a†), *ca.* 36 nm in size, which cannot be distinguished from the polymer nodules belonging to the PBI matrix at 10 wt% loading (Fig. 1b) to more than 1 μm at 32 wt% loading (Fig. 1d). Fig. S3b† shows the EDX-mapping image of the cross-section of the intermediate loading membrane (16 wt%) where the corresponding amount of Zn coming from the MOF can be appreciated. These changes in morphology were probably due to the interaction of the filler with the benzimidazole groups of the polymer, since this behavior was not observed when the material was dispersed in DMAc and dried under the same conditions of the membrane casting (see Fig. S4 and S5†). Neither this changes in morphology have been observed when the material was embedded in Matrimid® polyimide,[13] nor when it was ZIF-8 the one embedded in PBI, despite having the same casting conditions.[28] The morphological changes were more significant in the case of the nZIF-11 because of its nano-sized character, and the above mentioned lentil-shape particles appeared of considerably larger size than the initial particles. The evolution of ZIF-8 particles through an Ostwald ripening process has also been reported during the MMM preparation stages.[29]

FTIR spectra of the prepared MMMs and ZIF-11 powder (analogous to nZIF-11) are shown in Fig. 3. Despite the fact that PBI shows very intense bands in the 1300–740 cm^{-1} range,[30,31] the characteristic signals of this MOF can be distinguished. It can be seen that they become more intense as the filler loading increases. The absorbance peak at 1017 cm^{-1} is assigned to the benzene-ring vibration and the signal at 1287 cm^{-1} is related to the imidazole-ring breathing. The peak at 1222 cm^{-1} is caused by the in-plane C–H deformation of the disubstituted benzimidazole, while the peak at 902 cm^{-1} is due to the C–H out-of-plane bending of single hydrogen in substituted benzene rings.

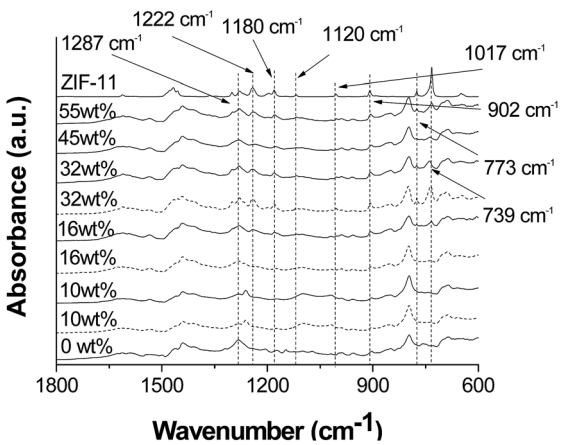

Fig. 3 FTIR spectra of the different PBI MMMs prepared with nZIF-11 (dotted line) and ZIF-11 (continuous line) at loadings up to 55 wt% and spectrum of micro-sized ZIF-11.

Finally, the signals at 1180, 1120 and 773 cm^{-1} are due to the benzimidazole in-plane C–H bending, the N–H in-plane bending and the imidazole in-plane ring bending, respectively.[32]

FTIR can assess the chemical environment in the ZIF-11 fillers but not their crystallinity. Fig. 4 shows the XRD spectra of all the membranes containing nZIF-11 and ZIF-11 and the pure PBI film together with the nano- and micro-sized ZIF-11 diffractograms for comparison.

The characteristic peaks of ZIF-11 are only visible at high loadings (over 16 wt% for ZIF-11 and 32 wt% for nZIF-11 MMMs) because at low loadings the amorphous band of the PBI matrix predominates. As expected, the larger the filler loading, the higher the intensity of these peaks, and the full diffractogram of ZIF-11 is visible at the highest filler loading. In any event, it can be observed how the MMM peaks coincide with those of the filler spectrum, and therefore the crystallinity of the filler remains unaltered when embedded in the polymeric matrix, despite all the morphological changes observed by SEM. The presence of narrow porosity of nZIF-11, a less crystalline material, was also confirmed by H_2 and CO_2 high pressure adsorption with uptakes about 50 and 30% lower, for H_2 and CO_2 respectively, than the amounts adsorbed by ZIF-11.[13]

In order to characterize in depth the chemical and structural evolution of both nZIF-11 and ZIF-11 when embedded in PBI polymeric matrix, ^{13}C NMR and XPS analyses were performed

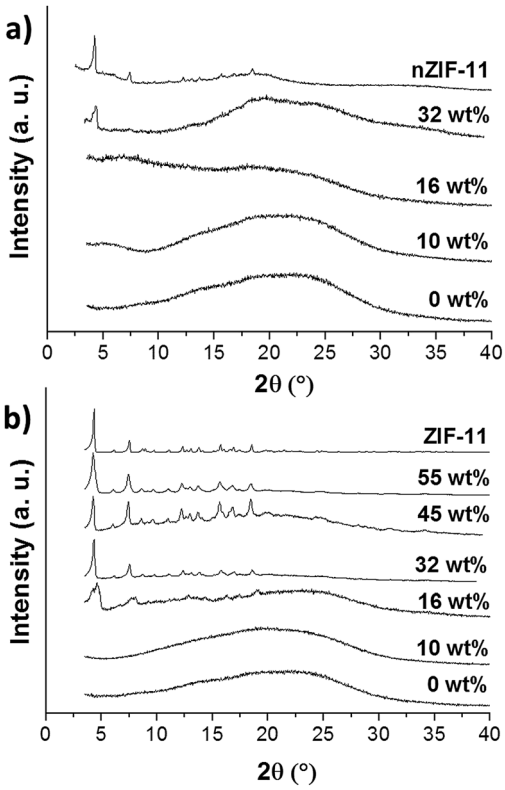

Fig. 4 XRD spectra of the different membranes prepared with nZIF-11 (a) and ZIF-11 (b) at loadings up to 55 wt% and spectrum of nano- and micro-sized ZIF-11.

with bare PBI membrane and MMMs containing both fillers at 32 wt% fixed loading.

MMM ^{13}C NMR spectra, as well as those of nZIF-11 and ZIF-11, can be seen in Fig. 5. Six clear peaks can be distinguished in the bare PBI spectrum. The carbon atom between the amino and the imidazole groups (C_1) resonates at 151.9 ppm, while the signals related to the other carbons (C_2–C_7) of the benzimidazole group resonate at 143.1, 134.6, 119.9 and 110.6 ppm. The signals are relatively broad, suggesting both consistent ^{1}H–^{13}C dipolar couplings and distributions of slightly different chemical environments, due to the packing of the polymer chains.[33] The peak at 129.3 ppm is attributed to aromatic carbons bearing a proton (C_9, C_{10}, and C_{11}). Finally, the signal related to the carbon in the 8 position is located at 134.6 ppm, on the basis of previous liquid NMR studies.[34]

Only four peaks can be distinguished in the spectra of the ZIF-11 and nZIF-11 fillers: at 115.9, 122.5, 141.8 and 150.0 ppm. In the case of the micro-sized ZIF-11, this last peak splits into two signals (151.4 and 148.7 ppm), probably due to differences in the chemical environment arising from the two adjacent benzimidazoles,[35] and from a higher crystallinity (for example, cellulose shows peaks at different ppm values in ordered and disordered structures that could be useful to quantify its crystallinity index[36]). When the MOFs are embedded in the polymeric phase, a slight shift of the peaks to lower ppm values can be appreciated (from 0.4 to 1.4 ppm).

The highest shifts are related to C_4 and C_6, both carbons contained in the benzyl group, substituent in the imidazole molecule, which may prove a π–π interaction between the benzyl rings of the polymeric bIm units and the linker of the ZIFs. In the spectra of both MMMs, the PBI signals at 151.9, 143.1, 119.9 and 110.6 ppm are barely noticeable, while the other two at the central part of the spectrum (134.6 and 129.3 ppm) remain unchanged.

Note that the signal at 150.7 ppm does not split in the case of the nZIF-11 MMM, suggesting that the material has not changed to a more crystalline phase (ZIF-11) during the membrane formation, which is consistent with the XRD results. Besides, the polymer spectrum dominates over that of the ZIF in this membrane, while it is the filler which dominates in the other MMM containing micro-sized ZIF-11.

The chemical states of nitrogen and carbon in the materials were also characterized by XPS. Recently, an analogous study was carried out by Japip *et al.*, to characterize the surface of ZIF-71/6FDA-Durene MMMs.[37] Fig. 6 shows the N 1s and C 1s core-level spectra of the pure PBI membrane, the MMMs containing nZIF-11 (10 and 32 wt%) and ZIF-11 (32 wt%) and the two ZIF fillers. The deconvolution of N 1s spectra involves two peaks (Fig. 6a), –NH– (binding energy BE 400.5 eV) and –N═ (BE

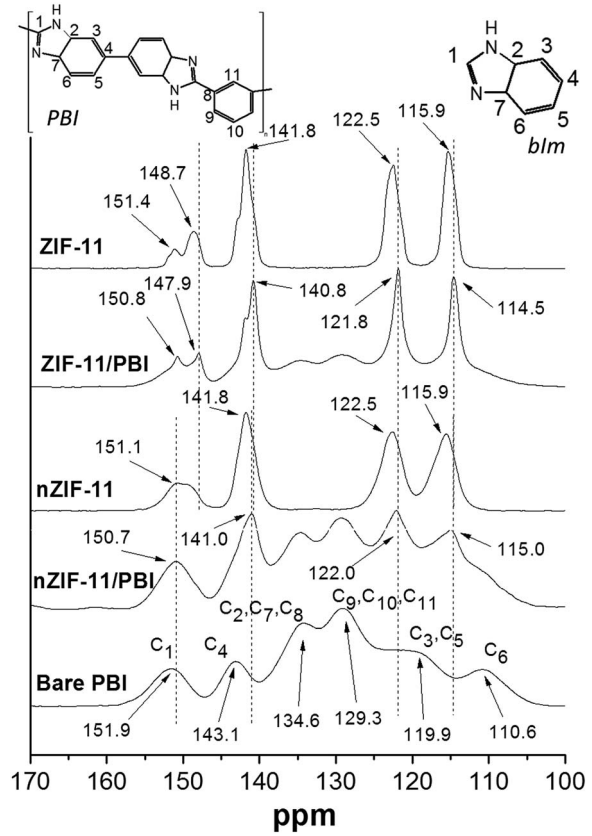

Fig. 5 ^{13}C NMR spectra of bare PBI, 32 wt% loading of nZIF-11 and ZIF-11 PBI MMMs and their corresponding fillers.

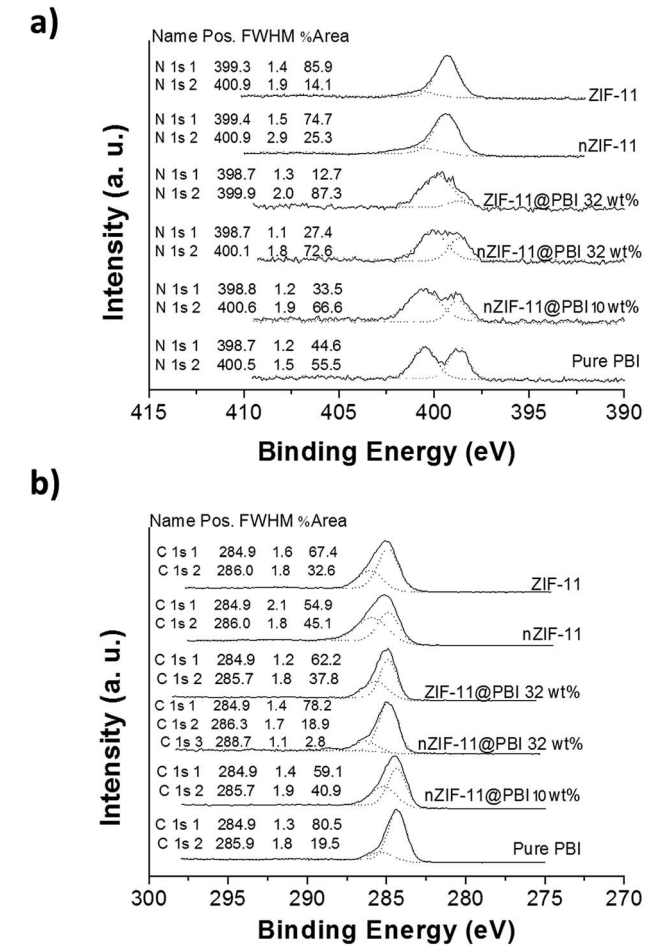

Fig. 6 XPS N 1s (a) and C 1s (b) signals of the cross-section of PBI based MMMs and of the corresponding fillers as powder.

398.7 eV), both of the polybenzimidazole molecule, according to the literature for secondary and tertiary amine, respectively.[38] Common XPS features in the nZIF-11 and ZIF-11 suggest that in both samples the chemical environment of nitrogen is similar.

However, the peak area ratio of these signals is slightly different. While micro-sized ZIF-11 shows an 85/15% ratio, in nZIF-11 this ratio is 75/25%, gaining importance the nitrogen at lower binding energy in the case of ZIF-11 samples, which may be related to its higher degree of crystallinity.[13]

In the case of the membranes' spectra, the pure PBI membrane shows a balanced proportion of both types of nitrogen atom. When embedding both MOFs in the polymeric matrix, this proportion is unbalanced, but unlike the spectra of the powder samples, it is the nitrogen at the higher binding energy which shows a greater peak area ratio. Chemical morphological changes of the filler may be behind this result and might also be indicative of the fact that the MOFs with benzimidazole organic linker are interacting with the PBI polymeric matrix, as appreciated in the NMR spectra. As expected, this imbalance increases with the amount of filler, as can be observed for the nZIF-11 MMMs. For nZIF-11 it can also be appreciated how the proportion between the areas of both types of nitrogen does not reach that of the ZIF-11 MMMs, indicating that the former is not able to crystallize during the membrane formation, as also revealed by NMR. Slight shifts in the signals can be observed for both types of nitrogen when comparing powder with membrane samples suggesting a different chemical environment.

The C 1s spectra for PBI (Fig. 6b) show two different signals, C–C (BE 284.9 eV) and C–N (BE 285.9 eV), in accordance with the literature.[39] Note that in the case of PBI containing 32 wt% of nZIF-11 an extra signal appears, referring to the single N=C–N bond of the benzimidazole structure. This group contributes to only 2.8% of all types of C-containing moieties and therefore it could not have been detected in the other samples, as also occurred with the 8 wt% nZIF-11 MMM. Unlike the N 1s spectra, the proportion in the area of both peaks is quite uneven for the pure polymer sample but becomes more balanced for the fillers, especially for the nZIF-11 sample. Differences between the proportions in both MOFs may again be related to differences in their crystallinity. Besides, the filler loading does not have such a big influence as in the case of N 1s spectra. In the C 1s spectra only the signal of the most energetic carbon slightly shifts, following the same tendency as in the N 1s spectra.

To sum up, the chemical environment provided by the monomeric units of PBI (bIm) is responsible for the changes in the morphology of both nZIF-11 and ZIF-11. There is no clear evidence that new bonds between filler and polymer are created, but there is a clear chemical interaction between both phases. This may be a π–π interaction between the benzyl rings of the polymeric bIm units and the linker of the ZIFs according to NMR results (also verified by XPS analysis). A similar behavior has been previously reported with ZIF-7[40] (same chemical composition as ZIF-11 but with a *sod* structure). This material also changes its form when it gets in contact with DMF at high temperature or with water for a long time, although in this case, the changes also entail a phase transformation.

Permeation performance

Pure PBI membranes and MMMs containing nZIF-11 and ZIF-11 with nominal loadings of 10, 16 and 32 wt% were prepared and tested for comparison. Moreover, micro-sized ZIF-11 membranes were further loaded up to 55 wt%.

Fig. 7a shows the H_2/CO_2 gas separation performance for a 50/50 mixture tested at 150 °C and 2 bar of driving force. At least 3 MMMs of each loading were fabricated and measured to provide error estimations. The integration of both MOFs in the PBI matrix enhanced the hydrogen permeability, achieving a higher H_2/CO_2 selectivity in comparison with the pure polymer in all cases.

MMMs fabricated with micro-crystalline ZIF-11 showed a similar performance than the analogous nano-sized MOF membranes at the same loading, except for the case of 32 wt% loading where H_2 permeability for the ZIF-11 membrane was about three times higher. As previously reported, nZIF-11 has lower crystallinity than micro-sized ZIF-11, which may lead to poorer separation ability and therefore a worse membrane performance.[13]

However, the more homogeneous distribution of nZIF-11 particles in the PBI phase results in similar performance values to ZIF-11 MMMs at low loadings. Once the membrane loading increases up to 32 wt%, both fillers occupy most of the space of the membrane cross-section leaving enough polymer to cover the particles efficiently. At this point, when both types of MOF

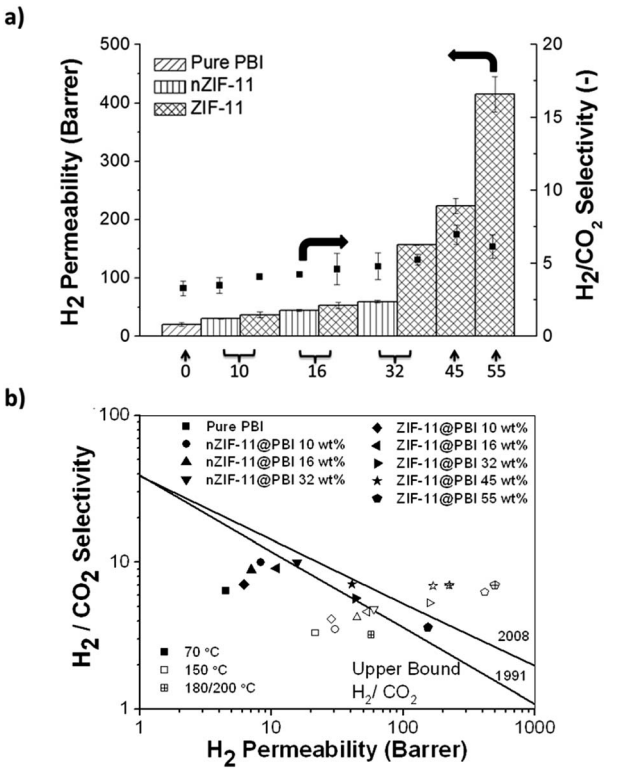

Fig. 7 H_2/CO_2 gas separation performance of PBI MMMs containing nZIF-11 and ZIF-11: (a) at 150 °C, and (b) as a function of the temperature (70 °C filled, 150 °C empty and 180/200 °C crossed). Robeson's upper bounds[1] are plotted for comparison.

are equally dispersed, crystallinity and microporosity start playing a more important role in the separation performance, leading to an enhancement of H_2 permeability for ZIF-11 MMMs. Loadings of 45 and 55 wt% produced membranes with a very little amount of polymer among the particles whose morphology and particle size were modified during the casting procedure (see SEM images in Fig. 2e and f). The gas separation is dominated by the MOF features providing the best membrane performances.

In addition to the previous testing at 150 °C, MMMs at 45 and 55 wt% loadings of ZIF-11 were also tested at 180–200 °C so as to improve the membrane performance, and at 70 °C to complete the study of the temperature influence. All the membranes tested at different temperatures are plotted in Fig. 7b. Note that PBI has an extraordinarily high thermal stability (Fig. S1 and S2†) with a glass transition temperature of about 426 °C.[41] Raising the temperature has a beneficial effect on the separation performance, surpassing the Robeson upper bound[1] beyond 32 wt% ZIF-11 loading. The permeability increased at higher temperatures because of the better diffusion of the penetrants while CO_2 adsorption on the MOF and solution in the polymer decreased.

Almost all the membranes show the highest selectivities at the lowest temperature (70 °C). This tendency has already been reported for PBI MMMs containing ZIF-7 and is due to the balance between the diffusivity selectivity and solubility selectivity for the H_2/CO_2 mixture.[18] At low temperatures the solubility selectivity increases while the diffusivity selectivity decreases. The augmentation of S_{H_2}/S_{CO_2} exceeds the reduction of D_{H_2}/D_{CO_2} and therefore the selectivity becomes higher.

All the membranes showed permeabilities at least four times higher at 150 °C than at 70 °C. The best result obtained with 55 wt% loading of ZIF-11 corresponds to 495 Barrer of H_2 with a H_2/CO_2 selectivity of 7.0, tested at 180 °C. These results are also in good agreement with the single published paper reporting MMMs with micro-sized ZIF-11 and PBI.[19] In this case the membranes were only tested at 35 °C and permeability improved when increasing the loading (17.2 Barrer of H_2 for pure polymer membrane to 67.8 Barrer for 16.1 wt% loading and 133.1 Barrer for 29.7 wt%). However, the selectivity barely improved or even decreased over the pure polymer (5.0 for pure PBI, 5.6 for 16.1 wt% loading and 3.7 for 29.7 wt%).

Additionally, in order to estimate the intrinsic properties of the fillers, the Maxwell–Wagner–Sillar equation[42] was applied using the performance results at 150 °C (see Tables S1 and S2†). nZIF-11 showed an average H_2 permeability of 4498 Barrer and a H_2/CO_2 selectivity of 64; while ZIF-11, of 9078 Barrer and 104, respectively.

Conclusions

MMMs based on PBI containing nano- and micro-sized ZIF-11 (nZIF-11 and ZIF-11, respectively) as fillers have been successfully prepared at loadings up to 55 wt%. A chemical morphology transformation for both materials was evident when embedded in the polymeric phase, but were especially acute in the case of the nZIF-11 because of its nano-sized character. While the ZIF-11 lost its rhombic dodecahedron form becoming particles with higher aspect ratio, those of the nZIF-11 grew and their final size was dependent on the membrane loading. These changes were attributed to the interaction of the filler with the benzimidazole groups of the polymer since this behavior was not observed when the material was dispersed in DMAc and dried under the same conditions of the membrane casting. Despite all these chemical morphological changes, the crystallinity of the fillers remained unaltered according to XRD analysis. Furthermore, π–π interactions between the fillers and the polymer were depicted by NMR analysis, while XPS spectra showed changes in the state of the N and C bonds in the fillers and membranes, verifying the NMR results.

The integration of both MOFs into the PBI polymer phase enhanced in all cases both the H_2 permeability and the selectivity in comparison with the pure polymer in the separation of H_2/CO_2 at 70–200 °C. Besides, MMMs fabricated with microcrystalline ZIF-11 showed a similar performance to the analogous nano-sized MOF membranes at low loadings (up to 16 wt%). As expected, the permeability increased at higher temperatures due to a better diffusion of the penetrants, while CO_2 adsorption on the MOF and solution in the polymer decreased. The best result of this work corresponded to 495 Barrer of H_2 with a H_2/CO_2 selectivity of 7.0 for the PBI MMM containing 55 wt% of ZIF-11.

Acknowledgements

The research leading to these results has received funding from the European Union Seventh Framework Programme (FP7/2007–2013) under grant agreement no. 608490, project M4CO2. In addition, financial support from the Spanish MINECO (MAT2013-40556-R), the Aragón Government and the ESF is gratefully acknowledged. All the microscopy work was done in the Laboratorio de Microscopías Avanzadas at the Instituto de Nanociencia de Aragón (LMA-INA). We thank Dr Guillermo Antorrena for our fruitful discussions on XPS. Finally, the authors would like to acknowledge the use of Servicio General de Apoyo a la Investigación-SAI, Universidad de Zaragoza.

Notes and references

1 L. M. Robeson, *J. Membr. Sci.*, 2008, **320**, 390–400.
2 B. Zornoza, S. Irusta, C. Téllez and J. Coronas, *Langmuir*, 2009, **25**, 5903–5909.
3 R. Mahajan, R. Burns, M. Schaeffer and W. J. Koros, *J. Appl. Polym. Sci.*, 2002, **86**, 881–890.
4 H. B. T. Jeazet, C. Staudt and C. Janiak, *Dalton Trans.*, 2012, **41**, 14003–14027.
5 T. Rodenas, M. van Dalen, E. García-Pérez, P. Serra-Crespo, B. Zornoza, F. Kapteijn and J. Gascon, *Adv. Funct. Mater.*, 2014, **24**, 249–256.
6 A. Sabetghadam, B. Seoane, D. Keskin, N. Duim, T. Rodenas, S. Shahid, S. Sorribas, C. L. Guillouzer, G. Clet and C. Tellez, *Adv. Funct. Mater.*, 2016, **26**, 3154–3163.
7 B. Zornoza, C. Tellez, J. Coronas, J. Gascon and F. Kapteijn, *Microporous Mesoporous Mater.*, 2013, **166**, 67–78.

8 Y. Lee, J. Kim and W. Ahn, *Korean J. Chem. Eng.*, 2013, **30**, 1667–1680.
9 H. Hayashi, A. P. Cote, H. Furukawa, M. O'Keeffe and O. M. Yaghi, *Nat. Mater.*, 2007, **6**, 501–506.
10 K. S. Park, Z. N. Ni, A. P. Côte, J. Y. Choi, R. Huang, F. J. Uribe-Romo, H. K. Chae, M. O'Keeffe and O. M. Yaghi, *Proc. Natl. Acad. Sci. U. S. A.*, 2006, **103**, 10186–10191.
11 M. He, J. Yao, Q. Liu, Z. Zhongb and H. Wang, *Dalton Trans.*, 2013, **42**, 16608–16613.
12 B. Seoane, J. M. Zamaro, C. Tellez and J. Coronas, *CrystEngComm*, 2012, **14**, 3103–3107.
13 J. Sánchez-Laínez, B. Zornoza, Á. Mayoral, Á. Berenguer-Murcia, D. Cazorla-Amorós, C. Téllez and J. Coronas, *J. Mater. Chem. A*, 2015, **3**, 6549–6556.
14 J. C. Tan, T. D. Bennett and A. K. Cheetham, *Proc. Natl. Acad. Sci. U. S. A.*, 2010, **107**, 9938–9943.
15 A. W. Thornton, D. Dubbeldam, M. S. Liu, B. P. Ladewig, A. J. Hilla and M. R. Hill, *Energy Environ. Sci.*, 2012, **5**, 7637–7646.
16 Z. Zhang, Z. Yao, S. Xiang and B. Chen, *Energy Environ. Sci.*, 2014, **7**, 2868–2899.
17 S. Choi, J. Coronas, E. Jordan, W. Oh, S. Nair, F. Onorato, D. F. Shantz and M. Tsapatsis, *Angew. Chem., Int. Ed.*, 2008, **47**, 552–555.
18 T. Yang, Y. Xiao and T. S. Chung, *Energy Environ. Sci.*, 2011, **4**, 4171–4180.
19 L. Li, Y. Jianfeng, X. Wang, Y. Chen and H. Wang, *J. Appl. Polym. Sci.*, 2014, **131**, 41056.
20 X. Li, R. P. Singh, K. W. Dudeck, K. A. Berchtold and B. C. Benicewicz, *J. Membr. Sci.*, 2014, **461**, 59–68.
21 S. Kumbharkar, Y. Liu and K. Li, *J. Membr. Sci.*, 2011, **375**, 231–240.
22 B. P. Biswal, A. Bhaskar, R. Banerjee and U. K. Kharul, *Nanoscale*, 2015, **7**, 7291–7298.
23 T. S. Chung, *J. Macromol. Sci., Rev. Macromol. Chem. Phys.*, 1997, **37**, 277–301.
24 T. Yang, G. M. Shi and T. S. Chung, *Adv. Energy Mater.*, 2012, **2**, 1358–1367.
25 T. Yang and T. S. Chung, *Int. J. Hydrogen Energy*, 2013, **38**, 229–239.
26 A. Bhaskar, R. Banerjee and U. Kharul, *J. Mater. Chem. A*, 2014, **2**, 12962–12967.
27 T. Yang and T. S. Chung, *J. Mater. Chem. A*, 2013, **1**, 6081–6090.
28 J. Sanchez-Lainez, B. Zornoza, S. Friebe, J. Caro, S. Cao, A. Sabetghadam, B. Seoane, J. Gascon, F. Kapteijn, C. Guillouzer, G. Clet, M. Daturi, C. Tellez and J. Coronas, *J. Membr. Sci.*, 2016, **515**, 45–53.
29 J. A. Thompson, K. W. Chapman, W. J. Koros, C. W. Jones and S. Nair, *Microporous Mesoporous Mater.*, 2012, **158**, 292–299.
30 P. Musto, F. Karasz and W. MacKnight, *Polymer*, 1993, **34**, 2934–2945.
31 P. Christensen and S. Jones, *Polym. Degrad. Stab.*, 2014, **105**, 211–217.
32 D. P. Drolet, D. M. Manuta, A. J. Lees, A. Katnani and G. J. Coyle, *Inorg. Chim. Acta*, 1988, **146**, 173–180.
33 A. S. Cattaneo, D. C. Villa, S. Angioni, C. Ferrara, E. Quartarone and P. Mustarelli, *J. Phys. Chem. C*, 2015, **119**, 18935–18944.
34 J. Grobelny, D. M. Rice, F. E. Karasz and W. J. MacKnight, *Macromolecules*, 1990, **23**, 2139–2144.
35 S. Zhu, L. Yan, D. Zhang and Q. Feng, *Polymer*, 2011, **52**, 881–892.
36 S. Park, J. O. Baker, M. E. Himmel, P. A. Parilla and D. K. Johnson, *Biotechnol. Biofuels*, 2010, **3**, 1.
37 S. Japip, K. Liao, Y. Xiao and T. S. Chung, *J. Membr. Sci.*, 2016, **497**, 248–258.
38 D. W. Mangindaan, N. M. Woon, G. M. Shi and T. S. Chung, *Chem. Eng. Sci.*, 2015, **122**, 14–23.
39 D. Mangindaan, W. Kuo, C. Chang, S. Wang, H. Liu and M. Wang, *Surf. Coat. Technol.*, 2011, **206**, 1299–1306.
40 P. Zhao, G. I. Lampronti, G. O. Lloyd, M. T. Wharmby, S. Facq, A. K. Cheetham and S. A. Redfern, *Chem. Mater.*, 2014, **26**, 1767–1769.
41 S. S. Hosseini and T. S. Chung, *J. Membr. Sci.*, 2009, **328**, 174–185.
42 R. Bouma, A. Checchetti, G. Chidichimo and E. Drioli, *J. Membr. Sci.*, 1997, **128**, 141–149.

Supporting Information

1. TGA analysis:

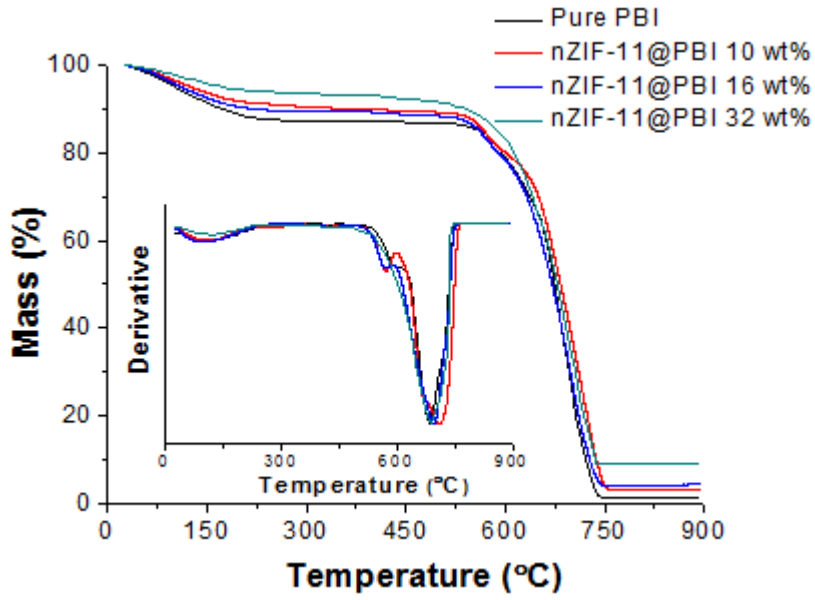

Figure S1. TGA and derivative curves (inset) of the PBI MMMs prepared with nZIF-11 at several loadings.

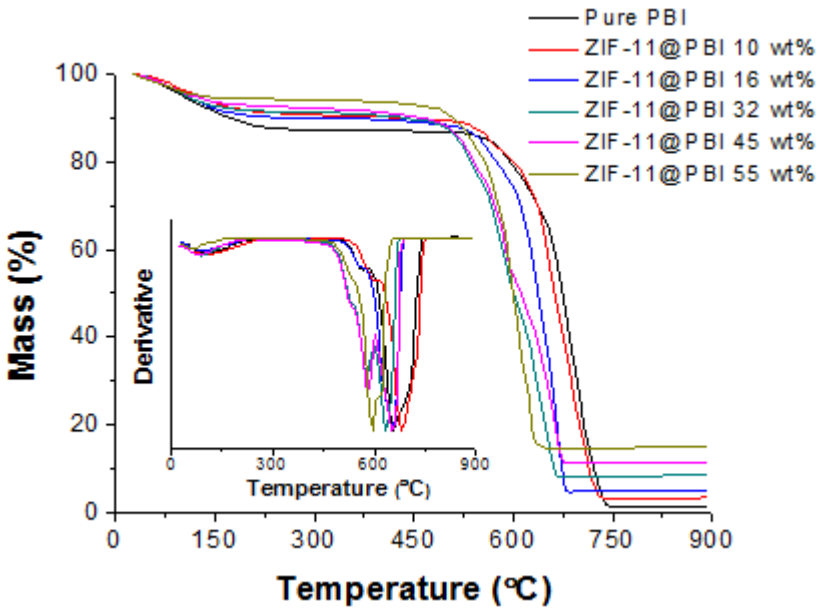

Figure S2. TGA and derivative curves (inset) of the PBI MMMs prepared with ZIF-11 at several loadings.

2. EDX mapping:

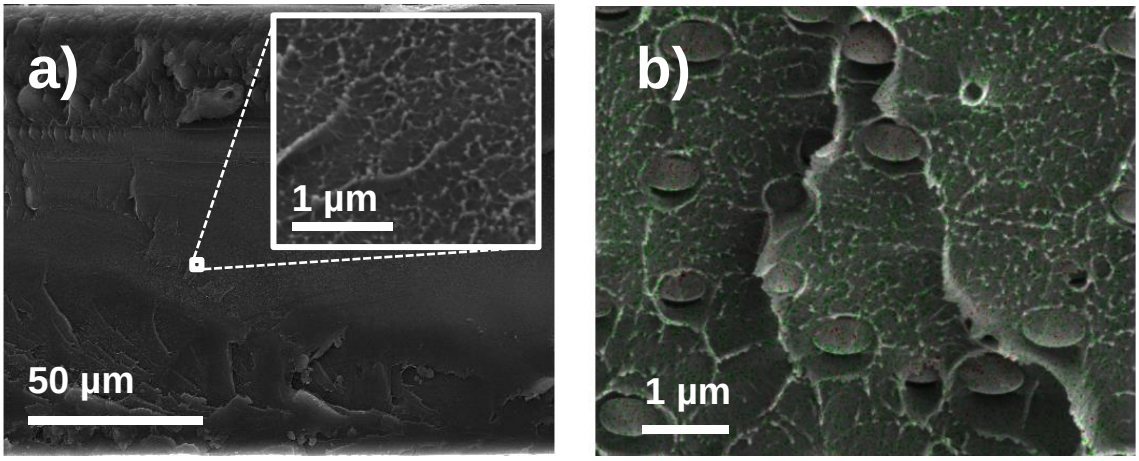

EDX (weight %)	C	O	Zn
10 wt% nZIF-11 PBI MMM	84.3	13.0	2.7
16 wt% nZIF-11 PBI MMM	84.2	11.3	4.5

Figure S3. SEM-EDX of the cross-section of a nZIF-11/PBI MMMs at 10 wt% loading (a) and 16 wt% loading (b). EDX-mapping for 16 wt% nZIF-11/PBi MMM is plotted where can be distinguished C (in green) and Zn (in red). Weight % calculated from the whole section in (a) and (b) are included in the table.

3. Stability in DMAc:

In order to know if the morphology changes of both fillers inside the membranes were due to the effect of the solvent at the hard casting conditions, the following experiment was performed. 2 g of ZIF-11 and nZIF-11 were separately dispersed in 2 g of DMAc and the resulting suspension was stirred overnight. The dispersions were three times stirred and sonicated alternately for 90 min total time and cast into a petri dish leveled inside an oven at 90 ^{0}C. The petri dishes were left uncovered overnight to allow the evaporation of the solvent. Finally, the resulting powder was characterized by SEM (Fig. S4) and XRD (Fig. S5) analyses.

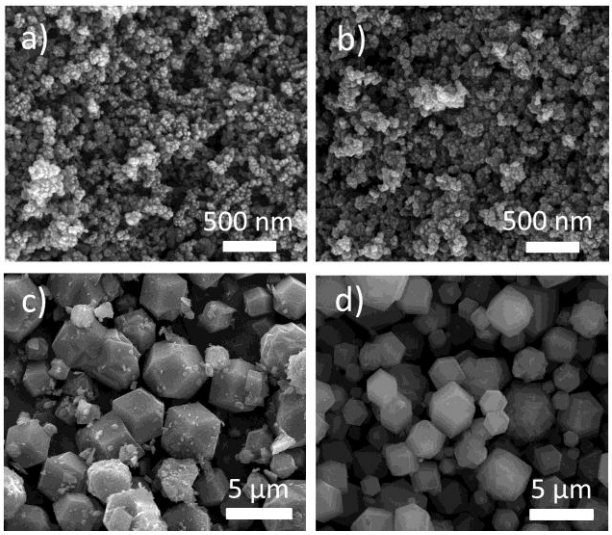

Figure S4. SEM images of nZIF-11 before (a) and after (b) being treated in DMAc and ZIF-11 before (c) and after (d) being treated in the same solvent.

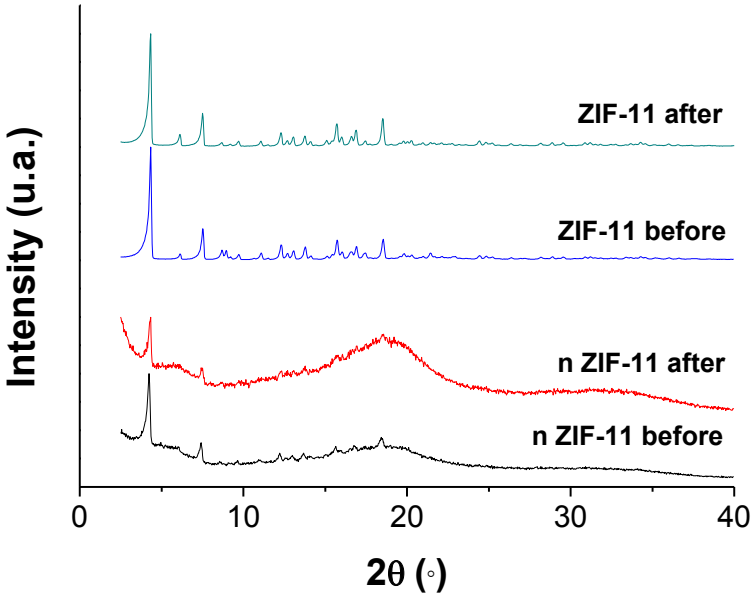

Figure S5. XRD spectra of nZIF-11 before (a) and after (b) being treated in DMAc and ZIF-11 before (c) and after (d) being treated in the same solvent.

As Fig. S4 shows, the morphology of the crystals remain unchanged after having been treated in DMAc. The same happens with their crystallinity, which can be seen from the XRD spectra on Fig S5. Therefore, the morphological changes previously observed in the MMMs images were probably due to the interaction of the filler with the benzimidazole groups of the polymer, which is the same molecule as the organic linker of the ZIFs.

4. Intrinsic properties of the fillers:

Table S1. Calculated intrinsic properties of nZIF-11 at different membrane loadings together with the average values.

nZIF-11 loading	n value	H_2 permeability (Barrer)	CO_2 permeability (Barrer)	H_2/CO_2 Selectivity (-)
10 wt%	-	-	-	-
16 wt%	0.20	4935	77	64
32 wt%	0.31	4061	64	63
Average	**-**	**4498**	**70**	**64**

Table S2. Calculated intrinsic properties of nZIF-11 at different membrane loadings together with the average values.

ZIF-11 loading	n value	H_2 permeability (Barrer)	CO_2 permeability (Barrer)	H_2/CO_2 Selectivity (-)
10 wt%	0.29	8459	26	325
16 wt%	0.18	8801	72	122
32 wt%	-	-	-	-
45 wt%	0.13	8601	75	114
55 wt%	0.08	10449	176	59
Average	**-**	**9078**	**87**	**104**

$$P_{eff} = P_c \cdot \frac{n \cdot P_d + (1-n)P_c + (1-n)(P_d - P_c)\cdot \Phi}{n \cdot P_d + (1-n)P_c - n(P_d - P_c)\cdot \Phi} \quad (1)$$

In order to get a deeper understanding of the MMMs permeation results, a permeation model was used to estimate the intrinsic properties of the fillers. The chosen model was the Maxwell-Wagner-Sillar equation (Eq. 1), that can calculate the permeability of a MMM (P_{eff}) for the case of a dilute dispersion of ellipsoids. Where n denotes the shape factor of the filler; P_d and P_c, the permeability of the dispersed and continuous phases, respectively; and φ, the fractional volume of the respective phases.

The performance values of the different MMMs at 150 ^{0}C were used to calculate P_d and P_c. For spherical filler particles, thus n = 1/3, the equation reduces to Maxwell equation, which leads to no logical solution in this case of study, since the permeabilities obtained have negative values. Therefore, a parametrization with different shape factor values was performed. The aim was finding matches in the solutions among the different loadings that could elucidate the intrinsic properties of the ZIFs. All those calculated values can be seen in tables S1 and S2, except for the loadings of 10 wt% and 32 wt% for nZIF-11 and ZIF-11, respectively, which resulted in no logical result for each n value.

As it is shown in table S2, there is a tendency in the n value for ZIF-11 MMMs since it tends to decrease as the membrane loading increases. This result is coherent, because the filler become laminar-shape at high loadings (see Fig. 2). On the other hand, there is not such a big difference for nZIF-11 MMMs (Table S2) because the form of the ellipsoids at 16 and 32 wt% loading is more similar between each other (see Fig. 1) Besides, both the permeabilities and the H_2/CO_2 selectivity of ZIF-11 is higher than those of nZIF-11, which can explaine the better performance result obtained with the membranes containing the former.

Chapter 7: Tuning the separation properties of zeolitic imidazolate framework core–shell structures *via* post-synthetic modification

J. Sánchez-Laínez, A. Veiga, B. Zornoza, S.R. Balestra, S. Hamad, A.R. Ruiz-Salvador, S. Calero, C. Téllez, J. Coronas. Journal of Materials Chemistry A, 5 (2017), 25601-25608. DOI: 10.1039/C7TA08778K. Reproduced by permission of The Royal Society of Chemistry.

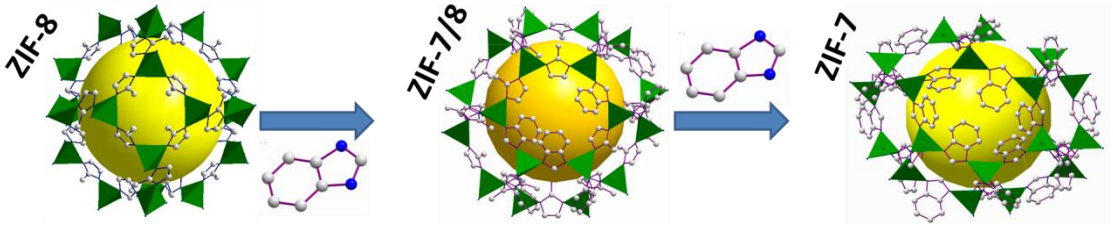

Category:

- Synthesis of new MOFs
- Type of membrane: self-supported MMMs
- Gas separation: pre-combustion CO_2 capture

Journal of Materials Chemistry A

PAPER

View Article Online
View Journal | View Issue

Cite this: J. Mater. Chem. A, 2017, 5, 25601

Tuning the separation properties of zeolitic imidazolate framework core–shell structures *via* post-synthetic modification†

Javier Sánchez-Laínez,[a] Adrián Veiga,[a] Beatriz Zornoza,*[a] Salvador R. G. Balestra,[b] Said Hamad,[b] A. Rabdel Ruiz-Salvador,[b] Sofia Calero,[b] Carlos Téllez[a] and Joaquín Coronas*[a]

Received 5th October 2017
Accepted 20th November 2017

DOI: 10.1039/c7ta08778k

rsc.li/materials-a

The conversion of ZIF-8 into ZIF-7 *via* post-synthetic modification with benzimidazole has been monitored by quantifying the liberated 2-methylimidazole by chromatography. The reaction kinetics have been adjusted to the shrinking core model, providing the diffusion coefficient of bIm inside the pores and the reaction kinetic constant (2.86×10^{-7} cm^2 s^{-1} and 1.36×10^{-4} cm s^{-1}, respectively). A wide variety of ZIF-7/8 hybrid core–shell frameworks have been obtained during this reaction. The most promising have been characterized by SEM/TEM, TGA, N_2 and CO_2 adsorption, FTIR and ^{13}C NMR, showing features of the coexistence of both phases inside the frameworks. Their structures have also been simulated, providing comparable XRD and adsorption results. The hybrid material has been used as a filler for PBI mixed matrix membranes (MMMs) applied to H_2/CO_2 separation, enhancing the performances of the bare PBI polymer and MMMs containing ZIF-8 or ZIF-7 as a filler, with a maximum H_2 permeability value of 1921 Barrer and a H_2/CO_2 selectivity of 11.8.

1 Introduction

Zeolitic Imidazolate Frameworks (ZIFs) are a subfamily of metal–organic frameworks (MOFs), where Zn^{2+} or Co^{2+} cations in tetrahedral coordination are covalently bound to organic linkers based on imidazole groups. In these frameworks, metal–imidazole–metal angles are close to 145°, which is coincident with the Si–O–Si angles typically found in zeolites. ZIFs constitute highly porous frameworks with extraordinarily high thermal and chemical stabilities and they have a great number of potential applications such as gas sorption and separation,[1–3] drug delivery[4] and catalysis.[5,6] Since they were first discovered independently by Yaghi's[7] and Chen's groups,[8] the number and variety of ZIFs has increased in the last few years, with significant use of a huge number of organic linkers.[9] The combination of different linkers inside the same crystalline structure has appeared as a novel route to develop new hybrid materials that can combine the beneficial properties of their original frameworks. Mixtures of linkers have already been reported for the direct solvothermal synthesis of hybrid ZIFs, such as ZIF-7-90,[10,11] ZIF-7-8 [11] and ZIF-9-67.[12] In addition, the series ZIF-68 to ZIF-70,[13] ZIF-78 to ZIF-82 [14] and ZIF-300 to ZIF-302 [15] constitute hybrid ZIFs with a mixture of linkers in their structure. However, some of the challenges of direct synthesis are limited linker solubility, chemical and thermal stability, functional group compatibility and particle size control. These problems may be avoided by employing post-synthetic modification routes. In this manner, materials of high complexity and functionality can be obtained by avoiding MOF destruction during the chemical reaction. This methodology has been successfully applied to a large number of MOFs,[16] including the aldehyde groups in ZIF-90 [17] and SIM-1.[18] Special ZIF/ZIF hybrid structures named core–shell structures can also be obtained as reported for ZIF-8 by Liu *et al.*[19] and Jayachandrababu *et al.*[20]

The pore architecture is a key element for gas separation of the H_2/CO_2 mixture, typically obtained at high pressure and temperature during hydrogen production *via* the steam reforming of methane. Two interesting frameworks for this gas separation are ZIF-8 and ZIF-7, both sharing a **sod** topology, built up of 2-methylimidazole (mIm) and benzimidazole (bIm), respectively. ZIF-8 crystallizes in a cubic symmetry, but the large size of bIm facilitates the crystallization of ZIF-7 in a rhombohedral symmetry, also featuring large ligand rotations. Despite the large size difference of the

[a]Instituto de Nanociencia de Aragon (INA), Chemical Engineering and Environmental Department, Universidad de Zaragoza, C/Mariano Esquillor, s/n., 50018 Zaragoza, Spain. E-mail: bzornoza@unizar.es; coronas@unizar.es

[b]Department of Physical Chemical and Natural Systems, Universidad Pablo de Olavide, Ctra. de Utrera km 1, 41013 Seville, Spain

† Electronic supplementary information (ESI) available: Study of the PSM reaction, reaction modelling, TEM reaction medium, XRD ZIF-7/8 core–shells (empirical and simulated), ZIF characterization (SEM-EDX, TEM, particle size distribution, TGA, N_2 and CO_2 adsorption, heat of adsorption of CO_2 and H_2, FTIR, and NMR), MMM characterization (SEM and XRD) and membrane performance (values). See DOI: 10.1039/c7ta08778k

ligands, these ZIFs show relatively similar pore apertures of 0.34 and 0.30 nm, respectively, close to the kinetic diameter of H_2 (0.29 nm), making them ideal for the separation of this gas over larger molecules such as CO_2 (0.33 nm) and CH_4 (0.38 nm). The use of polybenzimidazole (PBI) membranes for the separation of H_2/CO_2 mixtures has been widely reported[21–26] and several types of ZIFs, such as ZIF-7,[22] ZIF-8,[27–29] ZIF-11 [23,30] and ZIF-90,[31] have been embedded in PBI to create mixed matrix membranes (MMMs). Despite the smaller pore windows of ZIF-7 and ZIF-11, compared to those of ZIF-8, they showed worse gas separation performance when embedded in PBI.[22,30] A core–shell hybrid material of ZIF-7 and ZIF-8 is expected to result in a ZIF with enhanced separation performance.

This work presents the synthesis of hybrid ZIFs with a core–shell configuration, showing the tunable nature of this kind of materials. ZIF-7/8 core–shells were obtained through the post-synthetic modification of ZIF-8, a reaction that was monitored and adjusted to the shrinking core model. This kinetic model allowed defining with high accuracy the reaction conditions to obtain a great variety of hybrid frameworks with different compositions. The material can be therefore adapted to certain necessities according to its final application. In the case of this study, incorporating just 10% of ZIF-7 into ZIF-8 allowed an enhanced separation performance for H_2/CO_2 separation (CO_2 pre-combustion capture) when embedded in PBI MMMs owing to (a) the better filler–polymer compatibility provided by the benzimidazole ligand from ZIF-7, acting as the shell and (b) the reduced CO_2 adsorption and high H_2 diffusivity of ZIF-8, acting as the core. The concepts of core–shell and reaction monitoring may be extended to other MOFs and different applications, so that the properties of frameworks can be modified to enhance their performance.

2 Experimental section

2.1 Chemicals

Zinc nitrate hexahydrate ($Zn(NO_3)_2 \cdot 6H_2O$), 2-methylimidazole (mIm, $C_4H_6N_2$, >99%), benzimidazole (bIm, $C_7H_6N_2$, 98%) and *N*,*N*-dimethylacetamide (DMAc, ≥99.5%) were purchased from Sigma Aldrich. Methanol (MeOH, HPLC grade) and *N*,*N*-dimethylformamide (DMF, synthesis grade) were purchased from Scharlau. Commercial PBI solution comprising 26 wt% PBI with 1.5 wt% LiCl as a stabilizer in DMAc solvent was purchased from PBI Performance Products.

2.2 MOF synthesis

ZIF-8 was synthesized according to the following procedure based on the literature.[32] 470 mg of $Zn(NO_3)_2 \cdot 6H_2O$ was dissolved in 10 mL of MeOH and 10 mL of water. Besides, 1.0 g of mIm was dissolved in 10 mL of MeOH, and the two solutions were mixed and stirred for 2 h. The final product was collected by centrifugation, washed once with MeOH, and dried at 110 °C overnight. The resulting nanoparticles had a particle size of about 150 nm.

ZIF-7 was also synthesized in order to compare the effects caused on the ZIF-8 framework after its post-synthetic modification. The following procedure found in the literature was followed.[33] 1.63 g of bIm and 0.64 g of $Zn(NO_3)_2 \cdot 6H_2O$ were dissolved in 200 mL of DMF. The solution was stirred at room temperature for 48 h and the solid was collected by centrifugation. After that, the solid was activated in MeOH at 60 °C under reflux for 18 h.

The ZIF-7/8 core–shells were prepared by post-synthetic modification of ZIF-8. An initial amount of bIm was added to DMF at 65 °C to obtain a concentration of 13 g L^{-1}. When dissolved, ZIF-8 was added to the solution (3.3 g L^{-1}), which was stirred. The solid was collected at the corresponding reaction time by centrifugation and washed 3 times with MeOH and dried at 110 °C overnight. The mIm/bIm proportion in the ZIF-7/8 hybrid was calculated assuming that all the liberated mIm had been replaced by bIm during the reaction. Different initial bIm concentrations and temperatures were also tested to study their influence on the reaction time (see Table S1†).

2.3 Kinetic study

The kinetic study of the post-synthetic modification reaction of ZIF-8 was performed by quantifying the amount of mIm liberated by Gas Chromatography/Mass Spectrometry GC/MS, taking aliquots during the reaction. The ZIF-8 conversion was calculated as the amount of mIm quantified in the reaction medium divided by the total amount present in the original ZIF-8 structure. The equipment used was an Agilent 6850 GC system with a capillary column HP-5MS (30 m × 0.250 mm × 0.25 μm) coupled with an Agilent 5975 MSD. The detector and the injector temperature were 200 °C and helium was used as the carrier gas. The column temperature was set at 110 °C. An aliquot of 1.5 mL was taken from the reaction medium after the reaction had finished and it was injected at least three times to get the average concentration.

2.4 MMM preparation

The required amount of ZIF (ZIF-7/8 core–shell, neat ZIF-7 and neat ZIF-8) was weighed for each membrane loading, from 10 to 40 wt%, and the corresponding amount of PBI solution was added (previously diluted in DMAc to 15 wt% concentration to avoid problems deriving from viscosity). The resulting solution was further stirred overnight. The casting solution was stirred three times and sonicated alternately for a 90 min total time and cast into a Petri dish leveled inside an oven at 90 °C. The Petri dishes were left uncovered overnight to allow the evaporation of the solvent. After that, the membranes were peeled off from the Petri dishes and washed for 24 h in MeOH. Finally, the membranes were treated in an oven at 100 °C for 24 h for the complete removal of the remaining solvent. The membrane thicknesses were determined by using a Digimatic Micrometer (measurement range from 0 to 30 mm with an accuracy of ±1 μm). Several equally distributed points (9) on each membrane were measured and the arithmetic average was taken as the membrane thickness. The MMMs obtained in this work had a thickness of 88 ±

16 μm. For permeation testing of the membranes, circular areas of 3.14 cm^2 were cut from the films.

2.5 Characterization of samples

Powder X-ray diffraction (XRD) spectra of the MOFs and MMMs were acquired using a D-Max Rigaku X-ray diffractometer with a copper anode and a graphite monochromator to select CuKα radiation ($\lambda = 1.540$ Å), taking data from $2\theta = 2.5°$ to 40° at a scan rate of 0.03° s^{-1}. Thermogravimetric analyses (TGA) were carried out using a Mettler Toledo TGA/STDA 851e. Samples (5 mg) placed in 70 μL alumina pans were heated in an air flow from 30 to 900 °C at a heating rate of 10 °C min^{-1}. Scanning electron microscopy (SEM) images of the ZIFs and membranes were obtained using an Inspect F50 model scanning electron microscope (FEI), operated at 20 kV. The cross sections of the membranes were prepared by freeze-fracturing after immersion in liquid nitrogen and subsequent coating with Pt. Transmission electron microscopy (TEM, FEI TECNAI F30) images of the ZIF samples were acquired at an acceleration voltage of 300 kW. This TEM, fitted with a SuperTwin® lens allowing a point resolution of 1.9 Å, is employed for spectroscopy experiments performed in EDS (X-ray Microanalysis). Samples were prepared by placing one drop of a dilute suspension of powder in MeOH on a holey carbon-coated copper grid (300 mesh) and allowing the solvent to evaporate at room temperature. The particle size was obtained using ImageJ 1.49b software, where at least 60 particles were counted for each sample. Fourier transform infrared spectroscopy (FTIR) was performed on a Bruker Vertex 70 FTIR spectrometer equipped with a DTGS detector and a Golden Gate diamond ATR accessory. Both spectra were recorded by averaging 40 scans in the 4000–600 cm^{-1} wavenumber range at a resolution of 4 cm^{-1}. Nitrogen adsorption/desorption isotherms were obtained using a Micromeritics Tristar 3000 surface area and porosity analyzer, after previously degassing the samples, both powders and MMMs, at 200 °C for 8 h under vacuum. NMR spectra were recorded using a Bruker Avance III WB400 spectrometer with 4 mm zirconia rotors spun at the magic angle in N_2 at 10 kHz. ^1H–^{13}C CP spectra were measured using a ^1H π/2 pulse length of 3.0 μs, with a contact time (ramp) of 3 ms, a spinal 64 proton decoupling sequence of 5.3 μs pulse length, and a recycle delay of 5 s. 3000 scans were acquired for each spectrum. The chemical shifts were reported relative to tetramethylsilane (TMS).

2.6 Gas separation analysis

Mixed gas analyses were performed for PBI MMMs containing 10, 20 and 32 wt% loading of the ZIF-7/8 core–shell. The results were compared to those of neat PBI membranes and PBI based MMMs with ZIF-8 and ZIF-7. The membranes were placed in a module consisting of two stainless steel pieces and a 316L SS macroporous disk support (from Mott Co.) with a 20 μm nominal pore size, and gripped inside with Viton O-rings. The permeation module was placed in a UNE 200 Memmert oven to control the temperature of the experiments. Gas separation measurements were carried out by feeding a H_2/CO_2 equimolar mixture (25/25 cm^3(STP) per min) at 3 bar to the feed side by means of two mass-flow controllers (Alicat Scientific, MC-100CCM-D), while the permeate side of the membrane was swept with a 2 cm^3(STP) per min mass-flow controller stream of Ar at 1 bar (Alicat Scientific, MC-5CCM-D). The concentrations of H_2 and CO_2 in the outgoing streams were analyzed by using an Agilent 3000A online gas microchromatograph equipped with a thermal conductivity detector (TCD). Permeability was calculated in Barrer (10^{-6} cm^3(STP)/(cm^2 s cmHg)) once the steady-state of the exit stream was reached (for at least 3 h), and the separation selectivity was calculated as the ratio of permeabilities. At least 2–3 MMM samples of each loading were fabricated and measured to provide the corresponding error estimations.

2.7 Simulation

Simulations were performed with RASPA.[34] Adsorption isotherms of CO_2 and H_2 at 273 K were simulated using Grand Canonical Monte Carlo (GCMC, μVT) simulations, using 250 000 steps and the configuration bias MC algorithm in the insertion/deletion moves. The isosteric heats of adsorption of the guest molecules were computed after 200 000 sampling steps using the Widom insertion method. Host–guest interactions were modeled with Lennard-Jones (LJ) pairwise interatomic potentials plus electrostatic interactions. The atomic charges were taken from commuted values by Gutierrez-Sevillano *et al.*[35] The values of the LJ parameters used in the simulations were obtained through Lorentz–Berthelot mixing rules, for which the force field parameters of the atom of the MOF were taken from the UFF force field for the Zn atom and Dreiding force field for the ligands.[36,37] Diffusion coefficients were calculated through the linear fit of the Mean Square Displacement (MSD) of the guest in the infinite dilution regime at 453 K and 523 K. The MSD was simulated using molecular dynamics simulation in the canonical ensemble (NVT MD),[38] using a time step of 0.5 fs and 250 and 1000 ps of equilibration and production, respectively. Structures were always optimized to guarantee realistic adsorption and transport properties. The force field developed by Wu was used for the geometry optimization of the materials.[39]

3 Results and discussion

3.1 Reaction kinetics

To deduce the reaction kinetics, the reaction was monitored by measuring the liberation of mIm from ZIF-8 by GC/MS. The data obtained were fitted to the shrinking core model for spherical particles of unchanging size proposed by Yagi and Kunii.[40] This model for fluid–solid reaction considers that the reaction occurs first at the outer skin of the particle. The zone of the reaction then moves into the solid, leaving behind a completely converted material and inert solid (ash). We consider in our reaction the original ZIF-8 nanoparticles as the solid phase and the bIm (ZIF-7 benzimidazolate ligand) solution as the liquid phase. The converted material would be the ZIF-7, formed in the shell of the hybrid structure during the post-synthetic modification. The film resistance at the surface of the particle was

neglected, simplifying the model to the expression shown in eqn (S1).† To the best of our knowledge, this is the first time that this reaction in MOFs has been studied by means of a kinetic model.

The analysis of the exchange reaction reveals that the diffusion inside the pores appears to be the reaction controlling step, since it is responsible for around 90% of the total reaction time. The diffusion coefficient at the experimental temperature (65 °C), 2.86×10^{-7} cm^2 s^{-1}, as extracted from the fitting of the conversion curve (Fig. 1 and Table S2†), indicates a relatively large diffusivity of the ligands through the **sod**-type ZIFs. This is surprising since the kinetic diameter of bIm is at least that of benzene (0.585 nm) and therefore this is new evidence of the extremely high flexibility of this framework. Although it has been previously reported how long guest molecules can diffuse as quickly as short molecules in ZIF-8.[41] The calculated kinetic constant was 1.36×10^{-4} cm s^{-1}. The quality of the fitting of the experimental data to the kinetic model is good (see % error in Table S3†), with relatively larger errors (up to 20%) for the initial data at reaction times up to 5 h. This may be due to a different mechanism at the beginning of the reaction, probably related to desorption and partial dissolution processes, which may also explain the traces of Zn found in the reaction medium (Fig. S1†).

A full range of hybrid materials were obtained until the complete transformation of ZIF-8 into ZIF-7 occurred, showing intermediately the structure of a narrow pore ZIF-7.[42] This progression can be seen in the diffraction patterns of Fig. 1 (inset), indicating that a shrinking mechanism controls the process. The hybrid framework maintains the cubic structure of ZIF-8, while additional peaks can be observed at $2\theta = 8.4$, 9.4, 11.8, 15.2 and 16.6°, belonging to the ZIF-7(II) pattern.[42] Given that the contribution of bIm to the diffraction pattern of the ZIF-7/8 hybrid is as crystalline ZIF-7, its incorporation must have occurred by linker exchange with mIm during the post-modification reaction. Otherwise its interaction with the Zn^{2+} cations of ZIF-8 to build the ZIF-7 structure would have been impossible.

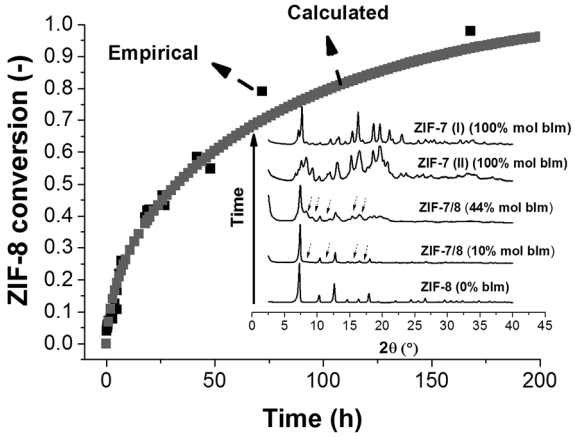

Fig. 1 Conversion of ZIF-8 *vs.* time at 65 °C: empirical (black) and calculated (grey) values with the shrinking core model.

3.2 Core–shell characterization

Two core–shells with different amounts of bIm (10 and 44 mol%) were chosen for further characterization, the former being the first with visible ZIF-7 XRD reflections and the latter having similar quantities of each linker. Note that ZIF-8 and ZIF-7(II) phases are clearly identified from the pattern of ZIF-7/8 (44% bIm) in Fig. 1 (inset). The large peak width supports this view, which can be interpreted as a consequence of the small particle size corresponding to each phase. The simulated XRD shows how the diffractogram of the hybrid material (Fig. S2†) better fits a linear combination of neat ZIF-7 and ZIF-8 patterns than the corresponding XRD pattern of a homogeneous mixed-ligand structure at the unit cell level, suggesting the existence of a core–shell arrangement of phases.

Regarding the particles' morphology, a single particle size population or morphology can be observed in the SEM/TEM images (Fig. S3†), consistent with the existence of one kind of particle, instead of a physical mixture of ZIF-7 and ZIF-8. The particle size decreased from 150 nm of the original ZIF-8 to 124 nm, according to the cumulative distribution graph shown in Fig. S4† and seems to be related to the partial dissolution of Zn found previously. EDX analysis performed on a single nanoparticle, revealed that the Zn and N amounts remain constant across the particle width (Fig. 3), with a consistent proportion in the framework structure (Table S4†).

The thermal stability of the core–shells was also tested. The TGA of the hybrid material in air (Fig. S5†) shows an intermediate behavior between ZIF-7 and ZIF-8, with two decomposition steps corresponding to the coexistence of mIm and bIm ligands in the structure. The onset temperatures are slightly different to those of the neat ZIFs (472 *vs.* 455 °C for mIm and

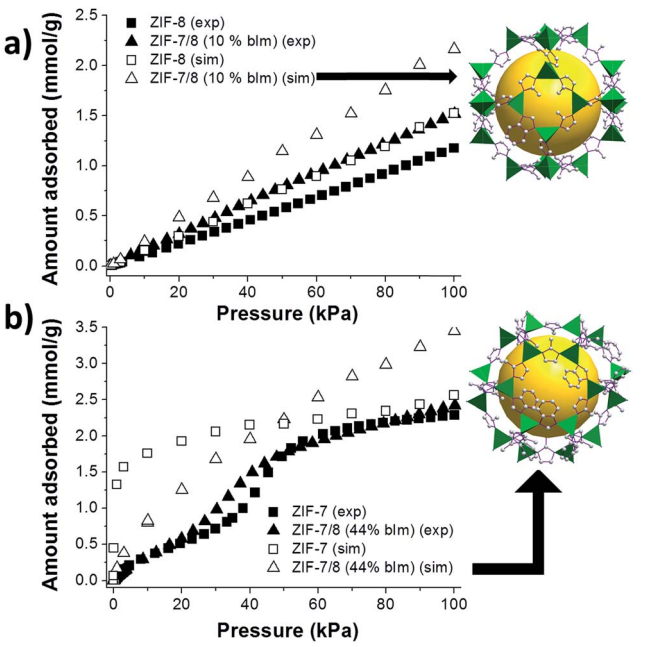

Fig. 2 Simulated and empirical CO_2 adsorption isotherms of ZIF-7 (a), ZIF-8 (b) and both hybrid materials (a and b) at 273 K and the simulated structure (inset).

527 *vs.* 576 °C for bIm). The mIm in the hybrid structure is more stable than that in ZIF-8, but the opposite happens to the bIm linker. This may be due to the fact that bIm is more exposed, as it is mainly located at the outer part of the framework, while mIm is more protected, basically remaining in the inner part.

The adsorption properties of the core–shells were also tested to study their microporosity in depth. The two 10% and 44% ZIF-7/8 hybrids show N_2 uptakes of 374 and 290 cm^3(STP) per g at $P/P_0 = 1$ (Fig. S6†), about one fourth and one half smaller than that of ZIF-8, respectively. The same occurs with the BET area, which is 20% smaller for the hybrid with the lowest amount of bIm (1050 $m^2\ g^{-1}$). This reduction is even higher for the other hybrid, having a value of 719 $m^2\ g^{-1}$. The inclusion of bIm in the ZIF-8 framework structure (in the form of ZIF-7 according to the XRD spectra) reduces the maximum quantity adsorbed in comparison to the original ZIF-8. This causes a partial reduction of the pore windows in the hybrid material, hindering the entrance of N_2 molecules inside the framework structure (in fact, ZIF-7 does not adsorb N_2).[43] Our adsorption measurement suggests that the shell part of our hybrid material is expected to have a small amount of the parent mIm ligand that creates percolative paths for the diffusion of N_2 in terms of the adsorption capacity.

The opposite tendency can be seen for CO_2 adsorption (Fig. 2 and S7†) since ZIF-8 is the framework with the lowest adsorption capacity. It is worth noting that the hybrid containing 44% bIm adsorbs the same quantity of CO_2 as the bare ZIF-7 despite containing half the amount of linker. The other hybrid (10 wt% bIm), as compared to ZIF-8, adsorbs about 20% more CO_2, which is consistent with a 90% core of ZIF-8. The simulated adsorption isotherms shown in Fig. 2 predict well the empirical results. CO_2 and H_2 heats of adsorption also increase as the amount of bIm in the framework becomes higher (Table S5†).

The chemical composition of the core–shells was studied by ^{13}C NMR (Fig. 4) and FTIR (Fig. S8†). ^{13}C NMR analyses show

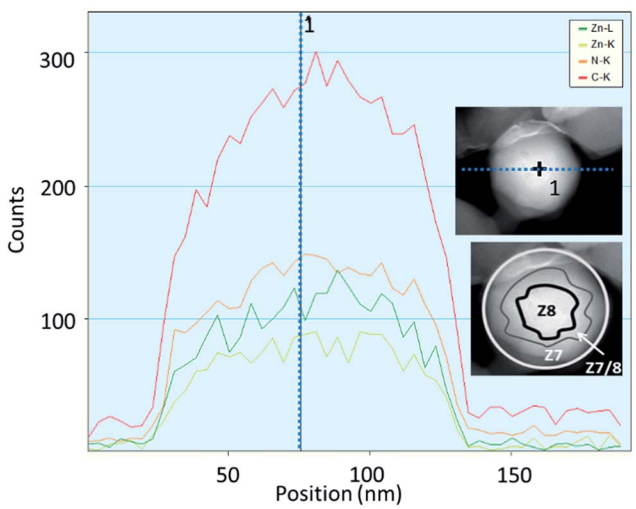

Fig. 3 EDX profile of a single 10% mol bIm hybrid nanoparticle in the top inset. From up to down: C–K, N–K, Zn–L and Zn–K. The bottom inset corresponds to a scheme of this particle.

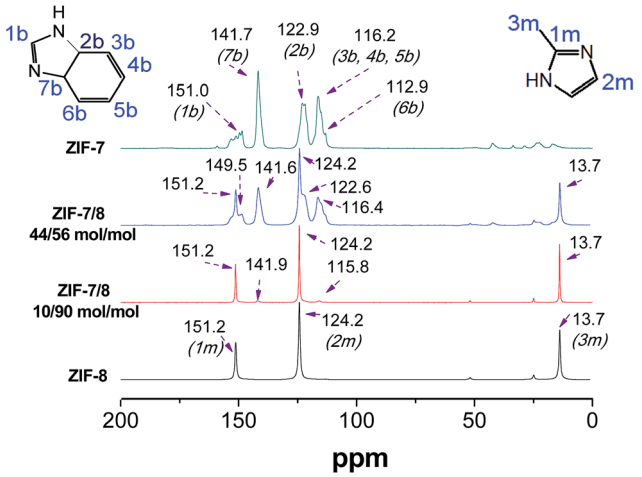

Fig. 4 ^{13}C NMR patterns of ZIF-7, ZIF-8 and two different ZIF-7/8 hybrids containing 10 and 44% mol of bIm.

the resonances of ZIF-8 and ZIF-7 in the hybrids' spectra without any shift, suggesting that the core of ZIF-8 remains unaltered after the post-synthetic modification reaction, and that the chemical environment of the carbon atoms of bIm in the hybrid framework is similar to that in neat ZIF-7. The ^{13}C NMR spectrum of ZIF-8 (Fig. 4) shows three resonances at 151.2, 124.2 and 13.7 ppm corresponding to the mIm linker. The former is due to the aromatic carbon linked to nitrogen (C_{1m}), the second to the –HC=CH– group (C_{2m}) and the latter to the methyl group (C_{3m}).[44] The ZIF-7 spectrum also shows the resonances of its linker (bIm). The carbon atom between the amino and the imidazole groups (C_{1b}) resonates as a multiplet at 151.0 ppm. The signal at 141.7 ppm corresponds to C_{7b}, while that at 116.2 to C_{3b}, C_{4b}, and C_{5b} resonances. Finally, the peak at 122.9 corresponds to C_{2b} and C_{6b} resonates at 112.9 ppm.[45–47]

The ^{13}C NMR experiments also quantified an amount of 18% mol of bIm in the framework (see Fig. S9†), in relative agreement with the GC-MS (10%), BET (20%) and CO_2 adsorption (10%). The simultaneous validity of diffraction, adsorption and spectroscopy characterizations allows one to depict a ZIF-8–ZIF-7 core–shell particle with a wide hybridized interface (see the scheme in the Fig. 3 inset).

3.3 Mixed matrix membrane performance

We considered that the hybrid ZIF could show a good performance as a filler in PBI MMMs for gas separation, especially that with the lowest amount of bIm because it retains a good part of the nature of ZIF-8, the ZIF with the best results in the literature,[27–29] while superficially exhibiting a bIm ligand highly compatible with PBI.[30] MMMs with loadings from 10 to 32 wt% (checked by TGA) were prepared and characterized by SEM and XRD. The cross section of the prepared MMMs at different loadings (10, 20 and 32 wt%) of the ZIF-7/8 hybrid (10 wt% mol bIm) is shown in Fig. S10,† where a good interaction between the filler and the polymer can be clearly distinguished. SEM images were reinforced with EDX analysis (Fig. S11†), in which the presence of Zn from the ZIF nanoparticles can be

distinguished across the MMM section. Additionally, XRD spectra of the MMMs (see Fig. S12†) show how the filler remains crystalline once embedded in the polymeric phase. N_2 adsorption was also performed on a MMM and the results can be seen in Fig. S13† in comparison to those of a bare PBI membrane and the ZIF-7/8 hybrid core–shell powder. As expected, the MMM shows an intermediate adsorption capacity because the polymer surrounding the hybrid particles hinders access to N_2. In any event, the reduction in the BET area is relatively low as compared to that achieved with ordered mesoporous sphere-polysulfone MMMs where the polymer chains penetrate into the filler pores.[48]

PBI MMMs containing ZIF-8 and ZIF-7 were also fabricated and tested under the same conditions for comparison. Fig. 5a shows the H_2/CO_2 gas separation performance of a 50/50 mixture at 180 °C and 3 bar feed pressure. MMMs with core–shell loadings up to 32 wt%, the maximal loading without the membranes being too brittle, were tested. The integration of the ZIF-7/8 hybrid material improved the membrane performance clearly. When embedding just 10 wt% of this hybrid filler, the H_2 permeability was seven-fold higher than that of the neat PBI and the selectivity was doubled. A significant enhancement in the H_2 permeability was observed with increasing loading, reaching a value of 1398 ± 88 Barrer at 32 wt% loading. However, the H_2/CO_2 selectivity showed an optimum value of 10.1 ± 0.2 at 20 wt% loading, which is three-fold that of the bare PBI at the same temperature. This suggests the presence of non-selective voids owing to some deterioration in the interaction between the MOF and the polymer at these high loadings.[49] The results evidence the important role that the presence of the microporous ZIF-7/8 hybrid plays in the gas transport through the membranes. In the Robeson graph of Fig. 5b, it can be seen how PBI MMMs containing the core–shells have a superior gas separation performance in terms of permeability and selectivity to analogous MMMs with ZIF-7 and ZIF-8 at the same loading, surpassing the Robeson upper bound in all cases.[50] This result is due to the best affinity of the hybrid ZIF with the polymer provided by the presence of bIm in its structure (see N_2 adsorption in Fig. S6†) and the reduction of the effective pore diameter, allowing a better CO_2 discrimination by the sieving process and thus enhancing the membrane selectivity. The increase in H_2 permeability may be related to the larger self-diffusion coefficient that the hybrid possesses according to the simulation results (Table S6†). It can also be seen how the ZIF-7 membrane performance was worse than that of ZIF-8. This proves that the amount of bIm in the hybrid material must be low (10% mol according to GC/MS analysis) to enable the improvement in the gas separation performance, minimizing the CO_2 adsorption. A MMM containing a physical mixture of ZIF-7 and ZIF-8 (10 wt% each) was also tested to compare the results with those of ZIF-7/8 hybrid core–shell MMMs. This membrane showed an inferior separation performance as well: a H_2 permeability of 277.4 Barrer and a H_2/CO_2 selectivity of 7.0. Finally, the PBI MMM with the highest loading of the hybrid ZIF, 32 wt%, was tested at a higher temperature (250 °C), showing a H_2 permeability of 1921 Barrer and a H_2/CO_2 selectivity of 11.8.

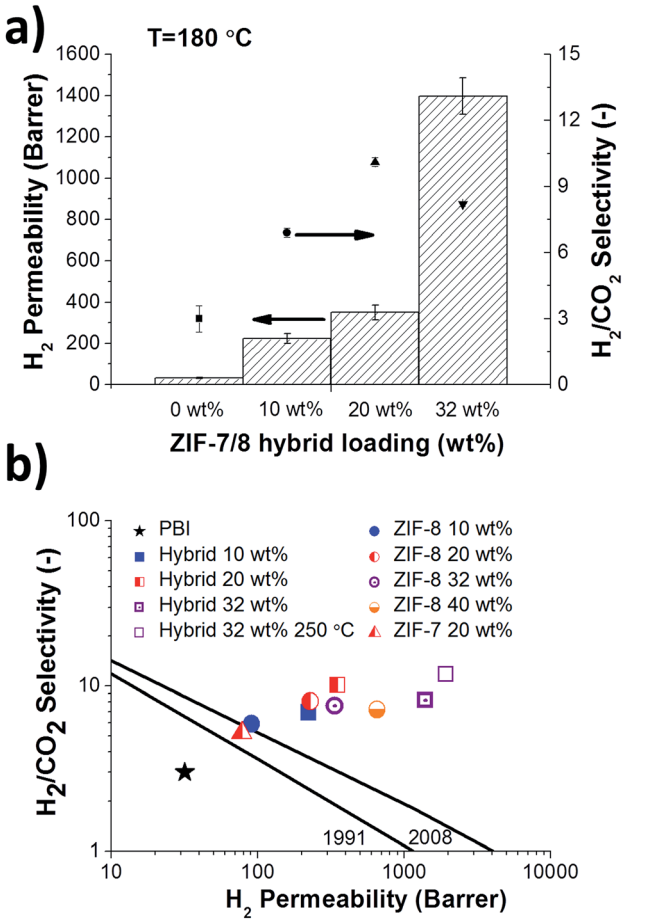

Fig. 5 Mixed gas separation performance at 180 °C of neat PBI and PBI MMMs containing the hybrid ZIF-7/8 at loadings of 10, 20 and 32 wt% (a) and gas separation performance at 180 and 250 °C of PBI MMMs of ZIF-8, ZIF-7 and ZIF-7/8 hybrids (10% bIm) with loadings up to 40 wt%. Continuous lines correspond to the Robeson upper bounds[50] (b).

4 Conclusions

The post-synthetic modification of ZIF-8 to ZIF-7 has been successfully adjusted to the shrinking core model. This kinetic model allowed defining with high accuracy the reaction conditions to obtain a great variety of hybrid frameworks with different compositions. Among them, hybrid ZIFs containing 10 and 44% mol of bIm with a **sod** topology were characterized in depth. The particles are envisioned as ZIF-8–ZIF-7 core–shells with a wide hybridized interface. XRD patterns revealed a linear combination of ZIF-7 and ZIF-8 diffractograms, while TGA analyses showed a combined curve with a single onset temperature. The hybrid framework also showed a decrease in the N_2 adsorption capacity due to the presence of bIm in its structure, with a BET reduction of about 20% of the original value for ZIF-8, and an increase in CO_2 adsorption that was corroborated by molecular simulation results. The use of the ZIF-7/8 hybrid as a filler in PBI membranes clearly enhanced the gas separation performance for CO_2 pre-combustion capture (H_2/CO_2 mixtures) at high temperatures due to (a) the better

filler–polymer compatibility provided by the benzimidazole ligand from ZIF-7, acting as the shell, and (b) the reduced CO_2 adsorption and high H_2 diffusivity of ZIF-8, acting as the core. The concepts of core–shell and reaction monitoring may be extended to other MOFs and different applications, so that the properties of frameworks can be modified to enhance their performance.

Conflicts of interest

There are no conflicts to declare.

Acknowledgements

The research leading to these results has received funding from the European Union Seventh Framework Programme (FP7/2007–2013) under grant agreement no 608490, project M4CO2. In addition, financial support from the Spanish MINECO and FEDER (MAT2016-77290-R and CTP2016-80206-P), the Aragón Government (T05) and the ESF is gratefully acknowledged. J. S.-L. thanks the Spanish Education Ministry Program FPU2014 for his PhD grant. S. R. G. Balestra also thanks the Spanish MINECO for his predoctoral fellowship (BES-2014-067825 from CTQ2013-48396-P). All the microscopy work was done at the Laboratorio de Microscopías Avanzadas at the Instituto de Nanociencia de Aragón (LMA-INA). Finally, the authors would like to acknowledge the use of the Servicio General de Apoyo a la Investigación-SAI, Universidad de Zaragoza.

Notes and references

1 G. Ferey and C. Serre, *Chem. Soc. Rev.*, 2009, **38**, 1380–1399.
2 B. Zornoza, C. Tellez, J. Coronas, J. Gascon and F. Kapteijn, *Microporous Mesoporous Mater.*, 2013, **166**, 67–78.
3 H. B. T. Jeazet, C. Staudt and C. Janiak, *Dalton Trans.*, 2012, **41**, 14003–14027.
4 P. Horcajada, C. Serre, M. Vallet-Regí, M. Sebban, F. Taulelle and G. Férey, *Angew. Chem.*, 2006, **118**, 6120–6124.
5 H. Jiang, T. Akita, T. Ishida, M. Haruta and Q. Xu, *J. Am. Chem. Soc.*, 2011, **133**, 1304–1306.
6 J. Gascon, U. Aktay, M. D. Hernandez-Alonso, G. P. M. van Klink and F. Kapteijn, *J. Catal.*, 2009, **261**, 75–87.
7 K. S. Park, Z. N. Ni, A. P. Côte, J. Y. Choi, R. Huang, F. J. Uribe-Romo, H. K. Chae, M. O'Keeffe and O. M. Yaghi, *Proc. Natl. Acad. Sci. U. S. A.*, 2006, **103**, 10186–10191.
8 X. Huang, Y. Lin, J. Zhang and X. Chen, *Angew. Chem.*, 2006, **118**, 1587–1589.
9 B. Chen, Z. Yang, Y. Zhu and Y. Xia, *J. Mater. Chem. A*, 2014, **2**, 16811–16831.
10 F. Rashidi, C. R. Blad, C. W. Jones and S. Nair, *AIChE J.*, 2016, **62**, 525–537.
11 J. A. Thompson, C. R. Blad, N. A. Brunelli, M. E. Lydon, R. P. Lively, C. W. Jones and S. Nair, *Chem. Mater.*, 2012, **24**, 1930–1936.
12 C. Zhang, Y. Xiao, D. Liu, Q. Yang and C. Zhong, *Chem. Commun.*, 2013, **49**, 600–602.
13 R. Banerjee, A. Phan, B. Wang, C. Knobler, H. Furukawa, M. O'Keeffe and O. M. Yaghi, *Science*, 2008, **319**, 939–943.
14 R. Banerjee, H. Furukawa, D. Britt, C. Knobler, M. O'Keeffe and O. M. Yaghi, *J. Am. Chem. Soc.*, 2009, **131**, 3875–3877.
15 N. T. Nguyen, H. Furukawa, F. Gándara, H. T. Nguyen, K. E. Cordova and O. M. Yaghi, *Angew. Chem., Int. Ed.*, 2014, **53**, 10645–10648.
16 S. M. Cohen, *Chem. Rev.*, 2011, **112**, 970–1000.
17 A. Huang and J. Caro, *Angew. Chem., Int. Ed.*, 2011, **50**, 4979–4982.
18 J. Canivet, S. Aguado, C. Daniel and D. Farrusseng, *ChemCatChem*, 2011, **3**, 675–678.
19 X. Liu, Y. Li, Y. Ban, Y. Peng, H. Jin, H. Bux, L. Xu, J. Caro and W. Yang, *Chem. Commun.*, 2013, **49**, 9140–9142.
20 K. C. Jayachandrababu, D. S. Sholl and S. Nair, *J. Am. Chem. Soc.*, 2017, **139**, 5906–5915.
21 S. Choi, J. Coronas, Z. Lai, D. Yust, F. Onorato and M. Tsapatsis, *J. Membr. Sci.*, 2008, **316**, 145–152.
22 T. Yang, Y. Xiao and T. Chung, *Energy Environ. Sci.*, 2011, **4**, 4171–4180.
23 L. Li, Y. Jianfeng, X. Wang, Y. Chen and H. Wang, *J. Appl. Polym. Sci.*, 2014, **131**, 41056.
24 X. Li, R. P. Singh, K. W. Dudeck, K. A. Berchtold and B. C. Benicewicz, *J. Membr. Sci.*, 2014, **461**, 59–68.
25 S. Kumbharkar, Y. Liu and K. Li, *J. Membr. Sci.*, 2011, **375**, 231–240.
26 B. P. Biswal, A. Bhaskar, R. Banerjee and U. K. Kharul, *Nanoscale*, 2015, **7**, 7291–7298.
27 T. Yang, G. M. Shi and T. Chung, *Adv. Energy Mater.*, 2012, **2**, 1358–1367.
28 T. Yang and T. Chung, *Int. J. Hydrogen Energy*, 2013, **38**, 229–239.
29 A. Bhaskar, R. Banerjee and U. Kharul, *J. Mater. Chem. A*, 2014, **2**, 12962–12967.
30 J. Sánchez-Laínez, B. Zornoza, C. Téllez and J. Coronas, *J. Mater. Chem. A*, 2016, **4**, 14334–14341.
31 T. Yang and T. Chung, *J. Mater. Chem. A*, 2013, **1**, 6081–6090.
32 N. Liédana, A. Galve, C. Rubio, C. Téllez and J. Coronas, *ACS Appl. Mater. Interfaces*, 2012, **4**, 5016–5021.
33 Y.-S. Li, F.-Y. Liang, H. Bux, A. Feldhoff, W.-S. Yang and J. Caro, *Angew. Chem., Int. Ed.*, 2010, 548–551.
34 D. Dubbeldam, S. Calero, D. E. Ellis and R. Q. Snurr, *Mol. Simul.*, 2016, **42**, 81–101.
35 J. J. G. Sevillano, S. Calero, C. O. Ania, J. B. Parra, F. Kapteijn, J. Gascon and S. Hamad, *J. Phys. Chem. C*, 2012, **117**, 466–471.
36 A. K. Rappé, C. J. Casewit, K. Colwell, W. Goddard III and W. Skiff, *J. Am. Chem. Soc.*, 1992, **114**, 10024–10035.
37 S. L. Mayo, B. D. Olafson and W. A. Goddard, *J. Phys. Chem.*, 1990, **94**, 8897–8909.
38 D. Dubbeldam and R. Snurr, *Mol. Simul.*, 2007, **33**, 305–325.
39 X. Wu, J. Huang, W. Cai and M. Jaroniec, *RSC Adv.*, 2014, **4**, 16503–16511.
40 S. Yagi and D. Kunii, *Symp. Combust.*, 1955, **5**, 231–244.
41 B. Zheng, L. Wang, L. Du, Y. Pan, Z. Lai, K. Huang and H. Du, *Mater. Horiz.*, 2016, **3**, 355–361.

42 S. Aguado, G. Bergeret, M. P. Titus, V. Moizan, C. Nieto-Draghi, N. Bats and D. Farrusseng, *New J. Chem.*, 2011, **35**, 546–550.
43 W. Morris, N. He, K. G. Ray, P. Klonowski, F. Hiroyasu, I. N. Daniels, Y. A. Houndonougbo, M. Asta, O. M. Yaghi and B. B. Laird, *J. Phys. Chem.*, 2012, **116**, 24084–24090.
44 U. Böhme, C. Paula, V. Reddy Marthala, J. Caro and M. Hartmann, *Chem. Ing. Tech.*, 2013, **85**, 1707–1713.
45 A. S. Cattaneo, D. C. Villa, S. Angioni, C. Ferrara, E. Quartarone and P. Mustarelli, *J. Phys. Chem. C*, 2015, **119**, 18935–18944.
46 J. Grobelny, D. M. Rice, F. E. Karasz and W. J. MacKnight, *Macromolecules*, 1990, **23**, 2139–2144.
47 R. M. Claramunt, C. López, I. Alkorta, J. Elguero, R. Yang and S. Schulman, *Magn. Reson. Chem.*, 2004, **42**, 712–714.
48 B. Zornoza, S. Irusta, C. Téllez and J. Coronas, *Langmuir*, 2009, **25**, 5903–5909.
49 R. Mahajan, R. Burns, M. Schaeffer and W. J. Koros, *J. Appl. Polym. Sci.*, 2002, **86**, 881–890.
50 L. M. Robeson, *J. Membr. Sci.*, 2008, **320**, 390–400.

Supporting Information

1. **Study of the post-synthetic modification reaction at different temperatures and bIm concentrations:**

Table S1. bIm amount in the reaction medium, reaction temperature and reaction time in the post-synthetic modification reactions of ZIF-8 and the resulting ZIF.

bIm concentration	6.5 g/L	6.5 g/L	13 g/L	26 g/L	26 g/L
ZIF-8 concentration	3.3 g/L	3.3 g/L	3.3 g/L	3.3 g/L	3.3 g/L
Temperature	30 ^{0}C	65 ^{0}C	30 ^{0}C	90 ^{0}C	90 ^{0}C
Time	7 days	3 days	3 days	1 day	3 days
Resulting ZIF	ZIF-7/8 hybrid (10 %mol bIm)	ZIF-7/8 hybrid (10 %mol bIm)	ZIF-7/8 hybrid (10 %mol bIm)	ZIF-7(II)	ZIF-7(I)

Different bIm concentrations and temperatures were tested to study the influence of these variables on the post-synthetic modification reaction of ZIF-8 (see Table S1), providing tunable reaction conditions. As a result, the ZIF-7/8 hybrid (10 %mol bIm) was obtained in 3 days at 65 ^{0}C and with an initial bIm concentration in the reaction medium of 6.5 g/L or at 30 ^{0}C with a bIm concentration of 13 g/L. The same hybrid material was obtained from a reaction at 30 °C during 7 days when the initial bIm concentration was 6.5 g/L.

2. **Reaction modeling:**

The post-synthetic modification reaction of ZIF-8 was adjusted using the shrinking core model for spherical particles of unchanging size of Levenspiel. Neglecting the contribution of the gas film resistance, the resulting integrated equation is shown in Eq. S1:

$$t = \frac{\rho_{ZIF-8} \cdot R^2}{6 \cdot b \cdot C_{bIm} \cdot D_e}\left[1 - 3(1 - X_{ZIF-8})^{\frac{2}{3}} + 2(1 - X_{ZIF-8})\right] + \frac{\rho_{ZIF-8} \cdot R}{b \cdot C_{bIm} \cdot k_s}\left[1 - (1 - X_{ZIF-8})^{\frac{1}{3}}\right] \quad [Eq.\,(S1)]$$

The values and meaning of the different terms of both equations can be seen in Table S1. Both the kinetic constant and the diffusion coefficient were calculated from the slopes resulting from a multiple regression fit of the empirical data recorded in Table S2.

Table S2. Values for the shrinking core model.

ρ_{ZIF-8}	ZIF-8 density	1.3 g/mL
R	Particle radius	124 nm
b	Stoichiometric factor	1
C_{bIm}	bIm concentration	13 g/L
D_e	Diffusion coefficient in the ash film	$2.86 \cdot 10^{-7}$ cm^2/s
k_s	Kinetic constant	$1.36 \cdot 10^{-4}$ cm/s

Table S3. Empirical and calculated values of the post-synthetic modification reaction.

Time (h)	Empirical X_{ZIF-8}	Calculated X_{ZIF-8}	$\%\ error = \frac{\lvert X_{empirical} - X_{calculated} \rvert}{X_{empirical}} \cdot 100$
0	0.00	0.00	0.0
0.50	0.05	0.04	16.4
0.75	0.06	0.06	4.5
1	0.07	0.07	2. 8
1.5	0.09	0.08	15.4
3	0.14	0.14	22.7
4.5	0.15	0.18	18.2
5	0.17	0.19	13.7
6	0.22	0.21	3.6
7	0.26	0.23	11.4
18	0.40	0.38	4.9
19	0.42	0.39	7.3
20	0.42	0.40	5.5
26	0.46	0.45	1.4
42	0.58	0.56	4.3
48	0.55	0.59	7.4
72	0.79	0.70	11.5
168	0.98	0.93	5.1

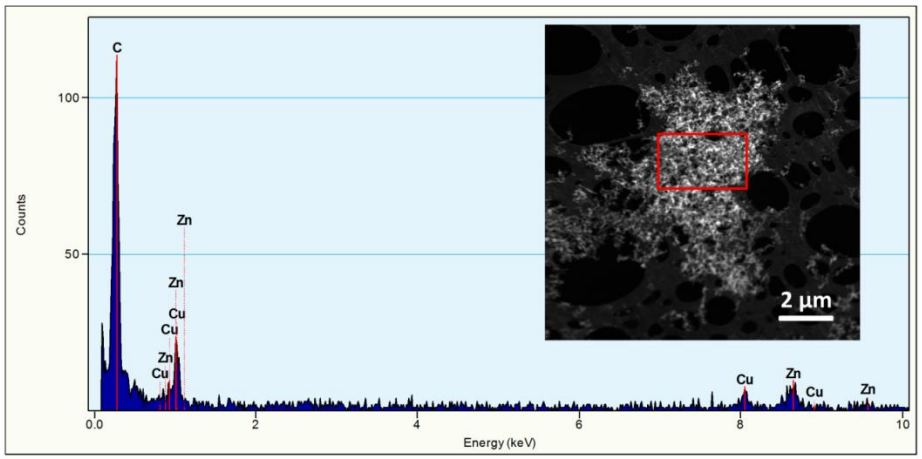

Fig. S1. TEM image and EDX analysis of the reaction medium after the post-synthetic modification reaction.

The reaction medium was evaluated by EDX once the post-synthetic modification had finished and the results are shown in Fig. S1. The dispersion was centrifuged and the supernatant was filtered twice using 0.14 µm filters to remove any remaining solid particles. The solvent was evaporated and replaced by MeOH. One drop of liquid was deposited onto a TEM grid for characterization. An amorphous solid could be found in the sample, where traces of Zn were detected, as well as Cu from the grid. This residual solid may come from part of the original ZIF-8 nanoparticles that was desorbed at the beginning of the post-synthetic modification reaction. This may explain the relative high fitting errors of the kinetic model (Table S3)

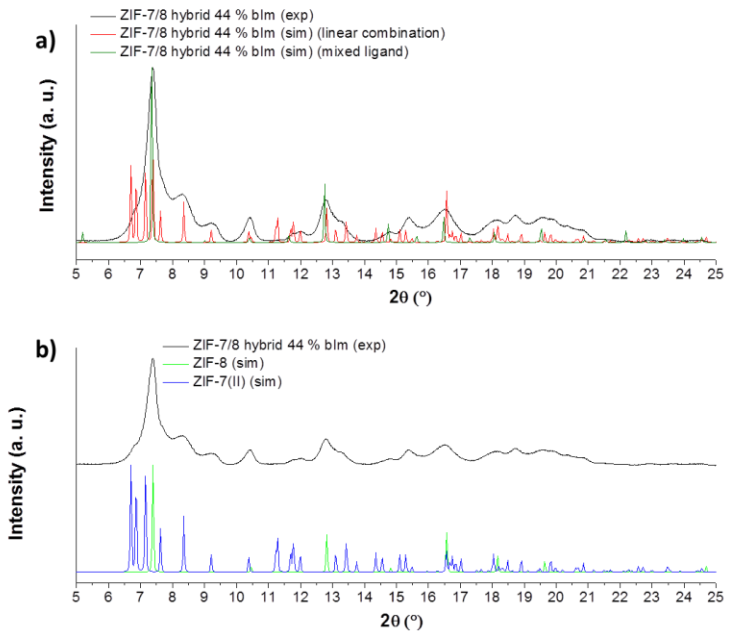

Fig. S2. XRD patterns of ZIF-7/8 hybrid 44% mol bIm, empirical and simulated according to a mixed-ligand structure and a linear combination of ZIF-7 and ZIF-8 (a) and comparison of empirical spectrum with simulated diffractograms of ZIF-8 and ZIF-7(II) from the literature (b).[9]

3. ZIFs characterization:

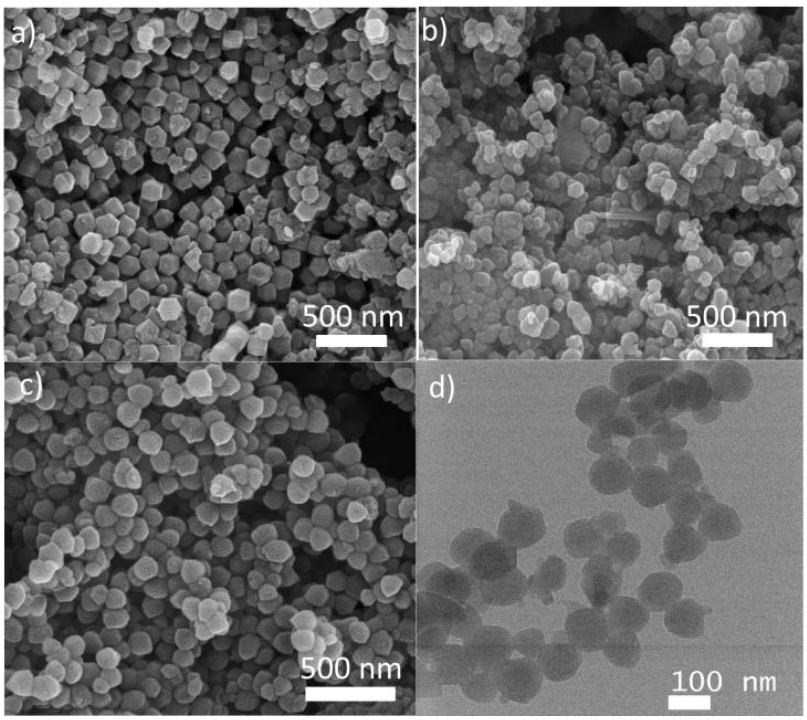

Fig. S3. SEM images of ZIF-8 (a), ZIF-7 (b) and ZIF-7/8 hybrid (c) and TEM image of ZIF-7/8 hybrid (d).

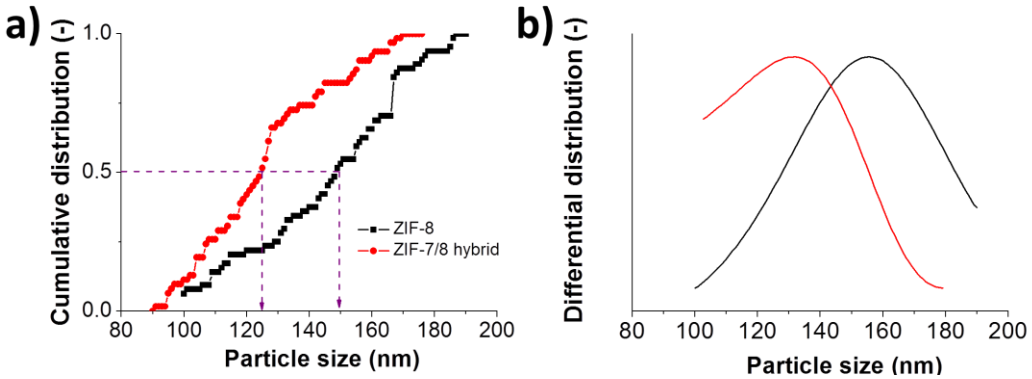

Fig. S4. Cumulative (a) and differential (b) particle size distribution of the ZIF-8 and ZIF-7/8 hybrid nanoparticle samples.

Fig. S4a shows the normalized cumulative number of particles as a function of the particle size. From this plot, average particle sizes for each sample (124 and 150nm) were obtained at N/N_T = 0.5, N and N_T being the number and total number of particles, respectively. In addition, the differential distributions were calculated (Fig. S4b), providing predominant particle sizes (modes), whose values are similar to the corresponding averages.

Table S4. EDX analysis of the ZIF-7/8 (hybrid) 10%mol bIm.

Element	Weight	Atomic %	Uncertanty %	Detector correction	k-Factor
C(K)	81.99	88.65	1.50	0.26	4.032
N(K)	10.66	9.89	0.59	0.26	3.903
Zn(K)	7.33	1.45	0.27	0.99	1.686

Table S4 shows the EDX quantification of the hybrid sample shown in Fig. 2. The average atomic N/Zn proportion was 7/1, which is similar to the theoretical 8/1 expected (one atom of Zn for every two imidazole molecules, thus four atoms of N).

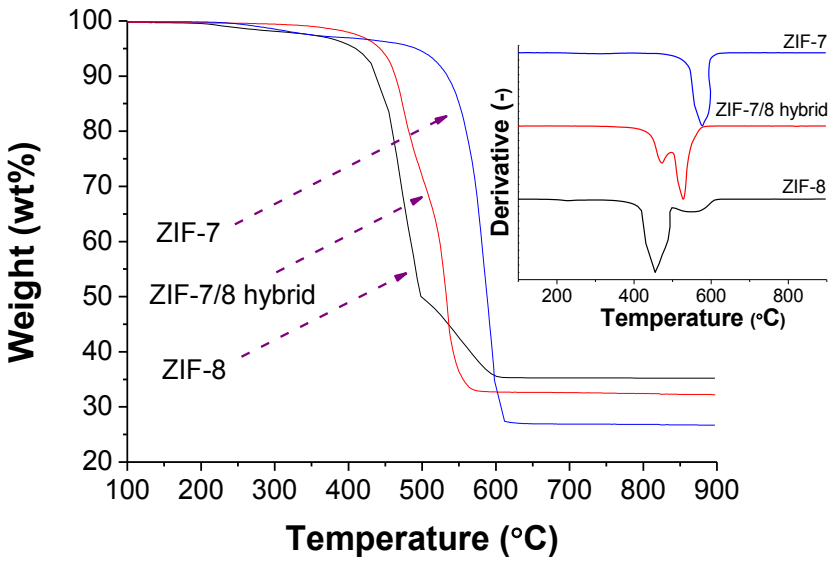

Fig. S5. TGA and derivative (inset) of ZIF-7, ZIF-8 and ZIF-7/8 hybrid in air.

Thermogravimetric analyses (TGA) in air can be seen in Fig. S5. ZIF-8 shows a big weight loss at 455 ^{0}C followed by a small one at 552 ^{0}C related to the decomposition of the mIm contained in its structure. In the case of ZIF-7, it shows a higher onset temperature (576 ^{0}C), due to the greater thermal stability of bIm (ZIF-7 linker). The existence of these two decomposition steps in the hybrid TGA corresponds to the coexistence of mIm and bIm in the framework structure. The existence of a continuous TGA curve, different to those of the neat ZIFs, instead of two isolated decomposition steps is indicative of the existence of a framework against a physical mixture of ZIF-7 and ZIF-8.

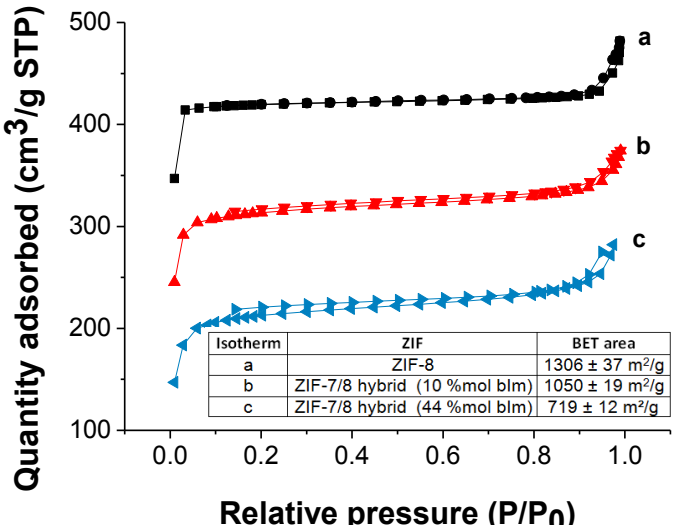

Fig. S6. Empirical N_2 adsorption isotherms of activated ZIF-8 and ZIF-7/8 hybrids at 77 K and calculated BET areas (inset).

N_2 adsorption was measured for ZIF-8 and the ZIF-7/8 hybrids to study their porosity (see Fig. S6) after the corresponding activation with MeOH. The adsorption isotherm of ZIF-7 is not included since this compound was unable to adsorb N_2 at this range of pressures. According to their shape, both isotherms can be classified as Type I, typical of microporous materials. The standard deviation for BET area is that provided by the sorption device.

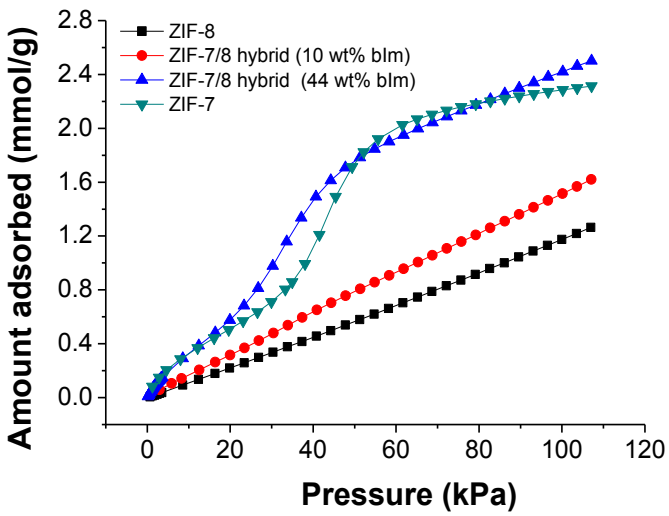

Fig. S7. Empirical CO_2 adsorption isotherms of activated ZIF-8, ZIF-7/8 hybrids and ZIF-7 at 273 K.

CO_2 adsorption was also measured for ZIF-7, ZIF-8 and both hybrids to study their porosity in deep (see Fig. S7). ZIF-8 shows a little CO_2 uptake (1.3 mmol/g at 110 kPa) since the pressure during the experiment is not high enough to open their pores.[10] The isotherm of ZIF-7 shows inflexion points, already reported in the literature.[11, 12] The framework containing a 10% of bIm increases this gas uptake a 20% at the same pressure, while the hybrid containing a 44 % of this linker is able to adsorb as much as bare ZIF-7, thus 2.4 mmol/g of CO_2 at 110 kPa.

Table S5. Heat of adsorption of CO_2 and H_2 in mixing ligands ZIF structures.

Structure (% bIm)	CO_2 Heat of adsorption (kJ/mol)	H_2 Heat of adsorption (kJ/mol)
100 (ZIF-7)	-30.3	-5.9
89	-28.2	-5.3
81	-27.8	-4.9
69	-24.5	-4.5
58	-18.4	-3.8
42	-16.0	-3.3
29	-13.5	-2. 9
21	-13.15	-2.9
8	-11.1	-2.6
0 (ZIF-8)	-11.1	-2.5

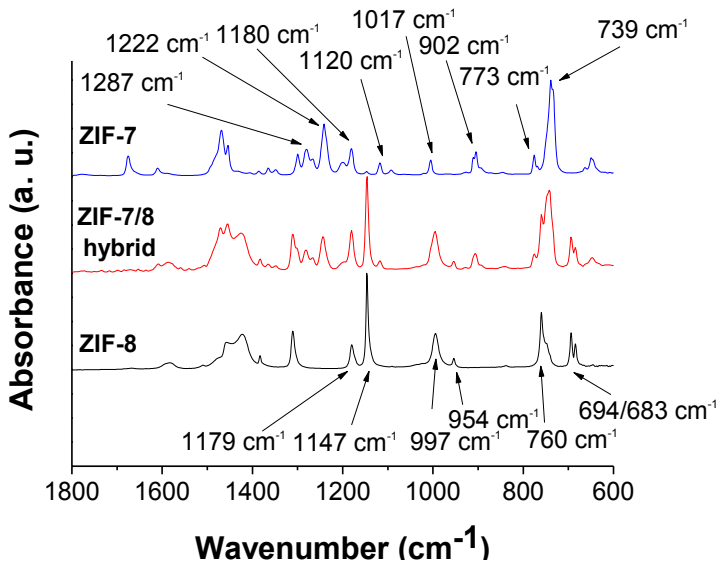

Fig. S8. FTIR spectra of ZIF-7, ZIF-8 and ZIF-7/8 hybrid.

The infrared spectra of ZIF-7, ZIF-8 and the hybrid material are shown in Fig. S8. ZIF-8 shows very intense bands in the 600-1700 cm^{-1} range. In this range ZIF-8 shows signals at 954 and 997 cm^{-1} and two intense bands at 1146 and 1179 cm^{-1}, the latter being attributed to C-N ring vibrations [13,14].In this range, peaks at 683, 694, 760 cm^{-1} are also clearly visible. These are mainly attributed to in-plane C-H deformation bands. [15] [16,17] In the case of ZIF-7, this framework also shows very intense bands in the 600-1700 cm^{-1} range but different to those of ZIF-8. The absorbance peak at 1017 cm^{-1} is assigned to the benzene-ring vibration and the signal at 1287 cm^{-1} is related to the imidazole-ring breathing. The peak at 1222 cm^{-1} is caused by the in-plane C-H deformation of the disubstituted benzimidazole, while the peak at 902 cm^{-1} is due to the C–H out-of-plane bending of single hydrogen in substituted benzene rings. Finally, the signals at 1180, 1120 and 773 cm^{-1} are due to the benzimidazole in-plane C-H bending, the N-H in-plane bending and the imidazole in-plane ring bending, respectively.[18] The hybrid material spectrum consists of the full combination of all the signals observed in ZIF-7 and ZIF-8 patterns, since all the vibration modes can be seen in it.

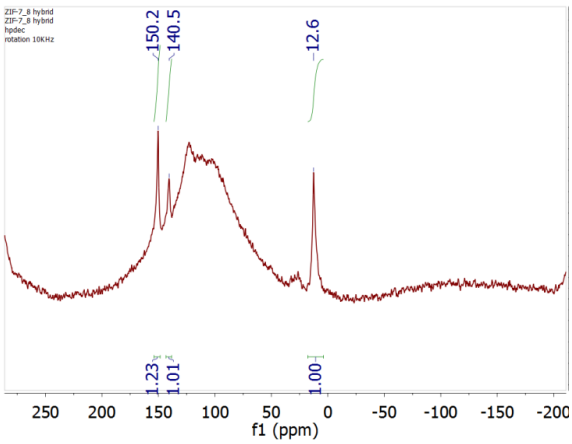

Fig. S9. Quantification of bIm by ^{13}C NMR in ZIF-7/8 (10 %mol bIm) framework.

The amount of bIm in the hybrid ZIF was also calculated with another experiment decoupling the ^{1}H signal in the ^{13}C NMR pattern (see Fig. S9). The resonance at 150.2 ppm corresponds to the contribution of two different carbons, one from mIm (C_{1m}) and another from bIm (C_{1b}). Adjusting the integration area of the peaks whose signal is only due to one carbon atom, thus C_{3m} (12.6 ppm)(mIm) and C_{7b} (140.5 ppm)(bIm) to unit, its integrated area was of 1.23. This means that an 18% of this signal is related to the bIm molecule.

4. Membrane characterization:

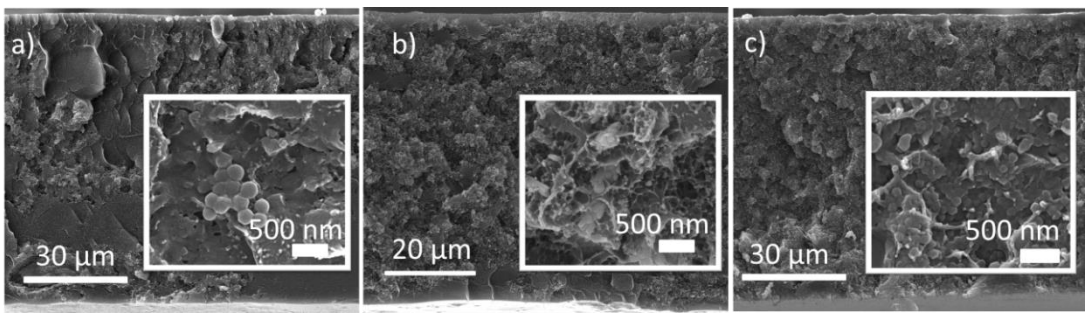

Fig. S10. SEM images of the PBI MMMs containing 10 wt% (a), 20 wt% (b) and 32 wt% (c) of the ZIF-7/8 hybrid (10 wt% mol bIm)

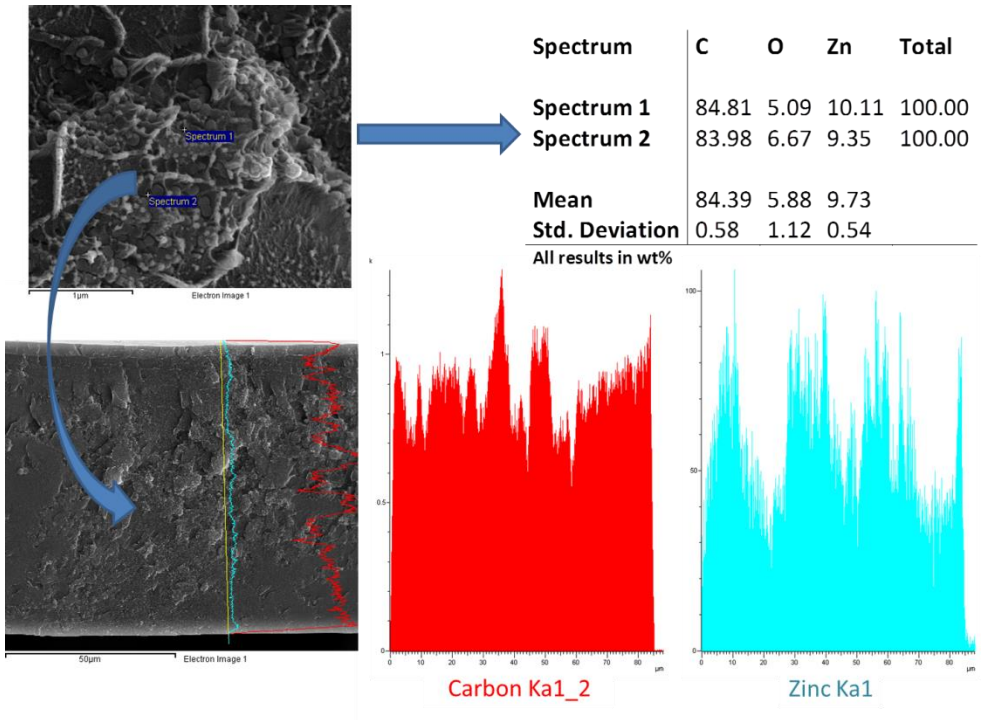

Spectrum	C	O	Zn	Total
Spectrum 1	84.81	5.09	10.11	100.00
Spectrum 2	83.98	6.67	9.35	100.00
Mean	84.39	5.88	9.73	
Std. Deviation	0.58	1.12	0.54	

All results in wt%

Figure S11. SEM-EDX of the cross-section of a 10 wt% loaded Hybrid/PBI MMM where can be distinguished C (in red) and Zn (in blue). Weight % calculated from the whole section in (a) and (b) are included in the table.

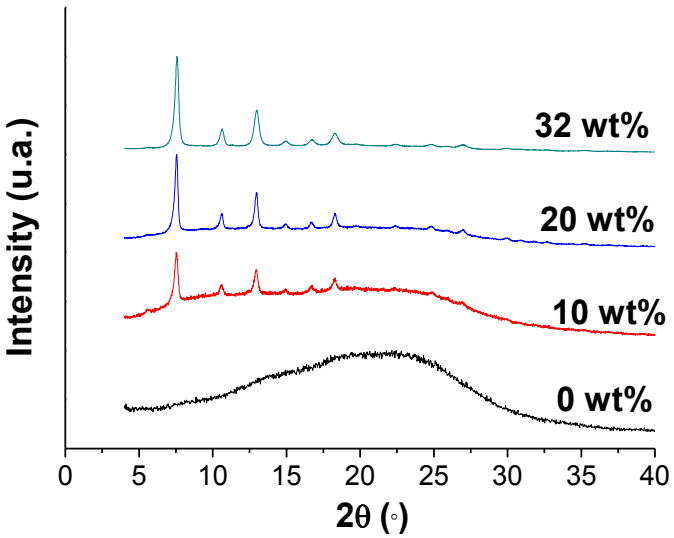

Fig. S12. XRD patterns of the PBI MMMs containing 10 wt% (a), 20 wt% (b) and 32 wt% (c) of the ZIF-7/8 hybrid

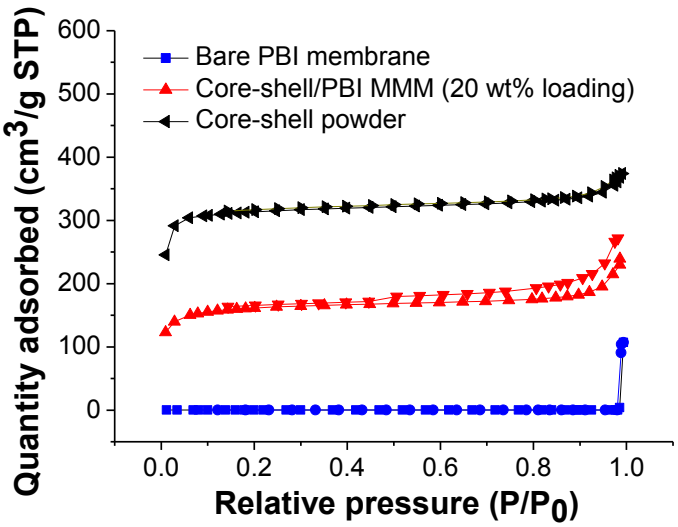

Fig. S13. Empirical N_2 adsorption isotherms of bare PBI membrane, 20 wt% core-shell MMM and activated core-shell (10 % bIm) powder.

5. Membrane performance:

Table S6. Permeation selectivity values of ZIF-7, ZIF-8 and both hybrids at 453 and 523 K.

Structure	T (^{0}C)	Gas	Loading, θ (mol/kg framework)	Self-diffusion, D (10^{-8} m^2s^{-1})	Adsorption selectivity (-)	Diffusion selectivity (-)	Permselectivity (-)
ZIF-8	180	CO_2	0.19	1.59	0.29	4.52	1.31
		H_2	0.06	7.23			
Hybrid (10 % bIm)	180	CO_2	0.21	2.50	0.25	6.92	1.73
		H_2	0.05	17.00			
Hybrid (44% bIm)	180	CO_2	0.22	0.32	0.14	57.79	8.09
		H_2	0.03	18.80			
ZIF-7	180	CO_2	0.47	0.01	0.03	100.67	3.02
		H_2	0.02	0.71			
ZIF-8	250	CO_2	0.12	3.04	0.38	4.00	1.52
		H_2	0.12	3.04			
Hybrid (10 % bIm)	250	CO_2	0.05	12.10	0.34	12.24	4.16
		H_2	0.04	27.80			
Hybrid (44% bIm)	250	CO_2	0.11	0.88	0.26	9.27	2.41
		H_2	0.03	8.08			

Structure	T (^{0}C)	Gas	Loading. θ (mol/kg framework)	Self-diffusion.D (10^{-8} m^2s^{-1})	Adsorption selectivity (-)	Diffusion selectivity (-)	Permselectivity (-)
ZIF-7	250	CO_2	0.18	0.01	0.07	217.14	15.2
		H_2	0.01	2.10			

Table S6 shows the permeation selectivities of ZIF-7, ZIF-8 and the hybrid ZIFs at 180 and 250^{0}C. All ZIFs are H_2 selective since their permselectivity values are over the unit. The H_2/CO_2 adsorption selectivities are in the range of 0.07-0.38 while diffusion selectivities show a huge range from 4 to over 200. Diffusion very strongly favors H_2 over CO_2. Noteworthy that the self-diffusion values are the highest for the hybrid material, especially for H_2, explaining how the PBI MMMs containing hybrid material show such high permeabilities, superior to that of MMMs containing neat ZIFs.

References

1 N. Liédana, A. Galve, C. Rubio, C. Téllez and J. Coronas, *ACS Appl. Mater. Interfaces*, 2012, **4,** 5016-5021.
2 Y.-S. Li, F.-Y. Liang, H. Bux, A. Feldhoff, W.-S. Yang, J. Caro, *Andgew. Chem. Int. Ed.*, 2010, 548–551.
3 D. Dubbeldam, S. Calero, D. E. Ellis and R. Q. Snurr, *Mol. Simul.*, 2016, **42,** 81-101.
4 J. J. G. Sevillano, S. Calero, C. O. Ania, J. B. Parra, F. Kapteijn, J. Gascon and S. Hamad, *J. Phys. Chem. C*, 2012, **117,** 466-471.
5 A. K. Rappé, C. J. Casewit, K. Colwell, W. Goddard Iii and W. Skiff, *J. Am. Chem. Soc.*, 1992, **114,** 10024-10035.
6 S. L. Mayo, B. D. Olafson and W. A. Goddard, *J. Phys. Chem.*, 1990, **94,** 8897-8909.
7 D. Dubbeldam and R. Snurr, *Mol. Simul.*, 2007, **33,** 305-325.
8 X. Wu, J. Huang, W. Cai and M. Jaroniec, *RSC Advances*, 2014, **4,** 16503-16511.
9 P. Zhao, G. I. Lampronti, G. O. Lloyd, M. T. Wharmby, S. Facq, A. K. Cheetham and S. A. Redfern, *Chem. Mater.*, 2014, **26,** 1767-1769.
10 D. Fairen-Jimenez, S. Moggach, M. Wharmby, P. Wright, S. Parsons and T. Duren, *J. Am. Chem. Soc.*, 2011, **133,** 8900-8902.
11 S. Aguado, G. Bergeret, M. P. Titus, V. Moizan, C. Nieto-Draghi, N. Bats and D. Farrusseng, New *J. Chem.*, 2011, **35,** 546-550.
12 J. van den Bergh, C. Gücüyener, E. A. Pidko, E. J. Hensen, J. Gascon and F. Kapteijn, *Chem. Europ. J.*, 2011, **17,** 8832-8840.
13 Q. Song, S. Nataraj, M. V. Roussenova, J. C. Tan, D. J. Hughes, W. Li, P. Bourgoin, M. A. Alam, A. K. Cheetham and S. A. Al-Muhtaseb, *Energy Environ. Sci.*, 2012, **5,** 8359-8369.
14 G. Kumari, K. Jayaramulu, T. K. Maji and C. Narayana, *J. Phys. Chem. A*, 2013, **117,** 11006-11012.
15 M. Cordes and J. Walter, *Spectrochim. Acta, Pt. A: Mol. Spectrosc.*, 1968, **24,** 1421-1435.
16 P. Musto, F. Karasz and W. MacKnight, *Polymer*, 1993, **34,** 2934-2945.
17 P. Christensen and S. Jones, *Polym. Degrad. Stab.*, 2014, **105,** 211-217.
18 D. P. Drolet, D. M. Manuta, A. J. Lees, A. Katnani and G. J. Coyle, *Inorg. Chim. Acta*, 1988, **146,** 173-180.

Chapter 8: Synthesis of ZIF-93/11 hybrid nanoparticles *via* post-synthetic modification of ZIF-93 and their use for H_2/CO_2 separation

J. Sánchez-Laínez, B. Zornoza, A. F. Orsi, M. M. Łozińska, D. M. Dawson, S. E. Ashbrook, S. M. Francis, P. A. Wright, V. Benoit, P. L. Llewellyn, C. Téllez, J. Coronas. Chemistry–A European Journal, 24 (2018), 11211–11219. DOI: 10.1002/chem.201802124. Permission conveyed through Copyright Clearance Center, Inc.

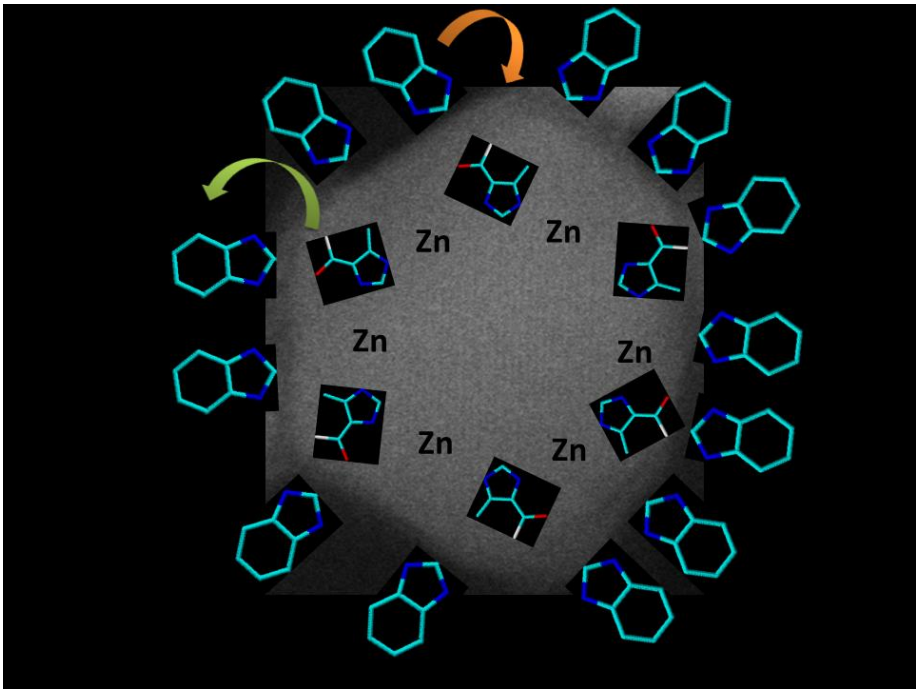

Category:

- Synthesis of new MOFs
- Type of membrane: self-supported MMMs
- Gas separation: pre-combustion CO_2 capture

ChemPubSoc Europe

DOI: 10.1002/chem.201802124

CHEMISTRY A European Journal Full Paper

Gas separation |*Hot Paper*|

Synthesis of ZIF-93/11 Hybrid Nanoparticles via Post-Synthetic Modification of ZIF-93 and Their Use for H_2/CO_2 Separation

Javier Sánchez-Laínez,[a] Beatriz Zornoza,[a] Angelica F. Orsi,[b] Magdalena M. Łozińska,[b] Daniel M. Dawson,[b] Sharon E. Ashbrook,[b] Stephen M. Francis,[b] Paul A. Wright,[b] Virginie Benoit,[c] Philip L. Llewellyn,[c] Carlos Téllez,[a] and Joaquín Coronas*[a]

Abstract: The present work shows the synthesis of nano-sized hybrid zeolitic imidazolate frameworks (ZIFs) with the **rho** topology based on a mixture of the linkers benzimidazole (bIm) and 4-methyl-5-imidazolecarboxaldehyde (4-m-5-ica). The hybrid ZIF was obtained by post-synthetic modification of ZIF-93 in a bIm solution. The use of different solvents, MeOH and *N*,*N*-dimethylacetamide (DMAc), and reaction times led to differences in the quantity of bIm incorporated to the framework, from 7.4 to 23% according to solution-state NMR spectroscopy. XPS analysis showed that the mixture of linkers was also present at the surface of the particles. The inclusion of bIm to the ZIF-93 nanoparticles improved the thermal stability of the framework and also increased the hydrophobicity according to water adsorption results. N_2 and CO_2 adsorption experiments revealed that the hybrid material has an intermediate adsorption capacity, between those of ZIF-93 and ZIF-11. Finally, ZIF-93/11 hybrid materials were applied as fillers in polybenzimidazole (PBI) mixed matrix membranes (MMMs). These MMMs were used for H_2/CO_2 separation (at 180 °C) reaching values of 207 Barrer of H_2 and a H_2/CO_2 selectivity of 7.7 that clearly surpassed the Robeson upper bound (corrected for this temperature).

Introduction

Zeolitic imidazolate frameworks (ZIFs) are crystalline structures in which imidazolate linkers join tetrahedral Zn^{II} or Co^{II} centers, building metal-imidazole-metal angles close to 145°, similar to the Si-O-Si angles typically found in zeolites. They are a class of metal-organic frameworks (MOFs) with high porosity, and good thermal and chemical stability. A large number of potential applications have been developed with them, such as gas sorption,[1] gas separation,[2] drug delivery,[3] and catalysis.[4]

A significant number of ZIFs have been reported since the first frameworks were discovered by Yaghi's group in 2006.[5] Among them, new hybrid structures with a combination of different linkers in the same framework have been obtained. Preparation of these mixed linker, hybrid structures of ZIFs by solvothermal synthesis can be found in the literature. Thompson et al.[6] reported the synthesis for the ZIF-7/90 and ZIF-7/8 hybrids. In their work, the combined frameworks were obtained by reactions in DMF/MeOH mixtures with fixed amounts of the metal source and both linkers (benzimidazole (bIm) and carboxaldehyde-2-imidazole for ZIF-7/90, and bIm and 2-methylimidazole for ZIF-7/8). The ZIF-7/8 hybrid has also been synthesized using Co^{II} as the metal source (ZIF-9/67).[7] The resulting hybrid ZIFs contained a combination of the different linkers in different proportions. Furthermore, the series ZIF-68 to ZIF-70,[8] ZIF-78 to ZIF-82,[9] and ZIF-300 to ZIF-302[10] comprise hybrid ZIFs with mixtures of linkers in their structure (2-methylimidazole or 2-nitroimidazole with benzimidazole derivatives). The latter series has the **cha** topology and the other two sets have the **gme** topology.

The direct synthesis of hybrid frameworks may not be always possible. Problems arising from limited linker solubility, chemical and thermal stability, or functional group compatibility can make the direct synthesis of hybrid ZIFs difficult. Post-synthetic modification routes are, therefore, a useful alternative approach. Through this technique, materials of high complexity and functionality can be obtained providing that the MOF is not destroyed during the chemical reaction. Post-synthetic modification of MOFs can be classified into three types: covalent, dative, and post-synthetic deprotection.[11] Covalent post-synthetic modification involves the use of a reagent to modify a component of the original MOF (generally the organic linker)

[a] *J. Sánchez-Laínez, Dr. B. Zornoza, Prof. Dr. C. Téllez, Prof. Dr. J. Coronas*
Chemical and Environmental Engineering Department
Instituto de Nanociencia de Aragón(INA)
Universidad de Zaragoza
50018 Zaragoza (Spain)
E-mail: coronas@unizar.es

[b] *Dr. A. F. Orsi, Dr. M. M. Łozińska, Dr. D. M. Dawson, Prof. S. E. Ashbrook, Dr. S. M. Francis, Prof. Dr. P. A. Wright*
EaStCHEM School of Chemistry
University of St. Andrews
St. Andrews, Fife KY16 9ST (United Kingdom)

[c] *Dr. V. Benoit, Dr. P. L. Llewellyn*
Aix Marseille University, CNRS, MADIREL, UMR 7246
13397 Marseille (France)

Supporting information and the ORCID identification number(s) for the author(s) of this article can be found under: https://doi.org/10.1002/chem.201802124.

to form a new covalent bond. In dative post-synthetic modification, the reagent modifies the MOF forming a dative bond instead, and usually a new linker or a metal source is incorporated to the framework in this manner. Finally, in post-synthetic deprotection the destruction of a target chemical bond inside an intact MOF results in the in situ formation of a linker with new chemical functionality.

Post-synthetic modification has been successfully applied for many MOFs, including: IRMOF-3,[12] MIL-53(Al),[13] MIL-53(Al)-NH_2,[14] MIL-101(Fe)-NH_2,[15] MIL-101(Cr),[16] UiO-66-NH_2,[17] UiO-66-Br,[18] and HKUST-1.[19] Post-synthetic modifications of ZIFs have also been demonstrated. Examples include the conversion of SIM-1 (also known as ZIF-94) to ZIF-91 and ZIF-92 (using $NaBH_4$ and ethanolamine, respectively),[20] the conversion of SIM-1 to SIM-2(C_{12}) using dodecylamine,[21] and the transformation of SIM-1 to ZIF-93 upon post-synthetic functionalization with amines.[22] Furthermore, Liu et al.[23] modified ZIF-8 through a shell-linker-exchange reaction in MeOH with different imidazole-like linkers, obtaining a core–shell structure with improved hydrothermal stability relative to the parent material. Very recently our group also developed the synthesis of ZIF-7/8 core–shell materials by post-synthetic modification.[24] These modification results of ZIFs represent an interesting way of controlling the particle size, chemical function, adsorption property, and pore size.

In the context of gas separation, it is of great importance that the framework has narrow porosity, especially when operating at high temperature, at which adsorption capacities are almost negligible, and the sieving process gains importance. This is the case for H_2/CO_2 mixtures, typically obtained at high pressure and temperature during hydrogen production via steam reforming of methane. One of the most interesting ZIFs for this gas separation is ZIF-11 (**rho** framework of Zn^{II} centers connected by bIm units), which has small pore windows of 0.30 nm diameter that are intermediate between the kinetic diameters of H_2 and CO_2 (0.29 and 0.33 nm, respectively). Simulation results have shown that this ZIF can achieve a H_2/CO_2 selectivity of 262.[25] ZIF-93 is another Zn^{II}-based **rho**-type framework composed of 4-methyl-5-imidazolecarboxaldehyde (4-m-5-ica) organic linkers with pore size 0.36 nm[26] and a high CO_2 uptake.[27]

The removal of CO_2 from H_2 is a critical requirement for hydrogen to be a sustainable energy system, as well as for the minimization of environmental impact, since it is a well-known pollutant. Among the different technologies for H_2/CO_2 separation, membrane technology is an alternative to other established methods such as amine-based absorption, pressure-swing adsorption, or cryogenic distillation.[28] However, this approach faces the challenge that both molecules have a similar kinetic diameter. The use of mixed matrix membranes (MMMs) is a widespread approach to enhance the H_2 selectivity of polymeric membranes.[29] MMMs comprise dispersions of generally porous fillers into a polymeric phase. The resulting membrane combines the advantageous properties of both phases: the good processability of polymers and the highest gas separation capacity of the filler. MOFs are particularly suitable as fillers, owing to their partial organic nature, they show a better affinity for the polymeric chains than wholly inorganic fillers. In addition, the MOF-polymer interface interactions are easier to control in order to avoid non-selective voids between the phases. Thus, MOFs have often been used in MMMs over the last few years.[2a]

The use of polybenzimidazole (PBI) membranes for the separation of H_2/CO_2 mixtures has been widely reported.[30] PBI is a polymer with high thermal stability, good chemical resistance, impressive compression strength, and high intrinsic H_2/CO_2 selectivity. However, its major drawbacks are low permeability and brittleness.[31] Several types of ZIFs, such as ZIF-7,[30b] ZIF-8,[32] ZIF-11,[30c,33] and ZIF-90[34] have been embedded in the PBI continuous phase. However, to date there have been no reports of the use of ZIF-93 for this purpose.

In the present work we show the synthesis of a ZIF-93/11 hybrid material, prepared from ZIF-93 nanoparticles following a post-synthetic modification route in different solvents. The post-synthetic method allowed a better control of the particle size and relative proportions of bIm and 4-m-5-ica than a direct synthesis. The nanoparticles were characterized by several techniques to study their physical and chemical properties. Finally, two types of hybrids were embedded in a commercial PBI continuous phase in the form of MMMs that were tested at high temperature (180 °C) to evaluate their performance in the separation of the H_2/CO_2 mixture.

Results and Discussion

ZIF characterization

The presence of both 4-methyl-5-imidazolecarboxaldehyde (4-*m*-5-ica) and benzimidazole (bIm) linkers inside the ZIF-93/11 framework structure, as well as their proportion, was determined by solution-state NMR analysis. Solution-state ^{1}H NMR spectra (Figures S1 and S2 in Supporting Information) of the digested ZIF-93/-11 hybrid materials confirmed that both linkers were present. Integration of signals of the aldehyde proton (H-1) of 4-m-5-ica and the imidazole ring proton (H-4) of bIm resulted in linker ratios of 3.3:1 and 12.5:1 for the hybrid materials synthesized in *N*,*N*-dimethylacetamide (DMAc) and MeOH, respectively (Table S1). The hybrid material synthesized in DMAc has more bIm linker present (23%) compared to the sample synthesized in MeOH (7.4%). This agrees with a higher solubility of the outgoing ligand (4-m-5-ica) in DMAc than in MeOH. To prove this, the calculated value of the solubility parameter *Ra* of 4-m-5-ica in DMAc is 6.6, whereas it is 14.9 in MeOH (both calculated with the Equation S1 using the Hansen Solubility Parameters (HSP) of Table S2).[35]

Solid-state ^{13}C CP MAS NMR spectra (Figure 1) were acquired for ZIF-93, ZIF-11, and the two hybrid materials synthesized in DMAc and MeOH solvents. Prior to analysis, ZIF-93, ZIF-11, and the hybrid material synthesized in DMAc were washed in MeOH (1 day) to remove residual solvents. The carbons of the 4-m-5-ica linker of ZIF-93 and the bIm linker of ZIF-11 are present in the spectra of the hybrid materials. The intensity of the bIm carbon signals in the hybrid material synthesized in MeOH are lower than those in the material synthesized in DMAc,

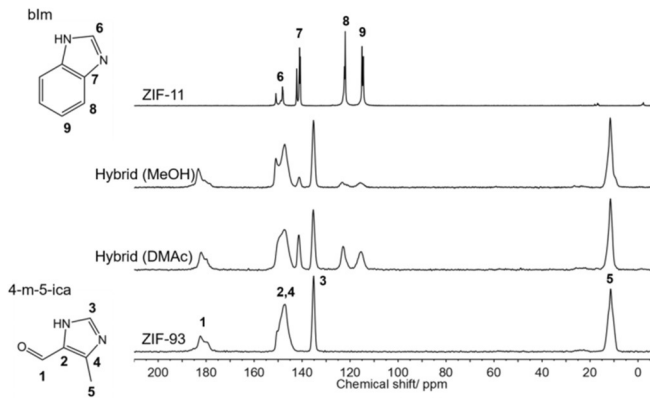

Figure 1. Solid-state ^{13}C CP MAS NMR spectra of ZIF-93 (bottom), hybrid materials synthesized in DMAc and MeOH (middle), and ZIF-11 (top). ZIF-93, ZIF-11 and hybrid synthesized in DMAc were washed in MeOH and dried prior to analysis.

which agrees well with the results from solution-state ^{1}H-NMR spectroscopy. The linewidths for the ^{13}C signals in ZIF-11 have high resolution, indicating ordered linkers in the framework. ZIF-93 has much broader ^{13}C signals suggesting orientational disorder of the linkers in the framework. The bIm signals in the hybrid materials are broadened compared to those in ZIF-11, suggesting that the disorder of the 4-m-5-ica linkers also affects the ZIF-11 areas of the hybrid materials. This confirms that the two linkers are within the same particles, and that there is not a sharp border separating both ZIF structures.

XPS analysis was performed to study the external surface of ZIF-93, ZIF-11, and the hybrid materials synthesized in DMAc (that with the highest concentration of bIm according to the NMR spectra). XPS is a surface sensitive technique, probing 1–12 nm thickness. The XPS survey scans, as well as the N 1s component region of the XPS spectra, in Figure 2 showed little difference between the surfaces of ZIF-93, ZIF-11, and the hybrid material. This agrees with the chemical similarity of both imidazolate ligands and with the bIm minority presence in both MeOH and DMAc hybrids (7.4–23%, as seen above).

Thermogravimetric analyses (TGA) in flowing air were used to elucidate the thermal stability of the different materials prepared in this work: ZIF-93, ZIF-11, and both hybrid materials. The results can be seen in Figure 3. ZIF-93 shows four clear decomposition steps at 366, 484, 554, and 612 °C corresponding to the progressive degradation of its 4-m-5-ica linker (ZIF-93 is highly hygroscopic and the mass loss below 200 °C corresponds to the loss of the ≈20 wt.% adsorbed water). ZIF-11 shows a higher onset temperature (576 °C), due to the greater thermal stability of bIm. The hybrid material shows an intermediate behavior, with two decomposition steps corresponding to the coexistence of 4-m-5-ica and bIm in the framework structure, as previously demonstrated by NMR spectroscopy. However, the onset temperatures are slightly different to those of the neat ZIFs (384 vs. 366 °C for 4-m-5-ica and 498 vs. 576 °C for bIm). The 4-m-5-ica in the hybrid structure is, therefore, more stable than that in ZIF-93, whereas the bIm is more stable in ZIF-11 than in the hybrid material. Moreover, the degradation of the hybrid ZIF synthesized in MeOH is more similar

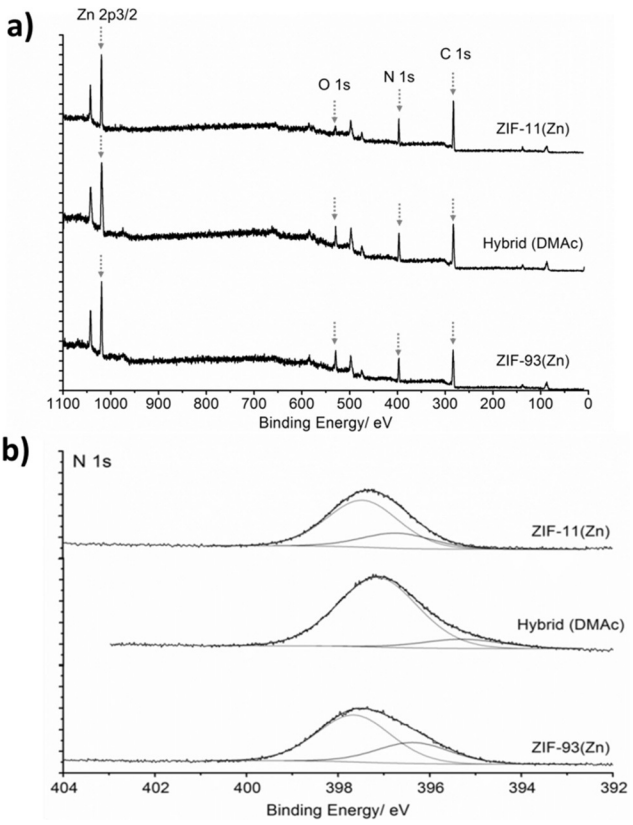

Figure 2. a) XPS survey scans of ZIF-93, the hybrid material synthesized in DMAc and ZIF-11. b) The N 1s component region of the XPS spectra of ZIF-93, the hybrid material synthesized in DMAc, and ZIF-11.

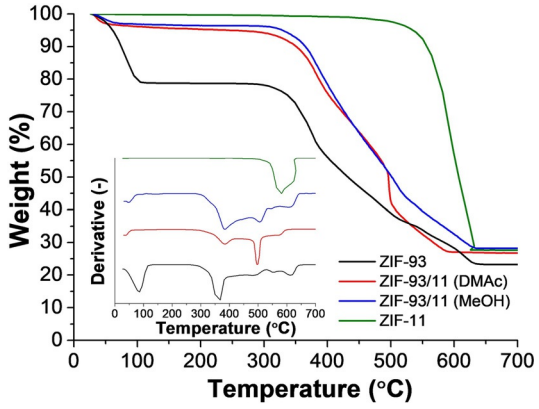

Figure 3. TGA curves and derivatives (inset) in flowing air. From bottom to top: ZIF-93 (black), ZIF-93/11 hybrid (DMAc) (red), ZIF-93/11 hybrid (MeOH) (blue), and ZIF-11 (green).

to that of ZIF-93, in agreement with low amount of bIm in this hybrid. In any event, the existence of a continuous mass loss process that does not correspond to the superposition of the TGA curves of the two neat ZIFs is strongly indicative of the existence of a unique hybrid phase, rather than a physical mixture of ZIF-93 and ZIF-11. Moreover, the weight loss regarding water adsorption (5 wt.%) is much lower than that in ZIF-93, which means that a small amount of bIm (7.4% for the MeOH hybrid) is enough to somehow increase the hydrophobicity.

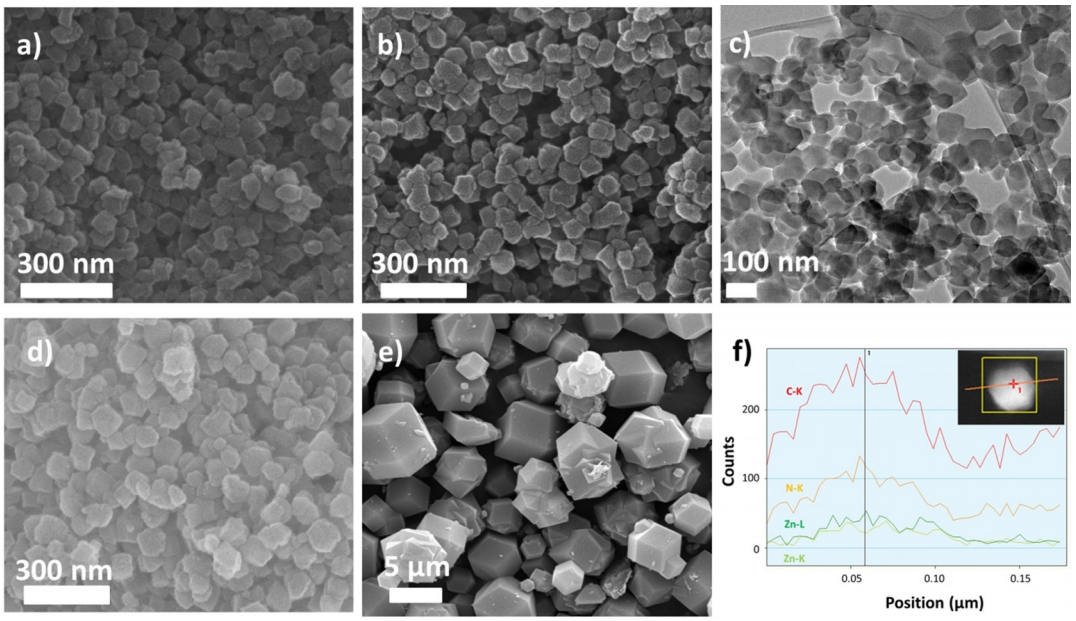

Figure 4. SEM images of a) ZIF-93, b) ZIF-93/11 hybrid material (DMAc), d) ZIF-93/11 hybrid (MeOH), and e) ZIF-11. TEM image of c) ZIF-93/11 hybrid material (DMAc) and f) TEM/EDX analysis of a single ZIF-93/11 hybrid nanoparticle synthesized in DMAc.

Figures 4a–d show the SEM/TEM images of ZIF-93 and ZIF-93/11 hybrid nanoparticles, whereby the similar morphology and particle sizes are observed. A narrow particle size distribution (around 72–73 nm for all the three ZIFs according to the cumulative distribution graph of Figure S3) can be observed, suggesting the existence of just one phase (i.e., a hybrid material, instead of a physical mixture of ZIF-93 and ZIF-11). Figure 4e shows the SEM image of the micro-sized ZIF-11 resulting from the chosen synthetic route. EDX analysis was performed on a single nanoparticle of ZIF-93/11 synthesized in DMAc, revealing, upon discounting the composition variation due to particle geometry, that the Zn and N amounts remain constant across the particle width (Figure 4f).

The XRD patterns of the ZIF-93/11 hybrid material, ZIF-11, and ZIF-93 are shown in Figure S4 of the Supporting Information for comparison. Both ZIF-93 and ZIF-11 have a rhombohedral topology, showing similar diffractograms, making distinction for the hybrid material by XRD difficult. No characteristic features are observed for the hybrid framework (synthesized in DMAc), which exhibits the same crystalline structure as ZIF-93. However, the ZIF synthesized in MeOH shows changes in some of the signal intensities. The peak at 4.3° (2θ) reduced its intensity by 90%, whereas the peak at 7.4° (2θ) increased in intensity, and was the most intense signal in the pattern.

The IR spectra of ZIF-93, ZIF-11, and the hybrid materials are shown in Figure S5. ZIF-11 shows very intense bands in the 600–1800 cm^{-1} range. The peak at 1222 cm^{-1} is caused by the in-plane C–H deformation of the disubstituted benzimidazole, whereas the peak at 902 cm^{-1} is due to the C–H out-of-plane bending of a single hydrogen in substituted benzene rings. Finally, the signal at 738 cm^{-1} is related to the imidazole in-plane ring bending.[36] ZIF-93 shows an intense band between 3000–3690 cm^{-1}, corresponding to the adsorbed water. Moreover, peaks at 1655 and 1629 cm^{-1} are related to the aldehyde group stretches of the 4-m-5-ica linker.[27] The spectra of the hybrid materials exhibit a combination of all the signals observed for ZIF-93 and ZIF-11, although some differences to the neat ZIFs spectra can be identified. Firstly, the vibration modes in the 3000–3690 cm^{-1} region have disappeared, showing that the hybrid framework is not as hygroscopic as ZIF-93. Secondly, the peak at 1629 cm^{-1} is not as intense. When comparing the spectra of both hybrid materials, the band at 738 cm^{-1} is less intense in the sample synthesized in MeOH perhaps as a consequence of the lower amount of bIm in the material (see Table S1).

N_2 isotherms at −196 °C were measured for ZIF-93 and the ZIF-93/11 hybrid material (synthesized in DMAc; it had the highest amount of bIm) to study their porosity (Figure 5a). ZIF-11 was deemed non-porous to N_2 (−196 °C) in this relative pressure range, especially since it has narrow microporosity and a pore aperture size smaller than the kinetic diameter of N_2 (0.36 nm).[37] ZIF-93 shows a N_2 uptake of around 290 cm^3 (STP) g^{-1} at $P/P_0 = 1$ and a BET specific surface area of 980 $m^2 g^{-1}$. The ZIF-93/11 hybrid material showed slightly inferior values (274 cm^3 (STP) g^{-1} and 926 $m^2 g^{-1}$, respectively). According to their shape, both isotherms can be classified as Type I, typical of microporous materials. The inclusion of bIm in the ZIF-93 framework structure has very little effect on the amount of N_2 adsorbed relative to ZIF-93. This suggests that a perfect core of ZIF-11 was not obtained, in agreement with the lack of a sharp border separating both ZIF structures, mentioned above when dealing with the NMR characterization. Regarding the CO_2 adsorption at 0 °C (Figure 5b), ZIF-93 shows an uptake of 2.84 mmol g^{-1}, which is 39% higher than that of ZIF-11. For the ZIF-93/11 hybrid material, only a slight reduction in the amount of CO_2 adsorbed was observed (≈2% rela-

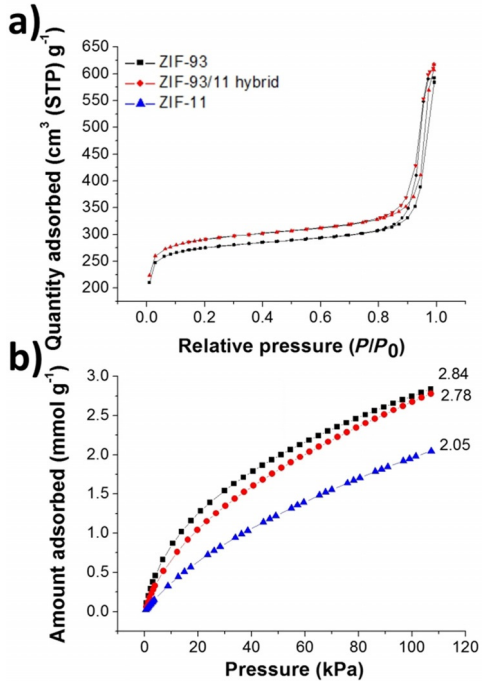

Figure 5. a) N_2 (−196 °C) and b) CO_2 (0 °C) adsorption isotherms of ZIF-93 (black), ZIF-11 (blue), and ZIF-93/11 hybrid material (synthesized in DMAc, red). Note that the N_2 adsoprtion of ZIF-11 is negligible.

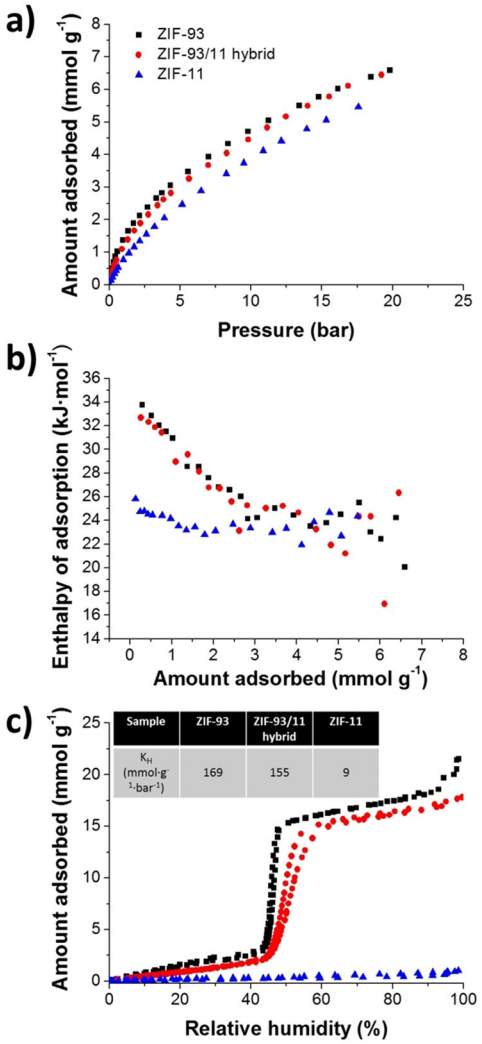

Figure 6. CO_2 adsorption at 30 °C a) of ZIF-93 (black), ZIF-93/11 hybrid material (synthesized in DMAc) (red) and ZIF-11 (blue); b) CO_2 adsorption enthalpies, and c) H_2O adsorption at 25 °C.

tive to ZIF-93). These results are further confirmed for the CO_2 calorimetry measurements at 30 °C, reaching higher pressures to explore the adsorption capacities of the frameworks in greater detail (Figure 6a). In this case the ZIF-93/11 hybrid material showed intermediate CO_2 uptakes (1.37 mmol g^{-1} at 1 bar and 4.43 mmol g^{-1} at 10 bar) between those of the neat ZIFs. Interestingly, the calorimetry signal can be used to calculate the enthalpies of adsorption and the two pure ZIF samples show quite different behaviors (see Figure 6b). The initial enthalpy observed with ZIF-93 is around 35 kJ mol^{-1} and decreases to around 25 kJ mol^{-1} and this can be interpreted by a slightly homogeneous surface with some different sorption centers. The ZIF-11 however, shows a flatter energy profile in the region of 25 kJ mol^{-1}, suggesting a more homogeneous surface. The enthalpy signal observed with the hybrid material closely resembles that of the ZIF-93, suggesting that this phase is dominant with respect to the CO_2.

Water adsorption analyses at 25 °C were performed on ZIF-93, ZIF-11, and the ZIF-93/11 hybrid material (Figure 6c). Whereas the pure ZIF-11 shows very little uptake throughout the experiment, the pure ZIF-93 is clearly a hygroscopic material, showing a water uptake over 20 mmol g^{-1} at a relative humidity of 95%. The Henry constants, obtained at low coverage, give an idea of the strength of interaction between the water and the various samples and again, this highlights that the ZIF-93 (k_H = 169 mmol g^{-1} bar^{-1}) is a far more hydrophilic material for water when compared to pure ZIF-11 (k_H = 9 mmol g^{-1} bar^{-1}). There is a marked, and quite sharp, pore filling step observed with the ZIF-93 in the region of RH = 40–50%. The hybrid material presents a water isotherm which resembles more the ZIF-93 material, however, with lower overall uptake and Henry constant (k_H = 155 mmol g^{-1} bar^{-1}), even though the presence of hydrophobic bIm linker was as high as 23%. The pore filling step observed with the hybrid material seems to be slightly shifted to higher relative humidity and takes place over a slightly larger domain of relative humidity. These observations can be related to the influence of the incorporated bIm and are in agreement with TGA and FTIR analyses (Figure 3 and S5, respectively).

MMMs characterisation and gas separation performance

In order to test the gas separation capacity of the different hybrid frameworks, PBI MMMs with 20 wt.% loading were prepared with the ZIF-93/11 hybrid materials synthesized in DMAc and MeOH. This 20 wt.% loading was in agreement with previous analogous MMMs with ZIFs.[24,33] ZIF-93 and ZIF-11 MMMs were also prepared for comparison. The morphology of the cross-section of these membranes is shown in Figure 7 (the whole characterization of ZIF-11-PBI MMMs can be found in a

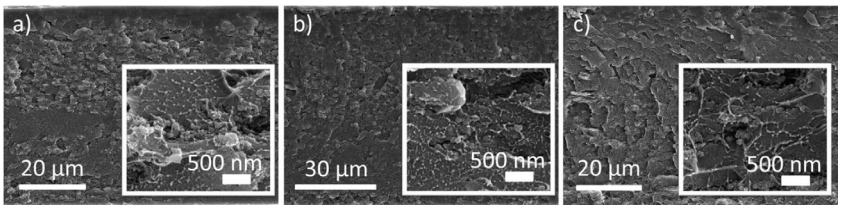

Figure 7. SEM images of the cross-sections of PBI membranes containing 20 wt.% loading of a) ZIF-93, b) ZIF-93/11 hybrid material (synthesized in DMAc), and c) ZIF-93/11 hybrid material (synthesized in MeOH).

previous work),[33] where a good dispersion and filler-polymer compatibility are observed.

All the membranes were tested at 180 °C and 3 bar of feed pressure for the separation of an equimolar H_2/CO_2 mixture, and the results in the Robeson-type graph are shown in Figure 8. As the Robeson upper bound was originally defined

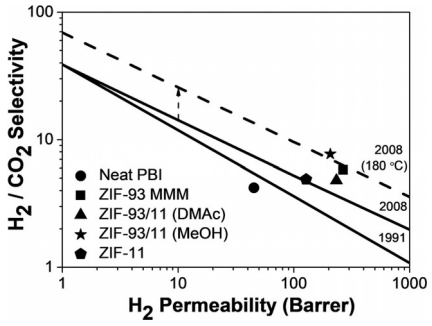

Figure 8. Gas separation performance of bare PBI membranes and 20 wt.% loaded MMMs containing ZIF-93, ZIF-11, and the ZIF-93/11 hybrid materials synthesized in DMAc and MeOH. The continuous lines correspond to the original Robeson upper bounds of 1991[39] and 2008[40] and the dashed line corresponds to the upper bound calculated for 180 °C.

at 35 °C, a correction for the elevated temperature was applied to acquire a more accurate bound. The upper bound shifts with the temperature according to Equation (1):[38]

$$\alpha_{H_2/CO_2} = \frac{k \cdot e^{\gamma/T}}{P_{H_2}^{n}} \quad (1)$$

where γ indicates the effect of temperature (in K) on the solubility and diffusivity of H_2 and CO_2, and k and n are the parameters that define the Robeson bound equation for this gas mixture (229 Barrer and 0.429, respectively). For H_2 and CO_2 in polymers, γ has a value of -543 K.[38] Increasing the temperature increases the upper bound, but has no effect on the selectivity-permeability slope.

For all of the MMMs the gas separation performances improved in comparison with those of the bare PBI membranes. Comparing the MMMs containing pure ZIFs, the ZIF-11 MMMs showed a H_2 permeability of 128 Barrer and a H_2/CO_2 selectivity of 4.9, whereas ZIF-93 MMMs were better (267 Barrer and 5.8, respectively). The MMMs containing the hybrid materials synthesized in MeOH had the highest gas separation performance reaching H_2 permeability values of 207 Barrer and 7.7 for H_2/CO_2 selectivity, which surpasses the Robeson upper bound, even when corrected for 180 °C. The larger amount of bIm in the hybrid material synthesized in DMAc may have led to the reduced performance of the corresponding MMM, since ZIF-93 was shown to have a better H_2/CO_2 separation than ZIF-11. In other words, only a small amount of bIm (7.4% of total ligand achieved with MeOH treatment) is enough to improve the compatibility with the polymer (as in case of ZIF-11-PBI MMMs)[33] and somehow constrain the microporosity of the ZIF, while maintaining a high value of open porosity. All this together makes the ZIF-93/11 hybrid material a suitable filler for the application of MMMs in the H_2/CO_2 mixture separation.

Finally, the industrial application of these membranes for H_2/CO_2 separation would involve some content of water in the feed stream. This water may cause competition for permeation paths through the membrane, decreasing the permeability of H_2. Future work would apply permeation tests with high water content in the feed, to quantify whether the high water activity affects the membrane separation performance.

Conclusions

Two hybrid frameworks (with 7.4 and 23% bIm) sharing features of ZIF-93 and ZIF-11 have been obtained through the post-synthetic modification of ZIF-93 nanoparticles in MeOH and DMAc. The use of these two solvents leads to a different proportion of bIm and 4-m-5-ica in the final hybrid material, which was quantified by solution-state ^{1}H NMR spectroscopy. The presence of both linkers was also verified by TGA analyses, proving that the inclusion of bIm led to a stabilization of the hybrid material. XPS analysis determined that both linkers were present on the surface of the nanoparticles, disproving the hypothesis of a core–shell type structure. The hybrid nanoparticles (72–73 nm) showed similar diffraction patterns to those of ZIF-93 and ZIF-11, and slight differences in their FTIR spectra, according to the proportion of the two linkers in their structures. N_2 and CO_2 adsorption experiments showed a reduction in the adsorption capacity of the hybrid materials related to the presence of bIm in their structure. Similar results were acquired for the water adsorption capacities, since the addition of bIm increases the hydrophobicity of the material. Both ZIF-93/11 hybrid materials were used as fillers in polymer PBI mixed matrix membranes that were tested for the separation of H_2/CO_2 mixtures at high temperatures. Loadings of 20 wt.% for the hybrid materials showed better results

(207 Barrer of H_2 and a H_2/CO_2 selectivity of 7.7 at 180 °C) than PBI membranes containing ZIF-93 and ZIF-11 at the same loadings.

Experimental Section

Chemicals: 4-Methyl-5-imidazolecarboxaldehyde (4-m-5-ica, $C_5H_6N_2O$, Sigma-Aldrich, 99%), benzimidazole (bIm, $C_7H_6N_2$, 98%), zinc acetate dihydrate ($Zn(CH_3COO)_2{\cdot}2H_2O$), *N*,*N*-dimethylacetamide (DMAc, ≥99.5%), ammonium hydroxide (NH_4OH, 28–30% aqueous solution), chloroform (anhydrous), toluene (≥99.5%), and trimethylamine (≥99.5%) were purchased from Sigma Aldrich. Methanol (MeOH, HPLC grade) was purchased from Scharlau. Commercial PBI solution comprising 26 wt.% PBI, with 1.5 wt.% LiCl as stabilizer, in DMAc was purchased from PBI Performance Products.

MOF synthesis: $Zn(CH_3COO)_2{\cdot}2H_2O$ (1.76 g, 8 mmol) was dissolved (room temperature, 15 min) in MeOH (80 mL). The linker 4-m-5-ica (1.76 g, 16 mmol) was dissolved (room temperature, 15 min) in water (200 mL). The linker/water solution was added to the Zn precursor/methanol solution followed by dropwise addition (room temperature) of trimethylamine (0.8 mL). The mixture gradually turned from clear to cloudy white. The mixture was stirred and heated (80 °C, 2 h), then allowed to cool to room temperature (15 min). The product was collected by centrifugation (15000 rpm, 20 min) and washed with water for eight cycles. The white powder product was dried in air (room temperature, overnight). The resulting nanoparticles of ZIF-93 were ≈73 nm wide.

The ZIF-93/11 hybrid material was prepared via post-synthetic modification of ZIF-93 in two different solvents: DMAc and MeOH. For the first synthesis, bIm (1.25 g, 11 mmol) was dissolved in DMAc (30 mL) and ZIF-93 (0.2 g, 0.7 mmol) was added to the solution. The suspension was stirred (30 °C, 3 days). The solid was collected by centrifugation, washed with MeOH under reflux (18 h), cooled, collected by centrifugation again and then dried (110 °C, overnight). For synthesis in MeOH, bIm (1.25 g, 11 mmol) was dissolved in a mixture of MeOH (6.4 g, 400 mmol), toluene (9.2 g, 100 mmol), and NH_4OH (2.4 g, 40 mmol). Then, ZIF-93 (0.2 g, 0.7 mmol) was added to the solution. The suspension was stirred (30 °C, 3 h) and the solid was collected by centrifugation and washed three times with MeOH. This solid was then dried (110 °C, overnight).

ZIF-11 was also prepared for comparison following a literature method.[41] The linker, bIm (0.24 g, 2 mmol) was dissolved in a mixture of MeOH (6.4 g, 400 mmol), toluene (9.2 g, 100 mmol) and NH_4OH (2.4 g, 40 mmol). $Zn(CH_3COO)_2{\cdot}2H_2O$ (0.22 g, 1 mmol) was dissolved in methanol (3.2 g, 200 mmol). Both solutions were mixed and stirred (room temperature, 3 h). The resulting solid was collected by centrifugation, washed with MeOH three times for the complete removal of toluene, and dried (100 °C, overnight). This synthesis results in micro-sized particles, which are larger than those of ZIF-93.

MMM preparation: The required amount of ZIF (ZIF-93/11 hybrid, ZIF-11, or ZIF-93) was weighed for a 20 wt.% membrane loading. The corresponding amount of PBI solution (15 wt.% in DMAc to reduce the viscosity) was added and the resulting solution was stirred overnight. The casting solution was subjected to three cycles of alternating stirring and sonication (90 min total treatment time) and then cast into Petri dishes (kept level) inside an oven (90 °C). The Petri dishes were left uncovered overnight to allow the evaporation of the solvent. Subsequently, the membranes were peeled off from the Petri dishes and washed with water (80 °C, 4 h) and then dried in an oven (100 °C, 24 h).

The membrane thicknesses were measured with a Digimatic micrometer (measurement range 0–30 mm with an accuracy of ±1 μm). Nine equally distributed sites on each membrane were measured and the arithmetic mean was taken as the membrane thickness. The MMMs obtained in this work had a thickness of 78±2 μm. For permeation testing of the membranes, circular areas of 3.14 cm^2 were cut from the films.

Characterization of samples: Powder X-ray diffraction (XRD) patterns of the MOFs were acquired using a Rigaku D-Max X-ray diffractometer with a copper anode and a graphite monochromator to select $Cu_{K\alpha}$ radiation ($\lambda = 1.540$ Å), taking data from 2.5 to 40° (2θ) at a scan rate of 0.03° s^{-1}. Thermogravimetric analyses (TGA) were carried out using a Mettler Toledo TGA/STDA 851e. Samples (5 mg) were placed in 70 μL alumina pans, which were heated in an air flow from 30 to 900 °C at a heating rate of 10 °C min^{-1}. Scanning electron microscopy (SEM) images of the ZIFs and membranes were obtained using an Inspect F50 model scanning electron microscope (FEI), operated at 20 kV. Cross-sections of membranes were prepared by freeze-fracturing after immersion in liquid nitrogen, and subsequent coating with Pt. Transmission electron microscopy (TEM, FEI TECNAI F30) images of the ZIF samples were acquired at an acceleration voltage of 300 kW. The TEM, fitted with a SuperTwin® lens allowing a point resolution of 1.9 Å, was also used for EDS (X-ray Microanalysis). Samples were prepared by placing one drop of a dilute suspension of powder in MeOH on a holey carbon-coated copper grid (300 mesh) and allowing the solvent to evaporate (room temperature). Particle size was obtained using ImageJ 1.49b software, where at least 60 particles were counted for each sample. Fourier transform infrared (FTIR) spectroscopy was performed on a Bruker Vertex 70 FTIR spectrometer equipped with a DTGS detector and a Golden Gate diamond ATR accessory. Both spectra were recorded by averaging 40 scans in the 4000–600 cm^{-1} wavenumber range at a resolution of 4 cm^{-1}. Nitrogen adsorption/desorption isotherms were obtained using a Micromeritics Tristar 3000 surface area and porosity analyzer, after previously degassing the samples (200 °C, vacuum, 8 h). CO_2 adsorption isotherms were measured using a volumetric adsorption analyzer (Micromeritics ASAP 2020) at 0 °C up to 120 kPa after degassing (200 °C, 8 h). The N_2, CO_2, and He gases used in the experiments were 99.9995% pure.

Solution-state ^1H nuclear magnetic resonance (^1H NMR) spectra were acquired using a Bruker Avance 500 (500 MHz) spectrometer at ambient temperature. The samples were digested in deuterated DMSO, with the addition of concentrated HCl (37%) to aid dissolution. Chemical shifts (δ) are reported in parts per million (ppm) relative to tetramethylsilane (TMS). Solid-state ^{13}C magic angle spinning (MAS) NMR spectra were recorded on a Bruker Avance III spectrometer equipped with a 9.4 T wide-bore superconducting magnet (Larmor frequencies of 400.13 and 100.61 MHz for ^1H and ^{13}C, respectively). Samples were packed into zirconia rotors with an outer diameter of 4 mm and rotated at the magic angle at a rate of 12.5 kHz. Spectra were recorded with cross polarization (CP) from ^1H with a contact pulse (ramped for ^1H) of 1 ms. High-power ($\nu 1 \approx 100$ kHz) two-pulse phase modulation (TPPM) decoupling of ^1H was applied during acquisition. Signal averaging was carried out for 2048–4096 transients with a recycle interval of 3 s. Chemical shifts are reported in ppm relative to TMS using the CH_3 resonance of L-alanine ($\delta = 20.5$ ppm) as a secondary reference.

The XPS spectra were collected on a Scienta 300 XPS spectrometer working at a base pressure $< 5\times10^{-9}$ mbar. Monochromated $Al_{K\alpha}$ X-rays were used throughout, generated from a rotating anode source operating at approximately 4 kW power. Wide energy survey scans were performed to determine the elements present

(2 scans, dwell time 200 ms and 200 meV step size) before more detailed scans were performed on the regions of interest (2 scans, dwell time 533 ms and 20 meV step size). A pass energy of 150 eV was used throughout and the energy scale referenced to Au $4f_7$ at 83.95 eV binding energy. The signals were collected by a multichannel plate/phosphor screen/video camera combination and all spectra were analyzed using the Casa XPS software.

Adsorption enthalpies were measured experimentally using a Tian–Calvet type microcalorimeter, coupled with a home-made manometric gas dosing system.[42] This apparatus allows the simultaneous measurement of the adsorption isotherm and the corresponding differential enthalpies. Gas is introduced into the system using a step-by-step method and each dose is allowed to stabilize in a reference volume before being brought into contact with the adsorbent located in the microcalorimeter. The introduction of the adsorbate to the sample is accompanied by an exothermic thermal signal, measured by the thermopiles of the microcalorimeter. The peak in the calorimetric signal is integrated over time to give the total energy released during this adsorption step. At low coverage the error in the signal can be estimated to around $\pm 0.2\ kJ\ mol^{-1}$.

Around 0.3 g of sample was used and was outgassed at 150 °C for 16 h under secondary vacuum prior to each experiment. For each injection of gas, equilibrium was assumed to have been reached after 90 min. This was confirmed by the return of the calorimetric signal to its baseline ($< 5\ \mu W$). The gas used for the adsorption was obtained from Air Liquide (99.997 % purity).

Gas separation analysis: Mixed gas analyses were performed for PBI MMMs containing a 20 wt.% loading of both ZIF-93/11 hybrid materials. The membranes were placed in a module comprised of two stainless steel pieces and a 316 L SS macroporous disk support (from Mott Co.), with a 20 μm nominal pore size, and gripped inside with Viton O-rings. The permeation module was placed in a UNE 200 Memmert oven to control the temperature of the experiments (180 °C). Gas separation measurements were carried out by feeding an equimolar mixture of H_2/CO_2 (25/25 $cm^3(STP)\ min^{-1}$) at 3 bar to the feed side by means of two mass-flow controllers (Alicat Scientific, MC-100CCM-D), while the permeate side of the membrane was swept with a 2 $cm^3(STP)\ min^{-1}$ mass-flow controller stream of Ar at 1 bar (Alicat Scientific, MC-5CCM-D). Concentrations of H_2 and CO_2 in the outgoing streams were analyzed by an Agilent 3000A online gas microchromatograph, equipped with a thermal conductivity detector. Permeability was calculated in Barrer ($1 \times 10^{-10}\ cm^3(STP)\ cm/(cm^2\ s\ cmHg)$) once the steady-state of the exit stream was reached (for at least 3 h), and the separation selectivity was calculated as the ratio of permeabilities. The membranes had to be handled with care because of the brittleness of PBI. This was truer for the MMMs, and they had to be cut carefully. In any event, the literature shows how brittle membranes have greater processability in the form of supported membranes, where thin selective layers are deposited on high performance polymeric supports that provide mechanical stability, solving the problem.[43]

Acknowledgements

The research leading to these results has received funding from the European Union Seventh Framework Programme (FP7/2007–2013) under grant agreement no. 608490, project M4CO2. In addition, financial support from the Spanish MINECO and FEDER (MAT2016-77290-R), the Aragón Government (T05) and the ESF is gratefully acknowledged. J.S.L. thanks the Spanish Education Ministry Program FPU2014 for his PhD grant. All the microscopy work was done in the Laboratorio de Microscopías Avanzadas at the Instituto de Nanociencia de Aragón (LMA-INA). The authors would like to acknowledge the use of the Servicio General de Apoyo a la Investigación-SAI, Universidad de Zaragoza. Prof. Dr. Steven Abbott is thanked for providing Hansen solubility parameters.

Conflict of interest

The authors declare no conflict of interest.

Keywords: H_2/CO_2 separation · hybrid zeolitic imidazolate framework · membranes · polybenzimidazole · synthesis design

[1] G. Férey, C. Serre, *Chem. Soc. Rev.* **2009**, *38*, 1380 – 1399.
[2] a) B. Zornoza, C. Tellez, J. Coronas, J. Gascon, F. Kapteijn, *Microporous Mesoporous Mater.* **2013**, *166*, 67 – 78; b) H. B. Tanh Jeazet, C. Staudt, C. Janiak, *Dalton Trans.* **2012**, *41*, 14003 – 14027.
[3] P. Horcajada, C. Serre, M. Vallet-Regí, M. Sebban, F. Taulelle, G. Férey, *Angew. Chem. Int. Ed.* **2006**, *45*, 5974 – 5978; *Angew. Chem.* **2006**, *118*, 6120 – 6124.
[4] a) H. Jiang, T. Akita, T. Ishida, M. Haruta, Q. Xu, *J. Am. Chem. Soc.* **2011**, *133*, 1304 – 1306; b) J. Gascon, U. Aktay, M. D. Hernandez-Alonso, G. P. M. van Klink, F. Kapteijn, *J. Catal.* **2009**, *261*, 75 – 87.
[5] K. S. Park, Z. N. Ni, A. P. Côte, J. Y. Choi, R. Huang, F. J. Uribe-Romo, H. K. Chae, M. O'Keeffe, O. M. Yaghi, *Proc. Natl. Acad. Sci. USA* **2006**, *103*, 10186 – 10191.
[6] J. A. Thompson, C. R. Blad, N. A. Brunelli, M. E. Lydon, R. P. Lively, C. W. Jones, S. Nair, *Chem. Mater.* **2012**, *24*, 1930 – 1936.
[7] C. Zhang, Y. Xiao, D. Liu, Q. Yang, C. Zhong, *Chem. Commun.* **2013**, *49*, 600 – 602.
[8] R. Banerjee, A. Phan, B. Wang, C. Knobler, H. Furukawa, M. O'Keeffe, O. M. Yaghi, *Science* **2008**, *319*, 939 – 943.
[9] R. Banerjee, H. Furukawa, D. Britt, C. Knobler, M. O'Keeffe, O. M. Yaghi, *J. Am. Chem. Soc.* **2009**, *131*, 3875 – 3877.
[10] N. T. Nguyen, H. Furukawa, F. Gándara, H. T. Nguyen, K. E. Cordova, O. M. Yaghi, *Angew. Chem. Int. Ed.* **2014**, *53*, 10645 – 10648; *Angew. Chem.* **2014**, *126*, 10821 – 10824.
[11] S. M. Cohen, *Chem. Rev.* **2012**, *112*, 970 – 1000.
[12] a) Z. Wang, S. M. Cohen, *J. Am. Chem. Soc.* **2007**, *129*, 12368 – 12369; b) K. K. Tanabe, Z. Wang, S. M. Cohen, *J. Am. Chem. Soc.* **2008**, *130*, 8508 – 8517; c) M. J. Ingleson, J. P. Barrio, J. Guilbaud, Y. Z. Khimyak, M. J. Rosseinsky, *Chem. Commun.* **2008**, 2680 – 2682; d) S. J. Garibay, Z. Wang, K. K. Tanabe, S. M. Cohen, *Inorg. Chem.* **2009**, *48*, 7341 – 7349; e) Z. Wang, S. M. Cohen, *Angew. Chem. Int. Ed.* **2008**, *47*, 4699 – 4702; *Angew. Chem.* **2008**, *120*, 4777 – 4780; f) D. Britt, C. Lee, F. J. Uribe-Romo, H. Furukawa, O. M. Yaghi, *Inorg. Chem.* **2010**, *49*, 6387 – 6389.
[13] M. Meilikhov, K. Yusenko, R. A. Fischer, *J. Am. Chem. Soc.* **2009**, *131*, 9644 – 9645.
[14] a) T. Ahnfeldt, D. Gunzelmann, T. Loiseau, D. Hirsemann, J. Senker, G. Férey, N. Stock, *Inorg. Chem.* **2009**, *48*, 3057 – 3064; b) C. Volkringer, S. M. Cohen, *Angew. Chem. Int. Ed.* **2010**, *49*, 4644 – 4648; *Angew. Chem.* **2010**, *122*, 4748 – 4752; c) S. J. Garibay, Z. Wang, S. M. Cohen, *Inorg. Chem.* **2010**, *49*, 8086 – 8091.
[15] K. M. Taylor-Pashow, J. D. Rocca, Z. Xie, S. Tran, W. Lin, *J. Am. Chem. Soc.* **2009**, *131*, 14261 – 14263.
[16] S. Bernt, V. Guillerm, C. Serre, N. Stock, *Chem. Commun.* **2011**, *47*, 2838 – 2840.
[17] a) V. Guillerm, F. Ragon, M. Dan-Hardi, T. Devic, M. Vishnuvarthan, B. Campo, A. Vimont, G. Clet, Q. Yang, G. Maurin, *Angew. Chem. Int. Ed.* **2012**, *51*, 9267 – 9271; *Angew. Chem.* **2012**, *124*, 9401 – 9405; b) M. Kandiah, S. Usseglio, S. Svelle, U. Olsbye, K. P. Lillerud, M. Tilset, *J. Mater. Chem.* **2010**, *20*, 9848 – 9851.
[18] S. J. Garibay, S. M. Cohen, *Chem. Commun.* **2010**, *46*, 7700 – 7702.
[19] S. S. Chui, S. M. Lo, J. P. Charmant, A. G. Orpen, I. D. Williams, *Science* **1999**, *283*, 1148 – 1150.

[20] A. Huang, J. Caro, *Angew. Chem. Int. Ed.* **2011**, *50*, 4979 – 4982; *Angew. Chem.* **2011**, *123*, 5083 – 5086.
[21] J. Canivet, S. Aguado, C. Daniel, D. Farrusseng, *ChemCatChem* **2011**, *3*, 675 – 678.
[22] F. Cacho-Bailo, M. Etxeberría-Benavides, O. Karvan, C. Téllez, J. Coronas, *CrystEngComm* **2017**, *19*, 1545 – 1554.
[23] X. Liu, Y. Li, Y. Ban, Y. Peng, H. Jin, H. Bux, L. Xu, J. Caro, W. Yang, *Chem. Commun.* **2013**, *49*, 9140 – 9142.
[24] J. Sánchez-Laínez, A. Veiga, B. Zornoza, S. R. Balestra, S. Hamad, A. R. Ruiz-Salvador, S. Calero, C. Téllez, J. Coronas, *J. Mater. Chem. A* **2017**, *5*, 25601 – 25608.
[25] A. W. Thornton, D. Dubbeldam, M. S. Liu, B. P. Ladewig, A. J. Hilla, M. R. Hill, *Energy Environ. Sci.* **2012**, *5*, 7637 – 7646.
[26] K. G. Ray, D. L. Olmsted, J. M. Burton, Y. Houndonougbo, B. B. Laird, M. Asta, *Chem. Mater.* **2014**, *26*, 3976 – 3985.
[27] W. Morris, B. Leung, H. Furukawa, O. K. Yaghi, N. He, H. Hayashi, Y. Houndonougbo, M. Asta, B. B. Laird, O. M. Yaghi, *J. Am. Chem. Soc.* **2010**, *132*, 11006 – 11008.
[28] P. Bernardo, E. Drioli, G. Golemme, *Ind. Eng. Chem. Res.* **2009**, *48*, 4638 – 4663.
[29] a) T. Chung, L. Y. Jiang, Y. Li, S. Kulprathipanja, *Prog. Polym. Sci.* **2007**, *32*, 483 – 507; b) P. Goh, A. Ismail, S. Sanip, B. Ng, M. Aziz, *Sep. Purif. Technol.* **2011**, *81*, 243 – 264.
[30] a) S. Choi, J. Coronas, Z. Lai, D. Yust, F. Onorato, M. Tsapatsis, *J. Membr. Sci.* **2008**, *316*, 145 – 152; b) T. Yang, Y. Xiao, T. Chung, *Energy Environ. Sci.* **2011**, *4*, 4171 – 4180; c) L. Li, J. Yao, X. Wang, Y. Chen, H. Wang, *J. Appl. Polym. Sci.* **2014**, *131*, 41056; d) X. Li, R. P. Singh, K. W. Dudeck, K. A. Berchtold, B. C. Benicewicz, *J. Membr. Sci.* **2014**, *461*, 59 – 68; e) S. Kumbharkar, Y. Liu, K. Li, *J. Membr. Sci.* **2011**, *375*, 231 – 240; f) B. P. Biswal, A. Bhaskar, R. Banerjee, U. K. Kharul, *Nanoscale* **2015**, *7*, 7291 – 7298.
[31] T. Chung, *J. Macromol. Sci. Part C* **1997**, *37*, 277 – 301.
[32] a) T. Yang, G. M. Shi, T. Chung, *Adv. Energy Mater.* **2012**, *2*, 1358 – 1367; b) T. Yang, T. Chung, *Int. J. Hydrogen Energy* **2013**, *38*, 229 – 239; c) A. Bhaskar, R. Banerjee, U. Kharul, *J. Mater. Chem. A* **2014**, *2*, 12962 – 12967.
[33] J. Sánchez-Laínez, B. Zornoza, C. Téllez, J. Coronas, *J. Mater. Chem. A* **2016**, *4*, 14334 – 14341.
[34] T. Yang, T. Chung, *J. Mater. Chem. A* **2013**, *1*, 6081 – 6090.
[35] C. M. Hansen, *Prog. Org. Coat.* **2004**, *51*, 77 – 84.
[36] D. P. Drolet, D. M. Manuta, A. J. Lees, A. Katnani, G. J. Coyle, *Inorg. Chim. Acta* **1988**, *146*, 173 – 180.
[37] W. Morris, N. He, K. G. Ray, P. Klonowski, F. Hiroyasu, I. N. Daniels, Y. A. Houndonougbo, M. Asta, O. M. Yaghi, B. B. Laird, *J. Phys. Chem.C* **2012**, *116*, 24084 – 24090.
[38] B. W. Rowe, L. M. Robeson, B. D. Freeman, D. R. Paul, *J. Membr. Sci.* **2010**, *360*, 58 – 69.
[39] L. M. Robeson, *J. Membr. Sci.* **1991**, *62*, 165 – 185.
[40] L. M. Robeson, *J. Membr. Sci.* **2008**, *320*, 390 – 400.
[41] M. He, J. Yao, Q. Liu, Z. Zhongb, H. Wang, *Dalton Trans.* **2013**, *42*, 16608 – 16613.
[42] P. L. Llewellyn, G. Maurin, *C. R. Chim.* **2005**, *8*, 283 – 302.
[43] Z. Dai, L. Ansaloni, L. Deng, *Green Energy Environ.* **2016**, *1*, 102 – 128.

Manuscript received: April 27, 2018
Accepted manuscript online: May 25, 2018
Version of record online: July 3, 2018

CHEMISTRY
A European Journal

Supporting information

1- Solution-state NMR

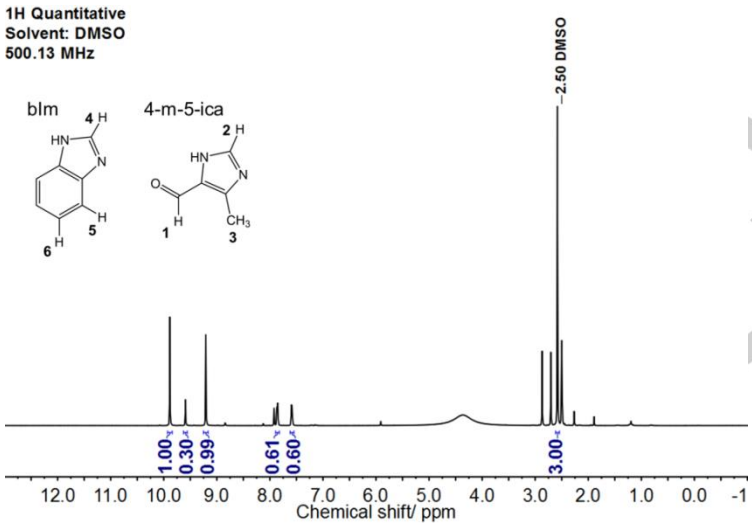

Figure S1. ^{1}H NMR spectrum of ZIF-93/-11 hybrid material synthesised in DMAc (500 MHz, DMSO-d_6). δ 9.89 (s, 1H, H-1 4-m-5-ica), 9.59 (s, 1H, H-4 bIm), 9.21 (s, 1H, H-2 4-m-5-ica), 7.87-7.85 (m, 2H, H-5/-6 bIm), 7.60-7.58 (m, 2H, H-5/-6 bIm), 2.58 (s, 3H, H-3 4-m-5-ica).

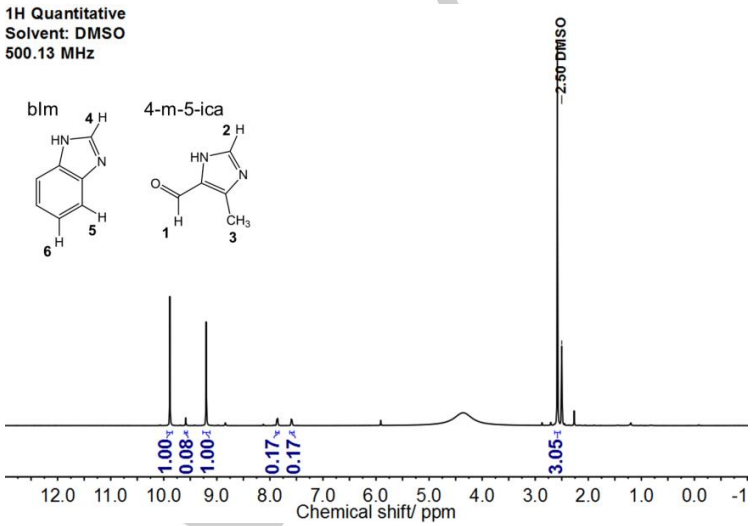

Figure S2. ^{1}H NMR spectrum of ZIF-93/-11 hybrid material synthesised in MeOH (500 MHz, DMSO-d_6). δ 9.89 (s, 1H, H-1 4-m-5-ica), 9.59 (s, 1H, H-4 bIm), 9.20 (s, 1H, H-2 4-m-5-ica), 7.87-7.85 (m, 2H, H-5/-6 bIm), 7.60-7.58 (m, 2H, H-5/-6 bIm), 2.58 (s, 3H, H-3 4-m-5-ica).

Table S1. Calculation summary for linker ratio from solution-state ^{1}H-NMR of dissolved hybrid materials from DMAc synthesis and MeOH synthesis.

Sample	Chemical shift/ ppm		Integration		Ratio of 4-m-5-ica : bIm
	4-m-5-ica	bIm	4-m-5-ica	bIm	
Hybrid from DMAc solvent	9.89 (1H)	9.59 (1H)	1.00	0.30	[1.00/1H] : [0.30/1H] = 1.00 : 0.30 **∴ 3.3 : 1**
Hybrid from MeOH solvent	9.89 (1H)	9.59 (1H)	1.00	0.08	[1.00/1H] : [0.08/1H] = 1.00 : 0. 08 **∴ 12.5 : 1**

2- Hansen Solubility Parameters (HSP)

$$Ra^2 = 4(\delta_{D1} - \delta_{D2})^2 + (\delta_{P1} - \delta_{P2})^2 + (\delta_{H1} - \delta_{H2})^2 \quad \text{(Equation S1)}$$

Table S2. Hansen solubility parameters for MeOH and DMAc solvents and the ligand 4-m-5-ica. Distances between materials obtained from Ra calculations with Equation S1

Solvent	HSP [MPa$^{0.5}$]			Ra
	δ_D	δ_P	δ_H	
4-m-5-ica	19.1	16.3	10.4	-
MeOH	15.1	12.3	22.3	14.9
DMAc	16.8	11.5	10.2	6.6

The interactions established between solvent or ligand can be of different nature, i.e. dispersion, polar or hydrogen bonds. These interactions can be discussed in terms of the so-called Hansen solubility parameters (HSP). These parameters (δ_D, δ_P and δ_H for dispersion or London interaction, polar interaction and hydrogen bonds, respectively) are given in Table S2 for the solvents used in the post-synthetic modification (MeOH and DMAc) and for the ZIF-93 ligand (4-m-5-ica). The solvent-ligand interaction can be estimated calculating the parameter Ra with the Equation S1. This way, the lower the Ra parameter is, the stronger the interaction becomes because the HSP values are more similar to each other.[1]. In general, HSP values were obtained from literature (solvents);[2] HSPs for ligand 4-m-5-ica, calculated using Y-MB technique with the commercial package Hansen Solubility Parameters in Practice.[3]

3- Particle size calculation

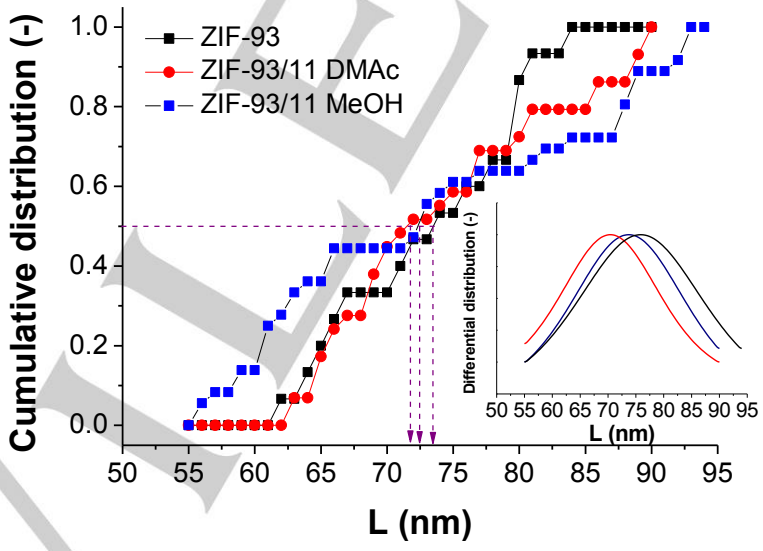

Figure S3. Cumulative and differential (inset) particle size distribution of the ZIF-93 and ZIF-93/11 hybrid materials (synthesised in DMAc and MeOH) nanoparticle samples.

4- XRD analysis

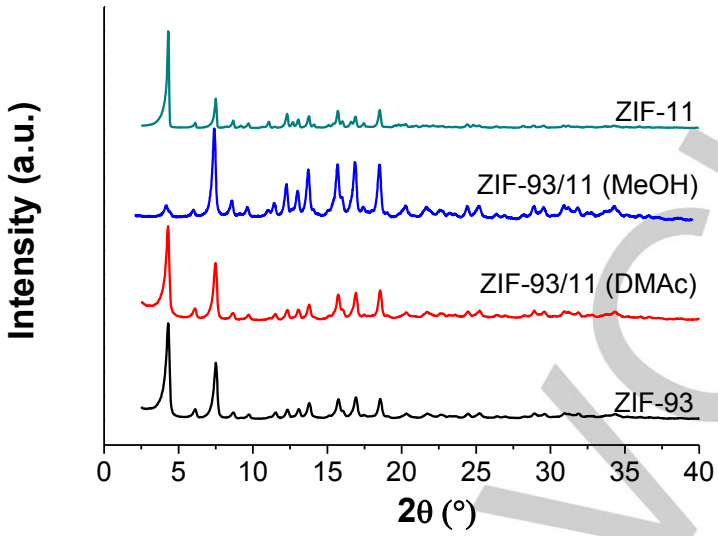

Figure S4. XRD patterns of ZIF-93, ZIF-11 and ZIF-93/11 hybrids materials.

5- FTIR analysis

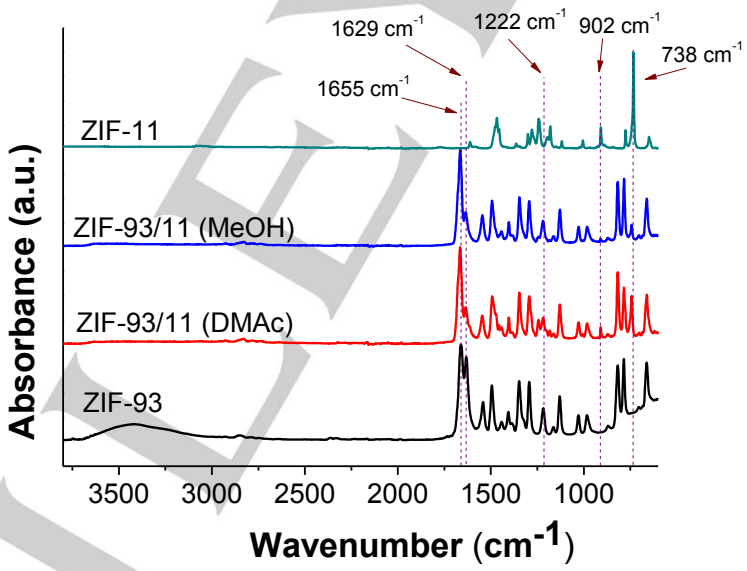

Figure S5. FTIR spectra of ZIF-93, ZIF-11 and ZIF-93/11 hybrid materials.

6- References

[1] C. M. Hansen, *Prog. Org. Coat.*,**2004**, *51*, 77-84.
[2] C. Hansen, Hansen solubility parameters: a user's handbook, 2nd edn Boca Raton, **2007**.
[3] S. J. Abbott, C. J. Hansen, H. Yamamoto, http://www.hansen-solubility.com, accessed September 2014.

Chapter 9: Asymmetric polybenzimidazole membranes with thin selective skin layer containing ZIF-8 for H_2/CO_2 separation at pre-combustion capture conditions

J. Sánchez-Laínez, B. Zornoza, C. Téllez, J. Coronas. Journal of Membrane Science, 563 (2018), (427-434). DOI: 10.1016/j.memsci.2018.06.009. Permission conveyed through Copyright Clearance Center, Inc.

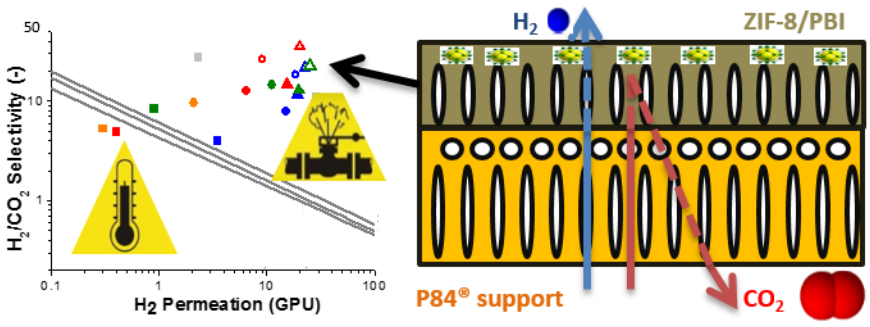

Category:

- Type of membrane: integrally skinned asymmetric membranes
- Gas separation: pre-combustion CO_2 capture

Journal of Membrane Science 563 (2018) 427–434

Contents lists available at ScienceDirect

Journal of Membrane Science

journal homepage: www.elsevier.com/locate/memsci

Asymmetric polybenzimidazole membranes with thin selective skin layer containing ZIF-8 for H_2/CO_2 separation at pre-combustion capture conditions

Javier Sánchez-Laínez, Beatriz Zornoza*, Carlos Téllez, Joaquín Coronas*

Chemical and Environmental Engineering Department, Instituto de Nanociencia de Aragón (INA), Universidad de Zaragoza, 50018 Zaragoza, Spain

ARTICLE INFO

Keywords:
CO_2 capture
Asymmetric membrane
Polybenzimidazole
Metal-organic-framework

ABSTRACT

This work addresses an optimization in the fabrication of flat PBI membranes containing ZIF-8 nanoparticles for gas separation purposes. The PBI membranes were prepared in an asymmetric configuration on P84® supports, representing a new way of preparing flat PBI membranes. An optimization of the conditions for the PBI phase inversion preparation method, including the dope composition (in the 15–26 wt% range), has been carried out to obtain PBI membranes with a 1 μm selective skin layer. The asymmetric membranes showed an unprecedented gas separation capacity in pre-combustion CO_2 capture, much superior to that of dense membranes, under harsh operating conditions (250 °C and 6 bar feed), performing up to 20.3 GPU of H_2 and a H_2/CO_2 selectivity of 35.6. Their much thinner selective layer made possible the increase in selectivity because of the saturation of the CO_2 flow at high pressures. The reduction in the amount of ZIF-8 for obtaining a membrane with the same filler loading (3.7 vs. 9.3 g/m^2) was also possible; the performance of this ZIF-8 containig membrane was 22.4 GPU of H_2 and a H_2/CO_2 selectivity of 22.3. The activation energy of the membranes, as well as the flow resistances, were calculated, providing a resistance in series model to understand the flow inside the membrane.

1. Introduction

Carbon capture and storage *via* pre-combustion processes involve the separation of H_2/CO_2 mixtures with a high CO_2 concentration (~ 45 vol%) at elevated pressure (15–20 bar) and temperature (190–210 °C) [1]. This mixture is the result of syngas generation from the steam reforming of hydrocarbon sources such as natural gas, heavy oils and naphtha, coal or biomass. The whole process consists of three steps: the catalytic reforming of methane, a water gas shift reaction and the purification of the resulting hydrogen flow [2]. Purification is needed to capture the CO_2, leaving a stream of nearly-pure hydrogen that will be burned in a combined cycle power plant to generate electricity [3]. In view of the high CO_2 concentration, pre-combustion capture is more efficient than post-combustion, but the severe operating conditions make the separation process more complicated.

Various approaches can be employed for CO_2 separation such as pressure swing adsorption, temperature swing adsorption and cryogenic distillation. However, membrane technology appears to be a more efficient alternative thanks to its attractive properties: simplicity, ease of operation, and versatility for a large number of potential uses. Besides, hydrogen separation is suited to membrane technology as hydrogen has a very high permeation rate relative to most other gases due to its small kinetic diameter, and thus its high diffusivity.

Currently, polymeric membranes rule the commercial scene for CO_2 capture. Very recently, Pinnau's group developed thin skin membranes by interfacial polymerization, able to reach a H_2 permeance of 500 GPU and a H_2/CO_2 selectivity of 50 [4]. However, these membranes could only withstand temperatures up to 140 °C due to the use of polysulfone supports. Pre-combustion capture needs membranes produced from materials with a high mechanical and thermal stability due to the harsh operating conditions involved. Polybenzimidazole (PBI) is a polymer with inherent mechanical, physical and chemical stability. This material retains its robustness up to 600–630 °C [5] and has a high glass transition temperature (427 °C) [6]. Furthermore, the high chain packing density of this material provides diffusivity selectivity at temperatures above 150 °C. However, its major drawbacks are low permeability and brittleness [7].

Polymeric membranes can be classified as symmetric or asymmetric according to their morphology [8]. Symmetric membranes constitute a dense or porous continuous matrix. They are prepared by evaporation of the casting solution and all their thickness is selective for gas separation. The main disadvantage of these membranes is their high

* Corresponding authors.
E-mail addresses: bzornoza@unizar.es (B. Zornoza), coronas@unizar.es (J. Coronas).

https://doi.org/10.1016/j.memsci.2018.06.009
Received 1 February 2018; Received in revised form 22 May 2018; Accepted 5 June 2018
Available online 06 June 2018
0376-7388/

resistance to flow, resulting in low flow rates and therefore low feasibility for commercial applications. Asymmetric membranes have a heterogeneous morphology. They consist of a dense layer integrally formed over a porous layer. The porous substructure provides mechanical support and prevents the membrane from breaking, whereas the dense skin layer is responsible for molecular discrimination and flow resistance. Such membranes are normally prepared in one step following the phase inversion technique developed by Loeb and Sourirajan [9], which consists of the precipitation of a casting solution by immersion in a non-solvent bath.

The use of PBI membranes for the separation of H_2/CO_2 mixtures has been widely reported in the form of flat dense membranes [10–20] and hollow fibers [21–25]. Although flat asymmetric PBI membranes can be found in the literature for applications such as nanofiltration or forward osmosis [26–28], they are not so developed for gas separation purposes. Only a few reports of gas separation with flat asymmetric membranes made from other polymers can be found in the literature [29–34].

This study provides a method for the preparation of defect-free flat asymmetric PBI membranes, showing their yet to be developed potential for the separation of H_2/CO_2 mixtures at high temperature and pressure. The membranes were prepared over non-selective polyimide P84® to provide mechanical strength to the composite. The results were compared with those of dense PBI films reported in previous studies and self-supported membranes. Moreover, ZIF-8 has also been embedded in the PBI phase with the aim of enhancing the gas separation properties of the membranes. ZIF-8 is a zeolitic imidazolate framework (a kind of metal-organic framework), with Zn cations coordinated to 2-methylimidazolate (2-mIm) ligands. It has the "**sod**" in bold zeolitic topology with cavities of 1.16 nm connected through smaller windows of 0.34 nm. This ZIF has been widely reported in the literature for the preparation of mixed matrix membranes (MMMs) for gas separation [15,19,35,36].

2. Experimental section

2.1. Materials

Zinc nitrate hexahydrate ($Zn(NO_3)_2{\cdot}6H_2O$), 2-methylimidazole (mIm, $C_4H_6N_2$, > 99%) and N,N-Dimethylacetamide (DMAc) were purchased from Sigma Aldrich. Methanol (MeOH, HPLC grade), isopropyl alcohol (IPA, 99.5%) and n-hexane were purchased from Scharlau. Commercial PBI solution comprising 26 wt% PBI with 1.5 wt % LiCl as stabilizer in DMAc solvent was purchased from PBI Performance Products and P84® was purchased from HP polymer GmbH.

2.2. ZIF-8 nanoparticle synthesis

This ZIF synthesis was adapted from the literature [37]. 0.47 g of ($Zn(NO_3)_2{\cdot}6H_2O$, > 98%, Sigma Aldrich) was dissolved in 10 mL of MeOH and 10 mL of deionized (DI) water. Besides, 1.0 g of mIm was dissolved in 10 mL of MeOH, and the two solutions were mixed and stirred for 2 h. The final product was collected by centrifugation, washed once with MeOH, and dried at 110 °C overnight. The resulting nanoparticles had an average size of 150 nm.

2.3. Preparation of P84® asymmetric supports

Asymmetric porous P84® supports were prepared following the phase inversion method. A 23 wt% dope solution of P84® was prepared, dissolving the corresponding amount of powder in DMAc. The polymer solution was cast onto a glass plate using an Elcometer 4340 Automatic Film Applicator placed in a fume hood and immediately immersed into a tap water bath at 25 °C. After precipitation, the membranes were kept in a DI water bath overnight and then rinsed with IPA in order to remove the remaining DMAc. The films were dried at 100 °C for one day prior to use [38].

2.4. PBI asymmetric membrane preparation

PBI asymmetric membranes were also prepared following the phase inversion method. A 20 wt% dope solution was directly obtained by diluting the 26 wt% PBI commercial solution in DMAc. The casting solution was left still overnight to remove any bubbles. The polymer solution was cast onto a P84® support using the same device as for the P84® films and immediately immersed into a DI water bath at 25 °C. After precipitation, the membranes were kept in a DI water bath for three days in order to remove all the DMAc. The membranes were then rinsed in MeOH and n-hexane for 90 min each, before drying at room temperature. Once dried, the membranes were healed following a dip-coating method. The coating solution was prepared mixing PDMS polymer base and hardener with a weight ratio of 10–1. The mixture was added to n-hexane to obtain a 3 wt% solution. The membranes were immersed in the coating solution for 5 min, and then allowed to evaporate at room temperature for 2 h. Finally, the membranes were cured in an oven at 100 °C for 18 h, resulting in a coated PDMS film of around 500 nm thickness. PBI membranes containing ZIF-8 were prepared analogously. In this case, ZIF-8 nanoparticles were dispersed in DMAc and commercial PBI solution (26 wt%) was added in three steps until a 20 wt% dope solution was obtained. As reported by Wang et al. [39], the PBI dope was selected near the critical concentration, obtained plotting the viscosity-concentration values from PBI Performance Products data (Fig. S1) [40]. A concentration near this critical value is necessary to form a thin skin layer with fewer defects [41]. Moreover, dopes with a PBI concentration of 15 and 26 wt% were also used to prepare membranes for characterization. These PBI self-supported membranes were also prepared on a glass plate, following the same procedure as for the P84® supports.

2.5. Membrane characterization

Thermogravimetric analyses (TGA) were carried out using a Mettler Toledo TGA/STDA 851e. Samples (10 mg) placed in 70 μL alumina pans were heated in an air flow of 40 mL from 25 to 900 °C at a heating rate of 10 °C/min. Scanning electron microscopy (SEM) images of MOFs and membranes were obtained using a FEI Inspect F50 model SEM, operated at 20 kV. Cross-sections of membranes were prepared by freeze-fracturing after immersion in liquid N_2 and subsequently coated with Pt. Membranes were also characterized by Raman spectroscopy using a WiTec Alpha300 Confocal Raman Microscope, with a 785 nm laser excitation beam. Carbon dioxide adsorption isotherms were measured using a volumetric adsorption analyzer (Micromeritics ASAP 2020) at 273 K up to 120 kPa after degassing at 200 °C for 8 h. In all cases, the hydrogen, carbon dioxide and helium gases used in the experiments were 99.9995% pure.

2.6. Gas separation performance

The membrane samples were placed in a module consisting of two stainless steel pieces and a 316LSS macroporous disk support of 3.14 cm^2 (from Mott Co.) with a 20 μm nominal pore size, and gripped inside with silicon O-rings. The permeation module was placed in a UNE 200 Memmert oven to control the temperature of the experiments. Gas separation measurements were carried out by feeding a H_2/CO_2 equimolar mixture (25/25 cm^3(STP)/min) from 3 to 6 bar to the feed side by means of two mass-flow controllers (Alicat Scientific, MC-100CCM-D), while the permeate side of the membrane was swept with a 2–10 cm^3(STP)/min mass-flow controlled stream of Ar at 1 bar. Concentrations of H_2 and CO_2 in the outgoing streams were analyzed by an Agilent 3000 A online gas microchromatograph equipped with a thermal conductivity detector. Permeation was calculated in GPU

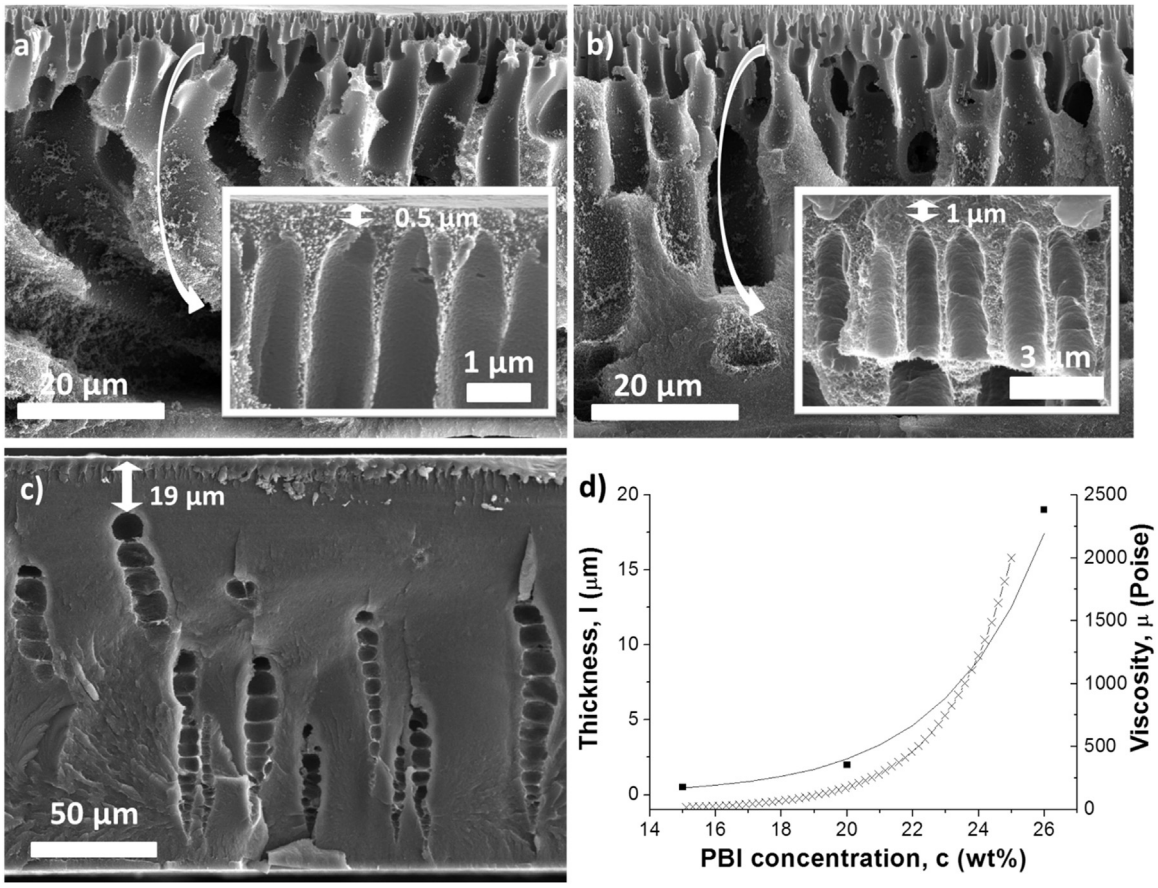

Fig. 1. SEM images of the cross-section of PBI self-supported asymmetric membranes fabricated from PBI dopes at 15 wt% (a), 20 wt% (b) and 26 wt% (c). PBI membrane skin layer thickness and PBI solution viscosity at 25 °C as function of PBI concentration in DMAc (d).

(10^{-6} cm^3(STP)/(cm^2 s cmHg)) once the steady-state of the exit stream was reached (after at least 3 h), and the separation selectivity was calculated as the ratio of permeances. At least 2–3 membrane samples of each type were fabricated and measured to provide the corresponding error estimations.

3. Results and discussion

3.1. Membrane characterization

The SEM images in Fig. 1 reveal how the polymer concentration of the casting solution has an effect on the differentiation and thickness of the selective skin layer and porous sponge substructure. The distance from the top of the finger-like macropores to the external part of the membranes is approximately 0.5, 1 and 19 µm when using PBI dopes of 15, 20 and 26 wt%, respectively. As seen in Fig. 1d, this increase follows an exponential trend, like the polymer solution viscosity with increasing concentration (fitting from the data of Fig. S1). Both fitting equations can be seen in Fig. S2. The polymer concentration also had an effect on the substructure and thus on the mechanical strength of the membrane, because only self-supported membranes prepared from 26 wt% dope solutions could be measured for gas separation. The rest of membranes were too brittle to support the feed pressure. The absence of a bore fluid, as used for hollow fiber fabrication [42], made the fingers (i.e. the large columnar macropores) grow from the bottom of the membrane, turning it into a fragile structure. Besides, the quantity of finger-like macropores decreased at high PBI concentrations, resulting in a denser membrane with the consequent reduction in permeation. Due to the brittleness of PBI, it was necessary to support the membranes on a polymeric substrate able to resist the handling for further characterization and the high temperatures and pressures of the gas separation test. Polyimide P84® was chosen since it is a high performance reliable polymer that has already been used as an inner layer in PBI hollow fibers [42]. Moreover, our research group has a previous practice P84® flat supports for nanofiltration issues [43,44].

Fig. 2 (left) shows the Raman spectra of the cross-section of a PBI supported membrane. Different points on zones corresponding to the PBI, the PBI/P84® interface and the P84® support were measured. The PBI Raman spectrum shows weak signals owing to fluorescence at lower Raman shifts. The band at 549–694 cm^{-1} is attributed to C–H out-of-plane ring deformation. The signals at 1374 and 1617 cm^{-1} are attributed to C–H in-plane bending vibrations and C=C/C=N benzimidazole ring stretching vibrations, respectively [45]. The P84® spectrum shows intense peaks in the 1000–1600 cm^{-1} band. The signal at 1535 and 1592 cm^{-1} corresponds to aromatic C-C stretching. The band at 1012 cm^{-1} is related to the C-H in-plane bending mode and that at 1290 cm^{-1} to the C=O in-phase stretching mode [46]. Signals of PBI cannot be distinguished in the interphase spectrum due to their low intensity, and only those of P84® are visible. Fig. 2 (right) shows the SEM image of this cross-section. The P84® support has a thickness of around 120 µm while the PBI film only of 30 µm (20 wt% PBI dope). The P84® support is constituted by two different porous layers, finger-like macropores and a ca. 15 µm thick porous sponge above them. No delamination can be observed at the interface between the two layers, indicating a good adhesion. This makes sense since PBI and P84® are highly compatible at molecular level [47]. The upper zone of the PBI layer reveals a dense structure at a high magnification (Fig. 2 inset), corresponding to the selective skin layer, while the inner zone is very porous, which is desirable for minimizing the transport resistance.

The thermal stability of supported PBI membranes was tested by

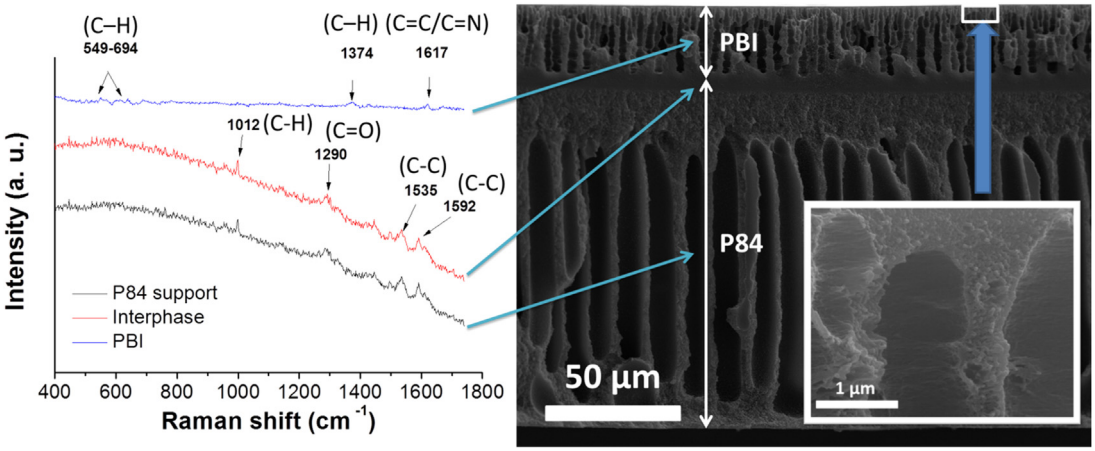

Fig. 2. Raman spectra on different zones of the cross-section of a PBI supported membrane (left) together with its SEM image (right) with a zoom into the PBI skin layer (inset). The membrane was prepared from a 20 wt% PBI dope.

thermogravimetric analysis in air (see Fig. S3). The membrane was stable up to 400 °C, making it suitable for H_2 separation at high temperature. Despite containing two different polymers, PBI as selective layer and P84® as support, the TGA obtained was a continuous curve in which it is difficult to distinguish one from the other. The major proportion of P84® in the composite is responsible for this behavior.

In order to improve the gas separation performance of the PBI asymmetric films, ZIF-8 was embedded into the PBI polymeric phase to form 10 wt% loaded MMMs, calculated from the TGA results of Fig. S4. The SEM images of cross-sections of these membranes (Fig. 3) reveal the presence of ZIF-8 nanoparticles in the PBI section over the P84® support (see arrows in inset). ZIF-8 nanoparticles were verified by EDX analysis (see Fig. 3 inset). The thin selective layer of PBI asymmetric membranes allowed the reduction in the necessary amount of ZIF-8 to prepare this kind of MMMs to 3.7 g/m^2. This means a 2.5 fold decrease in comparison with the value for obtaining an 80 µm dense membrane with the same filler loading (9.3 g/m^2).

3.2. Permeation results: dense vs. asymmetric PBI membranes

The P84® supports had no H_2/CO_2 selectivity when tested for gas separation. The use of a dope concentration below the critical value [25] prevents the formation of a selective skin layer and makes the films suitable for their use as low resistant, non-selective supports for PBI membranes.

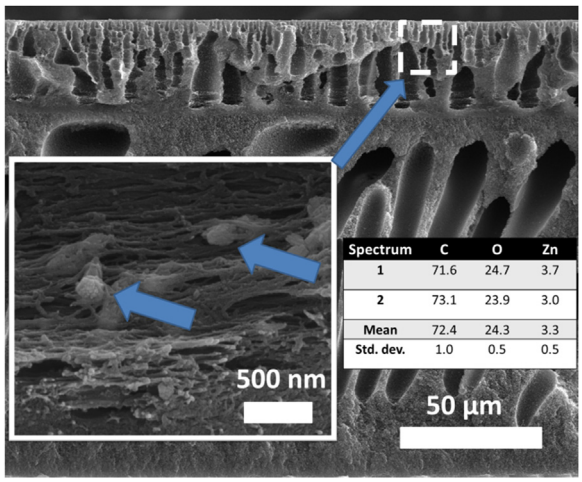

Fig. 3. SEM image of the cross-section of a supported PBI asymmetric MMM with 10 wt% loading of ZIF-8 including EDX analysis (inset).

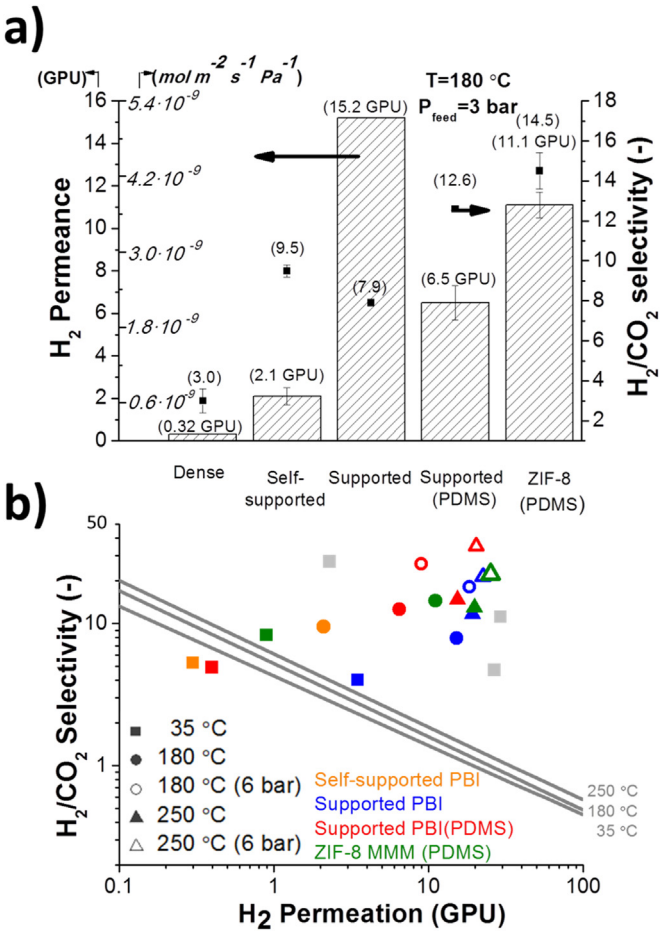

Fig. 4. Gas separation performance of dense PBI, self-supported asymmetric PBI, supported asymmetric PBI and asymmetric ZIF-8 10 wt% MMM. Histogram at 180 °C with feed and permeate pressures of 3 and 1 bar, respectively (a), and upper-bound plot (from 35 to 250 °C and pressure from 3 to 6 bar) with a comparison with hollow fiber literature values (in grey) [24–26] (b).

Fig. 4a shows the gas separation performance at 180 °C of dense PBI membranes (data from [20]) and four different PBI asymmetric membranes: self-supported membranes prepared from a 26 wt% concentration PBI dope (as seen above, lower concentration dopes gave rise to non-mechanically resistant membranes), supported membranes prepared from a 20 wt% dope before and after coating with PDMS, and

ZIF-8 MMMs healed with PDMS. The mean and standard deviation values corresponding to the measurement of 2–3 different membranes can be seen in Table S1.

The preparation of membranes *via* phase inversion resulted in an improvement in the H_2/CO_2 selectivity (9.5) in comparison with dense membranes prepared by evaporation (3.0), reaching values up to four-fold higher. The differences in these two values indicate that the polymer structure is different in the skin layer of the asymmetric membrane compared to that of the dense membrane. This can be associated to polymer molecular orientation or the motion of polymer chains [48]. As a result, the micropore volume of the skinned dense polymer is lower than that of the intrinsic material. It is worth noting that supported PBI membranes still have defects that need healing with PDMS since their selectivity is lower (7.9) than that of self-supported membranes, although the coating with PDMS also implies a substantial reduction in the H_2 permeance (with a better selectivity of 12.6). These defects may be related to the proximity of macrovoids to the outer surface of the membranes [21]. In any event, repairing techniques are usually employed to achieve effective membranes for practical applications [49]. As expected, H_2 permeance is higher for the asymmetric membranes due to the lower thickness of their selective layers, with maximum values of 15.2 GPU against the 0.32 GPU of dense PBI (with ca. 80 μm thickness). Regarding the MMMs, embedding ZIF-8 into the PBI matrix has a positive effect on the membrane performance. The H_2 permeance doubles in comparison with the value of the PBI membranes repaired with PDMS, and the H_2/CO_2 selectivity is 13% higher, reaching a value of 14.5. These membranes also show a better performance than that of ZIF-8/PBI hollow fibers found in the literature [35].

3.3. Influence of the temperature on the gas separation performance

The different PBI asymmetric membranes were tested at temperatures of 35, 180 and 250 °C. Their gas separation performances can be seen in the permeance-selectivity graph in Fig. 4b together with the literature values for PBI hollow fibers, given that no results for flat asymmetric membranes with this polymer have been published to date. Since the Robeson upper-bound [50] was originally defined for dense membranes at 35 °C, single gas permeability was set in Barrer. However, this unit is useless for asymmetric membranes, where the thickness of the selective thin layer is unknown. We have calculated an H_2/CO_2 upper-bound relationship in GPU, using the values from the literature that defined the original upper-bound but changing the permeation values from Barrer to GPU (see Table S2 and Fig. S5). As the temperature has an influence on the upper-bound (Eq. S1), we have also calculated the corresponding upper-bounds at 180 and 250 °C (Eq. S2 and S3). At 35 °C, supported PBI membranes surpassed the H_2/CO_2 upper-bound, as did all the membranes at high temperatures. Moreover, PBI supported membranes have superior permeation and selectivity than self-supported membranes once healed with PDMS. For example, at 180 °C and 3 bar of feed pressure they showed 6.5 GPU of H_2 and a H_2/CO_2 selectivity of 12.6. This means that the H_2 permeation was three-fold higher and the selectivity 25% higher in comparison with self-supported PBI. When increasing the temperature to 250 °C at the same feed pressure, PBI supported membranes showed values of 14.4 GPU of H_2 and a H_2/CO_2 selectivity of 13.8 at 3 bar. Increasing the feed pressure also had a positive influence on the membranes gas separation performance, which will be discussed in the following section. It can be seen in Fig. 4b how the literature values agree with our experimental results, despite referring to hollow fiber membranes. This is indicative of the huge gas permeance obtained using an asymmetric configuration.

In the case of ZIF-8/PBI asymmetric MMMs, Fig. 4b depicts how the H_2 permeance is at least one and a half times higher than that of the bare PBI membranes at each temperature. Besides, the H_2/CO_2 selectivity also shows an increase at 35 and 180 °C for the membranes containing ZIF-8, with a maximum value of 14.5. However, the selectivity value slightly decreases at 250 °C. This may be due to defects present in the membrane related to the integration of ZIF-8 that determine the flow at a higher temperature. The apparent activation energy was calculated for H_2, the fastest permeating compound in the binary mixture, resulting in values of 22.3 kJ/mol for the pure polymer and 19.5 kJ/mol for the MMMs (see Fig. S6). The apparent activation energy was also calculated for CO_2. This value slightly increased from 15.6 kJ/mol (bare polymer) to 16.3 kJ/mol when ZIF-8 was embedded in PBI. Both results are consistent with the increase in the H_2/CO_2 selectivity observed for most membranes at high temperature. This increase in selectivity is due to the fact that the diffusion selectivity becomes more important as the temperature rises, favoring the transport of the smallest H_2 gas molecules (kinetic diameter: 0.29 nm), that in turn has a higher value of apparent activation energy, over the largest of CO_2 (kinetic diameter: 0.33 nm). At the same time, the solubility of the most condensable gas (CO_2) becomes less significant.

3.4. Influence of feed pressure on the gas separation performance

As previously mentioned, the increase in the feed pressure led to an enhancement of the gas separation performance. For example, the supported PBI membranes healed with PDMS showed the best results at 250 °C and 6 bar, with a H_2 permeation of 20.3 GPU and an H_2/CO_2 selectivity of 35.6 (see Fig. 4b). This means an increase of 29% in the H_2 permeation while the H_2/CO_2 selectivity almost triples in comparison with the results of the same membrane at 3 bar. In the case of the ZIF-8 MMM, the H_2/CO_2 selectivity rises from 12.9 to 22.3 and the highest H_2 permeance of 22.4 GPU is reached. Defects produced by the integration of ZIF-8 into the PBI may be behind this behavior. In any event, the H_2/CO_2 selectivity almost doubles when the pressure increases from 3 to 6 bar while the H_2 permeance rises by 18%.

For a better understanding of the influence of the feed pressure on the gas separation performance of the different membranes tested, the permeation flows (m^3(STP) m^2 (membrane) s^{-1}) of H_2 and CO_2 measured in the permeate were represented as a function of the feed pressure. As shown in Fig. 5, the feed pressure has a clear influence on the gas separation performance depending on the nature of the PBI membranes. Regarding the PBI dense membranes, both H_2 and CO_2 flows increased almost equally with the increase in pressure resulting in a constant H_2/CO_2 separation factor. In the case of PBI uncoated asymmetric membranes, the H_2 flow increased more than that of CO_2, leading to a higher separation factor.

Finally, for PBI membranes healed with PDMS the flow of CO_2 remained constant as a function of the pressure while the H_2 flow increased. The small thickness of their skin layer caused the membranes to reach CO_2 saturation (Langmuir regime versus that of Henry in the two previous situations), significantly increasing the separation factor. Moreover, the PDMS coating healed the membrane defects avoiding possible viscous flow. CO_2 adsorption experiments in Fig. S7 proved that the adsorption capacity of the asymmetric PBI membrane, with a more porous structure (as the SEM observation revealed), is ten-fold higher than that of the dense membrane, making the former more suitable for CO_2 saturation at higher pressures. This result is in agreement with the dual-sorption model, which asserts that Henry sorption is the main mechanism of sorption into the matrix component, while Langmuir sorption governs the sorption into the microvoid region [51].

A similar tendency can be seen for ZIF-8 MMMs in dense and asymmetric configurations (Figs. S8 and 5d, respectively). The dense MMMs show a constant selectivity due to a parallel increase in both H_2 and CO_2 gas flows. In contrast, the asymmetric MMMs show an improvement in the selectivity with increasing feed pressure. Compared to neat asymmetric PBI membranes, the CO_2 flow is higher, making the H_2/CO_2 selectivity values decrease. This may be the explained by relatively poor adsorption capacity of ZIF-8 (ca. 1.2 mmol/g at 100 kPa and 273 K) together with the shape of its adsorption isotherm (see Fig. S7). The lack of a flattened portion in the curve, contrary to the tendency of the asymmetric PBI isotherm, means that ZIF-8 is far from

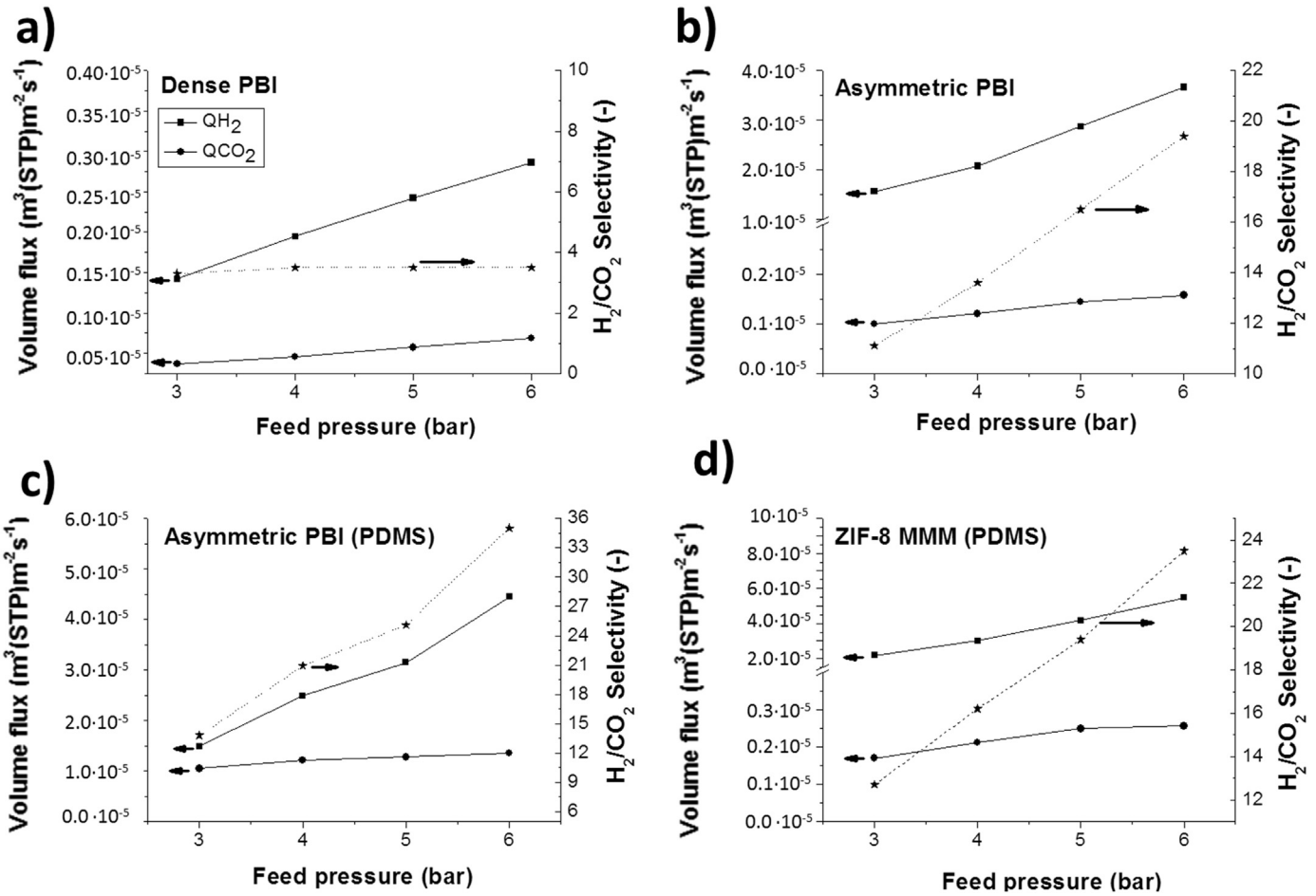

Fig. 5. Gas separation performance for the separation of H_2/CO_2 binary mixtures of flat PBI membranes, dense (a) and asymmetric before (b) and after coating with PDMS(c) and asymmetric ZIF-8 MMM healed with PDMS (d) at different operating pressures. Fluxes of H_2 and CO_2 in $m^3(STP)\cdot m^2$ (membrane)$\cdot s^{-1}$ are given. (a) was tested at 150 °C while (b), (c) and (d) at 250 °C.

saturation.

3.5. Membrane calculations

Pesek and Koros [52] considered that if the selectivity of an asymmetric membrane was higher than 80% of the intrinsic selectivity of the dense film, the gas transport was mostly controlled by the solution/diffusion mechanism. Otherwise the transport through membrane defects would predominate.The skin layer thickness can be estimated from the ratio of gas permeability measured from the flat membrane and the hollow fiber permeance under the same testing conditions. The thickness of the asymmetric PBI membranes of this work was calculated from the gas permeation data at 180 °C and a feed pressure of 3 bar (Fig. 4a) using Eq. (1):

$$l(\mu m) = \frac{H_2 Permeability \quad (Barrer)}{H_2 Permeance \quad (GPU)} \tag{1}$$

where the permeability represents the intrinsic permeation property of the polymeric material obtained from experiments with PBI dense membranes of known thickness. The calculated skin layer thickness for the self-supported and supported membranes were 15.2 and 2.1 μm, respectively. These values are in agreement with the SEM images in Fig. 1.

Fig. 4a shows how PBI supported asymmetric membranes coated with PDMS have higher selectivity values than self-supported membranes. Thus, the substructure of the former may contribute to their overall selectivity. The contribution of the substructure to the overall resistance (reciprocal to the permeance) can be estimated using a resistance model, considering that the skin layer, substructure and PDMS coating are connected in series (Eq. (2)) [53]:

$$\alpha_{H_2/CO_2} = \frac{(\alpha_1)_{H_2/CO_2} + (\alpha_2)_{H_2/CO_2}\left[\frac{(R_2)_{H_2}}{(R_1)_{H_2}}\right] + (\alpha_3)_{H_2/CO_2}\left[\frac{(R_3)_{H_2}}{(R_1)_{H_2}}\right]}{1+\left[\frac{(R_2)_{H_2}}{(R_1)_{H_2}} + \frac{(R_3)_{H_2}}{(R_1)_{H_2}}\right]} \tag{2}$$

where *1*, *2* and *3* refer to the resistance/selectivity of the skin layer, the substructure and PDMS coating, respectively. The known values in this equation, obtained from Fig. 4a, are: (*i*) those of the skin layer, considered the same as for self-supported asymmetric PBI ($(\alpha_1)_{H_2/CO_2} = 9.5$ and $R_1 = 1/2.1 GPU^{-1}$); (*ii*) the overall selectivity of the supported PBI asymmetric membrane ($\alpha_{H_2/CO_2} = 12.6$); and (*iii*) the values for PDMS ($R_3 = 1/1500 GPU^{-1}$ and $(\alpha_3)_{H_2/CO_2} = 0.8$), obtained from the literature [54]. Considering Kundsen selectivity as the substructure selectivity ($(\alpha_2)_{H_2/CO_2} = 4.7$), the calculated substructure layer resistance is 0.24 GPU^{-1}, meaning 33% of the total resistance of the membrane.

The contribution of the substructure to the overall resistance in the MMMs at 180 °C can also be estimated using Eq. (2). In this case the known values, different from the previous calculation, are: (*i*) those of the skin layer, obtained from the literature [14] ($(\alpha_1)_{H_2/CO_2} = 18$ and $R_1 = 1/3.0 GPU^{-1}$) and (*ii*) the overall selectivity obtained from Fig. 4 ($\alpha_{H_2/CO_2} = 14.5$). The estimated substructure layer resistance was 0.12 GPU^{-1}, thus, 26% of the total resistance of the membrane. The reduction in this resistance value compared to that of bare PBI membranes (33%) may suggest that the filler is also somehow dispersed in the PBI substructure and not only located in the skin layer. The

additional porosity of the ZIF-8/PBI composite, caused by the incorporation of the filler nanoparticles, enhances the diffusion of gases in the PBI layer, decreasing the flow resistance. Besides, the decrease in both the substructure resistance and the activation energy of H_2 may explain how the filler can be useful for the flow increase but not for an increase in the H_2/CO_2 selectivity (as seen in Figs. 4 and 5).

4. Conclusions

Asymmetric PBI flat membranes have been studied in this work. Neat polymeric membranes and ZIF-8 MMMs were prepared with this configuration. The concentration of the polymer dope strongly influenced the skin layer thickness and the mechanical resistance of the membrane. Dopes at 26 wt% led to self-supported and defect-free membranes, while 20 wt% dopes resulted in PBI membranes that needed a P84® support and PDMS healing. Characterization by SEM and Raman revealed that the latter membranes were constituted by a thin skin layer of around 1 μm on a finger-like macroporous structure. ZIF-8 was also successfully embedded in the polymer phase creating asymmetric PBI MMMs, with the nanoparticles clearly visible in the membrane cross-section. The necessary amount of ZIF was 2.5 fold smaller in comparison with equally loaded dense membranes. The membranes were tested for H_2/CO_2 pre-combustion mixed-gas separation up to 250 °C and 6 bar of feed pressure. The asymmetric PBI showed a better gas separation performance than PBI dense membranes, thanks to the different polymeric structure of the skin layer with this new membrane configuration. Embedding ZIF-8 into the PBI helped to enhance the gas separation performance of the membranes. Increasing the feed pressure had a positive effect on the performance of membranes with a thin skin layer. While the H_2 flow increased constantly with pressure, high pressures had a saturating effect on the CO_2 adsorption. This led to a change from the Henry to Langmuir regime that allowed a huge H_2/CO_2 selectivity increase. The substructure layer resistance in neat polymeric membranes was 33% of the total resistance of the membrane. For the MMMs this value was slightly smaller (26%). The same occurred with the calculated activation energy of the membranes, which decreased for H_2 when ZIF-8 was incorporated. Both facts indicate that the filler may only be useful in the current MMMs to increase the permeation flow.

Acknowledgments

The research leading to these results has received funding from the European Union Seventh Framework Programme (FP7/2007–2013) under grant agreement n° 608490, project M4CO2. In addition, financial support from the Spanish MINECO and FEDER (MAT2016-77290-R), the Aragón Government (T05) and the ESF is gratefully acknowledged. J. S-L. thanks the Spanish Education Ministry Program FPU2014 for his Ph.D. grant. All the microscopy work was done in the Laboratorio de Microscopías Avanzadas at the Instituto de Nanociencia de Aragón (LMA-INA). Finally, the authors would like to acknowledge the use of the Servicio General de Apoyo a la Investigación-SAI, Universidad de Zaragoza.

Appendix A. Supplementary material

Supplementary data associated with this article can be found in the online version at http://dx.doi.org/10.1016/j.memsci.2018.06.009.

References

[1] Z. Dai, L. Ansaloni, L. Deng, Precombustion CO_2 capture in polymeric hollow fiber membrane contactors using ionic liquids: porous membrane versus nonporous composite membrane, Ind. Eng. Chem. Res 55 (2016) 5983.
[2] S. Lee, J. Kang, K.T. Leung, W. Lee, D. Kim, S. Han, et al., Unique multi-phase Co/Fe/$CoFe_2O_4$ by water–gas shift reaction, CO oxidation and enhanced supercapacitor performances, J. Ind. Eng. Chem. 43 (2016) 69.
[3] J. Franz, P. Maas, V. Scherer, Economic evaluation of pre-combustion CO_2-capture in IGCC power plants by porous ceramic membranes, Appl. Energy 130 (2014) 532.
[4] Z. Ali, F. Pacheco, E. Litwiller, Y. Wang, Y. Han, I. Pinnau, Ultra-selective defect-free interfacially polymerized molecular sieve thin-film composite membranes for H_2 purification, J. Mater. Chem. A (2018) 30.
[5] M. Sadeghi, M.A. Semsarzadeh, H. Moadel, Enhancement of the gas separation properties of polybenzimidazole (PBI) membrane by incorporation of silica nano particles, J. Membr. Sci. 331 (2009) 21.
[6] S. Kumbharkar, M.N. Islam, R. Potrekar, U. Kharul, Variation in acid moiety of polybenzimidazoles: investigation of physico-chemical properties towards their applicability as proton exchange and gas separation membrane materials, Polymer 50 (2009) 1403.
[7] T. Chung, A critical review of polybenzimidazoles: historical development and future R&D, J. Macromol. Sci. Part C: Polym. Rev. 37 (1997) 277.
[8] R.W. Baker. Overview of membrane science and technology, Membr. Technol. Appl., Second Edition, 2004, p. 1.
[9] S. Loeb, S. Sourirajan, Saline water conversion-II, Adv. Chem. Ser. 38 (1963) 117.
[10] V. Giel, Z. Morávková, J. Peter, M. Trchová, Thermally treated polyaniline/polybenzimidazole blend membranes: structural changes and gas transport properties, J. Membr. Sci. 537 (2017) 315.
[11] V. Giel, M. Perchacz, J. Kredatusová, Z. Pientka, Gas transport properties of polybenzimidazole and poly (phenylene oxide) mixed matrix membranes incorporated with PDA-functionalised titanate nanotubes, Nanoscale Res. Let. 12 (2017) 3.
[12] H.S.M. Suhaimi, C.P. Leo, A.L. Ahmad, Hydrogen purification using polybenzimidazole mixed-matrix membranes with stabilized palladium nanoparticles, Chem. Eng. Technol. 40 (2017) 631.
[13] J.R. Klaehn, C.J. Orme, E.S. Peterson, Blended polybenzimidazole and melamine-co-formaldehyde thermosets, J. Membr. Sci. 515 (2016) 1.
[14] X. Li, R.P. Singh, K.W. Dudeck, K.A. Berchtold, B.C. Benicewicz, Influence of polybenzimidazole main chain structure on H_2/CO_2 separation at elevated temperatures, J. Membr. Sci. 461 (2014) 59.
[15] T. Yang, T. Chung, High performance ZIF-8/PBI nano-composite membranes for high temperature hydrogen separation consisting of carbon monoxide and water vapor, Int. J. Hydrog. Energy 38 (2013) 229.
[16] T. Yang, Y. Xiao, T. Chung, Poly-/metal-benzimidazole nano-composite membranes for hydrogen purification, Energy Environ. Sci. 4 (2011) 4171.
[17] S.C. Kumbharkar, P.B. Karadkar, U.K. Kharul, Enhancement of gas permeation properties of polybenzimidazoles by systematic structure architecture, J. Membr. Sci. 286 (2006) 161.
[18] D.R. Pesiri, B. Jorgensen, R.C. Dye, Thermal optimization of polybenzimidazole meniscus membranes for the separation of hydrogen, methane, and carbon dioxide, J. Membr. Sci. 218 (2003) 11.
[19] J. Sánchez-Laínez, B. Zornoza, S. Friebe, J. Caro, S. Cao, A. Sabetghadam, et al., Influence of ZIF-8 particle size in the performance of polybenzimidazole mixed matrix membranes for pre-combustion CO_2 capture and its validation through interlaboratory test, J. Membr. Sci. 515 (2016) 45.
[20] J. Sánchez-Laínez, B. Zornoza, C. Téllez, J. Coronas, On the chemical filler–polymer interaction of nano-and micro-sized ZIF-11 in PBI mixed matrix membranes and their application for H_2/CO_2 separation, J. Mater. Chem. A 4 (2016) 14334.
[21] R.P. Singh, G.J. Dahe, K.W. Dudeck, C.F. Welch, K.A. Berchtold, High temperature polybenzimidazole hollow fiber membranes for hydrogen separation and carbon dioxide capture from synthesis gas, Energy Proc. 63 (2014) 153.
[22] K.A. Berchtold, R.P. Singh, J.S. Young, K.W. Dudeck, Polybenzimidazole composite membranes for high temperature synthesis gas separations, J. Membr. Sci. 415 (2012) 265.
[23] S. Kumbharkar, K. Li, Structurally modified polybenzimidazole hollow fibre membranes with enhanced gas permeation properties, J. Membr. Sci. 415 (2012) 793.
[24] S. Kumbharkar, Y. Liu, K. Li, High performance polybenzimidazole based asymmetric hollow fibre membranes for H_2/CO_2 separation, J. Membr. Sci. 375 (2011) 231.
[25] S.S. Hosseini, N. Peng, T.S. Chung, Gas separation membranes developed through integration of polymer blending and dual-layer hollow fiber spinning process for hydrogen and natural gas enrichments, J. Membr. Sci. 349 (2010) 156.
[26] M.F. Flanagan, I.C. Escobar, Novel charged and hydrophilized polybenzimidazole (PBI) membranes for forward osmosis, J. Membr. Sci. 434 (2013) 85.
[27] R. Hausman, B. Digman, I.C. Escobar, M. Coleman, T. Chung, Functionalization of polybenzimidizole membranes to impart negative charge and hydrophilicity, J. Membr. Sci. 363 (2010) 195.
[28] K.Y. Wang, Y. Xiao, T. Chung, Chemically modified polybenzimidazole nanofiltration membrane for the separation of electrolytes and cephalexin, Chem. Eng. Sci. 61 (2006) 5807.
[29] S. Basu, A. Cano-Odena, I.F. Vankelecom, Asymmetric matrimid®/$[Cu_3(BTC)_2]$ mixed-matrix membranes for gas separations, J. Membr. Sci. 362 (2010) 478.
[30] H. Ren, J. Jin, J. Hu, H. Liu, Affinity between metal–organic frameworks and polyimides in asymmetric mixed matrix membranes for gas separations, Ind. Eng. Chem. Res. 51 (2012) 10156.
[31] J. Van't Hof, A. Reuvers, R. Boom, H. Rolevink, C. Smolders, Preparation of asymmetric gas separation membranes with high selectivity by a dual-bath coagulation method, J. Membr. Sci. 70 (1992) 17.
[32] S. Basu, A. Cano-Odena, I.F. Vankelecom, MOF-containing mixed-matrix membranes for CO_2/CH_4 and CO_2/N_2 binary gas mixture separations, Sep. Purif. Technol. 81 (2011) 31.
[33] T. Chung, L.Y. Jiang, Y. Li, S. Kulprathipanja, Mixed matrix membranes (MMMs) comprising organic polymers with dispersed inorganic fillers for gas separation, Prog. Polym. Sci. 32 (2007) 483.
[34] N. Nordin, A.F. Ismail, A. Mustafa, Synthesis and preparation of asymmetric PSf/ZIF-8 mixed matrix membrane for CO_2/CH_4 separation, J. Teknol. 69 (2014) 73.

[35] T. Yang, G.M. Shi, T. Chung, Symmetric and asymmetric zeolitic imidazolate frameworks (ZIFs)/polybenzimidazole (PBI) nanocomposite membranes for hydrogen purification at high temperatures, Adv. Energy Mater. 2 (2012) 1358.
[36] A. Bhaskar, R. Banerjee, U. Kharul, ZIF-8@ PBI-BuI composite membranes: elegant effects of PBI structural variations on gas permeation performance, J. Mater. Chem. A 2 (2014) 12962.
[37] N. Liédana, A. Galve, C. Rubio, C. Téllez, J. Coronas, CAF@ ZIF-8: one-step encapsulation of caffeine in MOF, ACS Appl. Mater. Interfaces 4 (2012) 5016.
[38] B.W. Rowe, L.M. Robeson, B.D. Freeman, D.R. Paul, Influence of temperature on the upper bound: theoretical considerations and comparison with experimental results, J. Membr. Sci. 360 (2010) 58.
[39] T. Chung, W.F. Guo, Y. Liu, Enhanced matrimid membranes for pervaporation by homogenous blends with polybenzimidazole (PBI), J. Membr. Sci. 271 (2006) 221.
[40] PBI Performance Products, Inc., Solutions brochure of polybenzimidazole (PBI) S26 solution 〈https://pbipolymer.com/wp-content/uploads/2016/05/Celazole-PBI-S26-Typical-Properties.pdf〉.
[41] T.S. Chung, S.K. Teoh, X. Hu, Formation of ultrathin high-performance polyethersulfone hollow-fiber membranes, J. Membr. Sci. 133 (1997) 161.
[42] K.Y. Wang, T. Chung, R. Rajagopalan, Dehydration of tetrafluoropropanol (TFP) by pervaporation via novel PBI/BTDA-TDI/MDI co-polyimide (P84) dual-layer hollow fiber membranes, J. Membr. Sci. 287 (2007) 60.
[43] C. Echaide-Górriz, S. Sorribas, C. Téllez, J. Coronas, MOF nanoparticles of MIL-68 (Al), MIL-101 (Cr) and ZIF-11 for thin film nanocomposite organic solvent nanofiltration membranes, RSC Adv. 6 (2016) 90417.
[44] C. Echaide-Górriz, M. Navarro, C. Téllez, J. Coronas, Simultaneous use of MOFs MIL-101 (Cr) and ZIF-11 in thin film nanocomposite membranes for organic solvent nanofiltration, Dalton Trans. 46 (2017) 6244.
[45] F. Conti, A. Majerus, V. Di Noto, C. Korte, W. Lehnert, D. Stolten, Raman study of the polybenzimidazole–phosphoric acid interactions in membranes for fuel cells, Phys. Chem. Chem. Phys. 14 (2012) 10022.
[46] J. Young, W. Tsai, F. Boerio, Characterization of the interface between pyromellitic dianhydride/oxydianiline polyimide and silver using surface-enhanced Raman scattering, Macromolecules 25 (1992) 887.
[47] S.S. Hosseini, T.S. Chung, Carbon membranes from blends of PBI and polyimides for N_2/CH_4 and CO_2/CH_4 separation and hydrogen purification, J. Membr. Sci. 328 (2009) 174.
[48] X.Y. Chen, S. Kaliaguine, D. Rodrigue, Correlation between performances of hollow fibers and flat membranes for gas separation, Sep. Purif. Rev. (2017).
[49] D.F. Sanders, Z.P. Smith, R. Guo, L.M. Robeson, J.E. McGrath, D.R. Paul, et al., Energy-efficient polymeric gas separation membranes for a sustainable future: a review, Polymer 54 (2013) 4729.
[50] L.M. Robeson, The upper bound revisited, J. Membr. Sci. 320 (2008) 390.
[51] M. Askari, M.L. Chua, T. Chung, Permeability, solubility, diffusivity, and PALS data of cross-linkable 6FDA-based copolyimides, Ind. Eng. Chem. Res. 53 (2014) 2449.
[52] S. Pesek, W. Koros, Aqueous quenched asymmetric polysulfone hollow fibers prepared by dry/wet phase separation, J. Membr. Sci. 88 (1994) 1.
[53] I. Pinnau, W.J. Koros, Relationship between substructure resistance and gas separation properties of defect-free integrally skinned asymmetric membranes, Ind. Eng. Chem. Res. 30 (1991) 1837.
[54] T. Merkel, R. Gupta, B. Turk, B. Freeman, Mixed-gas permeation of syngas components in poly (dimethylsiloxane) and poly (1-trimethylsilyl-1-propyne) at elevated temperatures, J. Membr. Sci. 191 (2001) 85.

Supporting Information

Membrane characterization

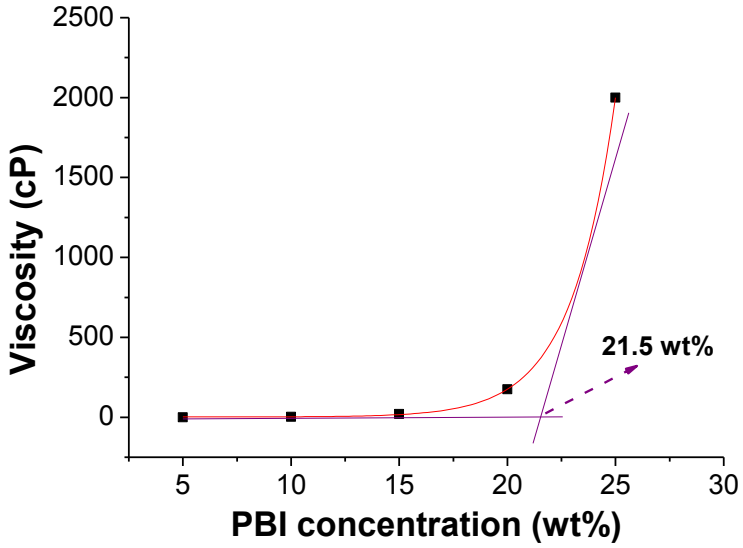

Figure S1. Viscosity of PBI solution as a function of PBI concentration in DMAc solvent at 25 °C from PBI Performance Products data [1]. The critical value for the fabrication of asymmetric membranes is indicated.

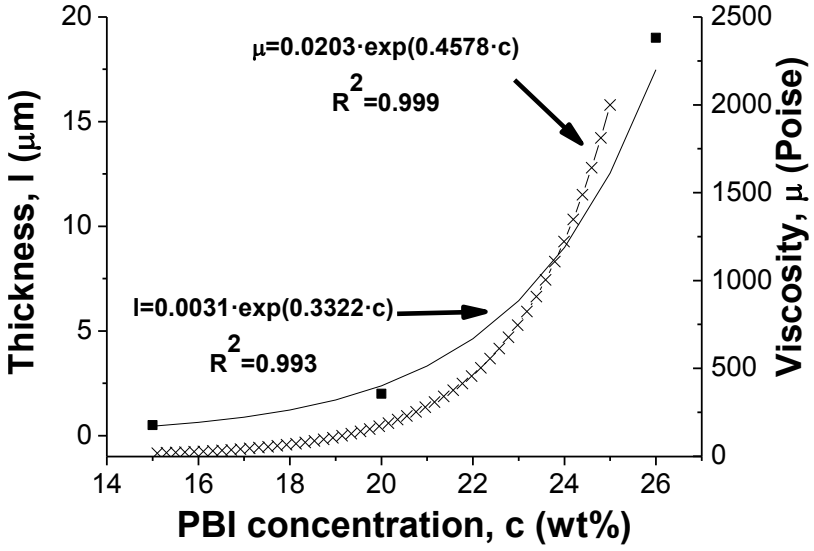

Figure S2. PBI membrane skin layer thickness and PBI solution viscosity at 25 °C as function of PBI concentration in DMAc. Both curves have been fitted to exponential functions that are also shown. Squares correspond to thickness values and crosses, to those of viscosity.

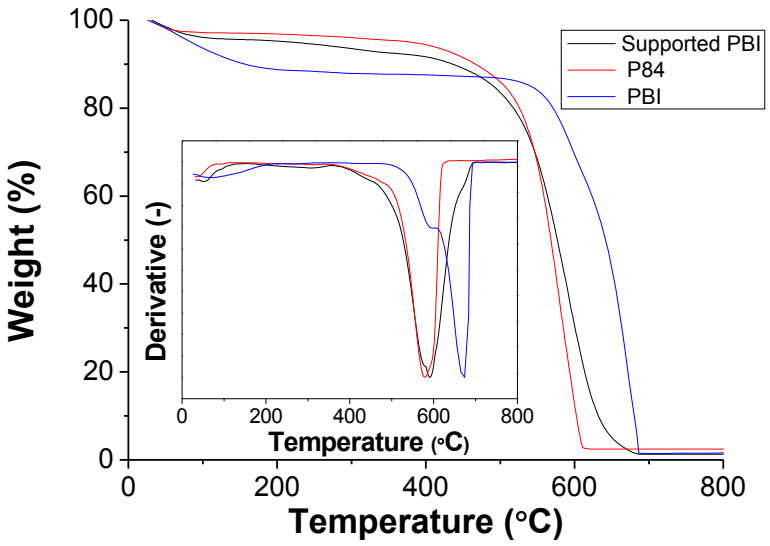

Figure S3. TGA analyses in air and their derivatives (inset) of a PBI supported membrane (black), a P84® support (red) and a PBI dense membrane (blue).

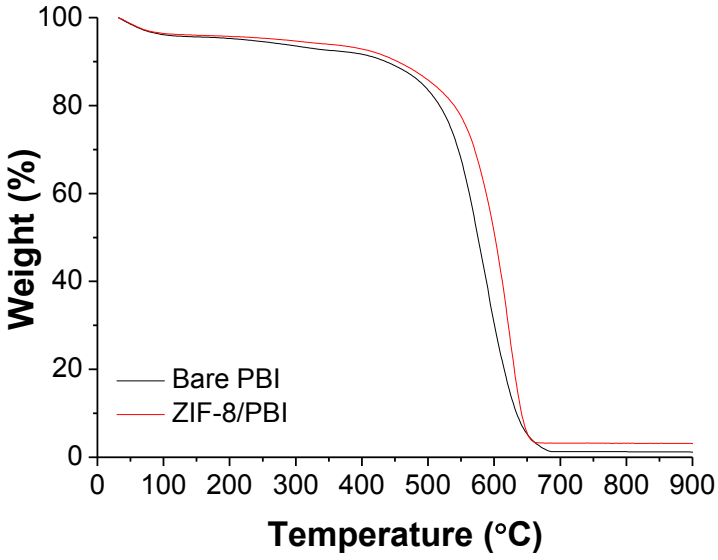

Figure S4. TGA analyses in air of a bare asymmetric PBI membrane (black) and a 10 wt% ZIF-8 MMM (red).

Table S1. Gas separation performance of the different PBI membranes shown in Figure 4a.

Membrane	H_2 Permeance (GPU)	H_2/CO_2 Selectivity (-)
Dense	0.32±0.01	3.0±0.6
Self-supported	2.1±0.4	9.5±0.3
Supported	15.2	7.9
Supported (PDMS)	6.5±0.8	12.6±0.1
ZIF-8 (PDMS)	11.1±0.6	14.5±0.9

Robeson upper-bound adapted

Table S2. Literature review with the values that defined the upper-bound in 2008, including membrane thickness, H_2 permeability in Barrer and H_2/CO_2 selectivity. The calculated H_2 permeance in GPU is given.

Polymer	Thickness (µm)	H_2 permeability (Barrer)	H_2 permeation (GPU)	α (H_2/CO_2)	Ref.
Liquid crystalline polyester (HBA/HNA 30/70)	75-130	0.0545	$5.317 \cdot 10^{-4}$	100.9	[2]
Polyaniline (redoped)	12	1.753	0.146	23.1	[3]
Polyimide(1,1-6FDA-DIA)	25-60	31.4	0.739	8.05	[4]
Poly(trimethylsilylpropyne)	400	13900	34.75	0.495	[5]
Poly(trimethylsilylpropyne-cophenylpropyne) (95/5)	400	20400	51	0.538	[6]
Poly(trimethylsilylpropyne)	400	23200	58	0.53	[6]

The Robeson upper-bound, revised in 2008 [7] was defined from pure component permeability data of dense membranes, allowing the determination of the state-of-the-art limits for polymeric membrane gas separation. The upper-bound relationship is expressed by $P_i = k \cdot \alpha_{ij}^{n}$, where P_i is the permeability of the more permeable gas, α is the separation factor (P_i/P_{ij}) and n is the slope of the log–log limit. It was observed that $-1/n$ vs. d_{ij} (where d_{ij} is the difference between the gas molecular diameters $(d_j - d_i)$) yielded a linear relationship. Since gas permeability was defined in Barrer, we have calculated an H_2/CO_2 upper-bound relationship in GPU, using the values from the literature that defined the original upper-bound but changing the flow values from Barrer into GPU (see Table S1). These values were represented in Fig. S5 and fitted to a logarithmic equation, resulting in the following upper-bound relationship: $P_{H_2} = 17.332 \cdot \alpha_{H_2/CO_2}^{-1.943}$. A factor k of 17.332 GPU was obtained and the slope n of -1.943 was near the value found in the original publication, implying that its inverse corresponds to the difference between the gas molecular diameters of H_2 (2.9 Å) and CO_2 (3.3 Å).

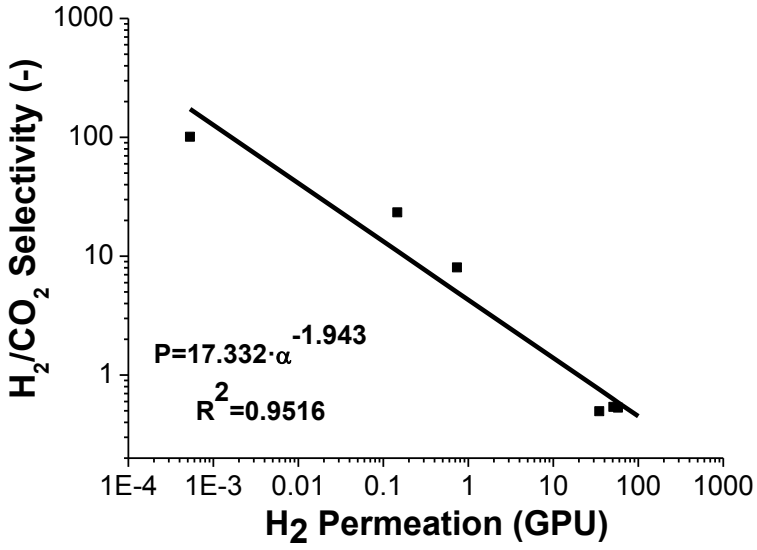

Figure S5. H_2/CO_2 upper-bound defined in GPU at 35 ^{0}C. Squares represent the values in GPU of Table S1. The fitting equation of the linear fitting is also given with the R^2 value**.**

The upper-bound shifts with the temperature according to Eq. S1 [8]:

$$\alpha_{H_2/CO_2} = \frac{k \cdot e^{\gamma/T}}{P_{H_2}^{1/n}} \quad (Eq.1)$$

where γ indicates the effect of temperature (in Kelvin) on the solubility and diffusivity of H_2 and CO_2, and k and n are the values previously calculated (17.332 GPU and -1.943, respectively). For H_2 and CO_2 in polymers, γ has a value of -543 K [8]. This way the upper-bound can be calculated at 180 and 250 ^{0}C (453.15 and 523.15 K, respectively) using the Eq. S2 and S3.

$$\alpha_{H_2/CO_2} = \frac{17.332 \cdot e^{-543/423.15}}{P_{H_2}^{1/-1.943}} \quad (Eq.2)$$

$$\alpha_{H_2/CO_2} = \frac{17.332 \cdot e^{-543/523.15}}{P_{H_2}^{1/-1.943}} \quad (Eq.3)$$

Gas separation performance

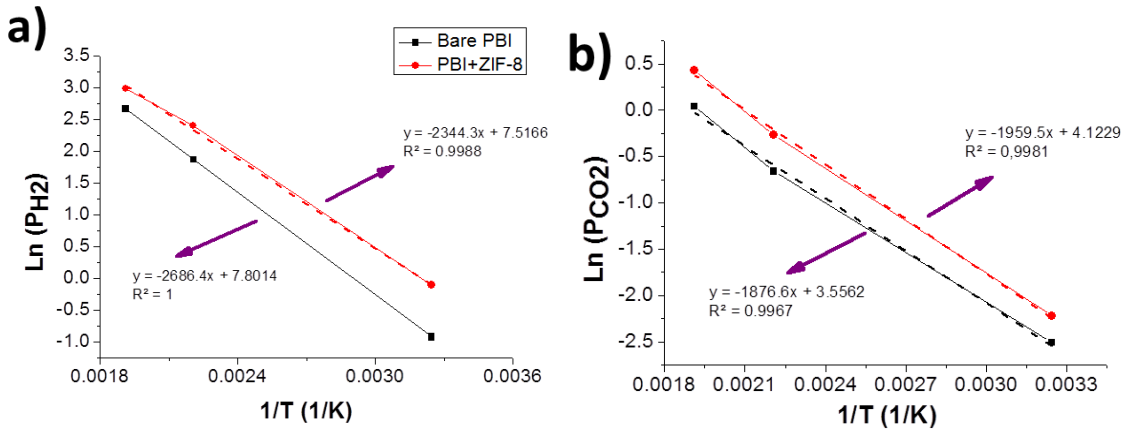

Figure S6. Activation energies of PBI membranes. The activation energies of bare PBI membranes and MMMs containing ZIF-8 were calculated from H_2 (a) and CO_2 permeation data (b), representing the logarithm of the corresponding permeance vs. the inverse value of the temperature. The graph was linear fitted according to the Arrhenius tendency. Values of bare PBI membranes are given in black and those of MMMs, in red. The fitting equations with the R^2 values are given.

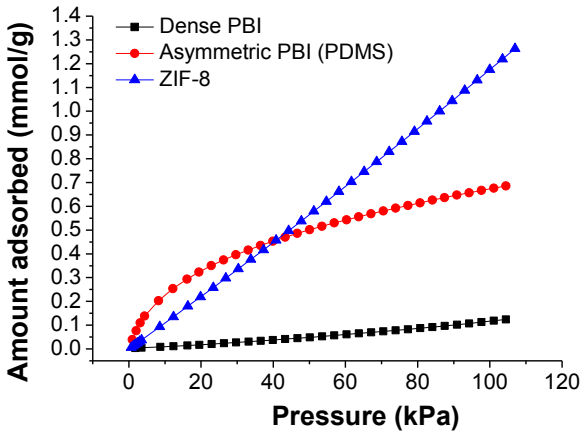

Figure S7. CO_2 adsorption isotherms of dense and asymmetric PBI membranes and ZIF-8 at 273K.

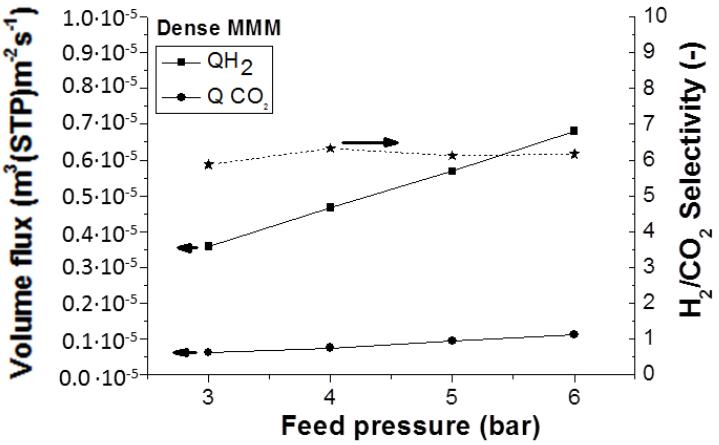

Figure S8. Gas separation performance for the separation of H_2/CO_2 binary mixtures at 150 °C of 10 wt% ZIF-8 dense MMM at different operating pressures. H_2 and CO_2 fluxes are given in $m^3(STP)\cdot m^2(membrane).s^{-1}$. The data were obtained from [9]. H_2 flux correspond to squares; CO_2 flux, to circles and H_2/CO_2 selectivities, to stars.

References

[1] PBI Performance Products, Inc., Solutions brochure of "polybenzimidazole (PBI) S26 solution. *https://pbipolymer.com/wp-content/uploads/2016/05/Celazole-PBI-S26-Typical-Properties.pdf*.

[2] D. Weinkauf, D. Paul. Gas transport properties of thermotropic liquid-crystalline copolyesters. II. The effects of copolymer composition. J. Polym. Sci. Part B: Polym. Phys., 30 (1992) 837.

[3] G. Illing, K. Hellgardt, M. Schonert, R. Wakeman, and A. Jungbauer. Towards ultrathin polyaniline films for gas separation. J. Membr. Sci., 253 (2005) 199.

[4] M.E. Rezac, B. Schöberl. Transport and thermal properties of poly (ether imide)/acetylene-terminated monomer blends. J. Membr. Sci., 156 (1999) 211.

[5] K. Nagai, A. Higuchi, and T. Nakagawa. Bromination and gas permeability of poly (1-trimethylsilyl-1-propyne) membrane. J. Appl. Polym. Sci., 54 (1994) 1207.

[6] K. Nagai, A. Higuchi, and T. Nakagawa. Gas permeability and stability of poly (1-trimethylsilyl-1-propyne-co-1-phenyl-1-propyne) membranes. J. Polym. Sci. Part B: Polym. Phys., 33 (1995) 289.

[7] L.M. Robeson. The upper bound revisited. J. Membr. Sci., 320 (2008) 390.

[8] B.W. Rowe, L.M. Robeson, B.D. Freeman, and D.R. Paul. Influence of temperature on the upper bound: Theoretical considerations and comparison with experimental results. J. Membr. Sci., 360 (2010) 58.

[9] J. Sánchez-Laínez, B. Zornoza, C. Téllez, and J. Coronas. On the chemical filler–polymer interaction of nano-and micro-sized ZIF-11 in PBI mixed matrix membranes and their application for H_2/CO_2 separation. J. Mater. Chem. A, 4 (2016) 14334.

Chapter 10: Hydrogen separation at high temperature with dense and asymmetric membranes based on PIM-EA(H_2)-TB/PBI blends

Reprinted with permission from (J. Sánchez-Laínez, B. Zornoza, M. Carta, R. Malpass-Evans, N. B. McKeown, C. Téllez and J. Coronas. Industrial & Engineering Chemistry Research, 57 (2018) 16909– 16916. DOI: 10.1021/acs.iecr.8b04209.).

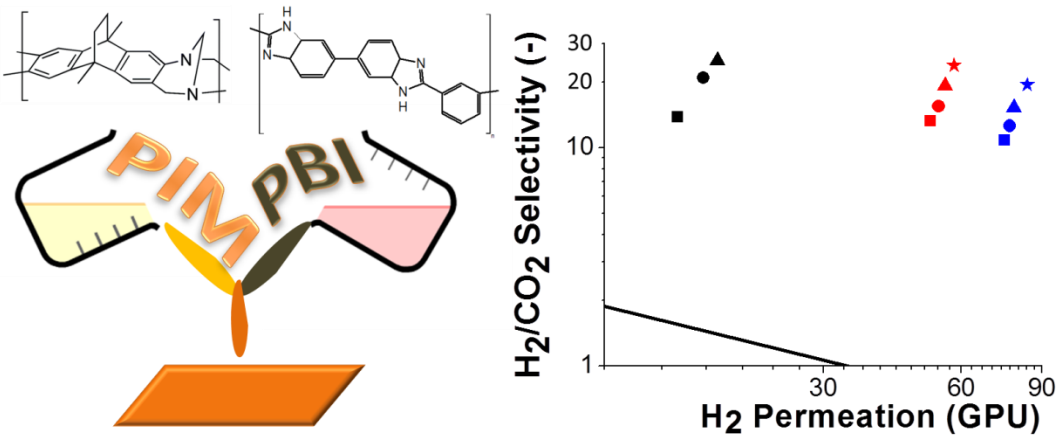

Category:

- Type of membrane: integrally skinned asymmetric membranes
- Gas separation: pre-combustion CO_2 capture

I&EC research
Industrial & Engineering Chemistry Research

Article

Cite This: Ind. Eng. Chem. Res. 2018, 57, 16909−16916

pubs.acs.org/IECR

Hydrogen Separation at High Temperature with Dense and Asymmetric Membranes Based on PIM-EA(H_2)-TB/PBI Blends

Javier Sánchez-Laínez,[†] Beatriz Zornoza,[†] Mariolino Carta,[‡] Richard Malpass-Evans,[‡] Neil B. McKeown,[‡] Carlos Téllez,[†] and Joaquín Coronas*,[†]

[†]Chemical and Environmental Engineering Department, Instituto de Nanociencia de Aragón (INA), Universidad de Zaragoza, 50018 Zaragoza, Spain

[‡]EastChem, School of Chemistry, University of Edinburgh, David Brewster Road, Edinburgh EH9 3FJ, U.K.

Supporting Information

ABSTRACT: The preparation of dense and asymmetric flat membranes from the blending of polybenzimidazole (PBI) and (1.5−20 wt %) of a polymer of intrinsic microporosity (PIM-EA(H_2)-TB) is reported. Thermal characterization validated the blend by revealing a single glass transition temperature, which suggests the absence of polymer phase segregation. In addition, the decomposition activation energy and *d*-spacing of the blends follow trends that correlate with the amount of PIM component. The membranes have been tested for the separation of H_2/CO_2 mixtures. The properties of the dense membranes, which also incorporate zeolitic imidazolate-8 (ZIF-8) nanoparticles, helped understanding of the behavior of the PIM/PBI blends by which phase inversion results in high separation performance asymmetric membranes. Asymmetric membranes show H_2/CO_2 selectivities of 23.8 (10/90 wt % PIM/PBI) and 19.4 (20/80 wt % PIM/PBI) together with respective H_2 permeances of 57.9 and 83.5 GPU at 250 °C and 6 bar feed pressure. The gas separation performance of these asymmetric blends has been fitted to an empirical model, showing the influence of the amount of PIM and the feed pressure.

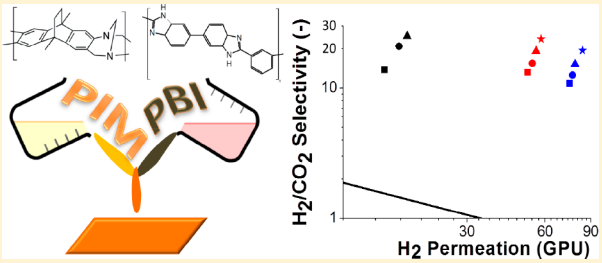

INTRODUCTION

Membranes are an energy-efficient technology for gas separation and purification compared to other technologies, such as those based on distillation and absorption processes. Because of their low energy cost and separation efficiency, as well as their small footprint and reliability, membrane units operate at large- and small-scale, across the globe, for liquid- and gas-phase separations. However, polymeric membranes show limitations in their gas separation performance, especially because of their relatively low permeance and limited operating temperature.[1] Several solutions have been proposed to develop high-performance gas separation membranes, among which polymer blending and the preparation of mixed matrix membranes (MMMs) are of particular importance. The blending of polymers seeks the synergistic combination of different materials that can overcome their individual deficiencies. Miscible polymer blends are desirable to prepare homogeneous membranes with uniform and stable thermal and mechanical properties.[2] MMMs consist of embedded particles (i.e., fillers, which are often crystalline and porous) within a processable polymer matrix within a polymeric phase. Various polymers have been modified with inorganic fillers, such as zeolites or mesoporous silicas,[3,4] and metal organic frameworks (MOFs)[5−7] to enhance their gas separation performance.

H_2/CO_2 separation has special relevance to hydrogen production and precombustion carbon capture. Many advances have been recently published on materials and membranes for this separation at high temperature.[8−11] Polybenzimidazole (PBI) is a polymer widely used to prepare membranes for H_2/CO_2 separation.[12−17] It possesses high thermal and chemical stabilities, good mechanical resistance, and a high intrinsic H_2/CO_2 selectivity. Nevertheless, its main disadvantages are low permeability and brittleness.[18] In contrast, polymers of intrinsic microporosity (PIMs) display huge H_2 permeability as self-standing films often well in excess of 1000 Barrer (1 Barrer = 10^{-10} cm^3(STP) cm cm^{-2} s^{-1} $cmHg^{-1}$) but with limited size selectivity for H_2 over CO_2 due to the relatively large voids present in their structure.[19] The fabrication of a film from the blend of both PBI and a PIM might result in one membrane with good H_2/CO_2 selectivity and enhanced permeability. PBI has already been blended with polyimides, such as Matrimid,[20,21] P84,[22] DPPD-IMM,[23] or Torlon,[20,22] obtaining interesting gas separation performance. The good miscibility between PBI and the polyimides is obtained because of the affinity between the N−H of the former and the C=O of the latter, allowing the formation of hydrogen bonds.[24] The polyimide segments reinforced the mechanical strength of the membranes while the PBI chains increased their

Received: August 30, 2018
Revised: November 7, 2018
Accepted: November 12, 2018
Published: November 12, 2018

thermal stability. Blends of PBI can also be found in the literature with polyaniline[25] and polyvinylidene fluoride (PVDF).[26] PIMs have also been blended with polyimides.[27−31] For instance, PIM-1 has been mixed with Matrimid, with even low amounts (∼10 wt %) increasing permeability by ∼75% with a minimal reduction of CO_2/CH_4 selectivity.[32] PIM-1 has also been blended with polyethylene glycol (PEG), giving excellent results for the separation of CO_2/N_2 and CO_2/CH_4 mixtures, superior to those of neat PIM-1, with CO_2 permeabilities close to 2000 Barrer and CO_2/N_2 and CO_2/CH_4 selectivities of 16 and 39, respectively.[33] The blending of PIM-1 with sulfonated polyphenylenesulfone (sPPSU) can also be found in the literature.[34,35] The increase in the degree of sulfonation in sPPSU/PIM-1 blends led to a decrease in chain−chain packing and therefore an enhancement in the CO_2/CH_4 selectivity.[35]

In this work we show the preparation of dense and asymmetric flat membranes from the blending of PBI and PIM-EA(H_2)-TB at different proportions. PIM-EA(H_2)-TB contains ethanoanthracene (EA) components linked by Tröger-base (TB) (2,8-dimethyl-6*H*,12*H*-5,11-methanol dibenzo[*b*,*f*][1,5]diazocina).[36] It possesses an extremely rigid backbone that allows it to display a small selectivity for H_2 over CO_2 at room temperature. Therefore, PIM-EA(H_2)-TB is more appropriate than other PIMs for blending to obtain membranes for H_2/CO_2 separation. Most of the blends involving PBI (and PIM-1) were implemented as dense membranes with the exception of Matrimid−PBI[20,21] and PVDF−PBI,[26] which reinforces the novelty of this work. Moreover, ZIF-8 has been used as a porous filler to prepare MMMs with this blended polymer mixture as matrix. ZIF-8 is a zeolitic imidazolate framework with sodalite topology based on the coordination of Zn with the organic linker 2-methyl-imidazolate. It possesses cavities of 1.16 nm connected through pore windows of 0.34 nm.[36] In this way, the permeance of H_2 is expected to be favored over that of CO_2 (kinetic diameter of 0.29 vs 0.33 nm, respectively). The effects of composition, miscibility, microstructure, and gas separation performance are investigated.

EXPERIMENTAL METHODS

Dense MMM Film Preparation. The required amount of PIM (synthesized as previously reported from the reaction of 2,6(7)-diaminoanthracene with dimethoxymethane in trifluoroacetic acid[37−39]) was weighed for each blending proportion, from 1.5 to 20 wt %, and dispersed in DMAc (Sigma-Aldrich) with stirring at room temperature until complete dissolution was obtained. PBI commercial solution (26 wt % concentration in DMAc, Celazole S26) was added so that the final concentration of the polymer blend (ca. 40 mg in dry basis) in solvent was 10 wt %, and the stirring was maintained overnight. The casting solution was sonicated three times for 15 min periods and then cast into a Petri dish, which was left uncovered and placed on a leveled surface inside an oven at 90 °C. Once dried, the films were peeled off from the Petri dishes and washed for 24 h in MeOH (HPLC grade, Scharlau). Finally, the membranes were activated in an oven at 100 °C for 24 h to remove any remaining traces of solvent. For the blends that incorporated ZIF-8 (prepared as nanoparticles in a MeOH/H_2O mixture[40]), the filler was dispersed in DMAc previous to the first addition of the PIM polymer. Pure PBI membranes were prepared following the same procedure without incorporating any PIM (see Table S1 for further details).

Pure PIM-EA(H_2)-TB membranes were prepared by dissolving 40 mg of polymer in 3.6 g of chloroform (anhydrous, Sigma-Aldrich). The casting solution was stirred overnight, sonicated three times for 90 min in total, and cast into a leveled Petri dish. The Petri dishes were left covered to allow a slow evaporation of the solvent at room temperature. After that, the membranes followed the same soaking and drying procedure as for the blends. Note that different solvents have been used depending on the membrane polymer. Even if PIM membranes could be affected by the casting solvent,[41] the typical solvents in which the membranes were prepared and optimized were preferred: DMAc for pure PBI and chloroform for PIM containing membranes. Besides, the alternatives to DMAc are similar harm solvents such as DMF or NMP, while PIMs can benefit from less toxic solvents.

The thickness of the membrane samples (88 ± 16 μm) was measured with a Digimatic Micrometer Mitutoyo (measurement range from 0 to 30 mm with an accuracy of ±1 μm), considering the average of 9 values obtained at different places.

PBI Asymmetric Membrane Preparation. PBI asymmetric membranes were prepared via a phase inversion method. The corresponding amount of PIM was dissolved in DMAc according to the blending proportion with stirring at room temperature, and the 26 wt % PBI commercial solution was added equally in three stages until the total amount was reached (see Table S1). The final concentration of the resulting polymer dope was 20 wt %. The casting solution was left still overnight to remove any bubbles present in it, cast on a P84 support[42] using the Elcometer 4340 Automatic Film Applicator, and immediately immersed into a deionized (DI) water bath at 25 °C. Afterward, the membranes were rinsed in DI water for 72 h to remove all the DMAc and then with MeOH and *n*-hexane (Scharlau) for 90 min. Then the membranes were dried and healed by immersing them in a coating solution of PDMS (Sylgard 184). A 3 wt % coating solution in *n*-hexane was used, mixing PDMS polymer base and hardener (10 to 1 weight ratio). The membranes were allowed to evaporate at room temperature for 2 h and then cured in an oven at 100 °C for 18 h. Neat PBI membranes were prepared following the same procedure and obtaining a 20 wt % dope solution from the dilution of the 26 wt % PBI commercial solution in DMAc.

Characterization of Samples. Thermogravimetric analysis (TGA) was performed with a Mettler Toledo TGA/STDA 851e. Samples of 5 mg were placed in 70 μL aluminum pans that were heated in air atmosphere from 30 to 900 °C at heating rates of 5, 10, and 20 °C min^{-1}. Differential scanning calorimetry (DSC) analysis was carried out with a Mettler Toledo DSC822e instrument. The 10 mg samples were placed in 70 μL aluminum pans and heated under 40 mL min^{-1} nitrogen flow from 25 to 500 °C using a heating rate of 20 °C min^{-1}. Scanning electron microscopy (SEM) images were acquired with an Inspect F50 model scanning electron microscope (FEI) operated at 20 kV and using a coating of Pt. The cross sections of the membranes were prepared by fracturing the samples during their immersion in liquid nitrogen. Infrared analysis (FTIR) was performed on a Bruker Vertex 70 FTIR spectrometer, which used a Golden Gate diamond ATR accessory and a DTGS detector, and with an FTIR microscope (Hyperion 2000). The spectra were recorded by averaging 40 scans in the 4000−600 cm^{-1}

DOI: 10.1021/acs.iecr.8b04209
Ind. Eng. Chem. Res. 2018, 57, 16909−16916

wavenumber range at a resolution of 4 cm^{-1}. Powder X-ray diffraction (XRD) spectra of ZIF-8 and MMMs were obtained with a D-Max Rigaku X-ray diffractometer that used a copper anode and a graphite monochromator to select Cu Kα radiation (λ = 1.540 Å). Data from $2\theta = 2.5°$ to 40° were taken at a scan rate of 0.03° s^{-1}.

Gas Separation Analysis. The membranes, consisting of circular areas of 2 cm diameter and sealed with silicon o-rings, were placed in a permeation module based on two stainless steel pieces and a 316LSS macroporous disk support (from Mott Co.) with a 20 μm nominal pore size. This module was placed in an UNE 200 Memmert oven that controlled the temperature of the experiment. The gas separation tests were performed feeding a 25/25 cm^3(STP) $min^{-1}H_2/CO_2$ mixture maintaining 3−6 bar at the feed side using two mass-flow controllers (Alicat Scientific, MC-100CCM-D), one for each gas. At the same time, Ar at 1 bar was used as sweep gas at the permeate side of the membrane, with a flow of 2−10 cm^3(STP) min^{-1} controlled by a mass-flow controller (Alicat Scientific, MC-5CCM-D and MC-100CCM-D). The concentrations of H_2 and CO_2 in the permeate were analyzed online with an Agilent 3000A gas microchromatograph using a thermal conductivity detector (TCD). After at least 3 h and once the steady-state was reached, the permeability was calculated in Barrer (10^{-10} cm^3(STP) cm cm^{-2} s^{-1} $cmHg^{-1}$), and the separation selectivity was calculated as the ratio of permeabilities. For asymmetric membranes, permeance was calculated instead in GPU (10^{-6} cm^3(STP) cm^{-2} s^{-1} $cmHg^{-1}$). At least 2 or 3 membranes of each type were measured to provide the corresponding standard deviations.

RESULTS AND DISCUSSION

Membrane Characterization. The polymers PBI and PIM-EA(H_2)-TB have been combined, where the latter is the minor component in the blend. Two polymers are considered to have built a homogeneous blending when they possess a single gas transition temperature (T_g), indicating the full miscibility of the system at the molecular level.[43] Blends of PBI and PIM-EA(H_2)-TB were prepared using amounts of PIM from 1.5 to 20 wt %, and the T_g of the different membranes was calculated from DSC data (see Table S2). The increase in the amount of PIM in the blend implies a reduction in the T_g of the membrane, almost following an arithmetic sequence.

The theoretical T_g of a polymer blend can be calculated with the Fox eq (eq 1).[44]

$$\frac{1}{T_{g,\text{blending}}} = \frac{X_{\text{PIM-EA}(H_2)\text{-TB}}}{T_{g,\text{PIM-EA}(H_2)\text{-TB}}} + \frac{(1 - X_{\text{PIM-EA}(H_2)\text{-TB}})}{T_{g,\text{PBI}}} \quad (1)$$

where $T_{g,\text{PIM-EA}(H_2)\text{-TB}}$ and $T_{g,\text{PBI}}$ are the glass transition temperatures in K of the individual polymers and $X_{\text{PIM-EA}(H_2)\text{-TB}}$ and X_{PBI} are related to the mass fractions of each component in the blend. For this study, this equation cannot be directly applied because the T_g of PIM-EA(H_2)-TB is unable to be measured empirically, its value being higher than the degradation temperature of the polymer. When the equation is reorganized, it can be expressed as eq 2. This way, the T_g of the blends should follow a linear tendency when represented against the amount of PIM in the composite.

$$\frac{1}{T_{g,\text{blending}}} = \left(\frac{1}{T_{g,\text{PIM-EA}(H_2)\text{-TB}}} - \frac{1}{T_{g,\text{PBI}}}\right)\cdot X_{\text{PIM-EA}(H_2)\text{-TB}} + \frac{1}{T_{g,\text{PBI}}} \quad (2)$$

As seen in Figure 1, the measured values fit to this reorganized Fox equation, and according to this fitting, the

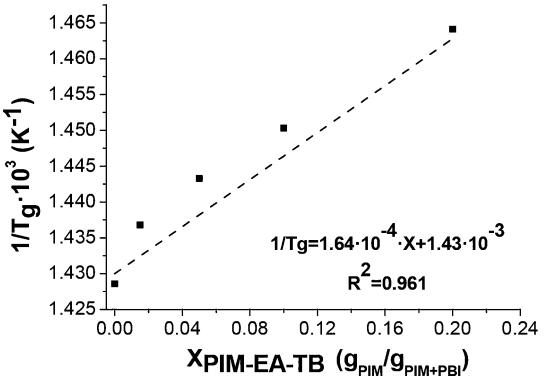

Figure 1. Glass transition temperature (T_g) values of the blends (scatter points) as a function of the amount of PIM-EA(H_2)-TB in them and its fitting to the Fox equation (dashed line).

calculated T_g value for neat PBI is 426 °C, meaning 0.2% error in comparison with its empirical value (427 °C, see Table S2). In addition, a hypothetical T_g for PIM-EA(H_2)-TB of 354 °C can also be obtained.

Thermogravimetric analyses in air were performed using three different heating rates of 5, 10, and 20 °C min^{-1} with bare PBI membranes and blends containing a 5 and 10 wt % PIM-EA(H_2)-TB. The temperatures corresponding to the maximum weight loss were obtained from the derivative curve of each thermogram (Figure S1), and they are collected in Table S3. It can be seen that the presence of PIM accelerated the thermal decomposition of the blend. The apparent activation energy (E_a) of these reactions was calculated for the different membranes using the Kissinger integral method.[45] The temperatures shown in Table S3 are represented and fitted according to the Kissinger eq (eq S1) in Figure S2. The incorporation of PIM in the blend is responsible for a significant reduction in the E_a (105, 87, and 83 kJ mol^{-1} for 0, 5, and 10 wt % PIM in the blend, respectively), because just 5 wt % polymer makes this parameter decrease by 17%. This agrees with a decrease of the polymer thermal stability as PBI is replaced by the PIM. In general, the lower the T_g value of a given polymer the higher its E_a value should be, e.g. ca. 190 °C (T_g) and 285 kJ mol^{-1} (E_a) for typical polysulfone.[46] It is worth noting that the TGA results may not show the true thermal stability of the membranes because the presence of oxygen could accelerate the decomposition or oxidation of certain functionalities. In addition, from the TGA analysis (see Figure S1) it can also be seen that all the DMAc was driven out by water during the membrane activation process.

FTIR spectroscopy can show the interaction of polymers in a blended structure. New vibration modes are usually detected when blends mean new strong interactions in terms of covalent bonds. A physical blending without any chemical reaction, i.e. involving only van der Waals, electrostatic or hydrogen interactions, would not produce new FTIR vibrations. Figure S3 spectra show the signals at 757 cm^{-1} and those at 1221−1120 cm^{-1}, present in the neat PBI spectrum and

DOI: 10.1021/acs.iecr.8b04209
Ind. Eng. Chem. Res. 2018, 57, 16909−16916

corresponding to in-plane bending of the imidazole and benzene rings, respectively.[47] These bands decreased in intensity in the blends. However, no new signals different from those of the bare polymer membranes could be found. This means that the interaction between PBI and the PIM follows the same kind of bonding already found in the neat polymers, which is logical because they have similar functional groups. FTIR analysis was also performed with a FTIR microscope, measuring several areas of 30 μm × 30 μm on the membrane surface of the blend with 20 wt % PIM (see Figure S4). The homogeneity among the different spectra confirmed the intimate mixing between PIM-EA(H_2)-TB and PBI, without segregation at a micrometer scale.

An XRD analysis was performed to gain insight into the effect of the blending on the microstructure and to obtain the *d*-spacing of the membranes. As shown in Figure 2, PBI is an

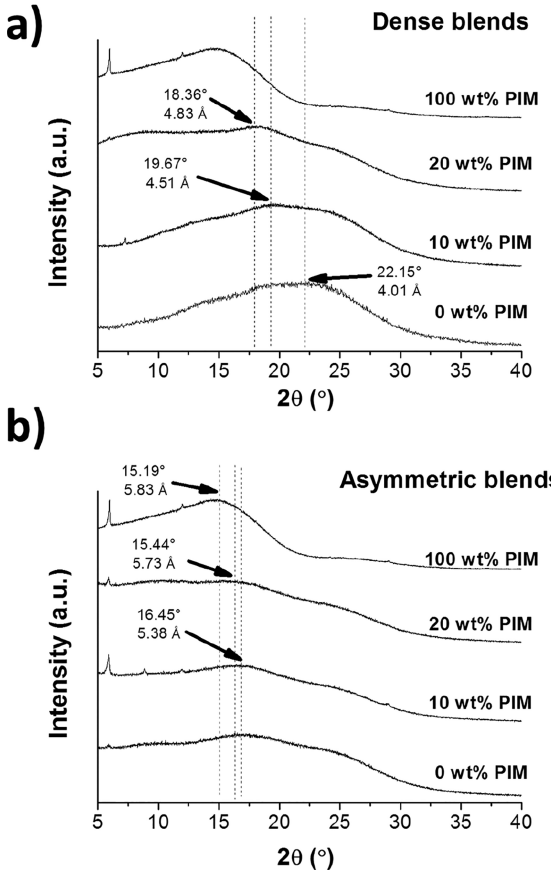

Figure 2. XRD patterns of membranes (bare PBI, bare PIM-EA(H_2)-TB, and blends containing 10 and 20 wt % PIM) in dense (a) and asymmetric configurations (b).

amorphous polymer with an indicative band at 2θ = 22.2°, corresponding to a *d*-spacing of 4.0 Å. PIM-EA(H_2)-TB is a glassy polymer with an amorphous band at 15.2°. As shown in Figure 2a, in the case of dense membranes, an increase in the PIM concentration gradually shifted the peak at 22.2° to lower values, increasing the interstitial space between the polymer chains up to 4.8 Å. In the case of asymmetric membranes (Figure 2b), the signal at 16.5° of PIM-EA(H_2)-TB was more visible, and it shifted to higher values with the decrease in the amount of PIM in the blend, showing again that the space between the polymer chains in the blend is higher with increasing PIM loading. The spectrum of PIM-EA(H_2)-TB in both figures corresponds to that of the dense membrane. It was impossible to prepare a pure PIM-EA(H_2)-TB asymmetric membrane because of the difficulty dissolving this polymer in DMAc at high loadings, which is necessary for the preparation of a defect-free asymmetric film. No XRD signals related to PIM-EA(H_2)-TB could be noticed in the patterns of the blends with 1.5 and 5 wt % PIM (in line with the fact that the 10 wt % sample already showed low XRD intensities), and they were not included in Figure 2.

Finally, Figure 3 shows the cross sections of membranes of bare PBI, neat PIM-EA(H_2)-TB, and the blend containing 10

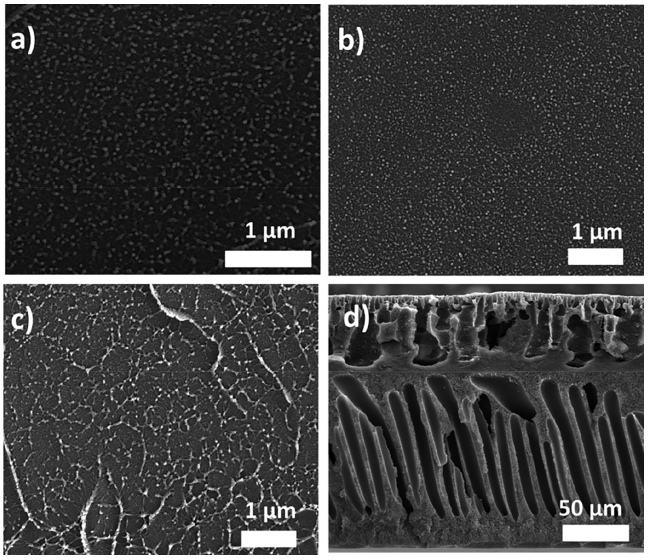

Figure 3. SEM images of the cross section of membranes: bare PBI (a), neat PIM-EA(H_2)-TB (b), and blend with 10 wt % PIM in dense (c) and asymmetric configurations (d).

wt % PIM in both dense and asymmetric morphologies. The appearance and texture of both neat polymers is quite similar, being difficult to distinguish one another. Besides, the image of the blend looks homogeneous, with no phase separation. The images of the blends containing ZIF-8 are shown in Figure S5, where the filler can be seen homogeneously dispersed across the section for all loadings.

Gas Separation Performance of Dense Membranes. The gas separation performance of dense membranes, blends in absence of filler, at 180 °C and 3 bar feed pressure can be seen in Figure 4. The numerical values are also collected in Table S4. PIM-EA(H_2)-TB (100 wt % PIM) shows a tremendous high H_2 permeability, 100 times that of PBI with 3857 Barrer, but poor H_2/CO_2 selectivity (ca. 2.2).

Blends at 1.5, 5, and 10 wt % PIM increased the H_2 permeability of the PBI from 31.9 to 72.2, 82.0, and 131 Barrer, respectively, but did not improve the membrane selectivity, because that of neat PIM-EA(H_2)-TB was not very high (2.2). This may be related to the increase in the *d*-spacing previously observed by XRD (see Figure 2). ZIF-8 nanoparticles were also added to the blended matrix in an attempt to enhance the separation performance of the membranes (see Table S4) All the results of dense membranes are represented in a Robeson type graph (Figure S6) where it can be seen that the best performing membranes surpass the Robeson upper bound corrected for 180 °C. Table S5 also shows the gas separation performance of dense membranes found in the

DOI: 10.1021/acs.iecr.8b04209
Ind. Eng. Chem. Res. 2018, 57, 16909−16916

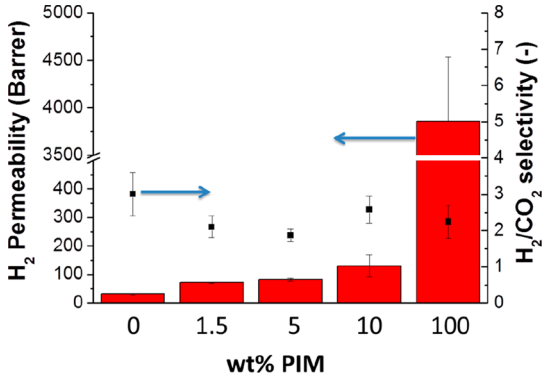

Figure 4. Gas separation performance of dense membranes at 180 °C and 3 bar pressure feed: pristine polymers and blends with different PIM-EA(H_2)-TB loadings. Bars stand for H_2 permeability, and scatter points stand for H_2/CO_2 selectivity.

literature for comparison; in general, the selectivity values with dense membranes are below those achieved with asymmetric membranes for this particular separation.

Gas Separation Performance of Asymmetric Membranes. In order to study in depth, the effect of PIM-EA(H_2)-TB/PBI blends in the gas separation performance of H_2/CO_2 mixtures, a new membrane configuration based on asymmetric blended membranes was tested. ZIF-8 was not incorporated in this kind of membranes because it did not achieved sufficient improvement with the previous dense blends. The higher permeances of this kind of membranes in comparison with those of dense blends allowed the measurements at several temperatures from 35 to 250 °C. Different feed pressures up to 6 bar were also applied (see Table S6). The membranes were prepared on P84 flat asymmetric supports and the results were compared with those corresponding to pristine PBI membranes of this kind previously reported.[42] The use of P84 is necessary because PBI asymmetric blends are extremely brittle and impossible to handle without the use of a support. This polymer has been selected for this purpose because of its compatibility with PBI, which allows the absence of delamination in the composite.[48] In order to discard a possible contribution of P84 to the gas separation, a PBI supported blend (10 wt % PIM) has also been tested for a different gas separation (i.e., equimolar CO_2/CH_4 mixture) at 35 °C and a feed pressure of 3 bar, showing a CO_2 permeance of 0.42 GPU and a CO_2/CH_4 selectivity of 1.4. Such a low selectivity proves that only the PBI layer is playing a role in the gas separation, because P84 usually shows a high CO_2/CH_4 selectivity while that of PBI is negligible.[49]

Figure 5a shows the gas separation performance of asymmetric PBI membranes (pristine polymer and blends containing 10 and 20 wt % PIM). Asymmetric membranes with 1.5 and 5 wt % PIM were not prepared because such low loading did not show a considerable improvement in comparison with the previous dense membranes (see Figure 4). The entire test was performed under a feed pressure of 3 bar and temperatures of 35, 180, and 250 °C. When these results are compared to those in Figure 4, the asymmetric membranes show a better gas separation performance than the dense membranes, presumably due to the different polymeric structure of the skin layer (less porous).[42] The content of PIM in the blends provided an enhancement in the H_2 transport. At 35 °C, the H_2 permeance increased from 0.4 to 8.9 GPU (22 times higher) when the content of PIM increased from 0 to 20

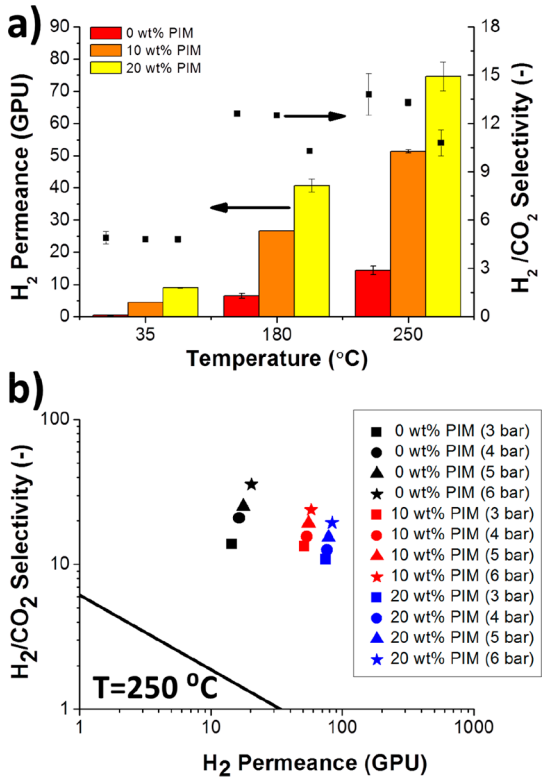

Figure 5. Gas separation performance of asymmetric blends: (a) at several operating temperatures and 3 bar feed pressure (bars stands for H_2 permeance, and scatter points stand for H_2/CO_2 selectivity); (b) gas separation performance at 250 °C and different feed pressures with the H_2/CO_2 upper bound at the same temperature.

wt %. At higher temperatures the increase in permeance was even greater, reaching the maximum H_2 permeance of 74.6 GPU for the blend containing 20 wt % PIM at 250 °C. Conversely, the H_2/CO_2 selectivity decreased slightly as the amount of PIM in the blend was increased, as previously seen for dense membranes, but H_2/CO_2 selectivity remained over 10 at the highest temperature. Increasing the operating temperature had a great impact on the H_2 permeation in all bare PBI membranes and blends. The H_2 permeance was around 5 times higher at 180 °C than at 35 °C (from 0.4−8.9 GPU to 6.5−40.7 GPU) and twice at 250 °C than at 180 °C (from 6.5−40.7 GPU to 14.4−74.6 GPU). The H_2/CO_2 selectivity also improved as the temperature rose, being 2.5-fold higher at 180 °C in comparison with that at the lowest temperature (4.8), and it even increased further when measuring at 250 °C (13.8). Measuring at different temperatures also allowed the calculation of the apparent activation energies of the membranes in terms of permeances for H_2 and CO_2 (see Figure S5 and Table S7). Calculated from H_2 permeances, pristine PBI membranes showed an apparent activation energy of 22.3 kJ mol^{-1}, a value that decreased to 14.9 and 13.9 kJ mol^{-1} as the amount of PIM increased to 10 and 20 wt %, respectively. The same happened with the values calculated from CO_2 permeances, which decreased from 15.6 to 7.6 kJ mol^{-1}. This activation energy shows the same tendency as that (corresponding to membrane stability) calculated by thermal analysis, previously shown in Figure S2. Because thermal treatments have been reported to be able to affect the transport properties of PIMs,[36] the blend with 20 wt % PIM was measured again after the membrane was cooled

DOI: 10.1021/acs.iecr.8b04209
Ind. Eng. Chem. Res. 2018, 57, 16909−16916

to room temperature. Its gas separation performance (see Table S6) was similar to the original at 250 °C, showing that the high-temperature operation had almost no effect on the gas separation properties of the blend.

Regarding the effect of pressure on the gas separation performance of the membranes, Figure 5b shows the separation selectivity results of PBI blends at 250 °C under feed pressures from 3 to 6 bar. As previously reported,[42] the increase in the feed pressure led to an enhancement of the gas separation performance. The disappearance of defects due to the membrane healing by PDMS coating together with the small thickness of their skin layer probably caused the membranes to reach CO_2 saturation, significantly increasing the gas transport and the separation factor, as observed in the case of pure PBI membranes.[42] The effect of pressure was less significant as the amount of PIM in the blend increased. For bare PBI membranes, the H_2 permeance was 29% higher at 6 bar than at 3 bar and the H_2/CO_2 selectivity was 61% higher, reaching values of 20.3 GPU and 35.6, respectively. However, for both blends, the H_2 permeance increased by 10% and the selectivity by 44%. The best values for the blends were obtained at 6 bar feed pressure with 57.9 GPU of H_2 and a H_2/CO_2 selectivity of 23.8 (10 wt % PIM) and 83.5 GPU of H_2 and a H_2/CO_2 selectivity of 19.4 (20 wt % PIM). All the permselectivity results surpass clearly the H_2/CO_2 upper bound defined in GPU at 250 °C.[42]

It can also be shown that the gas separation performance of the asymmetric blends follows a linear tendency based on the amount of PIM in the composite and the feed pressure of the process. The values of H_2 (P_{H2}) and CO_2 (P_{CO2}) permeances corresponding to Figure 5b were fitted by multiple linear regression, providing the empirical model described by eqs 3 and 4. No physical meaning is under these expressions as far as we are concerned. The fitting was successful (R^2 value >0.97) and can be seen in Figure S5.

$$P_{H_2} = 9.11 + 3.05\cdot\text{loading (wt \%)} + 2.30P \text{ (bar)} \quad (3)$$

$$P_{CO_2} = 3.03 + 0.24\cdot\text{loading (wt \%)} - 0.50P \text{ (bar)} \quad (4)$$

From the model, it can be seen how increasing the PIM content (loading) in the blend provides increases in gas transport for both H_2 and CO_2, because it is a positive term in both previous equations. The feed total pressure (P), however, has a different influence for each gas. Increasing this variable leads to simultaneous increase and decrease of the H_2 and CO_2 permeances, respectively. This fact is due to the saturation phenomena already explained above and supports the enhancement of the H_2/CO_2 with increasing pressure.

CONCLUSIONS

Blends of PBI and PIM-EA(H_2)-TB have been prepared in both dense and asymmetric configurations. The formation of a homogeneous blend between the two polymers was verified by the existence of a single glass transition temperature. The incorporation of PIM into PBI made the *d*-spacing of the resulting polymer increase, leading to higher gas permeances. The apparent activation energies of the blends, for thermal degradation and permeation, decreased as the amount of PIM in the composite was higher. The PIM/PBI blends were tested for the separation of H_2/CO_2 mixtures. Dense membranes also incorporated ZIF-8 nanoparticles to try to improve the gas separation due to the molecular sieving effect of this filler. The combination of PIM and PBI enhanced greatly the permeability of the membranes but reduced selectivity because of the poor H_2/CO_2 separation selectivity of PIM-EA(H_2)-TB. Asymmetric blends performed much better than the dense membranes because of their thin skin layer. With these composites, the increase in feed pressure had a positive effect on the gas separation performance, reaching a maximum H_2 permeance of 83.5 GPU with a H_2/CO_2 selectivity of 19.4. The empirical model developed corroborated the influence of the amount of PIM and the feed pressure on the gas separation performance. Finally, the presence of characterization and separation results with both dense and asymmetric membranes of the PIM-EA(H_2)-TB/PBI blend allows an interesting comparison not usually afforded in membrane gas separation publications. This allows envisioning the great potential that blends of high-performance polymers may have in the separation of H_2/CO_2 mixtures.

ASSOCIATED CONTENT

Supporting Information

The Supporting Information is available free of charge on the ACS Publications website at DOI: 10.1021/acs.iecr.8b04209.

Information about the thermal analysis, the characterization of membrane samples, and gas separation is included (PDF).

AUTHOR INFORMATION

Corresponding Author

*E-mail: coronas@unizar.es.

ORCID

Beatriz Zornoza: 0000-0002-9934-1707

Mariolino Carta: 0000-0003-0718-6971

Joaquín Coronas: 0000-0003-1512-4500

Notes

The authors declare no competing financial interest.

ACKNOWLEDGMENTS

The research comprising this work has received financial support from the European Union Seventh Framework Programme (FP7/2007-2013) under Grant Agreement No. 608490, project M4CO2. In addition, the authors acknowledge the funding received from the Spanish MINECO and FEDER (MAT2016-77290-R), the Aragón Government (T43-17R), and the European Social Fund. J.S-L. in particular thanks the Spanish Education Ministry Program FPU2014. All the microscopy work was performed in the Laboratorio de Microscopias Avanzadas at the Instituto de Nanociencia de Aragón (LMA-INA). Finally, the authors acknowledge the use of the Servicio General de Apoyo a la Investigación-SAI, Universidad de Zaragoza.

REFERENCES

(1) Robeson, L. M. The upper bound revisited. *J. Membr. Sci.* **2008**, *320*, 390−400.

(2) Chung, T.; Guo, W. F.; Liu, Y. Enhanced Matrimid membranes for pervaporation by homogenous blends with polybenzimidazole (PBI). *J. Membr. Sci.* **2006**, *271*, 221−231.

(3) Zornoza, B.; Irusta, S.; Téllez, C.; Coronas, J. Mesoporous silica sphere− polysulfone mixed matrix membranes for gas separation. *Langmuir* **2009**, *25*, 5903−5909.

(4) Mahajan, R.; Burns, R.; Schaeffer, M.; Koros, W. J. Challenges in forming successful mixed matrix membranes with rigid polymeric materials. *J. Appl. Polym. Sci.* **2002**, *86*, 881−890.
(5) Tanh Jeazet, H. B.; Staudt, C.; Janiak, C. Metal−organic frameworks in mixed-matrix membranes for gas separation. *Dalton Trans.* **2012**, *41*, 14003−14027.
(6) Rodenas, T.; van Dalen, M.; García-Pérez, E.; Serra-Crespo, P.; Zornoza, B.; Kapteijn, F.; Gascon, J. Visualizing MOF Mixed Matrix Membranes at the Nanoscale: Towards Structure-Performance Relationships in CO_2/CH_4 Separation Over NH2-MIL-53 (Al)@ PI. *Adv. Funct. Mater.* **2014**, *24*, 249−256.
(7) Sabetghadam, A.; Seoane, B.; Keskin, D.; Duim, N.; Rodenas, T.; Shahid, S.; Sorribas, S.; Guillouzer, C. L.; Clet, G.; Tellez, C.; et al. Metal Organic Framework Crystals in Mixed-Matrix Membranes: Impact of the Filler Morphology on the Gas Separation Performance. *Adv. Funct. Mater.* **2016**, *26*, 3154−3163.
(8) Smart, S.; Vente, J. F.; Diniz da Costa, J. C. High temperature H2/CO2 separation using cobalt oxide silica membranes. *Int. J. Hydrogen Energy* **2012**, *37*, 12700−12707.
(9) Japip, S.; Liao, K.; Chung, T. Molecularly tuned free volume of vapor cross-linked 6FDA-Durene/ZIF-71 MMMs for H_2/CO_2 separation at 150° C. *Adv. Mater.* **2017**, *29*, 1603833.
(10) Jang, E.; Kim, E.; Kim, H.; Lee, T.; Yeom, H.; Kim, Y.; Choi, J. Formation of ZIF-8 membranes inside porous supports for improving both their H_2/CO_2 separation performance and thermal/mechanical stability. *J. Membr. Sci.* **2017**, *540*, 430−439.
(11) Zhu, X.; Wang, Q.; Shi, Y.; Cai, N. Layered double oxide/activated carbon-based composite adsorbent for elevated temperature H_2/CO_2 separation. *Int. J. Hydrogen Energy* **2015**, *40*, 9244−9253.
(12) Choi, S.; Coronas, J.; Lai, Z.; Yust, D.; Onorato, F.; Tsapatsis, M. Fabrication and gas separation properties of polybenzimidazole (PBI)/nanoporous silicates hybrid membranes. *J. Membr. Sci.* **2008**, *316*, 145−152.
(13) Yang, T.; Xiao, Y.; Chung, T. Poly-/metal-benzimidazole nano-composite membranes for hydrogen purification. *Energy Environ. Sci.* **2011**, *4*, 4171−4180.
(14) Li, L.; Jianfeng, Y.; Wang, X.; Chen, Y.; Wang, H. ZIF-11/Polybenzimidazole composite membrane with improved hydrogen separation performance. *J. Appl. Polym. Sci.* **2014**, *131*, 41056.
(15) Li, X.; Singh, R. P.; Dudeck, K. W.; Berchtold, K. A.; Benicewicz, B. C. Influence of polybenzimidazole main chain structure on H_2/CO_2 separation at elevated temperatures. *J. Membr. Sci.* **2014**, *461*, 59−68.
(16) Kumbharkar, S.; Liu, Y.; Li, K. High performance polybenzimidazole based asymmetric hollow fibre membranes for H_2/CO_2 separation. *J. Membr. Sci.* **2011**, *375*, 231−240.
(17) Biswal, B. P.; Bhaskar, A.; Banerjee, R.; Kharul, U. K. Selective interfacial synthesis of metal−organic frameworks on a polybenzimidazole hollow fiber membrane for gas separation. *Nanoscale* **2015**, *7*, 7291−7298.
(18) Chung, T. A critical review of polybenzimidazoles: historical development and future R&D. *J. Macromol. Sci. Part C: Polym. Rev.* **1997**, *37*, 277−301.
(19) Budd, P. M.; McKeown, N. B. Highly permeable polymers for gas separation membranes. *Polym. Chem.* **2010**, *1*, 63−68.
(20) Hosseini, S. S.; Teoh, M. M.; Chung, T. S. Hydrogen separation and purification in membranes of miscible polymer blends with interpenetration networks. *Polymer* **2008**, *49*, 1594−1603.
(21) Hosseini, S. S.; Peng, N.; Chung, T. S. Gas separation membranes developed through integration of polymer blending and dual-layer hollow fiber spinning process for hydrogen and natural gas enrichments. *J. Membr. Sci.* **2010**, *349*, 156−166.
(22) Hosseini, S. S.; Chung, T. S. Carbon membranes from blends of PBI and polyimides for N_2/CH_4 and CO_2/CH_4 separation and hydrogen purification. *J. Membr. Sci.* **2009**, *328*, 174−185.
(23) Pérez-Francisco, J. M.; Santiago-García, J. L.; Loria-Bastarrachea, M. I.; Aguilar-Vega, M. Evaluation of Gas Transport Properties of Highly Rigid Aromatic PI DPPD-IMM/PBI Blends. *Ind. Eng. Chem. Res.* **2017**, *56*, 9355−9366.
(24) Musto, P.; Karasz, F.; MacKnight, W. Hydrogen bonding in polybenzimidazole/poly (ether imide) blends: a spectroscopic study. *Macromolecules* **1991**, *24*, 4762−4769.
(25) Giel, V.; Morávková, Z.; Peter, J.; Trchová, M. Thermally treated polyaniline/polybenzimidazole blend membranes: Structural changes and gas transport properties. *J. Membr. Sci.* **2017**, *537*, 315−322.
(26) Ahmad, N.; Leo, C.; Ahmad, A.; Mohammad, A. W. Separation of CO_2 from hydrogen using membrane gas absorption with PVDF/PBI membrane. *Int. J. Hydrogen Energy* **2016**, *41*, 4855−4861.
(27) Yong, W. F.; Li, F. Y.; Xiao, Y. C.; Chung, T. S.; Tong, Y. W. High performance PIM-1/Matrimid hollow fiber membranes for $CO_2/CH_4O_2/N_2$ and CO_2/N_2 separation. *J. Membr. Sci.* **2013**, *443*, 156−169.
(28) Yong, W. F.; Salehian, P.; Zhang, L.; Chung, T. Effects of hydrolyzed PIM-1 in polyimide-based membranes on C2−C4 alcohols dehydration via pervaporation. *J. Membr. Sci.* **2017**, *523*, 430−438.
(29) García, M. G.; Marchese, J.; Ochoa, N. A. Improved gas selectivity of polyetherimide membrane by the incorporation of PIM polyimide phase. *J. Appl. Polym. Sci.* **2017**, *134*, 44682.
(30) Salehian, P.; Yong, W. F.; Chung, T. Development of high performance carboxylated PIM-1/P84 blend membranes for pervaporation dehydration of isopropanol and CO_2/CH_4 separation. *J. Membr. Sci.* **2016**, *518*, 110−119.
(31) Panapitiya, N. P.; Wijenayake, S. N.; Nguyen, D.; Huang, Y.; Musselman, I. H.; Balkus, K. J.; Ferraris, J. P. Gas Separation Membranes Derived from High Performance Immiscible Polymer Blends Compatibilized with Small Molecules. *ACS Appl. Mater. Interfaces* **2015**, *7* (33), 18618−18627.
(32) Yong, W.; Li, F.; Xiao, Y.; Li, P.; Pramoda, K.; Tong, Y.; Chung, T. Molecular engineering of PIM-1/Matrimid blend membranes for gas separation. *J. Membr. Sci.* **2012**, *407*−*408*, 47−57.
(33) Mei Wu, X.; Gen Zhang, Q.; Ju Lin, P.; Qu, Y.; Mei Zhu, A.; Lin Liu, Q. Towards enhanced CO_2 selectivity of the PIM-1 membrane by blending with polyethylene glycol. *J. Membr. Sci.* **2015**, *493*, 147−155.
(34) Naderi, A.; Asadi Tashvigh, A.; Chung, T.; Weber, M.; Maletzko, C. Molecular design of double crosslinked sulfonated polyphenylsulfone /polybenzimidazole blend membranes for an efficient hydrogen purification. *J. Membr. Sci.* **2018**, *563*, 726−733.
(35) Yong, W. F.; Lee, Z. K.; Chung, T.; Weber, M.; Staudt, C.; Maletzko, C. Blends of a polymer of intrinsic microporosity and partially sulfonated polyphenylenesulfone for gas separation. *ChemSusChem* **2016**, *9*, 1953−1962.
(36) Park, K. S.; Ni, Z. N.; Côte, A. P.; Choi, J. Y.; Huang, R.; Uribe-Romo, F. J.; Chae, H. K.; O'Keeffe, M.; Yaghi, O. M. Exceptional chemical and thermal stability of zeolitic imidazolate frameworks. *Proc. Natl. Acad. Sci. U. S. A.* **2006**, *103*, 10186−10191.
(37) Carta, M.; Malpass-Evans, R.; Croad, M.; Rogan, Y.; Jansen, J. C.; Bernardo, P.; Bazzarelli, F.; McKeown, N. B. An efficient polymer molecular sieve for membrane gas separations. *Science* **2013**, *339*, 303−307.
(38) Carta, M.; Malpass-Evans, R.; Croad, M.; Rogan, Y.; Lee, M.; Rose, I.; McKeown, N. B. The synthesis of microporous polymers using Tröger's base formation. *Polym. Chem.* **2014**, *5*, 5267−5272.
(39) Tocci, E.; De Lorenzo, L.; Bernardo, P.; Clarizia, G.; Bazzarelli, F.; McKeown, N. B.; Carta, M.; Malpass-Evans, R.; Friess, K.; Pilnáček, K.; et al. Molecular Modeling and Gas Permeation Properties of a Polymer of Intrinsic Microporosity Composed of Ethanoanthracene and Tröger's Base Units. *Macromolecules* **2014**, *47*, 7900−7916.
(40) Liédana, N.; Galve, A.; Rubio, C.; Téllez, C.; Coronas, J. CAF@ ZIF-8: one-step encapsulation of caffeine in MOF. *ACS Appl. Mater. Interfaces* **2012**, *4*, 5016−5021.
(41) Shao, L.; Chung, T.; Wensley, G.; Goh, S. H.; Pramoda, K. P. Casting solvent effects on morphologies, gas transport properties of a novel 6FDA/PMDA−TMMDA copolyimide membrane and its derived carbon membranes. *J. Membr. Sci.* **2004**, *244*, 77−87.

DOI: 10.1021/acs.iecr.8b04209
Ind. Eng. Chem. Res. 2018, 57, 16909−16916

(42) Sánchez-Laínez, J.; Zornoza, B.; Téllez, C.; Coronas, J. Asymmetric polybenzimidazole membranes with thin selective skin layer containing ZIF-8 for H_2/CO_2 separation at pre-combustion capture conditions. *J. Membr. Sci.* **2018**, *563*, 427−434.
(43) Yong, W. F.; Chung, T. Miscible blends of carboxylated polymers of intrinsic microporosity (cPIM-1) and Matrimid. *Polymer* **2015**, *59*, 290−297.
(44) Fox, T. G. *Bull. Am. Phys. Soc.* **1957**, 123.
(45) Svoboda, R.; Málek, J. Is the original Kissinger equation obsolete today? *J. Therm. Anal. Calorim.* **2014**, *115*, 1961−1967.
(46) Cacho-Bailo, F.; Téllez, C.; Coronas, J. Interactive thermal effects on metal−organic framework Polymer composite membranes. *Chem. - Eur. J.* **2016**, *22*, 9533−9536.
(47) Drolet, D. P.; Manuta, D. M.; Lees, A. J.; Katnani, A.; Coyle, G. J. FT-IR and XPS study of copper (II) complexes of imidazole and benzimidazole. *Inorg. Chim. Acta* **1988**, *146*, 173−180.
(48) Wang, K. Y.; Chung, T.; Rajagopalan, R. Dehydration of tetrafluoropropanol (TFP) by pervaporation via novel PBI/BTDA-TDI/MDI co-polyimide (P84) dual-layer hollow fiber membranes. *J. Membr. Sci.* **2007**, *287*, 60−66.
(49) Sridhar, S.; Veerapur, R.; Patil, M.; Gudasi, K.; Aminabhavi, T. Matrimid polyimide membranes for the separation of carbon dioxide from methane. *J. Appl. Polym. Sci.* **2007**, *106*, 1585−1594.

DOI: 10.1021/acs.iecr.8b04209
Ind. Eng. Chem. Res. 2018, 57, 16909−16916

Supporting Information

1. Experimental section

Table S1. Preparation conditions of the membranes developed in this work.

Type of membrane	ZIF-8 (wt%)	PIM (wt%)	Mass of ZIF-8 (mg)	Mass of PIM-EA(H_2)-TB (mg)	Mass of PBI solution in DMAc (26 wt%) (g)	Mass of solvent (g)
Dense	**0**	**0**	0	0	1.54	2.46
		1.5	0	6	1.52	2.42
		5	0	20	1.46	2.34
		10	0	40	1.38	2.22
		100	0	400	0.00	3.60
	10	**0**	40	0	1.38	2.22
		5	40	18	1.32	2.10
		10	40	36	1.25	1.99
		100	40	360	0.00	3.60
	20	**0**	80	0	1.23	1.97
		5	80	16	1.17	1.87
		10	80	32	1.11	1.77
		100	80	320	0.00	3.60
Asymmetric	**0**	**0**	0	0	1.54	2.46
		10	0	40	1.38	2.22
		20	0	80	1.23	1.97

2. Differential Scanning Calorimetry

Table S2. Glass transition temperature of the different blends

PIM-EA(H_2)-TB (wt%)	T_g (^{0}C)
0	427
1.5	423
5	420
10	417
20	410

3. Apparent activation energy (E_a) for polymer decomposition through the Kissinger integral method

$$ln\frac{\beta}{T_m^2} = ln\frac{k_0 R}{E_a} - \frac{E_a}{RT_m}\ (Eq.S1)$$

The Kissinger equation to calculate the activation energy of the membranes is shown in Eq. S1.[2] Tm is the temperature with a maximum weight loss rate for a given reaction in K, E_a is the apparent activation energy in $kJ \cdot mol^{-1}$; k_0, the pre-exponential factor in s^{-1}; β, the heating rate applied to the sample in $K \cdot min^{-1}$, and R, the ideal gas constant in $J \cdot mol^{-1} \cdot K^{-1}$.

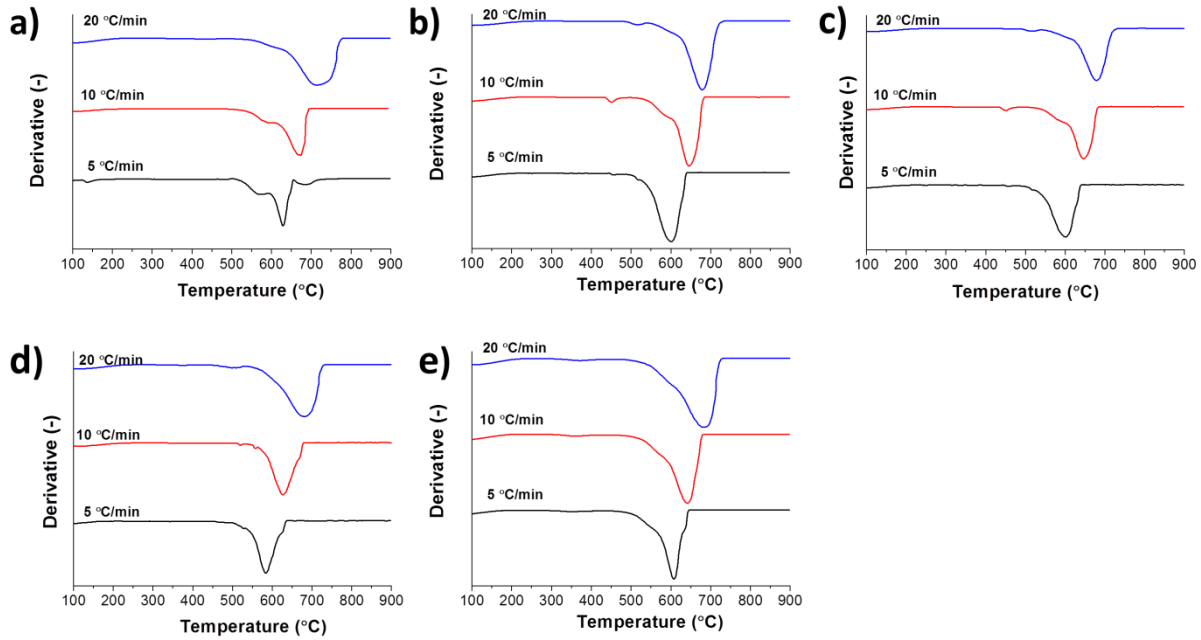

Figure S1. TGA derivatives at different heating rates for bare PBI membranes (a) and blends with 1.5 wt% (b), 5 wt% (c), 10 wt% (d) and 20 wt% (e) of PIM-EA(H_2)–TB.

Table S3. Temperatures corresponding to the maximum weight loss rates for the different blends at different heating rates.

PIM-EA(H_2) –TB amount	**Heating rate (°C min^{-1})**		
	5	**10**	**20**
0 wt%	629 ^{0}C	674 ^{0}C	713 ^{0}C
1.5 wt%	601 ^{0}C	646 ^{0}C	699 ^{0}C
5 wt%	601 ^{0}C	646 ^{0}C	699 ^{0}C
10 wt%	584 ^{0}C	626 ^{0}C	680 ^{0}C
20 wt%	587 ^{0}C	621 ^{0}C	670 ^{0}C

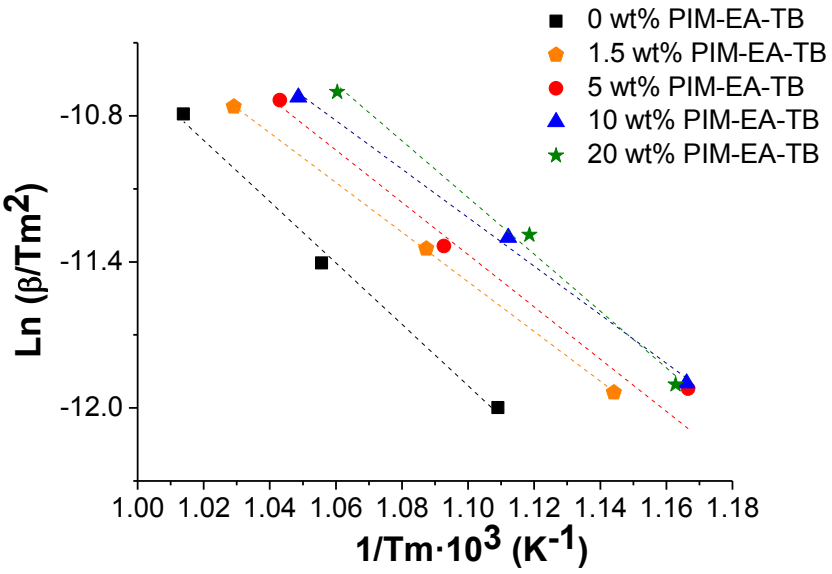

PIM loading % (w/v)	Fitting equation	E_a (kJ mol^{-1})
0	y = -12.602x + 1.9535 R^2 = 0.9939	105
1.5	y = -10.727x – 0.4297 R^2 = 0,9828	89
5	y = -10.2108x – 0.2505 R^2 = 0.9972	85
10	y = -9.9574x -0.2651 R^2 = 0.9932	83
20	y = -11.660x + 1,6902 R^2 = 0,9915	97

Figure S2. Calculation of the activation temperatures with the Kissinger method.

4. FTIR analysis

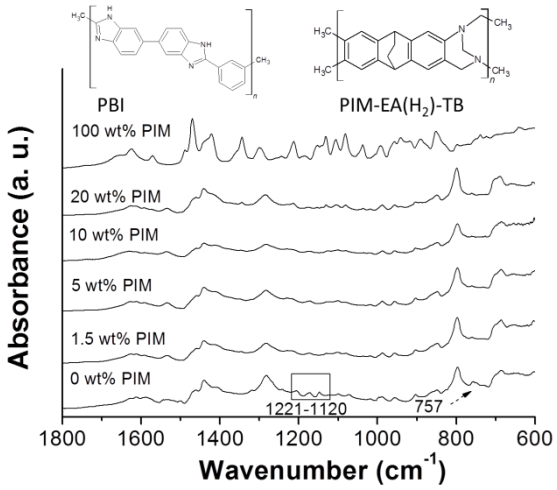

Figure S3. ATR-FTIR spectra of different PIM/PBI blends (1.5, 5, 10 and 20 wt% PIM) and pristine PBI and PIM-EA(H_2)-TB membranes for comparison. Chemical structures of PBI and PIM-EA(H_2)-TB are also shown.

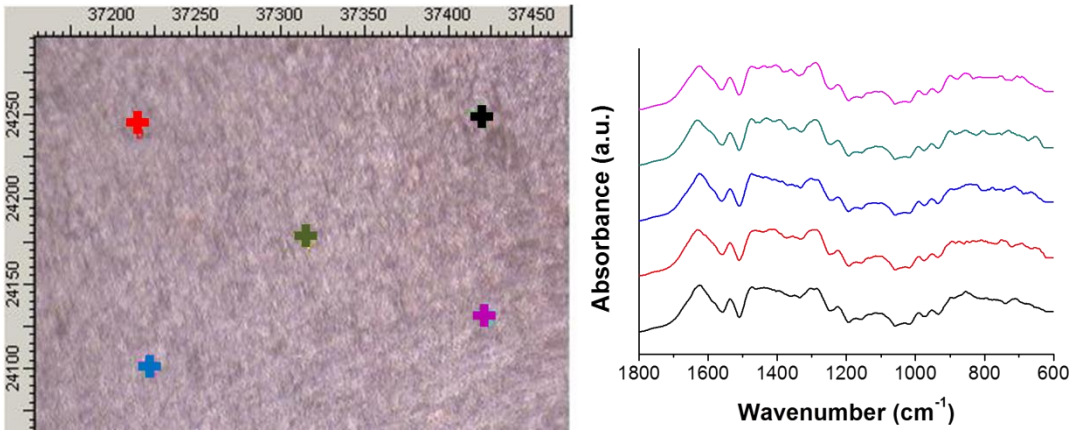

Figure S4. ATR-FTIR spectra of different points on the surface of the PIM/PBI blend with 20 wt% of PIM-EA(H_2)-TB. Each analyzed point corresponds to an area of 30µmx30µm.

5. SEM images

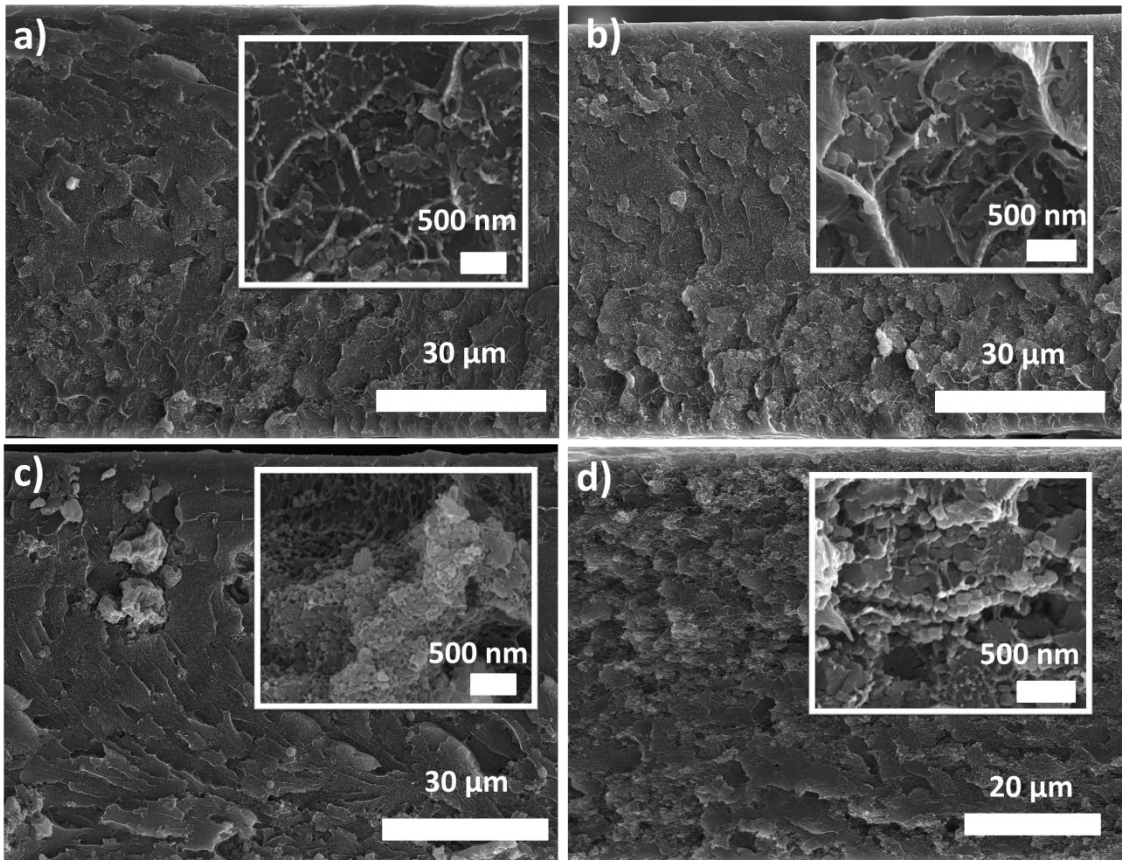

Figure S5. SEM images of the cross-section of PBI blends containing: 5 wt% of PIM and 10 wt% of ZIF-8 (a); 5 wt% of PIM and 20 wt% of ZIF-8 (b); 10 wt% of PIM and 10 wt% of ZIF-8 (c); and 10 wt% of PIM and 20 wt% of ZIF-8 (d). Insets show higher magnification details.

6. Gas separation analysis

Table S4. Gas separation performance of dense MMMs at 180 ^{0}C and 3 bar feed pressure.

ZIF-8 (wt%)	PIM (wt%)	Code	H_2 permeability (Barrer)	CO_2 permeability (Barrer)	Selectivity H_2/CO_2 (-)
0	0	0 wt% PIM, 0 wt% ZIF	31.9±1.9	10.7±0.3	3.0±0.6
	1.5	1.5 wt% PIM, 0 wt% ZIF	72.2±2.4	37.7±9.8	2.1±0.3
	5	5 wt% PIM, 0 wt% ZIF	82.0±5.0	43.8±1.3	1.9±0.2
	10	10 wt% PIM, 0 wt% ZIF	131±40	50.0±8.3	2.6±0.4
	100	100 wt% PIM, 0 wt% ZIF	3857±676	1753±10	2.2±0.5
10	0	0 wt% PIM, 10 wt% ZIF	90.7±10.4	15.4±2.0	5.9±0.1
	5	5 wt% PIM, 10 wt% ZIF	90.1±0.5	25.5±3.3	3. 6±0.5
	10	10 wt% PIM, 10 wt% ZIF	448±13	97.4±21.1	4.7±0.8
	100	100 wt% PIM,10 wt% ZIF	5422±48	1972±19	2.8±0.1
20	0	0 wt% PIM, 20 wt% ZIF	229±41	28.2±4.9	8.1±0.1
	5	5 wt% PIM, 20 wt% ZIF	144±5	32.6±2.0	4.4±0.1
	10	10 wt% PIM, 20 wt% ZIF	563±87	195±5	2.9±0.5
	100	100 wt% PIM, 20 wt% ZIF	-	-	-

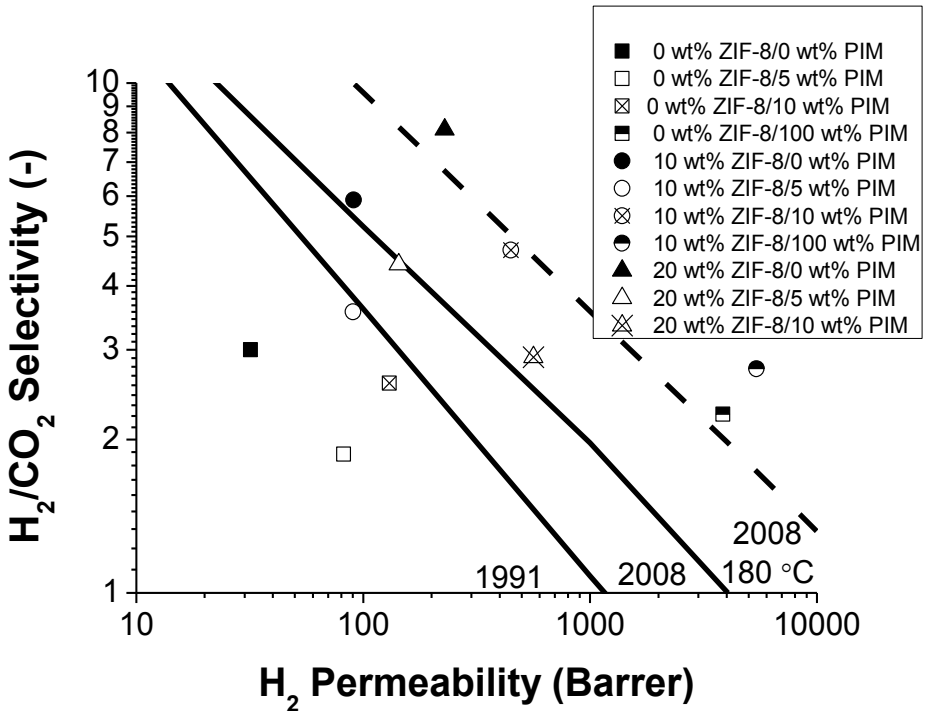

Figure S6. Gas separation performance of dense membranes at 180 ^{0}C and 3 bar feed pressure. Squares stand for membranes without filler and circles and triangles, for MMMs with 10 and 20 wt% of ZIF-8, respectively. Filled dots represent neat PBI membranes; empty dots, PBI blends with 10 wt% of PIM; crossed dots, PBI blends with 20 wt% of PIM and half-filled dots, neat PIM-EA(H_2)-TB membranes. The Robeson upper bounds of 1991,[3] 2008[4] and 2008 corrected for high temperature[5] are also plotted.

The gas separation performance of dense membranes at 180˚C and 3 bar of feed pressure can be seen in Table S4, where each membrane receives one code for clarification. Different types of membranes are shown : (i) bare PBI membranes (0 wt% PIM, 0 wt% ZIF-8), (ii) pure PIM-EA(H_2)-TB membranes (100 wt% PIM, 0 wt% ZIF-8), (iii) PBI/PIM blends containing different amounts of PIM-EA(H_2)-TB (5-10 wt% PIM, 0 wt% ZIF-8) and (iv) MMMs of both pristine

polymers and blends with ZIF-8 loadings of 10 and 20 wt% (0-100 wt% PIM, 10-20 wt% ZIF-8). PIM-EA(H_2)-TB membranes with loadings of ZIF-8 over 10 wt% were to brittle for manipulation and testing. Embedding ZIF-8 in both neat PBI and neat PIM-EA(H_2)-TB had a positive influence on the gas separation performance in terms of both permeability and selectivity. The enhancement was clearer for PBI, providing the best performance results at 20 wt% ZIF-8 loading (0 wt% PIM, 20 wt% ZIF) with 229 Barrer of H_2 and a H_2/CO_2 selectivity of 8.1. PIM-EA(H_2)-TB could only be loaded with ZIF-8 up to 10 wt% because of the extreme membrane brittleness. At this loading, it showed a H_2 permeability 1.5 fold higher that bare PIM membranes, with a H_2/CO_2 selectivity 10 % higher.

Embedding ZIF-8 in the blends had a positive influence in both permeability and selectivity. For the blends containing 5 wt% of PIM, both values increased as the filler loading was higher, reaching the optimal H_2/CO_2 selectivity of 4.4 with a H_2 permeability of 144 Barrer for the 20 wt% ZIF-8 loaded membranes (5 wt% PIM, 20 wt% ZIF). However, for the blends containing 10 wt% of PIM, the H_2/CO_2 selectivity reached an optimum (4.7) with 10 wt% of ZIF-8 (10 wt% PIM, 10 wt% ZIF) and then decreased at higher loadings (10 wt% PIM, 20 wt% ZIF). The preparation of MMMs with polymer blends (blending PIM and PBI and incorporating ZIF-8 to the matrix) led to opposing effects, while ZIF-8 tends to enhance the selectivity of the MMMs PIM-EA(H_2)-TB has the contrary behavior. Hence, MMMs were always more selective with neat PBI than in polymer blends, especially for larger amounts of PIM content. The optimum value of a MMM with a blended matrix was 448 Barrer of H_2 with a H_2/CO_2 selectivity of 4.7, corresponding to the PBI blend with 10 wt% of PIM and 10 wt% of ZIF-8 (10 PIM, 10 ZIF), which is close to the H_2/CO_2 upper bound (Figure S4). Besides, the highest H_2 permeability was 563 Barrer (10 wt% PIM and 20 wt% ZIF-8) with a H_2/CO_2 selectivity of 2.9. Summarizing this part, all the results of dense membranes are represented in a Robeson type graph (Figure S5).

Table S5. Gas separation performance of dense membranes found in the literature.

Filler	Polymer	Loading (wt%)	Temperature (ºC)	H_2Permeability (Barrer)	H_2/CO_2 selectivity (-)	Reference
-	PBI	-	30	5.2	12.5	6
-	PBI	-	30	5.4	6.5	7
			200	33.1	7.1	
-	PBI	-	35	2.9	7.1	8
			180	70.2	8.4	
-	PBI	-	150	45.5	1.4	9
			200	77.4	4.1	
ZIF-8	Matrimid®	40	35	71.22	2.90	10
ZIF-8	PBI	60	35	669.9	2.8	11
ZIF-8	PBI	60	35	1749.9	4.1	12
ZIF-8	PBI	20	150	124.9	7.6	13
ZIF-8	PIM-1	43	35	14430	0.74	14
MSS-Z8[a]	PSF	32	35	56.1	2.2	15

Table S6. Gas separation performance of asymmetric PBI blends.

Amount of PIM	T (^{0}C)	Feed pressure								Ref.
		3 bar		4 bar		5 bar		6 bar		
		H_2 permeation (GPU)	H_2/CO_2 selectivity (-)	H_2 permeation (GPU)	H_2/CO_2 selectivity (-)	H_2 permeation (GPU)	H_2/CO_2 selectivity (-)	H_2 permeation (GPU)	H_2/CO_2 selectivity (-)	
0 wt%	**35**	0.4±0.1	4.9±0.4	-	-	-	-	-	-	[16]
	180	6.5±0.8	12.6±0.1	-	-	-	-	9.0	26.3	
	250	14.4±1.4	13.8±1.3	16.4	20.9	17.6	25.1	20.3	35.6	
10 wt%	**35**	4.5	4.8	-	-	-	-	-	-	This work
	180	26.6	12.5	-	-	-	-	32.2	21.5	
	250	51.3±0.5	13.3±0.2	53.5±0.7	15.5±0.8	55.3±0.6	19.2±2.4	57.9±0.1	23.8±1.7	
20 wt%	**35**	8.9±0.1	4.8±0.2	-	-	-	-	10.7	7.0	This work
	180	40.7±2.1	10.3±0.1	-	-	-	-	50.3±0.8	17.3±2.0	
	250	74.6±4.5	10.8±0.8	76.5±4.9	12.6±0.3	78.2±4.1	15.3±0.5	83.5±2.3	19.4±0.9	
	250*	63.2	12.4	-	-	-	-	-	-	

* Measured again after cooling down to room temperature

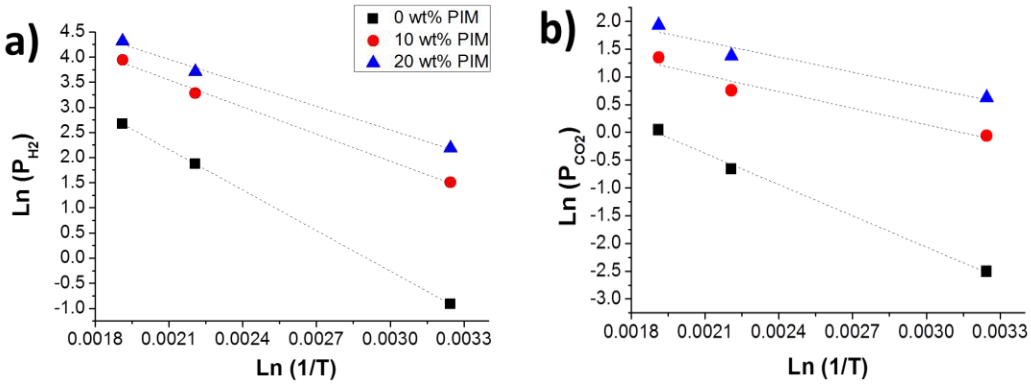

Figure S5. Arrhenius plots for the calculation of the H_2 permeance apparent activation energy of PBI blends for asymmetric membranes.

Table S7. Apparent activation energy corresponding to H_2 permeances of PBI blends for asymmetric membranes.

PIM loading wt%	Fitting equation H_2	Fitting equation CO_2	Ea (H_2) (kJ mol^{-1})	Ea (CO_2) (kJ mol^{-1})
0	y = -2686.4x + 7.8014 R^2 = 0.9999	y = -1875.2x + 3.5609 R^2 = 0.997	22.3	15.6
10	y = -1795.0x + 7.3133 R^2 = 0.997	y = -989.5x + 3.1089 R^2 = 0.95	14.9	8.2
20	y = -1560.0x + 7.2305 R^2 = 0.995	y = -918.64x + 3.5628 R^2 = 0.95	13.9	7.6

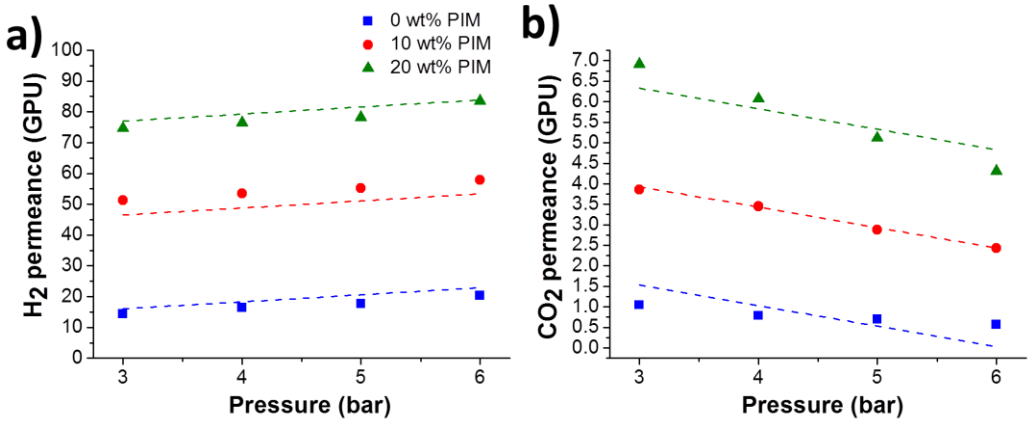

Figure S6. Empirical model for the gas separation performance of asymmetric blends at 250 ˚C. Dots stand for empirical values and lines to those calculated with the model.

7. Bibliography

(1) Fox T.G. ,*Bull Am Phys Soc* **1957**, 123.
(2) Svoboda, R.; Málek, J. ,Is the original Kissinger equation obsolete today? *J. Therm. Anal. Calorim.* **2014**, *2*, 1961-1967.
(3) Robeson, L. M. Correlation of separation factor versus permeability for polymeric membranes, *J. Membr. Sci.* **1991**, *2*, 165-185.
(4) Robeson, L. M. ,The upper bound revisited. *J. Membr. Sci.* **2008**, *1*, 390-400.
(5) Rowe, B. W.; Robeson, L. M.; Freeman, B. D.; Paul, D. R. ,Influence of temperature on the upper bound: Theoretical considerations and comparison with experimental results. *J. Membr. Sci.* **2010**, *1*, 58-69.
(6) Giel, V.; Perchacz, M.; Kredatusová, J.; Pientka, Z. ,Gas Transport Properties of Polybenzimidazole and Poly (Phenylene Oxide) Mixed Matrix Membranes Incorporated with PDA-Functionalised Titanate Nanotubes. *Nanoscale Res. Lett.* **2017**, *1*, 3.
(7) Klaehn, J. R.; Orme, C. J.; Peterson, E. S. ,Blended polybenzimidazole and melamine-co-formaldehyde thermosets. *J. Membr. Sci.* **2016**, 1-6.
(8) Yang, T.; Xiao, Y.; Chung, T. ,Poly-/metal-benzimidazole nano-composite membranes for hydrogen purification. *Energy Environ. Sci.* **2011**, *10*, 4171-4180.
(9) Suhaimi, H. S. M.; Leo, C. P.; Ahmad, A. L. ,Hydrogen Purification Using Polybenzimidazole Mixed-Matrix Membranes with Stabilized Palladium Nanoparticles. *Chem. Eng. Technol.* **2017**, *4*, 631-638.
(10) Ordonez, M. J. C.; Balkus, K. J.,Jr.; Ferraris, J. P.; Musselman, I. H. ,Molecular sieving realized with ZIF-8/Matrimid (R) mixed-matrix membranes. *J. Membr. Sci.* **2010**, *1-2*, 28-37.
(11) Yang, T.; Chung, T. ,High performance ZIF-8/PBI nano-composite membranes for high temperature hydrogen separation consisting of carbon monoxide and water vapor. *Int J Hydrogen Energy* **2013**, *1*, 229-239.
(12) Yang, T.; Shi, G. M.; Chung, T., Symmetric and asymmetric zeolitic imidazolate frameworks (ZIFs)/polybenzimidazole (PBI) nanocomposite membranes for hydrogen purification at high temperatures. *Adv. Energy Mater.* **2012**, *11*, 1358-1367.
(13) Sánchez-Laínez, J.; Zornoza, B.; Friebe, S.; Caro, J.; Cao, S.; Sabetghadam, A.; Seoane, B.; Gascon, J.; Kapteijn, F.; Le Guillouzer, C. ,Influence of ZIF-8 particle size in the performance of polybenzimidazole mixed matrix membranes for pre-combustion CO 2 capture and its validation through interlaboratory test. *J. Membr. Sci.* **2016**, 45-53.
(14) Bushell, A. F.; Attfield, M. P.; Mason, C. R.; Budd, P. M.; Yampolskii, Y.; Starannikova, L.; Rebrov, A.; Bazzarelli, F.; Bernardo, P.; Carolus Jansen, J.; Lanč, M.; Friess, K.; Shantarovich, V.; Gustov, V.; Isaeva, V. ,Gas permeation parameters of mixed matrix membranes based on the polymer of intrinsic microporosity PIM-1 and the zeolitic imidazolate framework ZIF-8. *J. Membr. Sci.* **2013**, *0*, 48-62.
(15) Sorribas, S.; Zornoza, B.; Téllez, C.; Coronas, J. ,Ordered mesoporous silica–(ZIF-8) core–shell spheres. *Chem. Commun.* **2012**, *75*, 9388-9390.
(16) Sánchez-Laínez, J.; Zornoza, B.; Téllez, C.; Coronas, J. Asymmetric polybenzimidazole membranes with thin selective skin layer containing ZIF-8 for H2/CO2 separation at pre-combustion capture conditions, *J. Membr. Sci.* **2018**, 427-434.

Chapter 11: Ultrapermeable thin film ZIF-8/polyamide membrane for H_2/CO_2 separation at high temperature without using sweep gas

J. Sánchez-Laínez, L. Paseta, M. Navarro, B. Zornoza, C. Téllez, and J. Coronas. Advanced Materials Interfaces, 2018, 1800647. DOI: 10.1002/admi.201800647. Permission conveyed through Copyright Clearance Center, Inc.

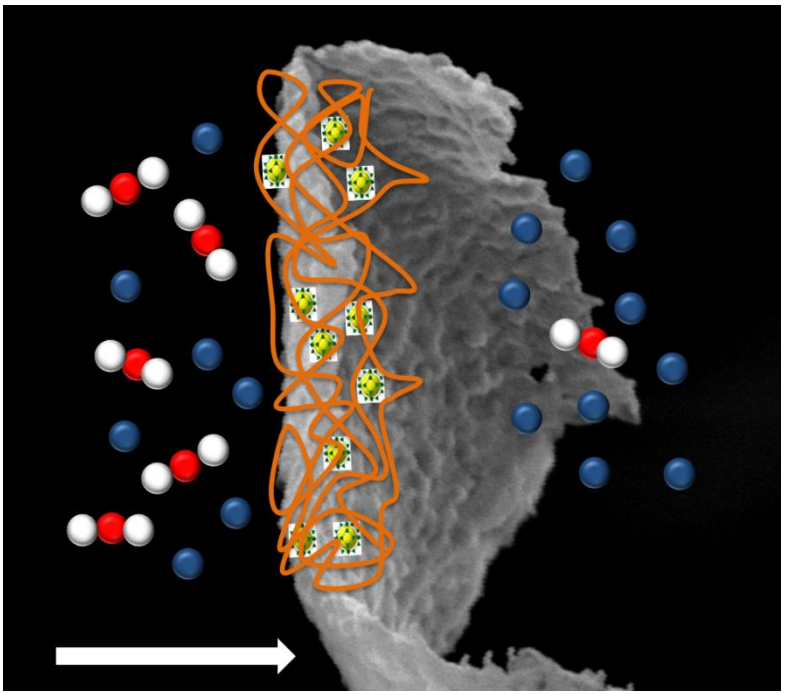

Category:

- Type of membrane: supported membranes
- Gas separation: pre-combustion CO_2 capture

ADVANCED MATERIALS INTERFACES

www.advmatinterfaces.de

Ultrapermeable Thin Film ZIF-8/Polyamide Membrane for H_2/CO_2 Separation at High Temperature without Using Sweep Gas

*Javier Sánchez-Laínez, Lorena Paseta, Marta Navarro, Beatriz Zornoza, Carlos Téllez, and Joaquín Coronas**

The use of thin film composites containing metal–organic frameworks (MOFs) as filler is of widespread interest for nanofiltration issues, since their thin selective layer allows a high permeation flow. The application of this kind of membranes for gas separation should provide a better permeance in comparison with other polymeric membranes and a reduction in the amount of MOF required for their fabrication. Here, the preparation of 50–100 nm thick polyamide flat membranes containing zeolitic imidazolate framework-8 (ZIF-8) nanoparticles is shown via interfacial polymerization, containing a lower amount of MOF (0.013 g m^{-2} membrane) as compared to other membranes used for gas separation. The membranes are applied for H_2/CO_2 separation at high temperatures and pressures, showing a stable performance at 180 °C for at least seven days. Outstanding separation values are 328 GPU of H_2 and a H_2/CO_2 selectivity of 18.1 at 180 °C and 6 bar feed without transmembrane pressure. These membranes, also measurable without sweep gas, are highly suitable for industrial application.

1. Introduction

Carbon capture and storage *via* pre-combustion processes involves the separation of H_2/CO_2 mixtures with a high CO_2 concentration (≈45 vol%) at elevated pressure (15–20 bar) and temperature (190–210 °C).[1] However, there is a considerable concern about the high costs of these processes.[2] Membrane technology is an efficient approach for this gas separation thanks to its simplicity, ease of operation and versatility for a large number of potential uses. Although polymeric membranes rule the commercial scene for CO_2 capture, their well-known trade-off between permeability and selectivity makes it difficult to manufacture commercially attractive membranes.[3]

J. Sánchez-Laínez, L. Paseta, Dr. M. Navarro, Dr. B. Zornoza, Prof. C. Téllez, Prof. J. Coronas
Chemical and Environmental Engineering Department
Instituto de Nanociencia de Aragón(INA)
Universidad de Zaragoza
50018, Zaragoza, Spain
E-mail: coronas@unizar.es

The ORCID identification number(s) for the author(s) of this article can be found under https://doi.org/10.1002/admi.201800647.

DOI: 10.1002/admi.201800647

Thin film composite (TFC) membranes consist of an ultrathin dense polymeric layer (thicknesses generally below 100 nm)[4,5] supported on a porous support. Several techniques have been applied to fabricate multilayer composites, such as solution casting, dip-coating, spin-coating, chemical vapor deposition, and interfacial polymerization.[6] Interfacial polymerization (IP) involves the polycondensation of two multifunctional monomers that are initially dissolved in different phases (aqueous and organic solvent). When both solutions make contact, a fast polymerization reaction occurs in the interphase, making the polymer precipitate and forming a dense thin film.[7]

The combination of high water flux and salt rejection, a result of the extremely thin selective polyamide (PA) layers, has led to the successful implementation of TFC membranes in large-scale industrial processes, especially in reverse osmosis and nanofiltration.[8] Some applications in gas separation processes can also be found in the literature, and TFC membranes prepared by IP have already been applied in CO_2 separation.[9–11] Regarding H_2/CO_2 separation, Ali et. al. developed thin skin membranes by interfacial polymerization, able to achieve a H_2 permeance of 500 GPU and a H_2/CO_2 selectivity of 50.[12] However, these membranes could only withstand temperatures up to 140 °C due to the use of polysulfone supports, and precombustion capture needs membranes produced from materials with a high mechanical and thermal stability due to the harsh operating conditions involved.

The incorporation of inorganic nanoparticles into TFC membranes gave rise to the so-called thin film nanocomposite (TFN) membranes.[13] These membranes have been widely developed for nanofiltration,[14] but the research into gas separation found in the literature to date is very scarce.[15] ZIF-8 may be a perfect filler to enhance the gas separation properties of the polyamide, since TFN membranes can be considered as supported ultrathin mixed matrix membranes (MMMs), in which these fillers have already been successfully used.[16–23] ZIF-8 is a zeolitic imidazolate framework (a subfamily of the so called metal–organic frameworks, MOFs) with **sod** zeolitic topology and cavities of 1.16 nm connected through smaller windows of 0.34 nm.[24] In addition, Hess et. al. were able to prepare

ZIF-8-poly(ether sulfone) (PES) composites with a selective layer thickness of about 5 µm that showed at room temperature a H_2 permeance of 1167 ± 785 GPU and a H_2/CO_2 selectivity of 9.3 ± 3.1.[25]

This work focuses on the preparation of polyamide-based TFN membranes on polyimide P84® asymmetric supports via the IP route. These membranes incorporate several loadings of ZIF-8, forming defect-free composites that show an extraordinary H_2/CO_2 gas separation performance at significantly high temperatures (250 °C), never before achieved with this particular type of membrane. Coating the membranes with polydimethylsiloxane (PDMS) allows keeping the gas separation performance stable for seven days, preventing the damage of the polyamide layer. TFN membranes represent a real opportunity to reduce the gas separation membrane cost to ≈US$50 per m^2 by using supports industrially available for reverse osmosis and nanofiltration.[26]

2. Results

2.1. Membrane Preparation and Characterization

TFC and ZIF-8-containing TFN membranes were synthesized by IP of polyamide on P84® asymmetric porous supports prepared following the phase inversion method. **Figure 1**a shows the scanning electron microscopy (SEM) images of the cross-section of a TFC membrane. The P84® support has a thickness of around 120 µm and is constituted by two different porous layers, finger-like macropores and a ≈26 µm thick porous sponge-like layer above them. The thickness of the top layer of polyamide was not easy to distinguish from the spongy polyimide zone (see below). The TFC membrane surface (Figure 1b) reveals the typical "ridge and valley" morphology of the polyamide (PA) layer, with a continuous morphology in the absence of visible defects. SEM images were also taken of TFN membranes containing different loadings of ZIF-8 from 0.2 to 0.8% w/v (see Figure S1 in the Supporting Information). The PA layer is well formed in the presence of the ZIF-8 nanoparticles but its morphology changes as the dense and smoother areas in combination with the "ridge and valley" morphologies become more frequent. This suggests that the introduction of the filler influenced the PA layer formation. Nevertheless, the concentration of the filler in the TFN membrane is very low, which hinders the detection of the ZIF-8 nanoparticles (≈30 nm as shown in Figure S2 in the Supporting Information) by this technique, whether using surface or cross-section images. In consequence, energy-dispersive X-ray spectroscopy (EDX) analysis was used to detect Zn (weight and atomic composition) in the cross-section images of TFN membranes with 0.2% and 0.4% w/v of ZIF-8 nanoparticles (Figure 1c; Figure S3, Supporting Information). The discrepancy between the nominal loading of the membranes (% w/v) and the actual amount of Zn detected is due to the fact that the first value is referred to the amount of ZIF-8 incorporated in the reaction medium during the interfacial polymerization. Only a part of this amount was effectively incorporated into the membrane. The presence of crystalline ZIF-8 nanoparticles was demonstrated by electron diffraction of the composite PA layer. Figure 1d,e shows schemes of the ZIF-8 and a TFN membrane for a better visualization and understanding of the prepared membranes.

To study the layout and interaction of the ZIF-8 nanoparticles and PA, a piece of TFN with 0.8% w/v of ZIF-8 was immersed in *N,N*-dimethylformamide (DMF) at room temperature for 5 min to dissolve the P84® support. The separated top PA selective layer was observed by transmission electron microscopy (TEM). Since the P84® support was not previously crosslinked, it was easily dissolved in the solvent. **Figure 2**a

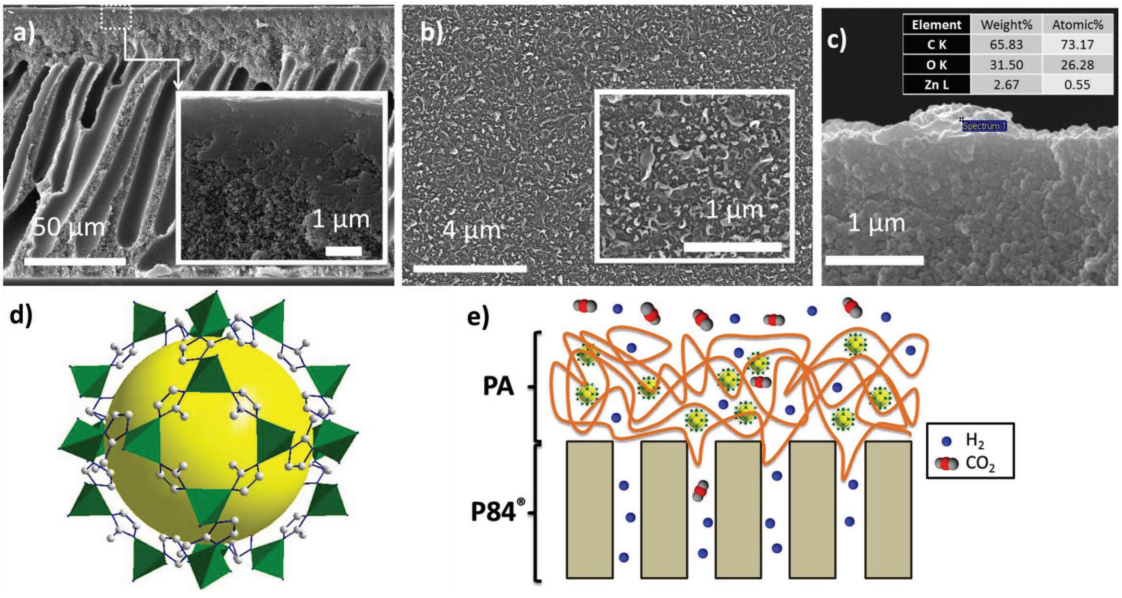

Figure 1. SEM characterization of TFCs & TFNs prepared on polyimide P84® supports. a) Image of the cross-section of a TFC with an inset at higher magnification. b) Image of the surface of the TFC with a zoom as inset. c) EDX analysis of a TFN containing a 0.8% w/v of ZIF-8. Schematic representations of d) ZIF-8 with the ZnN_4 tetrahedra in green and carbon atoms from ligand molecules in gray, and e) the TFN membrane.

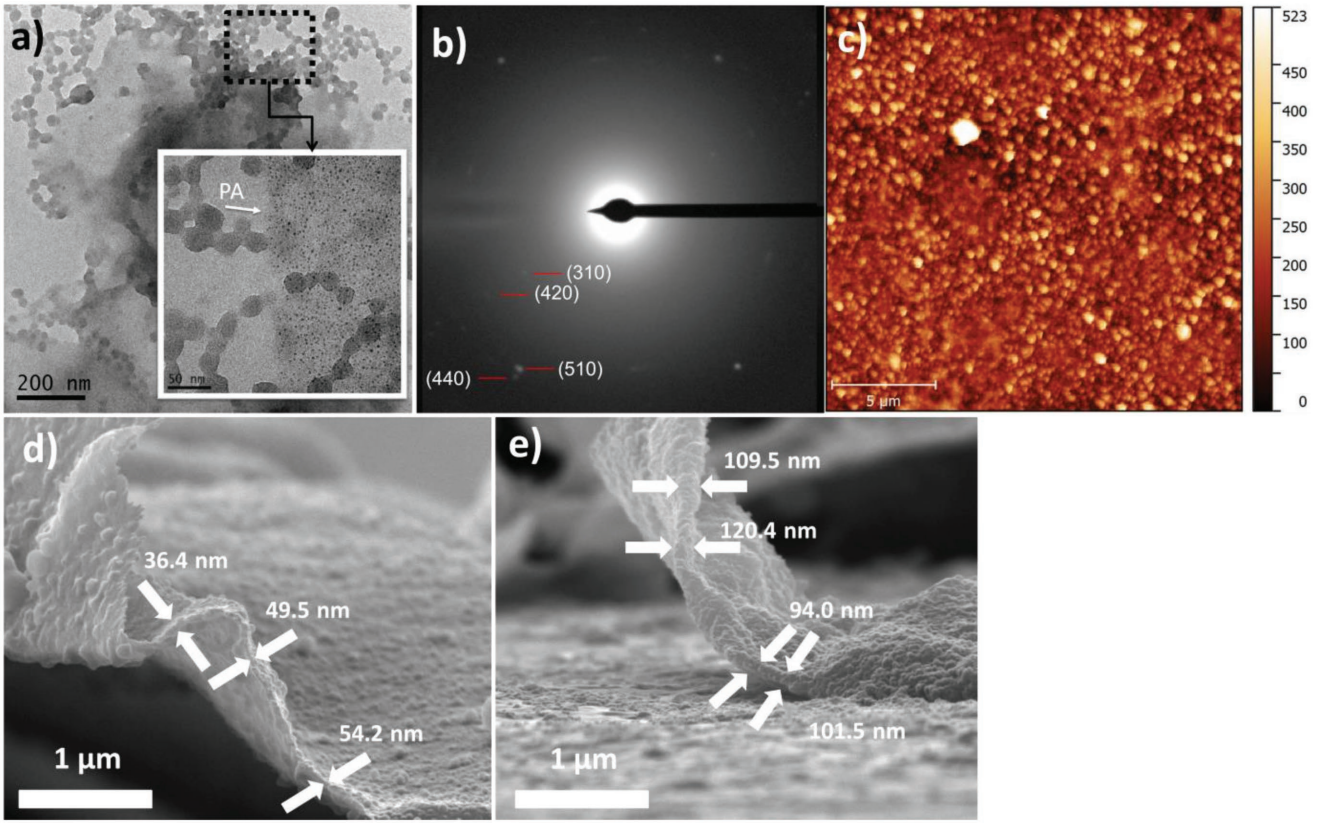

Figure 2. a) TEM image of the PA layer of a 0.8% w/v loaded TFN after the dissolution of the P84® support in DMF, with a higher magnified image as inset. b) Electron diffraction pattern in the [001] zone axis of a ZIF-8 crystal from inset (a). The diffraction spots are indicated by red lines and indexed according to the ZIF-8 crystal structure.[24] c) AFM characterization of the membrane surface of a 0.4% w/v loaded TFN with a color scale measuring the membrane roughness in nm. SEM images of the PA layer of a d) TFC and e) a TFN with 0.4% w/v of ZIF-8 nanoparticles removed from the P84® support. The arrows show the thickness of the PA layer.

illustrates small fragments of polymer with highly dispersed ZIF-8 nanoparticles embedded in them. Moreover, the electron diffraction pattern in Figure 2b of ZIF-8 in the [001] zone axis shows the spots indexed as the (310), (420), (510), and (440) diffractions consistent with the structure of ZIF-8 (*d*-spacings of 5.4, 3.8, 3.3, and 3.0 Å, respectively). The intensity of these spots was weak since the energy of the beam quickly degraded the sample. In any event, they provide evidence that the ZIF-8 structure remained unaltered during the interfacial polymerization process carried out to synthesize the TFN membrane. Moreover, Figure 2d,e shows the SEM images of the top thin PA layer detached from a TFC membrane and a TFN membrane with 0.4% w/v of ZIF-8 nanoparticles. Thicknesses of around 50 and 100 nm can be distinguished for the TFC and the TFN membranes with 0.4% v/w of ZIF-8, respectively. The thickness of the TFN is higher because of the presence of the ZIF-8 nanoparticles (again verified by EDX analysis), which can be found lodged between two sublayers of PA (see Figure S4 in the Supporting Information).

X-ray diffraction (XRD) and Fourier transform infrared spectroscopy (FTIR) analyses (Figures S5 and S6 in the Supporting Information, respectively) were also performed on TFN membranes with different loadings. Neither XRD reflections nor vibration modes of ZIF-8 were easy to distinguish, even using grazing incident diffraction (see Figure S5b in the Supporting Information). This may be because of the low concentration of the filler (maximum 0.8% w/v) dispersed in the PA membrane bulk. In any event, the XRD patterns in Figure S5 in the Supporting Information show some weak reflections at $2\theta = 9.5°$, 12.2°, and 24.8°) that may correspond to the PA layer. In the FTIR spectra in Figure S6a in the Supporting Information, two peaks related to the PA layer can be distinguished in the TFC and TFN membranes. The former at 1609 cm^{-1} corresponds to the N—H deformation vibration or C=C ring stretching vibration of the aromatic amide. The latter at 1541 cm^{-1} corresponds to the N—H in-plane bending and N—C stretching vibration of a —CO—NH— group.[27] Also, the FTIR spectra in Figure S6b in the Supporting Information show a signal at 1585 cm^{-1}, corresponding to the C=N stretching mode of the imidazole rings of mIm, the ZIF-8 linker.[28] Unfortunately, the low loading of filler makes that the accuracy of the FTIR spectra is not good enough to define the interaction between ZIF-8 and the PA. Nevertheless, physical interaction or chemical bonding cannot be discarded because of the flexibility of ZIF-8 and its partial organic nature, respectively. The TGA analysis in Figure S7 in the Supporting Information shows the thermal stabilities of all the composites. The analysis was performed under air flow (to calculate the real loading of the membranes) and N_2 flow (to simulate a reducing atmosphere similar to that present during the gas separation test). The thermograms show two

onset temperatures. The former at around 250 °C corresponds to the decomposition of the PA layer; and the latter at ≈600 °C is related to that of the P84® support. The real loading of ZIF-8 effectively incorporated in each TFN membrane was calculated to be: 0.26, 0.62, and 0.81 wt% for the 0.2, 0.4, and 0.8% w/v loadings used in the IP process, respectively. It is worth noting that these amounts correspond to the loadings of ZIF-8 with regard to the whole membrane volume, including the P84® support, and not only to the PA layer. Differential Scanning Calorimetry (DSC) analysis was also performed with the PA layer, shown in Figure S8 in the Supporting Information. Two endothermic peaks are distinguishable at 140 and 310 °C. The former may be a melting point and the latter the degradation temperature of the polymer, both usual in polyamides.[29]

The surface topography and roughness of the different membranes prepared were characterized by atomic force microscopy (AFM) and the results can be seen in Figure S9 in the Supporting Information. Each root-mean-square (RMS) roughness value was calculated from at least three images taken from 20 μm^2 of different substrates. The 0.2% w/v loaded TFN membrane presented a RMS value of 55 nm, almost double that of the TFC (RMS of 29 nm). Besides, the RMS value increased for the 0.4% w/v and 0.8% w/v TFN membranes, reaching full inhomogeneity in the latter, being 73 and 90 nm, respectively (see Figure 2c). Therefore, the increasing addition of the ZIF-8 nanoparticles, whose particle size (around 30 nm) is approximately one third of the polyamide layer thickness (Figure 2d,e), is responsible for the lower flatness of the membrane surface.

2.2. Gas Separation Performance

The TFC and the TFN membranes with ZIF-8 loadings of 0.2, 0.4, and 0.8% w/v were tested for H_2/CO_2 separation at temperatures from 35 to 250 °C and a feed pressure of 3 bar. The results are shown in the Robeson graph in **Figure 3** and also in Table S1 in the Supporting Information. Other membranes found in the literature based on ZIF-8 and tested at high temperature have also been included for comparison: ZIF-8 on P84® supports measured at 150 °C,[30] ZIF-8 on silicon nitride hollow fibers tested at 200 °C[31] and polybenzimidazole (PBI)/ZIF-8 hollow fibers measured at 180 °C.[17])

The use of a dope concentration below the critical value prevented the formation of a selective skin layer and made the films suitable for use as low resistant, non-selective supports.[33] Therefore, the P84® supports had no H_2/CO_2 selectivity. Polyimides exhibit a higher thermal and solvent resistance than polysulfone,[5,34] being more suitable for operating at the high temperatures necessary for H_2/CO_2 separation under industrial conditions, as explained above.

The TFC membrane showed good H_2 permeance, 99.7 GPU, at 35 °C but the selectivity remained poor (3.8). Increasing the temperature to 180 °C had an extremely positive effect on the gas separation performance. The H_2 permeance was fivefold higher and the H_2/CO_2 selectivity also increased, showing values over 500 GPU and H_2/CO_2 selectivity of 7.9. Additionally, a notable improvement in the gas separation performance was also experienced at the highest temperature tested, 250 °C. The H_2 permeance values were double than those achieved at

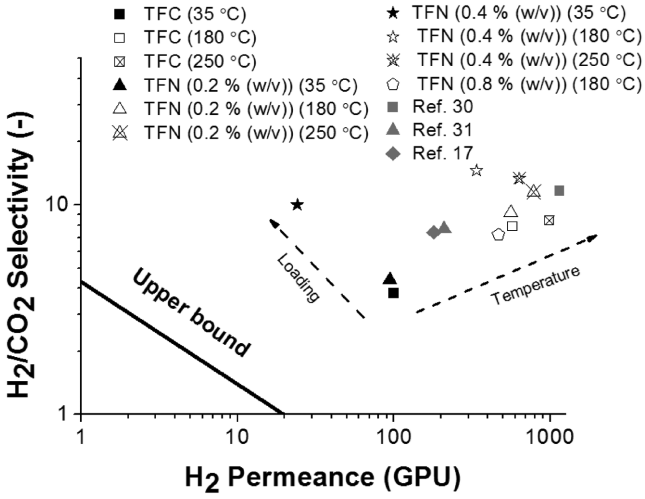

Figure 3. Gas separation performance of TFCs and TFNs at several temperatures and 3 bar feed pressure (black symbols): squares stand for TFCs; triangles for TFNs with 0.2% w/v of ZIF-8; stars for TFNs with 0.4% w/v of ZIF-8 and pentagrams for TFNs with 0.8% w/v of ZIF-8. Full symbols refer to measurements at 35 °C; crossed symbols, at 180 °C and crosses symbols, at 250 °C. The H_2/CO_2 upper bound calculated in GPU is also included[32] and bibliographical values can be seen in grey.

180 °C, being 988 GPU. There was also a 6% increase in the H_2/CO_2 selectivity, being 8.4.

Embedding ZIF-8 nanoparticles into the polyamide layer also had a positive effect on the gas separation performance. Even at the lowest temperature of 35 °C, incorporating just 0.2% w/v of ZIF-8 enhanced the gas separation performance. Besides, the H_2/CO_2 selectivity of the 0.4% w/v TFN membrane was threefold higher (10.0) than that of the TFC membrane. At 180 °C, TFNs containing 0.2% and 0.4% w/v of ZIF-8 showed respective increases in H_2/CO_2 selectivity of 42% (9.2) and 64% (14.6). However, at this high temperature, the H_2 permeance decreased as the membrane loading was higher: 338 GPU at 0.4% w/v. This is still a significantly high value for a flat membrane. The decrease in the H_2 flow may be related to the greater thickness of the PA layer as the loading of ZIF-8 increases, as already seen by SEM (see Figure 2d,e). Moreover, at the highest loading of 0.8% w/v a decrease in both permeance and selectivity could be seen. This phenomenon may be related to the defective formation of the PA layer in these TFN membranes, according to the previous characterization (see AFM results in Figure S9 in the Supporting Information), penalizing the activated and selective flow, and thus the optimum TFN membrane is observed at the intermediate 0.4% w/v loading. Raising the temperature to 250 °C led to an increase in the H_2 permeance of TFNs, but it had almost no effect on the selectivity. This may be due to defects present in the membrane related to the integration of ZIF-8 that conditions the flow at a higher temperature. It may also be due to the fact that this temperature is close to the onset temperature of the PA layer, according to the TGA and DSC analyses in Figures S7 and S8 in the Supporting Information.

The apparent activation energies of the TFC and 0.4% w/v TFN membranes were calculated for H_2 and CO_2, fitting their permeance values in Figure 3 with the Arrhenius equation

(see Figure S10 in the Supporting Information). The results in Table S2 in the Supporting Information reveal activation energies of 14.2 and 9.1 kJ mol^{-1} for H_2 and CO_2, respectively, for the TFC membrane. The TFN membrane with 0.4% w/v of ZIF-8 showed 20.6 kJ mol^{-1} for H_2 and 18.4 kJ mol^{-1} for CO_2. In line with the enhancement of gas transport through micropores, the incorporation of the ZIF nanoparticles into the polyamide layer increased the activation energy of both gases, but especially for CO_2, which almost equaled that of H_2. This fact may explain why the TFN membranes did not improve their selectivity so much with increasing temperatures, as would be expected in the case of polymeric membranes. In any event, the TFN membranes were very effective for the gas separation, even though their ZIF-8 loading was very low (below 1 wt% according to the TGA analysis shown in Figure S7 in the Supporting Information).

2.3. Membrane Stability

Although both the TFC and TFN membranes showed an outstanding H_2/CO_2 separation performance, the results were not constant when the experiment was run at 180 °C for several days. The membranes deteriorated from the first day onwards. **Figure 4**a shows the gas separation performance at 180 °C and 3 bar feed of a TFN membrane with a 0.4% w/v loading of ZIF-8, thus the optimal filler loading because it previously gave rise to the highest H_2/CO_2 selectivity at this same temperature (see Figure 3). It can be seen that the H_2 permeance of the membrane gradually increased with time while the H_2/CO_2 selectivity decreased its value. This deterioration may be due to working at an operating temperature close to the first melting point of the PA layer (see DSC analysis in Figure S8 in the Supporting Information).

In order to protect the PA layer from deteriorating, the membranes were coated with a 120 nm layer of PDMS (see Figure S11 in the Supporting Information) and tested at 180 °C for one week to check their stability. Figure 4b shows the gas separation performance of this 0.4% w/v loaded TFN membrane. The membrane was first tested under these conditions, then coated with PDMS and eventually tested again for seven days. Previous to the coating with PDMS, the membrane showed a H_2 permeance of 367 GPU and a H_2/CO_2 selectivity of 11.3. After coating, the H_2 permeance decreased to 258 GPU while the selectivity was maintained. This reduction in the H_2 flow is usual and is due to the new resistance in series added by the PDMS layer. The H_2 flow recovered during the operation time, reaching a constant value over 300 GPU after the fourth day. As the H_2/CO_2 selectivity was also stable during the whole measuring time, it can be concluded that PDMS coating sets the base for long-term stability, so that the TFN membranes may become suitable for operating under harsh conditions for long periods of time, which is industrially interesting.

The performance of the TFN membranes was also tested under different feed pressures to elucidate the influence of this variable on the gas separation performance. The results can be seen in Figure 4c. Upon increasing the feed pressure to 5 and 6 bar, the H_2 permeance increased by 5% for each pressure increase, reaching 334 GPU at 6 bar. The same occurred with the

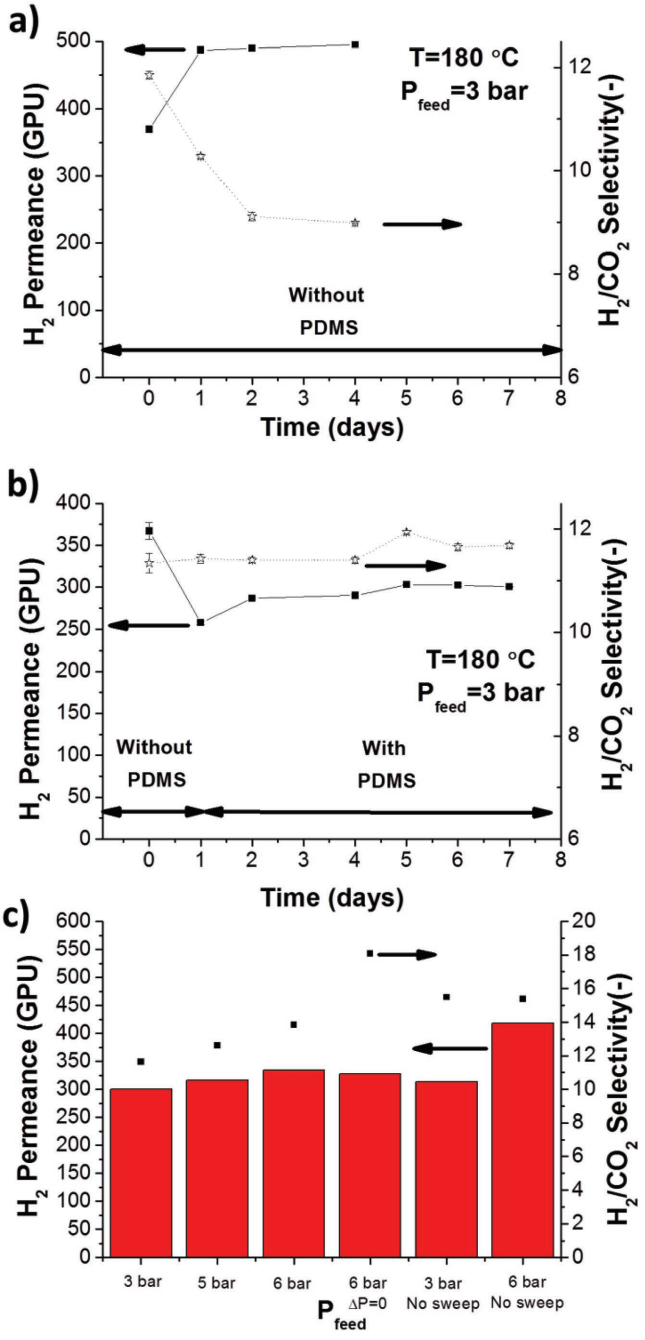

Figure 4. Gas separation performance of 0.4% w/v loaded TFN membrane. Stability test of the TFN a) without and b) with PDMS coating. The H_2 permeance (full symbols, continuous line) and H_2/CO_2 selectivity (empty symbols, dashed line) were monitored while the membrane was tested at 180 °C and 3 bar feed pressure for several days. c) Histogram of the gas separation performance of the TFN at different feed pressures: 3, 5, and 6 bar, at 6 bar feed pressure without transmembrane pressure and at 3 and 6 bar feed pressure without sweep gas. Bars refer to H_2 permeance and symbols to H_2/CO_2 selectivity.

H_2/CO_2 selectivity, which increased by 8% (13.9). Furthermore, the membranes were tested at 6 bar without transmembrane total pressure difference, setting the operating pressure at 6 bar at both the feed and the permeate side. Under these conditions,

the H_2 permeance dropped to 328 GPU, in comparison with previous values at 6 bar feed and 1 bar permeate, but the selectivity increased by 23%, reaching the highest value achieved in this work, 18.1 (Figure 4c). This enhancement may be related to the absence of viscous flow due to the lack of a total pressure gradient through the membrane. This result makes the membrane interesting for operating in cascade, since the permeate flow is obtained at high pressure, ready for the following stage. Finally, the membranes were also tested without sweep gas at 3 and 6 bar feed, showing a similar H_2 permeance and slightly higher H_2/CO_2 selectivities compared with the performance when using sweep gas (see Figure 4c). This result is of paramount importance, demonstrating the suitability of the membranes for industrial operation.

2.4. Amount of ZIF-8 for the Fabrication of Different Membranes

The amount of ZIF-8 necessary to fabricate 0.4% w/v TFN membranes, the optimal membrane loading as previously explained, has been calculated from the ZIF loading (0.62 wt% by TGA analysis) and the thickness of the membrane (150 µm). This quantity has been compared with those in other common membrane configurations in which this material has been used (see **Figure 5**). Supported ZIF-8 membranes (100% ZIF-8, thus pure MOF membranes) are the composites that need the highest amount of ZIF-8, ≈2500 g m^{-2} based on previous estimations found in the literature.[35] Using ZIF-8 in a dense mixed matrix membrane (MMM) configuration drastically reduces this amount to 9.3 g m^{-2} when the membrane has a loading of 10 wt% of ZIF.[36] As our group has recently reported,[32] when ZIF-8 is used as a filler in a membrane of the same loading but with an asymmetric configuration, the amount required was almost three times less (3.7 g m^{-2}). This reduction is related to the decrease in the skin layer thickness in comparison with dense MMMs of the same polymer. Finally, for the TFN membranes in this work, the necessary amount of filler is much

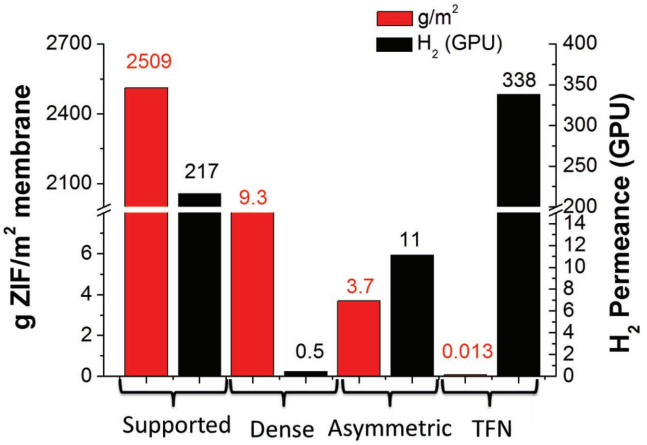

Figure 5. Histogram comparing the amount of ZIF-8 used for the membrane fabrication (red) and the H_2 permeance of the membrane (black) for: supported continuous membranes of ZIF-8 tested at 35 °C,[35] dense PBI membranes with 10 wt% of ZIF-8 tested at 180 °C,[36] asymmetric PBI membranes with 10 wt% of ZIF-8 tested at 180 °C[32] and the TFNs used in this work with 0.4% w/v of ZIF-8 tested at 180 °C.

lower, being only 0.013 g m^{-2}. This value is very attractive, since it would imply a significant reduction in the production cost in a hypothetical fabrication scale up. Besides, it is consistent with the 3.8 µg cm^{-2} (thus 0.038 g m^{-2}) quantified as the minimum amount of material added to the support when it is coated with a monolayer of MOF by the Langmuir–Schafer methodology.[37] The minimization of the amount of ZIF is important since all the membrane technologies designed to fight against global warming face severe economic restrictions due to the huge amounts of gases to be treated at low cost.[38] The H_2 permeance of all these membranes is also shown in Figure 5. TFN membranes show permeances 1.5 fold higher than supported membranes and 30 fold higher than asymmetric membranes, being clearly the best membrane configuration to obtain a high H_2 permeation flow. Besides, as shown above, they can selectively operate with no sweep gas, the driving force being established from a total pressure difference (5 bar).

3. Conclusion

Thin film composite membranes consisting of a selective polyamide layer on asymmetric P84® supports have been prepared in this work. ZIF-8 nanoparticles have been embedded in the polyamide matrix using different concentrations of this material from 0.2 to 0.8% w/v in the interfacial polymerization reaction medium. The polyamide layer, with a thickness between 50 and 100 nm, could be seen well formed on the membrane surfaces by SEM, with no visible defects. ZIF-8 nanoparticles were detected by TEM, where electron diffraction verified their crystallinity. FTIR also revealed weak signals of the C=N stretching mode in ZIF-8. AFM characterization showed that the membrane roughness increased with the ZIF-8 loading, until the membrane turned defective at 0.8% w/v. The membrane composites exhibited a high H_2/CO_2 separation performance at temperatures up to 250 °C. The optimal filler concentration of 0.4% w/v (real membrane loading of 0.62 wt%), produced a H_2 permeance of 338 GPU and a H_2/CO_2 selectivity of 14.6, and the high permeation flows allowed measurements without sweep gas. Coating the membranes with PDMS prevented polyamide damage, leading to membranes able to operate at high temperature during one week. The gas separation performance also improved with the feed pressure increase, especially when operating without total transmembrane pressure difference, and the H_2/CO_2 selectivity reached its maximum value (18.1). The TFN membranes could selectively operate with no sweep gas, the driving force coming from the total pressure difference (5 bar), which is important from the industrial point of view. The amount of ZIF-8 necessary to fabricate TFN membranes was calculated to be as small as 0.013 g m^{-2}, the lowest in comparison with other typical membrane configurations used for gas separation.

4. Experimental Section

Chemicals: Zinc nitrate hexahydrate ($Zn(NO_3)_2{\cdot}6H_2O$, >98%), 2-methylimidazole (mIm, $C_4H_6N_2$, >99%), trimesoyl chloride (TMC, 98%), m-phenylenediamine (MPD, 99%), and *N*,*N*-dimethylacetamide (DMAc) were purchased from Sigma Aldrich. Methanol (MeOH, HPLC grade), isopropyl alcohol (IPA, 99.5%), and n-hexane were purchased

from Scharlau. Polyimide Lenzing P84® was purchased from HP polymer GmbH and PDMS Sylgard 184, consisting of a polymer base (dimethylsiloxane, dimethylvinyl-terminated) and a hardener (dimethyl, methylhydrogen siloxane), was purchased from Dow Corning.

Synthesis of ZIF-8 Nanoparticles: ZIF-8 nanoparticles were synthesized following the method reported by Cravillon et. al.[39]: 2.93 g of zinc nitrate hexahydrate was dissolved in 200 mL of MeOH. Besides, 6.49 g of mIm was dissolved in 200 mL of MeOH, and the two solutions were mixed and stirred for 1 h. The final product was collected by centrifugation, washed once with MeOH, and dried at 110 °C overnight. The resulting nanoparticles had an average particle size of around 30 nm.

Preparation of P84® Asymmetric Supports: P84® was selected as support because it is a polymer with good mechanical and thermal stabilities, able to operate at high temperatures.[40,41] Besides, the group has previous experience in the preparation of polyamide/P84® composites for nanofiltration issues.[37] Flat asymmetric porous P84® supports were prepared following the phase inversion method. A 23 wt% dope solution of P84® was prepared dissolving the corresponding amount of powder in DMAc. This dope concentration was selected because it was found to be the optimum concentration between 15 wt% (too brittle supports) and 28 wt% (too dense supports) according to the SEM images of Figure S12 in the Supporting Information. The polymer solution was cast onto a glass plate using the Elcometer 4340 Automatic Film Applicator placed in a fume hood and set at a thickness of 250 µm. Immediately afterwards the resultant polymer sheets were immersed into a tap water bath at 25 °C for 10 min. After precipitation, the membranes were kept in a deionized (DI) water bath overnight and then rinsed with IPA in order to remove the remaining DMAc. The films were dried at 100 °C for one day prior to use.

Membrane Synthesis: TFC and TFN membranes were prepared by interfacial polymerization (IP) of polyamide on the P84® asymmetric porous supports described above. The P84® support was placed in a glass filtration holder and soaked with 30 mL of a 2% w/v solution of MPD in distilled water (i.e., 2 g of MPD for every 100 mL of water) for 2 min. Then 30 mL of a solution with 0.1% w/v of TMC in hexane and 0.2%–0.8% w/v of dispersed ZIF-8 nanoparticles (only for TFNs) was added for 1 min, followed by the addition of 10 mL of pure hexane to stop the polymerization reaction. After removing the excess, an extra 20 mL of hexane was added to remove unreacted trimesoyl chloride. The excess solution was discarded and the PA thin film was then synthesized. The remaining hexane was then washed out with 10 mL of distilled water. Finally, the membranes were soaked in DI water at 80 °C for 2 min to remove the rest of the unreacted monomers and dried at 100 °C for 18 h.

PDMS Coating: To avoid damage of the polyamide layer, the TFN membranes were healed with PDMS following a dip coating method. The coating solution was prepared mixing the PDMS polymer base and hardener with a weight ratio of 10 to 1. The mixture was added to n-hexane to obtain a 3 wt% solution. The membranes were immersed in the coating solution for 5 s and then allowed to evaporate at room temperature for 2 h. Finally, the membranes were cured in an oven at 100 °C for 18 h.

Membrane Characterization: Thermogravimetric analyses (TGA) were carried out using a Mettler Toledo TGA/STDA 851e. Samples (10 mg) placed in 70 µL alumina pans were heated in 40 mL (STP) of air or nitrogen flow from 25 to 900 °C at a heating rate of 10 °C min^{-1}. Differential Scanning Calorimetry (DSC) analysis was performed on a Mettler Toledo DSC822e. Samples (10 mg) placed in 70 µL aluminum pans were heated in 40 mL (STP) of nitrogen flow from 25 to 500 °C at a heating rate of 10 °C min^{-1}. Scanning electron microscopy (SEM) images of the MOFs and membranes were obtained using a FEI Inspect F50 model SEM, operated at 20 kV. Cross-sections of the membranes were prepared by freeze-fracturing after immersion in liquid N_2 and subsequently coated with Pt. Transmission electron microscopy (TEM) images of the MOF and PA were obtained using a FEI Tecnai T20 microscope, operated at 200 kV. A piece of membrane was immersed in DMF for 2 h until the complete dissolution of the P84® support. The layer of polyamide was then placed onto a holey carbon grid, which was allowed to dry for 48 h under ambient conditions. Fourier transform infrared spectroscopy (FTIR) was performed on the ZIF-8 powder sample and on the TFC and TFN membranes, using a Bruker Vertex 70 FTIR spectrometer equipped with a DTGS detector and a Golden Gate diamond ATR accessory. The spectra were recorded on the polyamide side by averaging 40 scans in the 4000–600 cm^{-1} wavenumber range at a resolution of 4 cm^{-1}. To detect the presence of MOF nanoparticles embedded in the polyamide layer in the TFN membranes, the spectrum of the TFC membrane was subtracted from the TFN membrane. Powder X-ray diffraction (XRD) patterns of the MOFs and MMMs were obtained with Panalytical Empyrean equipment, using CuKα radiation (λ = 1.540 Å), taking data from $2\theta = 2.5°$ to 40° at a scan rate of 0.03° s^{-1}. Atomic force microscopy (AFM) characterization was performed by means of a Veeco MultiMode 8 scanning probe microscope, in tapping mode under ambient conditions. A silicon cantilever provided by Bruker, with a force constant of 40 mN and operating at a resonant frequency of 300 kHz, was used in these experiments. Images were recorded with a scan rate of 1 Hz and an amplitude set-point lower than 1 V. After the AFM observation, the average plane roughness (R_a), the root-mean-square (RMS) and the relative surface area were obtained.

Gas Separation Analysis: The membrane samples were placed in a module consisting of two stainless steel pieces and a 316LSS macroporous disk support of 3.14 cm^2 (from Mott Co.) with a 20 µm nominal pore size, and gripped inside with silicon O-rings. The membrane was placed on the porous disk that acts as support, providing mechanical stability so that the membrane can stand the high feed pressure without breaking. The permeation module was placed in a UNE 200 Memmert oven to control the temperature of the experiments. Gas separation measurements were carried out by feeding a H_2/CO_2 equimolar mixture (25/25 cm^3(STP)·min^{-1}) at 3–6 bar to the feed side by means of two mass-flow controllers (Alicat Scientific, MC-100CCM-D), while the permeate side of the membrane was swept with a 10–30 cm^3(STP)·min^{-1} mass-flow controlled stream of Ar at 1–6 bar (Alicat Scientific, MC-5CCM-D). Concentrations of H_2 and CO_2 in the outgoing streams were analyzed by an Agilent 3000A online gas microchromatograph equipped with a thermal conductivity detector. Permeances were calculated in GPU (10^{-6} cm^3(STP) cm^{-2} s^{-1} $cmHg^{-1}$) once the steady-state of the exit stream was reached (for at least 3 h), and the separation selectivity was calculated as the ratio of permeances. At least 2–3 membrane samples of each type were fabricated and measured to provide the corresponding error estimations. Stability tests were performed maintaining the same flow conditions for 7 d at 180 °C. A scheme of the gas separation setup can be seen in Figure S13 in the Supporting Information.

Supporting Information

Supporting Information is available from the Wiley Online Library or from the author.

Acknowledgements

The research leading to these results has received funding from the European Union Seventh Framework Programme (FP7/2007-2013) under grant agreement no. 608490, project M4CO2. In addition, financial support from the Spanish MINECO and FEDER (MAT2016-77290-R), the Aragón Government (T05) and the ESF is gratefully acknowledged. J. S.-L. thanks the Spanish Education Ministry Program FPU2014 and L.P. the Ministry of Economy, Industry and Competitiveness Program FPI2014 for their PhD grants. All the microscopy work was done in the Laboratorio de Microscopías Avanzadas at the Instituto de Nanociencia de Aragón (LMA-INA). Finally, the authors would like to acknowledge the use of the Servicio General de Apoyo a la Investigación-SAI, Universidad de Zaragoza.

Conflict of Interest

The authors declare no conflict of interest.

Keywords

H_2/CO_2 separation, interfacial polymerization, membranes, metal–organic frameworks, polyamide

Received: April 26, 2018
Revised: June 1, 2018
Published online:

[1] Z. Dai, L. Ansaloni, L. Deng, *Ind. Eng. Chem. Res.* **2016**, *55*, 5983.
[2] D. M. Reiner, *Nat. Energy* **2016**, *1*, 15011.
[3] L. M. Robeson, *J. Membr. Sci.* **2008**, *320*, 390.
[4] S. Karan, Z. Jiang, A. G. Livingston, *Science* **2015**, *348*, 1347.
[5] M. F. Jimenez-Solomon, Q. Song, K. E. Jelfs, M. Munoz-Ibanez, A. G. Livingston, *Nat. Mater.* **2016**, *15*, 760.
[6] Z. Dai, L. Ansaloni, L. Deng, *Green Energy Environ.* **2016**, *1*, 102.
[7] S. V. Joshi, A. V. Rao, *J. Appl. Polym. Sci.* **1991**, *42*, 1773.
[8] M. J. Raaijmakers, N. E. Benes, *Prog. Polym. Sci.* **2016**, *63*, 86.
[9] J. Zhao, Z. Wang, J. Wang, S. Wang, *J. Membr. Sci.* **2006**, *283*, 346.
[10] X. Yu, Z. Wang, Z. Wei, S. Yuan, J. Zhao, J. Wang, S. Wang, *J. Membr. Sci.* **2010**, *362*, 265.
[11] M. Wang, Z. Wang, S. Li, C. Zhang, J. Wang, S. Wang, *Energy Environ. Sci.* **2013**, *6*, 539.
[12] Z. Ali, F. Pacheco, E. Litwiller, Y. Wang, Y. Han, I. Pinnau, *J. Mater. Chem. A* **2018**, *6*, 30.
[13] B. Jeong, E. M. Hoek, Y. Yan, A. Subramani, X. Huang, G. Hurwitz, A. K. Ghosh, A. Jawor, *J. Membr. Sci.* **2007**, *294*, 1.
[14] S. Sorribas, P. Gorgojo, C. Tellez, J. Coronas, A. G. Livingston, *J. Am. Chem. Soc.* **2013**, *135*, 15201.
[15] S. Yu, S. Li, S. Huang, Z. Zeng, S. Cui, Y. Liu, *J. Membr. Sci.* **2017**, *540*, 155.
[16] T. Yang, T. Chung, *Int. J. Hydrogen Energy* **2013**, *38*, 229.
[17] T. Yang, G. M. Shi, T. Chung, *Adv. Energy Mater.* **2012**, *2*, 1358.
[18] A. F. Bushell, M. P. Attfield, C. R. Mason, P. M. Budd, Y. Yampolskii, L. Starannikova, A. Rebrov, F. Bazzarelli, P. Bernardo, J. Carolus Jansen, M. Lanč, K. Friess, V. Shantarovich, V. Gustov, V. Isaeva, *J. Membr. Sci.* **2013**, *427*, 48.
[19] L. Xu, L. Xiang, C. Wang, J. Yu, L. Zhang, Y. Pan, *Chin. J. Chem. Eng.* **2017**, *25*, 882.
[20] J. A. Thompson, J. T. Vaughn, N. A. Brunelli, W. J. Koros, C. W. Jones, S. Nair, *Microporous Mesoporous Mater.* **2014**, *192*, 43.
[21] S. Shahid, K. Nijmeijer, *J. Membr. Sci.* **2014**, *470*, 166.
[22] Q. Song, S. Nataraj, M. V. Roussenova, J. C. Tan, D. J. Hughes, W. Li, P. Bourgoin, M. A. Alam, A. K. Cheetham, S. A. Al-Muhtaseb, *Energy Environ. Sci.* **2012**, *5*, 8359.
[23] M. J. C. Ordonez, K. J. Balkus, Jr., J. P. Ferraris, I. H. Musselman, *J. Membr. Sci.* **2010**, *361*, 28.
[24] K. S. Park, Z. N. Ni, A. P. Côté, J. Y. Choi, R. Huang, F. J. Uribe-Romo, H. K. Chae, M. O'Keeffe, O. M. Yaghi, *PNAS* **2006**, *103*, 10186.
[25] S. C. Hess, R. N. Grass, W. J. Stark, *Chem. Mater.* **2016**, *28*, 7638.
[26] B. Ghalei, K. Sakurai, Y. Kinoshita, K. Wakimoto, A. P. Isfahani, Q. Song, K. Doitomi, S. Furukawa, H. Hirao, H. Kusuda, *Nat. Energy* **2017**, *2*, 17086.
[27] C. Y. Tang, Y. Kwon, J. O. Leckie, *Desalination* **2009**, *242*, 149.
[28] Y. Hu, H. Kazemian, S. Rohani, Y. Huang, Y. Song, *Chem. Commun.* **2011**, *47*, 12694.
[29] I. Kolesov, R. Androsch, *Polymer* **2012**, *53*, 4770.
[30] F. Cacho-Bailo, M. Etxeberria-Benavides, O. David, C. Téllez, J. Coronas, *ACS Appl. Mater. Interfaces* **2017**, *9*, 20787.
[31] J. Wang, N. Li, Z. Li, J. Wang, X. Xu, C. Chen, *Ceram. Int.* **2016**, *42*, 8949.
[32] J. Sánchez-Laínez, B. Zornoza, C. Tellez, J. Coronas, *J. Membr. Sci.* **2018**, *563*, 427.
[33] S. S. Hosseini, N. Peng, T. S. Chung, *J. Membr. Sci.* **2010**, *349*, 156.
[34] B. Zornoza, C. Téllez, J. Coronas, *J. Membr. Sci.* **2011**, *368*, 100.
[35] S. Friebe, A. Mundstock, D. Schneider, J. Caro, *Chem.-A Eur. J.* **2017**, *23*, 6522.
[36] J. Sánchez-Laínez, B. Zornoza, S. Friebe, J. Caro, S. Cao, A. Sabetghadam, B. Seoane, J. Gascon, F. Kapteijn, C. Le Guillouzer, *J. Membr. Sci.* **2016**, *515*, 45.
[37] M. Navarro, J. Benito, L. Paseta, I. Gascón, J. Coronas, C. Téllez, *ACS Appl. Mater. Interfaces* **2017**, *10*, 1278.
[38] L. Giordano, D. Roizard, E. Favre, *Int. J. Greenhouse Gas Control* **2018**, *68*, 146.
[39] J. Cravillon, S. Muenzer, S. Lohmeier, A. Feldhoff, K. Huber, M. Wiebcke, *Chem. Mater.* **2009**, *21*, 1410.
[40] F. Cacho-Bailo, G. Caro, M. Etxeberría-Benavides, O. Karvan, C. Téllez, J. Coronas, *Chem. Commun.* **2015**, *51*, 11283.
[41] F. Cacho-Bailo, I. Matito-Martos, J. Perez-Carbajo, M. Etxeberría-Benavides, O. Karvan, V. Sebastián, S. Calero, C. Téllez, J. Coronas, *Chem. Sci.* **2017**, *8*, 325.

ADVANCED MATERIALS INTERFACES

Supporting Information

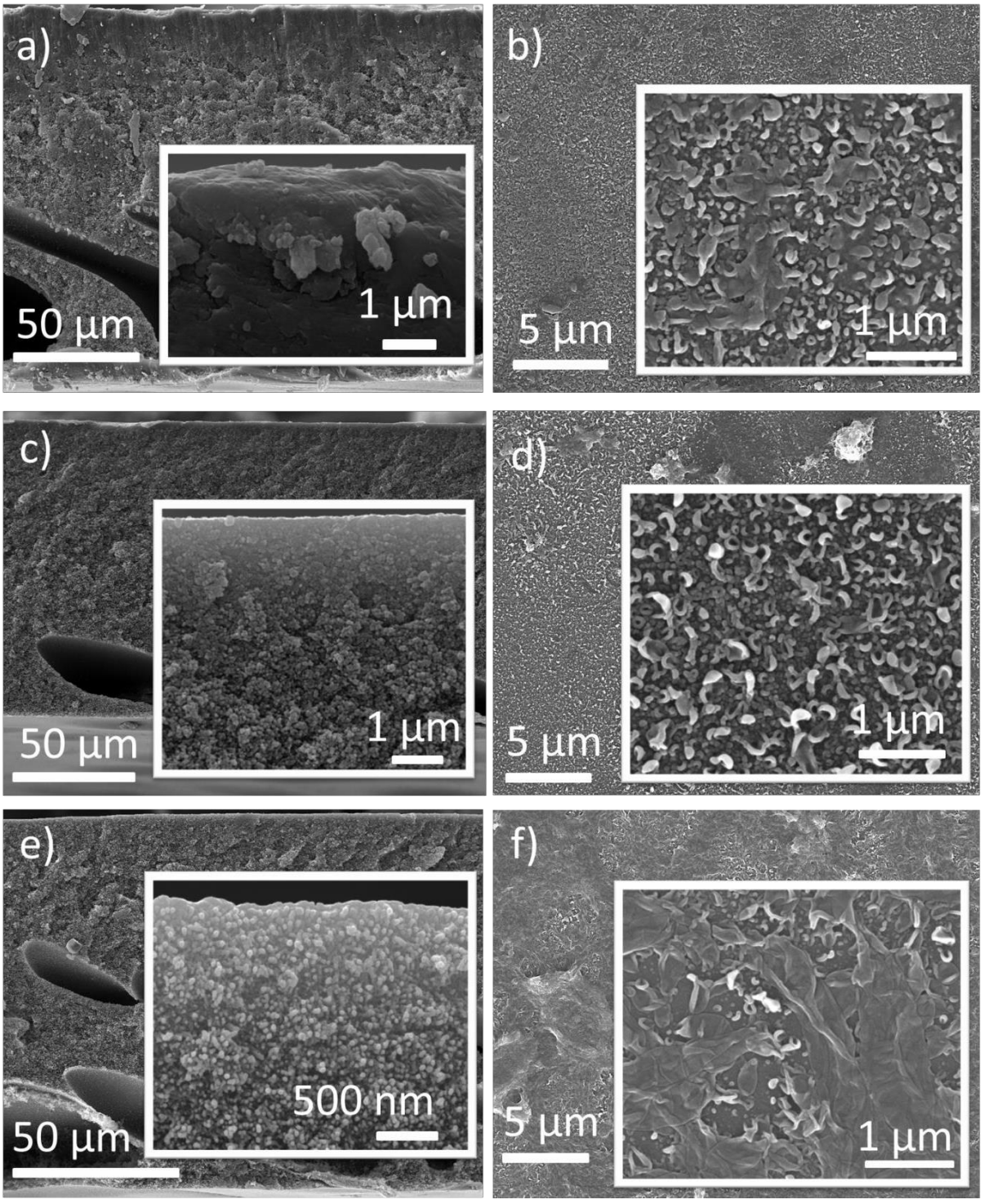

Figure S1. A,C,E) SEM images of the cross-section of the membranes. B,D,F) SEM images of the membranes surfaces. TFN membranes contain ZIF-8 loadings of: 0.2 %(w/v) (a, b), 0.4 %(w/v) (c, d) and 0.8 %(w/v) (e, f). All the images have an inset with a higher magnification of the top area of the membrane.

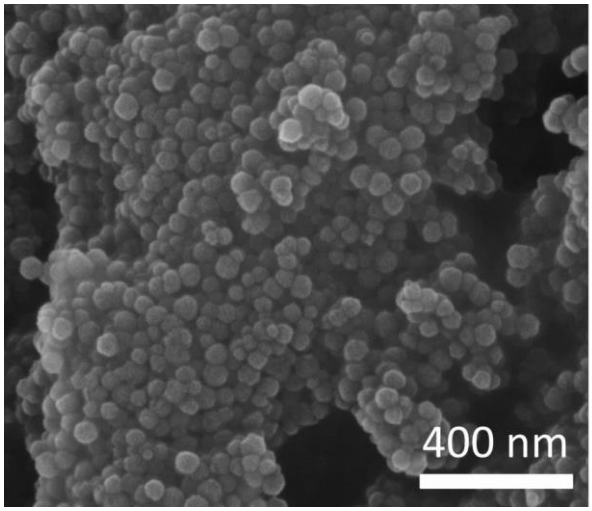

Figure S2. SEM image of the ZIF-8 nanoparticles. This ZIF with a particle size of ca. 30 nm is used as filler in TFN membranes.

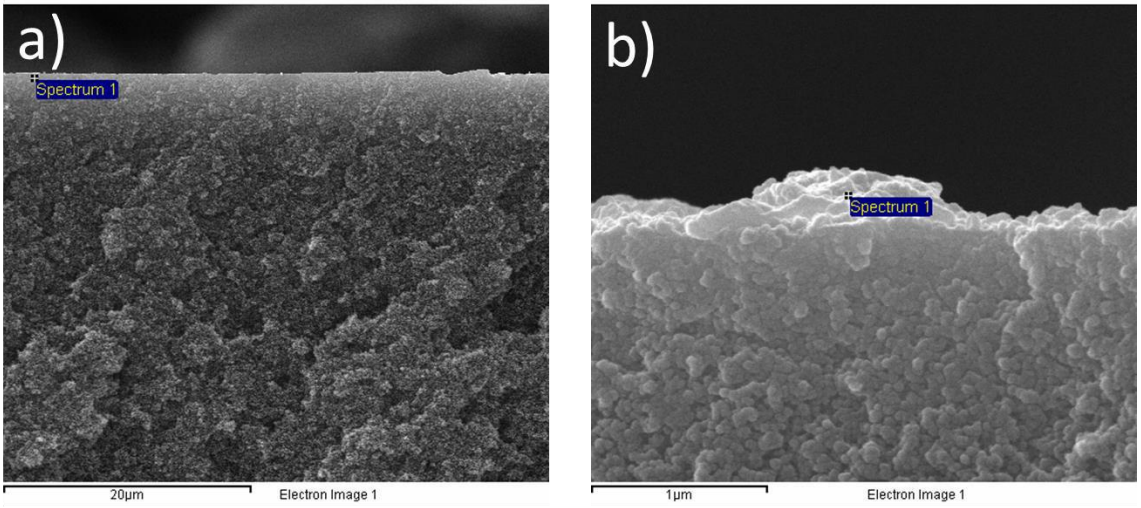

Element	Weight%	Atomic%
C K	69.67	76.11
O K	28.74	23.57
Zn L	1.60	0.32

Element	Weight%	Atomic%
C K	65.83	73.17
O K	31.50	26.28
Zn L	2.67	0.55

Figure S3. A,B) SEM image of the cross section of membranes containing 0.2 (a) and 0.8 %(w/v) (b) of ZIF-8 and the results of the EDX analysis in weight and atomic percentage displayed in the annexed tables.

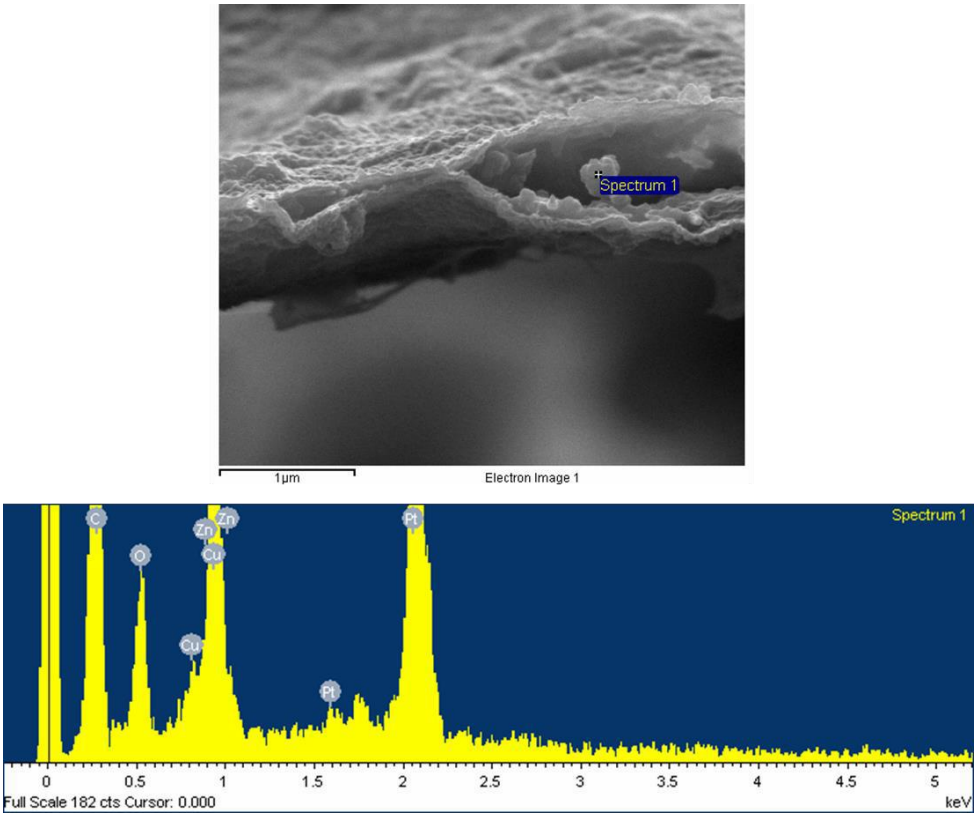

Figure S4. SEM image of the PA layer of a TFN membrane with 0.4 % (w/v) of ZIF-8 after being removed from the P84® support. The ZIF-8 nanoparticles can be found between two sublayers of PA and they are identified by EDX analysis. The Zn signal corresponds to the ZIF-8; that of Pt, to the coating; the Cu peak, to the TEM grid and C and O to the PA.

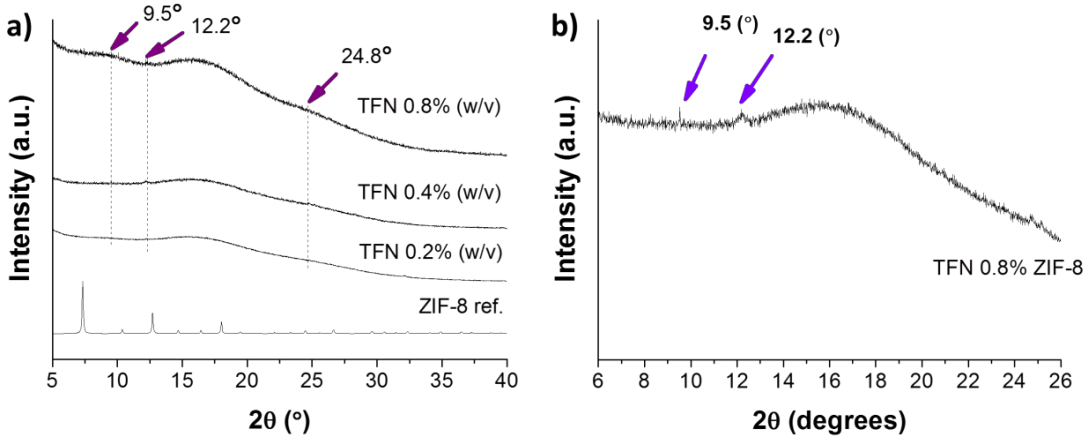

Figure S5. a) XRD diffraction patterns of TFN membranes with ZIF-8 loadings of 0.2, 0.4 and 0.8 % (w/v) and ZIF-8 powder as reference. b) Diffraction of the 0.8 % (w/v) TFN membrane in grazing incident mode. The signals detected in the membranes are pointed with arrows together with the corresponding numerical values.

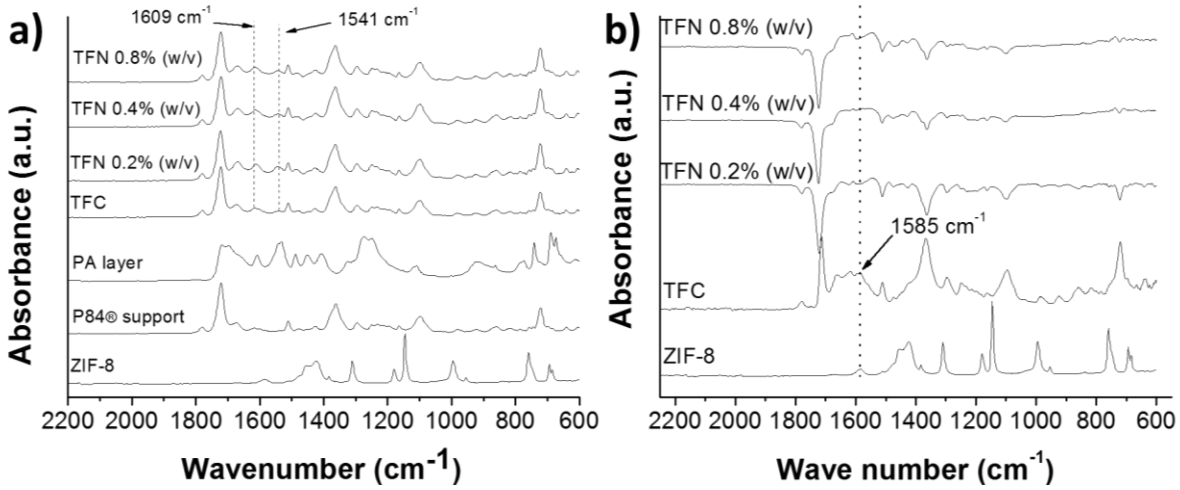

Figure S6. A) FTIR spectra of TFN membranes with ZIF-8 loadings from 0.2 to 0.8 % (w/v) and PA layer, P84® support and ZIF-8 powder as reference. B) Spectra of the TFN membranes after subtraction of that of the TFC membrane. The signals detected are pointed with arrows together with the corresponding numerical values.

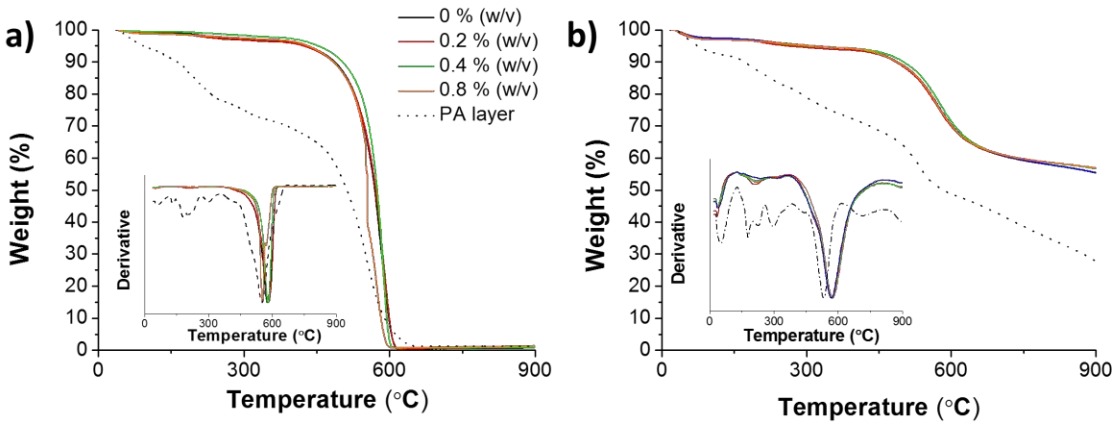

Figure S7. TGA curves and derivatives of TFN membranes and PA layer. A) TGA analyses in air atmosphere. B) TGA analyses in N_2 atmosphere. The black continues line refers to the TFC membrane; the red continues line, to the 0.2 % (w/v) loaded TFN membrane; the green continues line, to the 0.4 % (w/v) loaded TFN membrane; the orange continues line, to the 0.8 % (w/v) loaded TFN membrane and the dash black line, to the PA layer. Insets correspond to the corresponding derivatives.

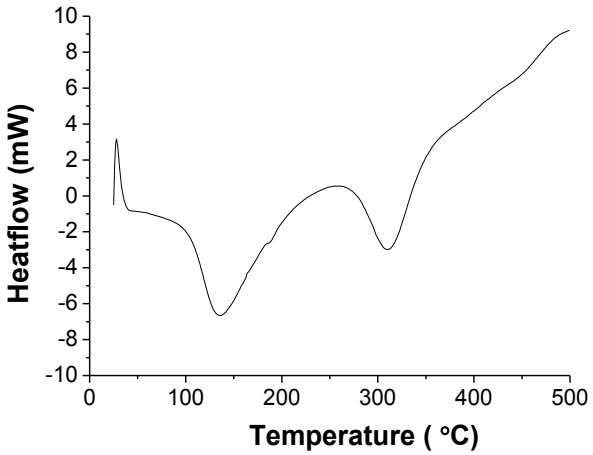

Figure S8. DSC analysis of the PA layer. The analysis was performed in N_2 atmosphere using a heating rate

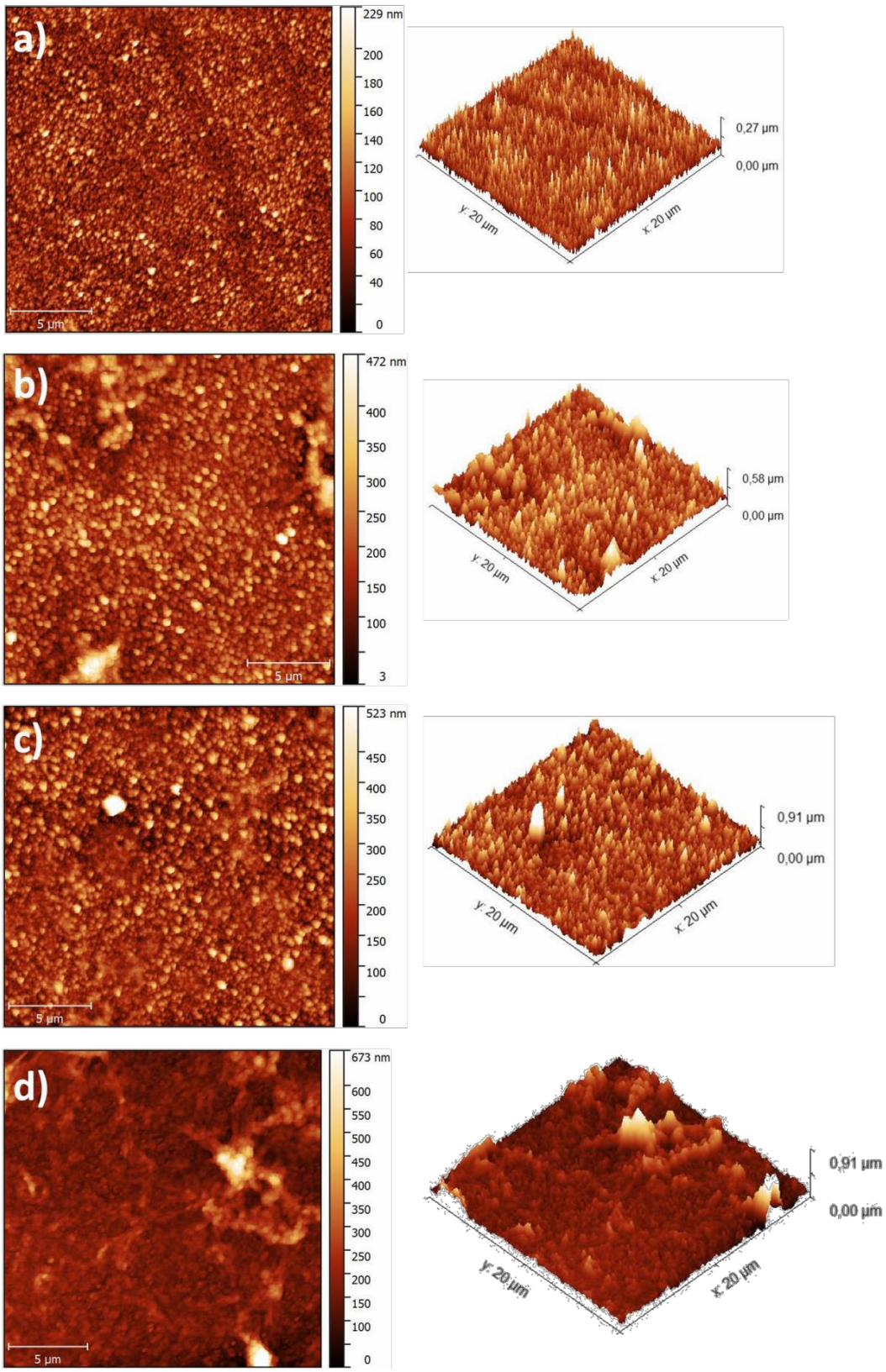

Figure S9. AFM characterization of TFN membranes showing a mapping of the membrane surface roughness of TFC (a), and TFN membranes containing 0.2 (b), 0.4 (c) and 0.8 %(w/v) (d) of ZIF-8. Dark colors stand for low roughness values and bright colors for high roughness values. The dimensions in µm of the surfaces studied are shown at the right.

Table S1. Gas separation performance of TFC and TFN membranes at several operating temperatures. The table shows the H_2 and CO_2 permeances in GPU and the H_2/CO_2 selectivity of the TFN test at 35, 180 and 250 ^{0} C. Average and standard deviation values for the different ZIF-8 loadings are provided.

ZIF-8 loading %(w/v)	**Temperature**	**Feed pressure (bar)**	**H_2 permeance (GPU)**	**CO_2 permeance (GPU)**	**H_2/CO_2 selectivity (-)**
0.0	**35**	3	99.7±7.4	26.2±0.1	3.8±0.3
0.2		3	94.5	21.7	4.4
0.4		3	27.3±4.5	3.1±0.1	9.0±1.4
0.0	**180**	3	576±4	74.3±12.0	7.9±1.2
0.2		3	561±51	61.3±7.9	9.2±0.3
0.4		3	338±32	23.2±1.1	14.6±0.7
		5	317	25.1	12.6
		6	334	24.1	13.9
		6*	328	18.1	18.1
		3**	313	20.2	15.5
		6**	418	27.2	15.4
0.8		3	468±21	72.7±15.7	7.2±0.9
0.0	**250**	3	988	117	8.4
0.2		3	783	68.3	11.5
0.4		3	635±71	47.3±4.8	13.4±0.1

* Without transmembrane pressure

** Without sweep gas

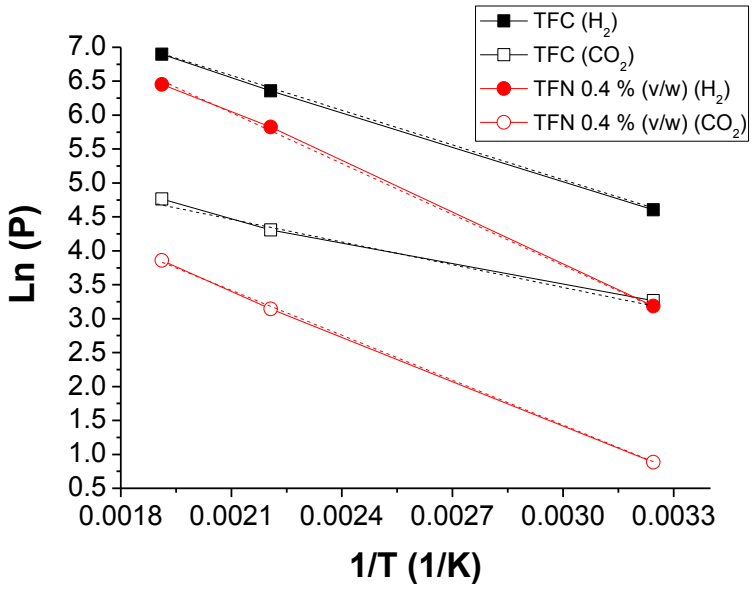

Figure S10. Arrhenius plots for the calculation of the activation energies. The logarithm of the H_2 (full symbols) and CO_2 permance (empty symbols) is represented as function of the inverse of the temperature for TFC (black) and 0.4 % (w/v) TFN membranes (red).

Table S2. Activation energies of TFC and 0.4 % (w/v) TFN membranes. The fitting equation and numerical value of the activation energy have been calculated from the H_2 and CO_2 permeances of the TFN membranes with 0.0 and 0.4 % (w/v) loading.

ZIF-8 loading % **(w/v)**	**Fitting equation** **H_2**	**Fitting equation** **CO_2**	**Ea (H_2)** **(kJ mol^{-1})**	**Ea (CO_2)** **(kJ mol^{-1})**
0.0	y = -1711.7x + 10.153 R^2 = 0.9998	y = -1091x + 6.79 R^2 = 0.9923	14.2	9.1
0.4	y = -2475.6x + 11.23 R^2 = 0.9991	y = -2215.3x + 8.0656 R^2 = 0.9996	20.6	18.4

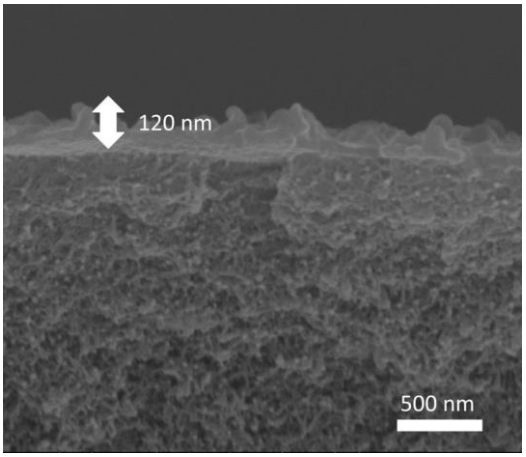

Figure S11. SEM image of the cross section of a TFN membrane 0.4 % (w/v) of ZIF-8 coated with PDMS. The white arrow indicates the thickness of the PDMS layer.

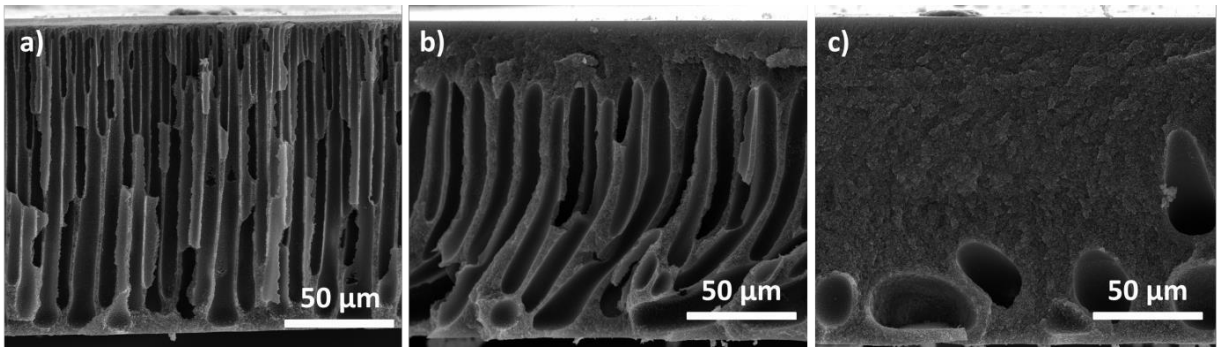

Figure S12. SEM image of the cross section of P84® supports prepared with different dope compositions in DMAc: 15 (a), 23 (b) and 28 wt% (c).

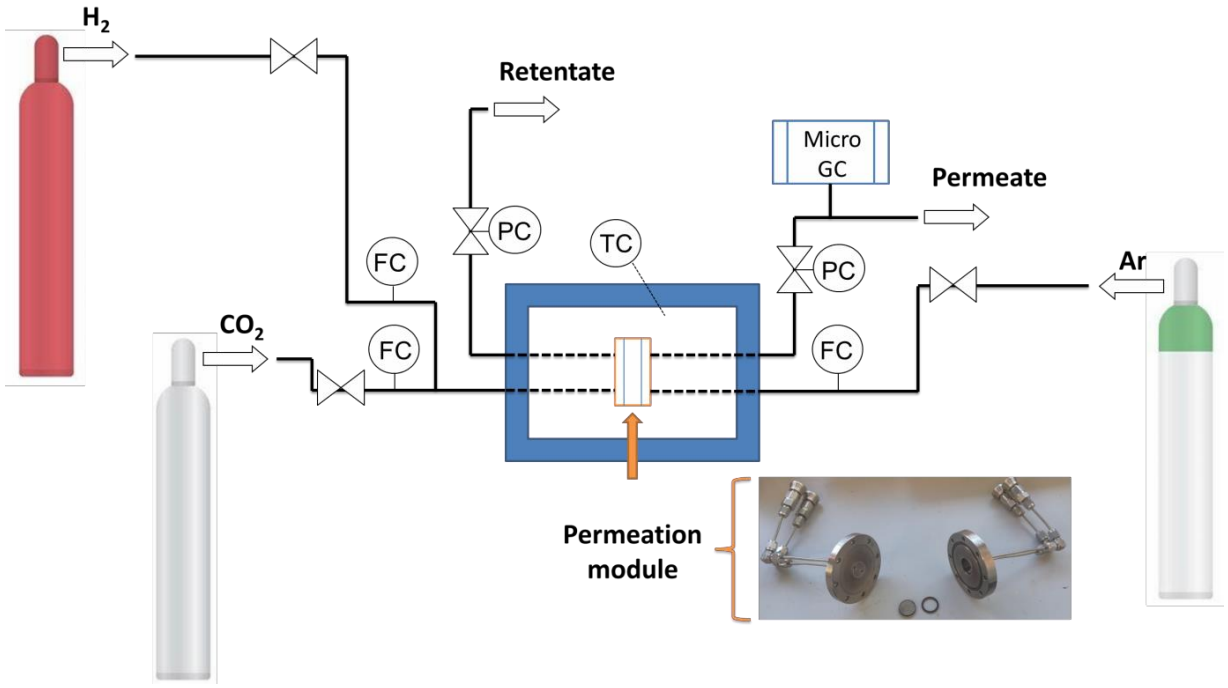

Figure S13. Scheme of the gas separation setup. FC, PC and TC stand for flow, pressure and temperature controllers, respectively.

Chapter 12: Polymer-Stabilized Percolation Membranes based on nano-sized zeolitic imidazolate frameworks for H_2/CO_2 Separation

J Sánchez-Laínez, S Friebe, B Zornoza, A Mundstock, I Strauß, C Téllez, J. Coronas. ChemNanoMat, 4 (2018), 698-703. DOI: 10.1002/cnma.201800126. Permission conveyed through Copyright Clearance Center, Inc.

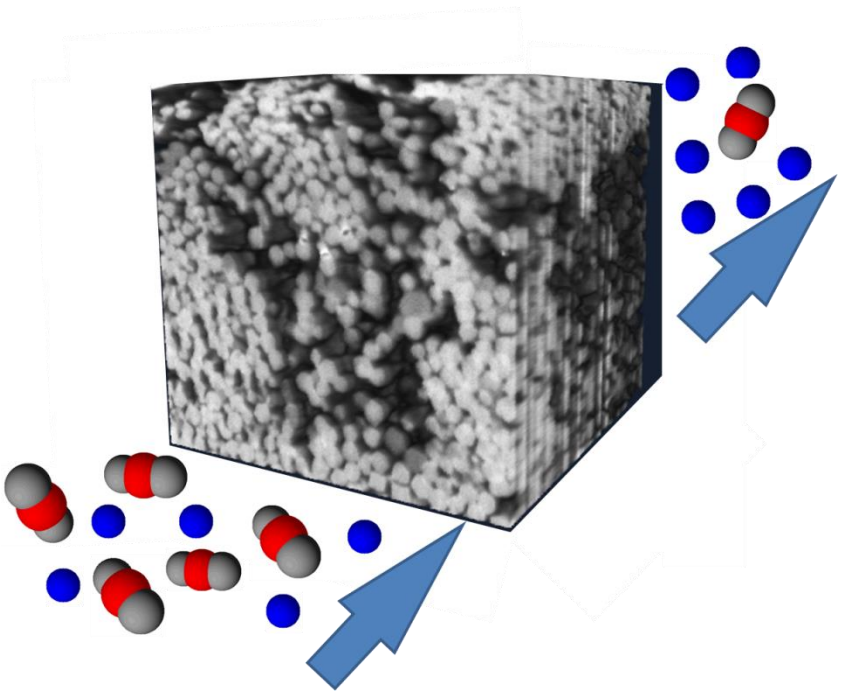

Category:

- Type of membrane: PSPMs
- Gas separation: pre-combustion CO_2 capture

ACES Asian Chemical Editorial Society

DOI: 10.1002/cnma.201800126

CHEMNANOMAT
Full Paper

Gas-Separation Membranes

Polymer-Stabilized Percolation Membranes Based on Nanosized Zeolitic Imidazolate Frameworks for H_2/CO_2 Separation

Javier Sánchez-Laínez[+],[a, b] Sebastian Friebe[+],*[a] Beatriz Zornoza,*[b] Alexander Mundstock,[a] Ina Strauß,[a] Carlos Téllez,[b] Jürgen Caro,[a] and Joaquín Coronas[b]

Abstract: This work shows the preparation of self-supported composite membranes prepared with the nano-sized zeolitic imidazolate frameworks (ZIFs): ZIF-8, ZIF-7(III) and ZIF-7/8 core-shells. The membranes consist of compressed pellets of ZIF nanoparticles (up to 74 wt% loading) stabilized with gas-impermeable epoxy resin, providing a gas transport-selective percolation network named polymer-stabilized percolation membrane (PSPM). The different PSPMs have been characterized by SEM, TGA, XRD, FTIR and Raman. FIB/SEM has provided a 3D reconstruction of the composite thanks to the slice and view technique, allowing a perfect visualization of the inside of the network. The N_2 adsorption properties have also been studied and compared with those of ZIFs in powder state. The gas separation performance of these membranes has been tested for the H_2/CO_2 mixture. The PSPMs were tested with feed pressures up to 5 bar, obtaining H_2 permeabilities of hundreds of Barrer and a maximum H_2/CO_2 selectivity of 12.3.

Introduction

Within the family of metal-organic frameworks (MOFs), the group of zeolitic imidazolate frameworks or ZIFs, discovered independently by Yaghi's[1] and Chen's[2] groups, can be highlighted. They form porous frameworks with high thermal and chemical stabilities, thank to which they have a great number of potential applications, such as gas sorption and separation,[3] drug delivery[4] and catalysis.[5] ZIFs consist of 3D networks where Zn or Co cations in tetrahedral coordination are connected to organic linkers based on imidazole groups, building metal–imidazole–metal angles close to 145°, which are coincident with the Si–O–Si angles typically found in zeolites.

The narrow microporosity and relative high chemical stability of ZIFs make them suitable for the H_2 separation, a gas which is usually produced *via* the steam reforming of methane together with high amounts of CO_2. ZIF-7 and ZIF-8 are two interesting frameworks for this gas separation. Both share the **sod** topology based on Zn(II) centers, but they contain different ligands in their structure: 2-methylimidazole (mIm) for ZIF-8 and benzimidazole (bIm) for ZIF-7. These ZIFs show relatively similar pore apertures of 0.30 (ZIF-7) and 0.34 nm (ZIF-8), close to the kinetic diameter of H_2 (0.29 nm). The combination of both ZIFs in a hybrid structure has also shown a positive influence in the gas separation performance. Very recently we published the synthesis of ZIF-7/8 core-shell particles that showed as Mixed Matrix Membrane (MMM) good results in the separation of H_2/CO_2 mixtures.[6] ZIF-7 also presents a denser phase called ZIF-7(III) obtained in a post-synthesis treatment by soaking a polar guest molecule like water or methanol into the activated ZIF-7. It is a laminar shaped material with an estimated pore aperture of 0.21 nm that once exfoliated has shown a high performance for the H_2/CO_2 membrane separation.[7]

Fabricating neat supported MOF films as membranes is possible if the frameworks are allowed to crystallize on ceramic, metallic or polymeric supports, either flat or tubular. There are different techniques that allow the formation of continuous MOF layers such as: layer by layer deposition, reactive seeding, spraying, micro-wave assisted synthesis and contradiffusion.[8] Regarding the ZIF family, supported membranes of ZIF-7,[9] ZIF-8,[10] ZIF-22[11] ZIF-69[12] and ZIF-90[13] can be found in the literature. Li et al.[14] prepared continuous membranes of ZIF-7 on Al_2O_3 supports that showed good results for the H_2/CO_2 separation at 220 °C. The membrane reached a H_2 permeance of 4.5×10^{-8} mol m^{-2} s^{-1} Pa^{-1} and a H_2/CO_2 selectivity of 13.6. Moreover, ZIF-9(III) (same ligand, bIm, like ZIF-7 but with Co instead of Zn) membranes on Ni hollow fiber supports gave rise at −10 °C to H_2/CO_2 selectivity of 22.2 and a H_2 permeance of 3.4×10^{-7} mol m^{-2} s^{-1} Pa^{-1}.[15] In the membranes prepared with ZIF-90 by Huang et al.[13] 3-aminopropyltriethoxysilane (APTES) was used as covalent bonding between the ZIF and the Al_2O_3 support. This allowed an enhancement in the selectivity of the membranes, especially for the H_2/CO_2 mixture, whose selectivity

[a] J. Sánchez-Laínez,[+] Dr. S. Friebe,[+] A. Mundstock, I. Strauß, Prof. Dr. J. Caro
Institut für Physikalische Chemie une Elektrochemie, Leibniz Universität, 30167, Hannover (Germany)
E-mail: sebastian.friebe@pci.uni-hannover.de
[b] J. Sánchez-Laínez,[+] Dr. B. Zornoza, Prof. Dr. C. Téllez, Prof. Dr. J. Coronas
Department of Chemical and Environmental Engineering and Instituto de Nanociencia de Aragón (INA), Universidad de Zaragoza, 50018 Zaragoza (Spain)
E-mail: bzornoza@unizar.es
[+] These two authors contributed equally to this work

Supporting information for this article is available on the WWW under https://doi.org/10.1002/cnma.201800126

was three-fold higher in comparison with their previous results, reaching values of 21, with a H_2 permeance of 3.0 10^{-7} mol m^{-2} s^{-1} Pa^{-1}.

Although the preparation of pure supported MOF films as membranes is quite widespread, this kind of membranes are sometimes difficult to reproduce, usually brittle and are not able to withstand high operating pressure.[16] Owing to this, their embedding in a polymeric phase building MMMs is usually preferred. However, an alternative to supported membranes and MMMs are the so-called *Polymer-Stabilized Percolation Membranes (PSPMs)*.[17] These membranes consist of a percolation network of a nanoporous component (zeolite or MOF) obtained by pressing a powder, followed by the infiltration of the intercrystalline space by a gas-impermeable polymer to force gas transport exclusively through the percolation network of the embedded nanoporous material. In previous work, MOFs such as MIL-140A and ZIF-8 were employed, obtaining performances of 9×10^{-10} mol m^{-2} s^{-1} Pa^{-1} of H_2 and a H_2/CO_2 selectivity of 8.2 for ZIF-8 and 2×10^{-8} mol m^{-2} s^{-1} Pa^{-1} of H_2 and a H_2/CO_2 selectivity of 8.0 for MIL 140-A. However, only frameworks with a micrometric particle size have been tested so far for the preparation of these kinds of composites. There are mainly two advantages for using nano-seized particles in PSPMs: (i) a higher mechanical stability because of the increased MOF-epoxy resin contact area, and (ii) an increased particle-particle contact area which rises the flux through the percolation network.

The present work shows the preparation of PSPMs with several ZIF nanoparticles. Microscopy techniques allowed a good characterization of the composites, building a 3D reconstruction of the membranes, thanks to which the percolation path of the filler was visible. Further characterization such as FTIR and Raman spectroscopy, gas adsorption and thermogravimetric analysis was also performed. The PSPMs have been tested for the H_2/CO_2 separation at pressures up to 5 bar, proving the good mechanical stability and gas separation performance of these composites with such a high ZIF loading (ca. 90 wt% as maximum).

The main novelty of this work lies in the use of i) MOFs such as ZIF-7(III) and the ZIF-7/8 core-shell that have shown good results for the H_2/CO_2 separation in MMMs, ii) nanoparticles, iii) a new reconstructing characterization technique that allows a perfect visualization of the composites in 3D helping to understand their internal architecture.

Results and Discussion

Membrane Characterization

Figure 1 shows the SEM images of the cross-sections of PSPMs containing ZIF-8, ZIF-7/8 core-shells and ZIF-7(III). It can be seen how the epoxy resin (dark zones) is located in the intercrystalline spaces formed by the compressed nanoparticles (brighter contrast). ZIF-8 and the ZIF-7/8 core-shell particles are spherical with average sizes of 150 and 120 nm, respectively. Conversely, ZIF-7(III) forms laminar shaped particles with a thickness of 500 nm (see Figure S1). To visualize the percolation path, focused ion beam (FIB) analysis was performed on the ZIF-7/8 core-shell PSPM sample, obtaining a 3D reconstruction of a volume of 3 μm × 3 μm × 1.5 μm (see Figure 2). A video of the reconstruction is also provided (see Additional Materials), in which the existence of hollow spaces, where the epoxy resin was not able to percolate, became visible. The infiltration depth of the epoxy in these composites is estimated to be around 100 μm.

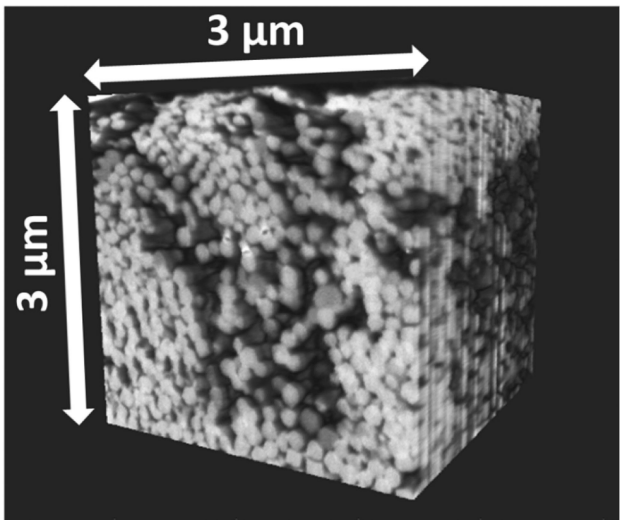

Figure 2. 3D reconstruction of the ZIF-7/8 core-shell PSPM from SEM-FIB images.

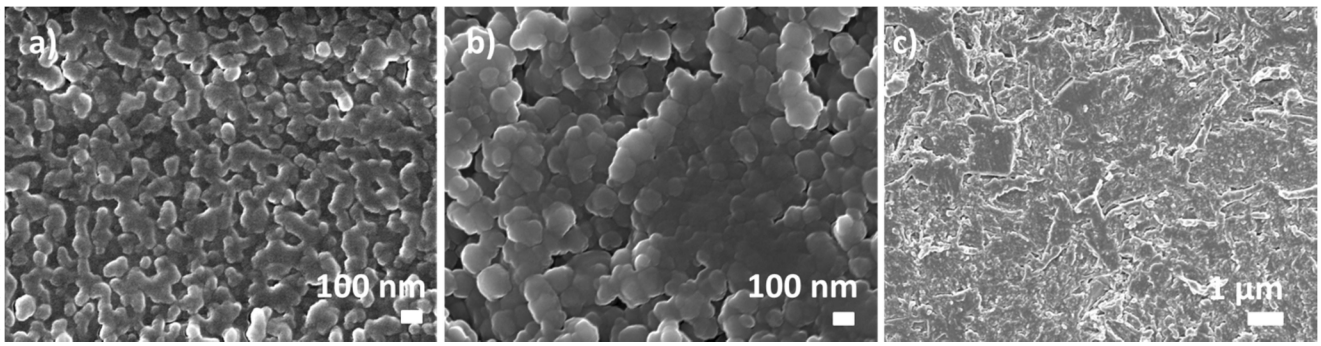

Figure 1. SEM images of the cross section of PSPMs with ZIF-8 (a), ZIF-7/8 core-shell (b) and ZIF-7(III) (c).

XRD analysis shown in Figure 3 proved that the ZIFs used for the PSPM fabrication remained crystalline after the membrane formation by pressing, as well as after the subsequent mechanical (polishing) and the extension to chemical stress (epoxy resin, water),[17] which is crucial for a high separation capability. The principal *hkl* planes of ZIF-8 and ZIF-7(III) can be seen in the PSPM diffraction patterns. ZIF-7 and ZIF-8 share the **sod** type structure, thus their corresponding XRD patterns and that of the core-shell are identical. ZIF-7/8 core-shell PSPM shows additionally a big amount of epoxy resin, visible as a wide band that rises between $2\theta = 12–23^{\circ}$. The compression pressure used for the pellet formation was 100 bar, far below the 1.5 GPa reported in the literature to modify the structure of ZIF-8.[18]

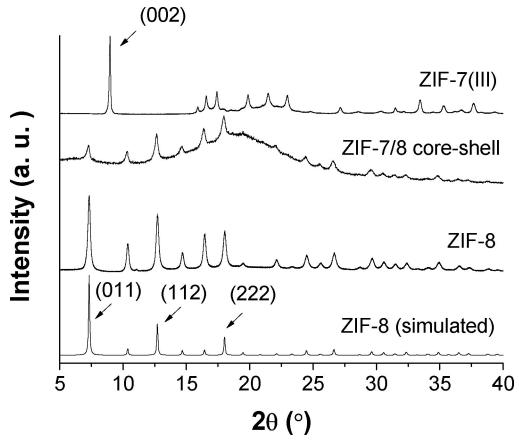

Figure 3. XRD patterns of the PSPMs containing ZIF-8, ZIF-7/8 core-shell and ZIF-7(III) and simulated ZIF-8 for comparison.

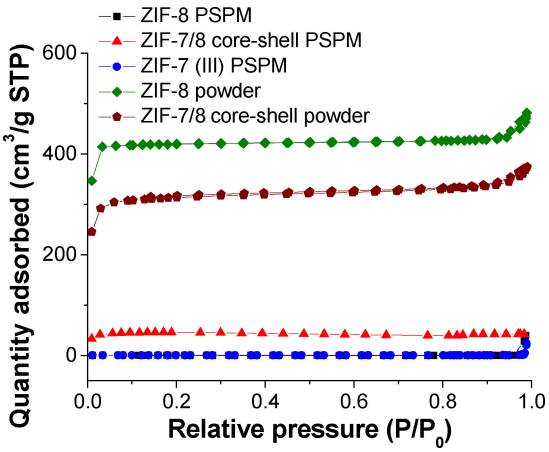

Figure 4. N_2 adsorption isotherms (77 K) of ZIF-8 PSPM, core-shell PSPM, ZIF-7 (III) PSPM and ZIF-8 and core-shell powders. Note that black and blue isotherms are overlapped.

The N_2 adsorption capacity of the PSPMs was tested and compared to that of the corresponding ZIFs as powder (see Figure 4). ZIF-7 (III) does not adsorb N_2 because of its pore size,[19] therefore its isotherm is not shown. Regarding the powder samples, ZIF-7/8 core-shell shows a N_2 uptake of 374 cm^3 (STP)/g at $P/P_0 = 1$, which is about one fourth smaller than that of ZIF-8. The same occurs with the BET specific surface area, which with a value of 1050 ± 19 m^2/g, is 20% smaller for the core-shell in comparison with ZIF-8. The inclusion of bIm in the ZIF-8 framework structure reduced the maximum quantity adsorbed in comparison to the original ZIF-8, due to the narrower pore windows of the core-shell ZIF-7/8.[6] The N_2 adsorption of all the PSPMs and their BET specific surface areas are almost negligible. The use of an impermeable epoxy resin caused a partial reduction in the gas access, hindering the entrance of N_2 molecules inside the composite membrane. Moreover, the core-shell PSPM adsorption isotherm shows a great increase at $P/P_0 = 0.85$ that may be related to interparticle adsorption as described for Figure 2. Due to the microporous character of the three ZIF fillers, the lack of N_2 adsorption should make the membranes ideal for the separation of small fast permeating molecules, such as hydrogen.

The IR as well as the Raman spectra in Figure 5 show the presence of both linker molecules within the core-shell material, that is, methylimidazolate and benzimidazolate. The spectra of the core-shell material can be understood as the sum of the two individual spectra (those corresponding to ZIF-8 & ZIF-7). Consequently, the IR and Raman spectroscopy results prove the

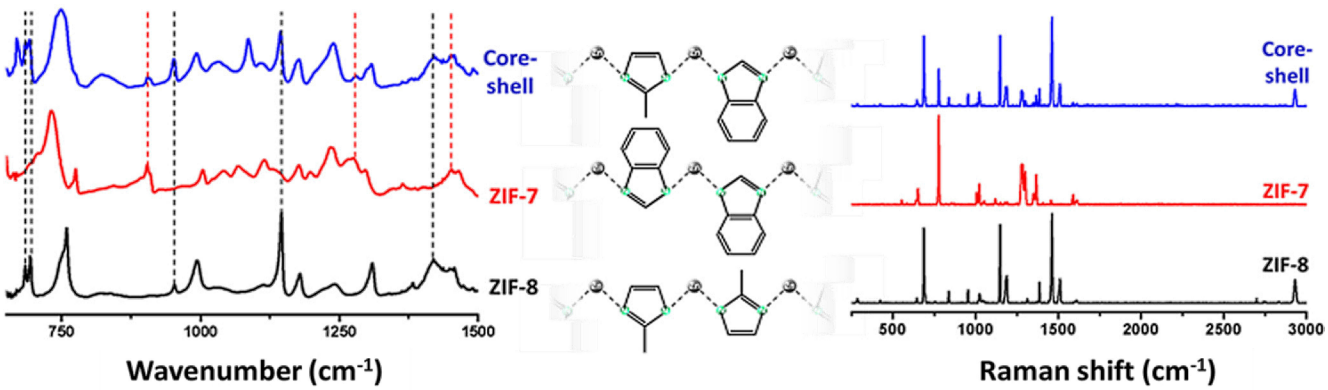

Figure 5. IR (left) and Raman spectra (right) for the different PSPMs (ZIF-8, ZIF-7, core-shell). The inset in the middle shows the linker composition within the materials.

successful formation of the ZIF-7/8 core-shell by linker exchange and the simultaneous existence of both ligands in the same ZIF particles.

The TG data for the three investigated materials in Figure 6 and S2 display that all PSPMs exhibit a similar stability towards

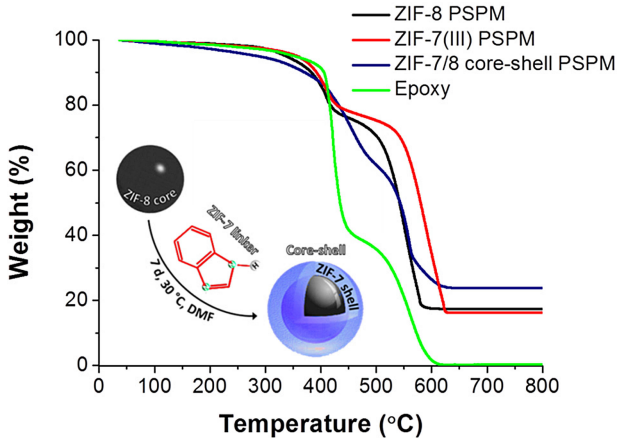

Figure 6. Thermogravimetric analysis results for the different PSPMs (ZIF-8, ZIF-7, core-shell) under study including a schematic representation of the core-shell formation. Analysis of the epoxy resin is also included for comparison.

higher temperature. Nonetheless, small differences can be observed at a temperature interval between 200–500 °C. The latter can be attributed to the removal of guest molecules (solvent, gases, etc.). The decomposition temperature is quite the same for all materials under study (ZIF-8: 621.7 °C, ZIF-7: 620.9 °C, core-shell: 621.1 °C), which was expected due to the very similar structure and composition. The pure epoxy resin, however, shows a lower onset temperature (around 400 °C) due to its full organic nature. The amount of ZIF in the composites was around 55 wt% for ZIF-8 and ZIF-7 (III) PSPM and of 74 wt% for the core-shell PSPM. These amounts were calculated from the residue of ZnO after the TG analysis (see Table S1). The concentration of nano-sized ZIFs is smaller than that in previous PSPMs prepared with micro-sized particles (~90 wt%).[17] This means that nanoparticles do not allow such densification by pressing like microparticles and, in any event, that the quality of the infiltration is better for the smallest particles. Nevertheless, their gas separation performance is excellent and the problem could be solved by applying a broad particle size distribution with nm-sized particles as "gap-filler" between the mico-sized.

Gas Separation Performance

The different PSPMs were tested in the gas separation performance of binary H_2/CO_2 mixtures at 35 °C and feed pressures of 3 and 5 bar (see Figure 7a and Table S2). The membranes were activated at 150 °C under vacuum for 3 h to remove any remaining humidity from the previous polishing step. ZIF-8 PSPM was the most permeable membrane, showing a H_2

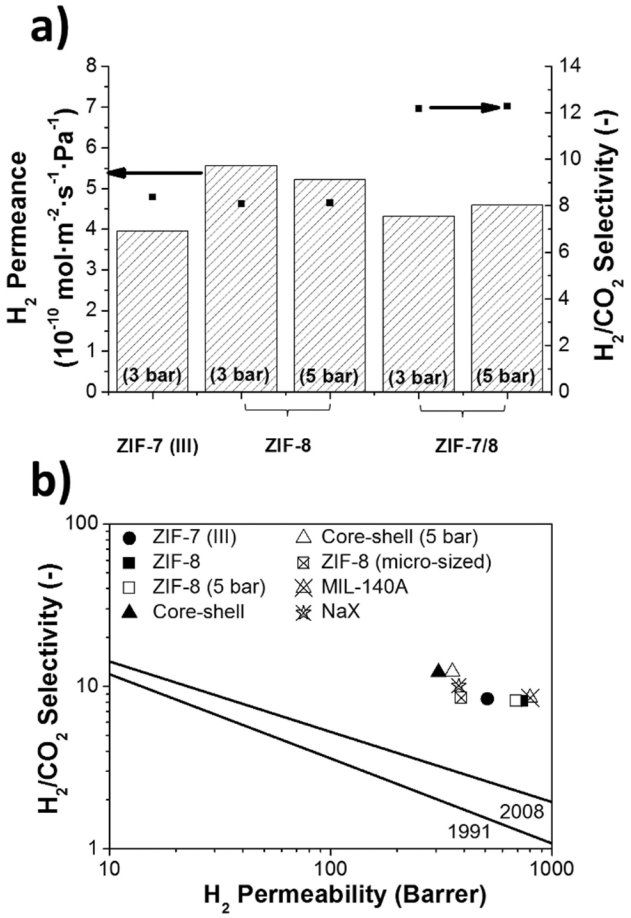

Figure 7. Gas separation performance of the different PSPMs. a) Histogram of the three membranes with H_2 permeances in mol m^{-2} s^{-1} Pa^{-1} and b) Robeson plot with the H_2 permeability in Barrer, including bibliographical data of previous PSPMs containing micro-sized ZIF-8, MIL-140A and the zeolite NaX.[17]

permeance superior to 5×10^{-10} mol m^{-2} s^{-1} Pa^{-1} at 3 and 5 bar. This result is consistent with that obtained in a previous publication with micro-sized ZIF-8 (9×10^{-10} mol m^{-2} s^{-1} Pa^{-1} of H_2 and a H_2/CO_2 selectivity of 8.2).[17] The ZIF-7/8 core-shell PSPM gave the best separation performance with a H_2 permeance of 4.6×10^{-10} mol m^{-2} s^{-1} Pa^{-1} and a H_2/CO_2 selectivity of 12.3 at 5 bar. This means that the H_2 permeance of both membranes is similar but the selectivity was around 33% higher in case of the ZIF-7/8 core-shell PSPM. This result agrees with the narrower microporosity of the core-shells provided by the linker exchange of bulkier bIm for mIm.[6] Finally, ZIF-7(III) PSPM showed a H_2/CO_2 selectivity of 8.4, slightly superior to that of ZIF-8 PSPM (8.1), but the lowest H_2 permeance (4.0×10^{-10} mol m^{-2} s^{-1} Pa^{-1}) due to the denser nature of its structure. Besides, all membranes showed similar permselectivity values at different feed pressures, proving the mechanical stability of these composites. Noteworthy, since the neat epoxy resin is impermeable for all gases under study, the separation performance of the PSPMs is solely a result of the filler material used and the quality of the percolation network formed.[17] The membrane thickness was calculated for each membrane according to the infiltration depth of the epoxy resin and it was

considered to allow plotting the H_2 permeability results in Barrer in a Robeson type graph (see Table S2). Figure 7b clearly shows that the gas separation performance of all PSPMs surpasses the Robeson upper-bound. The maximum H_2 permeability was obtained for the ZIF-8 PSPM with a value of 765 Barrer. It can also be seen in Figure 7b that the H_2 permeability is similar for the PSPMs in this work to those with ZIF-8 Basolite®, MIL-140A and the NaX, prepared in a previous related work.[17] Besides, the H_2/CO_2 selectivity obtained in this work is the highest, with a value of 12.3. PSPMs could be applied as disc membrane in gas separation, being able to predict the separation performance of supported thin-layer membranes. So far, these predictions have been made mainly "in silico", using the concept *permeability = solubility × diffusivity.*[20]

Conclusions

Polymer-stabilized percolation membranes (PSPMs) have been prepared with nanoparticles of ZIF-8, ZIF-7(III) and ZIF-7/8 core-shell. SEM microscopy gave insight into the cross-section of these composites and SEM-FIB allowed the reconstruction of a tridimensional volume of a membrane piece. Both techniques showed the percolation path through the MOF nanoparticles and the voids filled by the epoxy. FTIR and Raman spectroscopies helped to understand the chemical nature of the membranes, which have a high thermal stability according to TG analysis. XRD characterization also showed that the ZIF nanoparticles remained crystalline after the membrane preparation. The N_2 adsorption of all PSPMs was very low because of the effect of the epoxy resin, which hinders the entrance of the gas molecules into the pores of the ZIFs but not their separation ability for H_2/CO_2 mixtures. The PSPMs showed a high performance with an optimum result of 355 Barrer of H_2 and H_2/CO_2 selectivity of 12.3 for the PSPM containing ZIF-7/8 core-shell nanoparticles as filler. Finally, if cut in thin slices, our PSPMs could become mechanically stable self-supported membranes in disk geometry with high fluxes. Another advantage of PSPMs is their function as model system to predict the separation selectivity of supported thin-layer membranes.

Experimental Section

ZIFs Synthesis

ZIF-8 was synthesized according to the following procedure based on the literature.[21] 470 mg of Zinc nitrate hexahydrate ($Zn(NO_3)_2 \cdot 6H_2O$, Sigma Aldrich) was dissolved in 10 mL of methanol (MeOH, HPLC grade, Scharlau) and 10 mL of DI water. Besides, 1.0 g of 2-methylimidazole (mIm, $C_4H_6N_2$, >99%, Sigma Aldrich) was dissolved in 10 mL of MeOH, and the two solutions were mixed and stirred for 2 h. The final product was collected by centrifugation, washed once with MeOH, and dried at 110 °C overnight.

The ZIF-7/8 core-shells were prepared by post-synthetic modification of ZIF-8.[6] An initial amount of benzimidazole (bIm, $C_7H_6N_2$, 98%, Sigma Aldrich) was added to N,N-Dimethylformamide (DMF, synthesis grade, Scharlau) at 30 °C to obtain a concentration of 6.5 g/L. When dissolved, ZIF-8 was added to the solution (3.3 g/L); which was stirred for 7 days. The solid was collected at the corresponding reaction time by centrifugation, washed 3 times with MeOH, and dried later at 110 °C overnight.

ZIF-7(III) was obtained *via* micro-wave assisted synthesis. 0.22 g of $Zn(NO_3)_2 \cdot 6H_2O$ and 1.31 g of bIm were dissolved in 30 mL of N,N-Dimethylacetamide (DMAc, ≥99.5%, Sigma Aldrich). The solution was placed in a microwave oven at 150 °C for 30 min. After that, the solid was collected by centrifugation, washed 3 times with MeOH and dried at 110 °C overnight.

PSPM Preparation

PSPM composites were prepared following the procedure described in.[17] 400 mg of ZIF powder was pressed into disk-like pellets with 18 mm diameter and 2 mm height. Afterwards, they were coated with an epoxy resin (EPO-TEK 353ND) and transferred to a vacuum oven. Under vacuum (100 mbar) and at medium temperature (40–60 °C), the epoxy resin became more fluidic and infiltrated by gravity into the inter-crystalline space. Finally, the epoxy was hardened at 150 °C and the excess of it on the two sides was removed by polishing, thereby opening the percolation paths for molecules permeating through the pellet.

Characterization of Samples

Scanning electron microscopy (SEM) studies of the membrane cross-sections were performed with a field-emission SEM (JEOLJSM-6700F) at 2 or 5 kV and 3 mm working distance. Before the measurements, the cross-sections were polished with diamond lapping films. After that the polished samples were coated with a thin carbon film (Leica, EM SCD500) *via* evaporation to minimize surface charge effects. Focussed Ion Beam (FIB) characterization was performed with the dual beam Helios 650 after coating the samples with thin carbon and silver films. Ga atoms were used for etching slices every 25 nm to obtain a 3D reconstruction of the composite. XRD studies were carried out using a Bruker D8 Advance Diffractometer with Cu–Kα-radiation in a range between 5–40°. FTIR spectra were recorded on a Cary 630 (Agilent Technologies) spectrometer within the range of 650–4000 cm^{-1}. Each sample was scanned 15 times with a resolution of 4 cm^{-1} and averaged to obtain the final spectrum. Raman spectroscopy was performed using a Bruker Senterra spectrometer within the range of 200–3750 cm^{-1} with a laser excitation of 532 nm at 5 mW. The integration time was set to 10 s with a total sum of 1000 additions. Nitrogen adsorption/desorption isotherms were obtained using a Micromeritics Tristar 3000 surface area and porosity analyzer, after previously degassing the samples at 150 °C for 8 h under vacuum.

Gas Permeation Tests

The gas separation properties were evaluated by mixed gas separation tests of an equimolar mixture of hydrogen (25 mL(STP)/min) and carbon dioxide (25 mL(STP)/min) as feed gas. The permeate side was swept with nitrogen (1 mL(STP)/min). The membranes were sealed in the permeation cell with Viton O-rings (FKM 70 Vi 370). The neat MOF layers were tested at 35 °C and 3-5 bar. Gas chromatography (Agilent Technologies 7890B) was applied to investigate the permeated mixture. Permeance was calculated in GPU (10^{-6} cm^3(STP)/(cm^2 s cmHg)) once the steady-state of the exit stream was reached, and the separation selectivity was calculated as the ratio of permeances. Permeability was calculated in Barrer (10^{-10} cm^3(STP)·cm/(cm^2 s cmHg)) once the thickness of the membrane was estimated.

Acknowledgements

The research leading to these results has received funding from the European Union Seventh Framework Programme (FP7/2007-2013) under grant agreement n° 608490, project M4CO2. Financial support from the Spanish MINECO and FEDER (MAT2016-77290-R), the Aragón Government (T05) and the ESF is gratefully acknowledged. J. S-L. thanks Spanish Education Ministry Program FPU2014 his PhD grant. Part of the microscopy work was done in the Laboratorio de Microscopías Avanzadas at the Instituto de Nanociencia de Aragón (LMA-INA). F. Steinbach is acknowledged for technical assistance regarding the SEM.

Conflict of Interest

The authors declare no conflict of interest.

Keywords: Zeolitic imidazolate frameworks · nanoparticles · membranes · H_2/CO_2 separation · polymer-stabilized percolation membrane

[1] K. S. Park, Z. N. Ni, A. P. Côte, J. Y. Choi, R. Huang, F. J. Uribe-Romo, H. K. Chae, M. O'Keeffe, O. M. Yaghi, *PNAS* **2006**, *103*, 10186–10191.
[2] X. Huang, Y. Lin, J. Zhang, X. Chen, *Angew. Chem.* **2006**, *118*, 1587–1589, *Angew. Chem. Int. Ed.*, **2006**, *45*, 1557–1559.
[3] a) G. Ferey, C. Serre, *Chem. Soc. Rev.* **2009**, *38*, 1380–1399.; b) B. Zornoza, C. Tellez, J. Coronas, J. Gascon, F. Kapteijn, *Microporous Mesoporous Mater.* **2013**, *166*, 67–78; c) H. B. T. Jeazet, C. Staudt, C. Janiak, *Dalton Trans.* **2012**, *41*, 14003–14027.
[4] P. Horcajada, C. Serre, M. Vallet-Regí, M. Sebban, F. Taulelle, G. Férey, *Angew. Chem.* **2006**, *118*, 6120–6124, *Angew. Chem. Int. Ed.*, **2006**, *45*, 5974–5978.
[5] a) H. Jiang, T. Akita, T. Ishida, M. Haruta, Q. Xu, *J. Am. Chem. Soc.* **2011**, *133*, 1304–1306; b) J. Gascon, U. Aktay, M. D. Hernandez-Alonso, G. P. M. van Klink, F. Kapteijn, *J. Catal.* **2009**, *261*, 75–87.
[6] J. Sánchez-Laínez, A. Veiga, B. Zornoza, S. R. Balestra, S. Hamad, A. R. Ruiz-Salvador, S. Calero, C. Téllez, J. Coronas, *J. Mater. Chem. A* **2017**,.
[7] T. Rodenas, I. Luz, G. Prieto, B. Seoane, H. Miro, A. Corma, F. Kapteijn, i Xamena, Francesc X Llabrés, J. Gascon, *Nature Mater.* **2015**, *14*, 48–55.
[8] a) S. Qiu, M. Xue, G. Zhu, *Chem. Soc. Rev.* **2014**, *43*, 6116–6140. b) E. D. Bloch, W. L. Queen, R. Krishna, J. M. Zadrozny, C. M. Brown, J. R. Long, *Science* **2012**, *335*, 1606–1610; c) Y. Zhang, X. Feng, S. Yuan, J. Zhou, B. Wang, *Inorg. Chem. Front.* **2016**, *3*, 896–909. d) E. Adatoz, A. K. Avci, S. Keskin, *Sep. Purif. Technol.* **2015**, *152*, 207–237.
[9] F. Cacho-Bailo, S. Catalán, M. Etxeberría-Benavides, O. Karvan, V. Sebastián, C. Téllez, J. Coronas, *J. Membr. Sci.* **2014**, *464*, 119–126.
[10] a) J. Wang, N. Li, Z. Li, J. Wang, X. Xu, C. Chen, *Ceram. Int.*, https://doi.org/10.1016/j.ceramint.2016.02.153; b) X. Wang, M. Sun, B. Meng, X. Tan, J. Liu, S. Wang, S. Liu, *Chem. Commun.* **2016**, *52*, 13448–13451; c) K. Tao, L. Cao, Y. Lin, C. Kong, L. Chen, *J. Mater. Chem. A* **2013**, *1*, 13046–13049. d) Y. Pan, Z. Lai, *Chem. Commun.* **2011**, *47*, 10275–10277. e) T. Bae, J. S. Lee, W. Qiu, W. J. Koros, C. W. Jones, S. Nair, *Angew. Chem. Int. Ed.* **2010**, *49*, 9863–9866. f) S. R. Venna, M. A. Carreon, *J. Am. Chem. Soc.* **2009**, *132*, 76–78. g) L. Ge, W. Zhou, A. Du, Z. Zhu, *J. Phys. Chem. C* **2012**, *116*, 13264–13270. h) X. Gong, Y. Wang, T. Kuang, *ACS Sustainable Chem. Eng.* **2017**, *5*, 11204–11214.
[11] A. Huang, H. Bux, F. Steinbach, J. Caro, *Angew. Chem.* **2010**, *122*, 5078–5081, *Angew. Chem. Int. Ed.*, **2010**, *49*, 4958–4961.
[12] Y. Liu, E. Hu, E. A. Khan, Z. Lai, *J. Membr. Sci.* **2010**, *353*, 36–40.
[13] A. Huang, J. Caro, *Angew. Chem. Int. Ed.* **2011**, *50*, 4979–4982.
[14] Y.-S. Li, F.-Y. Liang, H. Bux, A. Feldhoff, W.-S. Yang, J. Caro, *Angew. Chem. Int. Ed.* **2010**, 548–551.
[15] F. Cacho-Bailo, M. Etxeberria-Benavides, O. David, C. Téllez, J. Coronas, *ACS Appl. Mater. Interfaces* **2017**, *9*, 20787–20796.
[16] J. Gascon, F. Kapteijn, B. Zornoza, V. Sebastian, C. Casado, J. Coronas, *Chem. Mater.* **2012**, *24*, 2829–2844.
[17] S. Friebe, A. Mundstock, D. Schneider, J. Caro, *Chem.-A Europ. J.* **2017**, *23*, 6522–6526.
[18] S. A. Moggach, T. D. Bennett, A. K. Cheetham, *Angew. Chem.* **2009**, *121*, 7221–7223, *Angew. Chem. Int. Ed.*, **2009**, *48*, 7087–7089.
[19] W. Morris, N. He, K. G. Ray, P. Klonowski, F. Hiroyasu, I. N. Daniels, Y. A. Houndonougbo, M. Asta, O. M. Yaghi, B. B. Laird, *J. Phys. Chem.* **2012**, *116*, 24084 – 24090.
[20] R. Krishna, *Sep. Purif. Techn.* **2018**, *194*, 281–300.
[21] N. Liédana, A. Galve, C. Rubio, C. Téllez, J. Coronas, *ACS Appl. Mater. Interfaces* **2012**, *4*, 5016–5021.

Manuscript received: March 26, 2018
Version of record online: May 22, 2018

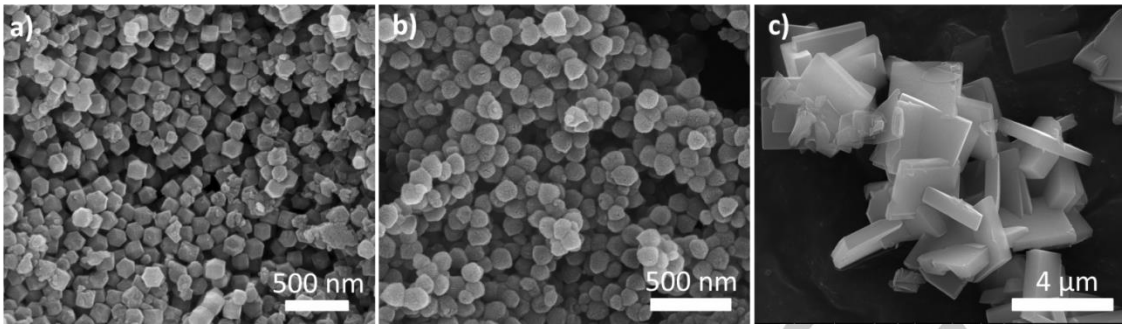

Figure S1. SEM images of ZIF-8 (a), ZIF-7/8 core-shell (b) and ZIF-7(III) samples as powder.

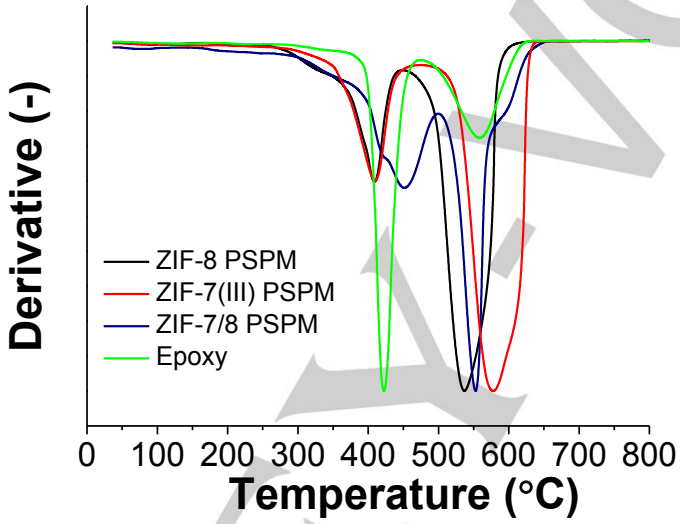

Figure S2. Derivatives of the thermogravimetric analysis for the different PSPMs (ZIF-8, ZIF-7, core-shell) and the epoxy resin.

Table S1. ZnO residue after TG analysis and calculated amount of ZIF and epoxy resin in the PSPMs composites.

PSPM	Residue of ZnO in TG (wt%)	Amount of ZIF in the composite (wt%)	Amount of epoxy in the composite (wt%)
ZIF-8	17.6	53.9	46.1
ZIF-7 (III)	16.2	56.5	43.5
ZIF-7/8 core-shell	23.9	74.1	25.9

The amount of ZIF for each PSPM was calculated from the residue of ZnO found after the TG analysis, since all the amount of Zn comes from the ZIF in the original sample. The amount of epoxy was calculated from the difference to reach a 100 wt%.

Table S2. Numerical values of the gas separation performance of the different PSPMs tested.

Sample	Thickness (µm)	Feed pressure (bar)	H_2 permeation (10^{-10} mol·m^{-2}·s^{-1}·Pa^{-1})	H_2 Permeability (Barrer)	H_2/CO_2 Selectivity (-)
ZIF-7 (III)	435	3	4.0	513	8.9
ZIF-8	461	3	5.6	765	8.1
		5	5.2	718	8.1
ZIF-7/8 core-shell	259	3	4.3	308	12.2
		5	4.6	355	12.3

The thickness of each membrane has been calculated from the amount of epoxy resin shown in Table S1, knowing that the total thickness of the composite is 1000 µm.

Chapter 13: Polymer engineering by blending PIM-1 and 6FDA-DAM for ZIF-8 containing mixed matrix membranes applied in CO_2 separation

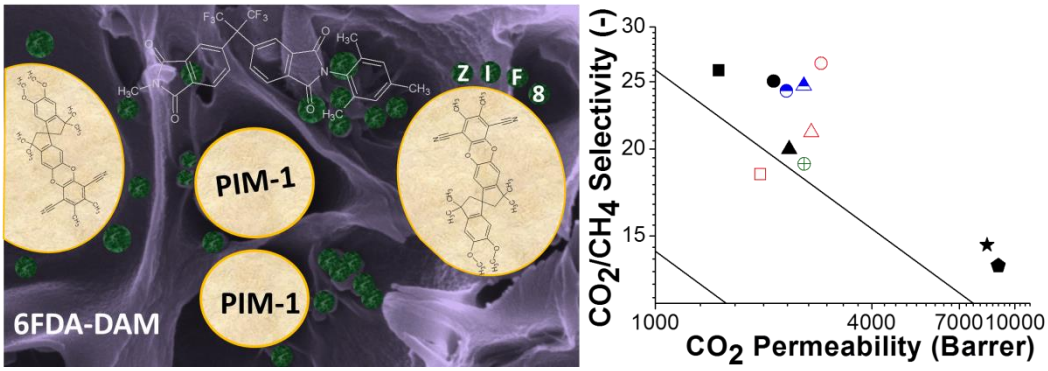

Category:

- Type of membrane: self-supported MMMs
- Gas separation: post-combustion CO_2 capture and biogas upgrading

Polymer engineering by blending PIM-1 and 6FDA-DAM for ZIF-8 containing mixed matrix membranes applied to CO_2 separations

KEYWORDS. PIM-1/6FDA-DAM heterogeneous blend, ZIF-8, mixed-matrix membrane, CO_2 separation.

ABSTRACT. The preparation of mixed matrix membranes (MMMs) for post-combustion CO_2 capture and biogas upgrading from PIM-1 (10-90 wt%)/6FDA-DAM heterogeneous blends with ZIF-8 as filler (3-20 wt% with regard to the polymer blend) is described. The heterogeneity of the blend, considered here as an advantage for the dispersion of the filler within the MMMs, has been confirmed by the existence of a single glass transition temperature, consistent with that of 6FDA-DAM. The segregation between the two polymeric phases and the filler dispersion have been studied by Raman spectroscopy, SEM microscopy and EDX analysis. Increasing the amount of PIM-1 in the blend makes the *d-spacing* of the polymer chains higher and increases gas permeability. When embedding filler nanoparticles of ZIF-8, a better compatibility with 6FDA-DAM than with PIM-1 is observed. The filler locates near the interphase between polymers helping its dispersion. The use of small loadings of ZIF-8 enhances the gas separation performance of the MMMs in terms of permeability and selectivity for 50/50 CO_2/CH_4 and 10/90 CO_2/N_2 mixtures. Importantly, the CO_2, N_2 and CH_4 permeabilities of the pure polymeric blends can be predicted using both the logarithmic and the Maxwell models. A new coupled Maxwell model has also been developed. This model is able to calculate the flow through the blends containing ZIF-8 and to predict the gas separation properties of the filler itself.

1. Introduction

One of the most common contaminants in the world is CO_2. It can be found in fossil fuels such as natural gas or biogas with concentrations of up to 50 %, which remarkably reduces the calorific value of the fuel and helps to corrode gas transport infrastructure[1]. In addition, the increase in the anthropogenic emissions of CO_2, precisely from the burning of such fossil fuels for power generation, is causing a serious environmental problem due to its contribution to the greenhouse effect[2]. Hence, it is necessary to remove CO_2 from fuels and exhaust gases to obtain a clean fuel and to reduce its environmental impact, respectively. For instance, in the case of natural gas and biogas, the CO_2 level should be reduced to less than 2% to meet the pipeline

specifications and to minimize corrosion[3]. The current technologies used for the removal of CO_2 from gas mixtures are absorption, adsorption and membrane technology, among others[4-6]. Membrane technology enjoys inherent advantages such as easy of operation, simplicity, high efficiency, low energy consumption and investment, adaptability and environmental friendliness[7].

Only a few polymers such as polysulfone, cellulose acetate and certain polyimides are used in commercial membranes[8] and there is still interest in developing new polymers with higher permeability and selectivity able to surpass the gas separation trade-off defined by Robeson[9]. The inhibited polymer chain packing and rigid backbone of 6FDA-DAM make it one of the most permeable polyimides for gas separation[10]. Another group of highly permeable polymers are the so-called polymers of intrinsic microporosity (PIMs), a class of rigid ladder-type polybenzodioxins with highly contorted chains. Budd et. al.[11] were the first to report these polymers, of which PIM-1 is possibly the most popular in the literature thanks to its relative ease of preparation with high molecular weight[12]. Both polymers have shown an interesting performance for the separation of CO_2 from CH_4 (natural gas/biogas upgrade) and from N_2 (post-combustion CO_2 capture). It has been reported that 6FDA-DAM can reach CO_2 permeabilities from 380 to 817 Barrer with CO_2/CH_4 selectivities between 15.9 and 31.0 and CO_2/N_2 selectivities around 15.0[13-15]. PIM-1 has usually shown 2300-5300 Barrer of CO_2 with CO_2/CH_4 and CO_2/N_2 selectivities of around 15 and 20, respectively[11,16-18]. Owing to the potential of these two polymers for the CO_2 separation, it was anticipated that mixtures of 6FDA-DAM and PIM-1 could lead to the formation of blends with superior separation properties. PIM-1 has been previously blended with polyimides such as Matrimid®[19], P84®[20], or polysulfone[21]. In all cases PIM-1 formed heterogeneous blends, where it was considered an organic phase dispersed in the matrix formed by the other polymer. The combination of 6FDA-DAM with polybenzimidazole (PBI) has also been reported, which also led to the formation of an immiscible polymer blend which demonstrated an improved performance for H_2/CO_2 separation[22,23].

The present work shows the preparation of membranes for CO_2 separation based on the heterogeneous blend of 6FDA-DAM with PIM-1. In order to improve the gas separation performance of the composites, nanoparticles of the zeolitic imidazolate framework ZIF-8 have been used as porous filler within this polymer mixture. Besides, the filler has located near the interphase between PIM-1 and 6FDA-DAM, helping its dispersion across the membrane section. ZIF-8 is a metal-organic framework (MOF) with a **sod** zeolitic topology, consisting of Zn cations coordinated with the organic linker 2-methylimidazolate, which forms large cavities of 1.16 nm connected through smaller windows of 0.34 nm[24]. Hence, the concept of mixed matrix membrane (MMMs) has been applied, where particles (i.e. fillers, which are often crystalline and porous) are embedded within a suitable polymer matrix to obtain a composite that combines the advantageous properties of both phases. ZIF-8 has

actually shown advantageous properties as filler in several polymers for the separation of CO_2/N_2 and CO_2/CH_4 mixtures[25-29].

2. Experimental

2.1 Membrane preparation

PIM-1/6FDA-DAM blends were prepared in the form of flat dense membranes following a two steps dissolution process. Amounts between 0.04-0.40 g of each polymer were used, being 8 wt% the total polymer concentration in the casting solution. Firstly, PIM-1 was dissolved at room temperature in 4.93 g of chloroform ($CHCl_3$, anhydrous, Sigma-Aldrich) under stirring. After some hours, a homogenous solution was obtained and 6FDA-DAM (purchased from Akron Polymer Systems, Inc., MW= 418 kDa) was added. The resulting solution was further stirred overnight. The composition of the blend was 0, 10, 20, 35, 55, 90 and 100 wt% of PIM, where the proportions of 0 and 100 wt% correspond to pure 6FDA-DAM and pure PIM-1 membranes, respectively. The following day, the polymer solution was left unstirred for 30 min to release air bubbles and then cast onto a glass Petri dish, allowing it to dry at room temperature for 24 h. The obtained film was immersed in MeOH, (HPLC grade, Scharlau) for another 24 h to remove traces of solvent and dried afterwards at 100 °C for 24 h more. The resulting films had a thickness of around 80 µm. In the case of blended MMMs, ZIF-8 was dispersed in the same volume of $CHCl_3$ previous to the addition of both polymers in the necessary quantities for obtaining nominal loadings of 1, 3, 10 and 20 wt%. ZIF-8 nanoparticles were synthesized following a route that can be found elsewhere and that uses a MeOH-water mixture as solvent[30].

2.2 Membrane characterization and gas separation analysis

Membrane characterization includes thermogravimetric analysis (TGA), differential scanning calorimetry (DSC) scanning electron microscopy (SEM), Fourier transform infrared (FTIR) and Raman spectroscopy and X-ray diffraction (XRD). The experimental details as well as those corresponding to the gas separation test can be found in the supporting information.

3. Results and discussion

3.1 Membrane characterization

Several PIM-1/6FDA-DAM blends have been prepared in this work containing PIM amounts of 10, 20 and 90 wt%. Figure 1 shows the SEM images of the cross-section of all these membranes. It can be deduced that 6FDA-DAM and PIM-1 are not full miscible due to the presence of two different morphologies.

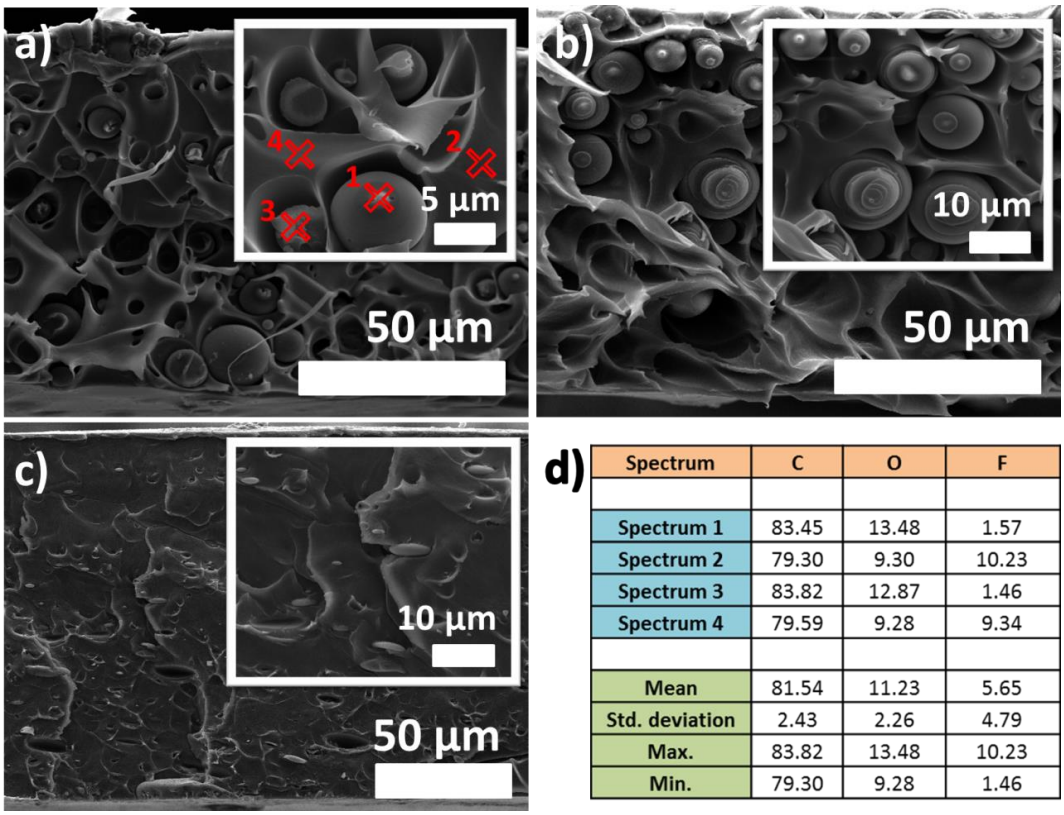

d)

Spectrum	C	O	F
Spectrum 1	83.45	13.48	1.57
Spectrum 2	79.30	9.30	10.23
Spectrum 3	83.82	12.87	1.46
Spectrum 4	79.59	9.28	9.34
Mean	81.54	11.23	5.65
Std. deviation	2.43	2.26	4.79
Max.	83.82	13.48	10.23
Min.	79.30	9.28	1.46

Figure 1. SEM images of the cross section of PIM-1/6FDA-DAM blends containing (a)10, (b) 20 and (c) 90 wt% of PIM-1 and (d) EDX analysis of the former.

The two polymers form a heterogeneous blend where the minor component builds the dispersed phase as spheres or lenticular shapes in a matrix consisting of the other polymer. In the case of PIM loadings of 10 and 20 wt% (Figure 1a and 1b, respectively), PIM-1 was the dispersed phase. This was verified by EDX analysis (see Figure 1d) since the signal of F (only contained in the 6FDA-DAM chains) appears in spectra 2 and 4, i.e. those corresponding to the polymeric matrix, while it cannot be detected in the dispersed phase of PIM-1 spheres (spectra 1 and 3). Confocal Raman microscopy analysis in Figure S1 also supported this phase segregation, obtaining different spectra for the dispersed phase and the matrix, where PIM-1 showed fluorescence while 6FDA-DAM did not. For the blend containing 90 wt% of PIM-1, the 6FDA-DAM formed the disperse phase with lentil shape particles. The existence of a heterogeneous blend between PIM-1 and 6FDA-DAM has also been verified by DSC analysis (see Table S1), since the same glass transition temperature (T_g) of around 320 °C was found for all the composites and this T_g corresponds to that of 6FDA-DAM[31]. Although typically two different T_g values are obtained in two-component heterogeneous blends, the T_g of PIM-1 cannot be measured because this value is higher than its decomposition temperature, and therefore only one value was obtained (that of 6FDA-DAM).

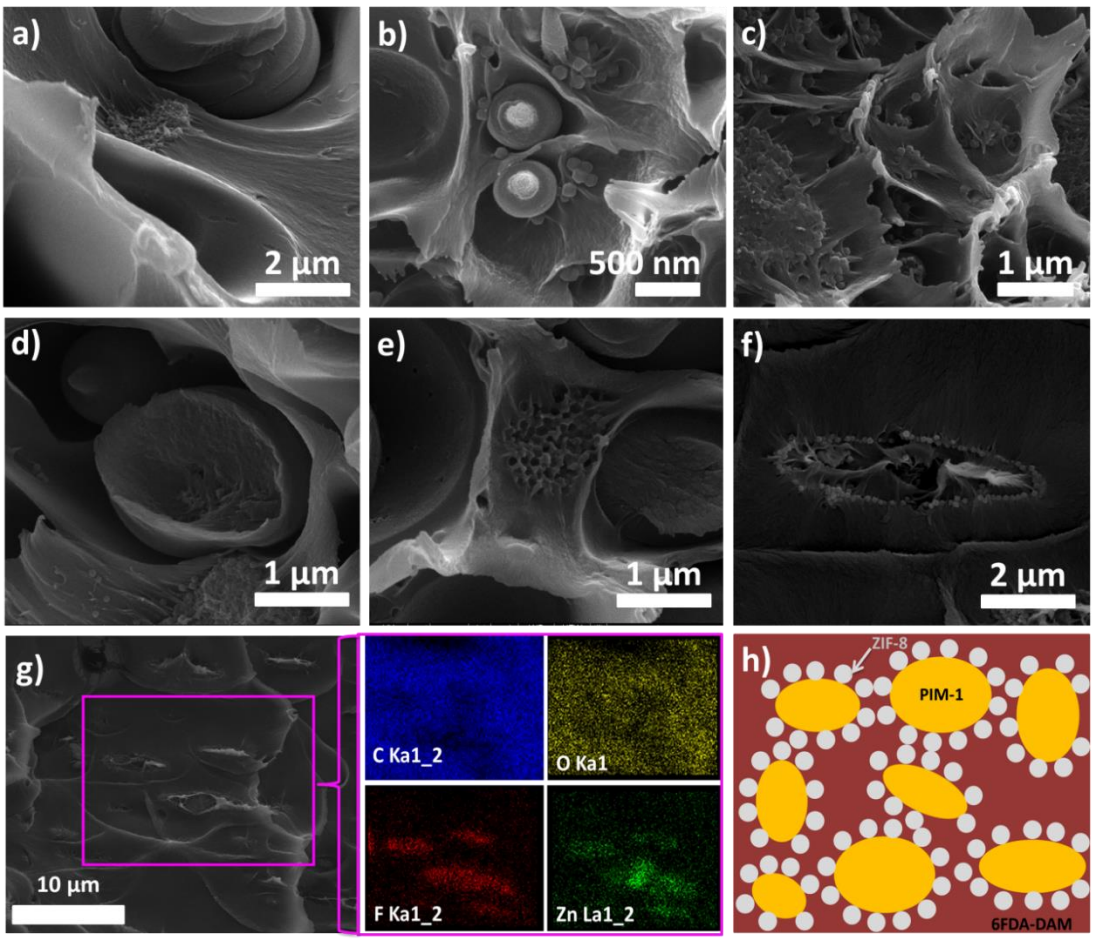

Figure 2. SEM images of MMMs with the 10/90 wt% PIM-1/6FDA-DAM blend containing (a) 1 wt%, (b) 10 wt% and (c) 20 wt% of ZIF-8; the MMMs with the 20/80 wt% PIM-1/6FDA-DAM blend containing (d) 3 wt% and (e) 10 wt% of ZIF-8; and 90/10 wt% PIM-1/6FD-DAM blend with (f) 10 wt% of ZIF-8 and (g) its EDX mapping. (h) A scheme of the MMMs explaining the filler distribution is also included.

Mixed matrix membranes (MMMs) have been prepared with the PIM-1/6FDA-DAM blends containing different loadings of ZIF-8. The cross-sections of all these membranes were observed by SEM and the corresponding images are shown in Figure 2. The blends containing 10 wt% of PIM-1 were loaded with 1, 10 and 20 wt% of ZIF-8. The blends consisting of 20 wt% of PIM-1 contained ZIF-8 amounts of 3 and 10 wt%. And the blends with the highest amount of PIM-1 (i.e. 90 wt%) were prepared with a ZIF-8 loading of 10 wt%. Table S2 summarizes the different membranes prepared, where the actual loadings obtained from TGA analysis are also shown. It can be determined from the SEM images that the filler is not distributed within the two polymeric phases, but it seems to possess more affinity for 6FDA-DAM. This fact was verified by the EDX analysis in Figure 2g, where it can be seen that the signals of F and Zn, corresponding to 6FDA-DAM and ZIF-8, respectively, are overlapped. Despite being firstly dispersed in PIM-1 for the preparation of the casting solution, ZIF-8 was mainly accumulated in the 6FDA-DAM phase during the film formation. In fact, the

filler nanoparticles are allocated near the interphase between polymers, which helped to enhance the filler dispersion across the membrane (see explanatory scheme of Figure 2h).

The thermal stability of the blends was studied performing TGA analysis in air oxidizing atmosphere. The thermograms in Figure S2 show that the pristine PIM-1 possesses two decomposition steps with maximum degradation temperatures of 501 and 617 °C, while the pure 6FDA-DAM membranes only have one at around 571 °C. PIM-1/6FDA-DAM blends show the same behavior as 6FDA-DAM for PIM loadings of 10 and 20 wt% and as PIM-1 when containing a PIM amount of 90 wt%. The absence of a combined pattern between the pure polymers with different decomposition steps is again indicative of the heterogeneity of the blend. Besides, the lack of weight loss below 400 °C proves the good activation of the films with no traces of solvent remaining. FTIR analysis was also performed with the different PIM-1/6FDA-DAM blends. Figure S3 shows that pristine PIM-1 exhibited its typical resonances at 1009 and 1445 cm^{-1}, corresponding to the imide C-N-C and C-N stretching, respectively[19]. Pure 6FDA-DAM membranes, however, showed characteristic peaks at 723 (imide ring deformation), 1101 and 1190 (C-C aromatic), 1356 (C-N stretching) and 1722 cm^{-1} (C=O stretching)[32]. As expected, the blends had the vibration modes of both polymers with different intensities depending on the amount of each other in the composite.

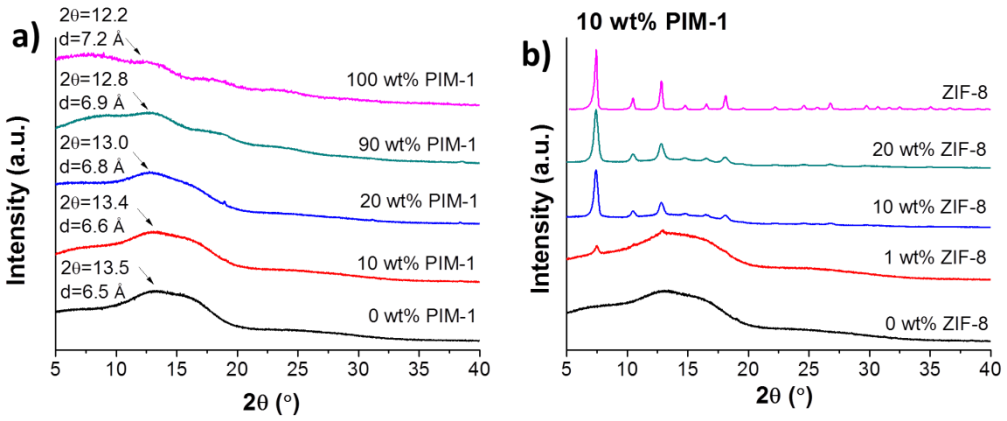

Figure 3. XRD patterns of the PIM-1/6FDA-DAM blends. (a) pure polymeric membranes and MMMs with (b) ZIF-8 as filler.

Figure 3a shows the XRD analyses performed on the PIM-1/6FDA-DAM blends without filler. All the XRD patterns form amorphous bands due to the lack of crystallinity in both polymers 6FDA-DAM and PIM-1. All the membranes show a band with a broad maximum in the range from 2θ = 10 to 15°, from which the *d-spacing* of the polymer could be calculated using the Bragg's law. This value was higher for pristine PIM-1 membranes (7.2 Å) than for those of 6FDA-DAM (6.5 Å) and showed an evolution in correlation with the amount of PIM in the blend. XRD analyses have also been performed with blends containing ZIF-8 (see Figure 3b and

S4), where it can be appreciated how the crystallinity of the filler remains unaltered after the membrane formation. In addition, the intensities corresponding to ZIF-8 became clearer as a function of the increasing loading in agreement with an even distribution of the filler in the MMMs.

3.2 Gas separation performance

The membranes were tested for gas separation with mixtures of CO_2/CH_4 (50/50 v/v) and CO_2/N_2 (10/90 v/v), corresponding to the industrial applications of biogas upgrading and post-combustion CO_2 capture, respectively. The gas separation performance of all the membranes is represented in the permeability-selectivity graphs of Figure 4 and the numerical values are collected in Table S3. It can be seen that pristine 6FDA-DAM and PIM-1 are both highly permeable polymers, with CO_2 permeabilities of 1503 and 8994 Barrer, respectively. In addition both CO_2/CH_4 and CO_2/N_2 selectivities in PIM-1 were lower than those in 6FDA-DAM (e.g., 26.0 and 20.1, respectively). The PIM-1 results are consistent with those found in the literature, while the permeability values for 6FDA-DAM are higher[14,16,33,34]. Increasing the amount of PIM-1 in the blend caused enhancement of the CO_2 flow and the resulting permeability is proportional to the polymer composition of the membranes. Both the CO_2/CH_4 and the CO_2/N_2 selectivities followed the opposite trend with values decreasing with a greater amount of PIM-1 in the blend. These results are consistent with the *d-spacing* obtained from XRD (Figure 3).

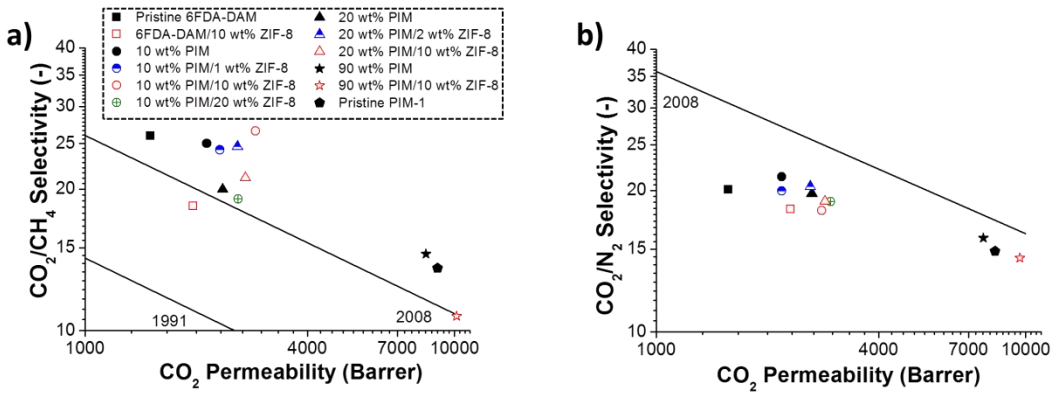

Figure 4. Gas separation performance of the PIM-1/6FDA-DAM blends for (a) CO_2/CH_4 and (b) CO_2/N_2 mixtures at 35 °C and 3 bar of feed pressure. The Robeson upper bounds of 1991 and 2008 are also represented[9,35].

Incorporating ZIF-8 nanoparticles in the matrix of the polymer blends had a positive effect on the gas separation performance of the membranes in comparison with the blends without filler. ZIF-8 was chosen as filler due to its good performance in previous studies[36-38]. The improvement was especially noticeable at low loadings. For example, the blend containing 10 wt% and 90 wt% of PIM-1 and 6FD-DAM (blend code 10% PIM-10% ZIF in Table S2) demonstrated increased CO_2 permeability from 2135 to 2891 Barrer, while the CO_2/CH_4 selectivity was maintained around 26.0 and the

CO_2/N_2 selectivity decreased from 20.1 to 18.1. For the blend with 20 wt% of PIM-1 and 3 wt% of ZIF-8 (blend 20% PIM-3% ZIF) the CO_2 permeability increased from 2356 to 2586 Barrer and the CO_2/CH_4 selectivity increased from 20.1 to 24.7, while the CO_2/N_2 selectivity remained almost stable at ca. 20. Higher loadings than 3 wt% always led to the enhancement of the CO_2 permeability but the selectivity values decreased. This behavior is typical in MMMs where high filler loadings result in the formation of non-selective voids due to a poor interaction between the filler and the polymeric matrix[39]. Noteworthy are the blends with 10 and 20 wt% of PIM-1 and 10 wt% of ZIF-8 (empty red circle and triangle, respectively), which showed a better separation performance than the MMMs of 6FDA-DAM with the same amount of ZIF-8 (empty red square). Finally, all the blends prepared in this work surpassed the 2008 Robeson upper bound for the CO_2/CH_4 separation and remained close to that of CO_2/N_2.

3.3 Membrane modeling

The gas transport through the bare polymeric blends is easy to predict since the permeabilities of both individual phases (6FDA-DAM and PIM-1) can be tested empirically. The permeability of the blends has been found to fit the logarithmic model of Hopfenberg and Paul[40]. This empirical model explains that the logarithm of the permeability of a blend consists of the linear combination of the logarithm of the permeability of each polymer. The formula for the blends in this study is shown in Equation 1:

$$\ln P_{blend} = \Phi \, lnP_{PIM-1} + (1 - \Phi) lnP_{6FDA-DAM} \quad (1)$$

where Φ is the volume fraction of PIM-1 in the composite($\Phi = V_{PIM\text{-}1}/(V_{PIM\text{-}1} + V_{6FDA\text{-}DAM})$), and P_{blend}, P_{PIM-1} and $P_{6FDA-DAM}$ are the respective permeabilities of the blend, PIM-1 and 6FDA-DAM. The volume fraction of PIM-1 was calculated with the polymer density values of 6FDA-DAM and PIM-1 (1.33 and 0.93 g cm^{-3}, respectively) obtained from the literature[41,42].

Figure 5a represents the logarithm of the mixed-gas permeabilities of CO_2, N_2 and CH_4 against the volume fraction of PIM-1 in the blends, showing that they follow a linear tendency. For CO_2 there are results available for the CO_2/CH_4 and the CO_2/N_2 separation, but only the gas permeability values from the former were chosen. The validity of the linear regression is shown in Table S4, with R^2 values higher than 0.99 and where the calculated permeabilities for the pure polymers can also be seen. They agree with the empirical values previously explained (see Figure 4 and Table S3), validating the model.

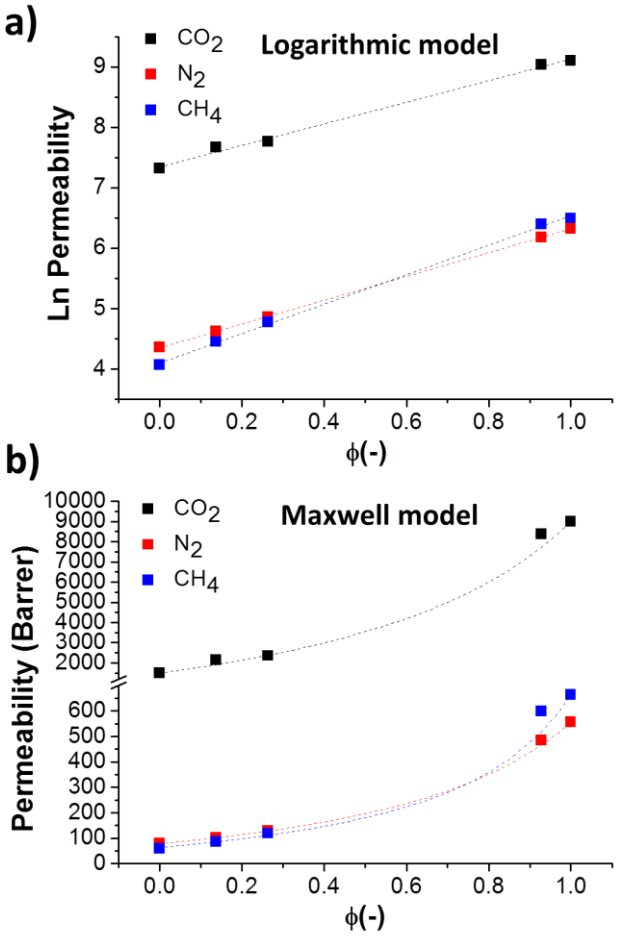

Figure 5. (a) Logarithmic and (b) Maxwell models for the permeability of CO_2, N_2 and CH_4 through the different PIM-1/6FDA-DAM blends. Scatters represent the empirical values and dashed lines those predicted by the models.

The Maxwell model[43] can also describe the gas transport though systems consisting in random distributed and non-interacting homogeneous solid spheres in a continuous matrix. It can be therefore used to model the gas flow though heterogeneous blends. In this case, the PIM-1 spheres were considered the disperse phase of the composite, providing the gas permeability described as seen in Equation 2.

$$P_{blend} = P_{6FDA}\left[\frac{P_{PIM}+2P_{6FDA}-2\Phi_{PIM}(P_{6FDA}-P_{PIM})}{P_{PIM}+2P_{6FDA}+\Phi_{PIM}(P_{6FDA}-P_{PIM})}\right] \quad (2)$$

Figure 5b shows the Maxwell prediction together with the empirical values. A good agreement between the empirical and calculated permeabilities of all gases was found, highlighting the suitability of the Maxwell model for this type of blend.

For the case of the blends containing ZIF-8 (giving rise to MMMs), according to the previous definition, these composites represent a ternary system, where the ZIF-8 nanoparticles were dispersed in the 6FDA-DAM continuous phase, while at the same

time PIM-1 spheres were also distributed within the same 6FDA-DAM matrix. For this model it is necessary to consider the dispersion of two different phases within a continuous polymeric matrix. To predict the flow across such membranes, the following model based on the Maxwell equation is proposed. This model is going to be called "coupled Maxwell model" since the Maxwell equation is used twice. Something similar was applied by Chung *et al.*[44] to consider the non-ideal performance of MMMs induced by interface voids.

Firstly, the Maxwell equation is used to describe the flux through the phase based on a mixture of 6FDA-DAM and the ZIF-8 nanoparticles (P_{2MM}) with Equation 3:

$$P_{2MM} = P_{6FDA}\left[\frac{P_{ZIF}+2P_{6FDA}-2\Phi_{ZIF}(P_{6FDA}-P_{ZIF})}{P_{ZIF}+2P_{6FDA}+\Phi_{ZIF}(P_{6FDA}-P_{ZIF})}\right] \quad (3)$$

Secondly, the permeability defined by the previous equation is introduced as that of the continue phase in the Maxwell equation, providing the gas permeability though the three-phase system (P_{3MM}) with Equation 4:

$$P_{3MM(6FDA)} = P_{2MM}\left[\frac{P_{PIM}+2P_{2MM}-2\Phi_{PIM}(P_{2MM}-P_{PIM})}{P_{PIM}+2P_{2MM}+\Phi_{PIM}(P_{2MM}-P_{PIM})}\right] \quad (4)$$

When the PIM phase is the major component in the blend, P_{2MM} is considered as the permeability of the disperse phase and Equation 5 is used instead:

$$P_{3MM(PIM)} = P_{\mathrm{PIM}}\left[\frac{P_{2MM}+2P_{\mathrm{PIM}}-2\Phi_{6FDA}(P_{\mathrm{PIM}}-P_{2MM})}{P_{2MM}+2P_{\mathrm{PIM}}+\Phi_{6FDA}(P_{\mathrm{PIM}}-P_{2MM})}\right] \quad (5)$$

Figure 6 represents the prediction of the coupled Maxwell model for the blends with the three PIM loadings used in this work together with the corresponding empirical values. It can be seen that the model is able to predict with reasonable accuracy the behavior of the blends with 10 and 20 wt% of PIM-1, but the calculated values differ for the highest PIM loading (90 wt%). This may be due to the high concentration of ZIF-8 (10 wt%) for the low amount of 6FDA-DAM in the blend (also 10 wt%), since all the filler is located within this polymer and the original Maxwell model is only accurate for low filler loadings. Finally, Table S5 summarizes the quality of the different models used, showing the corresponding errors between the empirical and the calculated values for the different blends. The calculated gas permeability of ZIF-8 as filler according to the coupled Maxwell model is also provided, with CO_2, N_2 and CH_4 permeabilities of 136483, 1553 and 415 Barrer, respectively.

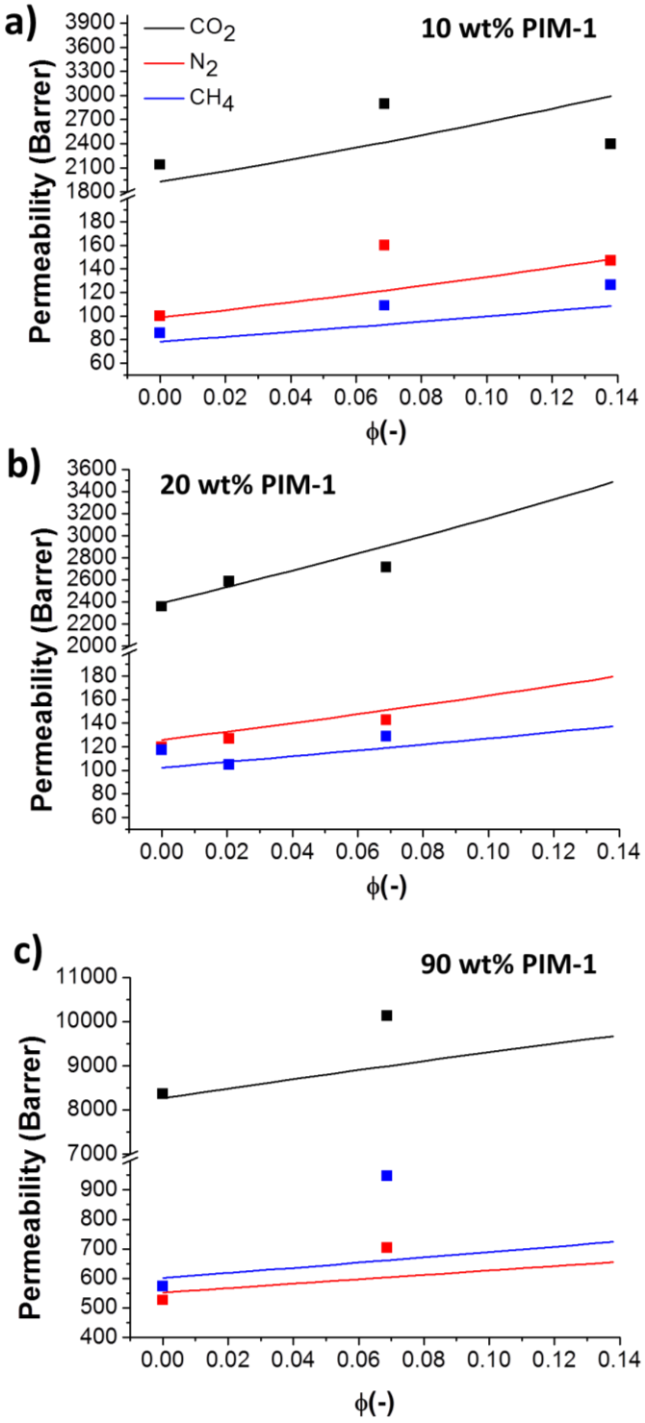

Figure 6. Gas permeabilities of CO_2, N_2 and CH_4 calculated with the coupled Maxwell model as a function of the ZIF-8 loading for the blends with (a) 10, (b) 20 and (c) 90 wt% of PIM. Scatter stands for the empirical values and lines for the model predictions.

4. Conclusions

Membranes based on polymer blends of 6FDA-DAM and PIM-1 have been prepared in this work. The existence of a single T_g confirmed that the mixture of these polymers form a heterogeneous blend, where the SEM microcopy revealed that the disperse phase form spheres and lenticular particles (3-5 μm) evenly distributed along the membrane cross-section. This phase segregation was also identified by Raman spectroscopy and EDX analysis, which detected the F signal of 6FDA-DAM only in certain domains of the composite. The *d-spacing* of the membranes was also calculated, finding that values became higher as the amount of PIM-1 in the blend increased. ZIF-8 nanoparticles were embedded in the blends to build MMMs where it was found that the heterogeneity of the blend contributed to achieving an even and efficient dispersion of the filler. In fact, the ZIF-8 showed a better affinity for 6FDA-DAM than for PIM-1. This resulted in the filler positioned preferably in the interphase between both polymers and embedded in 6FDA-DAM, which in turn allowed the improvement of the dispersion of the filler in the complex polymeric matrix. This behavior was also verified by EDX analysis, where the signals of F and Zn were found in the same positions.

Pure polymer and blend MMMs were tested for CO_2 separation in feed mixtures corresponding to biogas upgrading and post-combustion capture (50/50 CO_2/CH_4 and 10/90 CO_2/N_2, respectively). The increase in the amount of PIM-1 in the blend led to higher gas permeabilities, while the selectivity for both mixtures decreased. The addition of ZIF-8 at low loadings led to the enhancement of the gas separation performance and the best performing membranes were the blends PIM-1/6FDA-DAM 10/90 (w/w) with 10 wt% of ZIF-8, showing a CO_2 permeability of 2891 Barrer, a CO_2/CH_4 selectivity of 26.6 and 2802 Barrer of CO_2 with a CO_2/N_2 selectivity of 18.1. The gas separation performance of the membranes was predicted using the logarithmic and Maxwell models, providing successful fittings with the data. A coupled Maxwell model was also developed to calculate the gas flow through the blends containing ZIF-8, which showed minor errors for the blends with 10 and 20 wt% of PIM and allowed the determination of the separation properties of the ZIF-8 filler. This work demonstrates that even when thinking of highly permeable and moderately selective polymers as PIM-1 and 6FDA-DAM there remains some room to obtain additional performance enhancements by doing "polymer engineering" using MOFs as fillers.

ACKNOWLEDGMENT

Financial support from the Spanish MINECO and FEDER (MAT2016-77290-R), the Aragón Government (T43-17R) and the ESF is gratefully acknowledged. J. S.-L. thanks the Spanish Education Ministry Program FPU2014 for his PhD grant. All the microscopy work was done in the Laboratorio de Microscopías Avanzadas at the Instituto de Nanociencia de Aragón (LMA-INA). Finally, the authors would like to acknowledge the use of the Servicio General de Apoyo a la Investigación-SAI, Universidad de Zaragoza.

REFERENCES

[1] M. Harasimowicz, P. Orluk, G. Zakrzewska-Trznadel, and A. Chmielewski. Application of polyimide membranes for biogas purification and enrichment. J. Hazard. Mater., 144 (2007) 698-702.

[2] F.M. Orr Jr. CO_2 capture and storage: are we ready? Energy Environ. Sci., 2 (2009) 449-458.

[3] W. Burgers, P. Northrop, H. Kheshgi, and J. Valencia. Worldwide development potential for sour gas. Energy Procedia, 4 (2011) 2178-2184.

[4] G. Qi, Y. Wang, L. Estevez, X. Duan, N. Anako, A.A. Park, et al. High efficiency nanocomposite sorbents for CO2 capture based on amine-functionalized mesoporous capsules. Energy Environ. Sci., 4 (2011) 444-452.

[5] M. Mikkelsen, M. Jørgensen, and F.C. Krebs. The teraton challenge. A review of fixation and transformation of carbon dioxide. Energy Environ. Sci., 3 (2010) 43-81.

[6] Y. Xiao, T. Chung. Grafting thermally labile molecules on cross-linkable polyimide to design membrane materials for natural gas purification and CO_2 capture. Energy Environ. Sci., 4 (2011) 201-208.

[7] E. Favre. Carbon dioxide recovery from post-combustion processes: can gas permeation membranes compete with absorption? J. Membr. Sci., 294 (2007) 50-59.

[8] W.J. Koros, R.P. Lively. Water and beyond: Expanding the spectrum of large-scale energy efficient separation processes. AIChE J., 58 (2012) 2624-2633.

[9] L.M. Robeson, Correlation of separation factor versus permeability for polymeric membranes, J. Membr. Sci., 62 (1991) 165-185.

[10] W. Qiu, L. Xu, C. Chen, D.R. Paul, and W.J. Koros, Gas separation performance of 6FDA-based polyimides with different chemical structures, Polymer, 54 (2013) 6226-6235.

[11] P.M. Budd, B.S. Ghanem, S. Makhseed, N.B. McKeown, K.J. Msayib, and C.E. Tattershall. Polymers of intrinsic microporosity (PIMs): robust, solution-processable, organic nanoporous materials. Chem. Commun., (2004) 230-231.

[12] N.B. McKeown, P.M. Budd. Polymers of intrinsic microporosity (PIMs): organic materials for membrane separations, heterogeneous catalysis and hydrogen storage. Chem. Soc. Rev., 35 (2006) 675-683.

[13] A. Sabetghadam, B. Seoane, D. Keskin, N. Duim, T. Rodenas, S. Shahid, et al. Metal Organic Framework Crystals in Mixed-Matrix Membranes: Impact of the Filler Morphology on the Gas Separation Performance. Adv. Funct. Mater., 26 (2016) 3154-3163.

[14] L. Xu, C. Zhang, M. Rungta, W. Qiu, J. Liu, and W.J. Koros, Formation of defect-free 6FDA-DAM asymmetric hollow fiber membranes for gas separations, J. Membr. Sci., 459 (2014) 223-232.

[15] C.K. Yeom, J.M. Lee, Y.T. Hong, K.Y. Choi, and S.C. Kim, Analysis of permeation transients of pure gases through dense polymeric membranes measured by a new permeation apparatus, J. Membr. Sci., 166 (2000) 71-83.

[16] P. Li, T. Chung, and D. Paul. Gas sorption and permeation in PIM-1. J. Membr. Sci., 432 (2013) 50-57.

[17] C.R. Mason, L. Maynard-Atem, N.M. Al-Harbi, P.M. Budd, P. Bernardo, F. Bazzarelli, et al. Polymer of intrinsic microporosity incorporating thioamide functionality: preparation and gas transport properties. Macromolecules, 44 (2011) 6471-6479.

[18] S.J. Smith, B.P. Ladewig, A.J. Hill, C.H. Lau, and M.R. Hill. Post-synthetic Ti exchanged UiO-66 metal-organic frameworks that deliver exceptional gas permeability in mixed matrix membranes. Sci. Rep., 5 (2015) 7823.

[19] W. Yong, F. Li, Y. Xiao, P. Li, K. Pramoda, Y. Tong, et al. Molecular engineering of PIM-1/Matrimid blend membranes for gas separation. J. Membr. Sci., 407 (2012) 47-57.

[20] P. Salehian, W.F. Yong, and T. Chung. Development of high performance carboxylated PIM-1/P84 blend membranes for pervaporation dehydration of isopropanol and CO2/CH4 separation. J. Membr. Sci., 518 (2016) 110-119.

[21] L. Hao, P. Li, and T. Chung. PIM-1 as an organic filler to enhance the gas separation performance of Ultem polyetherimide. J. Membr. Sci., 453 (2014) 614-623.
[22] N.P. Panapitiya, S.N. Wijenayake, D. Nguyen, Y. Huang, I.H. Musselman, K.J. Balkus, et al. Gas Separation Membranes Derived from High Performance Immiscible Polymer Blends Compatibilized with Small Molecules. ACS Appl. Mater. Interfaces, (2015) 18618.
[23] N.P. Panapitiya, S.N. Wijenayake, Y. Huang, D. Bushdiecker, D. Nguyen, C. Ratanawanate, et al. Stabilization of immiscible polymer blends using structure directing metal organic frameworks (MOFs). Polymer, 55 (2014) 2028-2034.
[24] K.S. Park, Z.N. Ni, A.P. Côte, J.Y. Choi, R. Huang, F.J. Uribe-Romo, et al. Exceptional chemical and thermal stability of zeolitic imidazolate frameworks. PNAS, 103 (2006) 10186-10191.
[25] S. Shahid, K. Nijmeijer, Performance and plasticization behavior of polymer–MOF membranes for gas separation at elevated pressures, J. Membr. Sci., 470 (2014) 166-177.
[26] Q. Song, S. Nataraj, M.V. Roussenova, J.C. Tan, D.J. Hughes, W. Li, et al. Zeolitic imidazolate framework (ZIF-8) based polymer nanocomposite membranes for gas separation. Energy Environ. Sci., 5 (2012) 8359-8369.
[27] M.J.C. Ordonez, K.J. Balkus Jr., J.P. Ferraris, and I.H. Musselman. Molecular sieving realized with ZIF-8/Matrimid (R) mixed-matrix membranes. J. Membr. Sci., 361 (2010) 28-37.
[28] A.F. Bushell, M.P. Attfield, C.R. Mason, P.M. Budd, Y. Yampolskii, L. Starannikova, et al. Gas permeation parameters of mixed matrix membranes based on the polymer of intrinsic microporosity PIM-1 and the zeolitic imidazolate framework ZIF-8. J. Membr. Sci., 427 (2013) 48-62.
[29] L. Xu, L. Xiang, C. Wang, J. Yu, L. Zhang, and Y. Pan. Enhanced permeation performance of polyether-polyamide block copolymer membranes through incorporating ZIF-8 nanocrystals. Chin. J. Chem. Eng., 25 (2017) 882-891.
[30] N. Liédana, A. Galve, C. Rubio, C. Téllez, and J. Coronas. CAF@ ZIF-8: one-step encapsulation of caffeine in MOF. ACS Applied Mater. Interfaces, 4 (2012) 5016-5021.
[31] W. Xu, D.R. Paul, and W.J. Koros, Carboxylic acid containing polyimides for pervaporation separations of toluene/iso-octane mixtures, J. Membr. Sci., 219 (2003) 89-102.
[32] M. Safak Boroglu, A.B. Yumru, Gas separation performance of 6FDA-DAM-ZIF-11 mixed-matrix membranes for H_2/CH_4 and CO_2/CH_4 separation, Sep. Purif Technol, 173 (2017) 269-279.
[33] B. Zornoza, C. Téllez, J. Coronas, O. Esekhile, and W.J. Koros. Mixed matrix membranes based on 6FDA polyimide with silica and zeolite microsphere dispersed phases. AIChE J., 61 (2015) 4481-4490.
[34] C.L. Staiger, S.J. Pas, A.J. Hill, and C.J. Cornelius. Gas separation, free volume distribution, and physical aging of a highly microporous spirobisindane polymer. Chem. Mater., 20 (2008) 2606-2608.
[35] L.M. Robeson. The upper bound revisited. J. Membr. Sci., 320 (2008) 390-400.
[36] W. Zheng, R. Ding, K. Yang, Y. Dai, X. Yan, and G. He, ZIF-8 nanoparticles with tunable size for enhanced CO_2 capture of Pebax based MMMs, Sep. Purif. Technol., (2018) DOI: 10.1016/j.seppur.2018.04.010.
[37] N. Nordin, A.F. Ismail, and A. Mustafa. Synthesis and preparation of asymmetric PSf/ZIF-8 mixed matrix membrane for CO 2/CH 4 separation. J. Teknol, 69 (2014) 73-76.
[38] J. Sánchez-Laínez, B. Zornoza, S. Friebe, J. Caro, S. Cao, A. Sabetghadam, et al. Influence of ZIF-8 particle size in the performance of polybenzimidazole mixed matrix membranes for pre-combustion CO_2 capture and its validation through interlaboratory test. J. Membr. Sci., 515 (2016) 45-53.
[39] R. Mahajan, R. Burns, M. Schaeffer, and W.J. Koros. Challenges in forming successful mixed matrix membranes with rigid polymeric materials. J. Appl. Polym. Sci., 86 (2002) 881-890.
[40] D. Paul. S. Newman Eds., Polymer Blends. Aca-demic Press, New York, (1978).

[41] J.H. Kim, W.J. Koros, and D.R. Paul, Physical aging of thin 6FDA-based polyimide membranes containing carboxyl acid groups. Part I. Transport properties, Polymer, 47 (2006) 3094-3103.
[42] H. Frentrup, K.E. Hart, C.M. Colina, and E.A. Müller. In silico determination of gas permeabilities by non-equilibrium molecular dynamics: CO_2 and He through PIM-1. Membranes, 5 (2015) 99-119.
[43] C. Choy, K. Young. Thermal conductivity of semicrystalline polymers—a model. Polymer, 18 (1977) 769-776.
[44] T. Chung, L.Y. Jiang, Y. Li, and S. Kulprathipanja. Mixed matrix membranes (MMMs) comprising organic polymers with dispersed inorganic fillers for gas separation. Prog. Polym. Sci., 32 (2007) 483-507.

Supporting Information

1- Membrane characterization

Thermogravimetric analyses (TGA) were carried out using a Mettler Toledo TGA/STDA 851e. Samples (10 mg) placed in 70 µL alumina pans were heated in 40 cm^3(STP) min^{-1} of air flow from 35 to 900 °C at a heating rate of 10 °C min^{-1}. Differential scanning calorimetry (DSC) analyses were performed with a Mettler Toledo DSC822e. Samples (10 mg) placed in 70 µL aluminum pans were heated in 40 cm^3(STP) min^{-1} of nitrogen flow from 25 to 400 °C at a heating rate of 10°C min^{-1}. Scanning electron microscopy (SEM) images of the MOFs and membranes were obtained using a FEI Inspect F50 model SEM, operated at 20 kV. Cross-sections of the membranes were prepared by freeze-fracturing after immersion in liquid N_2 and subsequently coated with Pt. Fourier transform infrared spectroscopy (FTIR) was performed on the different membrane samples, using a Bruker Vertex 70 FTIR spectrometer equipped with a deuterated triglycine sulfate (DTGS) detector and a Golden Gate diamond ATR accessory. The spectra were recorded by averaging 40 scans in the 4000-600 cm^{-1} wavenumber range at a resolution of 4 cm^{-1}. Membranes were also characterized by Raman spectroscopy using a WiTec Alpha300 Confocal Raman Microscope, with a 785 nm laser excitation beam. Finally, X-ray diffraction (XRD) patterns of the MMMs were obtained with Panalytical Empyrean equipment, using CuK_α radiation (λ = 1.540 Å), taking data from 2θ = 2.5° to 40° at a scan rate of 0.03 ° s^{-1}.

2- Gas separation analysis

The membrane samples were placed in a module consisting of two stainless steel pieces and a 316LSS macroporous disk support of 3.14 cm^2 (from Mott Co.) with a 20 µm nominal pore size, and gripped inside with silicone o-rings. The permeation module was placed in a UNE 200 Memmert oven to control the temperature of the experiments. Gas separation measurements were carried out by feeding a CO_2/CH_4 equimolar mixture (25/25 cm^3(STP) min^{-1}) and CO_2/N_2 mixtures (10/90 cm^3(STP) min^{-1}) at 3 bar to the feed side by means of two mass-flow controllers (Alicat Scientific, MC-100CCM-D), while the permeate side of the membrane was swept with a 1 cm^3(STP) min^{-1} mass-flow controlled stream of He at 1 bar (Alicat Scientific, MC-5CCM-D). Concentrations of CO_2, N_2 and CH_4 in the outgoing streams were analyzed by an Agilent 3000A online gas microchromatograph equipped with a thermal conductivity detector. Permeabilities were calculated in Barrer (10^{-10} cm^3(STP) cm cm^{-2} s^{-1} $cmHg^{-1}$) once the steady-state of the membrane module exit stream was reached (for at least 3 h), and the separation selectivity was calculated as the ratio of permeabilities. At least 2-3 membrane samples of each type were fabricated and measured to provide the corresponding error estimations.

3- Results

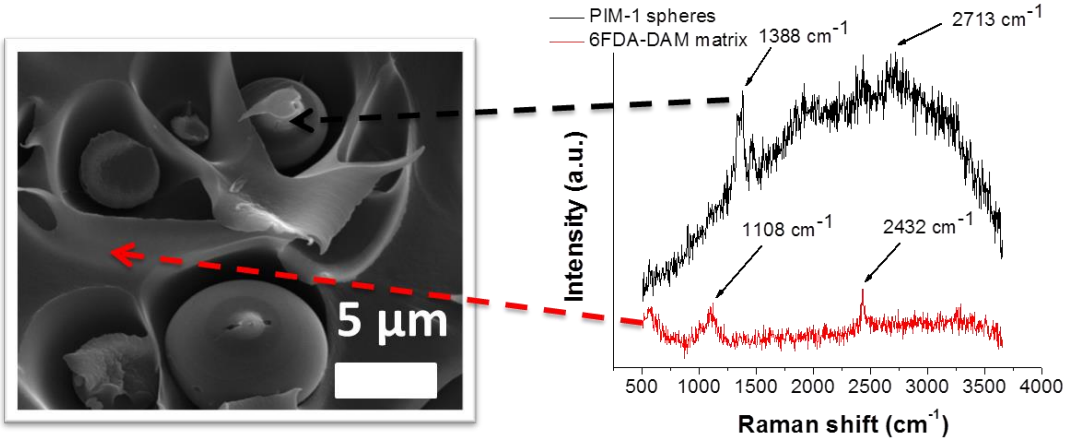

Figure S1. Raman spectra of the cross-section of a PIM-1/6FDA-DAM blend (10/90 w/w)

Table S1. Tg values of the blends containing 10 and 20 wt% of PIM-1 and pristine 6FDA-DAM (0 wt% PIM) and PIM-1 (100 wt% PIM)

PIM-1 amount (wt%)	Tg (° C)
0	**317**
10	**322**
20	**323**
100	**-**

Table S2. Composition of the different blends.

Blend code	PIM-1 amount (wt%)	Nominal ZIF-8 loading (wt%)	Real ZIF-8 loading (wt%)
10% PIM-1% ZIF-	**10**	1	0.6
10% PIM-10% ZIF		10	11.1
10% PIM-20% ZIF		20	22.2
20% PIM-3% ZIF	**20**	3	3.1
20% PIM-10% ZIF		10	7.8
90% PIM-10% ZIF	**90**	10	11.4

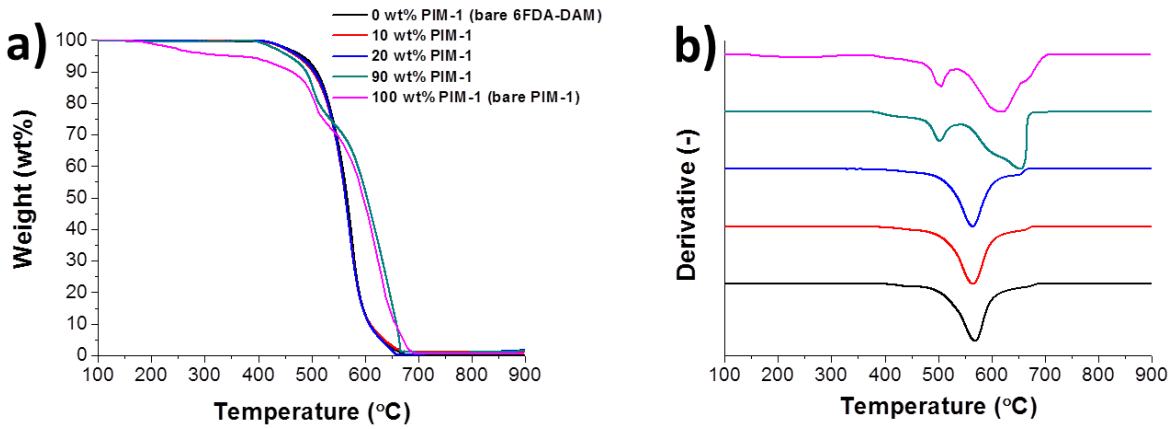

Figure S2. TGA curves in air of different PIM-1/6FDA-DAM blends.

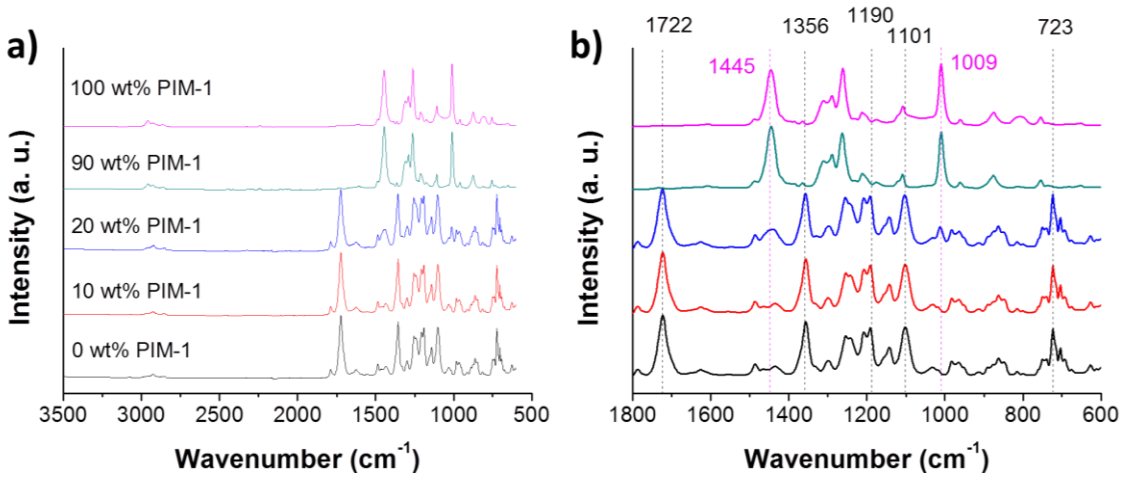

Figure S3. FTIR spectra of the different PIM-1/6FDA-DAM blends

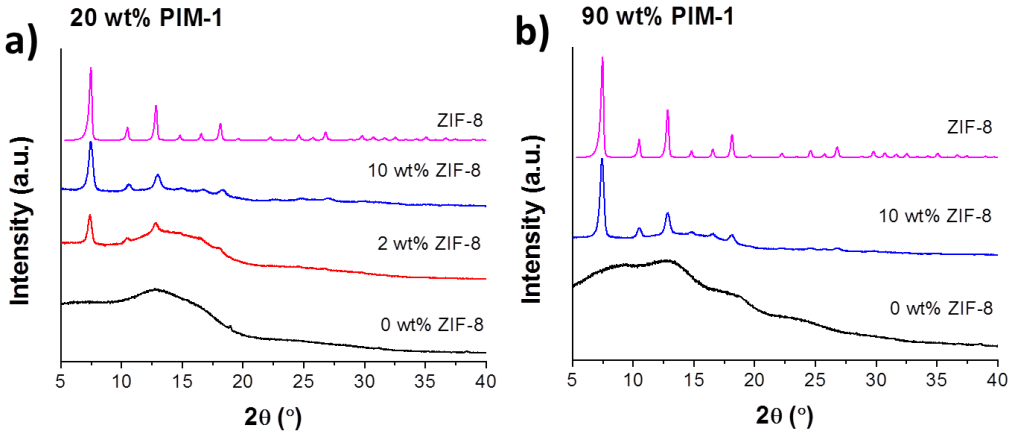

Figure S4. XRD patterns of PIM-1/6FDA-DAM blends containing several amounts of ZIF-8 as filler.

Table S3. Gas separation performance of the PIM-1/6FDA-DAM blends for CO_2/CH_4 (a) and CO_2/N_2 mixtures (b) at 35 °C and 3 bar of feed pressure

Blend	ZIF-8 loading (wt%)	CO_2/CH_4 separation		CO_2/N_2 separation	
		CO_2 Permeability (Barrer)	CO_2/CH_4 selectivity (-)	CO_2 Permeability (Barrer)	CO_2/N_2 selectivity (-)
0 wt% PIM (pristine 6FDA-DAM)	**0**	1503±126	26.0±1.8	1566±146	20.1±0.1
0 wt% PIM (pristine 6FDA-DAM)	**10**	1962±249	18.4±1.9	2310±183	18.3±0.5
10 wt% PIM	**0**	2135±150	25.0±2.7	2184±152	21.4±1.4
10 wt% PIM	**10**	2891±96	26.6±0.2	2802±149	18.1±0.9
10 wt% PIM	**20**	2396	19.0	1648	16.3
20 wt% PIM	**0**	2356±133	20.1±0.6	2638±36	19.7±0.9
20 wt% PIM	**3**	2586±67	24.7±1.3	2611±106	20.4±0.8
20 wt% PIM	**10**	2711±108	21.1±1.3	2863±35	19.0±0.2
90 wt% PIM	**0**	8364±366	14.6±1.4	7678±44	15.9±0.6
90 wt% PIM	**10**	10123±756	10.7±0.0	9651±674	14.4±1.0
100 wt% PIM (Pristine PIM-1)	**0**	8994±203	13.6±0.2	8263±37	14.9±0.2

Table S4. Fitting results of the logarithmic model.

Gas	Fitting	Ln ($P_{PIM-1}/P_{6FDA-DAM}$)	Ln (P_{PIM-1})	Calculated permeability (Barrer)	
				6FDA-DAM	PIM-1
CO_2	$y = 1.7841x + 7.3457$ $R^2 = 0.9961$	1.7841	7.3457	1503	8994
N_2	$y = 1.9716x + 4.3502$ $R^2 = 0.9999$	1.9716	4.3502	78	556
CH_4	$y = 2.4394x + 4.0985$ $R^2 = 0.9989$	2.4394	4.0985	58	663

Table S5. Comparison between empirical permeabilities and those calculated with the logarithmic, Maxwell and coupled Maxwell models for all the blends and the ZIF-8 as filler.

Model	Blend	ZIF-8 loading (wt%)	CO_2 permeability (Barrer)			N_2 permeability (Barrer)			CH_4 permeability (Barrer)		
			Empirical	Calculated	% error	Empirical	Calculated	% error	Empirical	Calculated	% error
Logarithmic	10 wt% PIM	0	2135	1979	7.3	99.8	101.5	1.7	85.4	84.2	1.4
Maxwell			2135	1917	10.2	99.8	101.7	1.9	85.4	85.8	0.4
Cupled Maxwell			2135	1925	9.8	99.8	98.7	1.1	85.4	78.5	8.1
Coupled Maxwell	10 wt% PIM	10	2891	2416	16.4	159.7	121.6	23.9	108.7	92.8	14.6
Coupled Maxwell	10 wt% PIM	20	2396	2993	19.9	147.0	148.2	0.8	126.1	108.8	13.7
Logarithmic	20 wt% PIM	0	2356	2479	5.0	119.6	130.2	8.2	117.2	114.5	2.3
Maxwell			2356	2381	1.1	119.6	128.3	6.8	117.2	111.2	5.1
Coupled Maxwell			2356	2390	1.4	119.6	125.7	4.9	117.2	102.4	12.6
Coupled Maxwell	20 wt% PIM	3	2586	2539	1.8	126.8	133.0	4.7	104.7	107.3	2.4
Coupled Maxwell	20 wt% PIM	10	2711	2906	6.7	142.7	151.0	5.5	128.5	119.1	7.3
Logarithmic	90 wt% PIM	0	8364	8113	3.0	526.0	482.8	8.2	572.9	579.4	1.1
Maxwell			8364	7706	7.9	526.0	464.9	11.6	572.9	516.9	9.8
Coupled Maxwell			8364	7710	7.8	526.0	494.2	6.0	572.9	505.5	11.8
Coupled Maxwell	90 wt% PIM	10	10123	7950	21.5	703.0	512.2	27.1	946.1	525.8	44.4
Coupled Maxwell	ZIF-8	100	-	136483	-	-	1553	-	-	415.0	-

Chapter 14: Thin supported MOF based mixed matrix membranes of Pebax® 1657 for biogas upgrade

J. Sánchez-Laínez, I. Gracia-Guillén, B. Zornoza, C. Téllez and J. Coronas, New Journal of Chemistry, 43 (2019) 312-319. DOI: 10.1039/C8NJ04769C. Reproduced by permission of The Royal Society of Chemistry (RSC) on behalf of the Centre National de la Recherche Scientifique (CNRS) and the RSC.

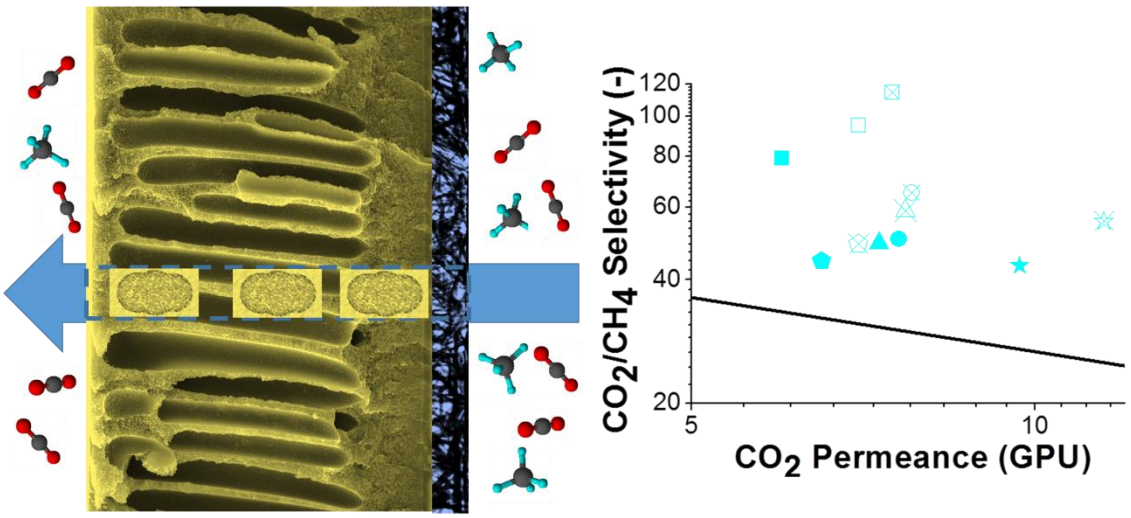

Category:

- Type of membrane: supported membranes
- Gas separation: biogas upgrading

NJC

PAPER

View Article Online
View Journal | View Issue

Cite this: *New J. Chem.*, 2019, **43**, 312

Thin supported MOF based mixed matrix membranes of Pebax® 1657 for biogas upgrade†

Javier Sánchez-Laínez, Inés Gracia-Guillén, Beatriz Zornoza, Carlos Téllez and Joaquín Coronas *

Received 19th September 2018,
Accepted 18th November 2018

DOI: 10.1039/c8nj04769c

rsc.li/njc

This work shows the preparation of thin mixed matrix membranes (MMMs) with a 2–3 μm thick Pebax® 1657 layer on two different supports: a porous asymmetric polyimide P84® and dense polytrimethylsilyl-propyne (PTMSP). Nanoparticles of metal–organic frameworks (MOFs) ZIF-8, MIL-101(Cr), UiO-66 and ZIF-7/8 core–shells were selected as fillers for the Pebax® 1657 based MMMs, all of them being MOFs with high CO_2 adsorption capacity but different pore size distribution. All the membranes were characterized by SEM, FTIR, Raman, TGA and XRD analyses, showing in all cases a perfect compatibility of the Pebax® layer with both supports and also a good dispersion of the fillers in the polymeric matrix. These membranes were applied for the separation of equimolar CO_2/CH_4 mixtures at 35 °C under feed pressures between 3 and 5 bar, where an improvement in the gas separation performance with increasing pressure was noticed, thanks to the favored solubility of CO_2. The synergistic compatibility between Pebax® 1657 and P84® gave rise to a 470% enhancement in CO_2/CH_4 selectivity, reaching a maximum value of 114 while the CO_2 permeance increased by 40% up to 7.5 GPU. The addition of fillers in the Pebax® polymeric phase produced an improvement in the gas separation performance of the membranes, especially in terms of permeance, where the MMMs containing a 10 wt% loading of UiO-66 reached the optimum value of 11.5 GPU of CO_2 (together with a CO_2/CH_4 selectivity of 55.6).

1. Introduction

Biogas production from renewable sources (*e.g.*, from agriculture, landfills, or sewage plants) is one of the fields where membrane technology can show its greatest potential.[1,2] The main components of biogas are methane (CH_4, the combustible component) and carbon dioxide (CO_2, the non-combustible component), although it also typically contains traces of H_2O, N_2, H_2S and other organic aromatics.[3] The high concentration of CO_2 and CH_4 in the mixture, basically in the same proportion, makes biogas upgrading appropriate to be carried out with polymeric membranes, a technology that offers advantages such as low energy costs and environmental benignity,[4] and that can be an alternative to other existing approaches, such as cryogenic upgrading or liquefaction.[5] For example, PVAm/PVA blends have shown a CH_4 recovery of 99% at a low running cost in a 2-stage recycled process.[6] Besides purifying the CH_4 flow, the captured CO_2 is also suitable for its conversion into high value-added products, such as MeOH.[7]

The major materials used for membranes are polyimides and fluoropolymers.[8] To obtain membranes with a good gas separation performance (*i.e.* high CO_2 permeation flux and CO_2/CH_4 selectivity), materials with intrinsic separation capacity for the target mixture are necessary. Poly(ether-*block*-amide), best known under the trademark Pebax®, constitutes a family of polymers that possess these advantageous properties. These polymers combine linear chains of rigid polyamide with flexible, CO_2-philic polyether segments, building crystalline/amorphous structures that show the properties of both thermoplastics and rubbers. It is believed that the hard amide block provides mechanical strength, whereas gas selective transport occurs primarily through the soft ether block.[9] The polyamide/polyether-oxide proportion in the blend determines the Pebax® grade. The membranes in this work were prepared with Pebax® 1657, consisting of 40 wt% polyamide.[10]

Membranes with high permeance are essential for large-scale applications, such as biogas upgrading.[11] This variable is not only related to the membrane permeability but also to the thickness of the membrane, and membranes consisting of a very thin selective layer are necessary to achieve this goal. Such high performance membranes can be prepared as composite materials, where the selective layer is deposited on a highly porous support that provides mechanical stability.[12] Pebax® 1657 can be found in the literature in the form of thin film

Chemical and Environmental Engineering Department, Instituto de Nanociencia de Aragón (INA) and Instituto de Ciencia de Materiales de Aragón (ICMA), Universidad de Zaragoza-CSIC, 50018 Zaragoza, Spain. E-mail: coronas@unizar.es

† Electronic supplementary information (ESI) available: MOF synthesis, membrane characterization and gas separation performance. See DOI: 10.1039/c8nj04769c

composites on several polymeric supports, such as polyvinylidene fluoride (PVDF),[13,14] polyacrylonitrile (PAN)[15,16] and polysulfones.[17,18] The CO_2 permeances vary from 13 to 670 GPU according to the membrane morphology and the CO_2/CH_4 selectivities are found to be between 13.6 and 18.0. These works also provide CO_2/N_2 selectivities, which show highly dispersed values (between 32 and 70).

In general, the gas separation performances of polymeric membranes can be enhanced through the concept of mixed matrix membranes (MMMs), consisting of the dispersion of inorganic fillers within a polymeric matrix so that either or both permeability and selectivity of the membrane can be improved through the synergistic combination of the two components.[19] Metal–organic frameworks (MOFs) are materials that have been widely used as fillers in MMMs. In the case of the Pebax® 1657 polymer, ZIF-8 has been used as the filler by Xu *et al.*[20] and Zheng *et al.*[21] The former found an increase in the CO_2 permeability from 79.2 to 156 Barrer as the ZIF-8 loading increased from 0 to 20 wt%, but the CO_2/N_2 selectivity decreased until 40.5. The latter showed fluctuating CO_2 permeabilities between 55.8 and 179 Barrer and practically constant CO_2/N_2 and CO_2/CH_4 selectivities. Within the ZIF family, ZIF-7 has also been used as the filler in Pebax® 1657 membranes. Li *et al.*[22] prepared thin Pebax® 1657 based MMMs supported on PAN that showed the best performance results at 34 wt% loading with a CO_2 permeance of 39 GPU, and CO_2/N_2 and CO_2/CH_4 selectivities of 105 and 44, respectively. ZIF-7 has also been used as a filler by Sutrisna *et al.*[13] who prepared MMMs on PVDF hollow fibers with optimum values of 300 GPU of CO_2, and with CO_2/N_2 and CO_2/CH_4 selectivities of 47.5 and 17.0, respectively. Other MOF-Pebax® 1657 combinations for dense MMMs included MOFs ZIF-94, NH_2-MIL-53(Al), MIL-69(Al) and MIL-96(Al), with the latter giving rise to the best CO_2/N_2 performance: permeability and selectivity were enhanced by 25 and 18%, respectively, as compared to the pure polymer.[23] Interestingly, the effect of the MOF functionalization (comparing the use of MIL-53(Al) and NH_2-MIL-53(Al) with better CO_2 permeability and CO_2/CH_4 selectivity values for the latter) has been recently studied on dense MMMs with Pebax® 1657.[24] There is no doubt that 1657 is the most used Pebax® code in the MMM field.

This work shows the preparation of thin film composite membranes with a thin mixed-matrix selective top layer of MOF/polymer Pebax® 1657 for biogas upgrade. The membranes have been prepared on different polymeric supports and the influence of the feed pressure on the gas separation performance has been studied. Different MOFs (ZIF-8, ZIF-7/8 core–shells, UiO-66 and MIL-101(Cr)) have been embedded in Pebax® 1657, dissolved in a water–ethanol mixture,[25] as fillers to obtain thin supported MMMs. Materials with a high CO_2 uptake (see Table 1) have been selected to favor the solubility of this gas in the membrane composite and thus enhance its CO_2/CH_4 separation performance.

Table 1 CO_2 adsorption capacities of different MOFs used in this work

MOF	Adsorption conditions	CO_2 uptake, (mmol g^{-1})	Pore aperture (nm)	Cavity (nm)	Ref.
ZIF-8	273 K, 1 bar 298 K, 30 bar	1.3 35	0.34	1.16	26,27
UiO-66	273 K, 1 bar 300 K, 35 bar	2.4 7.0	0.80	2.1	28–30
MIL-101(Cr)	303 K, 1 bar 304 K, 50 bar	1.6 40	1.2–1.6	2.9–3.4	31–33
ZIF-7/8 core–shells	273 K, 1 bar	2.5	0.29–0.34	0.43–1.16	26

2. Experimental section

2.1 Synthesis of MOF nanoparticles

Four different MOFs were synthesized to be used as fillers in the MMMs of this work. The synthesis of ZIF-8 was performed following a method based on a MeOH–water mixture as the solvent.[34] UiO-66 was synthesized solvothermally in *N*,*N*-dimethylformamide (DMF, 99.8%, Sigma-Aldrich).[35] The synthesis of MIL-101(Cr) was microwave assisted, with DI water as the solvent for the metal source and the ligand.[36] And finally, the ZIF-7/8 core–shells were prepared *via* post-synthetic modification of the previously described explained ZIF-8 nanoparticles.[26] The experimental details are described in the ESI.†

2.2 Membrane preparation

P84® asymmetric supports. Flat asymmetric porous P84® supports were prepared following the phase inversion method.[37] A 23 wt% doped solution of P84® (HP polymer GmbH) was prepared by dissolving the corresponding amount of powder in *N*,*N*-dimethylacetamide (DMAc, >99,8% Sigma Aldrich). The polymer solution was cast on a glass plate using the Elcometer 4340 Automatic Film Applicator placed in a fume hood and set at a thickness of 250 μm. Immediately afterwards the resultant polymer sheets were immersed into a tap water bath at 25 °C for 10 min. After precipitation, the membranes were kept in a deionized (DI) water bath overnight and then rinsed with IPA to remove the remaining DMAc. The films were dried at 100 °C one day prior to use.

Before testing the gas separation performance, several membranes were treated with PDMS (Sylgard® 184, Dow Corning) by dip coating. The coating solution was prepared by mixing the PDMS polymer base and the hardener (dimethyl, methylhydrogen siloxane) provided with the Sylgard® kit with a weight ratio of 10 : 1. The mixture was added to *n*-hexane to obtain a 3 wt% solution. The membranes were immersed in the coating solution for 5 min, and then allowed to evaporate at room temperature for 2 h. Finally, the membranes were cured in an oven at 100 °C for 18 h.

Dense PTMSP supports. For the preparation of dense PTMSP supports, the polymer was first dissolved at room temperature in hexane at 5 wt% concentration. The solution was then cast on a glass petri dish and allowed to dry at room temperature for 24 h. The obtained film was immersed in MeOH for another 24 h to remove traces of solvent and dried afterwards at 100 °C for 24 h more. The resulting films had a thickness of around 80 μm.

Pebax® 1657 membranes. Thin films of Pebax® 1657 were prepared on the two previously described supports (asymmetric porous P84® and dense PTMSP) following a solution-casting procedure. Pellets of Pebax® (kindly provided by Arkema) were

dissolved in a 70/30 (v/v) EtOH/H_2O mixture by refluxing at 90 °C for 1 h. The polymer solution was then cast on the corresponding support using the same film applicator as before. Afterwards, the membrane was kept at room temperature for 1 day for complete solvent evaporation. In the case of the Pebax® MMMs, the corresponding amount of MOF (ZIF-8, UiO-66, MIL-101(Cr) or ZIF-7/8 core–shells) was dispersed in the EtOH/H_2O mixture. Afterwards, the pellets of Pebax® were added and the suspension was heated at 90 °C until full dissolution of the polymer after *ca.* 1 h. Then the suspension was cast on the polymeric supports and allowed to dry, as explained above. The casting solution had to be used within a few hours because long storage times lead to defective films. Self-supported membranes of the bare polymer Pebax®, with an approximate thickness of 80 μm, were also prepared for comparison purposes. In this case the polymer solution was poured into a petri dish and the solvent was allowed to evaporate slowly for 72 h at room temperature.

2.3 Membrane characterization

Thermogravimetric analyses (TGA) were carried out using a Mettler Toledo TGA/STDA 851e. Samples (10 mg) placed in 70 μL alumina pans were heated under a 40 cm^3(STP) min^{-1} air flow from 25 to 900 °C at a heating rate of 10 °C min^{-1}. Differential scanning calorimetry (DSC) analyses were performed on a Mettler Toledo DSC822e. Samples (10 mg) placed in 70 μL aluminum pans were heated under a 40 cm^3(STP) min^{-1} of nitrogen flow from 25 to 500 °C at a heating rate of 10 °C min^{-1}. The scanning electron microscopy (SEM) images of the MOFs and membranes were obtained using a FEI Inspect F50 model SEM, operated at 20 kV. Cross-sections of the membranes were prepared by freeze-fracturing after immersion in liquid N_2 and subsequently coated with Pt. Fourier transform infrared spectroscopy (FTIR) was performed for the MOF powders and for the different membrane samples, using a Bruker Vertex 70 FTIR spectrometer equipped with a DTGS detector and a Golden Gate diamond ATR accessory. The spectra were recorded on the Pebax® side by averaging 40 scans in the 4000–600 cm^{-1} wavenumber range at a resolution of 4 cm^{-1}. Membranes were also characterized by Raman spectroscopy using a WiTec Alpha300 Confocal Raman Microscope, with a 785 nm laser excitation beam. X-ray diffraction (XRD) patterns of the MOFs and MMMs were obtained using Panalytical Empyrean equipment, using CuK_α radiation (λ = 1.540 Å), taking data from $2\theta = 2.5^\circ$ to 40° at a scan rate of 0.03° s^{-1}.

2.4 Gas separation analysis

The membrane samples were placed in a module consisting of two stainless steel pieces and a 316LSS macroporous disk support of 3.14 cm^2 (from Mott Co.) with a 20 μm nominal pore size, and gripped inside with silicon O-rings. The permeation module was placed in a UNE 200 Memmert oven to control the temperature of the experiments. Gas separation measurements were carried out by feeding a CO_2/CH_4 equimolar mixture (25/25 cm^3(STP) min^{-1}) at 3–5 bar to the feed side by means of two mass-flow controllers (Alicat Scientific, MC-100CCM-D), while the permeate side of the membrane was swept with a 1 cm^3(STP) min^{-1} mass-flow controlled stream of He at 1 bar (Alicat Scientific, MC-5CCM-D). The concentrations of CO_2 and CH_4 in the outgoing streams were analyzed using an Agilent 3000A online gas microchromatograph equipped with a thermal conductivity detector. Permeances were calculated in GPU (10^{-6} cm^3(STP) cm^{-2} s^{-1} $cmHg^{-1}$) once the steady-state of the membrane module exit stream was reached (for at least 3 h), and the separation selectivity was calculated as the ratio of permeances. At least 2–3 membrane samples of each type were fabricated and measured to provide the corresponding error estimations.

3. Results and discussion

3.1 Membrane characterization

Fig. 1 shows the cross-sections of three different membranes based on Pebax® 1657: a self-supported dense Pebax® 1657 membrane of around 80 μm thickness (Fig. 1a) and two supported Pebax® 1657 membranes prepared on dense PTMSP and asymmetric P84® supports (Fig. 1b and c, respectively). The cross-section of the Pebax® 1657/P84® composite shows a thickness of 120 μm for the P84® support, of which 15 μm corresponds to the denser top layer. Moreover, it can be observed in the inset at a higher magnification that the Pebax® 1657 layer is approximately 3 μm thick and shows a good adhesion to the polyimide support. A good compatibility can also be observed in the composite membrane prepared on PTMSP, the Pebax® 1657 layer in this case being 2 μm thick.

Fig. 1d shows the Raman spectra of the cross-section of the Pebax® 1657/P84® membrane. Two different points on the zones corresponding to the Pebax® 1657 layer and the P84® support were measured. Although the Pebax® 1657 Raman spectrum shows weak signals owing to its fluorescence, three peaks can be distinguished at 1133, 1305 and 1454 cm^{-1} related to the C–O and C═O vibration modes.[38] Signals in the 1300–1800 cm^{-1} range can be seen in the P84® spectrum. The signals at 1376 and 1435 cm^{-1} correspond to the C═O in-phase stretching mode. The band at 1613 cm^{-1} is related to the aromatic ring stretching mode, and that at 1780 cm^{-1} corresponds to the aromatic C–N stretching.[39]

Pebax® 1657 MMMs are shown in Fig. 2. Membranes containing a 10 wt% loading of ZIF-8, UiO-66, MIL-101(Cr) and ZIF-7/8 core–shell particles can be seen at three different magnifications. By visual inspection a good dispersion of the different fillers in the Pebax® thin layer can be observed, resulting in homogeneous membranes where a good filler–polymer adhesion is noticeable. The SEM images of the fillers are also provided (see Fig. S1 from the ESI†), from which the cumulative and differential particle size distributions were obtained using the ImageJ 1.49b software, together with median particle sizes of 150, 25, 33 and 124 nm for ZIF-8, UiO-66, MIL-101(Cr) and ZIF-7/8 core–shell particles, respectively (see Fig. S2 and Table S1 in the ESI†).

Fig. 3 shows the XRD patterns of the different membranes, MOFs and of the pure polymeric Pebax® 1657 membrane for comparison. Pristine Pebax® 1657 is a semicrystalline copolymer which consists of both crystalline and amorphous PEO and

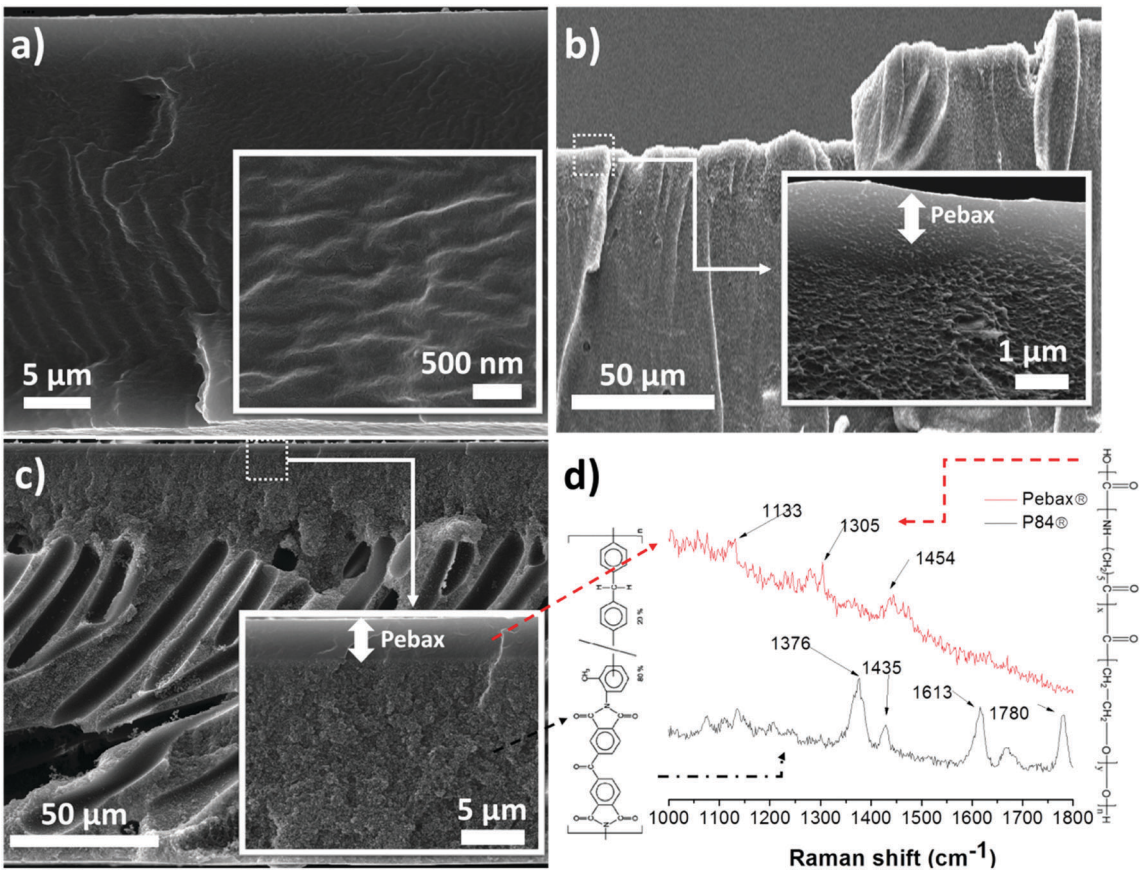

Fig. 1 SEM images with higher magnification insets of the cross-sections of: Pebax® 1657 self-supported dense membrane (a), Pebax® 1657 supported on PTMPS (b), and Pebax® 1657 supported on asymmetric P84® (c). The Raman spectra corresponding to the latter are also provided (d).

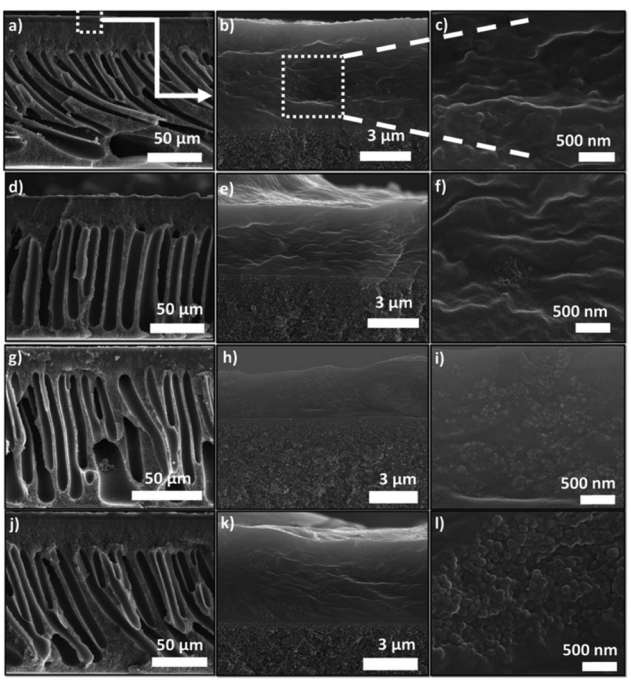

Fig. 2 SEM images of the cross-section of Pebax® supported (on asymmetric P84®) membranes containing the 10 wt% loading of ZIF-8 (a–c), MIL-101(Cr) (d–f), UiO-66 (g–i) and ZIF-7/8 core–shell particles (j–l).

PA6 phases, showing characteristic peaks at $2\theta = 5.8^\circ$, 12.6° and 24.4°.[40] These signals are also noticeable in the patterns of the MMMs, although with a lower intensity due to the higher crystallinity of the fillers. It is also clear that ZIF-8 and UiO-66 maintain their crystallinity in the polymer matrix since their XRD reflections dominate over the amorphous band of the polymer. In the case of the other two MOFs, the peaks are not so well defined. This is due to the lower crystallinity of MIL-101(Cr) and the fact that the ZIF-7/8 core–shells are not as crystalline as the original ZIF-8 from which they are synthesized, according to our previous study.[26] Besides, after the incorporation of the MOFs, the peak positions of Pebax® 1657 remained almost unaltered, proving that there were no changes in the *d*-spacing of the polymer.

The FTIR spectra were recorded to further characterize and analyze the Pebax® 1657 MMMs (see Fig. S3 in the ESI†). The observed peak at 1094 cm^{-1} is attributed to the stretching vibration of the C–O–C group of the soft segment part of PEO.[40] Regarding the hard segment of PA chains, the peak corresponding to the –N–H– linkages is found at 3298 cm^{-1} and the characteristic peak at 1636 cm^{-1} is assigned to the H–N–C═O group.[41] The most intense signals of each MOF can be found in the corresponding MMM spectrum. However, none of the membranes show new absorbance peaks, suggesting weak chemical interactions between the filler nanoparticles and the

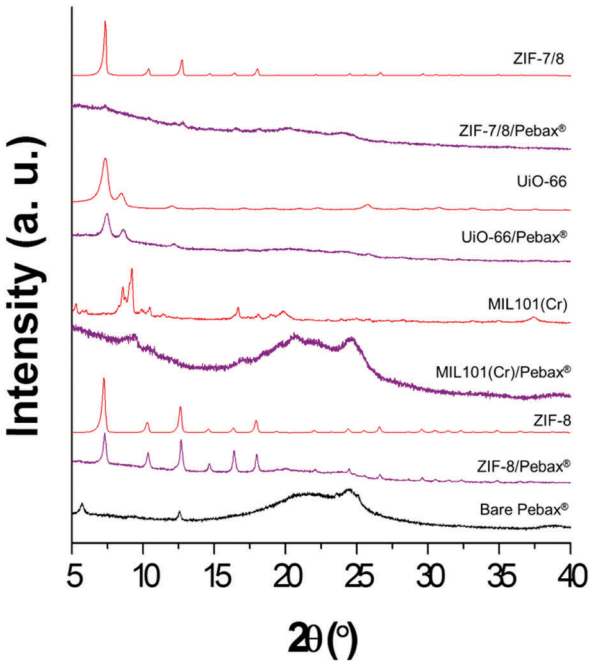

Fig. 3 XRD spectra of bare Pebax® 1657, MMMs and MOF powders.

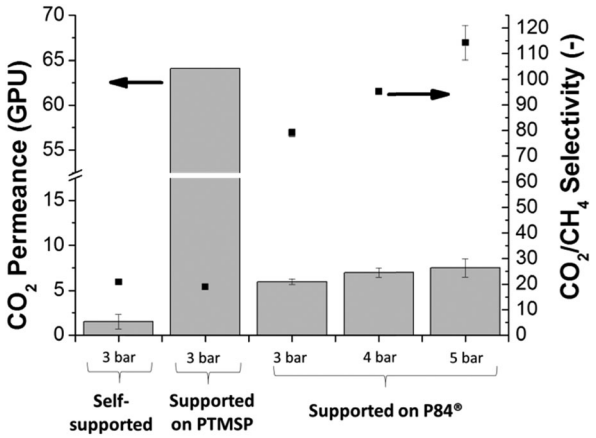

Fig. 4 Gas separation performance of pristine Pebax® 1657 membranes at 35 °C and under different feed pressures: self-supported and supported on PTMSP and P84®. Bars stand for CO_2 permeance and scatters for CO_2/CH_4 selectivity.

polymer chains or that the filler loading is too low for their visualization.

Thermogravimetric analyses (TGA) in flowing air were used to elucidate the thermal stability of the different membranes prepared in this work. As seen in Fig. S4 in the ESI,† while the P84® support shows an onset temperature of 592 °C, Pebax® 1657 was less stable since it started to degrade at around 400 °C. This is consistent with a slightly reduced thermal stability of the supported Pebax® 1657/P84® composite. Regarding the MMMs, the thermograms indicate that all the MOFs started to decompose over 300 °C. Besides, these TGA analyses helped to verify that the actual MOF content in the mixed matrix thin layer (12.5 wt% for ZIF-8, 8.2 wt% for MIL-101(Cr), 10.9 wt% for UiO-66 and 13.4 wt% for ZIF-7/8 MMMs) fits with the nominal (10 wt%). The thermal properties of Pebax® 1657 were further investigated by DSC (see Fig. S5 in the ESI†). Pristine Pebax® 1657 shows two endothermic peaks whose maxima occur approximately at 40 and 130 °C. These can be attributed to the fusion of the crystalline fraction of the blocks of poly(ethylene oxide) and polyamide, and limit the operating temperature of the membranes.[42]

3.2 Gas separation performance

The different membranes prepared were tested for the separation of the CO_2/CH_4 equimolar mixtures at 35 °C and under different feed pressures ranging from 3 to 5 bar.

Fig. 4 depicts the gas separation performance of pristine Pebax® 1657 membranes. Three different types of membranes were studied, self-supported Pebax® 1657 membranes and supported Pebax® 1657 using supports of two different polymers: a dense PTMSP and an asymmetric porous P84®. Thick self-supported Pebax® 1657 and thin Pebax® 1657 supported on PTMSP showed similar CO_2/CH_4 selectivities, with values around 20. However, the difference in CO_2 permeance was much more noticeable since the former showed only 1.5 GPU while that of the latter increased up to 64 GPU. This is consistent with the difference in thickness between both membranes: 80 μm of the self-supported membrane *vs.* 2 μm of the supported membrane. Taking into account the corresponding value of this parameter for each membrane, the calculated CO_2 permeability would be around 120 Barrer in both cases. This highlights the reliability of the membrane permeation characterization system.

When testing the Pebax® 1657 supported on P84® also at 3 bar, the CO_2 permeance was 6.0 GPU, the flow increase being smaller than for the previous PTMSP supported membrane. Nevertheless, the CO_2/CH_4 selectivity increased considerably, reaching a value of 79.2, four-fold higher than that of the self-supported membrane. This behavior indicates that the P84® support affects the gas separation performance of the composites, increasing the membrane selectivity and simultaneously decreasing the gas permeability. For a better understanding of the role that the P84® support was playing in the gas separation, the support itself was tested for the CO_2/CH_4 separation (see Table S2 from the ESI†). The results showed that the P84® support exhibited a CO_2 permeance of 270 GPU but showed no CO_2/CH_4 selectivity. When the P84® was coated with PDMS the permselectivity was enhanced by defect healing, but only the inherent CO_2/CH_4 selectivity of PDMS was noticeable (5.5), along with its CO_2 permeance (55.1 GPU).[43] This fact means that P84® and Pebax® 1657 possess a specific compatibility, giving a composite whose gas separation performance is much better than that of the bare polymers. Besides, coating the polyimide P84® support with a more selective polymer such as Pebax® 1657 may lead to a healing effect and the selectivity of the polyimide would approach values found in the literature for this polymer (CO_2/CH_4 selectivity of 33.4).[44]

The effect of the feed pressure on the gas separation performance of the CO_2/CH_4 mixture was also studied. As seen in Fig. 4, the supported Pebax® 1657/P84® membranes were

tested from 3 to 5 bar, showing that the increase in pressure implied an augment in both the CO_2 permeance and the CO_2/CH_4 selectivity, reaching optimum values at 5 bar with 7.5 GPU and 114, respectively. The higher permeance of CO_2 results from its smaller molecular diameter in combination with its enhanced solubility due to its high quadrupole moment (4.30 D Å for CO_2 *vs.* 0.02 D Å for CH_4), which enables strong specific interactions with the polar polyether groups in Pebax®.[10] Moreover, the CH_4 permeance showed a contrary tendency, decreasing at the higher feed pressures tested. A similar reduction of permeation flux resulting from compression has been reported for N_2 and CH_4 in rubbery polymers such as PDMS and poly(octylmethylsiloxane) (POMS).[45,46] Besides, as seen in Fig. S6 in the ESI,† both CO_2 and CH_4 permeances follow an exponential tendency as a function of feed pressure as described by Stern *et al.*[47] (eqn (S1)†), with beta (the constant characteristic of the penetrant–membrane system at the testing temperature, 35 °C in this case) values positive for CO_2 (0.11 bar^{-1}) and negative for CH_4 (-0.18 bar^{-1}).

Membranes based on Pebax® 1657 using ZIF-8, UiO-66, MIL-101(Cr) and ZIF-7/8 core–shell particles as fillers have been prepared on P84® supports, forming thin supported MMMs. These MOFs have been selected because of their high CO_2 uptake (1.3–2.5 mmol g^{-1} at 1 bar, see Table 1) in order to favor the solubility of this gas over CH_4 in the Pebax® 1657 based MMMs. Only MIL-101(Cr) has cavities in the mesoporous range, while other MOFs are microporous materials (see Table 1). Fig. 5a shows the gas separation performance of these MMMs at 35 °C. Two different feed pressures of 3 and 5 bar were tested showing that, as in the previous separation with pristine Pebax® 1657 (see Fig. 4), both the CO_2 permeance and the CO_2/CH_4 selectivity enhanced with increasing pressure. In terms of CO_2 permeance, the gas separation performance of the membranes improved with the incorporation of MOFs into the polymeric matrix. MMMs showed an average increase in CO_2 permeance of 6%, except for the UiO-66 MMMs, which showed a much greater improvement with a maximum value of 11.5 GPU at 5 bar, almost twice that of pristine Pebax® 1657 at the same feed pressure. Regarding the CO_2/CH_4 selectivity, its value decreased to one half when any of the fillers were incorporated into Pebax® 1657. Nevertheless, CO_2/CH_4 selectivities remained high with values between 50 and 60 for different MMMs, making them still very attractive. The best value was obtained for the ZIF-8 MMMs, with a CO_2/CH_4 selectivity of 65.1 (with 7.7 GPU of CO_2) at 5 bar. This result is logical since ZIF-8, besides having a moderate CO_2 adsorption, is the MOF with the narrowest pore access (0.34 nm), between the kinetic diameters of CO_2 and CH_4 (0.33 and 0.36 nm, respectively). The narrowest porosity of the ZIF-7/8 material (see Table 1), which is the worst performer in terms of CO_2/CH_4 selectivity, may hinder the transport of CO_2 in comparison to other MOFs.

Considering separately the effect of the diffusivity and selectivity of the MOFs in the gas separation performance of the membranes, ZIF-8 and ZIF-7/8 core–shells are expected to have a greater effect on the diffusivity thanks to their narrower pore distribution (see Table 1). In contrast, UiO-66 and MIL-101(Cr) may have a greater effect on the contribution of the solubility due to their higher CO_2 uptake (see Table 1).

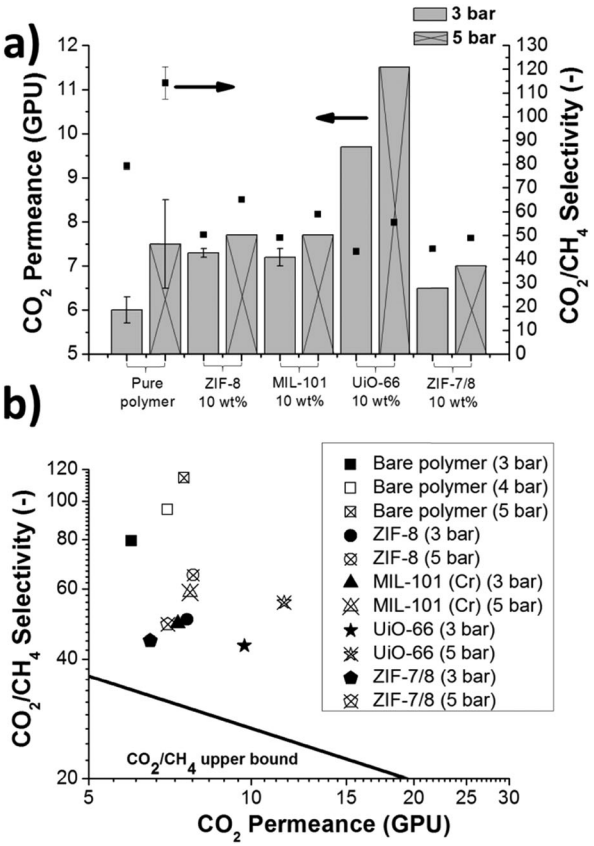

Fig. 5 Comparison of the gas separation performance of pristine Pebax® 1657 and the different supported on P84® MMMs in the form of histogram (a) and upper bound type graph (b).

The gas separation performances of all MMMs were plotted on a selectivity–permeance graph (Fig. 5b). Since the Robeson's upper bound was originally defined in Barrer[48](see the values in Table S3 from the ESI†), a new upper bound was calculated in GPU to obtain a more accurate comparison (Fig. S7 from the ESI†). The Robeson's upper bound, revisited in 2008[48] was defined from the pure component permeability data of dense membranes, allowing the determination of the state-of-the-art limits for gas separation with polymeric membranes. The upper bound relationship is expressed by $P_i = k{\cdot}\alpha_{ij}^{n}$, where P_i is the permeability of the more permeable gas, α is the separation factor (P_i/P_j) and n is the slope of the log–log limit. It was observed that the representation of $-1/n$ *vs.* d_{ij} (where d_{ij} is the difference between the gas molecular diameters ($d_j - d_i$)) yielded a straight line relationship. Since the gas permeability was defined for the explained purpose in Barrer, a new CO_2/CH_4 upper bound relationship in GPU has been calculated here. This used the values from the literature that defined the original upper bound but changing permeabilities in Barrer by permeances in GPU (see Table S3 from the ESI†), as done in a previous work for H_2/CO_2 mixtures.[37] The thicknesses used are those reported in the publications cited in Table S3 in the ESI,† although possible inaccuracies in the *ex situ* measurement

of this length, such as experimental errors or membrane swelling, might affect such values. These values are represented in Fig. S7 in the ESI† and fitted to a logarithmic equation, resulting in the following upper bound relationship: $P_{CO_2} = 8175 \cdot \alpha_{CO_2/CH_4}{}^{-2.086}$. A factor k of 8175 GPU was obtained and the slope n of −2.086 was not far from the value found in the original publication (−2.636). Fig. 5b shows that all the membranes prepared in this work clearly surpassed the new calculated upper bound, reaching the so-called commercially attractive region. UiO-66 MMMs exhibited the highest CO_2 permeances, followed by MIL-101(Cr) MMMs, thanks to their wide porosity (see Table 1). In contrast, ZIF-7/8 MMMs are the least permeable and they also contain fillers with the narrowest pore distribution. ZIF-8 MMMs are the best balanced membranes, showing a great CO_2/CH_4 selectivity with high CO_2 permeance.

4. Conclusions

Thin membranes of Pebax® 1657 have been successfully prepared on dense PTMSP and asymmetric porous P84® supports. The obtained supported Pebax® 1657 membranes, with a thickness ranging from 2–3 μm, have been found to exhibit a good compatibility and adhesion between the support and the selective layer. The membranes were tested for CO_2/CH_4 separation at 35 °C and different feed pressures (3–5 bar), showing an improvement in both the CO_2 permeance and the CO_2/CH_4 selectivity with increasing pressures, thanks to the favored CO_2 solubility. While the performance of Pebax® 1657/PTMSP membranes was similar to those of self-supported dense Pebax®, the Pebax® 1657/P84® composites showed a great enhancement in the CO_2/CH_4 selectivity thanks to the synergistic compatibility between the two polymers. Thin MMMs of Pebax® 1657 containing 10 wt% of ZIF-8, MIL-101(Cr), UiO-66 and ZIF-7/8 core–shell nanoparticles were also prepared supported on P84®. The incorporation of MOFs enhanced the CO_2 permeance of the membranes on average 6%, but especially embedding UiO-66, which allowed doubling the permeance of pristine Pebax® 1657 membranes. ZIF-8 MMMs are the best performing composites, maintaining a high CO_2 permeance with a good CO_2/CH_4 selectivity. In any event, it has been demonstrated that the good physicochemical interaction between polymer Pebax® 1657 and P84® support allowed an enhancement in the CO_2/CH_4 separation. The highest CO_2/CH_4 selectivity obtained along the work was that of the membrane made of bare Pebax® 1657 on P84®, with a value of 114 (at 7.5 GPU of CO_2).

Conflicts of interest

There are no conflicts to declare.

Acknowledgements

Financial support from the Spanish MINECO and FEDER (MAT2016-77290-R), the Aragón Government (T43-17R) and the ESF is gratefully acknowledged. J. S.-L. thanks the Spanish Education Ministry Program FPU2014 for his PhD grant. All the microscopy work were carried out in the Laboratorio de Microscopías Avanzadas at the Instituto de Nanociencia de Aragón (LMA-INA). Finally, the authors would like to acknowledge the use of the Servicio General de Apoyo a la Investigación-SAI, Universidad de Zaragoza.

References

1 M. Poloncarzova, J. Vejrazka, V. Vesely and P. Izak, *Angew. Chem., Int. Ed.*, 2011, **50**, 669–671.
2 Y. Zhang, J. Sunarso, S. Liu and R. Wang, *Int. J. Greenhouse Gas Control*, 2013, **12**, 84–107.
3 S. Rasi, A. Veijanen and J. Rintala, *Energy*, 2007, **32**, 1375–1380.
4 J. C. Chen, X. Feng and A. Penlidis, *Sep. Sci. Technol.*, 2005, **39**, 149–164.
5 A. Baccioli, M. Antonelli, S. Frigo, U. Desideri and G. Pasini, *Appl. Energy*, 2018, **217**, 328–335.
6 L. Deng and M. Hägg, *Int. J. Greenhouse Gas Control*, 2010, **4**, 638–646.
7 M. Pérez-Fortes, J. C. Schöneberger, A. Boulamanti and E. Tzimas, *Appl. Energy*, 2016, **161**, 718–732.
8 B. Li, Y. Duan, D. Luebke and B. Morreale, *Appl. Energy*, 2013, **102**, 1439–1447.
9 V. Bondar, B. Freeman and I. Pinnau, *J. Polym. Sci., Part B: Polym. Phys.*, 2000, **38**, 2051–2062.
10 J. H. Kim, S. Y. Ha and Y. M. Lee, *J. Membr. Sci.*, 2001, **190**, 179–193.
11 G. Valenti, A. Arcidiacono and J. A. N. Ruiz, *Biomass Bioenergy*, 2016, **85**, 35–47.
12 Z. Dai, L. Ansaloni and L. Deng, *Green Energy Environ.*, 2016, **1**, 102–128.
13 P. D. Sutrisna, J. Hou, M. Y. Zulkifli, H. Li, Y. Zhang, W. Liang, D. D'Alessandro and V. Chen, *J. Mater. Chem. A*, 2018, **6**, 918–931.
14 Y. Wang, T. Hu, H. Li, G. Dong, W. Wong and V. Chen, *Energy Procedia*, 2014, **63**, 202–209.
15 E. Esposito, G. Clarizia, P. Bernardo, J. C. Jansen, Z. Sedláková, P. Izák, S. Curcio, B. d. Cindio and F. Tasselli, *Chem. Eng. Process.*, 2015, **94**, 53–61.
16 A. Car, C. Stropnik, W. Yave and K. Peinemann, *Sep. Purif. Technol.*, 2008, **62**, 110–117.
17 P. Li, Z. Wang, W. Li, Y. Liu, J. Wang and S. Wang, *ACS Appl. Mater. Interfaces*, 2015, **7**, 15481–15493.
18 L. Liu, A. Chakma and X. Feng, *Chem. Eng. J.*, 2004, **105**, 43–51.
19 G. Dong, H. Li and V. Chen, *J. Mater. Chem. A*, 2013, **1**, 4610–4630.
20 L. Xu, L. Xiang, C. Wang, J. Yu, L. Zhang and Y. Pan, *Chin. J. Chem. Eng.*, 2017, **25**, 882–891.
21 W. Zheng, R. Ding, K. Yang, Y. Dai, X. Yan and G. He, *Sep. Purif. Technol.*, 2018, DOI: 10.1016/j.seppur.2018.04.010.
22 T. Li, Y. Pan, K. Peinemann and Z. Lai, *J. Membr. Sci.*, 2013, **425**, 235–242.
23 A. Sabetghadam, X. Liu, M. Benzaqui, E. Gkaniatsou, A. Orsi, M. M. Lozinska, C. Sicard, T. Johnson, N. Steunou, P. A. Wright, C. Serre, J. Gascon and F. Kapteijn, *Chem. – Eur. J.*, 2018, **24**, 7949–7956.

24 S. Meshkat, S. Kaliaguine and D. Rodrigue, *Sep. Purif. Technol.*, 2018, **200**, 177–190.
25 M. Isanejad, N. Azizi and T. Mohammadi, *J. Appl. Polym. Sci.*, 2017, **134**, 44531–44540.
26 J. Sánchez-Laínez, A. Veiga, B. Zornoza, S. R. Balestra, S. Hamad, A. R. Ruiz-Salvador, S. Calero, C. Téllez and J. Coronas, *J. Mater. Chem. A*, 2017, **5**, 25601–25608.
27 S. K. Nune, P. K. Thallapally, A. Dohnalkova, C. Wang, J. Liu and G. J. Exarhos, *Chem. Commun.*, 2010, **46**, 4878–4880.
28 J. H. Cavka, S. Jakobsen, U. Olsbye, N. Guillou, C. Lamberti, S. Bordiga and K. P. Lillerud, *J. Am. Chem. Soc.*, 2008, **130**, 13850–13851.
29 D. Sun, Y. Fu, W. Liu, L. Ye, D. Wang, L. Yang, X. Fu and Z. Li, *Chem. – Eur. J.*, 2013, **19**, 14279–14285.
30 H. Wu, Y. S. Chua, V. Krungleviciute, M. Tyagi, P. Chen, T. Yildirim and W. Zhou, *J. Am. Chem. Soc.*, 2013, **135**, 10525–10532.
31 J. Benito, S. Sorribas, I. Lucas, J. Coronas and I. Gascon, *ACS Appl. Mater. Interfaces*, 2016, **8**, 16486–16492.
32 G. Ferey, C. Mellot-Draznieks, C. Serre, F. Millange, J. Dutour, S. Surble and I. Margiolaki, *Science*, 2005, **309**, 2040–2042.
33 P. L. Llewellyn, S. Bourrelly, C. Serre, A. Vimont, M. Daturi, L. Hamon, G. De Weireld, J. Chang, D. Hong, Y. Kyu Hwang, S. H. Jhung and G. Férey, *Langmuir*, 2008, **24**, 7245–7250.
34 N. Liédana, A. Galve, C. Rubio, C. Téllez and J. Coronas, *ACS Appl. Mater. Interfaces*, 2012, **4**, 5016–5021.
35 L. Hou, L. Wang, N. Zhang, Z. Xie and D. Dong, *Polym. Chem.*, 2016, **7**, 5828–5834.
36 N. A. Khan, I. J. Kang, H. Y. Seok and S. H. Jhung, *Chem. Eng. J.*, 2011, **166**, 1152–1157.
37 J. Sánchez-Laínez, B. Zornoza, C. Téllez and J. Coronas, *J. Membr. Sci.*, 2018, **563**, 427–434.
38 F. H. Akhtar, M. Kumar and K. Peinemann, *J. Membr. Sci.*, 2017, **525**, 187–194.
39 J. J. Ge, G. Xue, F. Li, K. W. McCreight, S. Wang, F. W. Harris, S. Z. Cheng, X. Zhuang, S. Hong and Y. Shen, *Macromol. Rapid Commun.*, 1998, **19**, 619–623.
40 J. H. Kim and Y. M. Lee, *J. Membr. Sci.*, 2001, **193**, 209–225.
41 A. Ghadimi, M. Amirilargani, T. Mohammadi, N. Kasiri and B. Sadatnia, *J. Membr. Sci.*, 2014, **458**, 14–26.
42 S. Sridhar, R. Suryamurali, B. Smitha and T. Aminabhavi, *Colloids Surf., A*, 2007, **297**, 267–274.
43 K. Berean, J. Z. Ou, M. Nour, K. Latham, C. McSweeney, D. Paull, A. Halim, S. Kentish, C. M. Doherty, A. J. Hill and K. Kalantar-Zadeh, *Sep. Purif. Technol.*, 2014, **122**, 96–104.
44 S. Sridhar, R. Veerapur, M. Patil, K. Gudasi and T. Aminabhavi, *J. Appl. Polym. Sci.*, 2007, **106**, 1585–1594.
45 M. Askari, M. L. Chua and T. S. Chung, *Ind. Eng. Chem. Res.*, 2014, **53**, 2449–2460.
46 J. Schultz and K. Peinemann, *J. Membr. Sci.*, 1996, **110**, 37–45.
47 S. Stern, J. Mullhaupt and P. Gareis, *AIChE J.*, 1969, **15**, 64–73.
48 L. M. Robeson, *J. Membr. Sci.*, 2008, **320**, 390–400.

New Journal of Chemistry RSCPublishing

ARTICLE

Supporting Information

Synthesis of MOF nanoparticles

ZIF-8. This synthesis was performed following a recipe based on a MeOH-water mixture [1] as solvent. 0.47 g of zinc nitrate hexahydrate ($Zn(NO_3)_2 \cdot 6H_2O$, >98%, Sigma Aldrich) was dissolved in 10 mL of methanol (MeOH, HPLC grade, Sharlau) and 10 mL of water. Besides, 1.0 g of 2-methylimidazole (mIm, $C_4H_6N_2$, >99%, Sigma Aldrich), was dissolved in 10 mL of MeOH, and the two solutions were mixed and stirred for 2 h. The final product was collected by centrifugation at 10,000 rpm, washed once with MeOH, and dried at 110 ^{0}C overnight.

UiO-66[2]: 0.40 g of zirconium (IV) chloride ($ZrCl_4$, ≥99.5%, Sigma-Aldrich) was dissolved in 100 mL of N,N-dimethylformamide (DMF, 99.8%, Sigma–Aldrich) at room temperature with the help of a ultrasound bath, before the addition of 0.28 g of benzene-1,4-dicarboxylic acid (BDC, 98%, Sigma-Aldrich) and 0.13 mL of distilled water. The obtained solution was later transferred into a stainless steel teflon-lined autoclave for a solvothermal process in a pre-heated oven at 120 °C for 24 h. After cooling to room temperature, the colloidal suspension was centrifuged at 10,000 rpm and the precipitated solid was rinsed three times with fresh DMF, followed by washing three times more with the same amount of MeOH. Finally, the MOF was activated in a furnace at 300 °C for 3 h, with a heating rate of 15 °C·min^{-1}.

MIL-101(Cr): 0.5 g of chromium(III) chloride hexahydrate ($CrCl_3 \cdot 6H_2O$, 96%, Sigma-Aldrich) and 0.45 g of terephthalic acid (98%, Sigma–Aldrich) were dissolved in 26 mL of distilled water [3]. After mixing, the solution was maintained for 30 min at 180 °C in a microwave oven. The solid was separated by centrifugation at 10,000 rpm and washed with water. Then, the synthesized MOF was activated with DMF at 120 °C overnight and thereafter with MeOH for 12 h under reflux. Finally, the MIL-101(Cr) powder was dried at 100 °C overnight.

ZIF-7/8 core-shells. The ZIF-7/8 core-shells were prepared *via* post-synthetic modification of the above explained ZIF-8 nanoparticles[4]. An initial amount of benzimidazole (bIm, Sigma Aldrich) was added to DMF at 65 °C to obtain a concentration of 13 g/L. Once dissolved, ZIF-8 was added to the solution (3.3 g/L), which was stirred for 24 h. The solid was then collected by centrifugation at 10,000 rpm, washed three times with MeOH and dried at 110 °C overnight.

Membrane characterization

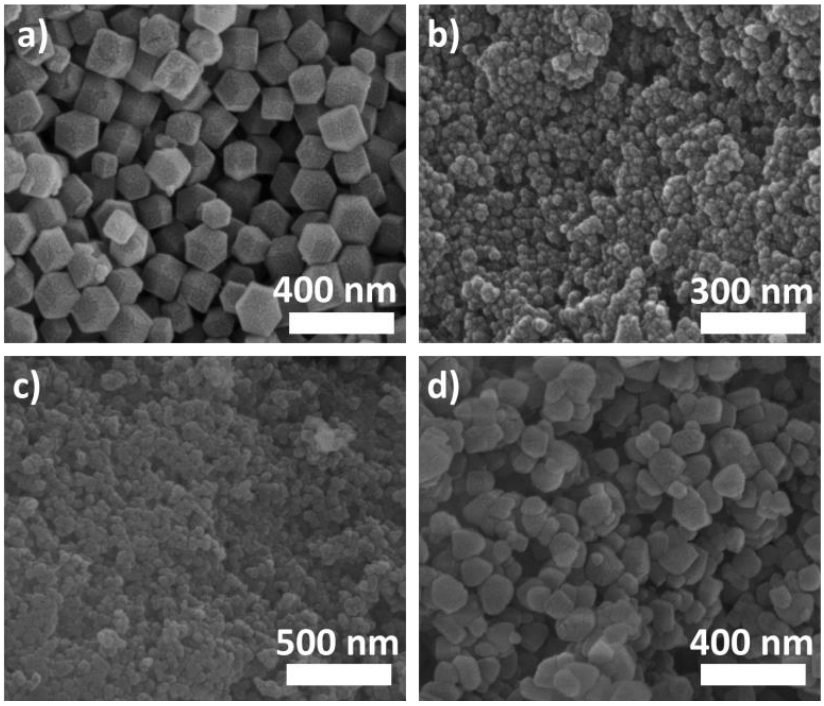

Fig. S1. SEM images of ZIF-8 (a), MIL-101(Cr) (b), UiO-66 (c) and ZIF-7/8 core-shell particles (d)

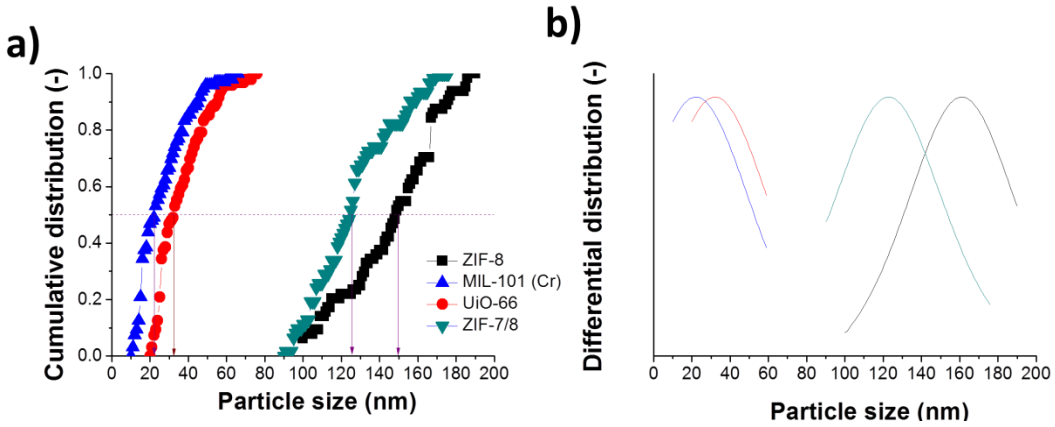

Fig. S2. Cumulative (a) and differential (b) particle size distribution of the ZIF-8, MIL-101(Cr), UiO-66 and ZIF-7/8 core-shells samples.

Table S1. Median particle sizes of the different MOFs used as filler according to the calculation of Fig. S2a.

MOF	ZIF-8	MIL 101 (Cr)	UiO-66	ZIF-7/8
Average particle size (nm)	150±60	25±19	33±13	124±22
Mode (nm)	161	22	32	123

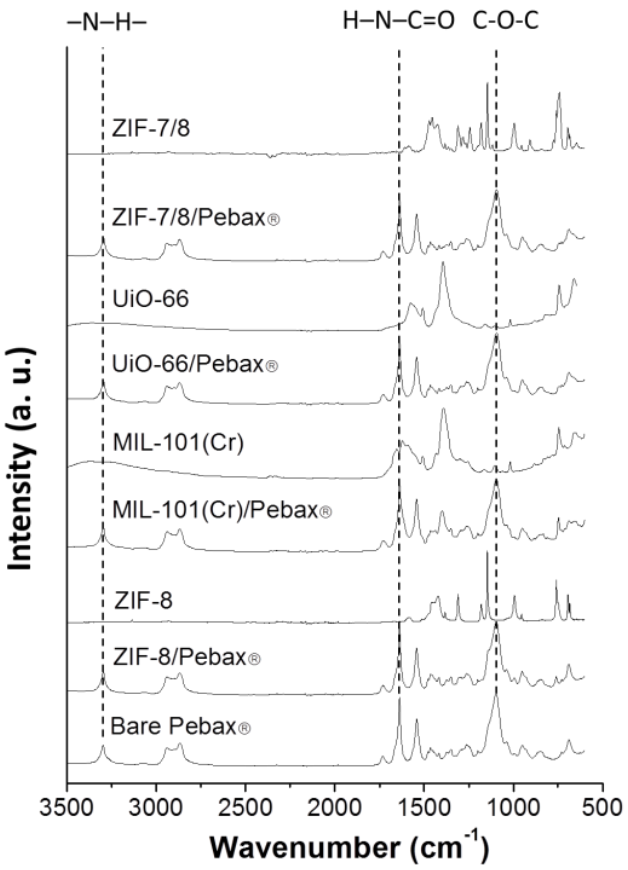

Fig. S3. FTIR spectra of Pebax® 1657 MMMs and MOF powders.

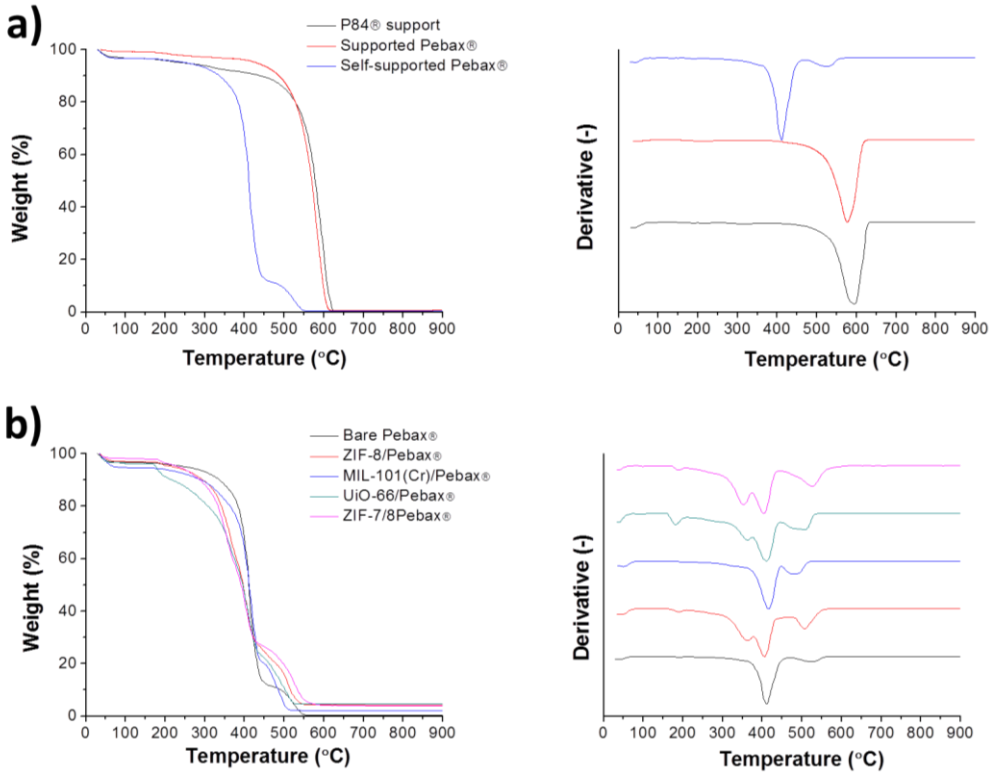

Fig. S4. TGA curves and derivatives in flowing air of pristine Pebax® 1657 membranes together with P84® support (a), and Pebax® 1657 MMMs (b).

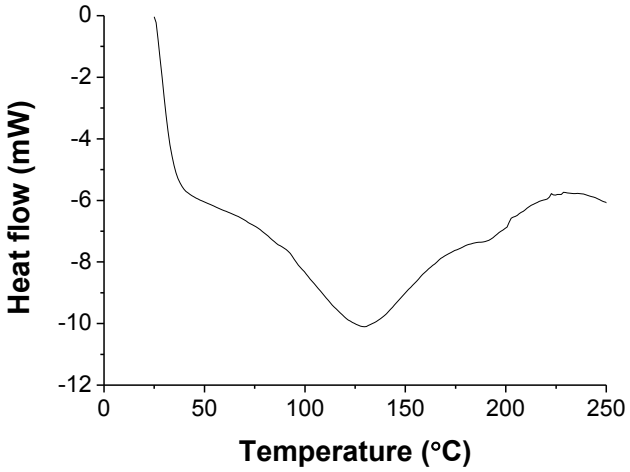

Fig. S5. DSC analysis of a Pebax® 1657 membrane. The analysis was performed in N_2 atmosphere using a heating rate of 10 ˚C·min^{-1}.

Gas separation performance

Table S2. Gas separation performance of P84® supports before and after PDMS coating. The testing conditions were 35 °C, 3 bar feed pressure and equimolar CO_2/CH_4 mixture.

Without PDMS			With PDMS		
CO_2 permeance (GPU)	**CH_4 permeance (GPU)**	**CO_2/CH_4 selectivity (-)**	**CO_2 permeance (GPU)**	**CH_4 permeance (GPU)**	**CO_2/CH_4 selectivity (-)**
270	256	1.1	55.1	10.0	5.5

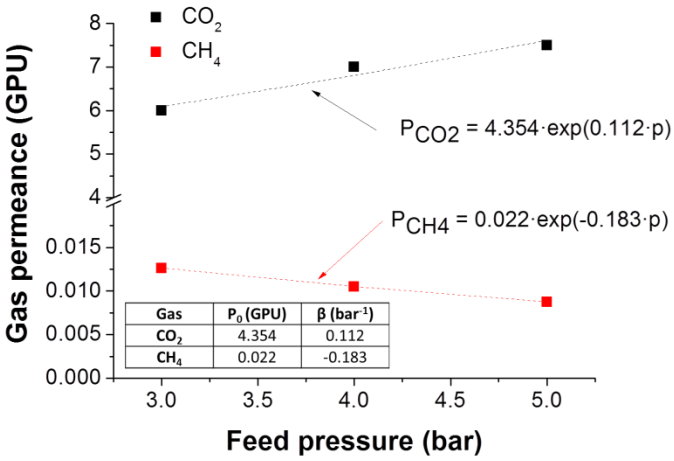

Fig. S6. Gas permeance of CO_2 and CH_4 with increasing pressure with numerical exponential fitting. The testing conditions were 35 °C, 3 bar feed pressure and equimolar CO_2/CH_4 mixture.

The CO_2 and CH_4 gas permeances of the Pebax® 16657/P84® supported membranes have been fitted to an exponential tendency according to Equation S1:

$$P = P_0 \cdot \exp(\beta \cdot p) \qquad (Eq\ \ 1)$$

Where P_0 is the permeance coefficient (GPU) at zero feed pressure, p is the feed pressure (bar) and β is a constant (bar^{-1}) characteristic of the penetrant-membrane system at a specified temperature.

Robeson upper-bound adapted

Table S3. Literature review with the values that defined the upper-bound until the present (2018), including membrane thickness, CO_2 permeability in Barrer and CO_2/CH_4 selectivity. The calculated CO_2 permeance in GPU is given.

Polymer	Thickness (µm)	CO_2 permeability (Barrer)	CO_2 permeance (GPU)	α (CO_2/CH_4)	Ref.
PVSH doped polyaniline	20-30	0.029	0.002	2200	5
Polypyrrole 6FDA/PMDA (25/75)-TAB	50-120	120	1.41	47.8	6
Poly(diphenyl acetylene) 3a	30-90	190	3.17	33.4	7
Polyimide PI-5	50-120	290	3.41	31.5	8
Poly(diphenyl acetylene) 3e	50-120	330	3.88	27.5	7
Poly(diphenyl acetylene) 3f	50	678	13.56	20.2	7
Polyimide 6FDA-durene	20-70	958	21.29	24.0	9
6FDA-based polyimide (8)	28	1100	39.28	17.7	10
PTMSP	46	2300	50.00	18.4	11

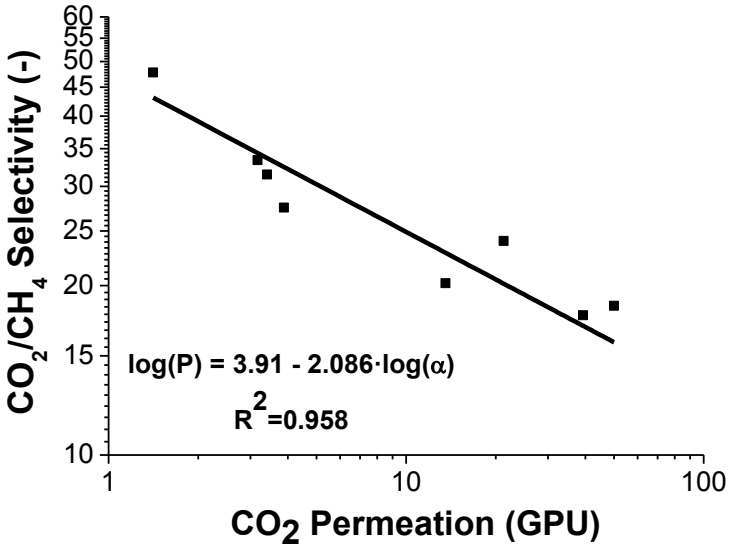

Fig. S7. CO_2/CH_4 bound defined in GPU at 35 ^{0}C. Squares represent the values in GPU of Table S3. The fitting equation of the linear fitting is also given with the R^2 value.

Bibliography

1 N. Liédana, A. Galve, C. Rubio, C. Téllez and J. Coronas, *ACS Appl. Mater. Interfaces*, 2012, **4,** 5016-5021.
2 L. Hou, L. Wang, N. Zhang, Z. Xie and D. Dong, *Polym. Chem.*, 2016, **7,** 5828-5834.
3 N. A. Khan, I. J. Kang, H. Y. Seok and S. H. Jhung, *Chem. Eng. J.*, 2011, **166,** 1152-1157.
4 J. Sánchez-Laínez, A. Veiga, B. Zornoza, S. R. Balestra, S. Hamad, A. R. Ruiz-Salvador, S. Calero, C. Téllez and J. Coronas, *J. Mater. Chem. A*, 2017, **5,** 25601-25608.
5 H. Hachisuka, T. Ohara, K. Ikeda and K. Matsumoto, *J Appl Polym Sci*, 1995, **56,** 1479-1485.
6 C. M. Zimmerman and W. J. Koros, *J. Polym. Sci., Part B: Polym. Phys.*, 1999, **37,** 1235-1249.
7 Y. Shida, T. Sakaguchi, M. Shiotsuki, F. Sanda, B. D. Freeman and T. Masuda, *Macromolecules*, 2006, **39,** 569-574.
8 M. Al-Masri, H. R. Kricheldorf and D. Fritsch, *Macromolecules*, 1999, **32,** 7853-7858.
9 W. Lin and T. Chung, *J. Membr. Sci.*, 2001, **186,** 183-193.
10 C. Nagel, K. Günther-Schade, D. Fritsch, T. Strunskus and F. Faupel, *Macromolecules*, 2002, **35,** 2071-2077.
11 T. Mizumoto, T. Masuda and T. Higashimura, *J. Polym. Sci., Part A: Polym. Chem.*, 1993, **31,** 2555-2561.

CHAPTER 15

CONCLUSIONS

From the initial objectives planned and the results presented throughout this thesis the following general conclusions can be drawn:

- **Three new MOF structures have been developed in this work: nano-size ZIF-11 (nZIF-11), ZIF-7/8 core-shells and ZIF-93/11 hybrids.** nZIF-11 has been synthesized through a new technique based on centrifugal acceleration for obtaining nanoparticles. From the characterization carried out, the nanoparticles (36±6 nm) showed the same thermal stability, a similar bond structure in terms of both FTIR and NMR and analogous H_2 and CO_2 adsorption capacities as the micrometric particles. The ZIF-7/8 core-shells and ZIF-93/11 hybrids have been synthesized *via* post-synthetic modification of ZIF-8 and ZIF-93, respectively, with benzimidazole. The conversion of ZIF-8 into ZIF-7, followed in real time by gas chromatography coupled with mass spectroscopy, was complete and it has been successfully adjusted to the shrinking core model. This kinetic model let define with high accuracy the reaction conditions to obtain a great variety of hybrid frameworks with different compositions and a particle size of around 124 nm. For the ZIF-93/11 nanoparticles (72-73 nm) the conversion was not complete and two hybrid frameworks with 7.4 and 23 % bIm were obtained. The presence of two linkers (bIm and mIm/4-m-5-ica) was verified by several characterization techniques in both hybrids: TGA analyses, gas adsorption, XRD, XPS, and NMR spectroscopy. Conversely to the core-shell structure found in the ZIF-7/8 crystals, both linkers were detected across the whole particles in the ZIF-93/11 hybrids.

- **The four different membrane configurations developed in this work have been: dense, integrally skinned asymmetric, supported and polymer stabilized percolation membranes (PSPMs).** Each of them contained MOFs embedded in the polymeric phase, building MMMs. While in dense membranes the whole thickness is gas-selective, in the others the gas separation capacity is only located in the thin selective layer of the composite.

- **The pre-combustion CO_2 capture (i.e. H_2/CO_2 separation) with dense membranes has been tackled with the polymer Matrimid® but above all with PBI. MMMs have been prepared with many ZIFs as fillers: ZIF-7, ZIF-8, ZIF-7/8 core-shells, nZIF-11, ZIF-11, ZIF-93** and the most interesting results at 180 and 200 °C are collected in **Figure 15.1**.

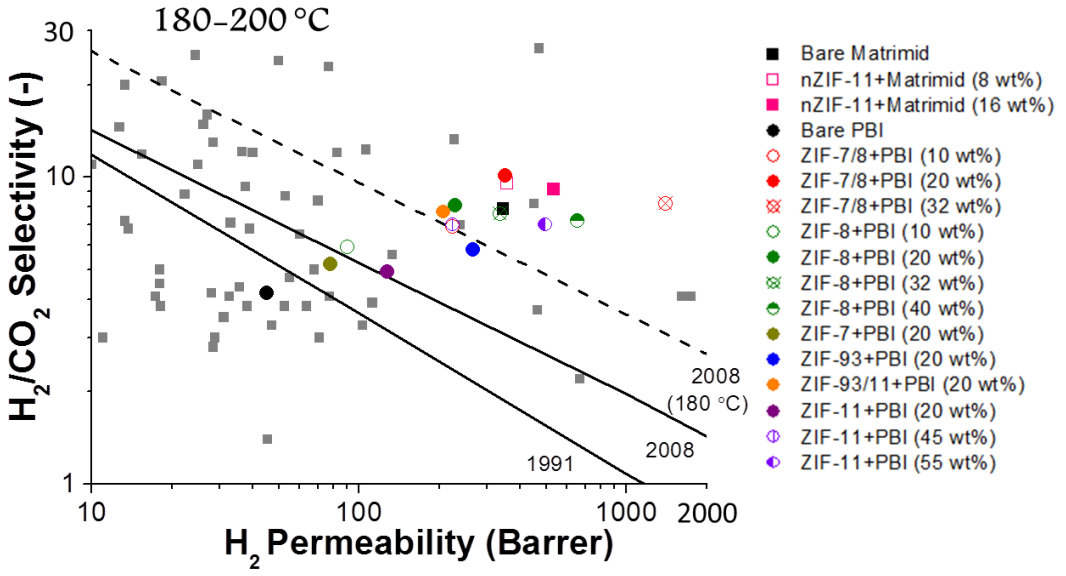

Figure 15.1. Robeson graph with the gas separation performance of the different dense MMMs prepared in this thesis at 180 (PBI membranes) and 200 °C (Matrimid® membranes). Gray scatter corresponds to bibliography data from tables 1.11, 1.12, and 1.14. The Robeson upper bounds of 1991[1] and 2008[2] at 35 °C and 2008 at 180 °C[3] are also plotted. Note that the best performing membranes (both permeability and selectivity) in literature corresponds to membranes tested at 230°C (reference 223).

The integration of each type of ZIF clearly enhanced the performance of the bare polymeric membranes, evidencing the important role that the microporous structure of the filler plays in the gas transport through the membranes. Comparing the different pure ZIFs, ZIF-8 can be considered the best filler since it has provided the highest gas separation results in terms of maximal selectivity (229 Barrer of H_2 and a H_2/CO_2 selectivity of 8.1 at 20 wt% loading) and maximal permeability (654 Barrer of H_2 and a H_2/CO_2 selectivity of 7.2 at 40 wt% loading). The improvement in the gas separation performance of ZIF-8 was more evident as the particle size of the filler increases from 50 to 150 nm, a result that was also validated by a European interlaboratory Round Robin test involving three different institutions.

The behavior of ZIF-11 as filler was different depending on the polymer in which it was embedded. When added to a Matrimid® matrix, the ZIF nanoparticles remained with a stable particle size. However, when it was used as filler in PBI MMMs, a chemical morphology transformation was evident for both materials. While the ZIF-11 lost its rhombic dodecahedron form becoming particles with higher aspect ratio,

[1] L. M. Robeson, *J. Membr. Sci.*, **1991**, *62*, 165-185.
[2] L. M. Robeson, *J. Membr. Sci.*, 2008, *320*, 390-400.
[3] B. W. Rowe, L. M. Robeson, B. D. Freeman, D. R. Paul, *J. Membr. Sci.*, **2010**, *360*, 58-69.

those of the nZIF-11 grew and their final size was dependent on the membrane loading. These changes were attributed to the interaction of the filler with the benzimidazole groups of the polymer favored by the high temperature casting in presence of DMAc.

Regarding the hybrid ZIFs, loadings of 20 wt% for the ZIF-93/11 hybrid showed a superior gas separation performance (207 Barrer of H_2 and a H_2/CO_2 selectivity of 7.7) than PBI membranes containing ZIF-93 and ZIF-11 at the same loadings. Also, PBI MMMs containing the ZIF-7/8 core-shells showed better results than analogous MMMs with ZIF-7 and ZIF-8. This result is due to the best affinity of the hybrid ZIF with the polymer provided by the bIm presence in its structure. PBI MMMs with 32 wt% loading of ZIF-7/8 core-shells provided the best results in this thesis with dense membranes for H_2/CO_2 separation (1398 Barrer of H_2 with a H_2/CO_2 selectivity of 8.2 and 1921 Barrer of H_2 with a H_2/CO_2 selectivity of 11.8, at 180 and 250°C, respectively).

- **Integrally skinned asymmetric membranes have been developed with pristine PBI and blends of PIM-EA(H_2)-TB with PBI.** Bare polymeric membranes and ZIF-8 MMMs were prepared with this configuration and they were applied for pre-combustion CO_2 capture. The concentration of the polymer dope strongly influenced the skin layer thickness and the mechanical resistance of the membrane, being necessary the use of P84® as support for the membranes with the thinnest skin layer (around 1 μm). The much thinner selective layer of these membranes in comparison with dense PBI made possible the increase in selectivity because of the saturation of the CO_2 flow, which changed from the Henry to Langmuir regime, at high pressures, providing the best performing membranes of this thesis in terms of selectivity (20.3 GPU of H_2 and a H_2/CO_2 selectivity of 35.6 at 250 °C and 6 bar feed pressure). PIM-EA(H_2)-TB and PBI formed a homogeneus blend (verified by the existence of a single glass transition temperature) that enhanced greatly the permeance of the membranes but reduced their selectivity, due to the worse H_2/CO_2 separation selectivity of PIM-EA(H_2)-TB. As before, the increase in the feed pressure had a positive effect on the gas separation performance of the membranes, reaching a maximum H_2 permeance of 83.5 GPU with a H_2/CO_2 selectivity of 19.4 for the blend with a 20 wt% of PIM.

- **Supported membranes have also been used for the separation of H_2/CO_2 mixtures. These membranes consisted of a thin selective polyamide layer (50-100 nm thick) containing ZIF-8 nanoparticles and supported on flat asymmetric P84®**. These composites meant the thinnest selective membranes with the highest gas fluxes obtained in this thesis. The optimal filler concentration of 0.4 %(w/v) produced a H_2 permeance of 338 GPU and a H_2/CO_2 selectivity of 14.6, value that raised to 18.0 when operating without total transmembrane pressure. The permeation fluxes were so high that the measurements could be performed without sweep gas. Besides, coating the membranes with PDMS prevented polyamide damage, leading to membranes able to operate at high temperature for one week.

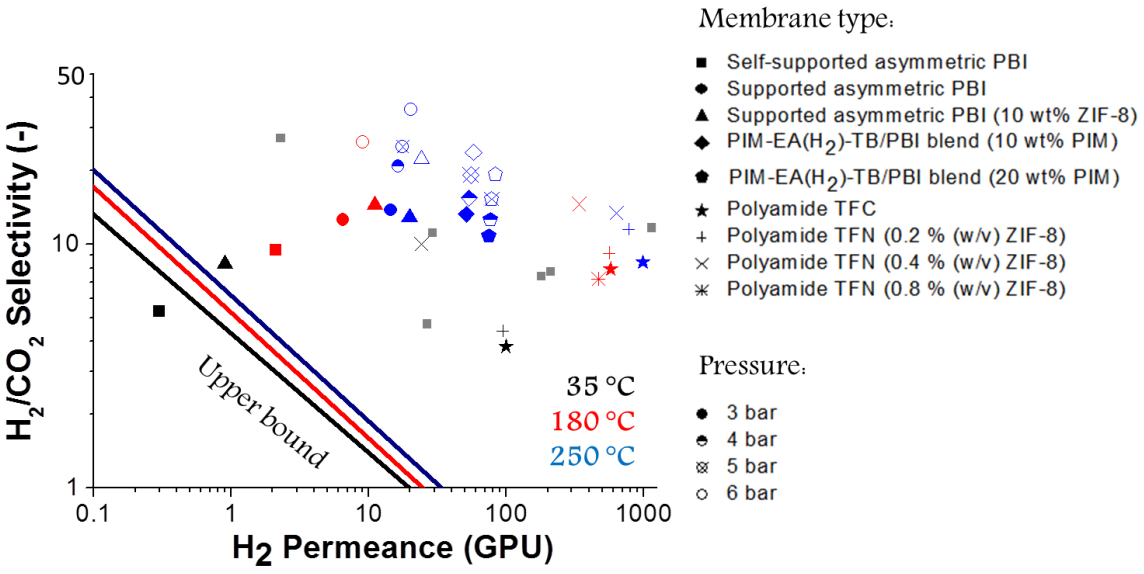

Figure 15.2. Gas separation performance of PBI asymmetric membranes, PIM-EA(H_2)-TB/PBI asymmetric blends and polyamide TFC and TFN membranes at several temperatures and pressures. The H_2/CO_2 upper bound calculated in GPU is also included and bibliographical values[4] can be seen in grey.

A comparison among the gas separation performance of the previous integrally skinned asymmetric PBI membranes and the supported polyamide membranes is shown in **Figure 15.2**.

[4] a) S. Kumbharkar, Y. Liu, K. Li, *J. Membr. Sci*., **2011**, *375*, 231.
b) S.S. Hosseini, N. Peng, T.S. Chung, *J. Membr. Sci*., **2010**, *349*, 156.
c) M.F. Flanagan, I.C. Escobar, *J. Membr. Sci*., **2013**, *434*, 85.
d)T. Yang, G. M. Shi, T. Chung, *Adv. Energy Mater*. **2012**, *2*, 1358.
e) F. Cacho-Bailo, M. Etxeberria-Benavides, O. David, C. Tellez, J. Coronas, *ACS Appl. Mater. Interfaces* **2017**, *9*, 20787.
f) J. Wang, N. Li, Z. Li, J. Wang, X. Xu, C. Chen, *Ceram. Int.* **2016**, *42*,8949.

- **PSPMs were prepared with nanoparticles of ZIF-8, ZIF-7(III) and ZIF-7/8 core-shells.** SEM-FIB allowed the reconstruction of a tridimensional volume of a membrane piece, showing the percolation path through the MOF nanoparticles and the voids filled by the epoxy resin. The composites showed a high performance with an optimum result of 355 Barrer of H_2 and H_2/CO_2 selectivity of 12.3 for the PSPM containing ZIF-7/8 core-shell nanoparticles as filler. This result validated the improved gas separation capacity of the hybrid material thanks to the reduction of the effective pore diameter, allowing a better CO_2 discrimination by the sieving process.

- **The post-combustion CO_2 capture (CO_2/N_2 separation) and biogas upgrading (CO_2/CH_4 separation) have been dealt with Pebax® 1657 supported membranes and dense PIM-1/6FDA-DAM blends**. Thin membranes of Pebax® 1657 (2-3 μm) were prepared on dense PTMSP and asymmetric porous P84® supports containing 10 wt% of ZIF-8, MIL-101(Cr), UiO-66 and ZIF-7/8 core-shell nanoparticles. Although the incorporation of MOFs enhanced the CO_2 permeance of the membranes, especially embedding UiO-66, the best gas separation performance was obtained with bare Pebax® on P84®, with 7.5 GPU of CO_2 and a CO_2/CH_4 selectivity of 114 (at 35 °C and 5 bar feed pressure).

6FDA-DAM and PIM-1 built heterogeneous blends where the minor component formed spheres and lenticular particles (3-5 μm) evenly distributed along the membrane cross-section. ZIF-8 nanoparticles were embedded in the blends to build three-phase MMMs (PIM-1, 6FDA-DAM and ZIF-8). The ZIF showed a better affinity for 6FDA-DAM than for PIM-1 and it is positioned near the interphase between both polymers, which allowed the improvement of the dispersion of the filler in the complex polymeric matrix. While the increase in the amount of PIM-1 in the blend led to higher gas permeabilities and to a decrease in the selectivity for both mixtures, the addition of ZIF-8 led to the enhancement of both variables. The best membranes of this work were the blends PIM-1/6FDA-DAM 10/90 (w/w) with 10 wt% of ZIF-8, showing a CO_2 permeability of 2891 Barrer, a CO_2/CH_4 selectivity of 26.6 and 2802 Barrer of CO_2 with a CO_2/N_2 selectivity of 18.1.

To sum up, the main achievents of this thesis have been:

- **The synthesis of new ZIF nanoparticles** (nZIF-11, ZIF-7/8 and ZIF-93/11) with tailored properties and adapted to the specific polymers of the membranes, showing better gas separation capacity than the original ZIFs due to the enhanced filler-polymer compatibility.

- **The optimization in the preparation of PBI membranes**, from dense to integrally skinned asymmetric membranes, as well as its blend with PIM-EA(H_2)-TB, improving the gas separation performance of the polymer for pre-combustion CO_2 capture.

- **The development of membranes with thin selective layers** (as thin as 50 nm) able to show superior gas fluxes, while maintaining a high gas selectivity for the separation of CO_2 from H_2, N_2 and CH_4.

It can therefore be concluded that improved membranes for the separation of H_2/CO_2, CO_2/N_2 and CO_2/CH_4 mixtures have been developed in this thesis, accomplishing the defined objectives and setting an interesting base for their further development as industrial products.

GLOSARIO DE TÉRMINOS

6

6FDA-DAM, 80

A

absorción química, 31
adsorción física a presión, 31
amina, 31
annealing, 42

B

Barrer, 52, 109
biogás, 30
blending, 46

C

CAC, 27
casting, 37, 101
CCS Technology Roadmap 2050, 27
CO_2, 27
condensabilidad, 57
COP 21, 27
COP 24, 27
core-shell, 71
crosslinking, 44

D

destilación criogénica, 31
diámetro cinético, 56
difusión Knudsen, 50
difusividad, 54
dip-coating, 39
disolución de *casting*, 37
DSC, 111

E

ecuación de Arrhenius, 58
EDS, 111
elastómero, 75
energía de activación, 58
entrecruzamiento, 44
envejecimiento, 78

F

factor de separación, 53
flujo de Poiseuille o viscoso, 50
FTIR, 112

G

gas natural, 29
gate-opening, 67
GPU, 53, 109

I

IGCC, 29
inversión de fases, 37

L

límite superior de Robeson, 41

M

Matrimid®, 79
membrana, 34
membrana asimétrica, 36
membrana integrada, 36
membrana soportada, 36
MIL-101(Cr), 97
mixed matrix membrane, 48
modelo de adsorción dual, 55
modelo de disolución-difusión, 51

Apéndice I: Factores de impacto de las publicaciones que componen el compendio

La **Tabla A.1** contiene los factores de impacto de las revistas científicas donde se han publicado los artículos que forman parte del compendio en que se estructura esta memoria, junto con las áreas temáticas a las que pertenecen y su clasificación dentro de ellas, incluyendo el cuartil.

Tabla A.1. Información sobre los artículos científicos que componen el compendio de publicaciones de esta tesis doctoral.

Referencia	Editorial	Índice de impacto	Categoría	Cuartil
J. Mater. Chem. A, 3 (2015) 6549-6556.	Royal Society of Chemistry	8,262	Materials Science, Multidisciplinary	Q1, 21/271
			Energy & Fuels	Q1, 4/88
			Chemistry, Physical	Q1, 16/144
J. Membr. Sci., 515 (2016) 45-53.	Elsevier Science BV	6,035	Chemical Engineering	Q1, 8/135
			Polymer Science	Q1, 4/86
J. Mater. Chem. A, 4 (2016), 14334-14341.	Royal Society of Chemistry	8,867	Materials Science, Multidisciplinary	Q1,19/275
			Energy & Fuels	Q1,4/92
			Chemistry, Physical	Q1, 15/146
J. Mater. Chem. A, 5 (2017), 25601-25608.	Royal Society of Chemistry	9,931	Materials Science, Multidisciplinary	Q1, 20/285
			Energy & Fuels	Q1, 6/97
			Chemistry, Physical	Q1, 14/147
Chem.–A Europ. J., 24 (2018), 11211–11219.*	Wiley-VCH Verlag	5,160	Chemistry-Multidisciplinary	Q1, 37/171
J. Membr. Sci., 563 (2018), 427-434.*	Elsevier Science BV	6,578	Chemical Engineering	Q1, 9/137
			Polymer Science	Q1, 3/87
Ind. Eng. Chem. Res., 57 (2018) 16909–16916.*	American Chemical Society	3,141	Chemical Engineering	Q1, 33/137
Adv. Mater. Interfaces, 2018, 1800647.*	Wiley-VCH Verlag	4,834	Chemistry-Multidisciplinary	Q1, 40/171
			Materials Science, Multidisciplinary	Q1, 49/285
ChemNanoMat, 4 (2018), 698-703.*	Wiley-VCH Verlag	3,173	Chemistry-Multidisciplinary	Q2, 66/171
			Nanoscience & Nanotechnology	Q2, 42/92
			Materials Science, Multidisciplinary	Q2, 78/285
New J. Chem., 43 (2019), 312-319.*	Royal Society of Chemistry	3,201	Chemistry-Multidisciplinary	Q2, 65/171
* Factores de impacto correspondientes al año 2017, el último año con datos disponibles				

La contribución del doctorando en las publicaciones que forman este compendio, en las que aparece como primer autor, ha comprendido el trabajo experimental, el análisis y tratamientos de datos y la posterior redacción de los documentos. Los co-autores no doctores de las publicaciones que forman parte del compendio de esta tesis han renunciado a su presentación como parte del compendio de otra tesis doctoral, en cumplimiento de la normativa.

Apéndice II: Resumen y conclusiones en español

La presente tesis doctoral está estructurada en 15 capítulos que se dividen en dos bloques: memoria y resultados. La memoria está formada por los capítulos 1, 2 y 3. El capítulo 1 contiene una introducción general donde se explican los procesos de separación de CO_2 y el papel que juega en ellos la tecnología de membranas. Desarrolla el concepto de membrana, desde los diferentes tipos existentes, los procesos de fabricación y los mecanismos de transporte de gas. Se detallan también los diferentes polímeros utilizados en este trabajo así como los compuestos organometálicos (*metal-organic frameworks* o *MOFs*) que se utilizarán como material de relleno, todo ello reforzado con una bibliografía actualizada sobre resultados de separación de gases. El capítulo 2 trata sobre la metodología seguida, incluyendo la síntesis de MOF, la preparación de membranas y la caracterización y medidas llevadas a cabo. Por último, el capítulo 3 contiene la lista de referencias de los anteriores capítulos. El segundo bloque corresponde con los apartados de resultados y discusión de los mismos. Comprende los capítulos 4-14 y se corresponde con las publicaciones científicas que componen el compendio de esta tesis y cuya unidad temática se justificará a lo largo de este resumen. La última sección (capítulo 15) detalla las principales conclusiones del trabajo en inglés.

El dióxido de carbono (CO_2) es uno de los contaminantes más importantes a nivel industrial. Debido al aumento de las emisiones de este gas de efecto invernadero, disminuir su concentración atmosférica se ha convertido en uno de los retos medioambientales más importantes. Además, el CO_2 es también un contaminante presente en combustibles como el gas natural o el biogás, siendo necesaria su eliminación para obtener un combustible limpio que cumpla con las especificaciones del mercado. La tecnología actual para la separación del CO_2 comprende la absorción química, la adsorción física y la destilación criogénica, todos ellos procesos con una alta penalización energética. La tecnología de membranas supone una alternativa atractiva por su bajo consumo energético, su baja huella de carbono y su facilidad de operación y escalado.

El objetivo principal de esta tesis doctoral ha sido el de desarrollar membranas mejoradas para la separación del CO_2. Gran parte de la investigación se ha centrado en la separación de H_2/CO_2 (mezclas de precombustión), pero también se han tratado mezclas de poscombustión (CO_2/N_2) y de gas natural y biogás (CO_2/CH_4). Estas membranas se han preparado a partir de polímeros con buenas propiedades de separación para la mezcla a tratar. Los polímeros elegidos para la mezcla H_2/CO_2 han sido la Matrimid®, el polibezimidazol (PBI) y la poliamida (PA) formada por la reacción de TMC con MPD. Las separación de mezclas de poscombustión y biogás se ha estudiado con membranas de PIM-1, PIM-EA(H_2)-TB, 6FDA-DAM y Pebax® 1657.

Para conseguir mejorar la capacidad de separación intrínseca de estos polímeros, se han preparado sistemas multicomponentes en forma de membranas mixtas (*mixed matrix membranes* o *MMMs*). Estas membranas han consistido en la dispersión de MOF en la fase continua constituida por la matriz polimérica, de manera que la permeabilidad y selectividad de las membranas aumentaba por la combinación sinérgica de ambas fases. Los MOF son materiales altamente cristalinos formados por la coordinación de iones o clústeres metálicos con ligandos orgánicos. Su naturaleza parcialmente orgánica hace que muestren una gran compatibilidad con las cadenas poliméricas convirtiéndolo en una fase dispersa ideal.

En el capítulo 4 se ha explicado el uso de membranas de Matrimid® para la separación de mezclas H_2/CO_2, donde el ZIF-11 es utilizado como material de relleno para desarrollar MMMs.

Sin embargo, ha sido el PBI el polímero más usado en esta tesis para la captura en precombustión. La preparación de MMMs de PBI con ZIF-8 como material de relleno se detalla en el capítulo 5, donde la influencia del tamaño de partícula y su incorporación en estado húmedo o seco han sido estudiadas. Además, la reproducibilidad de los resultados se confirmó mediante un *Round Robin test* llevado a cabo entre tres instituciones europeas. El ZIF-11 también se ha utilizado como material de relleno con el PBI y la mejora en la capacidad de separación de las memrbanas se muestra en el capítulo 6.

Aunque se han utilizado MOF existentes para la preparación de MMMs, también se ha realizado un gran esfuerzo en esta tesis doctoral para desarrollar nuevas estructuras con una compatibilidad mejorada con los polímeros. Así en el capítulo 4 se muestra la síntesis de ZIF-11 nanométrico (nZIF-11) con un tamaño de partícula de 36±6 nm. Este material se ha obtenido siguiendo una nueva ruta de síntesis basada en la centrifugación, que permitió la formación de partículas mucho más pequeñas que las del ZIF-11 tradicional (1.9±0.9 µm) pero manteniendo la misma composición química, estabilidad térmica y propiedades de adsorción de H_2 y CO_2. Su uso como material de relleno en Matrimid® y PBI se detalla en los capítulos 4 y 6, respectivamente. Además en este último se han estudiado los cambios en la morfología del material.

Los esfuerzos para obtener nuevos MOF se han centrado también en la síntesis de materiales híbridos. El capítulo 7 explica la formación de *core-shells* de ZIF-7/8 mediante la modificación postsintética del ZIF-8 con bezimidazol. Esta reacción ha concluido con la conversión completa del ZIF-8 en ZIF-7 y ha sido monitorizada por cromatografía de gases-espectroscopía de masas, cuantificando la cantidad de 2-metilimidazol liberada. Esto ha permitido el ajuste de la reacción al modelo cinético de núcleo decreciente, proveyendo datos de coeficiente de difusión del bezimidazol en el interior de los poros y de la constante cinética de la reacción. El modelo cinético permitió definir con gran precisión las condiciones de reacción para obtener una gran variedad de compuestos híbridos con un tamaño de partícula de alrededor de 124 nm. También se han desarrollado nanopartículas de ZIF-93/11 (72-73 nm) en el capítulo 8. Este ZIF híbrido se obtuvo por la modificación postsintética del ZIF-93 en una disolución de benzimidazol, pero al contrario que con el ZIF-7/8 la reacción no era completa. El uso de distintos disolventes (MeOH y DMAc) y tiempos de reacción dieron lugar a diferencias en la cantidad de benzimidazol incorporada, del 7,4 al 23 % en peso. La presencia de dos ligandos se constató mediante diferentes técnicas de caracterización en ambos híbridos: TGA, adsorción de gases, XRD, XPS y RMN. Ambos híbridos se han utilizado como material de relleno en membranas de PBI, y la capacidad de separación de mezclas H_2/CO_2 se compara con la de las MMMs conteniendo MOF puros (ZIF-7, ZIF-8, ZIF-11 y ZIF-93) en los capítulos correspondientes.

Además de añadiendo nanopartículas, la capacidad de separación de los polímeros se ha mejorado reduciendo el espesor de las membranas en favor de flujos de permeación más altos. Así en el capítulo 9 se han desarrollado membranas asimétricas de PBI sobre soportes de P84®. Estas membranas se han preparado por inversión de fases, obteniéndose capas selectivas de 1 µm de espesor que mostraban capacidades de separación sin precedentes para mezclas de precombustión, muy superiores a las de las membranas densas en condiciones de operación intensivas (250 °C y 6 bar). Estas membranas de PBI también se han optimizado en el capítulo 10 con un *blending* con PIM-EA(H_2)-TB. La mezcla homogénea de ambos polímeros consiguió mejora la permeación de los gases en comparación con la de las membranas asimétricas de PBI.

Las membranas con el espesor más fino obtenidas fueron las de tipo soportado desarrolladas en el capítulo 11. Consistían en una capa de 50-100 nm de PA, sintetizada mediante la

polimerización interfacial de MPD con TMC, con nanopartículas de ZIF-8 embebidas es ella. Estas membranas mostraron una capacidad de separación extraordinaria con flujos de permeado tan altos que se podía prescindir del gas de barrido para su medida. También mostraron una gran estabilidad térmica, ya que mantenían la capacidad de separación tras siete días operando en continuo a 180 °C.

La capacidad del ZIF-7, el ZIF-8 y las *core-shell de ZIF-7/8* para la separación de mezclas H_2/CO_2 se demuestra en el capítulo 12 con la preparación de *Polymer-Stabilized Percolation Membranes* (PSPM), que consisten en la compresión del ZIF en polvo en pellets que posteriormente se infiltran y estabilizan con una resina epoxi impermeable al gas, de manera que se obtiene una red de percolación selectiva al flujo de gas donde solo el ZIF es responsable de la separación.

Por último, las membranas aplicadas para poscombustión y purificación de biogás se explican en los capítulos 13 y 14. El capítulo 13 muestra la preparación de MMMs para la separación de mezclas CO_2/N_2 y CO_2/CH_4 mediante *blends* heterogéneos de PIM-1 y 6FDA-DAM con ZIF-8 como material de relleno. Las nanopartículas mostraban una mejor compatibilidad con el 6FDA-DAM que con el PIM-1, alojándose de manera preferencial cerca de la interfase entre polímeros, lo que ayudaba a la dispersión del material de relleno. El capítulo 14 detalla la preparación de MMMs finas (espesor de 2-3 µm) de Pebax® 1657 sobre P84® y politrimetilsililpropino (PTMSP). Nanopartículas de: ZIF-8, MIL-101(Cr), UiO-66 y ZIF-7/8 fueron elegidas como material de relleno, ya que todos ellos son MOF con alta capacidad de adsorción de CO_2 pero con diferente distribución de tamaño de poro. Estas membranas fueron utilizadas para la separación de mezclas de CO_2/CH_4 y se observó una compatibilidad sinérgica entre el Pebax® 1657 y el P84®.

Además del trabajo experimental, varios modelos matemáticos se han desarrollado en esta tesis para entender el flujo de gas a través de las membranas preparadas. En el capítulo 6 el modelo de *Maxwell-Wagner-Sillar* se ha utilizado para calcular las permeabilidades de H_2 y CO_2 a través del nZIF-11 y el ZIF-11. En el capítulo 9 se ha aplicado un modelo de resistencias en serie para explicar el flujo de gas a través de las membranas asimétricas de PBI. El capítulo 10 muestra un modelo empírico donde se correlaciona la influencia entre la cantidad de PIM en el *blend* y la presión de alimentación en la capacidad de separación de las membranas. Por último, se ha propuesto en el capítulo 13 un modelo de *Maxwell* acoplado para modelar la permeabilidad de los gases a través de los *blends* de PIM-1/6FDA-DAM. Con este modelo también se han calculado las propiedades de separación del ZIF-8.

A la finalización de este trabajo pueden arrojarse las siguientes conclusiones:

- **Se han sintetizado nuevas nanopartículas de ZIF (nZIF-11, ZIF-7/8 and ZIF-93/11)** con propiedades de separación mejoradas y adaptadas a los polímeros con los que se han preparado las membranas.

- **Se han preparado cuatro tipo de membranas diferentes: densas, asimétricas, soportadas y PSPMs.**

- **La captura de CO_2 en precombustión se ha llevado a cabo con membranas densas de Matrimid® y PBI. Se han preparado MMMs con diversos ZIF como material de relleno: ZIF-7, ZIF-8, core-shells de ZIF-7/8, nZIF-11, ZIF-11, ZIF-93;** mostrando los resultados más interesantes a 180 y 200 °C. Todos los ZIF mejoraban la capacidad de

separación de las membranas de polímero puro, evidenciando el importante papel que juega la microestructura porosa en la separación de gases. Respecto a los ZIF puros, el mejor material de relleno fue el ZIF-8, mostrando la mejor capacidad de separación en términos de mayor selectividad (229 Barrer de H_2 y selectividad H_2/CO_2 de 8,1 al 20 % peso de carga) y permeabilidad (654 Barrer de H_2 y selectividad H_2/CO_2 de 7,2 al 40 % peso de carga). Con este material de relleno también se observó como el rendimiento de la separación mejoraba al aumentar el tamaño de partícula de 50 a 150 nm.

El comportamiento del ZIF-11 como material de relleno dependía del polímero en el que se embebía. Al incorporarlo a la Matrimid® las nanopartículas permanecían estables; pero al hacerlo en PBI, su morfología cambiaba y el tamaño final dependía de la carga de la membrana. Estos cambios se atribuyeron a la interacción del material con los grupos bezimidazol del polímero en un medio de DMAc, lo que además se veía favorecido por la alta temperatura durante la formación de la membrana.

Respecto a los ZIF híbridos, las MMMs de ZIF-93/11 y PBI con cargas del 20 % peso mostraban capacidades de separación superiores (207 Barrer de H_2 y selectividad H_2/CO_2 de 7,7) que las correspondientes con ZIF-93 y ZIF-11 de la misma carga. Lo mismo se daba con las MMMs con ZIF-7/8 al compararlas con las membranas que contenían ZIF-7 y ZIF-8. Las MMMs con un 32% peso de carga de ZIF-7/8 fueron las membranas densas que dieron los mejores resultados de separación de gases, con 1398 Barrer de H_2 y una selectividad H_2/CO_2 de 8,2 y 1921 Barrer de H_2 con una selectividad H_2/CO_2 de 11,8 a 180 y 250°C, respectivamente.

- **Se han desarrollado membranas asimétricas con PBI puro y *blends* de PIM-EA(H_2)-TB con PBI**, conteniendo además ZIF-8 y aplicadas a la captura de CO_2 en precombustión. La concentración de polímero en la disolución de *casting* influenciaba claramente el espesor de la capa selectiva de las membranas y la resistencia mecánica de las mismas, siendo necesario el uso de soportes de P84® para las membranas con el espesor de capa selectivo más pequeño (1 µm). Esta capa selectiva tan fina en comparación con las membranas de PBI denso conllevó un aumento en la selectividad debido a la saturación del flujo de CO_2, que cambiaba del régimen de Henry al de Langmuir a altas presiones, consiguiendo los mejores valores de rendimiento de esta tesis en términos de selectividad (20,3 GPU de H_2 y selectividad H_2/CO_2 de 35,6 a 250 °C y 6 bar de presión de alimentación). El PIM-EA(H_2)-TB y el PBI formaban blends homogéneos que mejoraban la permeación de las membranas pero a costa de disminuir su selectividad, debido a la peor capacidad de separación del PIM-EA(H_2)-TB. Igual que con el PBI puro, el aumento de la presión de alimentación mejoraba el rendimiento de separación de las membranas, alcanzando un máximo de 83,5 GPU de H_2 con una selectividad H_2/CO_2 de 19,4 para el *blend* con un 20 % peso de PIM.

- **También se han utilizado membranas soportadas para la separación de mezclas H_2/CO_2. Consistían en una fina capa de PA de 50-100 nm de espesor con nanopartículas de ZIF-8 embebidas y soportada sobre P84® plano asimétrico.** Estas membranas supusieron las capas selectivas más finas y arrojaron los flujos más altos de esta tesis. La concentración óptima de material de relleno fue 0,4 %(w/v) y mostraba un permeación de H_2 de 338 GPU con una selectividad H_2/CO_2 de 14,6, valor que aumentó a 18,0 al operar sin presión transmembrana. Los flujos de permeación eran tan altos que se pudo trabajar sin gas de barrido. Además, al recubrir las membranas con PDMS se las protegía de daños y eran capaces de operar a alta temperatura durante una semana.

- **Se prepararon PSPMs con nanopartículas de ZIF**-8, ZIF-7(III) y ZIF-7/8. Mediante SEM-FIB se pudo reconstruir un volumen tridimensional de un trozo de membrana, mostrando el camino de percolación de la resina epoxi por los huecos disponibles entre partículas de MOF. Estas membranas mostraban un alto rendimiento de separación de gases, con un resultado óptimo de 355 Barrer de H_2 y una selectividad H_2/CO_2 de 12,3 para las que contenían ZIF-7/8 como material de relleno. Este resultado validó la capacidad de separación mejorada del material híbrido gracias a la reducción del tamaño de poro efectivo, permitiendo una mejor discriminación del CO_2 por el mecanismo de tamizado molecular.

- **La captura de CO_2 por poscombustión (separación CO_2/N_2) y la purificación de biogás (separación CO_2/CH_4) se llevó a cabo con Pebax® 1657 soportado y membranas densas basadas en *blends* de PIM-1 y 6FDA-DAM.** Se prepararon membranas de Pebax® 1657 de 2-3 µm de espesor sobre soportes de P84® asimétrico y PTMPS denso, que contenían un 10 % peso de ZIF-8, MIL-101(Cr), UiO-66 y ZIF-7/8 *core-shells*. Aunque la incorporación de MOF mejoró la permeación de las membranas, sobre todo las que contenían UiO-66, los mejores resultados se obtuvieron con Pebax® puro soportado sobre P84®, con 7,5 GPU de CO_2 y una selectividad CO_2/CH_4 de 114 (a 35 °C y 5 bar de presión de alimentación).

El 6FDA-DAM y el PIM-1 constituían *blends* heterogéneos donde el componente minoritario forma partículas esféricas de 3-5 µm distribuidas homogéneamente a lo largo de la sección transversal de la membrana. Se introdujeron nanopartículas de ZIF-8, formando una MMMs con tres fases (PIM-1, 6FDA-DAM and ZIF-8). Mientras que el aumento de la cantidad de PIM en el *blend* mejoraba la permeabilidad de los gases pero suponía la disminución de la selectividad para ambas mezclas, la adición de ZIF-8 mejoraba ambas variables. Las mejores membranas fueron los *blends* PIM-1/6FDA-DAM con un 10 % peso de PIM y 10 % peso de ZIF-8, mostrando una permeabilidad de CO_2 de 2891 Barrer, con una selectividad CO_2/CH_4 de 26,6 y 2802 Barrer de CO_2 con una selectividad CO_2/N_2 de 18,1.